

Liesbeth Birchall

Doctoral Thesis submitted to the University of Nottingham
for the degree of

Doctor of Philosophy

Reactive Inkjet of Quantum Dot-Silicone Composites

Faculty of Engineering
Centre for Additive Manufacturing
2021

Acknowledgments

I would like to thank my supervisors – Prof. Chris Tuck, Prof. Ricky Wildman, and Dr. Aleksandra Foerster – for their guidance, support, and considerable patience. Thank you for your reassurance and for helping me to get back on track every time it felt as if I had hit a wall. Aleksandra, you have been a friend to me in and out of the lab.

I would also like to give credit to the excellent support and expertise I have received from technicians at the NMRC (Nanoscale and Microscale Research Centre) and the SLIM (School of Life Sciences Imaging) centres in the University of Nottingham. Nicola Weston (NMRC) carried out ultrathin cryosectioning of QD-silicone monoliths and collected data using transmission electron microscopy. Dr. Graham Rance (NMRC) advised me on appropriate equipment and obtained Raman spectra, photoluminescent (PL) spectra, and PL maps of QD-silicone samples. Tim Self's expertise on confocal laser scanning microscopy was invaluable for advice on specialised sample heaters and imaging modes, and I am very grateful for his help with setting up temperature experiments and workflow for data collection. Likewise, Seema Rajani discussed experimental set-ups with me and trained me in the use of a well-plate reader, in addition to acquiring image stacks of QD clusters in a silicone composite. More generally, I would like to thank the technicians for CfAM (Centre for Additive Manufacturing), Mark East and Mark Hardy, for support with a wide range of equipment and lab management queries over the years. A range of post-doctoral researchers have also been of great assistance, in particular Dr. Craig Sturgess, for his advice on drop-on-drop reactive inkjet.

I would like to thank Prof. Lyudmila Turyanska, for advising me on all matters related to quantum dots and for great reassurance and support. Similarly, Prof. Derek Irvine advised me on polymer science, particularly with regards to dispersion of particles, although I did not carry out nearly as much experimental work on this topic as I would have liked. I would also like to thank my sponsor, AWE (Atomic Weapons Establishment), and my industrial supervisors for their support and productive discussions.

I am grateful to everyone at CfAM, especially to my friends and to our tireless administrators (who have helped me more times than I can count, with special thanks to Romina Davoudi). Special thanks to Chung Han Chua, for all his help with editing. Lastly, I thank my family for their support. I know my dad would have loved to read this (he is probably alone in this).

Extra special thanks to my chief editor, who kept me company on long days and late nights. Beta was the most codependently warm and loving animal I have ever known but suffered from chronic kidney disease; she passed away shortly after my viva. Though we only knew her for a short two years after adopting her, she can at least live on forever in the university archives.



Abstract

There is a need for high-resolution and high-sensitivity temperature sensing in fields such as micro/nanoelectronics, integrated photonics, and biomedicine; however, non-invasive integrated sensing is difficult and expensive to achieve in miniaturised devices, as fabrication is greatly complicated by multi-step processes, heat treatments, and material compatibility. Inkjet printing (IJP) is a direct writing technique in the material jetting AM category that is effective for maskless multi-material printing with $<50\ \mu\text{m}$ resolution, which enables production of end-use devices and could simplify sensor integration. Existing inkjet-printed temperature sensors comprise simple circuit devices, which use the change in the electrical resistance of a sensing area to measure temperature. While current examples are well-suited to wearable sensors, they do not achieve the spatial and thermal resolutions desired for printed devices such as microfluidics.

Development of inks for luminescence nanothermometry would enable inkjet-printable sensing geometries for planar and 3D thermal imaging with submicron and subdegree resolutions. Silicones are polymers suitable for optical sensing due to their ultraviolet (UV) and thermal stability, optical transparency, and high refractive indices. Composite inks for luminescence nanothermometry can be formulated with quantum dots (QDs), fluorescent semiconductor nanocrystals with intrinsic, reversible temperature quenching. Printable optical sensing materials would enable *in situ* temperature monitoring for applications and geometries that are otherwise impossible to monitor by conventional means.

This thesis describes the development of the first inkjet-printable QD-silicone composite, and the first ink for luminescence thermometry, for integrated optical sensing; these may also have use in lighting applications. 2-part addition cure silicone inks and 1-part UV cure silicone inks were explored and QD-silicone composites were synthesised; inkjet printing of an addition cure QD-composite was demonstrated.

Printing of reactive addition cure inks, where Ink A contained crosslinker and Ink B contained catalyst, was demonstrated using drop-on-drop IJP with the smallest average drop diameters reported for silicone IJP to date ($33\text{-}36\ \mu\text{m}$). To overcome poor contact pinning, a pinned grid strategy was used for single printhead IJP and a line-by-line strategy for dual printhead IJP. Curing was the greatest challenge in reactive inkjet of QD-silicone composites, as labile ligands on the QDs poisoned the platinum catalyst despite low QD loading (0.005 wt% QD-Ink A). PtCl_2 catalyst was added at low loading to enable curing and

to explore the interactions between QDs and the catalyst. However, quenching was observed, with 70% decrease in emission intensity as PtCl_2 concentration doubled; it was theorised that the QDs and catalyst competed for ligands, leading to metal-induced aggregation. Printing of fluorescent QD-silicone composites was demonstrated on a single printhead system using a pinned grid strategy; inks with no PtCl_2 had stronger fluorescence but did not cure, highlighting their greater vulnerability to delays or fluctuations in heating.

Novel UV curable silicone inks were formulated for inkjet using a high throughput screening method. Two photoinitiators (PIs) were trialled: DMPA (2,2-dimethoxy-2-phenylacetophenone) and TPO (phenylbis(2,4,6-trimethylbenzoyl)-phosphine oxide). DMPA was associated with rapid loss of fluorescence in QD-silicones, whereas quenching was not observed with TPO. Detachment of passivating ligands followed by photo-oxidation was suggested as a mechanism: TPO radicals are more susceptible to recombination with oxygen radicals than DMPA-derived radicals, which might result in better shielding of the QD surface. Printing of 1 wt% TPO silicone inks without quantum dots was carried out under nitrogen to prevent oxygen inhibition. Jetting was demonstrated with 34-42 μm average drop diameter on silanised glass slides, while printing of continuous films was demonstrated on glass slides coated in a release agent.

The temperature sensing performance of novel QD-silicone composites was assessed via fluorescence spectroscopy and imaging. 100 nm diameter QD clusters were observed in transmission electron microscopy and micron-scale QD aggregates in optical microscopy. QD emission appeared to be largely unchanged by immobilisation in silicone, although QD aggregation was expected to reduce photostability of the composite. Intensity- and spectral shift-based optical thermometry was demonstrated using well-plate reading and confocal laser scanning microscopy. Emission sensitivity at 627 nm was found to be approximately -0.7 to $-1.2\% \text{ } ^\circ\text{C}^{-1}$ between 30-50 $^\circ\text{C}$ and spectral sensitivity 0.07 to 0.08 $\text{nm } ^\circ\text{C}^{-1}$, in agreement with other values in QD-sensing literature. Intensity decreased between thermal cycles of the same sample, although values at 60 $^\circ\text{C}$ were unchanged, while spectral shift appeared repeatable without redshift. Overall, fluorescent QD-silicone composites were produced via IJP for the first time and were shown to have temperature-sensitive emission. These materials are suitable for inkjet-printable devices with embedded optical temperature sensors using luminescence nanothermometry.

Table of Contents

Acknowledgments	<i>i</i>
Abstract	<i>iii</i>
Table of Contents	<i>v</i>
List of Figures	<i>ix</i>
List of Tables	<i>xix</i>
Abbreviations	<i>xxii</i>
Chapter 1. Introduction	<i>1</i>
1.1. Context	<i>1</i>
1.2. Motivation, aims and objectives	<i>3</i>
1.3. Statement of novelty	<i>4</i>
1.4. Thesis structure	<i>5</i>
Chapter 2. Literature Review	<i>7</i>
2.1. Inkjet printing as a route for integrated thermal sensing	<i>8</i>
2.1.1. The inkjet printing process.....	<i>11</i>
2.1.2. Inkjet-printed temperature sensors.....	<i>16</i>
2.2. Silicones	<i>19</i>
2.2.1. Properties of silicones	<i>19</i>
2.2.2. Silicone cure systems	<i>22</i>
2.2.3. Silicones in inkjet.....	<i>28</i>
2.2.4. Functional silicone composites	<i>35</i>
2.3. Quantum dots	<i>40</i>
2.3.1. Properties of quantum dots.....	<i>40</i>
2.3.2. Inkjet printing of quantum dots.....	<i>43</i>
2.3.3. QD-polymer composites	<i>46</i>
2.3.4. QD-based temperature sensing	<i>49</i>
2.4. Research niche	<i>59</i>
Chapter 3. Methodology	<i>61</i>
3.1. Project workflow	<i>62</i>
3.2. Materials	<i>65</i>
3.1.1. Addition cure silicones	<i>66</i>
3.1.2. UV cure silicones	<i>67</i>
3.2. Methods	<i>68</i>
3.2.1. Pre-polymer characterisation	<i>68</i>
3.2.2. Ink formulation	<i>68</i>
3.2.3. Inkjet printing.....	<i>72</i>

3.2.4.	QD ink formulation	79
3.2.5.	QD composite curing.....	81
3.2.6.	Temperature sensing	84
Chapter 4. Results – Addition cure silicones		89
4.1.	Prepolymer characterisation.....	90
4.1.1.	Temperature sensor criteria	90
4.1.2.	Commercial silicone system.....	97
4.1.3.	Spectroscopy.....	100
4.1.4.	Rheology	108
4.1.5.	Summary of SiliGlass constituents	111
4.2.	Ink formulation	113
4.2.1.	Viscosity modification	113
4.2.2.	Octyl acetate-based inks	122
4.2.3.	Toluene-based inks	126
4.2.4.	Summary of SiliGlass inks.....	131
4.3.	Printing of SiliGlass inks	132
4.3.1.	Drop-on-drop inkjet process.....	132
4.3.2.	Optimisation of jetting.....	133
4.3.3.	Single-headed reactive inkjet.....	139
4.3.4.	Dual-headed reactive inkjet.....	143
4.3.5.	Summary of SiliGlass printing	151
4.4.	QD-ink formulation	153
4.4.1.	Minimum loading	153
4.4.2.	Viscosity prediction	156
4.4.3.	Solvent assessment.....	158
4.4.4.	Summary of QD-inks	165
4.5.	Printing of QD-composites.....	167
4.5.1.	Cure rate	167
4.5.2.	Single-headed reactive inkjet.....	178
4.5.3.	Summary of QD-composite printing	185
4.6.	Summary of addition cure silicones.....	187
Chapter 5. Results – UV cure silicones.....		188
5.1.	Prepolymer characterisation.....	189
5.1.1.	Temperature sensor criteria	189
5.1.2.	Commercial reagents	193
5.1.3.	Spectroscopy.....	200
5.1.4.	Rheology	203
5.1.5.	Summary of UV cure reagents	205
5.2.	Ink formulation	206
5.2.1.	PDMS inks	207
5.2.2.	2-EHA inks	211
5.2.3.	Summary of UV cure inks	215

5.3. DMPA-containing composites	216
5.3.1. PDMS and 2-EHA inks.....	217
5.3.2. Thiol-ene inks.....	220
5.3.3. Loss of photoluminescence.....	221
5.3.4. Summary of DMPA photoinitiator	223
5.4. TPO-containing composites	225
5.4.1. 2-EHA inks	226
5.4.2. Summary of TPO photoinitiator	228
5.5. Printing of UV cure silicone inks	229
5.5.1. Curing of silicone inks	230
5.5.2. Observation of jetting	232
5.5.3. Reactive inkjet.....	243
5.5.4. Summary of UV inkjet printing.....	246
5.6. Summary of UV cure silicones	247
Chapter 6. Results – Temperature sensing	248
6.1. Characterisation of QD addition cure silicone composite	250
6.1.1. TEM and EDS	250
6.1.2. PL spectra	252
6.1.3. Confocal LSM	253
6.1.4. Summary of QD-SiliGlass analysis	253
6.2. Well-plate reading.....	255
6.2.1. Octyl acetate-based addition cure composites.....	255
6.2.2. Toluene-based addition cure composites.....	259
6.2.3. UV cure composites	261
6.2.4. Summary of well-plate reading.....	265
6.3. Confocal microscopy.....	267
6.3.1. Octyl acetate-based addition cure composite with 0.00125 wt% PtCl ₂	269
6.3.2. Octyl acetate-based addition cure composite without added catalyst	276
6.3.3. Toluene-based addition cure composite without added catalyst	286
6.3.4. Summary of microscopy-based sensing.....	294
6.4. Summary of temperature sensing materials	296
Chapter 7. Discussion	297
7.1. Formulation and printing of addition cure silicone inks.....	297
7.2. Formulation and printing of addition cure QD-silicone composite inks.....	302
7.3. Formulation and printing of UV cure silicone inks.....	307
7.4. Temperature sensing with QD-silicone composites.....	315
Chapter 8. Conclusions	320

Chapter 9. Further work	323
9.1. Ink shelf life.....	323
9.2. Material development	325
9.3. Characterisation and applications	328
 Bibliography	 330
 Appendices	 373
Waveforms	373
W ₁ v ₁	373
W ₁ v ₂	373
W ₂	374
Silicones in alternate AM categories	375
Overview of AM.....	375
Commercial AM of silicones	377
Material extrusion	381
Vat photopolymerisation.....	393
Other AM processes	399
Summary of silicones in AM	401
QD dispersion in polymer matrices	402
Polymeric ligands.....	407
Bimodal silicone grafting	410
<i>In situ</i> passivation	412
Silica encapsulation	413
Sol-gel hybrimers.....	416
Macrocrystal embedding.....	419
Summary of dispersion strategies	422

List of Figures

Figure 1: Left: Inkjet printing using piezoelectric actuators for drop-on-demand inkjet. Reproduced from Chung et al. 2019. ⁹ Right: Multi-material IJP of photo-curable inks to produce 3D shapes via the Stratasys PolyJet process. Image taken from Wikimedia Commons (Projetbiblio800.jpg by user Bibliolmpression).	11
Figure 2: Parameter space of the jetting regime, plotted as Reynolds number versus Weber number. Reproduced with permission from Derby et al. ⁶	13
Figure 3: Parameter space of drop impact, plotted as Weber number versus Ohnesorge number. Reproduced with permission from Derby et al. ⁶	14
Figure 4: Schematic sequence of ink behaviour following drop impact with substrate in DOD inkjet. Reproduced with permission from Derby et al. ⁶	15
Figure 5: Stable line formation parameter space, plotted using dimensionless parameters: drop spacing as a function of static advancing contact angle $g(\rho^*, \theta)$ against print speed U_T^* (specifically, the traverse velocity of the printhead relative to the substrate). Reproduced with permission from Derby et al. ⁶	15
Figure 6: Condensation curing of a typical silicone formulation. Reproduced with permission from Wang et al. ⁵⁶	22
Figure 7: Metal-catalysed hydrosilylation of olefins via the Chalk-Harrod mechanism. Platinum catalysts follow the C_1 pathway and addition is anti-Markovnikov. Rhodium catalysts follow C_2 . Reproduced from Wang et al. ⁵⁶	23
Figure 8: Thermally-induced crosslinking of PDMS using a diacyl peroxide initiator. Adapted from Wang et al. ⁵⁶	24
Figure 9: Radical-mediated thiol-ene reaction mechanism with photoinitiator. Image adapted from Wikimedia Commons (Photoinitiated thiol-ene coupling reaction.gif by user Nkchenjx).	25
Figure 10: Photolysis of a diaryliodonium salt to produce a Bronsted acid catalyst. Reproduced with permission from Wang et al. ⁵⁶	26
Figure 11: Quantum confinement in CdSe QDs. At sizes above the exciton Bohr radius, molecular orbitals combine to form continuous energy bands, where the valence band (VB) is populated by electrons and the conduction band (CB) is empty. As particle sizes decrease below the Bohr radius, the bands increasingly split into quantised energy levels and bandgap increases, leading to emission of photons with higher energy wavelengths. Reproduced from de Mello Donegá 2011 ¹⁹ with permission from The Royal Society of Chemistry.	40
Figure 12: Types of core-shell quantum dots. The relative energies of the valence band and conductive band of the core (orange) and shell (green) material is shown, along with localisation of charge carriers and their ground state wavefunctions (electrons in blue, marked as \ominus ; holes in red, marked as \oplus). Adapted from de Mello Donegá 2011 ¹⁹ with permission from The Royal Society of Chemistry.	41
Figure 13: Intrinsic temperature quenching processes: a) thermally activated crossover and b) multiphonon relaxation. Trap-related temperature quenching processes: c) irreversible and d) reversible. Reproduced with permission from Zhao et al. ¹⁶⁰ Copyright 2012 American Chemical Society.	50

Figure 14: Multiplexed optical temperature probes using QDs composites with different $\lambda_{\text{emission}}$ in (a) reflection and (b) transmission configurations. A CCD spectrometer was used to collect signals in 595-600 nm and 620-625 nm. Reproduced with permission from Jorge et al. ¹⁵⁵	51
Figure 15: QD sensing film on circuit board. Left: Experimental set up. Top right: Micro-resistors on the printed circuit board with QD sensing layer, where the 200 x 140 μm^2 planar area measured on resistor H is outlined in red. Bottom right: Surface temperature measurement of resistor H, where each square measures 10 x 10 μm^2 . Reproduced with permission from Liu et al. ¹⁶⁵	52
Figure 16: Dual emitting Mn^{2+} doped CdSe QDs. (a) Energy level diagram. (b) PL spectra at varied temperatures 223 K – 403 K; peaks are seen at 500 and 570 nm. (c) Temperature dependence of the ratio between excitation intensity and total emission intensity. (d) Image of colloidal QDs at two temperatures, 400 K and 210 K. Reproduced with permission from Vlaskin et al. ¹⁵⁷ Copyright 2010 American Chemical Society.	52
Figure 17: Individual QD markers on a microheater. Left: Experimental set up. Centre: PL spectra at different temperatures, with peak plotted against temperature in inset. Right: Temperature variation with distance along microheater, calculated by peak wavelength. Reproduced with permission from Li et al. ¹⁶⁸ Copyright 2007 American Chemical Society..	53
Figure 18: Optofluidic device with waveguide. Left: Device layout with embedded waveguide. Right: Spatial temperature map of the microchannel. Reproduced from Choudhury et al. ¹⁷² with permission from The Royal Society of Chemistry.	54
Figure 19: Lifetime of CdTe QDs. (a) Luminescence decay curves of 1 nm CdTe QDs at 30 and 50 °C. (b) Variation of lifetime with temperature in 1 nm CdTe QDs. (c) Experimental set up for thermal measurement in a microchannel, with 1090 nm continuous laser and 532 nm pulsed laser for excitation of 3.8 nm CdTe QDs. Reproduced with permission from Haro-González et al. ¹⁷³	55
Figure 20: CdSe/CdS/ZnS QDs in PLMA matrix. (a) Fluorescent images at different temperatures, showing loss of intensity. (b) Variation of intensity against temperature during thermal cycles. Reproduced from Zhao et al. ¹⁶⁰ with permission from The Royal Society of Chemistry.	55
Figure 21: PL spectra variation in the temperature sensing range and response curves for $\text{Zn}_{1-x}\text{Mn}_x\text{Se/ZnS/CdS/ZnS}$. (a) TOPO capped in octadecene (b) encapsulated in n-octylamine-modified poly(acrylic acid), suspended in aqueous solution. Reproduced with permission from McLaurin et al. ¹⁷⁴ Copyright 2011 American Chemical Society.	56
Figure 22: Flowchart showing the workflow used to achieve research objectives, divided into six stages.....	62
Figure 23: Workflow for high throughput ink formulation. Arrays of potential inks are prepared in well-plates and the apparatus determines viscosity and surface tension to identify jettable inks. Reproduced from Zhou et al. ¹⁷⁸	71
Figure 24: Flowchart of fluorosilane deposition process.....	73
Figure 25: Left: Topside view of the printhead adaptor loaded with two Dimatix cartridges. On the left, the printhead angle is not correctly calibrated to align the jetting nozzle in use by each cartridge. On the right, the printhead turns to align in the X-axis. Right: Duplicated pattern for single pass printing with Y line offset. ¹⁷⁹	76
Figure 26: Histogram of emission from 0.00125 wt% PtCl_2 QD-silicone composite at 30 °C; data shown is the average of the three thermal cycles, with $\lambda_{\text{mean}} = 627.12$ nm. A normal	

distribution curve is plotted for illustrative purposes, showing how histograms obtained from the lambda scan relate to the QD emission peak.	88
Figure 27: Reaction scheme of SiliGlass crosslinking by hydrosilylation. Reproduced from Sturgess et al. ⁶⁰	98
Figure 28: ¹ H NMR spectrum of SiliGlass B with assigned peaks, corresponding to ¹ H environments as labelled in inset siloxane.	100
Figure 29: ¹ H NMR spectrum of SiliGlass A with assigned peaks, corresponding to ¹ H environments as labelled in inset siloxanes.	101
Figure 30: FTIR spectrum of SiliGlass A, which contains base polymer and crosslinker.....	105
Figure 31: FTIR spectrum of SiliGlass B, which contains base polymer and catalyst.....	105
Figure 32: Equilibrium flow curve of pure SiliGlass A. Black lines with square markers plot the shear stress as a function of shear rate, with a grey dotted trendline. Red lines with circular markers plot the dynamic viscosity as a function of shear rate. The linear region is enclosed between red dotted lines, with a black dotted trendline.	109
Figure 33: Equilibrium flow curve of pure SiliGlass B. Black lines with square markers plot the shear stress as a function of shear rate, with a grey dotted trendline. Blue lines with circular markers plot the dynamic viscosity as a function of shear rate. The linear region is enclosed between blue dotted lines, with black dotted trendline.....	109
Figure 34: Dynamic viscosity of 50 wt% octyl acetate-based inks against temperature, showing Ink A in red and Ink B in blue. Bars display the range of values measured. Viscosity in mPa s (25 °C, 30 °C, 35 °C): (A) 12.71, 11.75, 10.88; (B) 14.38, 13.35, 12.32.	123
Figure 35: Representative images of pendant drop analysis of Ink A (left) and Ink B (right) for octyl acetate-based inks.....	124
Figure 36: Dynamic viscosity of 60 wt% toluene-based inks against temperature, showing Ink A in red and Ink B in blue. Bars display the range of values measured. Viscosity in mPa s (25 °C, 30 °C, 35 °C): (A) 12.72, 11.95, 11.13; (B) 14.53, 13.66, 12.78.....	127
Figure 37: Dynamic viscosity of 50 wt% toluene-based inks against temperature, showing Ink A in red and Ink B in blue. Bars display the range of values measured. Viscosity in mPa s (25 °C, 30 °C, 35 °C): (A) 8.676, 8.265, 7.865; (B) 8.789, 8.371, 7.998.....	127
Figure 38: Drop-on-drop reactive inkjet scheme for addition cure silicone. Ink A (crosslinker) and Ink B (catalyst) are deposited drop-on-drop on the substrate and cure in situ via Pt-catalysed hydrosilylation. Here, Ink A is depicted as being deposited on Ink B using a dual printhead system; in practice, order of deposition was not seen to have a significant impact on printing.....	133
Figure 39: Droplet ejection of Ink A (top) and Ink B (bottom) at 32 V with waveform W ₁ v1 using the Dimatix.	133
Figure 40: Ink B deposited onto a silane-treated glass slide, as viewed through the DSA100 camera.	136
Figure 41: Droplet arrays of Ink A printed with 120, 70, 60 and 50 μm drop spacings, as viewed via fiducial camera. Droplets were ejected at 32 V with waveform W ₁ v1 using the Dimatix. Representative of both inks.....	137
Figure 42: Images of one layer of deposited Ink A as viewed via the fiducial camera of the Dimatix printer. Droplet spacings decrease left-to-right: 30, 15, and 5 μm.....	138

Figure 43: Micrographs of reactive inkjet-printed squares jetted at 32 V with waveform W_1 v1 using the Dimatix, demonstrating the effect of poor contact pinning. Left: A square printed at 60 μm spacing with 40A40B layers. Right: A 2 μm^2 square printed at 30 μm spacing with 20A20B, showing bulging at edges and round profile.	139
Figure 44: Stepwise printing of a 5 mm^2 square (consisting of layers 10A10B 20A20B 60A60B) at 32 V with waveform W_1 v1 and 60 μm drop spacing, as viewed in the fiducial camera of the Dimatix.	140
Figure 45: Micrograph of a 5 mm^2 square (consisting of layers 10A10B 20A20B 60A60B), printed at 32 V with waveform W_1 v1 and 60 μm drop spacing.	141
Figure 46: Stepwise printing of test pattern (with 1A1B grid) at 32 V with waveform W_1 v1 and 60 μm drop spacing, as viewed in the fiducial camera of the Dimatix. The print conformed to the pattern despite offsets.	141
Figure 47: Left: Micrograph of test print with 5x objective, with print bitmap superimposed in red. Right: Closer view of surface texture, taken with 10x objective.	142
Figure 48: Micrographs of unidirectional line-by-line square, printed as 20AB with 60 μm spacing at 30 V with generic waveform using the PiXDRO. Contrast has been enhanced in the central micrograph.	143
Figure 49: Consecutive runs of bidirectional stepped-line printing with alternating print direction, as viewed via fiducial camera. A 30AB square was printed with 40 μm spacing at 30 V (generic waveform) using the PiXDRO. The bottom row consists of the same images where brightness and contrast have been digitally enhanced.	145
Figure 50: Micrographs of printed square using a bidirectional stepped-line strategy with alternating print direction. From left to right, images show the top-left corner, centre, and top-right corner of the 30AB square printed with 40 μm spacing at 30 V with generic waveform using the PiXDRO.	145
Figure 51: Droplet ejection of Ink A (left) and Ink B (right) at 30 V with waveform W_1 v2 using the Dimatix.	146
Figure 52: Droplet array of Ink A jetted at 30 V with waveform W_1 v2 using the Dimatix, as viewed via fiducial camera (left) and optical microscope (right). The droplets in the micrograph are circled and labelled for sizing.	147
Figure 53: Droplet array of Ink B jetted at 30 V with waveform W_1 v2 using the Dimatix, as viewed via fiducial camera (left) and optical microscope (right). The droplets in the micrograph are circled and labelled for sizing.	147
Figure 54: Droplet array of Ink A jetted at 30 V with waveform W_1 v2 using the PiXDRO, as viewed via fiducial camera (left) and optical microscope (right). The droplets in the micrograph are circled and labelled for sizing.	148
Figure 55: Droplet array of Ink B jetted at 30 V with waveform W_1 v2 using the PiXDRO, as viewed via fiducial camera (left) and optical microscope (right). The droplets in the micrograph are circled and labelled for sizing.	148
Figure 56: Photographs of a test print on a silanised glass slide. The pattern was printed unidirectionally and line-by-line as 30AB layers with 45 μm spacing at 30 V with waveform W_1 v2 using the PiXDRO.	149
Figure 57: Stitched micrographs of representative elements of the 30AB pattern printed line-by-line with 45 μm spacing at 30 V with waveform W_1 v2 using the PiXDRO.	149

Figure 58: Absorbance (left) and photoluminescence (right) spectra of CdSe/ZnS quantum dots with 630 nm emission peak. Sourced from manufacturer Ocean Nanotech. ²³⁵	153
Figure 59: Detection limit experiment for serially-diluted quantum dots in addition cure silicone. Emission spectra with PL intensity on a logarithmic scale. Inset: Emission spectra with PL intensity on a linear scale.....	154
Figure 60: Representative measurement of 0.005 wt% QDs in octyl acetate at 20 °C. Left: Raw correlation data. Right: Size distribution by intensity.....	159
Figure 61: Representative measurement of 0.005 wt% QDs in hexane at 20 °C. Left: Raw correlation data. Right: Size distribution by intensity.	161
Figure 62: Photograph of 0.005 wt% QD composites excited by a UV lamp. The top sample has no additional platinum catalyst, whereas the bottom was synthesised with 0.005 wt% Pt-Ink B.....	171
Figure 63: Mean Raman spectra of the cured inks (N=10); inset shows the Si-H stretching vibration centred at 2150 cm ⁻¹ . The blue line corresponds to the control sample, which does not contain QDs or PtCl ₂ . Other samples contain QD-Ink A and Pt-Ink B: orange, grey, and yellow lines show data for 0.00125 wt%, 0.0025 wt%, and 0.005 wt% PtCl ₂ . Spectra have been normalised to the intensity of the Si-O-Si mode at 490 cm ⁻¹ and offset on the y-axis for visual clarity.....	173
Figure 64: PL maps of 0.005 wt% QD-silicone composites synthesised with additional platinum catalyst in Ink B.....	175
Figure 65: Photograph of glass slide of test prints of QD-silicone composites. Reactive inks were jetted at 30 V with waveform W ₁ v ₂ using the Dimatix printer.	178
Figure 66: Photograph of the test print of 0.005 wt% QD-Ink A and 0 wt% Pt-Ink B, excited by a 395 nm UV lamp. Test pattern was printed with a 1A1B 2A2B grid at 100 µm spacing (6.5 mm diameter print pattern) and 10A10B layers at 60 µm spacing (4 mm diameter print pattern).	179
Figure 67: Composite micrograph of test print of 0.005 wt% QD-Ink A and 0 wt% Pt-Ink B, taken with 5x objective. Test pattern was printed with 1A1B 2A2B grid at 100 µm spacing (6.5 mm diameter print pattern) and 10A10B layers at 60 µm spacing (4 mm diameter print pattern).	180
Figure 68: Photograph of the test print of 0.005 wt% QD-Ink A and 0.00125 wt% Pt-Ink B, excited by a 395 nm UV lamp. 1A1B 10A10B layers were deposited at 60 µm spacing (8 mm diameter print pattern).....	180
Figure 69: Composite micrograph of test print using 0.005 wt% QD-Ink A and 0.00125 wt% Pt-Ink B, taken with 5x objective. 1A1B 10A10B layers were deposited at 60 µm spacing (8 mm diameter print pattern).	181
Figure 70: Greyscale micrographs of bulk composite of printed composites, imaged at 24 °C. Left: 0 wt% Pt-Ink B. Right: 0.00125 wt% Pt-Ink B.	182
Figure 71: Composite micrographs of 1A1B grid deposited at 100 µm spacing, taken with 5x objective. Left: 1A1B grid using 0.005 wt% QD-Ink A and 0.00125 wt% Pt-Ink B, 4 mm diameter print pattern. Right: 1A1B 2A2B grid using 0.005 wt% QD-Ink A and 0 wt% Pt-Ink B, 6.5 mm diameter print pattern.....	182
Figure 72: Greyscale fluorescence micrograph of 1A1B 2A2B grid (0.005 wt% QD-Ink A and 0 wt% Pt-Ink B) with 100 µm drop spacing, imaged at 24 °C. Top: Raw data. Bottom: Contrast has been enhanced.	184

Figure 73: UV inkjet printing process diagram. Photopolymerisable ink is deposited onto the substrate and excited by a UV wavelength excitation source attached to the printhead assembly.	193
Figure 74: Precursors for UV-curable silicone and acrylate system.	194
Figure 75: ¹ H NMR spectrum of AB116678 with assigned peaks, corresponding to ¹ H environments as labelled in inset siloxane.	200
Figure 76: Viscosity of DMPA-PDMS inks as a function of DMPA loading. Error bars show standard deviation; the average viscosity is plotted as a grey dotted line (7.32 mPa s). Viscosity in mPa s (0.125, 0.25, 0.5, 1 wt% DMPA): 7.34, 7.34, 7.55, 7.03.....	208
Figure 77: Viscosity of TPO-PDMS inks as a function of TPO loading. Error bars show standard deviation; the average viscosity is plotted as a grey dotted line (7.52 mPa s). Viscosity in mPa s (0.125, 0.25, 0.5, 1 wt% TPO): 7.48, 7.63, 7.39, 7.59.	209
Figure 78: Viscosity of DMPA-2-EHA inks as a function of DMPA loading. Error bars show standard deviation; the average viscosity across all loadings is plotted as a grey dotted line (3.40 mPa s). Viscosity in mPa s (0.125, 0.25, 0.5, 1 wt% DMPA): 3.13, 3.34, 3.75, 3.38....	212
Figure 79: Viscosity of TPO-2-EHA inks as a function of TPO loading. Error bars show standard deviation; the average viscosity across all loadings is plotted as a grey dotted line (3.78 mPa s). Viscosity in mPa s (0.125, 0.25, 0.5, 1 wt% TPO): 3.08, 4.46, 3.96, 3.63.	213
Figure 80: Photolysis of DMPA, showing the formation of benzoyl and acetal fragments (top right) and their recombination products below. Reproduced with permission from Wang et al. ⁵⁶	216
Figure 81: Drop array printed onto a silanised glass slide, viewed through the fiducial camera of a Dimatix printer. Droplet diameter is approximately 35 μm.	218
Figure 82: Mercaptan monomers PETMP (left) and DODT (right).....	220
Figure 83: Photograph of vials of inks without DMPA, from left-to-right PETMP, DODT, 2-EHA, and PDMS inks. Right: Colour photograph of samples without photoinitiator after 48 hours, where only PETMP ink remains fluorescent. Left: Same image with the red channel isolated.....	222
Figure 84: Photolysis of TPO.	225
Figure 85: Samples prepared for initial feasibility tests with TPO, showing strong fluorescence after curing.	226
Figure 86: UV-DSC curves of 0.25, 0.5, and 1 wt% TPO-PDMS inks (grey, orange, and blue lines, respectively).	230
Figure 87: UV-DSC curves of 0.25, 0.5, and 1 wt% TPO-2-EHA inks (grey, orange, and blue lines, respectively).	231
Figure 88: Droplet ejection of PDMS ink at 25 V with waveform W ₂ using the Dimatix printer.	232
Figure 89: Droplet arrays of PDMS ink printed with 60 and 100 μm drop spacings, as viewed via fiducial camera. Droplets were ejected at 25 V with waveform W ₂ using the Dimatix printer.	233
Figure 90: Droplet array of PDMS ink jetted at 25 V with waveform W ₂ using the Dimatix, as viewed via optical microscopy. The droplets in the micrograph are circled and labelled for sizing.	233

Figure 91: Droplet ejection of PDMS ink at 20 V with waveform $W_1 v_2$ using the Dimatix printer.	234
Figure 92: Droplet arrays of PDMS ink printed with 60 and 100 μm drop spacings, as viewed via fiducial camera. Droplets were ejected at 20 V with waveform $W_1 v_2$ using the Dimatix printer.	234
Figure 93: Droplet array of PDMS ink jetted at 20 V with waveform $W_1 v_2$ using the Dimatix, as viewed via optical microscopy. The droplets in the micrograph are circled and labelled for sizing.	235
Figure 94: Droplet ejection of PDMS ink at 22 V with waveform $W_1 v_2$ using the Dimatix printer.	236
Figure 95: Droplet arrays of PDMS ink printed with 60 μm drop spacing, as viewed via fiducial camera. Droplets were ejected at 22 V with waveform $W_1 v_2$ using the Dimatix printer.	236
Figure 96: Droplet array of PDMS ink jetted at 22 V with waveform $W_1 v_2$ using the Dimatix, as viewed via optical microscopy. The droplets in the micrograph are circled and labelled for sizing.	237
Figure 97: Droplet array of PDMS ink jetted at 22 V with waveform $W_1 v_2$ using the Dimatix printer, as viewed via optical microscopy. Nozzles seem to deposit two smaller droplets, rather than one single drop, in a grid.	238
Figure 98: Droplet ejection of 2-EHA ink at 25 V with waveform W_2 using the Dimatix printer. Left shows jetting where the tail re-joins the head of the drop, while right shows formation of satellites.	239
Figure 99: Droplet arrays of 2-EHA ink printed with 60 and 100 μm drop spacings, as viewed via fiducial camera. Droplets were ejected at 25 V with waveform W_2 using the Dimatix printer.	239
Figure 100: Droplet array of 2-EHA ink jetted at 25 V with waveform W_2 using the Dimatix, as viewed via optical microscopy. The droplets in the micrograph are circled and labelled for sizing.	240
Figure 101: Droplet ejection of 2-EHA ink at 20 V (left) and 22 V (right) with waveform $W_1 v_2$ using the Dimatix.	241
Figure 102: Single layers of 1 wt% TPO-PDMS ink deposited at drop spacings of 5, 10, 15, and 30 μm with waveform $W_1 v_2$ at 22 V using the Dimatix, as viewed by fiducial camera. Larger-to-smaller drop spacing is shown, anti-clockwise from top-left.	243
Figure 103: Photograph of monolayers printed onto a glass slide with release coating. 1 wt% TPO-PDMS ink was deposited at drop spacings of 5, 10, 15, and 30 μm . Larger-to-smaller drop spacing is shown, anti-clockwise from top-left.	244
Figure 104: Composite micrographs of monolayers printed at unsuitable drop spacings. 1 wt% TPO-PDMS ink was deposited at drop spacings of 30 μm (left) and 5 μm (right) onto a glass slide with release coating.	244
Figure 105: Composite micrographs of monolayers printed at intermediate drop spacings. 1 wt% TPO-PDMS ink was deposited at drop spacings of 15 μm (left) and 10 μm (right) onto a glass slide with release coating.	245
Figure 106: Transmission electron micrographs of sectioned 0.005 wt% QD silicone composite in bright field mode. These micrographs feature a single QD agglomeration, as identified by EDS in Figure 107 below.	250

Figure 107: Electron-dispersive spectrogram of aggregate from 0.005 wt% QD-silicone sample, imaged in TEM.....	251
Figure 108: PL spectrum of 0.01 wt% QD-silicone composite ($\lambda_{\text{excitation}} = 532 \text{ nm}$).....	252
Figure 109: Representative fluorescent micrograph of QD aggregates in the silicone matrix of 0.005 wt% QD-silicone composite, in colour (left) and greyscale (right).	253
Figure 110: Emission of uncured QD-silicone composites. Bars display the range of values. Left: Emission as a function of temperature for each loading of additional catalyst. Right: Emission as a function of additional platinum catalyst at 30 °C.....	255
Figure 111: Emission of cured octyl acetate-ink QD-silicone composites. Bars display the range of values. Left: Emission as a function of temperature for each loading of additional catalyst. Right: Emission as a function of additional platinum catalyst at 30 °C.	257
Figure 112: Emission of cured toluene ink QD-silicone composites. Bars display the range of values. Left: Emission as a function of temperature for each loading of additional catalyst. Right: Emission as a function of additional platinum catalyst at 30 °C.....	259
Figure 113: Emission of UV cured DMPA QD-silicone composites. Emission as a function of temperature for each formulation. Bars display the range of values. Bottom: Comparison of formulations at 30 °C.	261
Figure 114: Emission of UV cured TPO QD-silicone composites. Emission as a function of temperature for each formulation. Bars display the range of values. Bottom: Comparison of formulations at 30 °C.	263
Figure 115: Left: Fluorescence micrograph of 0.00125 wt% PtCl ₂ octyl acetate ink-based QD-silicone composite (cycle 1) at 27.5 °C ($\lambda_{\text{emission}} = 627 \text{ nm}$). Right: Spectral profiles at 30, 45, and 60 °C.	269
Figure 116: Left: Spectral profiles of subsequent thermal cycles at 30, 45, and 60 °C (top to bottom) of 0.00125 wt% PtCl ₂ octyl acetate ink-based QD-silicone composite. Right: Normalised spectral profiles of subsequent thermal cycles at 30 °C.	270
Figure 117: Representative graph of emission intensity as a function of temperature for the imaging of clusters (left) and the analysis of the full captured image (right) of 0.00125 wt% PtCl ₂ octyl acetate ink-based QD-silicone composite at different emission wavelengths. Data shown is the average of the three thermal cycles.	271
Figure 118: Estimated mean emission wavelength λ_{max} as a function of temperature for 0.00125 wt% PtCl ₂ octyl acetate ink-based QD-silicone composite using three different image sectioning regimes. Data shown is the average of the three thermal cycles, with error bars denoting range.....	274
Figure 119: Left: Emission intensity of 0.00125 wt% PtCl ₂ octyl acetate ink-based QD-silicone composite (cycle 3) as a function of temperature from 30-99 °C at different emission wavelengths. Data shown is for loose thresholding of clusters.	275
Figure 120: Left: Fluorescence micrograph of sample A of octyl acetate ink-based QD-silicone composite at 27.5 °C ($\lambda_{\text{emission}} = 627 \text{ nm}$). Right: Spectral profiles at 30, 45, and 60 °C.	276
Figure 121: Emission intensity as a function of temperature for the imaging of clusters (left) and the analysis of the full image (right) of sample A of octyl acetate ink-based composite at different emission wavelengths.....	277

Figure 122: Estimated mean emission wavelength λ_{max} as a function of temperature for sample A of octyl acetate ink-based QD-silicone composite using three different image sectioning regimes.	278
Figure 123: Left: Fluorescence micrograph of sample B of octyl acetate ink-based QD-silicone composite (cycle 1) at 27.5 °C ($\lambda_{\text{emission}}= 627$ nm). Right: Spectral profiles at 30, 45, and 60 °C.	279
Figure 124: Emission intensity as a function of temperature for the imaging of clusters (left) and the analysis of the full captured image (right) of sample B of octyl acetate ink-based QD-silicone composite (cycle 1) at different emission wavelengths.	280
Figure 125: Estimated mean emission wavelength λ_{max} as a function of temperature for sample B of octyl acetate ink-based QD-silicone composite (cycle 1) using three different image sectioning regimes: strict and loose thresholding of clusters, and full image.	281
Figure 126: Left: Fluorescence micrograph of sample B of octyl acetate ink-based QD-silicone composite (cycle 2) at 27.5 °C ($\lambda_{\text{emission}}= 627$ nm). Right: Spectral profiles at 30, 45, and 60 °C.	282
Figure 127: Emission intensity as a function of temperature for the imaging of clusters (left) and the analysis of the full captured image (right) of sample B of octyl acetate ink-based QD-silicone composite (cycle 2) at different emission wavelengths.	283
Figure 128: Estimated mean emission wavelength λ_{max} as a function of temperature for sample B of octyl acetate ink-based QD-silicone composite (cycle 2) using three different image sectioning regimes: strict and loose thresholding of clusters, and full image.	284
Figure 129: Left: Emission intensity of 0 wt% PtCl ₂ octyl acetate ink-based composite (cycle 2) as a function of temperature from 30-99 °C at different emission wavelengths. Data shown is for loose thresholding of clusters.	285
Figure 130: Left: Fluorescence micrograph of sample A of toluene ink-based QD-silicone composite at 27.5 °C ($\lambda_{\text{emission}}= 627$ nm). Right: Spectral profiles at 30, 45, and 60 °C.	286
Figure 131: Emission intensity as a function of temperature for the imaging of clusters (left) and the analysis of the full image (right) of sample A of toluene ink-based QD-silicone composite at different emission wavelengths.	287
Figure 132: Estimated mean emission wavelength λ_{max} as a function of temperature for sample A of toluene ink-based composite using three different image sectioning regimes: strict and loose thresholding of clusters, and full image.	288
Figure 133: Left: Fluorescence micrograph of sample B of toluene ink-based QD-silicone composite (cycle 1) at 27.5 °C ($\lambda_{\text{emission}}= 627$ nm). Right: Spectral profiles at 30, 45, and 60 °C.	289
Figure 134: Left: Spectral profiles of subsequent thermal cycles at 30, 45, and 60 °C (top to bottom) of sample B of toluene ink QD-silicone composite. Right: Normalised spectral profiles of subsequent thermal cycles at 30 °C.	290
Figure 135: Representative graph of emission intensity as a function of temperature for the imaging of clusters (left) and the analysis of the full captured image (right) sample B of toluene ink-based QD-silicone composite at different emission wavelengths. Data shown is the average of the two thermal cycles.	291
Figure 136: Estimated mean emission wavelength λ_{max} as a function of temperature for sample B of toluene ink-based QD-silicone composite using loose thresholding of clusters.	

Data shown is the average of the two thermal cycles, where error bars denote range of values.	292
Figure 137: Left: Emission intensity of 0 wt% PtCl ₂ toluene ink-based QD-silicone composite (sample B cycle 2) as a function of temperature from 30-99 °C at different emission wavelengths. Right: Emission intensity of sample B (cycle 3) as a function of temperature from 30-99 °C. Data shown is for loose thresholding of clusters.	293
Figure 138: Single pulse waveform optimised for addition cure inks, jetting at 32 V. Referred to as W ₁ v1.	373
Figure 139: Single pulse waveform, optimised from previous in order to improve performance at lower jetting voltages. Referred to as W ₁ v2.	373
Figure 140: Single pulse waveform with forceful ink ejection; utilised here to demonstrate that UV cure inks can be jetted, but a waveform optimised from the Dimatix Model Fluid settings waveform is preferable. Referred to as W ₂	374
Figure 141: The seven AM process categories, as defined by the ASTM.	375
Figure 142: Top: A PDMS chain, created using MarvinSketch and Qutemol. Left to right: Representations of silicone fluids, elastomers, and resins.	376
Figure 143: Classification of bonds at quantum dot surfaces using covalent bond notation. Reproduced with permission from Anderson et al. 2013. ²⁸⁶ Copyright 2013 American Chemical Society.	403
Figure 144: Top: Nonradiative relaxation of excitons as a result of surface trap states. Bottom: Confinement of excitons to the CdSe core by the potential well of the ZnS shell. Reproduced with permission from Lim et al. ¹¹⁰	404
Figure 145: Classes of ligand exchange reactions at quantum dot surfaces. Reproduced with permission from Anderson et al. 2013. ²⁸⁶ Copyright 2013 American Chemical Society.	405
Figure 146: Dispersion strategies for QD-polymer composites utilising polymeric ligands. Reproduced with permission from Gill et al. ³⁶⁶	407
Figure 147: Reaction scheme for QD encapsulation in amphiphilic polymer followed by crosslinking between encapsulant and monomer to form QD-polymer composites. Reproduced with permission from Yoon et al. ³⁰⁶	408
Figure 148: Reaction scheme for self- or co-crosslinking of QDs with reactive ligands to form silicone elastomers. Reproduced with permission from Wang et al. ³⁰⁷ Copyright 2016 American Chemical Society.....	409
Figure 149: Reaction scheme for bimodal polymer grafting of CdSe QDs with phosphonic acid functionalised PDMS chains. Reproduced from Tao et al. 2013 ¹²² with permission from The Royal Society of Chemistry.....	411
Figure 150: Synthesis of quantum dots with in situ PDMS capping ligands. Reproduced from Xie et al. ²⁹¹ with permission from The Royal Society of Chemistry.	412
Figure 151: Schematic of silica sphere encapsulation of quantum dots, showing typical encapsulation and overcoating procedures. Reproduced from Cho et al. ³⁷² with permission from The Royal Society of Chemistry.....	413
Figure 152: Reaction scheme for synthesis of QD-siloxane sol-gel resin (a and b), followed by free radical crosslinking to produce a cured QD-siloxane hybrimer (c). Reproduced with permission from Kim et al. ¹³⁵ Copyright 2016 American Chemical Society.....	418

List of Tables

Table 1: Relative performance of common polymeric LED encapsulants, as described in Yazdan Mehr et al. ⁴⁶ Typical refractive indices are listed; optical formulations may achieve higher values.	18
Table 2: Selected properties of linear PDMS fluids with 600-62000 g mol ⁻¹ average mass; ¹⁷ where values change as a function of chain length, the value range is given from low to high mass.	21
Table 3: Direct additive manufacturing of bulk silicones via material jetting in academic research.	33
Table 4: Examples of materials used as fillers in silicones by material class.	36
Table 5: Semiconductor QD-based temperature sensors in academic literature.	57
Table 6: Selection criteria for a polymer matrix for an optical QD-based temperature sensor with an expected operating range of 0-100 °C.	94
Table 7: ¹ H NMR correlation table for SiliGlass A and SiliGlass B, relative to tetramethylsilane (SiMe ₄ , TMS) with chloroform-D solvent (CDCl ₃).	102
Table 8: Peak list of FTIR modes for SiliGlass A and B, with assignments based on literature data. ²⁰⁰⁻²⁰²	106
Table 9: Ideal solvent parameters for ink formulation for reduced volatility, good compatibility with solutes, and inkjet processability.....	118
Table 10: Suggested solvents for silicone inks for inkjet printing and their properties. Values are marked green (excellent), yellow (good), or orange (somewhat poor), in accordance with the ideal values stated above in Table 9.....	120
Table 11: Dynamic viscosity of 30, 40 and 50 wt% silicone in octyl acetate at 25 °C with a shear rate of 10 s ⁻¹ and the percentage difference from the ideal range (as applicable). ...	122
Table 12: Printability of 50 wt% silicone in octyl acetate at 25 °C. Values of shear viscosity, density, surface tension, and the printability parameter Z are given for each ink.....	125
Table 13: Dynamic viscosity of 50 and 60 wt% silicone in toluene at 25 °C with shear rate of 10 s ⁻¹ and the percentage difference from the ideal range (as applicable).....	126
Table 14: Printability of 60 and 50 wt% silicone in toluene at 25 °C. Values of shear viscosity, density, surface tension, and the printability parameter Z are given for each ink.	130
Table 15: QD parameters, as determined from the manufacturer's specifications and crystallography data for wurtzite CdSe and ZnS.	156
Table 16: Calculation of relative viscosity for 0.5 wt% QDs in 1 g of Ink A.....	157
Table 17: Average diameters obtained from DLS of 0.005 wt% QDs in octyl acetate at 20 °C.	160
Table 18: Average diameters obtained from DLS of 0.005 wt% QDs in hexane at 20 °C. ...	162
Table 19: Peak list of size distribution by intensity for 0.005 wt% QDs in hexane at 20 °C.	163
Table 20: Peak positions and intensities for Si-H and Si-O-Si modes obtained from cured samples.	174
Table 21: Performance of commercial classes of free radical photoinitiators.	198

Table 22: ¹ H NMR correlation table for AB116678, relative to tetramethylsilane (SiMe ₄ , TMS) with chloroform-D solvent (CDCl ₃).	201
Table 23: Viscosity of UV curing prepolymers at room temperature.	203
Table 24: Printability of UV curing prepolymers at room temperature. Values of shear viscosity, density, surface tension, and the printability parameter Z are given for each prepolymer.	204
Table 25: Viscosity of DMPA-PDMS inks at room temperature.....	207
Table 26: Printability of DMPA-PDMS inks at room temperature. Values of shear viscosity, density, surface tension, and the printability parameter Z are given for each ink.....	208
Table 27: Viscosity of TPO-PDMS inks at room temperature.	209
Table 28: Printability of TPO-PDMS inks at room temperature. Values of shear viscosity, density, surface tension, and the printability parameter Z are given for each ink.....	210
Table 29: Viscosity of DMPA-2-EHA inks at room temperature.	211
Table 30: Printability of DMPA-2-EHA inks at room temperature. Values of shear viscosity, density, surface tension, and the printability parameter Z are given for each ink.....	212
Table 31: Viscosity of TPO-2-EHA inks at room temperature.	213
Table 32: Printability of TPO-2-EHA inks at room temperature. Values of shear viscosity, density, surface tension, and the printability parameter Z are given for each ink.....	214
Table 33: Percentage emission intensity thermal coefficients for temperature-dependent emission in uncured octyl acetate inks for each loading of additional platinum catalyst... 256	
Table 34: Percentage emission intensity thermal coefficients for temperature-dependent emission in cured octyl acetate ink QD-silicone composites for each loading of additional platinum catalyst.....	258
Table 35: Percentage emission intensity thermal coefficients for temperature-dependent emission in cured toluene ink QD-silicone composites for each loading of additional platinum catalyst.....	260
Table 36: Percentage emission intensity thermal coefficients for temperature-dependent emission in UV cured DMPA ink QD-silicone composites for each ink formulation.....	262
Table 37: Percentage emission intensity thermal coefficients for temperature-dependent emission in UV cured TPO ink QD-silicone composites for each ink formulation.	264
Table 38: Percentage emission intensity thermal coefficients (30-50 °C) at different wavelengths from images of 0.00125 wt% PtCl ₂ octyl acetate ink-based QD-silicone composite using three image sectioning regimes.	271
Table 39: Values reported for percentage intensity thermal coefficient for CdSe/ZnS quantum dots in literature. Papers where coefficients were not listed in text but could be obtained from the data presented are marked with an asterisk.	273
Table 40: Spectral shift thermal coefficients (30-60 °C) from captured images of 0.00125 wt% PtCl ₂ octyl acetate ink-based QD-silicone composite using three different image sectioning regimes.	274
Table 41: Percentage emission intensity thermal coefficients (30-50 °C) at different wavelengths from images of sample A of octyl acetate ink-based QD-silicone composite using three different image sectioning regimes.	277

Table 42: Spectral shift thermal coefficients (30-60 °C) from images of sample A of octyl acetate ink-based QD-silicone composite using three different image sectioning regimes.	278
Table 43: Percentage emission intensity thermal coefficients (30-50 °C) at different wavelengths from sample B of octyl acetate ink-based QD-silicone composite (cycle 1) using three different image sectioning regimes.....	280
Table 44: Spectral shift thermal coefficients (30-60 °C) from images of sample B of octyl acetate ink-based QD-silicone composite (cycle 1) using three different image sectioning regimes.....	281
Table 45: Percentage emission intensity thermal coefficients (30-50 °C) at different wavelengths in sample B of octyl acetate ink-based QD-silicone composite (cycle 2) using three different image sectioning regimes.....	283
Table 46: Spectral shift thermal coefficients (30-60 °C) from images of sample B of octyl acetate ink-based QD-silicone composite (cycle 2) using three different image sectioning regimes.....	284
Table 47: Percentage emission intensity thermal coefficients (30-50 °C) at different wavelengths from images of sample A of toluene ink-based QD-silicone composite using three different image sectioning regimes.....	287
Table 48: Spectral shift thermal coefficients (30-60 °C) from images of sample A of toluene ink-based QD-silicone composite using three different image sectioning regimes.	288
Table 49: Percentage emission intensity thermal coefficients (30-50 °C) at different wavelengths from images of sample B of toluene ink-based QD-silicone composite using three different image sectioning regimes.....	291
Table 50: Spectral shift thermal coefficients (30-60 °C) from images of sample B of toluene ink-based QD-silicone composite using three different image sectioning regimes.	292
Table 51: Direct additive manufacturing of bulk silicones and silicone composites via material extrusion in academic research.....	384
Table 52: Direct additive manufacturing of bulk silicones via vat photopolymerisation in academic research.	395
Table 53: Direct additive manufacturing of bulk silicones via powder bed processes and other AM techniques in academic research.	400

Abbreviations

2-EHA	2-ethylhexyl acrylate
2PP	Two-photon polymerisation
3DP	Three-dimensional printing
AAAP	Alkylaminoacetophenone
AFM	Atomic force microscopy
AM	Additive manufacturing
ASTM	American Society for Testing and Materials International
AU	Arbitrary unit
BF	Benzoylformate ester
BP	Benzophenone
CAD	Computer-aided design
CB	Carbon black
CB	Conduction band
CCD	Charge-coupled device
CHB	Cyclohexylbenzene
CIJ	Continuous inkjet, a type of inkjet printing (contrast DOD)
CLIP	Continuous liquid interface production
cLSM	Confocal laser scanning microscopy
CNT	Carbon nanotube
COC	Cyclic polyolefin copolymer
CTE	Coefficient of thermal expansion
DAAP	Dialkoxyacetophenone
DIW	Direct ink writing; also known as robocasting
DLP	Digital light processing
DLS	Dynamic light scattering

- DMC** Dimatix material cartridge
- DMP** Dimatix material printer
- DMPA** 2,2-dimethoxy-2-phenylacetophenone; also known as 2,2-dimethoxy-1,2-diphenylethan-1-one or Omnirad 651 (formerly Irgacure 651)
- DoC** Degree of conversion
- DOD** Drop-on-demand, a type of inkjet printing (contrast CIJ)
- DoD** Drop-on-drop
- DODT** 2,2'-(Ethylenedioxy)diethanethiol; also known as 3,6-Dioxa-1,8-octanedithiol
- DS** Drop spacing
- DSA** Drop shape analysis
- DSC** Differential scanning calorimetry
-
- e-3DP** Embedded 3D printing, also known as EMB3D
- EDS** Electron-dispersive spectroscopy
- EGO** Expert-guided optimisation
- EHD** Electrohydrodynamic printing, a material jetting process
-
- FDM** Fused deposition modeling; trademarked by Stratasys, equivalent to FFF
- FFF** Fused filament fabrication
- FRE** Freeform reversible embedding
- FsDLW** Femtosecond direct laser writing
- FTIR** Fourier transform infrared spectroscopy
- FWHM** Full width at half maximum
-
- GPC** Gel permeation chromatography
-
- HAP** Hydroxyacetophenone
- HTS** High-throughput screening
- HTV** High temperature vulcanisation

IJP	Inkjet printing
IPA	Iso-propyl alcohol, also known as propan-2-ol, 2-propanol, or isopropanol
IR	Infrared
LC	Liquid crystal
LCD	Liquid crystal display
LCP	Liquid-crystal polymer
LED	Light-emitting diode
LOPP	Low one-photon polymerisation
LS	Laser sintering
LSM	Laser scanning microscopy
LSR	Liquid silicone rubber
LVER	Linear viscoelastic region
M_c	Critical molecular weight of chain entanglement
MJ	Material jetting
M_n	Number average molar mass (or molecular weight)
MPA	3-mercaptopropionic acid
M_w	Weight average molar mass (or molecular weight)
MW	Molecular weight, typically synonymous with molar mass
μSLA	Micro-stereolithography
NA	Numerical aperture
NMR	Nuclear magnetic resonance
NP	Nanoparticle
ODA	Octadecylamine
PAM	Pressure-assisted microsyringe
PBF	Powder bed fusion
PDI	Polydispersity index

PDMS Poly(dimethylsiloxane)
PDPS Poly(diphenylsiloxane)
PEG Polyethylene glycol
PETMP Pentaerythritol tetrakis(3-mercaptopropionate)
PFOTS 1H,1H,2H,2H-Perfluorooctyl-trichlorosilane
PL Photoluminescence
PMHS Poly(methylhydrogensiloxane)
PMPS Poly(methylphenylsiloxane)
PMT Photomultiplier tube
PO Phosphine oxide
ppm Parts per million
PTFE Polytetrafluoroethylene
PUF Physically unclonable function
PVA Poly(vinyl alcohol)

QD Quantum dot

RC Robocasting; also known as direct ink writing
RI Refractive index
RP Rapid Prototyping
RTD Resistance temperature detector
RTV Room temperature vulcanisation

sBP Substituted benzophenone
SD Standard deviation
SE Standard error
SEM Scanning electron microscopy
SLA Stereolithography
SLM Selective laser melting
SLS Selective laser sintering
SS Stainless steel

TEM	Transmission electron microscopy
TEOS	Tetraethyl orthosilicate
Tg	Glass transition temperature
TGA	Thermogravimetric analysis
TMS	Tetramethylsilane
ToF	Time of Flight
TPO	Phenylbis(2,4,6-trimethylbenzoyl)-phosphine oxide, also known as Omnirad 819 (formerly Irgacure 819)
TX	Thioxanthone
UV	Ultraviolet
UV vis	Ultraviolet-visible (typically in the context of UV vis spectroscopy)
VB	Valence band
vol%	Volume percent; percentage by volume
VP	Vat photopolymerisation
VTC	Viscosity-temperature coefficient
wt%	Weight percent; percentage by weight

Chapter 1. Introduction

1.1. Context

Temperature is an important physical parameter for the calibration of numerous systems, and temperature sensing methods must scale with device miniaturisation. Fields such as micro/nanoelectronics, integrated photonics, and biomedicine require high-resolution temperature sensing for the *in situ* detection of localised “hot-spots” that can arise in microdevices and for monitoring of complex biological systems. Nanothermometry can achieve submicron and subdegree resolution and is divided into electrical, mechanical, and optical categories.^{1,2} Electrical and mechanical nanothermometers involve micro-thermocouples and bi-material cantilevers respectively; mK thermal sensitivities are known with spatial resolution similar to atomic force microscopy, but they are surface techniques, require contact with the sample, and are expensive. Optical techniques are diverse; interferometric techniques are particularly sensitive, with micron resolution and mK thermal sensitivity, but are surface techniques that require transparent materials. Luminescence nanothermometry requires fluorescent materials but is a non-contact method which can achieve submicron and subdegree resolutions and enable planar thermal imaging and 3D image reconstruction of materials.

The drive towards device miniaturisation in electronics, optonics, and chemical and bio-analysis raises a corresponding need for non-invasive, *in situ* thermal sensing for accurate calibration and analysis during device operation.^{3,4} For instance, within the fields of microfluidics and lab- or organ-on-a-chip, integrated sensors eliminate the need for manual sample collection, which is time-consuming, requires large working volumes, and can disturb the system.⁵ Suitable strategies for temperature monitoring within these enclosed systems are therefore limited to electrical or luminescence thermometry with integrated sensing materials, or to embedded microsensors. However, direct sensor integration is challenging via conventional manufacturing: device fabrication is greatly complicated by multi-step processes, heat treatments, and material compatibility.

Inkjet printing (IJP) may be an economical route to devices with integrated sensors due to its capacity for maskless, high-resolution,⁶ multi-material printing.⁷ IJP is a direct writing technique which can produce electrodes and sensors on a range of substrates at low temperatures with high spatial resolution (typically 20-50 μm),⁶ which facilitates iterative design and reduces production time and cost. IJP has become an attractive manufacturing

process for end-use products (including electronics,^{8,9} chemisensors,¹⁰ and microfluidics¹¹) due to its capacity for multi-material deposition and the geometric freedom inherent to additive manufacturing techniques.^{7,12}

The inkjet-printed temperature sensors that have been reported so far are resistance temperature detectors (RTDs) or thermistors, both of which measure electrical resistance as a function of temperature. RTDs are a popular choice for printed temperature sensors due to their accuracy, response time, and simple fabrication;¹³ this has led to the development of wearable temperature sensors which can be made using economical inkjet printing processes.^{14,15} While typical existing inkjet-printable temperature sensors are well-suited for wearable sensors, they do not fulfil requirements for miniaturisation: sensors are typically on the order of cm² in size and sensing areas tens of mm² - which greatly limits spatial resolution and capacity for planar or 3D imaging - and the thermal coefficient of resistance of inkjet-printed materials is currently limited to 0.1 - 0.3 % C⁻¹ in all but one case.¹⁴⁻¹⁶ Novel inks for luminescence nanothermometry are needed to enable inkjet-printable sensing with microscale and subdegree resolution in the physiological range.

Silicones are amphiphilic polymers with a range of attractive properties including transparency, elasticity, biocompatibility, insulation, and temperature and radiation stability.¹⁷ Silicones and silicone composites used for LED encapsulation due to their UV transparency, refractive index, and thermal stability,¹⁷ and would be ideal matrices for optical sensing applications. Quantum dot-silicone composites are excellent candidates for luminescent sensing materials and are described in literature for LED films; reactive inks could be formulated to deposit and cure *in situ*.¹⁸ Quantum dots (QDs) are fluorescent semiconductor nanocrystals with including size-tunable and narrow emission bands with high quantum yield¹⁹ and show intrinsic, reversible temperature quenching of QD fluorescence.²⁰

Development of inks from temperature sensing materials capable of submicron and subdegree resolutions would enable controlled 3D patterning via inkjet and allow for *in situ* thermal monitoring. This may enable advanced designs for inkjet-printable devices and lead to more economical production of microfluidics and microelectronics with integrated, non-invasive sensing.

1.2. Motivation, aims and objectives

Current inkjet-printed resistance-based thermal sensors have limited spatial resolution and do not achieve sub-degree thermal resolution in the physiological range, which is a barrier to their use in microdevices and in cell culture and biomedical applications. Novel inks for luminescence nanothermometry could meet the requirements for integrated sensing in inkjet-printed microelectronic and microfluidic devices.

An ink formulation strategy utilising polymer composite inks can efficiently deposit and seal sensing materials simultaneously and the polymer matrix can provide processability, better enable 3D printing geometries, and improve dispersion and stability of the fluorescent species.^{21,22} Silicones are ideal polymer matrices for luminescence nanothermometry due to their optical transparency, UV and thermal stability, and high refractive indices.¹⁷ Printable QD-silicone composites for luminescence nanothermometry could enable *in situ* temperature monitoring for applications and geometries that are otherwise impossible to monitor by conventional means; it is anticipated that this will have particular use for monitoring microfluidic channels and thermal imaging of microelectronics.

The aim of this study is to produce an inkjet-printable quantum dot-silicone composite that can be used for optical thermometry. The aim will be met via the following objectives:

- O1 formulation of jettable silicone inks;
- O2 printing of silicone matrices;
- O3 formulation of jettable QD-silicone inks;
- O4 printing of QD-silicone composites;
- and O5 characterisation of temperature-sensing materials.

1.3. Statement of novelty

This PhD presents the first inkjet-printable quantum dot-silicone composite and the first ink demonstrated for luminescence nanothermometry via inkjet, enabling deposition of temperature sensing materials capable of greater spatial and thermal resolution than typical resistance-based inkjet-printed sensors. A range of silicones and a novel QD-silicone composite were printed; temperature sensitivity of composites was confirmed from photoluminescent measurements. Strategies were discussed and applied to improve substrate pinning, dispersion, and cure rate of printed materials. Novelty was demonstrated in the following areas:

- Rheological assessment of a range of silicone formulations
- Printing of novel UV curable silicones via inkjet
- Investigation of photoinitiator loading on photoluminescence in a range of UV curable QD-silicone inks for inkjet
- Use of additional platinum catalyst to enable curing of addition cure QD-silicone inks, with investigation of the effect of platinum catalyst on QD fluorescence
- Printing of the first reported inkjet-printable QD-silicone bulk composite
- Investigation of thermal sensitivities of composites to characterise the first inkjet materials formulated specifically for optical temperature sensing.

1.4. Thesis structure

This thesis details the first ink demonstrated for luminescence nanothermometry: the work carried out to develop reactive inks for quantum dot-silicone composites and the characterisation of materials produced.

Chapter 1 (Introduction) gives an overview of the research niche and sets out the motivation and aims and objectives of the project. It also outlines the framework of the rest of this thesis and what will be covered in each chapter.

Chapter 2 (Literature review) is a thorough discussion of the literature and theory relevant to the project, with an overview of nanothermometry and integrated thermal sensing. This is divided into three subsections: the inkjet process as a route to integrated thermal sensing; silicone polymers and their properties, crosslinking reaction mechanisms, inkjet of silicones, and potential QD-silicone composites for temperature sensing; and quantum dots and QD-polymer composites in inkjet and in luminescence nanothermometry. The research niche is summarised and covers context and the rationale for material selection.

Chapter 3 (Methodology) describes the materials, equipment and methods utilised, with justification and comparison to literature where appropriate. This chapter lists the research objectives and the methods used to meet them, including prepolymer characterisation, rheological characterisation, jetting optimisation, inkjet printing on single and dual printhead systems, assessment of QD dispersion, and cure optimisation and analysis of composite inks. Composite materials are interrogated using imaging and spectroscopic techniques, particularly in photoluminescent studies for temperature sensing.

Chapter 4 (Results – Addition cure silicones) details the development of 2-part reactive silicone inks, including selection of solvent, rheological characterisation, jetting optimisation, and drop-on-drop inkjet printing with single and dual printhead printers. QD-inks were then developed: QD loading was guided by PL detection limits and viscosity calculation, QD dispersion was assessed, and curing was optimised to demonstrate inkjet printing of QD-silicone composites.

Chapter 5 (Results – UV cure silicones) concerns the results of experiments carried out on 1-part UV-curable inks and covers rheological characterisation, photoinitiators and cure analysis, composite photostability, and inkjet printing trials on the single printhead printer. Both acrylate and thiol-ene free radical photopolymerisation mechanisms were investigated.

Chapter 6 (Results – Temperature-sensing) describes imaging and photoluminescence spectroscopy of QD-silicone composites and states the results of temperature-sensing experiments carried out via confocal microscopy and well-plate reading. Sensitivity is assessed using emission intensity- and peak shift-based measurements, and repeatability and limitations are discussed.

Chapter 7 (Discussion) contextualises the research findings, discussing limitations of the work and utility of the materials developed. Comparisons to literature are made and novel contributions to the field are identified.

Lastly, **Chapter 8 (Conclusions and further work)** summarises the research outcomes and what has been learned, highlighting novelty. Suggestions are given for improvements to the current work, potential applications, and which avenues of research may be of most interest to explore as the field expands.

Chapter 2. Literature Review

The goal of this work is to develop inks that enable economical production of devices with embedded temperature sensing via inkjet printing. High-resolution temperature sensing techniques are discussed in the context of device miniaturisation and inkjet printing is selected as a scalable process capable of multi-material deposition. The state-of-the-art of inkjet-printed temperature sensors is discussed and sensing materials for inks are selected. Silicones are polymers ideal for temperature sensing applications due to their thermal stability, optical transparency, and electrical resistance; an overview of silicones, their crosslinking mechanisms, their use in inkjet, and potential functional composites for temperature sensing is given. Quantum dots (QD) are selected as fillers for fluorescent QD-silicone composites at low QD loadings, for the development of the first inkjet-printable polymer composites for luminescence thermometry. 3D inkjet printing of such composites could enable high-resolution, *in situ* thermal monitoring with unprecedented geometries, with anticipated applications for thermal imaging within microfluidic channels and printed electronics.

This chapter:

- Presents an overview of high-resolution thermometry techniques and their applications and identifies research niches for inkjet printed thermal sensors
- Explains the inkjet process, its requirements, and directions for development of printed thermal sensors and sensing materials
- Identifies silicones as a suitable material for thermal sensing applications, describes its properties and crosslinking mechanisms, and reviews the current state-of-the-art in inkjet printing of silicones
- Discusses functional nanofillers for silicone composites for the formulation of electrical and luminescence-based temperature sensing inks
- Selects quantum dots (QD) as a fluorescent component for their intrinsic temperature dependence, describes existing QD-silicone composites, and reviews the QD-based temperature sensors reported in academic literature.

2.1. Inkjet printing as a route for integrated thermal sensing

Temperature is an important physical parameter for the calibration of numerous systems, as thermal energy has wide-ranging effects on materials properties, reaction kinetics, optonics, and biological systems. Fields such as micro/nanoelectronics, integrated photonics, and biomedicine require temperature sensing with high resolution: submicron and sub-degree resolutions are needed for the *in situ* detection of localised “hot-spots” that can arise in microdevices and for monitoring of complex biological systems, where small changes in temperature can have profound effects.^{1,2} Nanothermometry, the measurement of temperature with submicron resolution, is divided into electrical, mechanical, and optical categories.

Electrical nanothermometers use the same principles as conventional electronic thermometers, which obtain thermal measurements based on changes in the voltage, conductivity, resistance, or capacity of conductive materials; devices include thermistors, resistance temperature detectors (RTD), and thermocouples. Thermistors and RTDs use the temperature-based resistance of materials, typically metal oxides and metal wires respectively, while thermocouples consist of an electrical junction of two dissimilar conductors; the voltage across the device is temperature-dependent due to the Seebeck effect. Microthermocouples or thin-film resistors are used as probes for Scanning Thermal Microscopy (SThM). This approach offers high spatial resolution (>100 nm) and can achieve large scanning areas (hundreds of μm^2); scanning areas on the order of mm^2 are possible in theory, but area is limited by the challenge of fabricating probes at the microscale.²³

Mechanical nanothermometry uses microcantilever probes, which consist of two materials with different thermal expansion coefficients; when heat is applied, the cantilever deflects. These probes can be used for SThM, with a reported spatial resolution of 400 nm and 0.14 K thermal resolution, although the maximum theoretical resolutions are estimated to be on the order of nm and mK.²⁴

The key disadvantage of the Scanning Thermal Microscopy approach is that it is a contact, surface technique, which means that it can only collect 2D images, that it cannot collect data from internal or obscured geometries, and that measurements may be affected by heat transfer between the probe and surface. In contrast, optical nanothermometry methods are non-contact measurement techniques and may address these limitations.

Optical nanothermometry comprises a range of techniques, including interferometric, which uses temperature-dependent changes in optical pathlength of transparent materials;

spectroscopic, such as scanning Raman thermal microscopy; and luminescent, which relies on materials with fluorescence that changes with temperature. Interferometric techniques are capable of submicron and subdegree resolution, but require transparent materials;²⁵ thermoreflectance microscopy methods, where material reflectivity changes with temperature, have achieved mK thermal resolutions with submicron spatial resolution, though the approach is limited by the lack of literature values for thermoreflectance coefficients.^{26,27} Both are surface measurements, limiting data collection to 2D imaging.

Spectroscopic methods examine emission from materials as a function of temperature and are theoretically universal techniques. Scanning Raman thermal microscopy examines the vibrational modes of bonds that are affected by structural changes associated with heat. In practice, the specifications for Raman modes limit the number of compatible materials; it is most commonly used for characterisation of GaN transistors.²⁸ The typical resolutions achieved using this method have been 10 °C and 1 µm,^{28,29} with 5 °C being the highest thermal resolution reported.³⁰ Pyrometric and infrared thermometry measure the electromagnetic radiation emitted as materials are heated and are compatible with all materials. However, these techniques are limited to 2D imaging and require long wavelengths (>1 µm), which limits the spatial resolution (5-30 µm) and necessitates expensive infrared detectors.¹

Luminescence nanothermometry requires materials with temperature-sensitive fluorescence but is capable of 3D thermal imaging; spatial resolution is limited by the emissive species size and the data collection method, and subdegree thermal resolutions are achieved. This may enable non-invasive *in situ* measurement of systems with submicrometer resolution and capacity for 3D image reconstruction.¹ However, this approach requires specific materials under constant excitation from illumination sources.

Each of these types of nanothermometry have their own niche and applications in which they are most effective. In brief, mechanical and electrical nanothermometry are capable of the highest spatial resolutions and subdegree thermal resolutions but are contact measurements which are not suitable for non-invasive *in situ* temperature measurements. Interferometric techniques also achieve subdegree temperature resolution but are surface measurements that are only suitable for transparent materials; Scanning Raman thermal microscopy similarly has specific material requirements that limit its use, primarily to measurement of GaN transistors, with the lowest thermal resolution of the techniques listed. Pyrometric and infrared techniques are compatible with all materials but have the

lowest spatial resolution of the techniques listed due to the long wavelengths emitted. Luminescence nanothermometry is capable of 3D image reconstruction and is suitable for temperature monitoring within enclosed systems with submicron and subdegree resolutions, although specialised materials are required; spatial resolutions on par with confocal microscopy are achievable with subdegree thermal resolution. For applications which do not require planar imaging nor spatial resolution $<30\ \mu\text{m}$, microsensors or optical fibres may be embedded into systems to enable sensing within enclosed systems, although microsensors are expensive to manufacture.

The drive towards device miniaturisation in electronics, optonics, and chemical and bio-analysis raises a corresponding need for non-invasive, *in situ* thermal sensing for accurate calibration and analysis during device operation.^{3,4} For instance, within the fields of microfluidics and lab- or organ-on-a-chip, integrated sensors eliminate the need for manual sample collection, which is time-consuming, requires large working volumes, and can disturb the system.⁵ Suitable strategies for temperature monitoring within these enclosed systems are therefore limited to electrical or luminescence thermometry with integrated sensing materials, or to embedded microsensors. However, direct sensor integration is challenging via conventional manufacturing: device fabrication is greatly complicated by multi-step processes, heat treatments, and material compatibility. In contrast, inkjet printing (IJP) is a direct writing technique which can produce electrodes and sensors on a range of substrates at low temperatures with high spatial resolution (typically $20\text{-}50\ \mu\text{m}$),⁶ which facilitates iterative design and reduces production time and cost. IJP has become an attractive manufacturing process for end-use products (including electronics,^{8,9} chemisensors,¹⁰ and microfluidics¹¹) due to its capacity for multi-material deposition and the geometric freedom inherent to additive manufacturing techniques.^{7,12}

The inkjet printing process and its formulation requirements are elaborated on below, with a focus on potential inks to enable non-invasive *in situ* thermal sensing to be integrated into printed devices. As discussed in more detail below, almost all current inkjet-printed temperature sensors use electrical sensing materials and fail to meet requirements for spatial resolution, in addition to having limited capacity for embedding in complex geometries or for planar sensing. The following sections will explore the research gaps and identify classes of materials of interest for this application and discuss their compatibility with inkjet printing to guide formulation of novel inks.

2.1.1. The inkjet printing process

Material jetting is defined by ISO/ASTM 52900 as "an additive manufacturing process in which droplets of build material are selectively deposited".³¹ Of this class of manufacture, inkjet printing is by far the best established process. In conventional inkjet printing (IJP), low viscosity inks ($<40 \text{ mPa s}$)³² are jetted through a nozzle; the stream spontaneously separates into 10-150 μm diameter droplets due to Plateau-Rayleigh instabilities.⁶ Similar processes which enable higher viscosity jetting include piezo-pneumatic jetting and electrohydrodynamic printing (EHD). Figure 1 below shows process diagrams of conventional IJP and of 3D printing (3DP) using the photopolymerisation-based Stratasys PolyJet process: droplets are deposited and solidify to form shapes layer-by-layer.

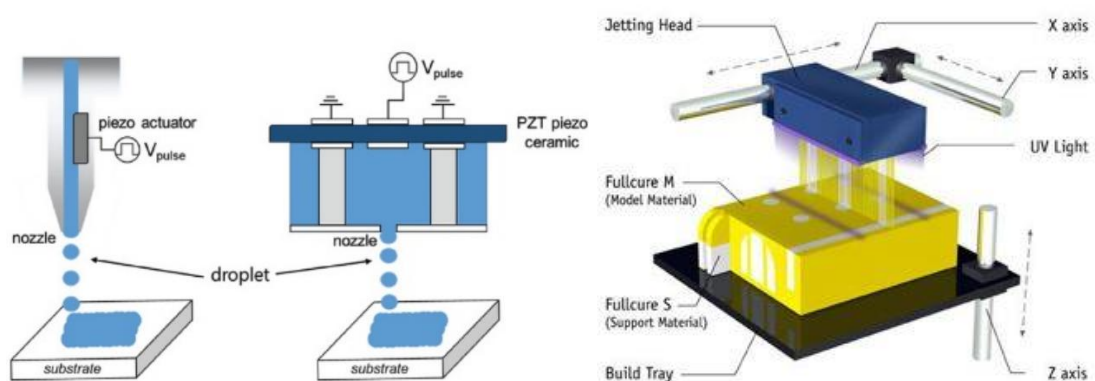


Figure 1: Left: Inkjet printing using piezoelectric actuators for drop-on-demand inkjet. Reproduced from Chung *et al.* 2019.⁹ Right: Multi-material IJP of photo-curable inks to produce 3D shapes via the Stratasys PolyJet process. Image taken from Wikimedia Commons (Projetbiblio800.jpg by user Bibliolmpression).

Conventional inkjet (hereafter referred to as inkjet) is compatible with a diverse variety of material classes and is therefore advantageous for production of parts requiring multiple or functionally graded materials.⁷ Inkjet printing enables mask-free deposition of materials with low material waste and high resolution: drop-on-demand IJP can deposit drops on the order of picolitres or less, which has led to use in high-throughput materials development. These properties are ideal for the deposition of fine, high-value sensing materials for temperature sensing. While other material jetting processes may be used, inkjet printing is most economical and offers higher repeatability than EHD printing and higher resolution than piezo-pneumatic jetting. As inkjet is scalable and capable of multi-material deposition onto a wide range of substrates, it is used as a route to functional devices and could streamline manufacture of devices with embedded temperature sensing features.⁷

Inkjet printing is divided into two types: continuous inkjet (CIJ) and drop-on-demand (DOD). In CIJ-type inkjet, inks are continuously ejected and field plates are used to control drop trajectory; drops are directed to a catcher for recycling when no deposition is required. CIJ

achieves higher drop velocities but resolution is typically lower than for DOD (typically 100 μm , compared to 20-50 μm)⁶ and ink recycling can lead to issues with contamination, thermal cycling, and solvent evaporation. DOD-type inkjet is more widely used: drops are generated as required by thermal or piezoelectric actuators, which leads to low material waste, though nozzle clogging may occur when the printhead is inactive. The vast majority of IJP for materials science has utilised DOD;⁶ henceforth, ‘inkjet’ refers to DOD inkjet.

A wide variety of materials are inkjet printable including polymers, biomaterials, and metal, metal oxide and carbon nanomaterial suspensions,³³ with applications in biomedical and electronic devices, but the materials portfolio of optimised inks is limited by stringent rheological requirements, as summarised in a key paper by Derby *et al.*⁶

The printability indicator Z - also known as the inverse Ohnesorge number Oh^{-1} - is used to identify the range of stable droplet formation, as defined in Equation 1 below. This dimensionless parameter relates inertia, surface tension, and viscosity: the Reynolds number is the ratio of inertial forces to viscous forces, while the Weber number relates the inertial forces to surface tension. Stable jetting is seen for Z parameters between 1 - 10.⁶

$$Z = Oh^{-1} = \frac{\sqrt{\rho\sigma L}}{\mu} = \frac{Re}{\sqrt{We}}$$

Equation 1: Printability Indicator Z , where Oh , Re , and We are the Ohnesorge, Reynolds and Weber numbers, and ρ , η , σ , and L are density, dynamic viscosity, surface tension, and nozzle diameter respectively.

The jetting regime is plotted on a chart of Reynolds number versus Weber number in Figure 2 below. The printable region is found where $1 < Oh^{-1} < 10$. Where We is high and Re low (i.e. $Oh^{-1} \leq 1$), inks are too viscous for jetting (Rayleigh instabilities are resolved by viscous dissipation) and a continuous stream is seen, as in material extrusion. Where We is low and Re high (i.e. $Oh^{-1} \geq 10$), inks are too thin, leading to satellite droplets. Drop ejection is not observed for $We \leq 4$, due to insufficient energy for drops to overcome the energy barrier of the liquid/air surface tension at the nozzle. Lastly, flow from when drops contact the substrate must be considered: ordered printing requires that inks form single, individual drops. For smooth, flat substrate surfaces, splashing is seen where $We^{1/2}Re^{1/4} \geq 50$. Further parameters, as related to 3DP, are discussed by Guo *et al.* 2017.³³

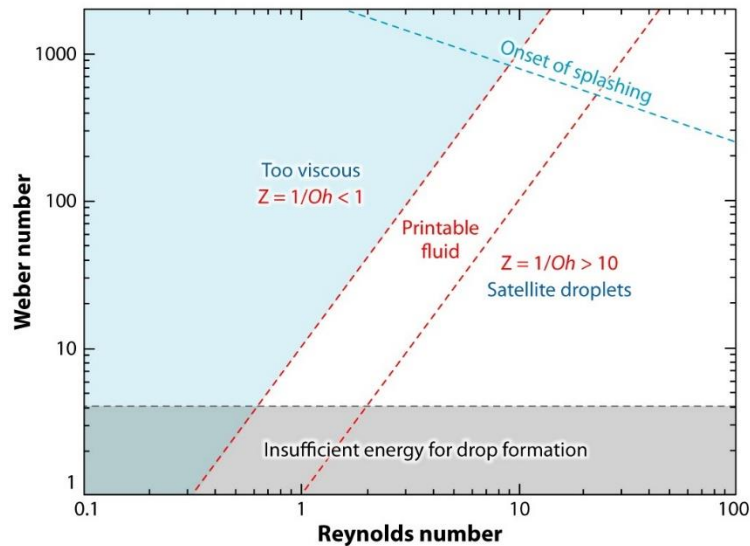


Figure 2: Parameter space of the jetting regime, plotted as Reynolds number versus Weber number. Reproduced with permission from Derby *et al.*⁶

There are five stages of jetting: droplet ejection, droplet flight, droplet impact, droplet spreading, and droplet solidification. In brief, material is ejected from the nozzle and falls as droplets. Upon impact with the substrate, these spread and solidify via cooling, solvent evaporation, or chemical reaction such as photopolymerisation.

As stated earlier, ejection occurs when the surface tension energy barrier at the nozzle is overcome. Nozzle blockage is a noted problem in DOD inkjet: during inactive phases, ink does not circulate and may thicken and clog the printhead. Solvent evaporation is a leading cause of this as solvents are often required to obtain the correct fluid parameters. Colloidal suspensions of particles are also associated with nozzle failure: if not well-dispersed, particle aggregation and/or sedimentation occur which block the nozzles. The diameter of particles should not exceed 5% of the nozzle diameter.³⁴ Regular cleaning cycles and spitting and tickle pulses may be used to minimise latency, deviating jets, and blockage.

Droplet flight and impact are determined by surface activity of the ink, but also the distance from - and choice of - substrate. Flight time should ensure that drops impact the substrate with the correct velocity and do not have excess kinetic energy. Splashing may arise with low surface tension, contact angle, or viscosity; bouncing, with high. There is also a possibility of inks solidifying prematurely during long flight times due to cooling, solvent evaporation, or excessively rapid reaction. Substrates should be selected for the correct surface energy to give an intermediate contact angle with the ink for ideal droplet pinning, film formation, and printing resolution.

As inks are subjected to high shear during ejection ($10^3 - 10^6 \text{ s}^{-1}$),^{34,35} inks with Newtonian properties are ideal as their viscosity is independent of shear rate, leading to consistent fluid behaviour during jetting. Long polymers and concentrated particle dispersions show non-linear behaviour, and it may be difficult to optimise printability as their behaviour during or after ejection deviates. However, some non-linear character can be beneficial for printing, where inks are ejected with trailing filaments called ‘tails’: Newtonian inks with long tails tend to break up into satellite droplets due to Rayleigh instabilities, whereas tails do not destabilise in weakly viscoelastic inks, and instead elastically retract to re-join the head.⁶ It is standard practice, and often sufficient, to optimise the jetting waveform and voltage to reduce or eliminate tails, though viscoelastic character can be achieved by adding a low concentration of polymer with suitable chain length if required.

As shown in Figure 3, there are two regimes for drop impact, which occur above and below the critical Weber number, respectively: impact-driven, where behaviour is inertia-dominated and drop velocity is important; and capillarity-driven, where capillary forces dominate and drop velocity is unimportant. Additionally, two viscosity-related regimes are noted – inviscid and viscous – which describes resistance to spreading. In DOD inkjet, substrate interaction is impact-driven and inviscous: the schematic sequence of drop impact and spreading in a typical DOD ink droplet is shown below in Figure 4.

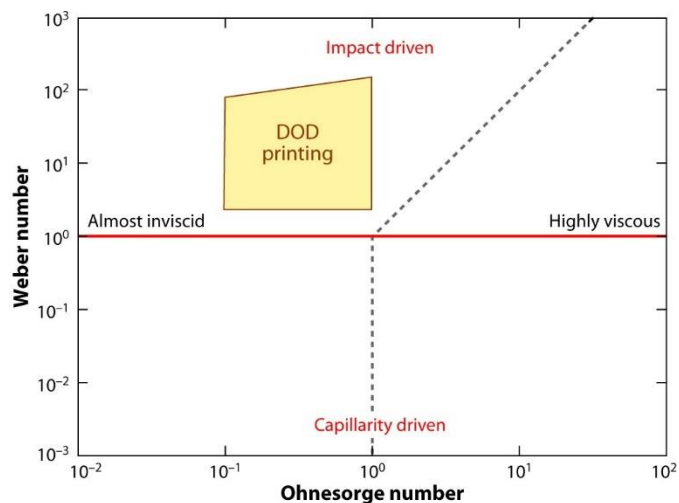


Figure 3: Parameter space of drop impact, plotted as Weber number versus Ohnesorge number. Reproduced with permission from Derby *et al.*⁶

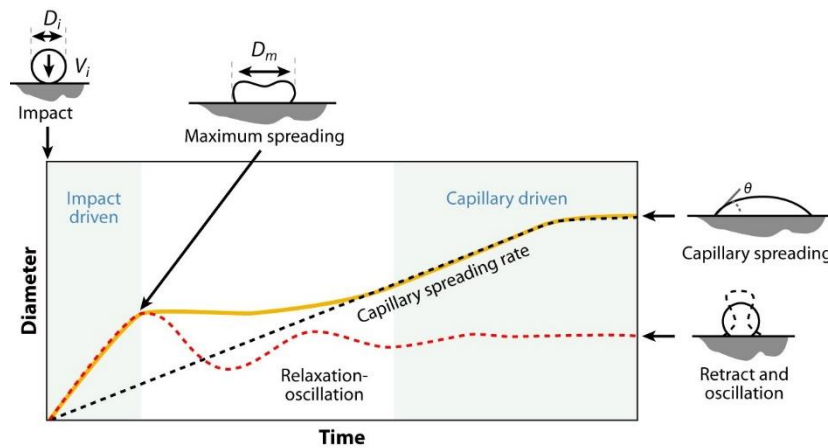


Figure 4: Schematic sequence of ink behaviour following drop impact with substrate in DOD inkjet. Reproduced with permission from Derby *et al.*⁶

Contact pinning is important for coalescence of overlapping drops into beads, lines, and layers. The contact angle of the ink on the substrate determines sessile drop shape and diameter: after impact, a droplet spreads to a static advancing contact angle; where drops contact other drops, flow reversal may occur with receding contact angle. Contact angle hysteresis is needed for stable line formation, which is defined by three parameters, as shown in Figure 5 below: drop spacing, static advancing contact angle, and print speed.

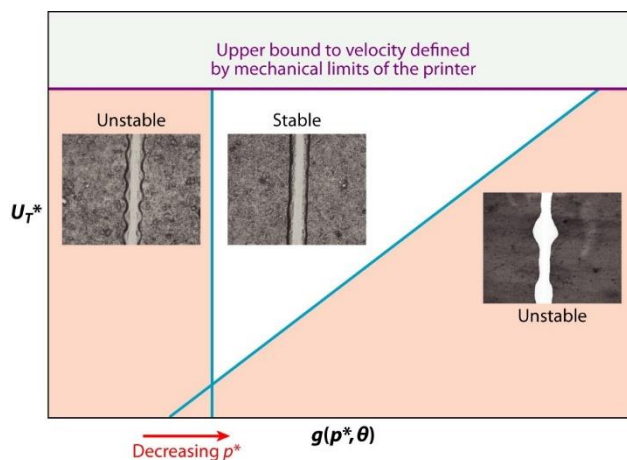


Figure 5: Stable line formation parameter space, plotted using dimensionless parameters: drop spacing as a function of static advancing contact angle $g(p^*, \theta)$ against print speed U_T^* (specifically, the traverse velocity of the printhead relative to the substrate). Reproduced with permission from Derby *et al.*⁶

In inks containing a large volume of solvent, the Marangoni effect may be observed. As evaporation is fastest at the edge of a droplet, solute is deposited there and forms a pinned contact line. Ink flows from the centre of the drop outwards to replenish the fluid at the contact line; this leads to an uneven, ‘coffee ring’ pattern of material deposition. As conductive and fluorescent fillers are needed for inks for temperature sensing materials, as discussed below, this can make even deposition challenging, affecting sensor performance.

2.1.2. Inkjet-printed temperature sensors

The vast majority of inkjet-printed temperature sensors reported are resistance temperature detectors (RTDs) or thermistors, both of which measure electrical resistance as a function of temperature. RTDs are a popular choice for printed temperature sensors due to their accuracy, response time, and simple fabrication;¹³ this has led to the development of wearable temperature sensors which can be made using economical inkjet printing processes.^{14,15} Resistance-based sensing materials for inkjet typically require post-processing heat treatments at around 150 °C and include silver,^{13,16,36–38} nickel oxide,³⁹ carbon nanomaterials,^{40–42} and PEDOT:PSS polymer.^{40–42}

A few variations of device designs for inkjet-printed RTDs are reported. For example, Dankoco *et al.* deposited organic silver ink to produce a meander-line structure RTD with 0.223 % C⁻¹ sensitivity between 20-60 °C; the wearable patch had dimensions of 2.85 x 2.26 cm.¹³ Bali *et al.* produced a fully inkjet-printed Wheatstone bridge sensor using a carbon nanoparticle ink (positive temperature coefficient, PTC) and a PEDOT:PSS ink typically containing 10 wt% dimethyl sulfoxide (negative temperature coefficient, NTC). The bridge sensor was around 2 cm² in size and had a sensitivity of 4 mV C⁻¹ between 20-70 °C; the PTC and NTC sensing materials had sensitivities of 0.0022 and 0.0025 % C⁻¹, respectively.⁴¹ In a departure from the typical conductive inks used for temperature sensing, Tao *et al.* fabricated an 8 cm² IJP sensing array by depositing an ionic liquid onto paper substrates with 25mm² pixel sizes. Temperature changes were measured between 25-45 °C as a function of conductivity of the ionic liquid-impregnated cellulose fibres.⁴³ This is the first report of a fully-inkjet printed sensor capable of planar thermal imaging, although the spatial resolution demonstrated was limited to 1 cm².

Aside from resistance-based devices, a few other sensing mechanisms are explored in literature of IJP temperature sensors. Vena *et al.* produced a split ring resonator RFID sensor using a conductive silver ink and a resistive PEDOT:PSS ink containing single walled carbon nanotubes.⁴⁰ Split rings were 18.5 mm² in size and required a planar substrate; the need for visibility makes this approach unsuitable for conformal or obscured geometries. Wang *et al.* proposed a pyroelectric temperature sensor based on a web-shaped silver electrode by depositing a zinc oxide ink and a silver ink onto an aluminium substrate.⁴⁴ However, the zinc oxide was annealed at 500 °C, which is not ideal for fully printed devices where materials or components may be degraded at such a high temperature.

While typical existing inkjet-printable temperature sensors are well-suited for wearable sensors, they do not fulfil requirements for miniaturisation: sensors are typically on the

order of cm^2 in size and sensing areas tens of mm^2 , which greatly limits spatial resolution and capacity for planar or 3D imaging.^{14,15} The thermal coefficient of resistance of inkjet-printed materials is currently limited to 0.1-0.3 % C^{-1} , with one exception: the thermistor-like sensor by Trudeau *et al.* Trudeau *et al.* produced a fully inkjet-printed bolometer (a device which measures the intensity of incident electromagnetic radiation) consisting of silver interdigitated electrodes and an 8mm^2 perovskite layer for absorption.¹⁶ The resistance of the device increases by six orders of magnitude from 17 to $36\text{ }^\circ\text{C}$, showing polymer PTC thermistor-like behaviour; however, this is below body temperature and therefore unsuitable for a range of biological applications and other applications requiring a wider or higher temperature range.

In summary, IJP resistance-based thermal sensors have limited spatial resolution and do not achieve sub-degree thermal resolution in the physiological range, which is a barrier to their use in microdevices and in cell culture and biomedical applications. Novel inks for luminescence nanothermometry could meet the requirements for such niche applications. Materials with fluorescence compatible with temperature sensing have included organic dyes and inorganic nanomaterials,^{1,2} both of which may be inkjet printed if inks are formulated to meet the rheological requirements of jetting. These functional species require a carrier medium to enable ink deposition and solidification to securely position the printed sensing material; while solvents are effective diluents, achieving uniform film formation may be challenging and the sensing material is likely to require sealing to immobilise it and/or protect it from degradation and environmental factors.

Given that sensing materials are commonly sealed by glass or polymer layers, an ink formulation strategy utilising polymer composite inks can efficiently deposit and isolate sensing materials in tandem. The polymer matrix can provide processability, better enable 3D printing geometries, and improve dispersion and stability of the fluorescent species.^{21,22}

For thermal sensing, it is imperative that the material is stable within the operating conditions and thermal range, resisting both thermal and photo-aging. Candidates for LED encapsulants have similar material requirements to optical thermosensors due to the heat generated at the junction ($\sim 120\text{ }^\circ\text{C}$ junction temperature in white LEDs⁴⁵). Encapsulants are selected for “good chemical resistance, high resistance against UV radiation, high refractive index, strong adhesion and bond strength, good mechanical strength, and stable microstructure”⁴⁶; typical polymers are polycarbonate (PC), acrylates (i.e. PMMA), epoxy resins, and silicones, as summarised in Table 1. In brief, PC is limited by its lower

transparency, PMMA its poorer heat and moisture resistance, epoxy resins their poorer UV resistance, and silicones their lower refractive indices and poorer processability. As silicones have the greatest stability against heat and UV light, the intended working conditions for the sensing material, they are best suited to luminescent thermometry.

*Table 1: Relative performance of common polymeric LED encapsulants, as described in Yazdan Mehr *et al.*⁴⁶ Typical refractive indices are listed; optical formulations may achieve higher values.*

	PC	PMMA	Epoxies	Silicones
Thermal and chemical stability	Good	Poor	Excellent	Excellent
Moisture resistance	Good	Poor	Excellent	Excellent
UV resistance	Good	Excellent	Poor	Excellent
Optical transparency	Good	Excellent	Excellent	Excellent
Refractive index n_D^{25}	Excellent 1.59 ⁴⁷	Good 1.49 ⁴⁸	Excellent 1.50-1.56 ⁴⁹	Poor-Good 1.40-1.50 ¹⁷
Mechanical properties	Excellent	Good	Good	Good
Cost of manufacture	Good	Excellent	Excellent	Poor

In summary, ideal polymer matrices for luminescence nanothermometry have: high transparency at excitation and emission wavelengths of the functional species; high refractive index for maximum light extraction, and high thermal stability. These specifications overlap with those of polymers for LED encapsulation; of these polymers, silicones are the material of choice for microfluidics⁵⁰ and are also known to enhance temperature sensitivity in IJP thermal sensors due to thermal expansion.¹⁴ Therefore, the following section discusses the properties and reaction mechanisms of silicones in detail to contextualise silicone IJP in literature and to identify promising formulations for inkjet-printable composite materials for integrated nanothermometry.

2.2. Silicones

Silicones - also known as polysiloxanes - are semi-inorganic, amphiphilic polymers that consist of $-\text{Si}(\text{R}_2)\text{O}-$ repeating units. The most industrially-important silicone fluid is poly(dimethylsiloxane) (PDMS), in which the R groups are methyl groups.^{17,51} The Si-O backbone is flexible and thermodynamically stable, which gives rise to properties distinct from hydrocarbons. Silicones are ideal for use in electronic or optical temperature sensing applications due to their thermal stability, electrical insulation, high refractive index, and optical transparency at UV and visible wavelengths. The low surface energy of silicones also leads to good biocompatibility, which makes them suitable for non-invasive temperature monitoring of biological and microfluidic systems. Silicones are processible via inkjet and therefore compatible with inkjet-printed sensors; a range of printable silicone formulations are known for inkjet and Additive Manufacturing (AM) as a whole, and their elastic properties are desirable for the AM material portfolio. A number of functional composites can be prepared using silicone matrices which have applications in flexible electronics and lighting, both of which may be utilised for temperature sensing applications.

2.2.1. Properties of silicones

The Si-O bond is polarised and is stabilised by the difference in electronegativity between the two atoms; the bond energy is 443-452 kJ mol⁻¹ with 40% ionic character.⁵¹⁻⁵³ The ionic nature of the bond is reflected in its reactivity: the siloxane backbone is very stable against homolytic scission, and less so against heterolytic.⁵² Overall, this strong bond leads to chemical inertness, temperature stability, and radiation resistance.

The polar polymer backbone is shielded by apolar organic constituents, i.e. methyl groups in PDMS; intermolecular forces between pendant methyl groups are weak so there is little interaction between PDMS chains (barring entanglement), which results in hydrophobic, inviscous fluids compared to hydrocarbons. There is also little steric hindrance as the oxygen atoms have no constituents and methyl groups have a small van der Waal radius of 200 pm.⁵¹ Additionally, the Si-O and Si-C bonds are longer than the carbon-based analogues (indeed, this is the case for bonds to any given element⁵²) and the Si-O-Si bond angles wide (143 °).^{52,53} Together, this enables extreme conformational flexibility along the siloxane backbone: the energy barrier to rotation is just 2.5 kJ mol⁻¹, compared to 17 kJ mol⁻¹ in alkanes, and results in the low glass transition temperature (T_g) of -127 °C.^{51,52}

The backbone flexibility allows silicones to orient their chain groups to interface with low and high energy surfaces, and methyl groups lead to hydrophobic surfaces (water contact angle 80-110 °).^{17,51} Silicone fluids have low surface tension (approx. 20.4 mN m⁻¹) and therefore effectively wet a wide variety of materials; in PDMS, the critical surface tension of wetting (24 mN m⁻¹) is higher than their surface tension and the polymer is self-wetting, promoting film formation and adhesion.^{51,52} For these reasons, silicones are used in coatings, surfactants, and adhesives.

The low steric hindrance and the conformational freedom of silicones leads to further characteristic physical properties. Silicones have high free volume which leads to high gas permeability (60 Barrer for oxygen⁵³) and compressibility (100 x 10⁻¹¹ m² N⁻¹ in PDMS¹⁷).⁵² Conversely, transition from coiled to extended chains is facile, leading to elasticity in silicone rubbers (430-725% elongation, from a selection of commercial silicones).^{17,53} Silicone fluids have notable lubricating properties: PDMS has the lowest recorded surface shear viscosity.⁵¹ Lack of intermolecular forces between chains leads to low viscosity in short chain PDMS (i.e. below 21000-33000 g mol⁻¹, corresponding to approximately 1000 mPa s viscosity⁵³) in comparison to hydrocarbons, and with lower temperature-dependence as the activation energy for movement is lower. Increased viscosity in higher molecular weight (MW) PDMS is associated with chain entanglement.^{17,52}

Silicones are of interest as biocompatible elastomers: their low surface energy is in the range of interest to prevent cell adhesion (20-30 mN m⁻¹).⁵² This results in low adhesion (26.6 times lower than for PTFE),⁵⁴ which is antifouling and prevents colonisation. The chemical inertness of silicones results in non-toxicity and biodurability, while their hydrophobicity ensures that they are insoluble in the body and do not absorb moisture and swell.⁵⁵ However, their open volume does allow gas-permeability and drug-permeability, making them attractive exchange and delivery matrices.⁵⁵ Lastly, their low T_g, high thermal stability, and high radiative and oxidative stability enable silicones to withstand cold storage and sterilisation procedures.⁵⁵

Silicones are used for potting agents, wire insulation, and sealants in devices as they are thermally and electrically insulating. They are also noted for their optical and UV transparency down to ~240 nm,⁵⁰ which leads to applications in optical fibre coatings and lighting encapsulants. The refractive index (RI) of PDMS is n_D^{20} 1.39 and may be increased to 1.43-1.47 by incorporation of phenyl pendant groups, although this reduces UV transparency.¹⁷ The high RI value and transparency is of use for lenses, waveguides, contact

lenses, optical coatings, and LED encapsulation.^{17,55} Silicones are particularly important in microfluidics: PDMS is the most commonly used elastomer in production of microfluidic devices.⁵⁰

Table 2: Selected properties of linear PDMS fluids with 600-62000 g mol⁻¹ average mass;¹⁷ where values change as a function of chain length, the value range is given from low to high mass.

Property	Value for PDMS fluids
<i>Density (25 °C), g cm⁻³</i>	0.90-0.97
<i>Surface tension, mN m⁻¹</i>	19.3-21.5
<i>Viscosity (25 °C), mPa s</i>	3-12500
<i>Viscosity-temperature coefficient</i>	0.55-0.61
<i>Refractive index, n_D²⁵</i>	1.390-1.404
<i>Dielectric constant (25 °C, 50 Hz)</i>	2.5-2.8
<i>Dielectric strength, kV mm⁻¹</i>	13-15
<i>Resistivity (25 °C), Ω cm</i>	2 x 10 ¹⁴

Some key physical properties of silicones are summarised above in Table 2. Overall, silicones have properties that are distinct from hydrocarbon polymers; their thermal, electronic, and optical properties make silicone a suitable material for temperature sensing applications, and the rheology of PDMS fluids is compatible with formulation for inkjet.

Silicone elastomers consist of crosslinked networks and are thermoset, meaning that they are not melt-processable. While silicone elastomers do have limited solubility in compatible solvents, such solutions need to be dilute to meet the viscosity limit for inkjet and this limits the polymer deposition rate. Higher solvent loadings also require time to dry and may be associated with uneven film formation and/or disturb the preceding layers; additionally, there may be material compatibility issues in devices requiring multimaterial deposition, which is exacerbated by higher solvent loadings. In order to achieve efficient inkjet printing of solid silicone elastomers, reactive silicone macromers are used to meet processability requirements for inkjet. The next section presents an overview of cure systems for silicones and assesses their utility for inkjet-printed sensors.

2.2.2. Silicone cure systems

Silicone crosslinking reactions can broadly be divided into two classes: addition cure, where two molecules combine to form a single adduct; and condensation cure, where two molecules combine to form a product and eliminate a simple by-product. Addition reactions of silicones are subdivided into radical-based reactions and metal-catalysed reactions. This comprises the three well-known cure systems for silicone rubbers: condensation, hydrosilylation or addition, and radical.

Condensation

Hydroxy-functional silicones react with hydrolysable silane crosslinkers to form elastomeric networks, as shown in Figure 6 below; tin or titanium catalysts are used to enhance cure. As linkers react with water, this system is also known as moisture cure. Hydrolysis proceeds via nucleophilic acyl substitution, resulting in the elimination of volatile organic compounds which may be acidic, neutral, or basic; this leads to significant shrinkage (3 vol% compared to 0 vol% for hydrosilylation) and to byproduct leaching.⁵⁶

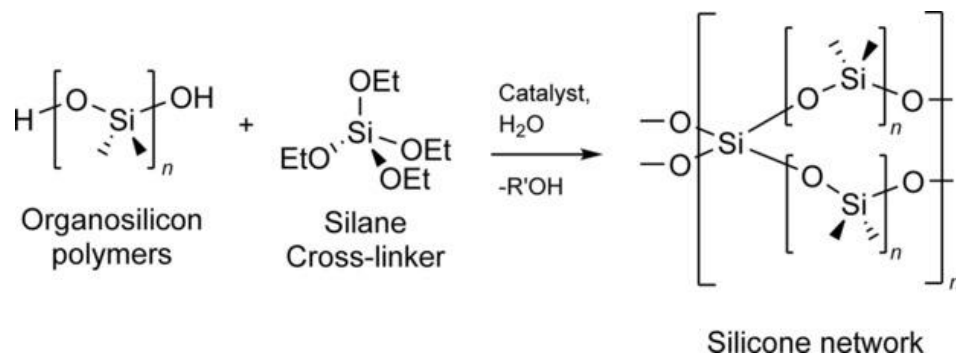


Figure 6: Condensation curing of a typical silicone formulation. Reproduced with permission from Wang *et al.*⁵⁶

Both 1-part and 2-part room temperature vulcanisation (RTV) formulations are known. 1-part RTVs contain excess crosslinker, which leads to formation of silicones with reactive end groups; when the container is opened and exposed to atmospheric water, these crosslink to form an elastomeric network and cure from the surface inward.¹⁷ 2-part RTVs contain alkoxy crosslinkers, which require tin catalysts. The selectivity of the catalytic mechanism ensures reaction of the hydroxy terminals, even in the presence of excess crosslinker, leading to even cure.¹⁷

Addition

Hydrosilylation is the addition of silicon hydrides to multiple bonds; in the context of silicone rubbers, the typical system consists of short hydride-functionalised silicone crosslinkers (poly(methylhydrosiloxane), PMHS) and longer vinyl-terminated PDMS chains (also written as α,ω -divinyl PDMS, where α and ω denote polymer chain terminals). The molar ratio of the functional groups is important in determining the properties of the cured polymer.^{17,57} No by-products are produced during reaction, leading to minimal leaching and shrinkage; this is useful for size-control and biomedical applications. Hydrosilylation may be thermally-activated – and is sometimes known as thermal or heat curing – though metal catalysts are commonly used to enable 2-part RTVs,¹⁷ as shown below in Figure 7.

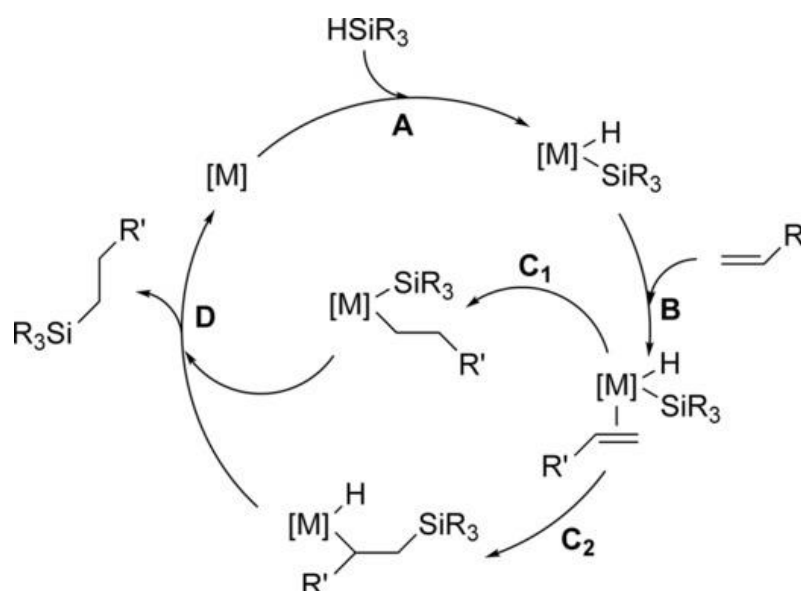


Figure 7: Metal-catalysed hydrosilylation of olefins via the Chalk-Harrod mechanism. Platinum catalysts follow the C_1 pathway and addition is anti-Markovnikov. Rhodium catalysts follow C_2 . Reproduced from Wang *et al.*⁵⁶

Platinum catalysts are by far the most widely used^{17,56} and therefore 2-part RTVs may be known as platinum-cure: platinum catalysts have sufficient selectivity, catalytic activity, and stability against heat, oxygen, and moisture, that inert conditions are not needed. A brief discussion of types of platinum catalyst can be found in Wang *et al.*⁵⁶ Catalysis of hydrosilylation is efficient, often requiring only a few ppm of catalyst for effective curing,¹⁷ and the reaction rate can be varied over a wide range using catalyst concentration, temperature and inhibitors. However, the catalyst is poisoned by a wide range of chemicals; residual catalyst may also lead to yellowing and poor biocompatibility.⁵⁶

Radical

There are two common types of radical-based crosslinking in silicones: thermally-induced peroxide crosslinking and photo-induced polymerisation. For the former, peroxides undergo thermal decomposition at 150-200 °C and the O-O bond breaks (homolysis) to form reactive radicals.^{17,56} Diaryl peroxides are used for pressureless crosslinking and decompose at 60-90 °C, but produce carboxylic acid by-products while dialkyl peroxides do not. A simple scheme is shown below in Figure 8 for the crosslinking of unmodified PDMS using a diacyl peroxide, where the primary radical undergoes β -scission to produce a secondary carbon radical.

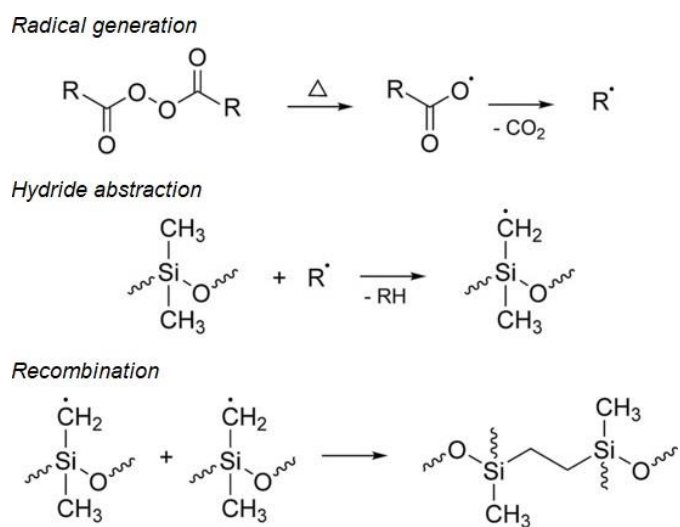


Figure 8: Thermally-induced crosslinking of PDMS using a diacyl peroxide initiator. Adapted from Wang *et al.*⁵⁶

Silicone fluids are modified with reactive, unsaturated moieties to control crosslinking density: a typical formulation contains 0.003-2 wt% methylvinylsiloxy groups.¹⁷ Hydrogen is abstracted from either a methyl group or a vinyl group to produce a silicone macroradical and a hydrocarbon by-product from the peroxide, which is removed post-curing. Reaction is terminated when two radicals combine: in vinyl-functionalised silicones, a combination of methyl-methyl, vinyl-vinyl, and methyl-vinyl crosslinks are seen in cured products.

Alternatively, UV curable silicones can be formulated by modification with photopolymerisable functional groups such as epoxide, vinyl, acrylate, and thiol groups. Acrylate moieties are the most commonly used functionality in UV curable silicone formulations due to rapid curing at ambient temperature without the need for solvents, which can enable higher printing resolutions.⁵⁶ While reaction proceeds rapidly via free radical chain growth, the radicals produced are oxygen-sensitive: in industrial coating applications, oxygen levels are maintained at 50 ppm or lower to prevent inhibition and ensure that high conversion - and the desired mechanical properties - are reached.⁵⁶

Thiol and vinyl moieties can be used together to formulate photopolymers which do not require an inert atmosphere. Thiol-ene reactions result in anti-Markovnikov addition of thiols to alkenes; photopolymerised thiol-ene reactions proceed via a step-growth mechanism, as shown below in Figure 9. A radical abstracts a hydrogen from a thiol group to generate a thiyl radical; in the propagation step, the thiyl radical reacts with a vinyl group to form a radical thioether bridge. This species can then regenerate the thiyl radical by hydrogen abstraction from another thiol moiety in the chain transfer step. The kinetics of the overall reaction rate depends on the ratio of the rates for propagation and chain transfer, as the slower reaction is rate limiting; when the rates are close to equal, the reaction is half-order with respect to both thiol and ene concentrations. The primary mechanism of termination is radical-radical recombination, which can lead to a variety of termination products.⁵⁸

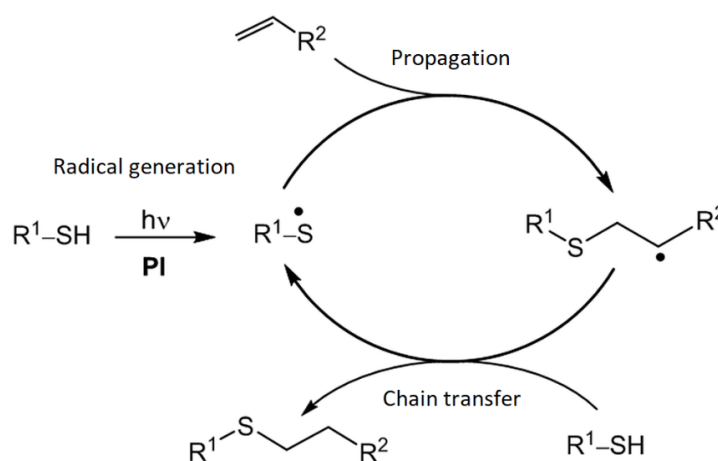


Figure 9: Radical-mediated thiol-ene reaction mechanism with photoinitiator. Image adapted from Wikimedia Commons (Photoinitiated thiol-ene coupling reaction.gif by user Nkchenjx).

In comparison to acrylate-based photopolymerisation, thiol-ene reactions offer higher conversions, low oxygen inhibition, and less shrinkage.⁵⁶ While oxygen does not significantly alter polymerisation rate, it is incorporated into polymer chains: oxygen reacts with thioether radicals to form peroxy radicals, which do not participate in propagation but do undergo chain transfer with thiols to regenerate thiyl radicals.⁵⁸ The disadvantages of thiol-ene formulations are offensive smell and reduced pot-life, as reaction proceeds spontaneously over time. As reaction occurs even in the absence of an initiator, many formulations use stabilisers to achieve suitable stability.⁵⁸

Lastly, it is also possible to formulate cationic photopolymerisable silicones using epoxide- or vinyl ether-modified silicones, rather than using radical-based photopolymerisation. Diaryliodonium or arylsulfonium salts with soft metal-halides undergo photolysis to liberate a strong Brønsted acid, which initiates cationic polymerisation (see Figure 10).

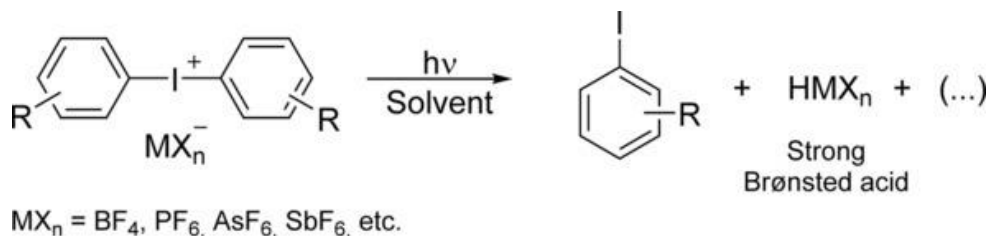


Figure 10: Photolysis of a diaryliodonium salt to produce a Brønsted acid catalyst. Reproduced with permission from Wang *et al.*⁵⁶

The reaction does not require inert conditions and can be carried out at room temperature. However, a solvent is essential by the nature of the reaction and solvation will be greatly important to reaction rate.

Considerations for inkjet and sensing

In order to be utilised as jetting inks, crosslinking reactions must proceed under the operating conditions of the printer, which are typically close to ambient. For example, the platen heating limit of the Fujifilm Dimatix is 60 °C, which is lower than the conditions required for thermally-induced peroxide crosslinking (60-90 °C for diaryl peroxides⁶) and hydrosilylation in the absence of a catalyst (around 100-120 °C for curing in solvent-free formulations⁶). Of the reactions discussed above, tin-catalysed condensation cure, platinum-catalysed addition cure, and various photoinitiated cure mechanisms meet this requirement and are feasible for ink formulation.

A further consideration to make is the generation of by-products and harsh chemicals, which can lead to material compatibility issues for device design. Poor inertness and leaching of by-products interfere with the system being measured if the material is not sealed, which limits utility for non-invasive *in situ* temperature sensing and applications requiring biocompatible materials. Functionality may also be affected by material compatibility issues with metals or semiconductors for electronic devices, or by by-products reducing the transparency of materials for optical sensing. For example, photo-induced cationic polymerisation generates Brønsted acids that are strong enough to attack glass, in addition to hydrolysing or decomposing to HF, a toxic and volatile species. The

material compatibility and handling issues make this class of photopolymers unsuitable for IJP of functional devices.

Of the remaining cure mechanisms, tin-catalysed condensation cure systems are economical but have slower curing and greater shrinkage than other silicone crosslinking mechanisms, which are detrimental for inkjet print speed and fidelity. 1-part RTV inks have poor shelflife as cure proceeds spontaneously upon contact with water, and jetting nozzles may become blocked during idle time. The reaction also produces volatile by-products which may affect the performance of a functional device. While condensation cure silicones have been used in other AM processes (see *Appendices: Silicones in alternate AM categories*), these properties make them ill-suited as the primary crosslinking mechanism for IJP of functional devices.

In contrast, platinum-catalysed addition cure systems do not produce by-products and are not associated with shrinkage. While platinum is expensive and can reduce the transparency of the cured polymer, typical catalyst loadings are on the order of 10-100 ppm. The main drawback is that the platinum catalyst is poisoned by a range of materials and contamination should be avoided during crosslinking. Addition cure systems are used for LED encapsulants and present an attractive material for optical sensors.

Radical photopolymerisable formulations based on acrylate chain growth or thiol-ene step growth are known to lead to rapid crosslinking and high conversion, which allows less time for droplet spreading; this is attractive for jetting inks as this can enable higher print resolution (smaller drop diameter), particularly on substrates that inks may wet. While acrylate photopolymerisation is oxygen sensitive and may require an inert atmosphere for efficient jetting, thiol-ene reactions are not slowed by the presence of oxygen and thiol-acrylate photopolymers benefit from this property. The photoinitiator and photo-products may cause yellowing and leach out of the cured polymer, reducing the transparency and inertness of the material, but this can be minimised through photoinitiator selection and reducing the photoinitiator loading.

In summary, addition cure and radical UV cure mechanisms are likely to be most promising for the inkjet of silicones for temperature sensing applications. The next section discusses considerations for inkjet printing of silicones and the state-of-the-art in industry and academic research.

2.2.3. Silicones in inkjet

Silicones are attractive for a wide range of applications, particularly medical devices, microfluidics, soft robotics, and electronics. Conventional manufacturing using moulds or lithography is expensive and time-consuming as there are individual fabrication steps for each part plus assembly: some intricate geometries are impossible to achieve via conventional methods and small volume production – such as for personalised medical devices – is not economically viable using moulds. Device manufacturing may require complex steps including mask alignment, sputter or spin coating, vapour deposition, and etching. Inkjet printing, a process in the Material Jetting category of Additive Manufacturing, can streamline production.

Additive manufacturing (AM) – also known as rapid prototyping (RP) and 3D printing (3DP) – selectively adds and fuses material to produce parts with controlled shapes. This enables geometric freedom, facile customisation and small batch production, minimal assembly, and low material waste: production of end-use parts is possible, which can enable economical *in situ* temperature sensors.⁷

AM categories compatible with silicones are described in detail in *Appendices: Silicones in alternate AM categories*; the majority of silicone AM uses processes that require liquid feedstocks. Of these (material jetting, extrusion, and vat photopolymerisation), inkjet printing (IJP) has the strictest requirements for fluid properties: ink viscosity is limited to $<40 \text{ mPa s}$,^{32,59} which makes achieving particular material properties difficult, e.g. elastomers with $\geq 1 \text{ MPa}$ elastic moduli require $>20 \text{ kg mol}^{-1}$ PDMS chains in the network,⁵⁷ which are on the order of 1000 mPa s .¹⁷ IJP also does not have inherent overhang support for printed geometries (unlike vat photopolymerisation where the vat provides some support), so another ink is required to deposit a sacrificial support structure if overhangs are needed, which necessitates a post-processing removal step. The resolution of inkjet printing is typically $20\text{-}50 \text{ }\mu\text{m}$;⁶ this is superior to typical material extrusion processes which use nozzles with diameters of hundreds of microns, but vat polymerisation processes can achieve sub-micron resolution. However, inkjet printing has the greatest capacity for multi-material deposition and functionally-graded materials, in addition to being compatible with a variety of materials, scalable, and having micron-scale resolution.⁷ Therefore, inkjet printing is the most suitable AM technique for the production of functional devices that consist of multiple materials and has been selected as a route to embedded thermal sensing.

In terms of inkjet, silicones have a number of characteristic qualities that need consideration during ink development. Firstly, silicones are thermoset polymers and are therefore not melt-processable. Cured rubbers and resins have limited printability; while crosslinked silicones can be dissolved in some solvents, concentration is limited by poor solubility and even dilute solutions may have viscosity too high for jetting. Therefore, crosslinking reactions are used to deposit inks which cure *in situ* to materials with desired properties. Formulation strategies such as the use of chain extenders can be used to increase the elastic moduli achievable from precursors of suitably low viscosity for inkjet.⁵⁷

Silicones have very low surface tension ($\sim 20.4 \text{ mN m}^{-1}$),⁵¹ which can cause satellite droplets and splashing. Linear PDMS is Newtonian until high molecular weight ($>21000\text{-}33000 \text{ g mol}^{-1}$, M_c^{53}), which aids ink formulation as rheological behaviour will be consistent despite the high shear forces generated during jetting. As chain length increases, viscosity increases and silicones become viscoelastic due to chain entanglement.¹⁷ Viscoelastic behaviour can help to overcome the tendency of silicone filaments to destabilise into satellite droplets during jetting due to low surface tension: this elasticity can produce ink droplets where tails re-join the head instead of separating.

The high chain mobility of silicones, in comparison to hydrocarbon polymers, makes them effective lubricants and therefore less likely to block jetting nozzles. Nonetheless, as solvents are required to lower the viscosity of reactive silicones, blockage may occur during idle time via increased viscosity resulting from local solvent evaporation. Sturgess *et al.* reported reliable, consistent jetting with no nozzle blockage during operation with cleaning cycles. Nozzles were easily cleared after a period of disuse by jetting at a higher temperature to clean the printhead.⁶⁰

Silicones are amphiphilic and able to orient pendant groups at interfaces, meaning that they wet both high and low energy surfaces, forming films on almost everything except fluorocarbopolymers.⁵¹ Drop diameters of 160-400 μm are typically achieved when jetting onto non-optimised substrates;⁶¹⁻⁶³ prudent substrate selection can enhance resolution. Sturgess *et al.* compared glass slides (untreated; spin-coated PDMS; fluoroalkylsilane-treated) and PTFE film as substrates: contact angles were 2, 15-20, 55, and 25 $^\circ$ respectively. Lower surface energy substrates were able to achieve higher resolution – drop diameters were $64 \pm 2 \mu\text{m}$ and $48 \pm 2 \mu\text{m}$ for PTFE and silane-treated glass respectively – although specialised print strategies were required to overcome poor ink pinning.⁶⁰ Mikkonen *et al.* achieved similar resolution on spin-coated PDMS on glass slides using a

1-part ink (25 wt% PDMS in octyl acetate) and obtained a 46 ° contact angle on spin-coated PDMS, compared to the 15-20 ° observed by Sturgess *et al.* for both of their 2-part inks.⁶⁴ An alternative strategy to prevent wetting is to ensure rapid curing so that ink does not have time to spread. Stieghorst *et al.* used an IR laser to accelerate curing of addition cure silicones on a range of plasma-treated, low adhesion polymer substrates. Spreading was found to decrease with increasing ink viscosity, irradiation, and substrate surface energy. Cure acceleration was therefore most beneficial for higher viscosity polymers and for relatively high energy substrates, as these took longer to reach the surface tension-dependent spreading limitation and could therefore be cured to pin droplets in place.⁶⁵

A range of commercial materials and specialised 3D printing systems for silicone exist – see *Appendix: Commercial AM of silicones* – with typical resolutions of 200-400 µm (range 100-900 µm) and Shore hardness 20-60A (range 10-90A). However, these processes have a limited range of materials; current jetting processes require proprietary UV cure silicones.

In June 2015, Wacker announced the first commercial 3D printer for silicones and the first 3D-printable silicone elastomers: ACEO by Wacker uses material jetting valves with highly viscous, UV-curable silicones. They offer printable formulations with 400 µm resolution, 20-60A Shore hardness, and 200-800% elongation at break, as well as medical grade silicones. In 2018, ACEO printed conductive silicone composites and in 2019 they opened an Open Print Lab to interface with and offer training to customers. The ACEO Imagine Series K2 printer was announced in 2019 and is set to offer multi-material printing (four materials simultaneously) and novel automatic control technology (which measures silicone layers during printing and compares to the CAD file). In 2021, ACEO added a thermoset epoxy to its material portfolio which can be used to print composites with hard epoxy and soft silicone; this enables reinforcement of silicone parts.

Shortly after Wacker announced ACEO, in 2015 Keyence announced UV cure silicone inks for its AGILISTA 3200 inkjet printer: AR-G1L and AR-G1H are soft and hard silicone rubbers respectively, with 300 µm print resolution.

The capacity for advanced materials has not been fully explored: while ACEO demonstrated jetting of a conductive silicone composite, the focus so far has been on enabling elastomers with specific mechanical properties despite the rheology requirements for inkjet. However, conductive or fluorescent composites could be effective temperature sensing materials for inkjet printing and enable non-invasive *in situ* sensing in printed devices.

Within academic literature, the majority of research has been on dispersion-based material extrusion, followed by vat photopolymerisation-based processes; material jetting and powder bed fusion-based processes are also increasingly reported. Ligon *et al.* have written a review on all polymer AM processes,⁶⁶ while Liravi and Toyserkani³² and Herzberger *et al.*⁶⁷ have produced detailed reviews of silicone AM.

Research on the jetting of reactive silicones (Table 3) has typically been towards microfluidic or electronic applications. Much of the work on silicone AM in general has primarily or solely investigated silicone elastomers, where desirable mechanical properties include high flexibility, elongation, and tear strength. As material jetting processes typically have stringent viscosity limits (<40 mPa s for inkjet³²), this limits the mechanical properties that can be achieved with inks: stronger elastomers are made with longer polymer chains – specifically, high average chain length between crosslinks – and reinforcing fillers such as fumed silica. As both are associated with high viscosity, there is a trade-off between printability and mechanical properties. Silicones are thermoset and have low temperature-dependence for viscosity compared to hydrocarbon polymers; therefore, diluents are used to dilute PDMS fluids in all inkjet printing of silicones reported.^{60–64}

The majority of inkjet printing has been carried out with 2-part addition cure RTVs; a UV curable ink formulation was investigated by McCoul *et al.*⁶³ 2-part RTVs are typically mixed to make a single ink^{61–64} as two-part inks are more complicated to deposit, requiring alignment and mix ratio calibration, and are much slower to print on printers with single printheads. However, this leads to short working time (2 hours was reported by Mamidanna *et al.*)⁶² and renders cartridges unusable after this. While Mikkonen *et al.* produced a 1-part ink with a longer shelf life, this was still limited to 48 hours.⁶⁴ Reactive drop-on-drop jetting of 2-part inks with long term stability has been demonstrated^{60,68} and allows control over mixing ratios, which can enable functionally-graded materials.⁵⁷ Silicone inkjet is capable of high resolution, typically under $50\ \mu\text{m}$ drop diameter with suitable substrate.^{60,64} Silicone inks are particularly effective for thin films, leading to high Z resolution: McCoul *et al.* produced fine membranes with 2-4 μm thickness.⁶³

There is also research into other material jetting processes, such as using jetting valves for viscous polymers, as commercialised by ACEO Wacker. Dual piezoelectric/pneumatic jetting valves have a much wider viscosity range (≥ 1 kPa s)³² and high-viscosity jetting has been explored using Nordson Pico Pulse printheads, using either reactive drop-on-drop jetting of a 2-part addition cure RTV⁶⁸ or a UV curable formulation with a dual UV/moisture cure

system.^{69,70} While resolution is lower than with inkjet – around $\geq 500 \mu\text{m}$, similar to that achieved with electrohydrodynamic (EHD)⁷¹ – piezo-pneumatic jetting valves can print 20 times faster than conventional inkjet.⁷⁰ Aerosol jetting has also been investigated: this technique has a low viscosity limit of up to 5 mPa s or 1000 mPa s, depending on the type of atomiser used.³² While thin layer thicknesses are achieved ($\leq 40 \mu\text{m}$), printing is slow with a $5\text{-}10 \text{ mm s}^{-1}$ throughput.³² Electro spray deposition has achieved 90 nm layer thickness.^{72,73}

Overall, inkjet has been demonstrated to be a viable route to cured silicone elastomers - despite the rheology limits ($< 40 \text{ mPa s}$ viscosity in standard printers³²) - by a number of groups. The research has typically been towards applications that are systems of interest for embedded temperature sensors, namely microfluidics and electronics, which suggests that a sensing ink would be well-utilised in these printed devices.

Of the material jetting processes investigated for silicones, inkjet is capable of the highest spatial resolutions. While piezoelectric/pneumatic jetting valves deposit materials with much higher viscosity ($\geq 1 \text{ kPa s}$)³² and electro spray deposition can deposit films with around 100 nm thickness, the spatial resolution of inkjet is the best suited for embedded sensors within printed devices. Silicone IJP has been demonstrated with print resolutions $< 50 \mu\text{m}$ (roughly 10x smaller than that achieved with piezo-pneumatic valves), and inkjet is scalable with capacity for multi-material deposition,⁷ ideal for printing functional devices.

Print resolution $< 100 \mu\text{m}$ has required substrates with surface energy close to that of silicones ($\leq 20 \text{ mN m}^{-1}$),¹⁷ which may complicate material compatibility for devices. Strategies for controlled deposition on a variety of materials could include minimising droplet spreading by achieving fast cure rates using UV cure silicones or IR lasers to accelerate hydrosilylation.⁶⁵ Alternatively, a thin film could coat the surface to produce a silicone substrate for printing, as has been demonstrated with 2-4 μm thickness.⁶³

Solvents have been used in all reported silicone inks but may lead to material incompatibilities in devices and affect the physical properties of the polymer. The solvents used are flammable and volatile, with the exception of octyl acetate,^{60,64} which is non-hazardous. If elasticity is not a desired property, solvent-free inks with shorter macromers and/or higher crosslinking density may be viable, particularly using radical polymerisation to achieve high conversion.

While not yet explored in academic research of IJP, silicones may form composites that are suitable for temperature sensing; such materials are discussed in the next section.

Table 3: Direct additive manufacturing of bulk silicones via material jetting in academic research.

<i>Paper</i>	<i>AM category</i>	<i>Application</i>	<i>Printer set-up</i>	<i>Silicone</i>	<i>Resolution</i>
Stieghorst <i>et al.</i> 2016 ⁶⁵	Material jetting (hypothetical; drop-casting using material extrusion)	Medical implants using IR curing	Arduino-controlled XY gantry and step motor, dispensing system with 200 μm nozzle diameter, ULR-25 9.3 μm laser	Wacker Silpuran 2430 or Dow Corning Sylgard 184	Minimum 3.24% spreading, 2 s cure time, penetration depth 1.67-1.71 μm , Drop diameter 1924-2720 $\mu\text{m} \pm \leq 10\%$ Drop volume 1.85-2.11 μL
Peng <i>et al.</i> 2017 ⁶¹	Material jetting (Inkjet printing (IJP))	Patterned elastic microstructures for pressure sensors	MicroFab jetlab II inkjet printer with a 50 μm diameter printhead	Dow Corning Sylgard 184 2-part RTV n-butyl acetate solvent, 1:3 PDMS:solvent	Approx. 160 μm drop diameter, 1.6 μm height
Sturgess <i>et al.</i> 2017 ⁶⁰	Material jetting (IJP)	3D reactive drop-on-drop inkjet	Dimatix DMP-2800 inkjet printer and cartridges (21 μm diameter nozzles)	60 wt% PolyTek SiliGlass (A or B) with 40 wt% octyl acetate solvent	Drop diameter 48 \pm 2 μm Layer thickness 7 \pm 3 μm
Mamidanna <i>et al.</i> 2017 ⁶²	Material jetting (IJP)	Microfluidics Mixing device	Microfab Jetlab II inkjet printer 40 μm nozzle	Dow Corning Sylgard 184 2-part RTV in toluene solvent, 1:5 by volume	200–300 μm line width
McCoul <i>et al.</i> 2017 ⁶³	Material jetting (IJP)	Dielectric elastomer actuators	MicroFab jetlab 4 inkjet printer 80 μm nozzle	Wacker Elastosil P7670, NuSil CF18-2186, Bluestar Silbione LSR 4305, Wacker Silpuran 6000/05, and Momentive Silopren UV Electro 225-1. All diluted with Dow Corning OS-2 solvent	Drop diameter >200 μm 2-4 μm layer thickness, DPI 152-254, 50 mm s^{-1} throughput
Mikkonen <i>et al.</i> 2020 ⁶⁴	Material jetting (IJP)	Multi-layered soft electronics	Dimatix DMP-2800 inkjet printer and cartridges (21 μm diameter nozzles)	Dow Corning Sylgard 184 2-part RTV Octyl acetate solvent, typically 1:3 PDMS:solvent	Drop diameter 45 μm Minimum line width 85 μm

Foerster <i>et al.</i> 2017 ⁶⁸	Material jetting (piezo-pneumatic)	3D reactive drop-on-drop jetting	Aerotech 3-axis stage piezo-pneumatic jetting printheads (Nordson Pico Pμlse), 300 μm drop spacing, 150 and 50 μm nozzle diameters (Ink A and Ink B, respectively)	Dow Corning SE 1700 α, ω-vinyl PDMS (Gelest) and SO-100 silicone oil viscosity modifiers Support ink PF127 triblock copolymer with 10 wt% carbon paste	Unknown resolution; grids with line width ≤500 μm were produced
Liravi <i>et al.</i> 2018 ⁶⁹	Hybrid (piezo-pneumatic material jetting and extrusion)	Print optimisation	Custom: three piezo-pneumatic jetting printheads (Pico Pμlse, Nordson); two extrusion printheads (xQR41 MicroDot and Optimeter, Nordson); 365 nm UV lamp	Novagard RTV 800-400 with 3 wt% Omnirad 1173 photoinitiator Dual UV/moisture curing mechanism	580 μm line width 8.1 μm surface waviness 100 mm s ⁻¹
Davoodi <i>et al.</i> 2020 ⁷⁰	Material jetting (piezo-pneumatic)	Flexible sensors	Piezo-pneumatic jetting printhead (Pico Pμlse, Nordson) with 150 μm nozzle	Novagard RTV 800-400 with 3 wt% Omnirad 1173 Photoinitiator, 30 wt% milled carbon fibres, Smooth-On Thinner	Unknown resolution; 150 μm nozzle diameter 100 mm s ⁻¹ velocity
Wilkinson <i>et al.</i> 2020 ⁷¹	Material jetting (electrohydrodynamic (EHD))	Capacitive sensors	Syringe pump, 160 μm ID stainless steel blunt nozzle	Sylgard 1-4128 2-part addition cure RTV	≥500 μm sessile drop diameter ≥800 pL mass
Weiss <i>et al.</i> 2016 ^{72,73}	Material jetting (electrospray)	Dielectric elastomer actuators	Aladdin six-syringe pump, 160 μm SS blunt nozzle	5 vol% α,ω-vinyl-PDMS in ethyl acetate (Gelest) UV cured under Ar (210 nm max, 180-450 nm emission)	Layer thickness 91 ± 10 nm RMS roughness 0.2-0.28nm
Araromi <i>et al.</i> 2011 ⁷⁴	Material jetting (aerosol jet printing (AJP))	Dielectric elastomer actuators	Revell Starter Class airbrush system, 2.0 bar air pressure	Dow Corning Silastic 3481 Dichloromethane solvent, 1:5 PDMS:solvent	Layer thickness 40 μm
Reitelshöfer <i>et al.</i> 2015, ⁷⁵ 2016 ⁷⁶	Material jetting (AJP)	Dielectric elastomer actuators	Custom system, dual pneumatic atomisers	Wacker Elastosil P 7670 2-part RTV	Layer thickness >10 μm

2.2.4. Functional silicone composites

The material portfolio for 3D IJP printing is limited: Waheed *et al.* 2016 reported that, although an enormous range of materials are used in conventional manufacturing of microfluidic devices, only 100 raw materials were available across all AM processes.¹¹ There is also increasing demand for functional materials for jetting to enable inkjet-printed devices including soft robotic actuators, flexible electronics, and lab on a chip chemosensors.^{8-10,77}

Silicones can be excellent matrices for composites, able to provide processability to a range of nanoparticle fillers which may impart specific functionalities; for example, conductive silver silicone nanocomposites may have use in stretchable electronics,^{78,79} which could also be of use for resistance-based thermometry. Inkjet may be a viable route to functional silicone composites for sensing applications.

Nanoparticles (NPs) are very well established in inkjet printing, where submicron particles are needed to avoid nozzle blockage.³⁴ NPs have high surface activity which makes dispersion challenging at high concentrations as viscosity increases; loadings of up to 40 vol% have been seen for the jetting of alumina suspensions in wax.⁸⁰ Particulate inks are also vulnerable to 'coffee staining', where solute is deposited at the edge of drying droplets. A common strategy to eliminate this is through the use of two solvent systems, where the major solvent has a lower boiling point and higher surface tension than the co-solvent.^{81,82} Typically, a few tens of vol% co-solvent is used; Marangoni numbers are on the order of 10^5 - 10^6 .^{83,84}

Examples of materials used in silicone composites are shown below in Table 4. The most industrially-important silicone filler is silica, which is primarily used for reinforcement; carbon black is also used, and nanoclays may be used in high performance rubbers. Metal oxides are inert but confer scratch resistance, while heat transfer silicones typically contain boron nitride, aluminium nitride, alumina, or zinc oxide to increase thermal conductivity. The standard flame retardants are aluminium trihydrate (ATH) and magnesium dihydrate (MDH). Dielectric silicones contain inorganic oxides, while commercial conductive silicones contain carbon black, nickel graphite, or silver.¹⁷ A detailed review of silicone elastomer fillers is given by Paul and Mark.⁸⁵

Table 4: Examples of materials used as fillers in silicones by material class.

<i>Material class</i>	<i>Examples</i>
Inorganic oxides	Silica, alumina, titanium dioxide, zinc oxide
Inorganic compounds	Aluminium trihydrate, magnesium dihydrate Calcium carbonate Boron nitride, aluminium nitride, silicon nitride
Nanoclays	Montmorillonite, bentonite, kaolinite, hectorite, halloysite
Carbon-based materials	Carbon black, expanded graphite, nickel graphite, carbon nanotubes (SWNT or MWNT)
Metals	Nickel, iron, copper, zinc, aluminium, silver

Reinforcing fillers, by definition, have strong interactions with the polymer they reinforce and form high viscosity networks. Literature on material jetting of silica-reinforced silicone nanocomposites is therefore limited to piezo-pneumatic jetting systems.⁶⁸ However, surface-modified silica nanoparticles have been used in inkjet printing as a means of imparting functionality for fluorescence,⁸⁶ optics,⁸⁷ and conductivity.⁸⁸ Typical commercial nanodispersions, such as AERODISP[®], have ~20 wt% loadings and viscosity on the order of 100 mPa s; this can be diluted to give jettable nanoinks.

For integrated thermal sensing materials for IJP, conductive and fluorescent fillers are required for electrical and luminescent thermometry, respectively. Ideally, a species should confer a high signal-to-noise ratio at low ink loadings to enable effective sensing with simple ink formulation. Resistance-based sensing materials for inkjet typically require post-processing heat treatments at around 150 °C and include silver,^{13,16,36–38} nickel oxide,³⁹ and carbon nanomaterials.^{40–42} Inks for luminescence nanothermometry via inkjet printing have not been demonstrated, although some compatible material classes have been jetted previously; materials with suitable fluorescence include organic sensing dyes, rare earth metal ions, and quantum dots.^{1,2}

Conductive fillers

There is much interest in conductive inks for inkjet, as summarised in a recent review by Nayak *et al.*,⁸ although high loadings are required for adequate conductivity in bulk polymer matrices (>10 wt%), which makes formulating printable inks challenging due to the increase in viscosity associated with the addition of nanoparticles. Inks with conductive fillers are divided into carbon-based inks and metal-based inks.

Carbon nanotubes (CNTs) and graphene have strong tendency to aggregate; inks are formulated with concentrations of 0.01-10 gL⁻¹ and 0.002-0.1 wt%, respectively. Graphene oxide inks have higher loadings (0.1-1 wt%) but require reduction post-sintering. While the majority of inkjet processes deposit conductive carbon onto a substrate as a layer, some polymer nanocomposites are reported: electrodes and luminescent nanocomposites have both been made with inks containing PVA and either graphene oxide or graphene QDs,^{89,90} and conductive polymer nanocomposites are reported from PEDOT:PSS and single walled CNTs.⁹¹ Extrusion-based AM has been carried out on silicones containing carbon black (CB)^{92,93} or CNTs.^{94,95} Material jetting is currently limited to high viscosity systems: one paper reports piezo-pneumatic jetting of silicone ink containing 30 wt% milled carbon fibres for flexible sensors.⁷⁰

Metal nanoinks are well-established with various commercial dispersions, most commonly nanosilver; for conductivity, high loadings are needed in the range of 20-80 wt%. Conductive silver-silicone elastomer nanocomposites are of interest for stretchable electronics^{78,79} and have been printed by extrusion AM at up to 80 wt% AgNPs.^{79,96,97} While metal-silicone nanocomposites have not been inkjet-printed, other polymer nanocomposites have; for example, resistors have been printed with an aqueous ink of PEGDA and silver nanoparticles (10-50 wt%).⁹⁸

Inkjet of conductive silicone inks is challenging due to the high loadings required to achieve conductivity, where the resulting increase in viscosity may result in inks that are incompatible with jetting. Furthermore, resistance-based IJP devices in literature typically require sensing areas that are tens of millimeters in size; this limits the applicability of this approach for integrated sensing in small devices and for planar imaging.

In contrast, luminescence-based thermal sensing inks are not yet described and may enable planar or 3D thermal imaging with subdegree and submicron maximum resolutions. This is a gap in the IJP material portfolio where formulation of novel inks could enable embedded thermal sensing in inkjet-printed devices where specific needs are not being met by the current materials available, such as temperature monitoring and imaging within a microfluidic mixer.

Fluorescent fillers

Organic sensing dyes are one type of material that can be used for luminescence thermometry, of which the most commonly-employed is Rhodamine B.¹ This approach is typically used in solution to monitor microfluidic channels; in a key paper by Ross *et al.*, this enabled thermal imaging with submicron resolution.⁹⁹ Rhodamine B is readily absorbed by PDMS, which has made dyeing PDMS a route to temperature sensitive films for microfluidics;¹⁰⁰ however, the film had to be isolated with glass slides to prevent diffusion into the liquid and the bulk silicone. Additionally, organic dyes are more susceptible to photobleaching than quantum dots,¹⁰¹ which will limit the lifespan of a sensing device. Therefore, while IJP of dyed PDMS inks is a feasible route to temperature-responsive fluorescent materials, inorganic species may provide more stable device performance for continuous temperature monitoring and are prioritised in this thesis.

Quantum dots (QD) are fluorescent semiconductor nanoparticles with particle size-dependent emission wavelength, narrow emission peak, and inherent thermal quenching mechanisms. They are well-established as photostable markers for fluorescence microscopy and in lighting applications, which leads to good performance as nanothermometers.¹ Numerous QD-silicone composites have been described in literature for lighting applications¹⁰² and Additive Manufacturing of QD-polymers is known: CdSe/ZnS quantum dots were added to silicones to aid imaging of a microfluidic mixing printhead for extrusion-based AM,¹⁰³ while Elliot *et al.* demonstrated inkjet printing of an acrylate QD-photopolymer, producing composites with visible fluorescence at sufficiently low QD loading (0.5 wt%) that ink viscosity was virtually unchanged upon addition of QDs.¹⁸

The trivalent lanthanide ions from cerium to ytterbium contain unfilled 4f orbitals that are shielded by the filled 5s and 5p shells, which leads to numerous optical transitions with narrow luminescent lines that are insensitive to host environment (excepting degradation).¹ Therefore, a range of lanthanide-doped nanocrystals have been used for thermometry; temperature-dependency of luminescent line intensities results from a combination of phenomenon and is difficult to model. Materials used for thermometry include Er³⁺,Yb³⁺:NaYF₄ co-doped nanocrystals,¹⁰⁴ Eu³⁺,Tb³⁺: γ -Fe₂O₃ co-doped nanocrystals,¹⁰⁵ and Ce³⁺:YAG nanocrystals.¹⁰⁶ Bulk silicone composites containing lanthanide-doped nanocrystals have been of interest for optical applications such as random lasers and waveguides; examples include Nd³⁺:YAG^{107,108} and Er³⁺:CeO₂.¹⁰⁹

Both quantum dots and lanthanide-doped nanocrystals are promising for luminescence thermometry and are worthy of study. Both have bright emission and good photostability, so that visible fluorescence is possible at <1 wt% loadings; such low loadings are not expected to lead to significant increases in viscosity and do not present a challenge for ink rheology. The photoluminescence (PL) of QDs is efficient due to a down-conversion mechanism, where one higher energy photon is converted into two lower energy photons. Lanthanide-doped nanocrystals can be down-converting or up-converting, the latter of which enables the use of near-infrared excitation wavelengths which are lower power and cheaper than UV or visible wavelengths. A key advantage of lanthanide-doped nanocrystals is that their complex emission spectra can be self-calibrating, which enables absolute temperature measurement. However, this requires more data processing and more expensive equipment to resolve, in comparison to the single QD emission peak where change in intensity and peak shift is linear across the physiological temperature range.

Both materials can be degraded by various mechanisms and may be vulnerable to oxygen and/or moisture; core-shell QDs are well-known and are protected by an overcoated layer. Lanthanide-doped nanocrystal PL is insensitive to environment and size, which is advantageous for controlled temperature sensing in a range of systems and reduces the need for controlling diameter and surface science during particle synthesis and device operation. However, this can be advantageous for QDs: the quantum yield can be enhanced by stabilising ligands and the PL can be used for chemosensing applications. Most importantly for imaging, the particle diameter can be tuned to enable emission wavelengths across the entire visible spectrum with narrow emission peak and broad absorption peaks, which has established QDs as versatile fluorescent probes for imaging.

Overall, both are excellent candidates for temperature-sensing composites; however, while lanthanide-doped nanocrystals are ideal for absolute temperature measurement, they are not as well-established or widely used as quantum dots. A wide range of QDs are commercially available, with different core-shell compositions, surface treatments, and emission wavelengths, making them accessible for a wider range of markets and applications. They are also well-established within fluorescent imaging, particularly within biosciences, and their behaviour is better understood and easier to resolve. For these reasons, quantum dots are explored in the scope of this thesis, although lanthanide-doped nanocrystals remain recommended for future work. The following section describes quantum dots in more detail and describes their use in inkjet printing, QD-polymer composites, and their performance in optical temperature-sensing.

2.3. Quantum dots

2.3.1. Properties of quantum dots

Quantum dots (QDs) are metal or semiconductor nanocrystals which are sufficiently small – typically 2-12 nm diameter – so that the QD radius is smaller than the exciton Bohr radius and therefore they display quantum confinement effects in all three dimensions.¹⁹ This leads to particle-size-dependent energy level quantisation and bandgap, as predicted by the particle-in-a-box model. In semi-conductors, fluorescence occurs when light excites an electron from the valence band to the conduction band, leaving behind a hole. When the electron-hole pair (a.k.a. exciton) recombines, a photon is emitted with energy equal to the bandgap. Therefore, QDs emit light at wavelengths that are dependent on particle size: emission blue-shifts as particle size decreases, as shown in Figure 11.

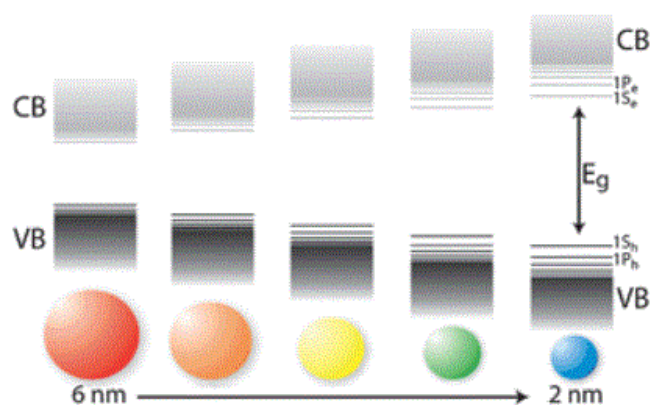


Figure 11: Quantum confinement in CdSe QDs. At sizes above the exciton Bohr radius, molecular orbitals combine to form continuous energy bands, where the valence band (VB) is populated by electrons and the conduction band (CB) is empty. As particle sizes decrease below the Bohr radius, the bands increasingly split into quantised energy levels and bandgap increases, leading to emission of photons with higher energy wavelengths. Reproduced from de Mello Donegá 2011¹⁹ with permission from The Royal Society of Chemistry.

QDs are of practical application for LEDs and LCDs as they have tuneable, narrow emission bands, broad absorption bands, and have high efficiency due to a down-conversion mechanism: QDs absorb higher energy light (typically ultraviolet (UV) wavelengths) and emit two lower energy photons (visible wavelengths) via impact ionisation, a process known as carrier multiplication or multiple exciton generation.¹¹⁰ The first commercial QD-LED display was released by Sony in 2013.¹¹¹

Quantum dots have very high surface-area-to-volume ratios and have significant interaction with stabilising ligands. Emission is sensitive to quantum dot surface environment; therefore, it is common to passivate surface traps, or otherwise modify the excitonic properties of quantum dots, with a layer of another semi-conductor. There are two types of core-shell QDs, shown in Figure 12, depending on relative bandgaps. In type-I,

the bandgap of the core is smaller than that of, and falls within, the bandgap of the shell; electrons and holes are confined to the core. In type-II, the valence band edge of the core is within the shell bandgap and the conduction band edge of the shell is within the core bandgap; this leads to a separation of charge carriers, where electrons and holes are confined to the core and shell or vice versa. Inverse types are noted where the core and shell bandgaps are reversed in the above types; inverse type-II QDs have similar conduction band edge energies between core and shell, which leads to delocalisation of electrons and holes confined to the core.

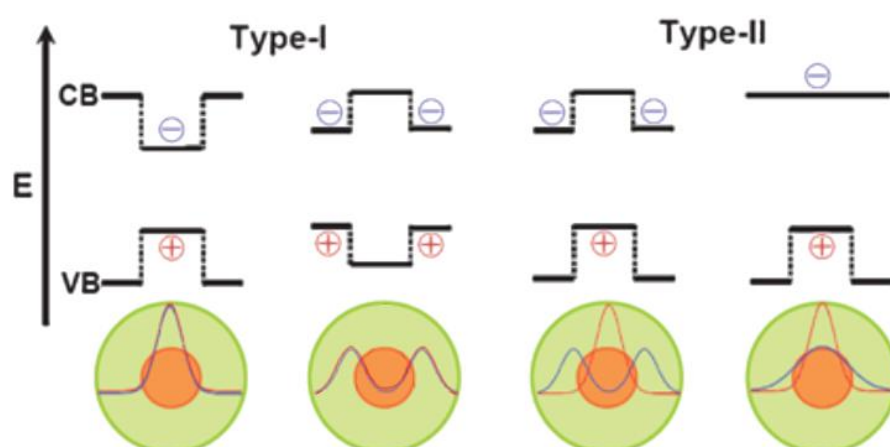


Figure 12: Types of core-shell quantum dots. The relative energies of the valence band and conductive band of the core (orange) and shell (green) material is shown, along with localisation of charge carriers and their ground state wavefunctions (electrons in blue, marked as \ominus ; holes in red, marked as \oplus). Adapted from de Mello Donegá 2011¹⁹ with permission from The Royal Society of Chemistry.

Type-I QDs have the greatest utility for lighting and temperature sensing as they have greater quantum yields (QY) and greater long-term stability as excitons are confined to the core and shielded from the environment. However, their small Stokes shift does mean that photon reabsorption by neighbouring quantum dots is an issue. Additionally, the excitons are not perfectly confined: exciton leakage into the shell is observed in Type-I core-shell QDs, which leads to redshift of the core emission.^{19,110,112} CdSe/ZnS is the most well-studied core-shell QD as it was the first published (1996), has high quantum yield, and emission can be tuned across the visible colour spectrum (red to blue, for 6 nm to 2 nm core diameter respectively).^{110,112}

Greater energy barriers and thicker shells are preferred to prevent exciton quenching by surface defects, but lattice mismatch between core and shell limits the maximum thickness due to the interfacial strain. For example, while a ZnS shell has the best energy offset for a CdSe core, the 12% lattice mismatch makes it hard to overcoat more than 2-3 monolayers: however, materials with less mismatch have smaller offsets.¹⁹ For these reasons, QDs may

be synthesised with multiple shells to give a sequential increase in energy offset but with small lattice mismatches between layers; gradient alloy shells are also effective at overcoming these limitations. Such quantum dots may be significantly more challenging and time-consuming to prepare.

In addition to their aforementioned utility for temperature-sensing, quantum dots have a wide range of applications as summarised in the review by Bera *et al.*¹¹³ High attenuation coefficients and high density of states makes quantum dots attractive for a range of optical and electronic applications.¹¹⁴ Downconversion gives them utility for LEDs, photodetectors, amplifiers, and sensors, while their activity as triplet photosensitisers enables solar cells and photocatalysis. Quantum dots may also be used for optical encoding as they can show nonlinear optoelectronic properties, such as photorefractivity.

Quantum dots are also of great importance for biological imaging and sensing.¹¹⁵ Their narrow emission and small size enable high resolution imaging, particularly for intracellular imaging: high photostability enables allows 3D image reconstruction and real-time tracking. For biosensing applications, QDs have surface plasmon resonance with gold nanoparticles, enabling surface enhanced Raman spectroscopy (SERS). QDs are also commonly used as FRET probes (Förster resonance energy transfer) to monitor biomolecules such as proteins. Quantum dots have particular use in cancer research, where they are used variously to image, label, target, and/or kill cancerous cells (phototherapy).

As quantum dots have utility in a range of applications, these materials are established in inkjet printing with various formulation strategies to meet the specifications of different devices, such as solar cells and LEDs. The following section discusses inkjet printing of quantum dots to produce films, composites and devices, and identifies strategies that are most suitable for sensing devices containing QD-silicone composites.

2.3.2. Inkjet printing of quantum dots

The most common approach to inkjet of quantum dots is as a colloidal dispersion in solvent; devices can be made with QD layers sandwiched between other materials. Uniformity of QDs is usually vital for functionality, particularly for solar cells and electroluminescent QD-LEDs, which require close-packed QD layers for charge transfer. However, even QD films are difficult to achieve due to a range of challenges: coffee ring formation; QD close-packing being dependent on the flatness of the underlying layer; composite film flatness being disturbed by deposition of the subsequent layer; selection of suitable orthogonal solvents; and nozzle blockage from volatile solvents. The large solvent component of inks also allows significant time for solvent-polymer interactions during drying, leading to diffusion of impurities or residual monomers and surface roughness.¹¹⁶ In 2009, Haverinen *et al.* used a low vapour pressure solvent (chlorobenzene, 11 mmHg) to suppress coffee ring formation in single-solvent CdSe or CdSe/ZnS QD inks.¹¹⁶

It is known that two-solvent mixtures can be used to counteract Marangoni flow that leads to coffee ring formation of droplets in inkjet;⁸² in 2005, Coe-Sullivan *et al.* used a mixture of chloroform and chlorobenzene to obtain ordered QD layers following spin-casting.¹¹⁷ Jiang *et al.* 2016 demonstrated coffee ring-free inkjet of two-solvent QD inks using 20 vol% 1,2-dichlorobenzene with 80 vol% cyclohexylbenzene (CHB),¹¹⁸ the latter of which became widely used in two-solvent QD inks. In 2017, Liu *et al.* produced a fully solution-processed QD LED using orthogonal solvents, i.e. solvents in which the previously deposited material will not dissolve. The coffee ring effect was eliminated in CdSe/ZnS QD inks using a two-solvent ink: 10 vol% toluene and 90 vol% CHB.¹¹⁹ High resolution, coffee ring-free inkjet was achieved (20 μm drop diameters) for QDs in 5 vol% octane and 95 vol% CHB by Yang *et al.* 2019 using a PiXDRO LP50 printer with 9 μm nozzle diameter (nominal drop volume 1 pL, obtained drop volume 2-4 pL).¹²⁰

Recently, Ho *et al.* 2020 demonstrated inkjet printing of aqueous salt-encapsulated QDs with the highest resolution to date: as the drops dried on a hydrophobic surface, they contracted to form uniform cuboid pixels ($3.74 \pm 0.5 \mu\text{m}$ diameter). As this was achieved using 10 pL printheads (21.5 μm nozzle diameter), there is potential for an even higher resolution to be achieved if 1 pL printheads (9 μm nozzle diameter) can be used.¹²¹

A range of QD-polymer composites have also been produced by inkjet printing for QD-LED applications, where the QD layer is used for colour conversion or correction, as layers are not required to be as thin as in solar cells. There are three routes to inorganic polymer nanocomposites: prepared nanoparticles, metal salt precursors, and sol-gel approaches.

The majority of QD-polymer inks are prepared by mixing colloidal QD solution with a polymer solution. Embedding QDs in polymer matrices improves dispersion and reduces quenching to improve the photoluminescent efficiency.^{21,22} Choice of stabilising agent also affects dispersion; bimodal PDMS-brush-grafted QDs were found to enhance dispersion in high molecular weight silicone (>21000-33000 g mol⁻¹, M_c⁵³), i.e. Sylgard 184.¹²² Dispersion medium is similarly important: α,ω -hydride PDMS-co-PDPS silicone fluids have been found to be effective for dispersion of dodecyl amine-capped CdSe/ZnS QDs.¹²³ Strategies to enhance QD dispersion in polymer matrices are discussed in detail in *Appendices: QD dispersion in polymer matrices*.

Single solvent systems are known: Kim *et al.* 2009 used chloroform to print 3.4 nm CdSe/ZnS QDs (with TOPO surfactant) in 5 wt% polystyrene solution (MW=5200 g mol⁻¹) using DOD inkjet with 70 μ m nozzles.¹²⁴ Schnee *et al.* 2016 inkjet-printed CdSe QDs and poly(benzyl methacrylate) in toluene (5.0 and 3.3 mg mL⁻¹ respectively) to produce QD-polymer arrays for testing vapour sensitivity.¹²⁵

Mixed solvent systems have been effective at reducing coffee-staining in the inkjet printing of QD-polymer nanocomposites. Tekin *et al.* 2007 printed CdTe QDs in aqueous poly(vinyl alcohol) (PVA) solution; addition of 1-2 vol% ethylene glycol suppressed coffee ring formation.¹²⁶ In 2009, Wood *et al.* used thermal inkjet printing to produce thin films of QD-polymer composites, demonstrating that full-colour AC-EL displays can be produced by jetting. Polyisobutylene solution (MW 400,000 g mol⁻¹, 0.1 g, 10 mL hexane, 1 mL octane) was mixed with 2 mg mL⁻¹ QDs in hexane at ratios of 1:2 to 1:4.¹²⁷

Solvent-free printing of nanocomposites has also been carried out by adding freeze-dried QDs directly to photopolymer. Elliott *et al.* 2013 used an Objet PolyJet printer to print QD-polymer composites: 0.5 wt% suspensions of CdSe QDs in VeroClear gave visible fluorescence and did not hinder printability; however, aggregation of inks occurred within 2-3 days once stirring ceased, and the nanocomposites were not homogeneously dispersed.¹⁸ Recently, Hu *et al.* 2020 prepared inkjet-printed QD colour conversion layers using 15 wt% QD inks in either a volatile solvent (cyclohexylbenzene) or in a photocurable acrylic resin. Drop diameter was <50 μ m for both inks but the solvent ink showed coffee ring formation, whereas the rapid photopolymerisation of the polymer ink led to improved morphology of solidified droplets and excellent dispersion of QDs without aggregates. A 6.6-inch full colour display was demonstrated using the QD-photoresin ink.¹²⁸

In contrast, Bao *et al.* 2015 used reactive inkjet to produce QDs *in situ*. Aqueous polyacrylic acid solutions containing Cd²⁺ ions were jetted and solidified on the surface; subsequent treatment with HS gas produced the nanocomposite. The coffee ring effect was eliminated by using PDMS substrates to obtain a high contact angle, which avoided contact line pinning.¹²⁹ Applying this strategy to silicones is challenging due to their low surface energy ($\sim 20.4 \text{ mN m}^{-1}$),⁵¹ which begets a strong tendency to form films, but could be feasible with the correct substrate *cf.* Sturgess *et al.*⁶⁰

Overall, a range of strategies exist for incorporating QDs into polymer composites by inkjet, both as sandwiched QD layers or as bulk nanocomposites. QDs have been added directly to photoresins; this has advantages of rapid curing and no coffee ring formation, but it is challenging to prevent QD aggregation, which can reduce the thermal and photo-stability of QD-polymer composites. Single-solvent inks make use of solvents with low vapour pressure (<15 mmHg) to reduce Marangoni flow in drying droplets; two-solvent systems have been used to enhance QD dispersion by eliminating coffee-staining. Further strategies to drive resolution and dispersion include *in situ* QD synthesis and the use of hydrophobic substrates to prevent contact pinning; while these are exciting topics of research, they are difficult to develop and are beyond the scope of this thesis, as well as being more difficult to implement in a range of devices due to the need for specific substrates and material compatibilities.

Polymer composite ink formulations, though not well-established in literature, may be beneficial for printed sensors as fluorescent species can be deposited and sealed simultaneously, which may improve dispersion and stability of the fluorescent species.^{21,22} No inkjet-printable QD-silicones are currently described, nor are reactive composite inks which crosslink via mechanisms other than photopolymerisation; however, such materials have been explored for LEDs and may enable a range of applications, in addition to non-invasive temperature sensing. The following section discusses existing QD-silicone composites in literature and the applications of fluorescent QD-polymers, highlighting the formulations, challenges, and applications of QD-silicone composites, before reviewing QD-based temperature sensing.

2.3.3. QD-polymer composites

QD-silicone composites are fluorescent materials with properties ideal for optical temperature sensing and lighting applications. Quantum dots are used in lighting applications,¹¹¹ while silicones are used as LED encapsulants due to their thermal insulation, optical transparency, and UV stability; silicone elastomers are of further interest for flexible electronics. While the aim of this work is to use inkjet printing as a route to devices with integrated thermal sensors, bulk QD-silicones nanocomposites in literature have been investigated solely for QD-based displays and have been utilised in QD-LEDs for two main tasks: efficient colour filters for coloured LEDs, and colour correction for white LEDs.

A range of QD structures are used; core-shell QDs in QD-silicone composites for lighting applications are type-I, as these have higher quantum yields and are better passivated than other core-shell types as excitons are isolated to the core.^{19,112} CdSe-based QDs are the most commonly used in QD-silicone composites and include CdSe core QDs,^{122,130,131} CdSe/ZnS^{132–136} and other core-shell QDs,^{137,138} and multi-shell and/or gradient QDs^{138–144} which offer increased stability.¹⁰² These have been used in silicone composite films for LEDs alone^{133,136–139,143} or with other phosphors.^{134,140–142,144} Due to the high toxicity of cadmium, there is great interest in Cd-free QDs; other QD cores in silicone composites include ZnO,¹⁴⁵ InP,^{146–148} and CuInS₂.^{131,149,150}

The silicone matrices explored in literature have near-unanimously cured via hydrosilylation mechanisms; this is likely because their lack of shrinkage and photo- or by-products leads to higher optical clarity than is the case for condensation cure or UV cure silicones. The majority of research using Dow Corning Sylgard 184 or a Dow Corning LED encapsulating resin such as OE6630, although there are limited reports of alternative formulations. Li *et al.* 2018 synthesised a solid-liquid hybrid-state QD-LED via hydrosilylation by dispersing CdSe/ZnS in a α,ω -vinyl PDMS solid network with a PDMS fluid,¹³⁶ and both condensation and UV cure mechanisms are known: Xuan *et al.* 2015 used a 2-part resin containing an anhydride curing agent (YD65-5 from Raypower Optoelectronics – likely a silicone epoxy),¹³⁴ and Kim *et al.* 2016 dispersed 0.5 wt% CdSe/ZnS QDs in an α,ω -diacrylate PDMS (Miramer M244) with 0.2 wt% Omnirad 651 and cured the composite via free radical photopolymerisation.¹³⁵

Although immobilisation in polymer matrices can enhance QD dispersion and stability by shielding QDs from environmental factors,^{21,22} both quantum dot films and QD-polymer films for LEDs have been limited by issues with stability to UV radiation, heat, moisture, and oxygen, the latter of which is most critical in QD-silicones. All of the above papers describe

composites made from QDs with minimal surface modifications; strategies for QD dispersion, as pertaining specifically to QD-silicones, are discussed in *Appendices: QD dispersion in polymer* matrices with examples from literature. A recent review of strategies to prevent quenching in QD LEDs is given by Moon *et al.* 2019,¹⁰² while Kim *et al.* 2016 investigates the role of capping ligand on the thermal stability of CdSe and CuInS₂ QDs.¹³¹ These limitations, degradation mechanisms, and stabilising strategies will be applicable to the temperature-sensors where these materials are used as sensing materials and are important to consider for understanding and improving device performance.

In addition to lighting applications and thermometry, quantum dots are used in various optical sensing applications, most notably biological ones,¹¹⁵ and QD-based optical sensing is an evolving field, as evidenced by a recent review by Chern *et al.* 2019.²⁰ QD-silicones composites may find application in QD-based vapour sensors in the future as silicones are gas-permeable – QD-polymer nanocomposite film sensors have been demonstrated by making use of QD size¹⁵¹ and surface modification.¹⁵² Gases detected include methanol,¹⁵¹ toluene,^{151,152} xylene,¹⁵² formaldehyde,¹⁵³ and nitrogen dioxide.¹⁵⁴

Although QD-based physical sensors have received less attention in comparison to biological and chemical probes, the intrinsic temperature quenching of QDs makes them desirable for thermometry in dispersions, films, and polymer composites. CdSe/ZnS and CdTe/ZnS QDs are well-known to have emission intensities which decrease linearly with temperature, and are suitable for optical temperature probes when immobilised in a sol-gel¹⁵⁵ or polymer matrix.¹⁵⁶

Dual emission is observed in doped QDs, and a colour change is seen for fluorescence between two temperatures as the relative intensity of the two emission peaks changes. Certain Mn-doped QDs also display temperature- and pressure-dependent luminescence: Zn_{1-x}Mn_xSe/ZnCdSe core/shell QDs can be tuned to different temperatures by varying the shell thickness.^{157,158} While doped QDs with dual emission are desirable for ratiometric temperature sensing – which enables self-referenced thermal measurement with simple instrumentation¹ and is therefore ideal for future sensing formulations – these QDs have not yet been widely commercialised.

Optimisation of LED QD-silicone films and QD optical sensors can have similar specifications, and therefore may overlap with needs for ink formulation for QD-silicone luminescent thermal sensing materials. Review of QD-silicone composites found that addition cure silicones are preferred, as they likely lead to less optical aberrations as there are no shrinkage or by-products associated with hydrosilylation. Addition cure was identified as a promising crosslinking mechanism for inkjet in Section 2.2, alongside radical-based photopolymerisation, which was valued for comparatively rapid crosslinking which are beneficial for print speed and resolution; these mechanisms are therefore strongly recommended for inkjet-printing of silicones for use in optical applications and have been selected for ink formulation.

CdSe/ZnS is the most well-studied core-shell QD as it has high stability and quantum yield (>50%¹¹²) and emission can be tuned across the visual colour spectrum, making it attractive as a fluorescent marker. As these are comparatively well-established in imaging and temperature sensing, with a wide range of commercial particles available that can be used as supplied, these are ideal for sensing material formulation and are selected in this work.

Lower toxicity and cadmium-free QDs are an important direction in quantum dot development, particularly for biological applications. QD-microbeads and gradient core-shell CdSe/ZnS QDs with similar QY are sold by specialist suppliers; these particles have better stability and lower toxicity than typical CdSe/ZnS QDs but are more expensive. InP/ZnS are much less toxic QDs with wide emission range (500-800 nm) and can achieve similar QYs to CdSe/ZnS,¹¹² and are commercially available with similar pricing to core-shell CdSe/ZnS QDs. InP/ZnS QDs have not yet been demonstrated in temperature sensing applications but have suitable fluorescence, and their PL temperature-dependence is beginning to be characterised in literature.¹⁵⁹ As the inks will be formulated to contain low loadings of QDs (>1 wt%), jetting behaviour is expected to be near-identical between QD types where the surface treatments and particle size are similar, so it may be possible to substitute CdSe/ZnS QDs with analogous InP/ZnS QDs without the need for reformulation.

Quantum dot-based nanothermometry has been carried out using various instrumentation as they have multiple PL parameters which are temperature-sensitive. Literature examples of QD-based temperature sensing are reviewed in the following section and the different approaches to measurement are discussed with regards to sensing performance.

2.3.4. QD-based temperature sensing

As discussed above in Section 2.1, current inkjet-printed temperature sensors are based on measurement of resistance across a circuit. However, there is a need for high-resolution and high-sensitivity temperature sensing in fields such as micro/nanoelectronics, integrated photonics, and biomedicine; an inkjet-printable QD-silicone composite for luminescence thermometry could meet these requirements and enable *in situ* sensing for a wider range of printed devices.

Luminescence nanothermometry is a method of thermal measurement which is capable of planar imaging, 3D image reconstruction, and monitoring of enclosed systems, depending on the device design and the experimental set-up employed. Submicron spatial resolution can be obtained via confocal fluorescence microscopy with high numerical optics and spatial filters, or microscale resolution with near-field optical microscopes with low aperture optic fibres; the resolution is also limited by fluorescent particle size.^{1,2} QDs have large quantum yields, tuneable and narrow emission, high photostability, and very small size (2-12 nm diameter¹⁹); if homogenous distribution can be achieved, they are ideal for luminescence nanothermometry. The minimum size of sensing area in a printed device would therefore be determined by the drop diameter in IJP ($\sim 20\text{-}50\ \mu\text{m}$)⁶ and does not determine the spatial resolution of thermal sensing, unlike in resistance-based materials.

The typical temperature sensing range reported is in the ambient region ($\sim 10\text{-}50\ ^\circ\text{C}$), although temperatures in the region of $200\ ^\circ\text{C}$ have been investigated.¹⁶⁰ QD nanothermometry may be conducted based on changes in photoluminescent (PL) intensity, band shape, spectral position, and lifetime;^{1,2} literature examples are described below in detail and summarised in Table 5. Much of these have been for microfluidics and microelectronics, areas in which there are efforts to enable printable devices:^{8,9,11} a novel sensing ink would be well-positioned to meet emerging demands for integrated sensors.⁵

Several mechanisms give rise to variation of QD luminescence with temperature, as shown in Figure 13. Thermally activated crossover reduces the energy separation of excited states so that the bandgap shrinks and energy transfer to non-radiative states is sped up. Multiphonon relaxation via electron-hole recombination is another intrinsic quenching mechanism where the energy gap is bridged by the emission of multiple phonons; however, the gap is too large for efficient multiphonon relaxation in semiconductor QDs. Surface states or defects which trap charge carriers are thermally induced at higher temperatures as ions become more mobile; trap formation may be reversible or irreversible.^{2,160,161}

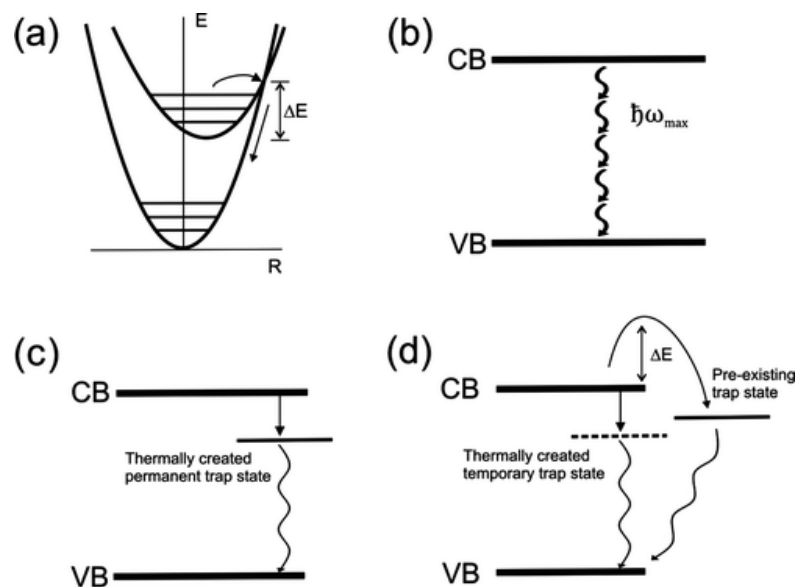


Figure 13: Intrinsic temperature quenching processes: a) thermally activated crossover and b) multiphonon relaxation. Trap-related temperature quenching processes: c) irreversible and d) reversible. Reproduced with permission from Zhao *et al.*¹⁶⁰ Copyright 2012 American Chemical Society.

Intensity based: Temperature is obtained from the spatial variation in emission intensity. Luminescence intensity of QDs in ambient temperature ranges is well-noted to decrease linearly as temperature increases due to thermally activated crossover and phonon mediated processes. This linearity is ideal for sensing, as the sensitivity is consistent across the range of interest so that calibration and analysis are simple. However, the intensity is dependent on the concentration of QDs and the laser power, so measurements are affected by fluctuations.

Jorge *et al.* developed optical fibre temperature probes by encapsulating CdSe/ZnS or CdTe/ZnS QDs in a sol-gel matrix. To overcome the dependence of intensity on optical power, two signals from narrow spectral windows 595-600 nm and 620-625 nm were normalised to $(S1-S2)/(S1+S2)$. This enabled self-referenced optical fibre probes in the temperature range of 10-50 °C with a resolution of 0.3 °C. This enables simultaneous sensing for chemicals and temperature, where *in situ* calibration is needed for temperature-dependent sensing dyes. Multiplexed point probes, both transmission and reflection configurations, were then tested using QD composites with different emission wavelengths to demonstrate simultaneous interrogation of two independent point sensors as shown in Figure 14.¹⁵⁵

Further work in ensuring accurate measurements has been carried out Munro *et al.*, who used CdSe/ZnS as thermomarkers on silk fibres to investigate the use of neural networks trained with steady state temperature conditions.¹⁶²

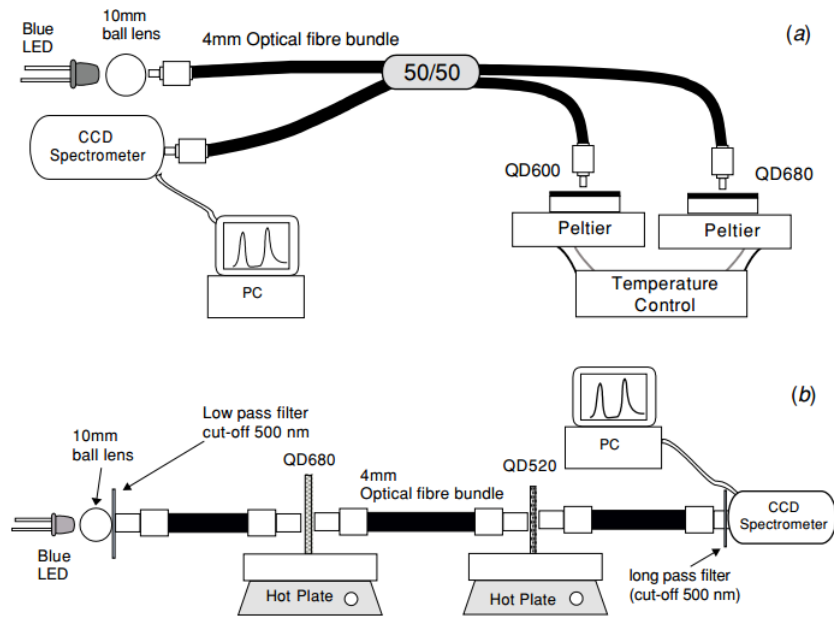


Figure 14: Multiplexed optical temperature probes using QDs composites with different $\lambda_{\text{emission}}$ in (a) reflection and (b) transmission configurations. A CCD spectrometer was used to collect signals in 595-600 nm and 620-625 nm. Reproduced with permission from Jorge *et al.*¹⁵⁵

Thermal imaging can be carried out where QDs are incorporated into the system of interest; the spatial variation of the emission intensity is then recorded by microscopy or CCD camera to give an image. Examples from literature include Han *et al.*, who used a CCD camera to non-invasively monitor the temperature inside cancer cells,¹⁶³ and Liu *et al.*, who utilised a polymer nanocomposite where CdSe/ZnS QDs were encapsulated in a polystyrene matrix for use in lock-in photothermal spectroscopy.¹⁶⁴

Liu *et al.* deposited ZnCuInS/ZnSe/ZnS QDs directly onto a circuit board for planar *in situ* measurement of resistors, as shown in Figure 15.. Calibration was carried out using normalised intensity for 20-105 °C by comparison to the intensity of each pixel at 20 °C. Microscale resolution was obtained using optical microscopy with fibre optics and a spectrometer: a 10 μm x 10 μm resolution was obtained for the measurement of surface temperature distribution for a plane-array with sensitivity of 0.66% °C⁻¹ and under 2% relative error.¹⁶⁵

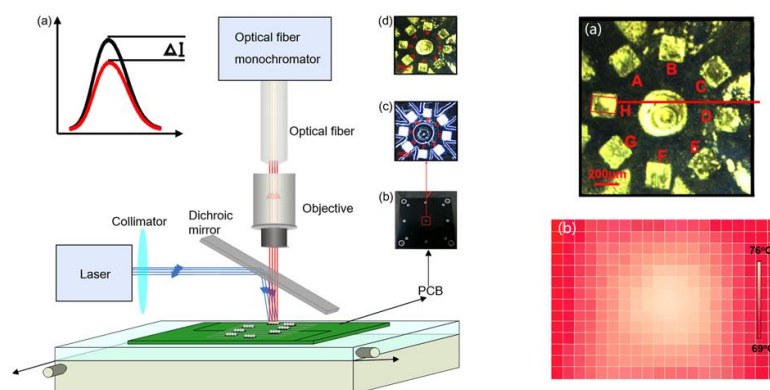


Figure 15: QD sensing film on circuit board. Left: Experimental set up. Top right: Micro-resistors on the printed circuit board with QD sensing layer, where the $200 \times 140 \mu\text{m}^2$ planar area measured on resistor H is outlined in red. Bottom right: Surface temperature measurement of resistor H, where each square measures $10 \times 10 \mu\text{m}^2$. Reproduced with permission from Liu *et al.*¹⁶⁵

Band shape based: Temperature is obtained from the relative intensities of two or more luminescence bands. Dual emission is seen in doped QDs, as detailed below in Figure 16 for Mn-doped CdSe. An energy transfer mechanism to Mn^{2+} energy levels (k_{ET}) quenches the excitonic emission k_{exc} and leads to a band for k_{Mn} luminescence. This is dependent on temperature and the bandgap (ΔE): k_{Mn} dominates at low temperature and yellow luminescence is seen, whereas at high temperature k_{exc} dominates with green luminescence, resulting in a visible colour change between the two regimes. The thermal range can be tuned via the size-dependent bandgap, which could enable a range of sensing applications. The onset of the linear sensing region was 300 K for 4.7 nm diameter QDs and 150 K for 3.5 nm QDs, and a thermal resolution of $0.2 \text{ }^\circ\text{C}$ was demonstrated.¹⁵⁷

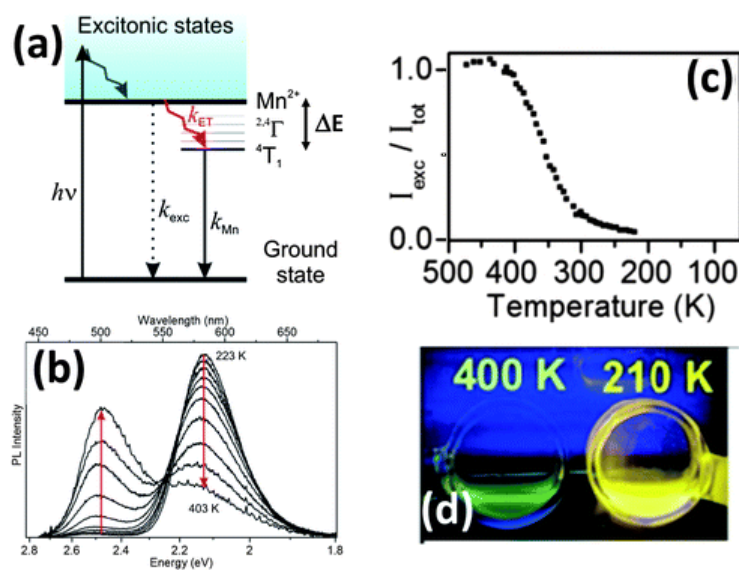


Figure 16: Dual emitting Mn^{2+} doped CdSe QDs. (a) Energy level diagram. (b) PL spectra at varied temperatures 223 K – 403 K; peaks are seen at 500 and 570 nm. (c) Temperature dependence of the ratio between excitation intensity and total emission intensity. (d) Image of colloidal QDs at two temperatures, 400 K and 210 K. Reproduced with permission from Vlaskin *et al.*¹⁵⁷ Copyright 2010 American Chemical Society.

The key advantage of band shape based sensing is that ratiometric sensing enables self-referenced thermal measurement with simple instrumentation,¹ in contrast to the need for calibration when using other PL parameters. Qiu *et al.* 2020 demonstrated ratiometric upconversion nanothermometry using dual-emission from silica-overcoated nanoclusters containing PbS QDs and lanthanide-doped upconversion nanoparticles; these were both excited by an 865 nm laser. This enabled monitoring of intra-tumoral temperature in rats *in vivo* during photothermal therapy with 0.5 °C resolution and 5.6% °C⁻¹ sensitivity.¹⁶⁶

Spectral based: Temperature is obtained from shifts in spectral position of emission and is unaffected by variations in concentration of fluorescent species. Spectral shift in QDs arises from multiple phenomena - particularly bandgap shrinkage caused by thermally activated crossover - which are dependent on intrinsic material properties and on QD size; therefore, smaller QDs show greater sensitivity. 1 nm diameter CdTe QDs have thermal spectral coefficients of 0.8 nm °C⁻¹, which theoretically allows for resolution <0.25 °C.¹⁶⁷

Li *et al.* used the peak shift of individual QDs as temperature markers (Figure 17). Total internal reflection fluorescence microscopy was used to capture images and spectra of QDs excited at 532 nm, and the thermal sensitivity of single QDs was found to be 0.1 nm °C⁻¹. An aluminium MEMS microheater (1200 x 40 x 0.1 μm³) was then coated with CdSe/ZnS QDs for imaging where temperature was measured against voltage. A spatial resolution of 230 nm was achieved; 1 °C precision was estimated to require 1200 QDs.¹⁶⁸

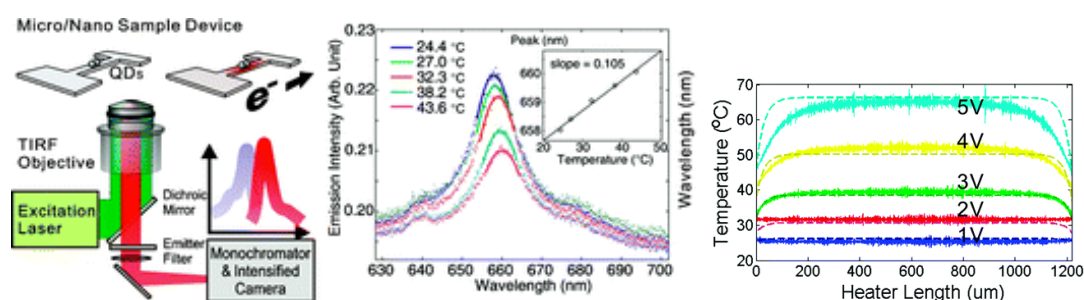


Figure 17: Individual QD markers on a microheater. Left: Experimental set up. Centre: PL spectra at different temperatures, with peak plotted against temperature in inset. Right: Temperature variation with distance along microheater, calculated by peak wavelength. Reproduced with permission from Li *et al.*¹⁶⁸ Copyright 2007 American Chemical Society.

Gu *et al.* used PbSe QDs as real-time temperature probes on GaN LED chips. QDs were deposited in hexane solution via an AFM tip to create a 40 μm diameter sensing region on GaN chips, which were then coated in silicone resin. A thermal camera was used to calibrate the peak shift, which was found to be linear in the region of 30-120 °C with 0.15 nm °C⁻¹ thermal coefficient and 3 °C precision.¹⁶⁹

Peak shift has also been used for planar imaging applications: Maestro *et al.* reported the first use of QDs to enable high-resolution two-photon fluorescence thermal imaging¹⁷⁰ and to aid the thermal characterisation of optical plasmonic recording material in order to better understand the memory writing process.¹⁷¹

Choudhury *et al.* used QD peak shift for thermal imaging inside an optofluidic device. 0.3 wt% aqueous CdTe QDs were sealed in a microchannel and the effects of thermal loading from a laser were investigated, as shown below in Figure 18. This was calibrated by comparison to simple theoretical models of laser heating of a water-filled channel. This experiment was repeated with an aqueous solution of CdTe QDs and CNTs, acting as nanoheaters: the optofluidic device was thermally and fluorescently imaged along the channel, and emission peaks converted into temperature ($0.35 \text{ nm } ^\circ\text{C}^{-1}$) to obtain the induced spatial temperature variation with thermal uncertainty below $0.2 \text{ } ^\circ\text{C}$.¹⁷²

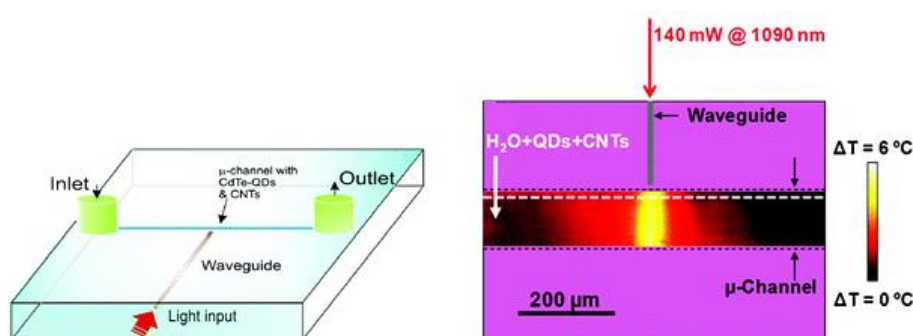


Figure 18: Optofluidic device with waveguide. Left: Device layout with embedded waveguide. Right: Spatial temperature map of the microchannel. Reproduced from Choudhury *et al.*¹⁷² with permission from The Royal Society of Chemistry.

Lifetime based: Temperature is obtained from luminescence decay times; luminescence lifetime of QDs decreases with temperature as thermally activated crossover and phonon mediated processes increase. Lifetime measurements are much faster to collect than high-resolution PL spectra, which typically take tens of seconds per point. Haro-González *et al.* investigated the variation in lifetime of CdTe QDs in the range of 20-50 °C for application in Fluorescence Lifetime Thermal Imaging (FLTI), which can achieve hundreds of points per second. Lifetime was found to decrease linearly for all QDs but smaller QDs had greater sensitivity: 1 nm CdTe QDs were found to have a lifetime thermal coefficient of $0.017 \text{ } ^\circ\text{C}^{-1}$, one of the largest values reported so far for any material.¹⁷³ 3.8 nm CdTe QDs were demonstrated to find thermal loading caused by a laser in a microfluidic system, as shown below in Figure 19.

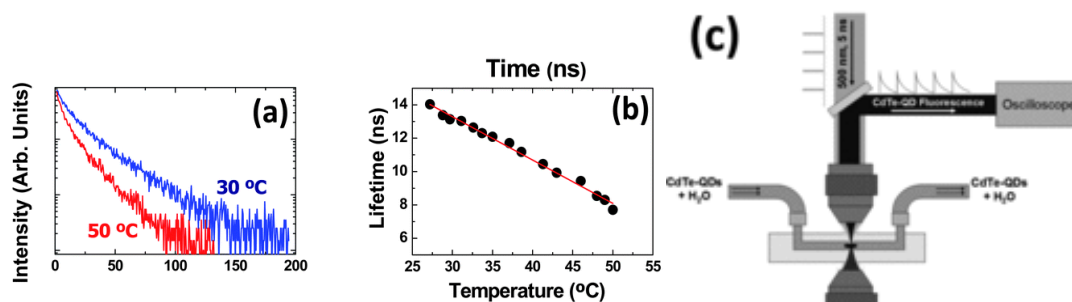


Figure 19: Lifetime of CdTe QDs. (a) Luminescence decay curves of 1 nm CdTe QDs at 30 and 50 °C. (b) Variation of lifetime with temperature in 1 nm CdTe QDs. (c) Experimental set up for thermal measurement in a microchannel, with 1090 nm continuous laser and 532 nm pulsed laser for excitation of 3.8 nm CdTe QDs. Reproduced with permission from Haro-González *et al.*¹⁷³

High temperature: While the majority of sensors have utilised the linear regime in the ambient temperature region, there are reports of temperature response above 90 °C.

Zhao *et al.* investigated quenching of a range of colloidal CdSe-based quantum dots between 25-210 °C, where QDs were measured in octadecene solution and in crosslinked polymer matrices (either PMMA or PLMA, shown in Figure 20).¹⁶⁰ Reversible quenching was seen between 100-180 °C for all QDs investigated. In CdSe/CdS/ZnS QDs in PLMA, no intrinsic quenching was seen until 100 °C, and irreversible quenching was seen after 150 °C; after cooling down from 210 °C, partial recovery of lifetime and intensity was seen with full recovery from red-shift. Temperature quenching in CdSe/CdTe QDs in PMMA was completely reversible up to 200 °C. In terms of sensing material and sensor design, further data on the reversible and irreversible quenching of QDs at elevated temperatures may enable the design of sensors which can give data on thermal history, which are known as thermal history sensors.

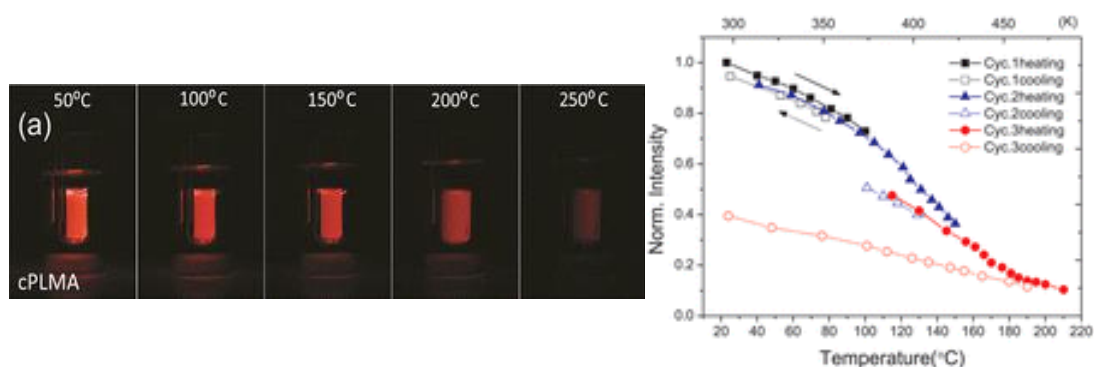


Figure 20: CdSe/CdS/ZnS QDs in PLMA matrix. (a) Fluorescent images at different temperatures, showing loss of intensity. (b) Variation of intensity against temperature during thermal cycles. Reproduced from Zhao *et al.*¹⁶⁰ with permission from The Royal Society of Chemistry.

McLaurin *et al.* synthesised water-soluble dual-emitting $Zn_{1-x}Mn_xSe/ZnS/CdS/ZnS$ QDs which are suitable for sensing at temperatures >100 °C, as seen in Figure 21 below. Tuning of the bandgap is possible by altering the shell thicknesses; this allows the temperature behaviour to be controlled to obtain a sensing range to match the intended application.¹⁷⁴ Water-insoluble QDs with peaks at 267 °C and 17 °C had a sensitivity of 7×10^{-3} °C⁻¹. Water-soluble QDs were suitable for measuring up to ~ 90 °C with similar sensitivity and a precision of ± 0.14 °C. This approach enables wide temperature sensing ranges with suggested application for biological imaging via ratiometric thermometry; the water-insoluble QDs could be incorporated into polymer composites for jetting inks.

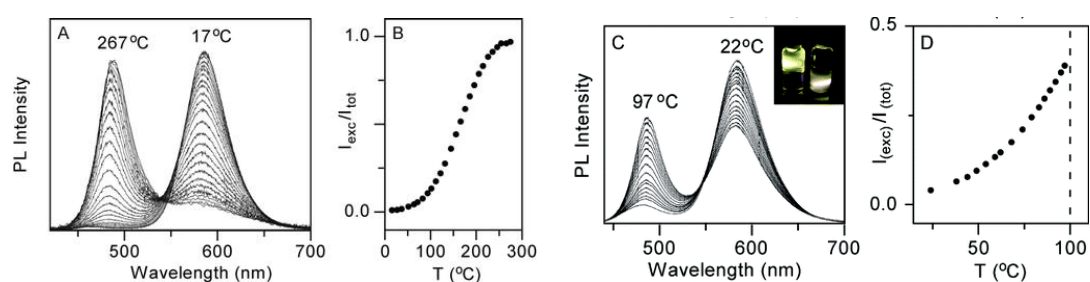


Figure 21: PL spectra variation in the temperature sensing range and response curves for $Zn_{1-x}Mn_xSe/ZnS/CdS/ZnS$. (a) TOPO capped in octadecene (b) encapsulated in *n*-octylamine-modified poly(acrylic acid), suspended in aqueous solution. Reproduced with permission from McLaurin *et al.*¹⁷⁴ Copyright 2011 American Chemical Society.

In summary, quantum dots have been of interest for temperature measurement of microdevices with high spatial and thermal resolution, and there has been active research into IJP as a route for economical production of devices, particularly those with integrated sensing.⁵ There is a clear research gap in that no ink has been developed for luminescence nanothermometry which could facilitate such devices. The intrinsic temperature quenching of QDs means that a single ink formulation can enable a broad range of approaches to thermal measurements: intensity and spectral measurements are commonly employed as they have linear temperature-dependence in the ambient temperature region, which enables simple calibration. Lifetime measurement of CdTe QDs is less established but the data collection rate can be ten-fold that of high-resolution spectral imaging (such as spectral and band shaped measurement). These measurements may be difficult to reference and intensity-based sensing is susceptible to fluctuations in laser power and QD concentration; while band shape-based sensing enables self-referenced measurement with simple instrumentation, this requires specialised doped-QDs.¹ The literature shows that commonly-used commercial QDs, such as CdSe/ZnS or CdTe, are sufficient to formulate versatile sensing inks capable of microscale and subdegree resolution.

Table 5: Semiconductor QD-based temperature sensors in academic literature.

Paper	Type	Application	QD	Form	Temperature range	Resolution, sensitivity, % error
Walker <i>et al.</i> 2003 ¹⁵⁶	Intensity	Quantum dots as optical temperature probes	CdSe/ZnS	In PLMA matrix	250-315 K (~-23-42°C) 278-313 K (~-5-40 °C)	-1.0 %°C ⁻¹ (~-23-42°C) -1.3 %°C ⁻¹ (~-5-40 °C)
Jorge <i>et al.</i> 2006 ¹⁵⁵	Intensity	Self-referenced temperature probe	CdSe/ZnS, CdTe/ZnS	In non-hydrolytic sol-gel matrix	10-50 °C	0.3 °C, -0.7 %°C ⁻¹ to -1.6 %°C ⁻¹
Munro <i>et al.</i> 2015 ¹⁶²	Intensity, various	Neural network to select parameters for highest accuracy in reconstructing photothermal temperature oscillations	CdSe/ZnS	On surface of silk fibre	300-312 K (~27-39 °C)	0.29 °C
Han <i>et al.</i> 2009 ¹⁶³	Intensity	Imaging of photothermal heating of cancer cells	CdSe/ZnS	0.5 wt% in 60 µm polymer film; In cancer cell	20-70 °C	-0.7 %°C ⁻¹ (aqueous) -1.6 %°C ⁻¹ (polymer) 2.2% in cancer cell
Liu <i>et al.</i> 2014 ¹⁶⁵	Intensity	Planar thermal imaging of printed circuit board (PCB)	ZnCuInS/ZnSe/ZnS	Deposited on PCB	20-105 °C	10 µm x 10 µm, -0.66 %°C ⁻¹ , <2%
Liu <i>et al.</i> 2016 ¹⁶⁴	Intensity	Lock-in photothermal spectroscopy	CdSe/ZnS	13.1 µm film polystyrene matrix on black paint on Cu	30-60 °C	-1.3 %°C ⁻¹
Qiu <i>et al.</i> 2020 ¹⁶⁶	Band shape	Ratiometric upconversion nanothermometry with time-resolved dual emission for <i>in vivo</i> temperature monitoring of tumours	PbS	With lanthanide doped NPs in silica coated clusters	20-60 °C	0.5 °C, 5.6% °C ⁻¹

Li <i>et al.</i> 2007 ¹⁶⁸	Peak shift	Single QDs as temperature markers for microheater	CdSe/ZnS from Invitrogen	Deposited on surface, then sealed with silicone	24.4-43.6 °C	1 °C (theory 1200 QDs), -0.3 %°C ⁻¹ (intensity), 0.1 nm°C ⁻¹ , 230 nm
Gu <i>et al.</i> 2013 ¹⁶⁹	Peak shift	40 µm in-situ temperature probe on GaN LED chips	PbSe	Deposited on surface, then sealed with silicone	30-120 °C	±3 °C, 0.15 nm°C ⁻¹
Maestro <i>et al.</i> 2010 ¹⁷⁰	Peak shift	Two-photon fluorescence thermal imaging of HeLa cells	CdSe	In PBS solution; In cells	30-70 °C (solution) 25-50 °C (cells)	1 °C (solution) ±2 °C (cells), 0.16 nm°C ⁻¹
Choudhury <i>et al.</i> 2012 ¹⁷²	Peak shift	Thermal imaging of optofluidic microchannel	CdTe	0.3 wt% solution in water	25-31 °C	0.2 °C, 0.35 nm°C ⁻¹
Maestro <i>et al.</i> 2014 ¹⁷¹	Peak shift	Thermal characterisation of optical plasmonic recording material	CdSe	In 20 µm film PVA matrix, 10 QDs/µm ³ and 72 GNRs/µm ³	25-65 °C	0.11 nm°C ⁻¹ , ≤67%
Haro-González <i>et al.</i> 2012 ¹⁷³	Lifetime	Fluorescence lifetime thermal imaging of microchannel	CdTe	0.3 wt% solution in water	27-50 °C	0.017 °C ⁻¹

2.4. Research niche

Inkjet printing may be an economical route to devices with integrated thermal sensors due to its capacity for maskless, high resolution (typically 20-50 μm),⁶ multi-material printing. However, current inkjet-printed resistance-based thermal sensors have limited spatial resolution and do not achieve sub-degree thermal resolution in the physiological range, which is a barrier to their use in microdevices and in cell culture and biomedical applications. Novel inks for luminescence nanothermometry could meet the requirements for such niche applications; an ink formulation strategy utilising polymer composite inks can efficiently deposit and isolate sensing materials simultaneously and the polymer matrix can provide processability, better enable 3D printing geometries, and improve dispersion and stability of the fluorescent species.^{21,22}

Silicone was selected as the polymer matrix of inks for luminescence nanothermometry due its high optical transparency and UV stability, which enables compatibility with excitation and emission wavelengths of a variety fluorescent species; high refractive index for efficient light extraction; and high thermal stability which enables longer device lifespan. Silicones are also commonly used in the devices of interest: electronics, for their insulation, and microfluidics, for their biocompatibility.⁵⁰ Reactive silicone precursors are used for ink formulation due to rheological limitations of the inkjet process, and addition cure and radical photopolymerisation crosslinking mechanisms were identified as being best suited for inkjet as they proceed at ambient temperatures with comparatively rapid crosslinking. Addition cure inks were selected for optical sensing applications for their optical clarity; it is likely fewer optical aberrations arise during this curing mechanism as there are no shrinkage or by-products associated with hydrosilylation, and this mechanism is used in published and commercialised films for LEDs. Radical-based photopolymerisation was identified as having reactivity ideal for inkjet printing: the rapid silicone crosslinking is beneficial for print speed and resolution, allowing geometrically controlled deposition on a wider range of printing substrates, which may be required for fully-inkjet printed devices.

Quantum dots were selected as the functional filler for fluorescence nanothermometry: these are fluorescent semiconductor nanoparticles with outstanding emission (tuneable emission, narrow emission peak, and high quantum yields). QD-silicone composites are described for colour filter or correction layers in LEDs; while inkjet printing of bulk QD-polymer composites is not well-established, visible fluorescence of QD-polymer composites can be achieved at <1 wt% QD loadings which are not expected to lead to increases in viscosity that are impede jetting.¹⁸

Temperature sensing is based on intrinsic thermal quenching of QDs and linear, reversible changes in emission are observed in common commercial QDs below ~ 60 °C. The literature shows that means that a single ink formulation can enable a broad range of approaches to thermal measurements and that commonly-used commercial QDs, such as CdSe/ZnS or CdTe, are sufficient to formulate versatile sensing inks capable of microscale and subdegree resolution. CdSe/ZnS QDs have been selected for ink formulation as they are the most well-studied core-shell QD due to high stability and quantum yield ($>50\%$),¹¹² are comparatively well-established in fluorescence microscopy and temperature sensing, and a wide range of commercial particles are available that can be used as supplied. Specialised quantum dots, including core-shell gradient QDs and doped dual-emitting QDs, are of interest to further work, while commercial CdTe-based QDs and InP/ZnS QDs were identified as ideal candidates for formulations for lifetime based nanothermometry and biological applications, respectively.

Overall, development of the first inkjet-printable luminescent sensing material would enable high resolution, low waste production of devices with integrated sensing features with geometries that are otherwise impossible to achieve via conventional manufacturing. This is likely to be particularly beneficial for *in situ* calibration of other sensing devices or for production of microfluidic devices.

Chapter 3. Methodology

This chapter describes the methods by which objectives were met in the course of this PhD. Reactive inks were developed for inkjet printing of QD-silicone composites using both addition cure and UV cure mechanisms, and the photoluminescence of composites was assessed for temperature sensing applications with the goal of enabling integrated, non-invasive, high-resolution thermal sensing in printed devices. This chapter states the materials, equipment, and methods used to:

- Formulate silicone inks with suitable rheology
- Optimise jetting and print silicone films
- Formulate QD-silicone inks with suitable loading, dispersion, and rheology
- Print QD-silicone composite materials
- Carry out temperature-sensing experiments on composite materials.

A detailed project workflow to achieve research objectives is given below, followed by an overview of the silicone materials explored. The finding and outcomes of the work carried out are detailed later in the corresponding results chapters as follows.

Chapter 4 discusses the formulation and printing of addition cure silicones, noting challenges in printing composite materials. Characterisation of composite materials is carried out to guide strategies to enable composites to be printed with suitable properties.

Chapter 5 presents the work carried out into UV cure silicones. This study is less thorough than for addition cure silicones due to issues with PL stability, but printing is demonstrated for silicone matrices and composites are investigated.

Lastly, Chapter 6 shows the imaging of QD clusters in cured composites and shows the results of temperature sensing experiments conducted using well-plate reading and confocal microscopy.

3.1. Project workflow

This section details the methods used to achieve the research objectives, which were: *O1* formulation of jettable silicone inks; *O2* printing of silicone matrices; *O3* formulation of jettable QD-silicone inks; *O4* printing of QD-silicone composites; and *O5* characterisation of temperature-sensing materials. As shown in Figure 22, the workflow to achieve the project aim consisted of six stages, corresponding to research objectives. Each of the experimental stages are described below, with the equipment and methods used and their rationales.

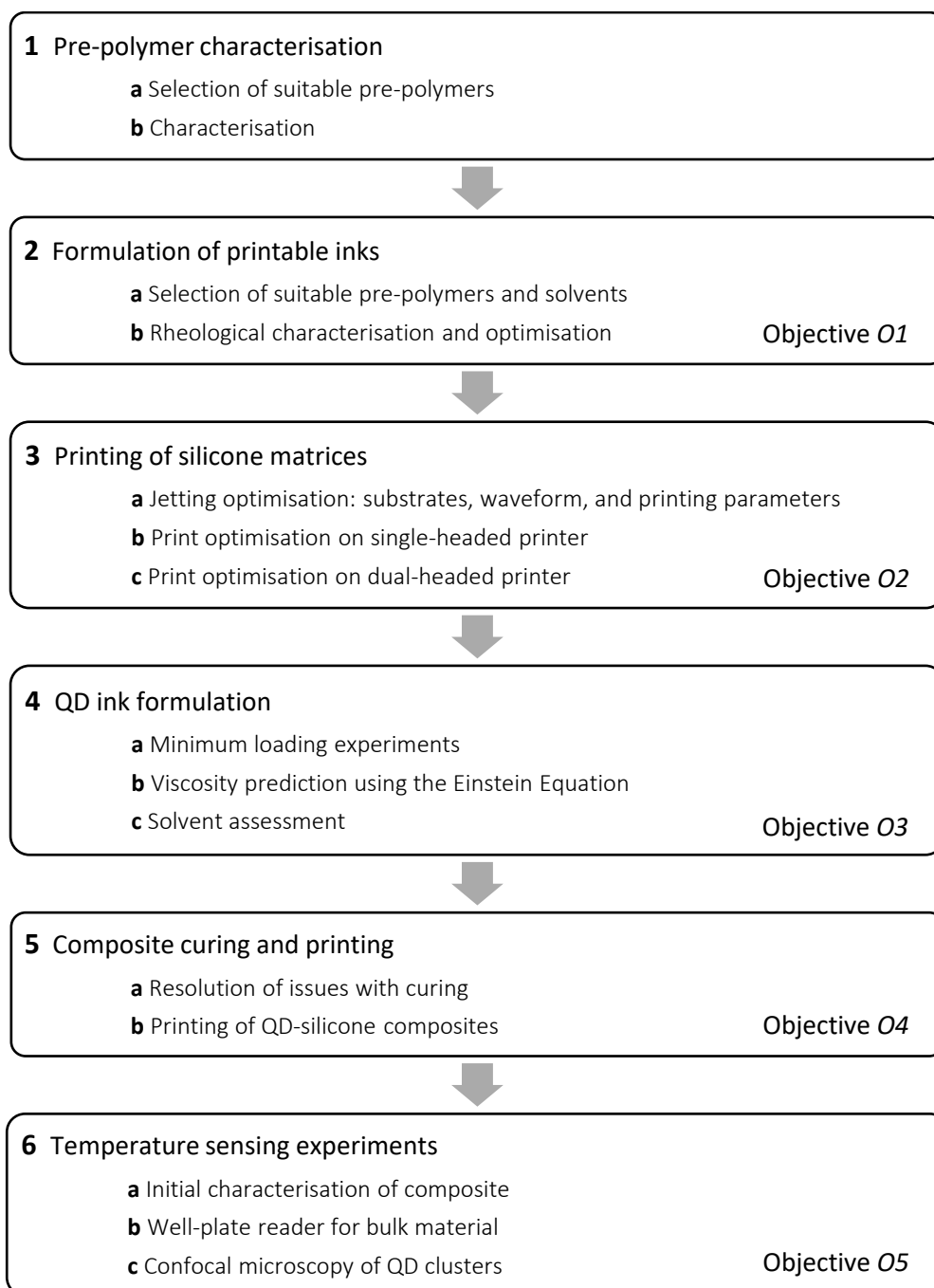


Figure 22: Flowchart showing the workflow used to achieve research objectives, divided into six stages.

Stages 1 and 2 used the following techniques to achieve *O1* by formulating ink candidates and confirming their printability.

Stage 1a involved reviewing literature on silicones in AM and silicones in industry, followed by selecting precursors. In **1b**, data on pre-polymers was collected from datasheets, spectroscopy and rheometry. Pre-polymers were interrogated using nuclear magnetic resonance (NMR) spectroscopy (Bruker, USA), Fourier transform infrared (FTIR) spectroscopy (Perkin Elmer, USA) and rheometry (Malvern, UK). This data informed **2a**.

In **Stage 2a**, solvents were selected as required to enable jettable inks. In **2b**, formulations were made and their densities measured by weighing aliquots from a syringe. Rheological characterisation of addition cure silicones was carried out using a Kinexus Pro rheometer (Malvern, UK), and a drop shape analyser DSA100 (KRÜSS, Germany). Shear-rate dependent viscosity of inks was determined for different temperatures in order to assess the need for viscosity modifiers such as the use of solvent or nozzle heating. Drop shape analysis was used in pendant and sessile droplet modes to find the surface tension of the ink and to assess printing substrates. A high-throughput rheometer was similarly used to find the viscosity and surface tension of the UV cure inks at room temperature. The printability of inks was calculated using the inverse Ohnesorge number as indicator (*O1*).

O2 was achieved in Stage 3 by optimising print parameters and testing a range of print strategies to produce printed patterns.

Stage 3 was carried out once *O1* was achieved i.e. the printability of inks had been calculated to be in the jettable range. **3a** and **3b** were conducted on the Fujifilm Dimatix printer. Printing parameters were optimised using the drop watcher to observe the jetting process. Deposited droplet diameter and mass were determined. In **3b**, print trials were carried out, utilising a pinned grid technique for addition cure silicones. In **3c**, printing of addition cure silicones was carried out on a dual-headed printer, which was more efficient for 2-part reactive inkjet.

Stage 4 comprised the work needed to formulate QD-inks with ideal loading, adequate dispersion, and printability to satisfy *O3*.

In **Stage 4**, QD composite inks were formulated. Minimum loading experiments were carried out in **4a** by finding the minimum loading for visible fluorescence and by determining detection limits using fluorescence microscopy (Horiba, Japan). In **4b** the Einstein Equation was used to predict viscosity increase with QD loadings to ensure that

inks remained printable. **4c** assessed octyl acetate as a solvent in comparison to hexane using dynamic light scattering (DLS) with a Zetasizer Nano ZS (Malvern, UK) to ensure that the solvent used led to good QD dispersion.

However, further work was required for *O4* as the curing of inks was not yet sufficient for printing. Stage 5 resolved issues with curing before conducting print trials.

Stage 5 demonstrated printing of QD-silicone composites. Addition of quantum dots to addition cure silicone was associated with hindered curing; in **5a**, work was carried out to resolve issues with curing that prevented printing of composites. Drop casting experiments were carried out with increased platinum catalyst loadings to find the minimum additional platinum catalyst needed for a sufficient reaction rate. FT-IR spectroscopy was trialled with a Frontier MIR/FIR spectrometer (Perkin Elmer, USA) by sampling every 3 minutes. Raman spectroscopy was carried out on cured samples using a LabRAM microscope (Horiba, Japan).

5a differed in the case of UV cure silicones due to different reaction mechanism. Experiments with photoinitiator concentration were carried out using a drop casting method to suggest ideal concentrations. DSC was carried out (Perkin Elmer, USA) to quantify the curing of QD-silicone composites with different concentrations of photoinitiator.

5b was carried out once issues with curing of addition cure silicone composites had been resolved. Composites were printed using a Fujifilm Dimatix printer (*O4*).

Lastly, the composite materials were characterised as potential temperature-sensing materials. A range of techniques were carried out in Stage 6 to fulfil *O5*.

Stage 6 assessed the performance of composites as temperature sensing materials (*O5*). **6a** involved initial characterisation of composites: PL spectra were taken (fluorescence microscopy) and imaging techniques (TEM, confocal microscopy) were used to identify QD agglomerates in the silicone matrix and give an indication of their size and dispersion through the bulk composite. Subsequent experiments measured the fluorescence of composites as a function of temperature: bulk measurements were taken using a plate reader (FlexStation, USA) in **6b**, while individual clusters were imaged using confocal microscopy (Zeiss, Germany) in **6c**. A specialised sample heater (Linnovave, Germany) was used to control temperature during microscopy.

3.2. Materials

Silicone fluids may crosslink to form thermoset polymers, which is of interest for reactive ink jetting processes. There are three main curing mechanisms: condensation cure (hydrolysis); addition cure (hydrosilylation); and UV cure (photopolymerisation). These mechanisms and their pros and cons are discussed in Literature Review, Section 2.2.2.

For the addition cure formulation, PlatSil® SiliGlass was obtained from Polytek and used as received. Octyl acetate ≥99% (Sigma Aldrich) and anhydrous toluene 99.8% (Sigma Aldrich) were used as solvents. Platinum (II) chloride 98% (Sigma Aldrich) was later used as additional catalyst to account for catalyst poisoning (*Stage 5a*).

UV cure formulations explored a small range of materials. Methacryloxypropyl-terminated PDMS (abcr, 4-6 cP), 2-ethylhexyl acrylate 98% (Sigma Aldrich), pentaerythritol tetrakis(3-mercaptopropionate) >95% (Sigma Aldrich), and 2,2'-(ethylenedioxy)diethanethiol 95% (Sigma Aldrich) were used as supplied. Photoinitiators 2,2-dimethoxy-2-phenylacetophenone 99% (Sigma Aldrich) and phenylbis(2,4,6-trimethylbenzoyl)-phosphine oxide 97% (Sigma Aldrich) were trialled.

CdSe/ZnS core-shell quantum dots (Ocean Nanotech, emission wavelength 630 nm, 9.5 nm diameter) were supplied in powder form with octadecylamine stabilising ligands.

Glass slides were coated in 1H,1H,2H,2H-Perfluorooctyl-trichlorosilane (PFOTS) 97% (Sigma Aldrich) to prepare sufficiently hydrophobic substrates for printing, as described in Section 3.2.3.1, and a thin layer of Elastosil® Aux mould release agent 32 (Wacker) was manually spread onto untreated glass slides for printing UV cure silicones (Section 3.2.3.2).

3.1.1. Addition cure silicones

Addition cure silicones are a class of 2-part silicones in which vinyl groups react with hydrosilane groups to crosslink. Addition reactions were selected as the starting point for this research due to the lack of by-products and shrinkage, which leads to their use as LED encapsulants; the optical properties were of interest to the sensing application.

A commercial RTV addition cure silicone rubber system was obtained from Polytek. PlatSil® SiliGlass is a low viscosity 1A:1B mix used to mimic glass for the production of moulded objects and safe shards. This system offered fast curing under ambient conditions, relatively low viscosity, and excellent optical clarity. SiliGlass is composed of unspecified organofunctional siloxanes, most likely linear methyl and/or phenyl siloxane chains capped with vinyl monomers. Part A contains < 20% siloxane hydride crosslinkers, while Part B contains < 0.1% platinum catalyst. Mix viscosity was given by the manufacturer as 190 mPa s. As the viscosity limit of inkjet printers is typically <40 mPa s for standard printers,³² it was necessary to dilute each part in a miscible solvent to create suitable inks.

Octyl acetate (≥99%) and toluene (anhydrous, 99.8%) were used as diluents as supplied from Sigma-Aldrich. Octyl acetate-based inks are used unless stated otherwise as their lower volatility was advantageous to printing.

Quantum dots (QD) were purchased and used as supplied from Sigma Aldrich. The 9.5 nm diameter CdSe/ZnS core-shell particles were supplied in powder form with octadecylamine stabilising ligands.

When preparing composites, it was observed that QDs inhibited curing of addition cure silicones and printing of composites was not possible with the 50 wt% SiliGlass inks as a result. Platinum (II) chloride 98% (Sigma Aldrich) was used as an additional catalyst to replace poisoned catalyst.

3.1.2. UV cure silicones

A brief screening of UV cure silicone formulations was carried out, investigating pre-polymers for radical polymerisation reactions with thiol-ene and/or (meth)acrylate moieties. This curing mechanism would enable vat photopolymerisation AM processes, such as micro-stereolithography (μ SLA) and two-photon polymerisation (2PP), in addition to being compatible with inkjet-based processes.

Two monomers were investigated for an acrylate-based photopolymerisable silicone ink: Methacryloxypropyl-terminated PDMS (abcr **AB116678**, 4-6 cP), and 2-ethylhexyl acrylate 98% (**2-EHA**).

Thiol-ene reactions are another notable mechanism for UV-curable silicones, as discussed in Chapter 5. This reaction was of interest for low oxygen inhibition, but thiols often quench QD fluorescence. Preliminary experiments were carried out to assess their potential utility. Two mercaptan monomers were obtained from Sigma Aldrich: Pentaerythritol tetrakis(3-mercaptopropionate) >95% (**PETMP**) and 2,2'-(Ethylenedioxy)diethanethiol 95% (also known as 3,6-Dioxa-1,8-octanedithiol or **DODT**).

Two well-known photo-initiators from different classes were explored. Photoinitiators 2,2-dimethoxy-2-phenylacetophenone 99% (**DMPA**) and phenylbis(2,4,6-trimethylbenzoyl)-phosphine oxide 97% (**TPO**) were obtained from Sigma Aldrich and used as received.

3.2. Methods

3.2.1. Pre-polymer characterisation

Physical and spectral data of pre-polymers was collected during *Stage 1b*. ^1H NMR spectra were collected in CDCl_3 solvent using a Bruker DPX 400 MHz spectrometer and IR spectra were taken as an average of four scans between $4000 - 650 \text{ cm}^{-1}$ using a PerkinElmer Frontier FT-IR spectrometer fitted with a diamond ATR plate. Viscosity data of constituents has been collected using the methods described below for *Stage 2*; other data was taken from the manufacturer's specifications.

3.2.2. Ink formulation

As described in Chapter 2, inkjet printing ejects droplets of liquid inks, which solidify on the printing substrate; as silicones are thermoset polymers, this work uses reactive inkjet, where silicone fluid precursors are deposited and crosslink *in situ*. The inkjet process has strict ink rheology requirements (i.e. $<40 \text{ mPa s}$ viscosity³² and $20\text{-}50 \text{ mN m}^{-1}$ surface tension³⁵) and the ink properties must fit the specifications of the equipment. During *Stage 2b*, jettable inks were formulated (Objective *O1*) to meet the specifications of the Dimatix Material Cartridge DMC-11610, a disposable system acting as both ink reservoir and printhead. This cartridge has 16 nozzles arranged in a row with $254 \mu\text{m}$ spacing, $21.5 \mu\text{m}$ nozzle diameter, 10 pL nominal droplet volume, and 1.5 mL capacity.⁵⁹ The LCP version has been employed in the case of addition cure silicones due to a need for higher chemical stability than the standard cartridge to ensure compatibility with the solvent. This cartridge is composed of Kalrez[®] and Liquid Crystal Polymer (LCP), as well as the standard silicon, silicon dioxide, and chemically-resistant epoxy.⁵⁹

To determine whether inks are printable, Equation 1 can be used to confirm that the ink rheology is within the jettable regime. Printability of inks is determined by three key rheological parameters: viscosity, density, and surface tension. Inks have been formulated to have rheological properties within the specific guidelines given by the manufacturer, as discussed in the following subsections. The cartridge has a built-in nozzle heater capable of $60 \text{ }^\circ\text{C}$ heating to help ink to meet these guidelines; however, inks have been formulated to jet at $30 \text{ }^\circ\text{C}$ to reduce potential thermal effects on unreacted material.

$$Z = Oh^{-1} = \frac{\sqrt{\rho\sigma L}}{\mu} = \frac{Re}{\sqrt{We}}$$

Equation 1: Printability Indicator Z , where Oh , Re , and We are the Ohnesorge, Reynolds and Weber numbers, and ρ , η , σ , and L are density, dynamic viscosity, surface tension, and nozzle diameter respectively.

3.2.2.1. Viscosity

According to the manufacturer's formulation guidelines, the ideal ink viscosity for the Fujifilm Dimatix printer is 10-12 mPa s,^{175,176} with a maximum extended range of 2-30 mPa s.⁵⁹ To ensure that the formulated ink is close to ideal, a Malvern Kinexus rotary rheometer was used to find the dynamic viscosity. Dynamic viscosity is defined as shear stress divided by shear rate, meaning the tangential force per unit area required to achieve a rate of change of deformation in a layer of fluid.

This rheometer is capable of shear rates of 0.1-2000 s⁻¹. While this measurement range is orders of magnitude lower than the typical shear during jetting processes,^{34,35} this is not an issue if inks are Newtonian fluids as their viscosity is independent of shear rate by definition. At low shear rates (<10 s⁻¹), the rheometer did not reach steady state because the torque generated from the low viscosity sample was low. At high shear rates (>100 s⁻¹), the measured viscosity increased as secondary flow was generated in the sample. This was not indicative of non-Newtonian behaviour and did not give rise to issues with printability. Therefore the 2.5-400 s⁻¹ approximate range is presented as representative of the sample and the value at 10 s⁻¹ is used in subsequent printability calculations.

A cone-and-plate geometry was used in this study as this system was effective for measuring low-viscosity fluids and only required small sample volumes. Steady-state viscosity was measured for a logarithmic set of shear rates and equilibrium flow curves were plotted to confirm Newtonian behaviour. Steady-state viscosity at a constant shear rate was then measured against temperature steps to find ink concentrations and nozzle temperatures suitable for jetting.

Dynamic viscosity was measured using a Malvern Kinexus pro+ rotational rheometer with a cone and plate geometry (4 °/40 mm SS). Equilibrium flow curves were taken using the rSpace Toolkit regime V001: shear viscosity was measured at steady-state against a logarithmic set of shear rates between 10⁻¹-10³ s⁻¹ at 25 °C.

The dynamic viscosity of solvent compositions was measured against temperature steps at constant shear (10 s⁻¹) using Toolkit regime V004 on a Malvern Kinexus pro+ rotational rheometer with a cone and plate geometry (4 °/40 mm SS) with a solvent trap. 60 data points each were taken over 300 s at steps of 25, 30, and 35 °C. The first 3 points of each step were discounted to ensure steady state. Standard error was >0.004 mPa s for each step.

3.2.2.2. Density

While the Dimatix DMP-2800 Series User Manual does not give a range of suitable densities, it notes that specific gravities greater than one are beneficial.¹⁷⁶ Ink density was found by weighing 1 mL of ink on an analytical balance with a 1 ± 0.01 mL syringe. This measurement was repeated three times with separate aliquots.

3.2.2.3. Surface tension and contact angle

According to the manufacturer's formulation guidelines,¹⁷⁵ the ideal range of surface tension for the Dimatix DMP-2830 is 28-33 mN m^{-1} , while the manual lists surface tension up to 42 mN m^{-1} as acceptable.¹⁷⁶ The extended range of surface tension typically recommended for inkjet is 20-50 mN m^{-1} ,³⁵ though the manufacturer notes that jetting is possible with surface tensions as high as 70 mN m^{-1} (albeit with limited performance).¹⁷⁵ Larger contact angles are associated with higher resolution, although contact angles above 90° may be associated with bulging.¹⁷⁷

Drop shape analysis is an optical method of contour analysis and contact angle measurement. Droplets are imaged and the shape is fit to mathematical models to determine properties. Surface tension was determined from pendant droplets and contact angle from sessile droplets in order to assess the printability of ink formulations and to identify substrates with compatible surface energies for inkjet patterning.

Surface tension was determined by static pendant drop shape analysis using the Young-Laplace model with a Krüss DSA100S drop shape analyser. Solutions were placed in 1 mL syringes with a flat-tip 1.25 mm diameter needle and 20 μL dosing applied gradually for the largest possible stable drops. Ten droplet measurements were recorded at room temperature for each test with octyl acetate-based inks and five droplets for toluene-based.

Contact angle measurements were carried out with sessile drop shape analysis using the Tangent – 2 computation method with a Krüss DSA100S. Solutions were placed in 1 mL syringes with a flat-tip 1.25 mm diameter needle and droplets were deposited onto different substrates with a 4.5 μL dispensing volume at a dosing rate of 100 $\mu\text{L}/\text{min}$. The baseline was manually set to the substrate surface. The test substrates were silane-treated glass, untreated glass, and glass coated with a release agent (Elastosil® Aux mould release agent 32, Wacker): the latter two led to wetting and the contact angle was too small to measure. Measurements were obtained for silane-treated glass (see Section 3.2.3.1). Five droplets were recorded at room temperature for 5 minutes for each test.

3.2.2.4. High-throughput screening

The viscosity and surface tension values of UV cure inks were rapidly determined using a high-throughput rheometer to screen potential formulations and investigate the effect of photoinitiator loading on printability. This quickly indicated which formulations were jettable and which would need further work to optimise formulation.

Rheological characterisation of UV curable formulations was carried out with a high throughput screening (HTS) method as described by Zhou *et al.*; their workflow is reproduced below in Figure 23.¹⁷⁸ Ninety-six-well-plates were prepared with 500 μL sample volume per well (Thermo Scientific 260252) in Stage 1. A four-channel liquid handling apparatus (Microlab STARlet, Hamilton Robotics) was used to handle samples via air displacement pipetting for viscosity (Stage 2) and surface tension determination (Stage 3).

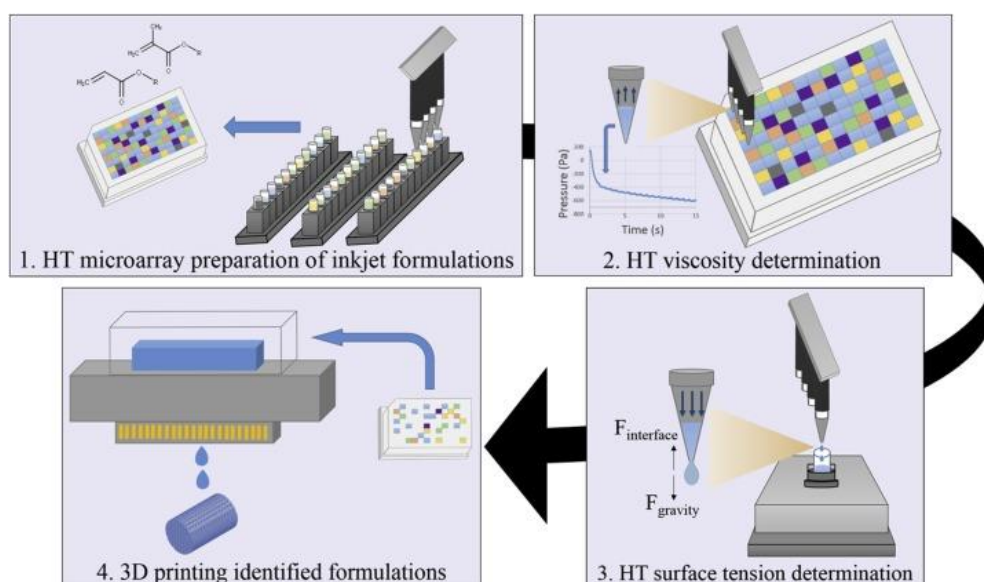


Figure 23: Workflow for high throughput ink formulation. Arrays of potential inks are prepared in well-plates and the apparatus determines viscosity and surface tension to identify jettable inks. Reproduced from Zhou *et al.*¹⁷⁸

For viscosity measurements, four samples were simultaneously aspirated into 300 μL pipettes (Hamilton Robotics 235902 CO-RE tips) at $10 \mu\text{L s}^{-1}$ for 15 s then re-dispensed into the well-plate to conserve material. Viscosity was calculated from pressure versus time curves. Three measurements were taken per sample.

For surface tension measurements, 110 μL of one sample was aspirated into a 300 μL pipette and dispensed into a receptacle on a high-precision balance (Mettler Toledo WXS205SDUV/15) at $5 \mu\text{L s}^{-1}$ for 20 s. As a droplet detaches from the pipette tip when the forces arising from droplet weight are equal to adhesive forces, it is possible to determine the surface tension. Typically, 12 droplets were measured for each sample.

3.2.3. Inkjet printing

As discussed in Chapter 2, inkjet printing is a versatile method of material deposition which is limited by its strict rheological requirements (i.e. $<40 \text{ mPa s}$ viscosity³² and $20\text{-}50 \text{ mN m}^{-1}$ surface tension³⁵). This in turn can limit the silicone materials that can be deposited using inkjet, as crosslinked silicones do not melt and have poor solubility; even dilute solutions of polymer networks may be non-Newtonian and viscous.

To circumvent issues with silicone elastomer inks, reactive inkjet has been employed. This uses low viscosity silicone fluids ($>1000 \text{ mPa s}$) to formulate pre-polymer inks that react *in situ* to form the final product. Two variations of reactive inkjet have been used in Stage 3b and 3c respectively. For the addition cure inks, 2-part inks (Ink A and Ink B, crosslinker and catalyst) were deposited drop-on-drop and crosslinked on the substrate (see Chapter 4 for details). For the UV cure inks, a single ink was used and a UV lamp induced photopolymerisation on the substrate (see Chapter 5 for details).

Printing optimisation has been carried out on two printer systems, one single- and one dual-head printer. The dual-head printer was ideal for the deposition of reactive 2-part addition cure inks, but it was not possible to observe jetting drop formation on this system nor obtain droplet mass using the custom-build assembly. The single printhead printer was therefore used for testing and optimisation of jetting and for deposition of 1-part UV inks.

Equation 1 was used to calculate whether inks meet the process requirements for stable jetting, as described in the previous section and Chapter 2. This is calculated from the viscosity, surface tension, and density of the ink, and the nozzle diameter of the printhead.

$$Z = Oh^{-1} = \frac{\sqrt{\rho\sigma L}}{\mu} = \frac{Re}{\sqrt{We}}$$

Equation 1: Printability Indicator Z, where Oh, Re, and We are the Ohnesorge, Reynolds and Weber numbers, and ρ , η , σ , and L are density, dynamic viscosity, surface tension, and nozzle diameter respectively.

Aside from optimisation of ink rheology, printing is refined via selection of print parameters to suit the material and ideally yield stable jetting, fast droplet velocity, and high jetting frequency. A frequency of 5 kHz was used: development of higher frequency inks, as is typically carried out for industrial processes, was not considered a priority at this stage of material development. In addition to ink formulation and jetting optimisation, a suitable substrate was selected and prepared prior to printing to prevent wetting, reduce sessile drop diameter, and therefore improve print resolution.

3.2.3.1. Substrate preparation

Due to the wetting behaviour of the silicone inks, glass slides were treated with fluorosilane (1H,1H,2H,2H-Perfluorooctyl-trichlorosilane, PFOTS), as described in Figure 24, to produce a low surface energy substrate in *Stage 3a*. Glass slides were oxidatively cleaned with 70% nitric acid before immersion in 1 vol% PFOTS solution in anhydrous toluene and then baking at 100 °C. This follows the preparation method used by Sturgess *et al.*⁶⁰

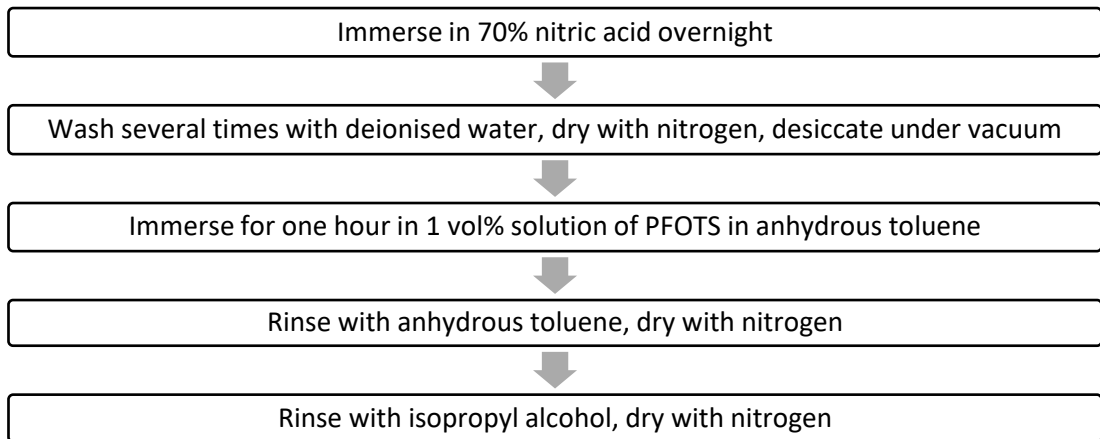


Figure 24: Flowchart of fluorosilane deposition process.

3.2.3.2. Printing of silicone matrix with single-printhead

In *Stage 3a* and *3b* for development of addition cure silicone inks, inkjet was carried out at room temperature on a Fujifilm Dimatix DMP-2830 with 10 pL LCP cartridges; LCP cartridges were used as curing did not occur with standard cartridges. A single pulse waveform was optimised from the Dimatix Model Fluid waveform (SiliGlass waveform version 1, henceforth referred to as $W_1 v_1$; see Figure 138, appendix). Drop formation and ejection with 30 °C nozzle temperature were observed via the Drop Watcher camera; images were taken from video using the Scene Filter option in VLC and reconstructed to show the droplet trajectory over time.

During *Stage 3a*, waveform $W_1 v_1$ was refined from the Dimatix Model Fluid with minimal modifications. A single jetting pulse with dwell time 1.9 μ s was used for optimal droplet velocity; 32 V jetting voltage was selected to achieve reliable jetting performance with suitable drop velocity and mass. The high viscosity and low surface tension of the silicone inks was observed to tend towards nozzle wetting, droplet tails, and satellite droplets. A meniscus cancellation pulse (55% level, 3.6 μ s pulse width) was used to straighten and

detach droplet tails during ejection from nozzles. The fill level was also set to 7% to reduce nozzle wetting.

Drop arrays were printed onto silane-treated glass slides using one nozzle at 60 μm drop spacing; size distribution was assessed using an optical microscope (Nikon Eclipse LV100 ND). Micrographs using the 20x objective lens were thresholded and analysed in ImageJ. Droplet mass was found by jetting one million drops into an aluminium DSC pan and weighing by difference; this was repeated until three measurements were found in agreement.

In *Stage 3b*, reactive printing was carried out with 40 $^{\circ}\text{C}$ platen heating as it was observed that crosslinking of SiliGlass was greatly slowed by the addition of solvent. At room temperature, the inks took hours to cure during dropcasting experiments, and at 60 $^{\circ}\text{C}$, inks took 10 min to fully cure. As cure rate is diffusion-based and the droplet volumes are much smaller during printing - leading to an increased rate of solvent evaporation - 40 $^{\circ}\text{C}$ platen heating was used to minimise any thermal cycling on QDs.

Inks did not converge to a single layer as the ink showed poor pinning to the silane-treated substrate. Reactive printing on the Dimatix required a pinned grid to be printed and solidify on the surface before continuous patterns could be produced with accuracy. Printing was carried out with 60 μm spacing as the smallest spacing that did not lead to ink coalescence.

As the Dimatix printhead holds only one cartridge, Ink A and Ink B needed to be swapped regularly. As offset needed to be recalibrated each time, it was prudent to deposit multiple layers of ink at a time rather than alternate. The pinned grid was typically 10 layers of A followed by 10 layers of B.

In *Stage 3a* and *3b* for UV curable silicone formulations, inkjet was carried out on a Fujifilm Dimatix DMP-2830 with standard 10 pL cartridges. Material was printed at room temperature in a nitrogen-filled glovebox (0.5% O_2) to prevent oxygen inhibition. Inks are referred to using shorthand notation below: methacryloxy-terminated PDMS (AB116678) was used, henceforth referred to as 'PDMS' in the context of UV cure inks. This was also combined with 2-ethylhexyl acrylate (2-EHA) in a 1:1 weight ratio, henceforth referred to as '2-EHA' in the context of inks.

In *Stage 3a*, jetting was investigated for PDMS and 2-EHA inks at 25 V with a single pulse waveform (henceforth referred to as W_2 ; see Figure 140, Appendices). Waveform W_2

consists of a single pulse waveform for forceful ink ejection and long, slow recovery; a meniscus cancellation pulse is used to cut off tails during ink ejection. This waveform is not optimised towards efficient jetting of a specific ink but is compatible with a range of fluid properties and was used to demonstrate jetting of UV cure ink. Additionally, PDMS was jetted at 20 V with a waveform developed for jetting of addition cure inks on the dual-printhead system ($W_1 v2$, Figure 139, Appendices). Ejection of inks without photoinitiator was investigated as rheology was similar between formulations of the same precursor composition. Drop formation and ejection were observed via the Drop Watcher camera, as described for addition cure inks, and drop arrays were similarly deposited and analysed using optical microscopy as described above.

Printing was then demonstrated for 1 wt% TPO-PDMS ink at 22 V using waveform $W_1 v2$ (Figure 139, Appendices) in *Stage 3b*. Convergence tests were carried out to determine ideal droplet spacing for printing a continuous film. Squares were printed onto a glass substrate coated with release agent at drop spacings of 5, 10, 15, and 30 μm and were cured with a 365 nm lamp affixed to the printhead. Continuous, non-bulging films were produced with 10 μm drop spacing.

3.2.3.3. Printing of silicone matrix with dual-printhead

Dual-headed printing (*Stage 3c*) was carried out for addition cure inks on a PiXDRO LP50 with a custom-built assembly for compatibility with Dimatix cartridges, as developed by Sturgess.¹⁷⁹ A printhead with two slots for cartridges fits onto the gantry of the LP50. The two inks are controlled by an arbitrary function generator (Tektronic AFG3102) – which outputs the jetting waveform in response to the data and signals from the LP50 and computer – connected to two controllers which select the nozzle and nozzle temperature. Only one of the 16 Dimatix jetting nozzles can be controlled at one time using this set-up. The deposition of the two inks is aligned in the X axis by the angle of the printhead, as shown in Figure 25; this enables line-by-line printing in the X-direction with simultaneous deposition of both inks. The alignment angle is calculated from drop offset and controlled by a MATLAB script: a test pattern is deposited by each cartridge to calculate the offset of ink deposition in the X and Y axes (ΔX_{off} and ΔY_{off} , respectively) from which the angle correction required for line-by-line printing is calculated (Equation 2). This leads to a line offset in the Y-axis for single pass printing (Equation 3): a duplicated pattern is printed, leading to a central overlapping pattern and individual inks, separated by the Y line offset.

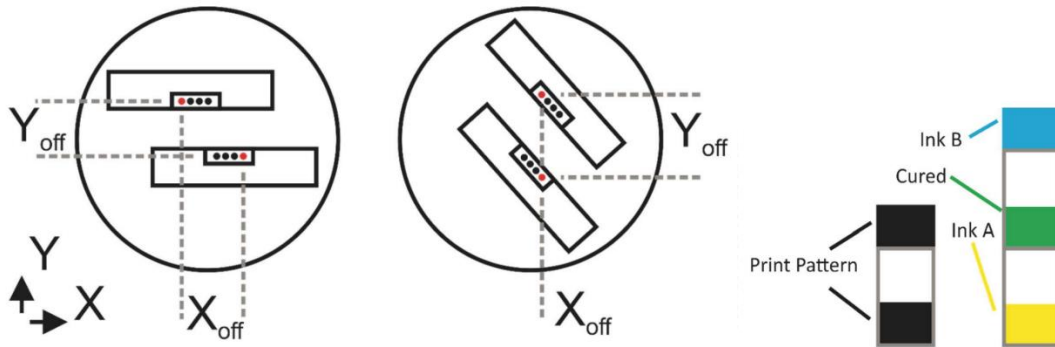


Figure 25: Left: Topside view of the printhead adaptor loaded with two Dimatix cartridges. On the left, the printhead angle is not correctly calibrated to align the jetting nozzle in use by each cartridge. On the right, the printhead turns to align in the X-axis. Right: Duplicated pattern for single pass printing with Y line offset.¹⁷⁹

$$\theta_{line\ off} = \text{atan}\left(\frac{\Delta X_{off}}{\Delta Y_{off}}\right)$$

Equation 2: Calculation of printhead angle offset for line-by-line printing from the offset between the two cartridges, where $\theta_{line\ off}$ is printhead angle offset, and ΔX_{off} and ΔY_{off} are offset in the X and Y axes.¹⁷⁹

$$Y_{line\ off} = \sqrt{\Delta X_{off}^2 + \Delta Y_{off}^2}$$

Equation 3: Calculation of the Y-axis offset between the two cartridges during line-by-line printing, where $Y_{line\ off}$ is the distance between the duplicated print pattern to enable single pass printing.¹⁷⁹

The simultaneous deposition of two inks was beneficial for printing 2-part addition cure inks as this approach did not require the user to load and unload cartridges to alternate materials. Line-by-line deposition aided the mixing of Ink A (crosslinker) and Ink B (catalyst), eliminated the need for pinned grids, and improved surface finish of printed films.

Printing was carried out using the waveform developed on the Dimatix - with slight modifications for lower voltage (Figure 139, Appendices) - using the same nozzle and platen temperatures. Waveform $W_1 v_2$ was adapted from $W_1 v_1$ to enable printing on the modified LP50, as the jetting voltage was limited to 30 V. This consisted of the same single jetting pulse (slew rate 0.65, dwell time 1.8 μ s) and meniscus cancellation pulse (55% level, 3.6 μ s pulse width) as $W_1 v_1$. Consistent jetting at 30 V was enabled by reducing the fill segment length and setting its level to 0%. Drop arrays were jetted with 60 μ m spacing and analysed via optical microscopy as described previously.

Printing was carried out at 40 or 45 μ m, spacings at which stable lines are formed; simultaneous jetting of both inks enabled line-by-line printing and eliminated the need for pinned grids. Printing was typically unidirectional and left-to-right. Bidirectional jetting refers to jetting in both the forward and backward y direction, aligning the droplets using time of flight; this deposited two reactive lines per pass.

3.2.3.4. *Printing of QD-silicone composites*

Once suitable inks had been optimised for printing of addition cure silicone matrices, QD-inks were formulated (see Section 3.2.4). The first attempt to print QD-silicone composites was unsuccessful, therefore further work was carried out to identify and overcome the issues associated with printing. In the interim, the dual-headed printer became unavailable and so all further printing was carried out on the Fujifilm Dimatix during *Stage 5b*. Successful jetting of quantum dots was visually confirmed by inspecting for fluorescence under a UV lamp.

Composite printing was demonstrated for the 50 wt% octyl acetate addition cure inks, which were sonicated for 30 min prior to loading into LCP cartridges. QD-Ink A (0.005 wt% QDs) was printed with either Ink B or Pt-Ink B (0.00125 wt% additional platinum catalyst) using a Fujifilm Dimatix printer (DMP-2830) and a pinned grid strategy as described above. Ink was jetted using waveform W_1 v2 at 30 V and 60 μm spacing was used with 60 °C substrate heating; inks were jetted with nozzle temperature 35 °C, as that was the lowest stable temperature with this platen heating. Pinned grids were deposited with one layer of QD-Ink A and one layer of Ink B or Pt-Ink B, or 1a1b, and were allowed to cure for 5 min. Subsequent material was deposited on top of the grid as 10a10b.

Jetting of UV cure inks with QDs was demonstrated for inks prepared with 0.25 wt% DMPA-2-EHA; 10 μL of QD solution (0.005 wt% in octyl acetate) was added to 1 mL of ink pre-polymer and loaded into a Dimatix cartridge. Printing was carried out in a Dimatix printer inside a glove box in a nitrogen atmosphere (1.1% O_2) to prevent oxygen inhibition and ink was jetted using waveform W_2 at 25 V.

3.2.4. QD ink formulation

Addition cure QD-silicone formulations were characterised to ensure that fluorescence of composites was adequate for optical sensing and to establish the minimum loading required to meet detection limits for sensing (*Stage 4a*). The Einstein equation was used to predict the change in viscosity associated with the addition of quantum dots and calculate printability (*Stage 4b*), and the effect of the solvent on dispersion was assessed (*Stage 4c*). The following techniques were used to refine the formulation of QD inks to ensure that inks would meet requirements for inkjet and sensing (to complete Objective O3).

3.2.4.1. Minimum loading

Minimum loading was assessed during *Stage 4a* using samples produced by mixing QD-Ink A with Ink B. Addition cure composites are listed with the weight percent of the QD-ink used to make them, which is equivalent to the weight percent of QDs to silicone matrix in the cured composites when disregarding residual solvent.

In order to rapidly assess the loading required for visible fluorescence in cured composites, samples were prepared in vials by mixing 0.2 mL of Ink A with different QD loadings with 0.2 mL of Ink B. Initial experiments added QDs to Ink B but, after the first print trial resulted in inks that did not cure, this experiment was repeated and all subsequent work adds QDs to Ink A to minimise catalyst poisoning.

Vials containing Ink B were heated to 60 °C on a hotplate. QD dispersions in octyl acetate were diluted to the desired loading, mixed with SiliGlass A, sonicated, and added to vials containing Ink B. Composites made from 0.02, 0.01, 0.005, 0.001, and 0.0001 wt% QD inks were left to cure at 60 °C. All cured composites appeared transparent.

To guide the QD loading for the inks, the detection limit was found for the addition cure QD-silicone composite using fluorescence microscopy. A well-plate was prepared by serial 10x dilution of QDs in Ink A followed by addition of 90 µL of Ink B (180 µL total sample volume per well) to produce wells with 0.01, 0.001, 0.0001, 0.00001, and 0.000001 wt% QD-Ink A and Ink B. Point spectra were taken from the centre of each sample with a Horiba LabRAM microscope using a 532 nm laser, a 600 lines mm⁻¹ grating, and a 10x or 50x objective.

3.2.4.2. Viscosity prediction

In *Stage 4b*, the Einstein equation was used to predict the change in viscosity upon addition of QDs,³⁵ as defined below in Equation 4.

$$\mu_r = 1 + 2.5\phi$$

Equation 4: The Einstein equation, where μ_r is relative viscosity and ϕ is the volume fraction of hard sphere particles.

3.2.4.3. Solvent assessment

Dynamic light scattering (DLS) is a technique used to measure particle size in dry or wet conditions. This was of interest to confirm the suitability of the solvent used in this ink by comparison to typical nonpolar solvents for QD suspensions (*Stage 4c*). Toluene is a notorious scatterer and was not investigated using DLS, while chloroform led to faster QD settling than octyl acetate. Therefore, hexane was used as a comparative typical solvent.

Dynamic light scattering (DLS) was carried out using a Malvern Zetasizer Nano ZS with 0.005 wt% solutions of QDs to mimic the ink loading. QD solutions in octyl acetate or hexane were sonicated for 30 minutes prior to measurement. 1 mL was then loaded into a Starna Spectrosil® Quartz-1/Q/10 cuvette and loaded into the machine.

3.2.5. QD composite curing

Cure rate had proved to be a major challenge in printing of composites; therefore, work was carried out to optimise and quantify ink curing in *Stage 5a*. Inks were prepared with varying amounts of additional platinum catalyst (addition cure) or photoinitiator (UV cure). Drop casting experiments were carried out to quickly assess suitability of formulations followed by quantitative assessment of curing. Addition cure inks were interrogated using Raman spectroscopy and Fourier transform infrared spectroscopy (FTIR). UV cure inks were assessed using differential scanning calorimetry (DSC).

3.2.5.1. Addition cure inks

Ink preparation

Work was carried out to formulate curable inks using additional platinum catalyst. Henceforth, QD-Ink A refers to 0.005 wt% CdSe/ZnS QDs in SiliGlass A with 50 wt% octyl acetate solvent. Pt-Ink B similarly consists of additional catalyst in SiliGlass B with 50 wt% octyl acetate solvent, which refers to a series of formulations with 0, 0.005, 0.0025, 0.00125, and 0.00075 wt% platinum (II) chloride unless otherwise stated. Ink A mixed with Ink B, with no additional QDs or catalyst, serves as control sample unless specified otherwise. Toluene analogues, where noted, are formulated using SiliGlass with 40 wt% toluene solvent and identical QD or catalyst loadings as described above. All inks were sonicated for 30 min immediately prior to use.

Drop casting experiments

Drop casting experiments were carried out to quickly assess suitability of formulations.

To assess whether lower QD loadings could achieve suitable cure rates, Ink A was prepared with 0.005 wt%, 0.001 wt%, or 0.0005 wt% QD loadings, which were selected to be within detection limits. 20 μ L of Ink A was deposited on top of 20 μ L of Ink B on a glass slide on a hotplate at 60 °C; this temperature was selected as a feasible temperature for substrate heating on the Dimatix if required. Samples were monitored at 30 s intervals to see how long it took for the silicone to solidify, using a micro-spatula to confirm the change in state. This was repeated three times for each formulation.

Minimum additional catalyst experiments were carried out using the same method as above with QD-Ink A and Pt-Ink B. Controls were run with unadulterated Ink A and Ink B and their toluene-based analogues (60 wt% SiliGlass in toluene).

Raman spectroscopy

Raman spectroscopy was carried out using a Horiba LabRAM HR Raman microscope. Measurements were carried out using a 785 nm wavelength laser (~20 mW power), 300 lines mm⁻¹ grating and a 100x objective. Wavelength was selected to avoid QD fluorescence.

Raman spectra were obtained for SiliGlass A and B separately. Cured samples were prepared for QD-Ink A with Pt-Ink B, with undiluted SiliGlass reagents ('pure') and Ink A with Ink B ('solvent') as controls. 175 µL of each ink (350 µL total) was mixed in a PTFE/silicone SEPTA closed top vial cap and heated on a hotplate at 60 °C for 15 minutes.

Ten Raman spectra were taken from the surface of each cured sample and averaged. The peak of interest corresponds to the Si-H group at ~2150 cm⁻¹, which is depleted as the silicone crosslinks via a Pt-catalysed reaction. The Si-O-Si stretch at ~490 cm⁻¹ was used to normalise data: intensity ratios were calculated from peak areas. Degree of conversion (DoC) was calculated using mean intensity ratios in comparison to cured SiliGlass. XY PL maps were taken of samples containing quantum dots.

Fourier transform infrared spectroscopy

A pilot study for time-dependant FTIR was carried out. IR spectra were taken as an average of four scans taken between 4000 – 650 cm⁻¹ (0.2 cm⁻¹ resolution) using a PerkinElmer Frontier FT-IR spectrometer fitted with a diamond ATR plate. QD-Ink A was mixed with Pt-Ink B; Ink A mixed with Ink B was used as a control. 15 µL of each ink was added to aluminium DSC pans (40 µL pan volume) on a hot plate at 60 °C. 1 µL was sampled at 3 minute intervals. The sample holder was cleaned with IPA and a background scan run between samples.

While FTIR was shown to be feasible for monitoring of the Si-H peak – particularly if the resolution and range were optimised to increase the number of scans – sample peaks were inconvenient for normalisation and experiments were time-consuming. While it is possible to use FTIR spectroscopy, the data collected during the pilot study could not be analysed.

3.2.5.2. UV cure inks

Sample preparation

The UV-curable silicone used was a methacryloxy-terminated PDMS (AB116678), henceforth referred to as 'PDMS' in the context of UV cure inks. This was also combined with 2-ethylhexyl acrylate (2-EHA) in a 1:1 weight ratio, henceforth referred to as '2-EHA' in the context of UV cure inks.

Formulation was carried out with two different photoinitiators: DMPA and TPO.

DMPA: Prepolymer inks were prepared in vials as 0.5 wt% DMPA-PDMS ink; 0.5 wt%, 1.25 wt%, and 2.5 wt% DMPA-2-EHA inks; and with 0.2 mL PDMS, 0.1 mL DODT, 2 drops of the more viscous PETMP, and 2.5 wt% DMPA. Curing was typically carried out in a glove box under nitrogen (0.5 % O₂) under a 365 nm UV lamp. 10 µL of QD solution (0.005 wt% in octyl acetate) was mixed with 90 µL of pre-polymer to produce QD-loaded inks. 10 µL of sample was placed onto a glass slide and cured to investigate formulations with and without QDs. Vials of prepolymers were put under a 365 nm lamp to produce cured composites.

TPO: Vials were prepared with 0.01, 0.1 and 1 wt% TPO-2-EHA inks. 25 or 50 µL of QD solution (0.01 wt% in octyl acetate) was added to 0.2 mL ink in a vial. The vials were then cured under a 365 nm lamp to produce composites.

Differential scanning calorimetry

DSC was carried out using a Perkin Elmer DSC 8000 under isothermal conditions (25 °C) and nitrogen gas (20 mL min⁻¹ flow rate) with an OmniCure S2000 laser unit (Hg lamp, 250-450 nm filter, 23 mW, 15% iris). PDMS and 2-EHA inks were prepared with 0.25, 0.5 and 1 wt% TPO photoinitiator. Samples were accurately weighed by difference with a Kern ABT 100-5m scale into aluminium pans, using approximately 18 mg per test. The test programme was 5 minutes long with a sampling interval of 0.1 s; the lamp shutter was triggered to open for 10 s at 0.5 minutes and 3.5 minutes.

3.2.6. Temperature sensing

Experiments were carried out to monitor emission of the QD-silicone composites as a function of temperature to achieve Objective *O5* during the final phase of experiments, *Stage 6*. As the UV cure composites had been observed to have less stable fluorescence, sensing experiments focused on addition cure silicone formulations.

The properties of the addition cure composites were investigated using imaging techniques to obtain PL point spectra and to assess QD cluster size and dispersion through the silicone matrix. In *Stage 6b*, a fluorescence plate reader was used to assess changes in emission of bulk material as intensity counts, demonstrating utility for high-throughput methods.

In *Stage 6c*, confocal fluorescence microscopy was used to assess changes in emission intensity and wavelength as a function of temperature by imaging individual quantum dot clusters within the silicone matrix. This was used for assessing dispersion of quantum dots, homogeneity of response, and peak shift, as well as imaging any potential structural changes resulting from heating.

3.2.6.1. Sample preparation

QD composite characterisation

QD-silicone composite test samples were prepared in glass vials using 0.01 and 0.005 wt% QD-Ink A as described in Section 3.2.4.1.

Fluorescence plate reader

Formulations were prepared in a Corning 4580 flat bottom half-area black well-plate: this is constructed of cyclic polyolefin and glass and was chosen for solvent compatibility. The procedure for well-plate preparation was refined during preliminary experiments; the final method is given here. The well-plate was sequentially washed with acetone and iso-propyl alcohol and allowed to dry fully before use to remove any possible surface treatments that could interfere with silicone curing.

Addition cure formulations were prepared with QD-Ink A mixed with Pt-Ink B as according to ink preparation in Section 3.2.5.1, with SiliGlass A mixed with SiliGlass B ('pure') and Ink A mixed with Ink B ('solvent') as controls. Toluene-based analogues were also prepared.

Addition cure inks were sonicated for 30 min before 75 μL of each ink was pipetted into wells (150 μL sample per well) and cured by heating the well-plate on a hotplate at 60 $^{\circ}\text{C}$ for 2 hours, the first 15 minutes of which was accompanied by heating from above with a heat gun. The well-plate was allowed to cool to room temperature before filling wells with UV cure silicones.

PDMS and 2-EHA UV cure inks were prepared with high or low loadings (0.1 or 0.001 wt%) of either DMPA or TPO photoinitiator. A 0.01 wt% stock solution of QDs in PDMS was obtained by adding 0.5 wt% QDs in octyl acetate to PDMS and sonicating for 30 min. 0.01 wt% QD-PDMS or PDMS was added to PDMS or PDMS/2-EHA containing 0.2 or 0.002 wt% DMPA or TPO to produce 0.005 wt% QD-composite inks and control inks.

UV cure silicone formulations were sonicated for 30 min and 75 μL of each sample was pipetted into wells. The wells with addition cure samples were covered with aluminium foil before curing the UV cure samples under a 365 nm wavelength UV lamp in a glovebox (0.5% O_2). UV samples were cured for 5 min, moving the lamp between wells to ensure even exposure.

Confocal fluorescence microscopy

Initial work was carried out to image QD clusters in the silicone matrix. Samples were prepared by depositing 10 μL of QD-Ink A and Ink B (20 μL total) onto a glass slide and placing a glass coverslip on top to prepare a thin film; slides were heated to 60 $^{\circ}\text{C}$ on a hotplate for 1 hr to cure.

Equipment for controlling the temperature of samples necessitated a different preparation procedure: samples were prepared on glass coverslips to fit on top of the smart substrate. 10 μL of each addition cure ink (QD-Ink A and Pt-Ink B, 20 μL total) was deposited onto a coverslip and sets of samples were heated on a hotplate at 60 $^{\circ}\text{C}$ for 15 min and then left at room temperature overnight. QD-Ink A with Ink B was prepared using both octyl acetate and toluene analogues; octyl acetate-based QD-Ink A with Ink B was prepared by heating at 60 $^{\circ}\text{C}$ for 1 hr and did not cure under the other conditions listed.

3.2.6.2. QD composite characterisation

For *Stage 6a*, imaging was carried out to analyse the size and dispersion of QD clusters through the silicone matrix, and photoluminescence (PL) spectra were taken.

Point spectra were taken with a Horiba LabRAM microscope to assess PL of 0.01 and 0.005 wt% samples synthesised in vials as described in Section 3.2.4.1.

Samples were prepared for TEM by cryo-section with a CR-X Cryo Ultramicrotome and were ultramicrotomed to 70 nm thick with a diamond knife with liquid nitrogen cooling (T_g of silicone rubber = -127 °C). The sliced sample was then transferred using a wire loop with a drop of 5% sucrose solution and mounted onto a copper TEM grid. Mounted sections were imaged in bright field mode using a JEOL 2100+ TEM with an UltraScan 1000XP CCD camera and elemental analysis was carried out using an Oxford Instruments XMax^N 80 TLE EDS detector.

3.2.6.3. Fluorescence plate reading

Fluorescence plate readers are commonly used for high-throughput and screening methodologies, monitoring changes in emission, and for imaging of arrays. This technique was used for investigating bulk properties of the composites in *Stage 6b*.

Well-plates were loaded into a Flexstation 3 multi-mode microplate reader (Molecular Devices) and fluorescence intensity counts taken from the centre of each well, taking 6 readings from the bottom. The excitation wavelength used was 561 nm and the emission wavelength for detection was set to 630 nm. Measurements were taken between 25-40 °C with 2.5 °C intervals; measurements were taken when the emission intensities ceased to vary with time, so 15-20 minutes were allowed between tests for the samples to attain thermal equilibrium. 5 measurements were then taken at 1.5 min intervals.

3.2.6.4. Confocal fluorescence microscopy

Confocal fluorescence microscopy can be used to image the dispersion of quantum dot clusters through the silicone matrix without the need for cryo-sectioning, as well as allow controlled collection of PL data from a narrow focal plane.

Confocal fluorescence microscopy was performed using a Zeiss LSM 710 laser scanning microscope: a Zeiss inverted microscope consisting of an Axio Observer.Z1 base with scanning stage 130x100 STEP, fitted with a Zeiss LSM 710 laser unit.

For higher resolution imaging under ambient conditions (*Stage 6a*), a Zeiss Plan-Apochromat 63x 1.4 N_A oil-immersion objective was used. QDs were excited with a 514 nm argon laser with a 514 nm long-pass filter (MBS 458/514 nm). Images and z-stacks were taken from 526-685 nm emission (1024x1024 and 512x512 pixels respectively; averaging of 2 frames). Lambda scans were taken from 540-714 nm with approximately 10 nm intervals (1024x1024 pixels; averaging of 2 frames).

Temperature-sensing experiments used a Zeiss EC Plan-Neofluar 20x 0.50 N_A objective without immersion (*Stage 6c*). QDs were excited with a 561 nm DPSS laser with a 561 nm long-pass filter (MBS 458/561 nm) and Z-stacks were taken from 568-712 nm (1024x1024 pixels; averaging of 2 frames). Lambda scans were taken from 569-704 nm with approximately 10 nm intervals (1024x1024 pixels; averaging of 4 frames): nominal emission wavelengths of interest are 598 (592.9-602.5), 607 (602.5-612.2), 617 (612.2-621.8), 627 (621.8-631.5), 636 (631.5-641.1), 646 (641.1-650.8), and 656 (650.8-660.4) nm.

A prototype VAHEAT temperature control unit was used to ensure rapid and accurate temperature control: room temperature was measured using a thermometer and set as the reference value. Lambda scans have been taken from 25-99 °C with 2.5 °C intervals, with 25-60 °C as typical cycle; higher temperatures were also explored to investigate the impact on PL. Although the sample temperature rapidly stabilised according to the control unit, data has been collected after a waiting period - as silicones have poor thermal conductivity^{17,53} - to ensure thermal equilibrium: 2 minutes for intervals of 2.5 °C; 5 minutes for larger intervals; and 10-15 minutes when returning to ambient temperature.

Gain was optimised at the start for each individual sample at 25 °C to avoid saturated pixels: while this prevents direct comparison between samples, each run is internally consistent. Thermal drift was found to be a non-issue and refocusing was not necessary: the same confocal plane has been imaged consistently for each sample. Thermal drift did not exceed 2 pixels in the x or y direction and images were stabilised using an ImageJ plugin. In some datasets, a sinusoidal pattern of error was observed in data, which averaged out between thermal cycles and correlated with the stabilisation constants used and background removal (see below): thresholding led to larger observed changes in grey value as pixel values could be averaged across the mask boundary.

Micrographs were aligned and analysed using ImageJ: histograms were obtained for grey values of micrographs with and without background removal. Background removal was carried out on the brightest slice (621.85-631.50 nm) of a sample imaged under ambient

conditions and a threshold was applied to obtain a background mask, which was applied across all slices and stacks of the same sample region for consistency.

Particle measurement was carried out on the 621.85-631.50 nm slice of ambient micrographs after background removal and thresholding to collect mean, modal, minimum, and maximum grey values of individual QD clusters. Grey values were obtained for all slices and stacks of the same sample region by using the binary background image as a mask, redirecting to greyscale slices of interest in the Set Measurements options. Additionally, particle sizing was carried out using stricter thresholding to isolate the brightest areas, obtaining values for area and Feret diameter from the ambient 621.85-631.50 nm slice. Collection of grey value data for all slices and stacks was repeated with this threshold using the method described above. QD cluster sizes obtained are estimates as optical effects interfere in how large fluorescent particles appear.

In addition to estimated emission intensity-based sensing, it was also possible to estimate the average emission wavelength based on the emission spectra histograms collected by comparison of mean greyscale values. An exemplary histogram is plotted below in Figure 26; the mean emission wavelength λ_{mean} was estimated as described in Equation 5.

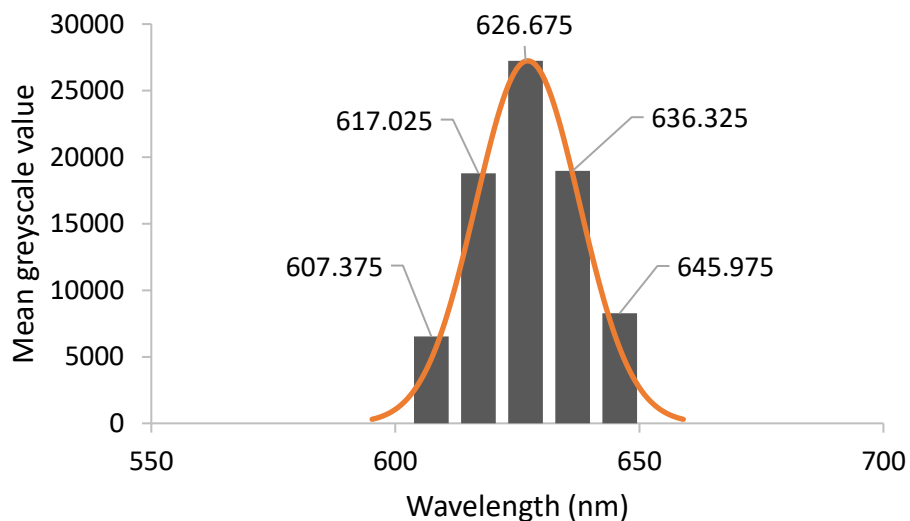


Figure 26: Histogram of emission from 0.00125 wt% PtCl₂ QD-silicone composite at 30 °C; data shown is the average of the three thermal cycles, with $\lambda_{mean} = 627.12$ nm. A normal distribution curve is plotted for illustrative purposes, showing how histograms obtained from the lambda scan relate to the QD emission peak.

Equation 5: Estimated mean emission wavelength λ_{mean} , where λ is the midpoint emission wavelength of each frame and g_{λ} is the mean greyscale value.

$$\lambda_{mean} = \frac{\sum(\lambda \cdot g_{\lambda})}{\sum g_{\lambda}}$$

Chapter 4. Results – Addition cure silicones

In this chapter, addition cure silicone inks were formulated for inkjet using octyl acetate or toluene solvent to reduce viscosity. A Fujifilm Dimatix DMP-2830 and a Suss Microtec PiXDRO LP50 were used to print 50 wt% silicone octyl acetate-based inks. Reactive jetting of the two parts was carried out using a drop-on-drop (DoD) method. The Dimatix had a single printhead and a pinned-grid strategy was required to control patterning. The PiXDRO had a dual printhead which enabled simultaneous jetting of both parts and was much more efficient to operate than the Dimatix.

This chapter:

- Discusses the choice of commercial silicone and characterises the 2-part system
- Identifies suitable solvents
- Characterises several jettable ink formulations
 - Viscosity
 - Density
 - Surface tension
 - Z number
- Outlines the printing optimisation of 50 wt% silicone octyl acetate-based inks
 - Preparation of substrates with suitable contact angle
 - Optimisation of printing parameters
 - Assessment of printed patterns and print strategies
- Formulates jettable quantum dot (QD) inks
 - Detection limit experiments to find minimum loadings
 - Viscosity prediction using the Einstein equation
 - Comparison of QD dispersion in octyl acetate and hexane
- Describes work carried out to enable printing of composites
 - Addition of platinum catalyst to enhance curing of composites
 - Characterisation of cure using FTIR and Raman spectroscopy
 - Printing of QD-silicone composites.

Several challenges arose, involving solvent compatibility, substrate pinning, dispersion, and catalyst poisoning. Multilayer silicone films with complex geometries were printed using both single and dual printhead assemblies. Printing of a QD composite was then demonstrated: the first inkjet printable QD-silicone composite.

4.1. Prepolymer characterisation

This section discusses the selection of a commercial 2-part room temperature vulcanisation (RTV) system, collates data from the manufacturer, and discusses the data collected to characterise the prepolymers. Datasheets for commercial silicone systems do not give full details of their proprietary formulations; however, formulation choices can determine the rheological, mechanical, and optical properties of the cured material. Therefore, work was done to obtain data on the selected commercial silicone to inform ink formulation and to aid understanding of the properties of printed material and composites as relates to the temperature sensing application.

In this section:

- ^1H Nuclear Magnetic Resonance (NMR) spectroscopy and Fourier Transform Infrared (FTIR) spectroscopy are used to identify principal components of the formulation and their parameters (chain groups, molecular weight, molar ratio of reactive moieties)
- The rheological behaviour of the two parts is examined to predict changes in viscosity when under high shear during the inkjet process and to assess the need for viscosity modifiers.

4.1.1. Temperature sensor criteria

As stated in Section 2.1.2, silicones are preferred encapsulants for high-brightness white LEDs – which have similar material requirements to optical thermosensors due to the heat generated at the junction ($\sim 120\text{ }^\circ\text{C}$ junction temperature in white LEDs⁴⁵) – due to their optical properties and their thermal, moisture, and UV stability. These properties and others are discussed below in the context of the formulation of inks for printable sensing materials to be used for optical thermometry; the specifications for matrices for QD-based luminescent sensing materials are listed in Table 6 below.

Thermal stability

In composite materials for optical temperature sensing applications, matrices must have thermal stability in the operating temperature range, as well as resistance to thermal aging. The linear region of temperature-dependent fluorescence of QDs is typically measured from $\sim 10\text{-}50\text{ }^\circ\text{C}$ in QD-based sensing (Section 2.3.4), though a wider sensing range may be feasible: in an investigation of thermal quenching of QD-polymer fluorescence by

Zhao *et al.*,¹⁶⁰ no intrinsic quenching was observed until 100 °C and quenching was fully reversible until 150 °C. Therefore, an ideal matrix will have an operating range and long-term thermal stability in the ~0-100 °C range.

Silicone elastomers have “the widest operating temperature range of commercially important rubbers”¹⁷ at approximately -50 to 250 °C,¹⁸⁰ with a maximum continuous service temperature of 120-180 °C, depending on formulation.⁵² While the onset of thermal decomposition is 350-420 °C for silicone fluids⁵³ and oxidation resistance is “adequate” ≤ 200 °C¹⁷ – both of which greatly exceed the intended sensing range – thermal aging and yellowing is a concern. Above 150-200 °C, the network density of PDMS elastomers increases and the material becomes more brittle: oxygen cleaves pendant methyl groups and vinyl crosslinks, and residual Si-H groups in the elastomer undergo condensation reactions with water, both of which lead to the formation of new crosslinks.¹⁷ Reversion (chain scission via hydrolysis; anaerobic) can also generate siloxanols, which crosslink by reaction with Si-H or Si-Me, leading to volatile by-products.¹⁸¹ The above reactions occur gradually with chronic heating at lower temperatures (12 months, 50-90 °C), which accelerates aging. While hydrosilylation-related post-curing occurred even at room temperature and concluded within 2 months at 50-90 °C, trace water-related crosslinking did not plateau and increased with both temperature and time.¹⁸¹ Overall, progressive embrittlement was observed even at low temperature (50 °C), and significant yellowing at 50 °C or 80 °C depending on formulation, both of which may degrade optical performance.

UV resistance

Similarly, photo-degradation can occur upon exposure to UV light, which is used an excitation source for luminescence sensing. The absorbance spectrum of CdSe/ZnS QDs with 630 nm emission (see Figure 58) shows small peaks at around 580 and 620 nm, and absorption which rapidly increases at wavelengths under 550 nm. Therefore, any wavelength ≥ 500 nm is feasible as an excitation source and may be preferable to reduce photo-degradation from high energy photons. The downconversion mechanism of QD fluorescence means that higher energy photons are converted into multiple lower energy photons, which enables high signal-to-noise ratios even with low intensity sources. As QDs are excited efficiently by longwave UV, compatible with typical UV-LEDs (350-400 nm), the selected matrix should be stable to photodegradation at these wavelengths to enable temperature monitoring.

Silicones are noted for their UV resistance as the ionic nature of the siloxane bond makes them stable to chain scission until UVC (<280 nm).¹⁸² PDMS is >90% UV transparent down to ~240 nm;⁵⁰ the low absorptivity aids UV photo-stability, although thermal aging can reduce this transparency.¹⁸³ However, the organic pendant groups are susceptible to UV >280 nm and form radicals, leading to increasing crosslinking density and brittleness,¹⁸² as observed for thermal aging in air. Photo-induced radical generation in silicones is also associated with yellowing via the formation of metallic nanoclusters.⁴⁶ As some studies have observed that room temperature photodegradation at long UV wavelengths ≥ 350 nm is limited,^{183,184} PDMS elastomers are suitable matrices for the sensor operating conditions, the effects of thermal aging notwithstanding.

Optical properties

The optical transparency of an encapsulating polymer must match the desired wavelengths of the system. For QD-based sensing, maximal transmittance from ~350-700nm is ideal, to accommodate both excitation and emission wavelengths and to better enable imaging via optical microscopy. Addition cure silicone elastomers can meet this requirement as they have >90% transmittance from 400-750 nm, as long as any fillers present do not act to reduce transparency.¹⁸⁵ Discoloration is a key problem for polymer encapsulants, as polymers undergo yellowing as they age, accelerated by thermal and photo-aging.⁴⁶ This issue is not limited to silicones, which are noted to have better stability against yellowing at elevated temperatures than materials such as epoxies.⁴⁵

For optical sensing materials, parameters affecting light propagation are key. Refractive index (RI) matching between the polymer and emissive species is important for achieving maximum light extraction efficiency (LEE) in LEDs; the RI values of typical semiconductor materials are higher than those of typical polymers, which leads to significant back-reflection and heat generation.^{186,187} While the quantum dots in a QD-polymer composite are distributed randomly, rather than as a layer as is the case for QD-LEDs, RI matching is still beneficial for reducing scattering to improve composite transparency;¹⁸⁸ as scattering is greater for larger particles, RI matching will be more beneficial where QDs form large aggregates in matrices. The refractive indices of bulk wurtzite CdSe and ZnS are approximately 2.5 and 2.4 n_D^{25} respectively,¹⁸⁹ while typical LED encapsulants have much lower RI values (~1.4-1.6 n_D^{25}) and the highest RI achieved in a polymer is ~1.8 n_D^{25} ;¹⁹⁰ therefore, the sensing material matrix should achieve a target RI value of $\geq 1.4 n_D^{25}$.

Mechanical properties

The mechanical requirements of sensing materials will vary with intended application. In broad terms, these materials are not expected to be load-bearing, but it is desirable that deposited materials retain their shape and are not displaced, so gel-like consistencies should be avoided and a minimum Shore A hardness of 30A is recommended. The ideal elastic modulus may also vary; some flexibility in materials is advantageous for thermal sensing as it can prevent cracking that arises from thermal expansion, where the different materials in a device may have different coefficients of thermal expansion (CTE).⁴⁶ Another consideration is that thermal and photo-aging can increase the crosslinking density of polymers as described above and may lead to reduced flexibility and increased brittleness over time, making crack formation more likely.⁴⁶

Flexible silicone elastomers have higher CTE than metals, ceramics, and typical organic polymers ($\sim 260\text{-}360\text{ ppm K}^{-1}$ for Sylgard 184),¹⁹¹ which can act to enhance the temperature sensitivity of thermal sensors¹⁴ but may also complicate emission intensity calibration and lead to changes in measured response as the polymer ages and CTE decreases. Silicone elastomers with higher crosslinking density or shorter crosslinks have greater shape retention in terms of expansion – smaller CTE and reduced swelling with solvents^{57,181} – and will undergo smaller overall changes in expansion with aging, which may enable more consistent measurements but the materials will be less able to absorb thermal stresses. The ideal material properties depend on the sensing application, the materials that the sensing device or environment consists of, and the measurement method. Therefore, a print strategy which uses 2-part inks is advantageous in that the elastic modulus can be controlled using the mix ratio of the inks to vary the molar ratio of silane and vinyl groups.⁵⁷

Rheological properties

The rheological properties of materials determine their printability via inkjet: for the Fujifilm Dimatix print cartridges, the ideal properties are 10-12 mPa s viscosity,^{175,176} 28-33 mN m⁻¹ surface tension,¹⁷⁵ and $>1\text{ g cm}^{-3}$ density.¹⁷⁶ Of these, the viscosity limit is by far the most limiting for polymer formulations as greater elasticity is achieved using longer precursors, but viscosity and pseudoplasticity also increase with increasing chain length.¹⁷ The greater conformational freedom of the siloxane backbone, as compared to hydrocarbon polymers, combined with weak intermolecular forces (dispersive only) between PDMS chains, results in lower viscosity than typical polymers,¹⁷ but viscosity still

presents a challenge as low-viscosity silicone elastomers are formulated with $<20 \text{ kg mol}^{-1}$ base polymers, equivalent to $<1000 \text{ mPa s}$ viscosity.^{53,57} It is possible to use carrier vehicles to dilute polymers, though higher polymer loadings are preferable for higher deposition rates in printing and to minimise deposition issues that arise from ink drying;¹¹⁶ therefore, low-viscosity formulations, i.e. $<1000 \text{ mPa s}$, are preferred for sensing applications, and ideal viscosity is as low as possible while retaining the required mechanical properties. While the surface energy of pure PDMS is low ($\sim 20.9 \text{ mN m}^{-1}$),⁵³ this is just within the extended range for inkjet ($20\text{-}50 \text{ mN m}^{-1}$ surface tension)³⁵ and may be modified by an additive; low surface energy may be desirable for biological applications or for planar sensing, as it leads to materials that are hydrophobic, resist cell adhesion and material adhesion in general, and tend towards film formation.^{51,52}

Table 6: Selection criteria for a polymer matrix for an optical QD-based temperature sensor with an expected operating range of 0-100 °C.

Property	Specifications
Thermal stability	Decomposition does not occur under operating conditions Oxidative resistance up to 100 °C minimum Minimal thermal aging under operating conditions
UV stability	Long-term resistance to photo-aging at $\geq 350 \text{ nm}$ to match UV LED excitation wavelengths; but visible light ($\sim 400\text{-}500 \text{ nm}$) is a viable alternative excitation source
Optical transparency	$\geq 90\%$ transmission $\sim 350\text{-}700 \text{ nm}$ Minimal yellowing under operating conditions
Refractive index n_D^{25}	≥ 1.4
Shore A hardness	$>30A$
Elastic modulus	2-part inks to enable control
Viscosity	$<1000 \text{ mPa s}$, or minimal value to achieve optical and mechanical specifications

In terms of silicone formulation, addition cure room temperature vulcanisation (RTV) silicones (which consist of a vinyl-terminated base polymer, a hydride-functionalised crosslinker, and a platinum catalyst) are suitable for formulating 2-part inks, which can enable control over mechanical properties via the molar ratio of silane to vinyl moieties.⁵⁷

Although the temperature range of interest for the sensing material, 0-100 °C, is below that of the maximum continuous service temperature of silicones (120-180 °C),⁵² Brounstein *et al.* found that long-term aging and changes in mechanical properties were observed in Sylgard 184-based elastomers after 12-months of continuous heating, even at temperatures as low as 50 °C,¹⁸¹ which could alter sensor performance. For industrial rubbers, the thermal stability of silicones can be enhanced by the addition of stabilisers at 0.001-10 wt% loading¹⁷; acidic or alkaline impurities accelerate the depolymerisation process,¹⁷ and so reinforcing silica fillers without surface treatment are not recommended for temperature sensing applications. However, none of these stabilisers and fillers are recommended for formulations for optical applications as they reduce transparency,⁵⁷ and they are to be avoided in the sensing material. As higher initial crosslinking density has been found to correlate to smaller overall change in mechanical properties with aging,¹⁸¹ precursors with lower molecular weights (<20 kg mol⁻¹) may be preferable if mechanical stability is a priority, and experiments with reaction conditions or use of silane cross-linking agents may be of interest for the stability testing phase of material development in future work.

The UV stability of PDMS is also suitable for the intended excitation sources (≥ 350 nm), as long-term aging has been observed to be minimal at room temperature.^{183,184} The CdSe/ZnS QDs ($\lambda_{\text{max}} = 630$ nm) can be excited with blue light instead to reduce photoaging if photoaging is problematic within the temperature range of sensing; the QDs themselves are further expected to prevent photodegradation by absorbing and downconverting UV wavelengths due to the difference in transmittance between the QDs and the silicone matrix. Silicones which contain pendant phenyl groups can reduce embrittlement from photodegradation by reducing the cross-linking efficiency.¹⁹² Phenyl groups also increase the thermal stability¹⁷ and the refractive index (1.5 n_D^{25} PMPS¹⁹³ compared to 1.4 n_D^{25} PDMS⁵³), which is desirable for optical sensing; however, π -stacking interactions between chains increase the viscosity and degree of crystallinity.^{17,193,194} As photodegradation of the sensing material can be mitigated by changing the excitation wavelength, silicones with and without phenyl groups may both present valid options for formulation, as long as the selected polymer has rheology compatible with inkjet.

However, long-term yellowing may present a challenge for sensor performance, as significant yellowing has been reported even at ≤ 50 °C (12 months accelerated aging),¹⁸¹ which reduces optical and UV transparency and accelerates further photodegradation. Discoloration is a complex process but a key mechanism is the formation of metallic nanoclusters during thermal aging or by photo-induced radical generation;⁴⁶ therefore, yellowing can be reduced by minimising the amount of platinum catalyst used,^{181,192} and to some extent by the choice of catalyst. Yellowing is “nearly independent” of the composition of the silicone chain⁴⁶ and is affected by the molar ratio of silane to vinyl moieties and the chain mobility within the elastomer, which determine the type of metallic cluster and the rate of formation: while equimolar or excess silane is associated with Pt clusters and grey-brown discoloration, excess vinyl is observed to lead to Si-Pt and C-Pt clusters with darker brown discoloration.¹⁹² In a study of thermal aging, the onset of yellowing was delayed until 80 °C by the addition of tetrakis (dimethylsiloxy) silane (TDS) crosslinking agent, at which point the resulting discoloration was significantly darker than in the sample without TDS;¹⁸¹ this suggests that elastomers with high crosslinking density (>5 mol g⁻¹ in the above study), or the use of TDS as an additive to increase crosslinking density, are suitable for a sensing range between 0-70 °C.

While the above strategies and potential additives are of interest for future studies to improve long-term sensing performance, many complex material interactions are possible in composite materials, and it is prudent to limit this at the outset. Therefore, investigation of a commercial formulation with minimal fillers and modifications is desirable for initial work. Commercial RTVs that have been demonstrated to be viable for inkjet printing are discussed below, and the rationale for selecting SiliGlass is given.

4.1.2. Commercial silicone system

The rationale in selecting candidates for inkjet is given below; as discussed in Chapter 2, addition cure formulations were identified as ideal for optical sensing due to their use in commercial LED encapsulants, in addition to having suitable reactivity at ambient temperatures for inkjet printing.

Sylgard 184 from Dow is considered a benchmark for commercial silicones with viscosity under 10 Pa s and is one of the most widely-used 2-part RTVs in literature.^{57,67} It is a flexible Shore A43 rubber¹⁹⁵ used as an electronics encapsulant, valued for its transparency and dielectric properties, and would be an excellent matrix. However, its 10:1 mixing ratio and viscosity (5100 mPa s base; 3500 mPa s mixed)¹⁹⁵ necessitates dilute inks, raised nozzle temperatures, and premixing, the latter of which reduces ink shelf-life.⁶⁴ It has been inkjet printed in mixed 1-part inks at ≤ 25 wt% loading with a maximum ink working life of 48 hours.^{61,62,64}

Polytek SiliGlass is another commercial silicone which has been demonstrated for inkjet printing by Sturgess *et al.*⁶⁰ It is a brittle rubber (Shore 40A)¹⁹⁶ used to mimic water and glass shards for special effects, noted for its optical transparency. This system has a mixing ratio of 1:1 and the viscosities of the two parts are more similar to each other than is the case for Sylgard 184; this enables drop-on-drop printing of 2-part inks, as inks can be formulated to mix on the substrate with the correct ratio. The cure time is also shorter than for Sylgard 184 (24 hours at room temperature, compared to 48 hours) so inks are expected to react more rapidly which may increase the maximum printing rate. As SiliGlass is an order of magnitude less viscous than Sylgard 184 (200 mPa s mixed),¹⁹⁶ SiliGlass has been chosen to enable inks with higher polymer concentrations. As discussed above in Section 4.1.1, the shorter chain length base polymer in SiliGlass may also be beneficial to reduce solvent swelling, coefficient of thermal expansion, yellowing, and the overall magnitude of changes in mechanical properties with aging, although the resultant sensing material may be more susceptible to cracking.^{46,181,192}

Other commercial silicones have been used in inkjet, as reviewed in Section 2.2.3. However, the alternative addition cure silicones that were inkjet-printed by McCoul *et al.* were optically opaque, viscous (20-75 Pa s), and/or had low Shore A hardness (5-7A),⁶³ which do not meet the requirements for the sensing material (see Table 6).

Polytek SiliGlass

Polytek SiliGlass is a commercial 2-part room temperature vulcanisation (RTV) silicone formulation; these crosslink via hydrosilylation and are also called addition cure silicones. Low viscosity RTVs are typically used for moulding as their flowability prevents air pockets.¹⁷ SiliGlass is a transparent silicone rubber marketed for special effects and is used to safely mimic glass for moulded objects and fake glass shards.

The formulation of SiliGlass is typical for 2-part RTVs, where both parts contain the base polymer while the crosslinker (A) and catalyst (B) are separated,^{17,57} as shown in the reaction scheme below in Figure 27; Part A and Part B are formulated for mixing in a 1:1 ratio by weight.

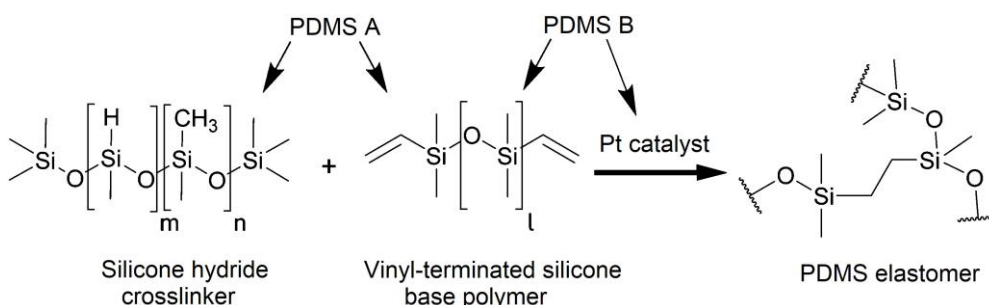


Figure 27: Reaction scheme of SiliGlass crosslinking by hydrosilylation. Reproduced from Sturgess *et al.*⁶⁰

The base polymer is a telechelic vinyl-terminated siloxane (Oligomer $M^vD_nM^v$ in Figure 27). As indicated in the Material Safety Data Sheet (MSDS), this may be a copolymer with organofunctional groups in the chain, but poly-dimethylsiloxane (PDMS) is most common.¹⁷ The vinyl groups are terminal in low viscosity formulations (where the crosslinked chain has molar mass $<20 \text{ kg mol}^{-1}$, equivalent to $<1000 \text{ mPa s}$ viscosity⁵³) to achieve good network density and maximum hardness with the short chain lengths required for low viscosity systems.^{17,57} Additionally, hard silicone elastomers (elastic modulus $\geq 1 \text{ MPa}$) are formulated with an excess of silane groups to ensure all vinyl groups react.^{17,57}

In SiliGlass, Part A contains ≤ 20 weight percent (wt%) crosslinker¹⁹⁷: a low molecular weight PDMS-co-PHMS (Hydride $MD_m^H D_n M$ in Figure 27). Part B contains ≤ 0.1 wt% platinum catalyst,¹⁹⁸ which is a proprietary platinum salt likely chosen to maximise transparency. The MSDS does not note any solvents, resins, or silica particles in the formulation. Both parts contain 75-100 wt% organofunctional siloxanes, which can include base polymer, chain extenders, and copolymers containing phenyl groups.⁵⁷

Polymer formulations are proprietary and so manufacturers do not release precise details on their formulas. However, as formulation choices impact the resultant viscosity, surface energy, polymer microstructure, mechanical properties, and other properties, it is prudent to characterise precursors before ink formulation. Crosslink chain length, which is determined by the base polymer chain length and the amount of chain extenders present, is important in determining the elongation at break of cured elastomers, while the hydride (a.k.a. silane) to vinyl ratio is a determining factor for the elastic modulus.⁵⁷ Polymer architecture and fillers, such as fumed silica or resins, may also have profound impact on precursor viscosity and the mechanical properties of the elastomer.

As discussed in Section 4.1.1, the expected features of SiliGlass (low molecular weight base polymer, high elastic modulus, and excess silane) may be beneficial for a sensing material: it can result in more consistent temperature response across device lifetime by reducing the coefficient of thermal expansion (CTE), solvent swelling, yellowing, and the overall magnitude of changes in mechanical properties with aging.^{46,181,192} However, this would also lead to a brittle material which may be susceptible to crack formation from thermal stresses and differences in CTE between device materials.⁴⁶ It is necessary to confirm whether the SiliGlass constituents are as expected in order to understand the effect that the matrix will have on the performance of the printed sensing material.

SiliGlass is marketed as 'water-clear' and mimics glass; this precludes the use of typical fillers like silica, although resins may be used to strengthen transparent formulations.⁵⁷ Pendant groups on the siloxane backbone may also be used to alter functionality: the incorporation of pendant phenyl groups is associated with higher refractive index and greater optical transparency,¹⁷ ideal for optical sensors. However, this is also associated with factors that are detrimental for sensing inks, such as higher viscosity and ultraviolet (UV) absorbance,^{17,57,193,194} which must be considered during ink formulation. Phenyl groups modify the physical properties of silicones through steric factors and π -stacking interactions; increasing phenyl content is associated with greater thermal and photostability,^{17,192} lower CTE,¹⁹³ and changes in crystallinity, phase transition temperatures, and flexibility^{17,193,194} which can affect how cracks arise from aging and thermal stresses in the sensing material.

Spectroscopy and viscometry are used to interrogate precursors in the following sections, to identify the likely constituents and their implications for sensing, and to ensure that the silicone precursors have rheological properties which are compatible with inkjet.

4.1.3. Spectroscopy

¹H NMR spectroscopy

¹H NMR was used to estimate the number average molar mass (M_n) of prepolymers and to quantify functional groups in the siloxanes. The hydride to vinyl ratio determines the amount of residual silane groups in the cured polymer, which contribute to hydrolysis-based post-curing.⁵⁷ Peaks indicating organic pendant groups (alkyl or phenyl) can be detected using NMR; as these groups can affect viscosity, surface energy, elastomer microstructure and mechanical properties, and refractive index, it is important to quantify them to inform ink formulation and predicted composite properties as sensing materials.

As seen in the reaction scheme above (Figure 27), SiliGlass B contains a vinyl-terminated siloxane as well as the platinum catalyst; this siloxane was identified in the ¹H NMR spectrum as PDMS (Figure 28). The vinyl group leads to a triplet, subdivided into a triplet (b) and two doublets (a&a') at approximately 6 parts per million (ppm), with each vinyl group containing one hydrogen atom per peak. The methyl groups on the chain (c, d) generate the strong multiplet at 0.1 ppm which contains six hydrogen atoms per silicon atom. The intensity ratios can be used to estimate chain length (see Equation 6 below).

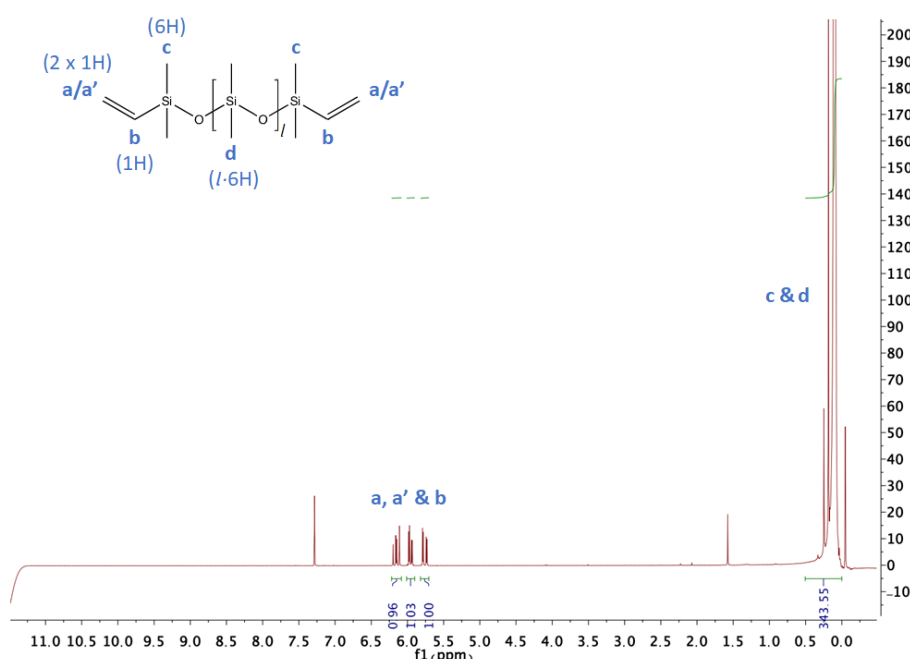


Figure 28: ¹H NMR spectrum of SiliGlass B with assigned peaks, corresponding to ¹H environments as labelled in inset siloxane.

SiliGlass A contains both the base polymer and the short crosslinker, as shown in Figure 29. Again, the vinyl groups on the base polymer produce a triplet at approximately 6 ppm, with

the same splitting pattern observed for SiliGlass B and the same species assigned to the peaks. The silane of the crosslinker (**h**) is identified as a single peak with complex splitting at approximately 4.75 ppm. However, the methyl groups of both siloxanes (**c-g**) all show similar chemical shifts and are assigned to the multiplet at 0.1 ppm. It is more difficult to estimate the molecular weights of these chains from intensity ratios as methyl groups from both species contribute towards the peak intensity.

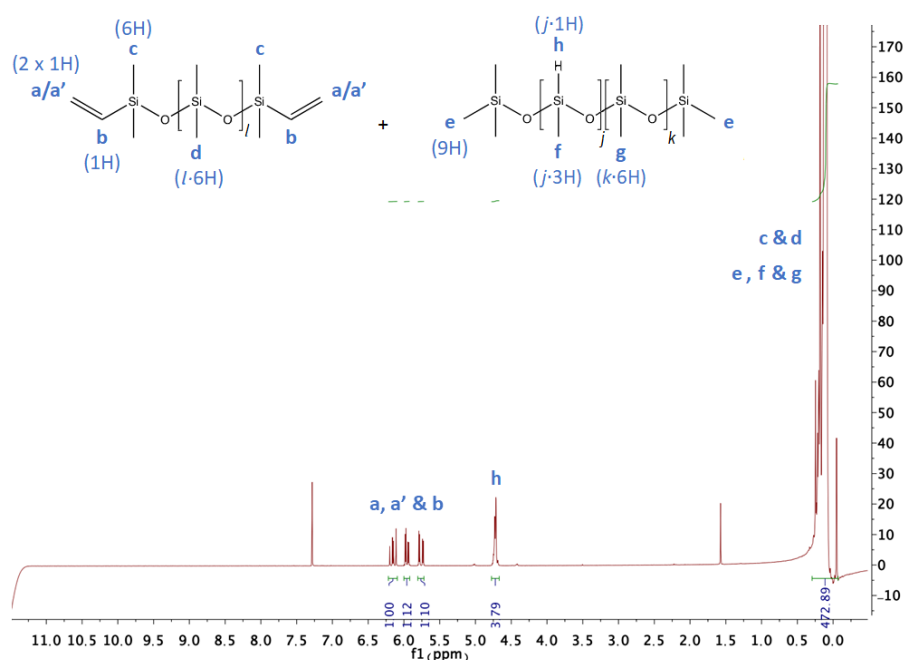


Figure 29: ^1H NMR spectrum of SiliGlass A with assigned peaks, corresponding to ^1H environments as labelled in inset siloxanes.

The peaks observed in the SiliGlass ^1H NMR spectra are listed below in Table 7 alongside typical ^1H NMR chemical shifts in siloxanes, to summarise the assigned groups, observed and literature shift, and observed intensities. Peaks seen around 7.3 and 1.6 ppm correspond to the chloroform-D solvent: 7.24 ppm is associated with chloroform-D while 1.6 ppm is associated with water or deuterated water.

There is no evidence for the presence of phenyl groups in any of the components, indicating that SiliGlass does not contain any PDPS, PMPS, or PDMS-co-PDPM polymers. While these polymers do have higher refractive index than PDMS ($1.5 n_D^{25}$ PMPS¹⁹³ compared to $1.4 n_D^{25}$ PDMS⁵³), which is desirable for optical sensing, π -stacking between chains can lead to much higher viscosity and a higher degree of crystallinity,^{17,193,194} which can be detrimental for ink formulation. As SiliGlass does not appear to contain any phenyl groups, it is expected to have the properties of bulk PDMS in terms of glass transition temperature T_g , microstructure and mechanical properties, and rheology.

Table 7: ¹H NMR correlation table for SiliGlass A and SiliGlass B, relative to tetramethylsilane (SiMe₄, TMS) with chloroform-D solvent (CDCl₃).

Group	Observed	Literature ¹⁷	Intensity (SiliGlass A)	Intensity (SiliGlass B)
≡Si-CH ₃	0.1	0	427.89 c,d,e,f,g	343.55 c,d
≡Si-CH ₂ -	-	0.5	-	-
≡Si-OCH ₃	-	3.5	-	-
≡Si-H	4.75	4.7	3.79 h	-
≡Si-CH=CH ₂	5.75, 5.95, 6.15	5.8-6.2	1.00, 1.12, 1.10 a,a',b	0.96, 1.03, 1.00 a,a',b
≡Si-C ₆ H ₅	-	7.3, 7.6	-	-

As the peak intensities correspond to the number of hydrogen atoms, and the number of end groups in the chain is known, the peak intensity ratios can be used to determine the degree of polymerisation (number of repeat units) according to Equation 6, where x and y are repeat unit (SiMe₂) and end group (Vi) moieties, a is peak area, n is the number of moieties in the average chain, and m is number of protons in a moiety. The repeat moiety here is taken to be SiMe₂ rather than the repeat unit SiMe₂O, as the peaks of the terminal SiMe₂ groups (**f**) are not resolved separately (from **g**) in the spectrum.

Equation 6: Calculation of number of repeat units n_x (i.e. degree of polymerisation) from ¹H NMR data, where x and y are the repeat unit and end group respectively, and a is area of peak, m is number of protons in the moiety, and n is number of moieties in the average polymer chain.¹⁹⁹

$$n_x = \frac{a_x \cdot m_y \cdot n_y}{a_y \cdot m_x}$$

In the case of SiliGlass B, estimation can be based on the peak for one of the protons in the vinyl group so that $n_{SiMe_2} = (343.55 \times 1 \times 2)/(1.00 \times 6) = 114.5$, or based on all three peaks associated with the vinyl group where $n_{SiMe_2} = (343.55 \times 3 \times 2)/(2.99 \times 6) = 114.9$. As each of the three peaks are associated with the same number of protons and an area of 3.00 is divisible by 3, $n_{SiMe_2} = 114.5$ is an acceptable estimate. The number average molar mass M_n can then be calculated using Equation 7, which is the degree of polymerisation n multiplied by the molar mass of the repeat unit M_0 , plus the total molar mass of the end groups M_e .

Equation 7: Calculation of number average molar mass M_n , where n is the average number of repeat units, M_0 the molar mass of the repeat unit, and M_e the sum of molar masses of the end groups.¹⁹⁹

$$M_n = nM_0 + M_e$$

If the average chain contains 114.5 SiMe₂ moieties (average $l = 112.5: M^{Vi}D_{112.5}M^{Vi}$), then $M_n = (\text{SiMe}_2\text{O} \times 112.5) + \text{SiMe}_2\text{OVi} + \text{SiMe}_2\text{Vi}$ and corresponds to 8528.28 g mol⁻¹ for the bifunctional base polymer. Base polymers under 20 kg mol⁻¹ lead to brittle elastomers due to tension from short polymer chains;⁵⁷ while a low M_n could indicate the presence of chain extenders, brittleness is a design feature in SiliGlass as it mimics glass shards and so a base polymer with low molar mass in the absence of chain extenders is not unexpected.

SiliGlass A contains both base polymer and crosslinker, which are not resolved separately in the spectrum. However, if assumptions are made, some simple cases may be constructed to fit the molar ratios observed in the spectrum of SiliGlass A: for a given mixture of base polymer and crosslinker, the expected molar ratios of vinyl to hydride groups and hydride to methyl groups can be calculated for possible crosslinker identities and compared and matched to the spectral data.

From the peak areas observed in the spectrum, the molar ratio of vinyl groups to hydride groups in the SiliGlass A mixture is approximately 1 : 3.79. In a simple case where SiliGlass A is a 1:1 mixture of crosslinker and base polymer by number, a crosslinker species would need an average of ~7.6 hydrides in the chain to match the ratio as the base polymer is bifunctional. If the base polymer is identical in parts A and B, then the area of the vinyl peak in the SiliGlass spectra can also be used to estimate the number of methyl protons belonging to the base polymer chain, using the 1 : 343.55 ratio observed in the spectrum of SiliGlass B. When this amount is subtracted from the methyl peak, an area of approximately 84.35 remains, which yields an expected 1 : 22.26 ratio of hydride:methyl protons in the crosslinker species. By calculating the hydride:methyl ratio for different chain lengths of PMHS with 7 or 8 hydride groups, cases can be constructed that fit the ratios observed in the spectrum of SiliGlass A.

Under these assumptions, SiliGlass A comprising a 1:1 ratio by number of base to crosslinker would correspond to an average crosslinker where $j = 7.6$ and $k = 21.4$ (i.e. $MD_{7.6}^H D_{21.4}^M$) with an M_n of 2206.21 g mol⁻¹. This is a likely candidate as this is very similar in weight to crosslinkers recommended for hard silicone elastomers (elastic modulus ≥ 1 MPa), with similar functionality ($f=7.6$ compared to $f=8$).⁵⁷

The molar excess can be estimated using this crosslinker candidate. From the NMR data, the ratio of vinyl to silane moieties in the SiliGlass A mixture is 1 : 3.79. When parts A and B are mixed in a 1:1 weight ratio, this gives a molar excess of silane of approximately 1.68 with the estimated crosslinker, which is within the expected range for hard silicone

elastomers.⁵⁷ It is expected that all vinyl moieties will react, and that there will be residual silane that may be converted to silanol and hydrolyse to yield Si-O-Si bridges as a post-curing reaction.⁵⁷ The values obtained for molar mass are also in agreement with the upper limit given in the MSDS (which states that SiliGlass A contains ≤ 20 wt% silicone hydride¹⁹⁷).

While the estimated molar masses of the constituents fit the available data well and match typical specifications of low viscosity formulations for hard elastomers, a number of assumptions have been made which may reduce the accuracy of the prediction. Furthermore, NMR spectroscopy is an averaging technique and can only be used to estimate the number average molecular weight M_n ; it does not give data on how uniform a sample is. For example, it is possible that a chain extender (hydride-terminated PDMS, >0.2 crosslinker:chain extender ratio) is used to increase chain length during curing, as is a common strategy for low viscosity formulations,⁵⁷ which would be indistinguishable in the NMR spectrum above.

In order to obtain data on how uniform the polymer chains are by size, weight average molar mass M_w is required to enable calculation of polydispersity. Viscometry is one technique that is capable of this: viscosity is related to M_w as increasing chain length leads to greater chain entanglement.¹⁷

Other physical and spectral data of SiliGlass

Fourier transform infrared (FTIR) spectroscopy was carried out on samples to assess the presence of various functional groups. IR-active modes are assigned based on literature studies of silicones.^{200–202} FTIR spectra for SiliGlass A and B, shown below in Figure 30 and Figure 31, are identical except for peaks associated with Si-H in the FTIR spectrum of SiliGlass A (crosslinker): a very weak peak at 2161 cm^{-1} and a weak peak in the fingerprint region at 912 cm^{-1} . None of the modes that would indicate the presence of phenyl groups are present in the FTIR spectra, such as peaks in the $1600\text{--}1450\text{ cm}^{-1}$ region.²⁰⁰ This confirms again that there are no phenyl groups present, in agreement with the NMR data.

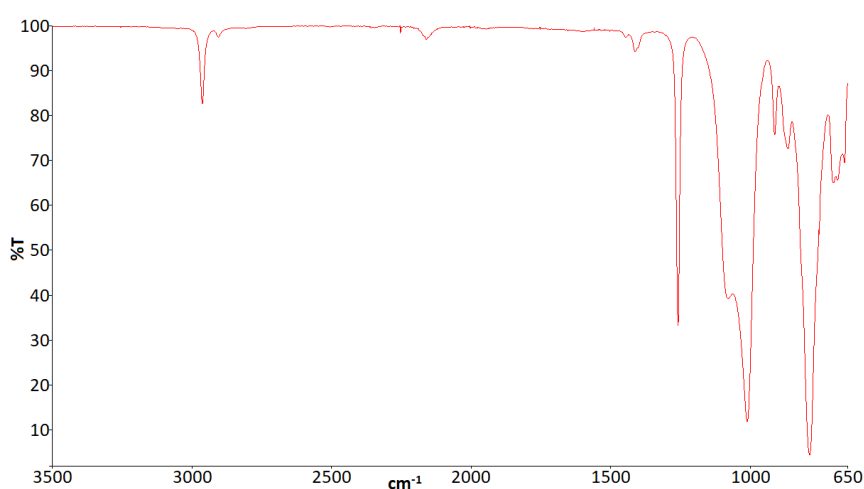


Figure 30: FTIR spectrum of SiliGlass A, which contains base polymer and crosslinker.

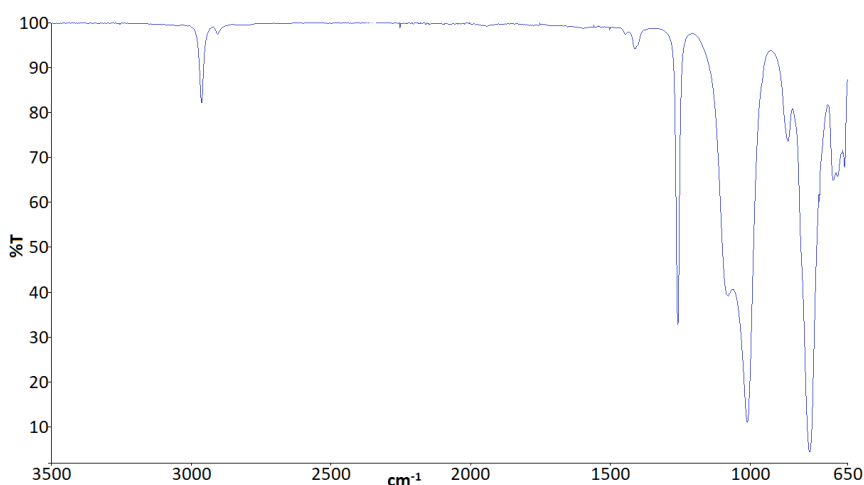


Figure 31: FTIR spectrum of SiliGlass B, which contains base polymer and catalyst.

The full peak list of the FTIR spectra of SiliGlass A and B is given in Table 8 below, and peaks are assigned specific modes based on studies in the literature.^{200–202} Alkyl stretching modes are observed at 2963 and 2905 cm^{-1} , pendant methyl bending modes at 1412 and 1258 cm^{-1} , and siloxane chain stretching modes at 1079 and 1010 cm^{-1} . In the fingerprint region, peaks at 787 and 752 cm^{-1} are assigned to the siloxane backbone and are correlated to modes that combine Si-C stretch and in-plane CH_3 rocking. 702 cm^{-1} represents a weak CH_3 rocking mode and peaks at 686 and 661 cm^{-1} correspond to SiC, either as SiC rocking modes or as SiC stretching modes that are coupled to CH_3 rocking.

Table 8: Peak list of FTIR modes for SiliGlass A and B, with assignments based on literature data.^{200–202}

SiliGlass A		SiliGlass B		Assignment
Wavenumber cm^{-1}	Transmission %	Wavenumber cm^{-1}	Transmission %	
2963.00	82.64	2962.86	82.15	Alkane $\nu_{\text{as}}(\text{CH})$ C-H asymmetric stretch
2905.16	97.50	2905.79	97.48	Alkane $\nu_{\text{s}}(\text{CH})$ C-H symmetric stretch
2160.58	96.98			Silane $\nu(\text{SiH})$ Si-H stretch
1412.05	94.23	1411.97	94.19	Methyl $\delta_{\text{as}}(\text{Si}(\text{CH}_3)_2)$ Chain methyl asymmetric bend
1257.99	33.37	1257.92	32.59	Methyl $\delta_{\text{s}}(\text{Si}(\text{CH}_3)_2)$ Chain methyl symmetric bend
1079.33	39.30	1079.00	39.09	Siloxane chain $\nu_{\text{as}}(\text{SiOSi})$ Si-O-Si asymmetric stretch
1010.35	11.89	1009.30	10.92	Siloxane chain $\nu_{\text{s}}(\text{SiOSi})$ Si-O-Si symmetric stretch
911.86	75.72			Silane $\omega(\text{SiH})$ Si-H wag
863.29	72.68	863.48	73.55	Methyl $\rho_{\text{s}}(\text{CH}_3)$ Me symmetric rock
786.53	4.45	785.31	4.20	Methyl $\nu_{\text{as}}(\text{SiC})//\rho_{\text{as}}(\text{CH}_3)$ Si-C stretch in-plane Me rock
751.73	53.56	751.35	60.12	Methyl $\rho_{\text{as}}(\text{CH}_3)//\nu_{\text{s}}(\text{SiC})$ Si-C stretch in-plane Me rock
702.60	65.07	701.35	64.79	Methyl $\rho(\text{CH}_3)$ Me rock
685.86	65.54	686.31	65.72	Organosilicon (SiC) Si-C rock or coupled stretch
661.07	69.57	660.73	67.76	Organosilicon (SiC) Si-C rock or coupled stretch

Further physical data for SiliGlass has been collated from the manufacturer's datasheets. The boiling point of SiliGlass is listed as >200 °C with a vapour pressure of <0.1 mmHg, which indicates that the formulation is non-volatile and therefore does not contain cyclic or short chain silicone oils such as MM. This is beneficial as evaporation of volatile constituents can pose safety risks, reduce the product lifetime, and cause printing issues. The cure time is defined for pour, demould, and total cure at room temperature: 5 min, 0.5-1 hour, and 24 hours, respectively. As these cure times are short in comparison to Sylgard 184, which has total cure in 48 hours, SiliGlass is expected to cure to hold its shape sufficiently rapidly for inkjet printing with substrate heating. The technical datasheet states that SiliGlass cures to an elastomer with 40A Shore hardness; this is above the suggested minimum to prevent displacement during sensor operation (30A, Table 6).

Rheological data is supplied for the 1:1 wt Part A and B mixture: specific gravity is 0.97 and viscosity is 200 mPa s. The specific gravity is compatible with the print cartridge of the Dimatix inkjet printer and, while this viscosity is an order of magnitude greater than the limit,^{175,176} the viscosity is below the suggested limit for sensing inks (1000 mPa s, Table 6) which enables formulation of jettable inks without extensive dilution; for reference, 1-part addition cure inks have been formulated from Sylgard 184 (which has a 3500 mPa s mix viscosity)¹⁹⁵ at ≤25 wt% loading.^{61,62,64} As the stated viscosity is therefore compatible with inkjet, rheological characterisation is carried out on SiliGlass Part A and Part B in Section 4.1.4 below, to identify any non-Newtonian behaviour and obtain individual values for viscosity at room temperature to inform ink formulation for 2-part inks. The M_w obtained from viscosity data is then compared with the M_n estimated from NMR data to obtain the polydispersity index (PDI).

4.1.4. Rheology

Rotational viscometry of SiliGlass A and SiliGlass B was carried out to assess the precursors as described in Chapter 3 Section 3.2.2.1. Viscosity values were obtained to inform ink formulation – ideal inks for the Dimatix printer are Newtonian fluids with 10-12 mPa s viscosity^{175,176} – and to estimate weight average molar mass M_w to obtain the dispersity index to assess the uniformity of polymer chains and the likelihood of phase separation.

It is non-trivial to measure the dynamic viscosity of an ink at a shear rate that is representative of jetting. Shear stress is typically in the region of 10^5 - 10^6 s⁻¹ during inkjet operation³⁵ - outside the measurable range of rotational viscometers - and so it is practical to measure shear-dependant viscosity from 1-1000 s⁻¹. Therefore, it was important to determine whether the silicones displayed Newtonian behaviour to ensure that the measured dynamic viscosity would be consistent for jetting.

Short to medium length silicone fluids are Newtonian fluids, meaning that their dynamic viscosity is independent of the shear rate and will be consistent throughout the jetting process.¹⁷ The viscosity of silicone fluids increases with increasing chain length due to entanglement between chains; in long chain PDMS, i.e. above the critical molecular weight of entanglement (21000-33000 g mol⁻¹, M_c ⁵³), this leads to pseudoplastic behaviour.¹⁷

More complex behaviours are possible when silicones are mixed with other components. For example, fumed silica is widely used to reinforce silicone elastomers, leading to higher viscosity (where loading is >2 wt%)¹⁷ and thixotropic behaviour in silicone fluids. Silica strongly interacts with silicones through hydrogen-bonding, which forms a solid-like percolating network that is broken down at shear rates higher than the yield stress, leading to time-dependent shear thinning.²⁰³ Shear thickening is also seen at high shear rates, particularly above ~20 wt% loading.²⁰⁴ However, as silica is associated with reduced transparency, it is not expected in SiliGlass.⁵⁷

The rheological behaviour of SiliGlass can also yield information about fillers or reinforcements in the formulation. If nonlinear behaviour is seen, it may potentially be resolved by dilution in a chosen solvent to decrease the percentage of polymer chains bridged by particles or to disrupt intramolecular bonding. Ideally, however, SiliGlass will show Newtonian behaviour and be confirmed to have consistent viscosity for jetting.

Equilibrium flow curves were obtained for SiliGlass A and SiliGlass B at 25 °C (Figure 32 and Figure 33 respectively) by measuring the dynamic viscosity of a sample against a logarithmic series of shear rates, allowing the sample to equilibrate at each rate.

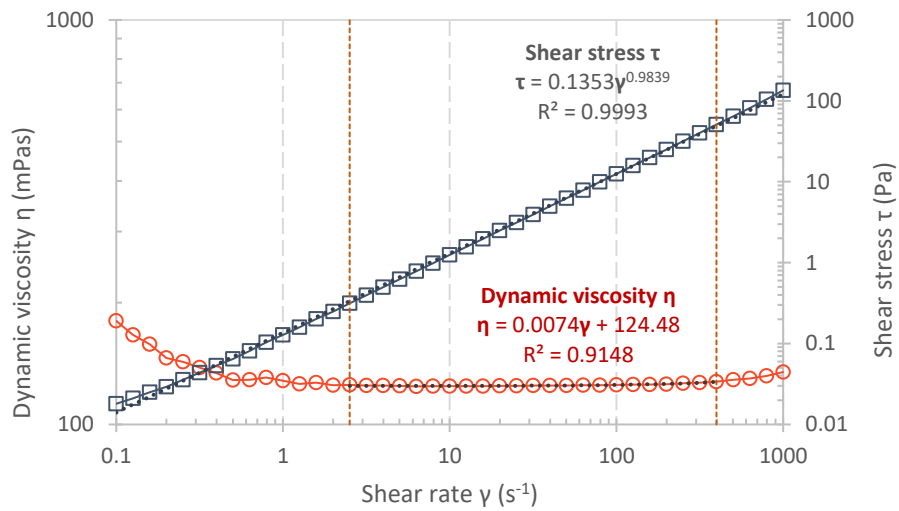


Figure 32: Equilibrium flow curve of pure SiliGlass A. Black lines with square markers plot the shear stress as a function of shear rate, with a grey dotted trendline. Red lines with circular markers plot the dynamic viscosity as a function of shear rate. The linear region is enclosed between red dotted lines, with a black dotted trendline.

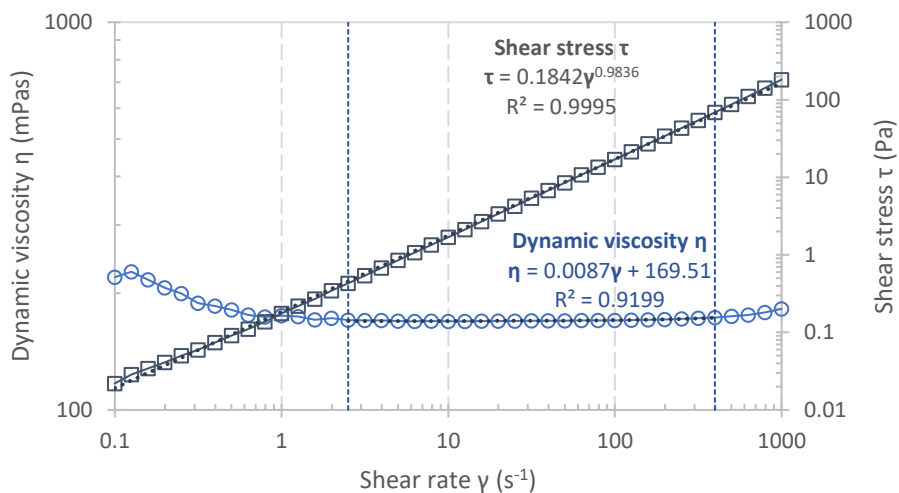


Figure 33: Equilibrium flow curve of pure SiliGlass B. Black lines with square markers plot the shear stress as a function of shear rate, with a grey dotted trendline. Blue lines with circular markers plot the dynamic viscosity as a function of shear rate. The linear region is enclosed between blue dotted lines, with black dotted trendline.

For both SiliGlass parts, shear stress varies linearly with shear rate, with power laws indices close to one. This indicates that they are Newtonian within this measurable range. Mid-range shear rate values, i.e. from 2.5 to 400 s^{-1} , show a near-constant value of dynamic viscosity in SiliGlass A and B, indicating Newtonian behaviour. 10 s^{-1} has been selected as a representative value for viscosity: at 10 s^{-1} , Part A is 124.3 mPa s and Part B is 169.3 mPa s . The viscosity of SiliGlass A is lower than SiliGlass B, as expected with the presence of a shorter crosslinker. The low viscosity ($<500 \text{ mPa s}$) and linear behaviour of both parts implies that there are no reinforcing fillers present in the formulation.^{57,203}

The dynamic viscosity of each part shows an upwards trend as the shear rate approaches the minimum and maximum of the experimental range. This is due to the limitations of the equipment. At low shear rates ($<10 \text{ s}^{-1}$), the rheometer did not reach steady state, as the torque generated from the sample was very low. Silicones are highly lubricating; PDMS has the lowest recorded surface shear viscosity.⁵¹ The data shows a “kink” in the flow curve, which is characteristic of wall slip at low shear rates.²⁰⁵

At high shear rates ($>100 \text{ s}^{-1}$), the measured viscosity increased. While reinforcing fillers for silicones are often shear thinning,^{57,203} thickening at high shear is known;²⁰⁴ however, these fillers are associated with high viscosity due to strong filler-polymer interactions. Rather, the high speed likely generated secondary flow in the low viscosity SiliGlass.²⁰⁶

The viscosity of PDMS silicone fluids is related to temperature and weight average molar mass M_w . As the chain length of silicones increases, there is an increasing tendency for entanglement of polymer chains, and so viscosity increases as chains form an increasingly tangled network that impedes movement.²⁰⁷ The molecular weight of linear PDMS chains may be estimated from their viscosity at room temperature using Equation 8.

$$M = \frac{464 \cdot (\eta_{25^\circ\text{C}})^{0.825}}{2 + 0.0905 \cdot (\eta_{25^\circ\text{C}})^{0.555}}$$

Equation 8: Relationship between molecular weight and viscosity of linear PDMS fluids at 25 °C.¹⁷

The weight average molar mass of SiliGlass B is estimated to be 8985.08 g mol⁻¹ from its viscosity of 169.3 mPa s. This value of 8985.08 g mol⁻¹ for SiliGlass B is in close to the estimate of 8528.60 g mol⁻¹ obtained from the NMR spectrum (Figure 28). For the SiliGlass A mixture, its 124.3 mPa s viscosity leads to an estimated 7480.18 g mol⁻¹ M_w , compared to the 5367.25 g mol⁻¹ M_n estimated from the constituents based on NMR data.

Comparison of the weight and number average molecular masses of a sample yields information about its uniformity. The polydispersity index (PDI) is a metric for how homogeneous a polymer sample is in chain size. It is calculated as weight average molar mass M_w divided by the number average molar mass M_n , as shown in Equation 9. From the estimated molecular masses, the PDI of SiliGlass A and B is 1.39 and 1.05, respectively.

Equation 9: Calculation of polydispersity index PDI , where M_w and M_n are weight average and number average molar mass, respectively.¹⁹⁹

$$PDI = \frac{M_w}{M_n}$$

4.1.5. Summary of SiliGlass constituents

PolyTek SiliGlass, a commercial 2-part RTV silicone, was selected for its low viscosity (<1000 mPa s), optical transparency from 350-700 nm, and Shore A hardness (40A). These properties would enable formulation of inks with jettable viscosity even at high polymer loading (>25 wt%) and/or ambient temperature; allow efficient transmission of excitation and emission wavelengths; and limit displacement of sensing material during operation. SiliGlass was further characterised to gain a greater understanding of the system prior to ink formulation.

NMR data was used to identify the bifunctional base polymer in SiliGlass B as a vinyl-terminated PDMS with an average of 112.5 repeat units, corresponding to 8528.28 g mol⁻¹ M_n . The dynamic viscosity at room temperature was 169.3 mPa s, which is calculated to correspond to 8985.08 g mol⁻¹ M_w and 1.05 PDI, near monodisperse. SiliGlass A contains the crosslinker and was seen to contain a vinyl-terminated PDMS and a methyl hydrogen silicone fluid in its NMR spectrum, and had a dynamic viscosity of 124.3 mPa s at room temperature. FTIR spectroscopy peaks corresponding to silane moieties were seen solely in SiliGlass A. Assuming that the vinyl base polymer is the same in both parts, the crosslinker was estimated to be a short PDMS-co-PMHS polymer with 2206.21 g mol⁻¹ M_n and $f=7.6$. The viscosity of Part A corresponds to 7480.18 g mol⁻¹ M_w and therefore 1.39 PDI, higher than for Part B as Part A is a mixture of base polymer and shorter crosslinker; as the PDI was under 1.5, it is unlikely that shorter, bifunctional chain extenders were present in the formulation. However, the accuracy of the M_w value estimated from viscosity data may have been affected by the fact that Part A is a mixture of base polymer and crosslinker, as the viscosity of mixtures can be complex to predict, and by the substitution of methyl groups for vinyl or hydride moieties, which may have an impact on intermolecular behaviour.

The estimated constituents fit the properties of the SiliGlass system based on formulation guidelines⁵⁷: a low viscosity base polymer (>20 kg mol⁻¹) which cures to a brittle, rubber-like material (40A) used to mimic glass shards. The ratio of vinyl groups to silane groups in the NMR spectrum of SiliGlass A was 1 : 3.79, calculated to correspond to a 1.68-fold molar excess of silane when SiliGlass A and SiliGlass B are mixed in a 1:1 weight ratio. As shorter base polymers lead to reduced flexibility and higher crosslinking density, as well as high elastic modulus (≥ 1 MPa) in the presence of excess silane,⁵⁷ the elastomer is expected to have reduced solvent swelling and coefficient of thermal expansion than Sylgard 184 (260-360 ppm K⁻¹ CTE)¹⁸¹; this may result in a sensing material with more consistent sensing

performance across device lifetime as the overall magnitude of change in expansion associated with material aging is reduced,^{46,181} as are changes in emission intensity, which are dependant on QD concentration.¹ Furthermore, the reduced chain mobility and the excess silane can both hinder discoloration associated with the formation of metallic clusters as the material ages,^{181,192} which impedes optical sensing by altering the transparency of the matrix and therefore the observed fluorescence. The disadvantage of brittleness in a sensing material is that the ability to absorb thermal stresses is lower, so that the material is more vulnerable to crack formation than a more flexible elastomer would be and this may reduce sensor lifespan.⁴⁶

No evidence was seen for the presence of PMPS, PDPS copolymers, resins, or silica particles in either part: no identifying peaks are seen in FTIR or NMR spectroscopy, and both parts have low viscosity and Newtonian behaviour. The material is therefore expected to have the characteristic properties of bulk PDMS elastomers, **without phase separation associated microstructures.**

Overall, estimates were given for the components of SiliGlass and its properties are expected to resemble bulk PDMS. While Newtonian, the viscosity of the parts were found to exceed jetting limits, which indicates that further viscosity modification is required in order to formulate jettable inks.

4.2. Ink formulation

SiliGlass was selected as a low viscosity commercial silicone, but its viscosity was still above the printable limit for inkjet. The results below detail the work to establish jettable formulations (objective *O1*) using a carrier vehicle to reduce viscosity and collecting rheological data to calculate printability, as detailed in Section 3.2.2.

In this subsection:

- Inks were formulated with selected solvents to reduce viscosity
- Rheological parameters were obtained for inks (viscosity, density, surface tension)
- The Z parameter was calculated to confirm printability of inks.

4.2.1. Viscosity modification

The goal of ink formulation is to produce inks which meet the process requirements of the inkjet printer, while ensuring that all constituents are mutually compatible (i.e. silicones, QDs, and any processing aids) and that inks are compatible with the cartridge and printhead, as well as the processing temperature used.

The ideal ink properties for the Fujifilm Dimatix print cartridge are as follows:

- 10-12 mPa s viscosity^{175,176}
- 28-33 mN m⁻¹ surface tension¹⁷⁵
- >1 g cm⁻³ density¹⁷⁶

The viscosities of SiliGlass Part A (crosslinker) and Part B (catalyst) as supplied were 124.3 mPa s and 169.3 mPa s at room temperature, respectively. However, the maximum extended range of viscosity for the Fujifilm Dimatix printer is 2-30 mPa s.⁵⁹ Therefore, strategies for viscosity modification were required to meet the processing requirements.

One method of reducing ink viscosity is to increase the jetting temperature; however, silicones have a smaller viscosity-temperature coefficient than hydrocarbons (0.6 VTC for PDMS fluids of 100 mPa s viscosity at 25 °C).⁵³ Given that the maximum nozzle temperature of the print cartridge is 60 °C,⁵⁹ and the room temperature SiliGlass viscosities were >100 mPa s, increasing the jetting temperature alone would be insufficient to reduce viscosity to jettable levels. A change in formulation was required to reduce viscosity, such as by reducing the average chain length of the precursors or by adding a processing aid.

Solvents are commonly used as carrier vehicles in ink formulations and are effective at reducing viscosity without being permanently incorporated into the polymer matrix, although complete solvent removal requires post-processing. Dilution by addition of solvent is a facile way to reduce viscosity while preserving the crosslink chain length in the cured material, as compared to reducing the average molecular weight (MW) of precursors, which limits the Shore hardness and elasticity of a cured elastomer (barring the use of chain extenders).⁵⁷ Rheological modification is reversible as solvent is removed during drying; this can be used to control adhesion, contact pinning, and reaction kinetics, which can influence print resolution. Solvents also facilitate the mixing and homogenisation of constituents, which can increase polymer conversion and aid dispersion of species within a polymer ink; this could stabilise QD dispersion in the composite ink.

There are a number of drawbacks to the use of solvents: in terms of printing performance, dilution reduces the material deposition rate, print speed may be delayed by interlayer drying times, and Marangoni flow may be generated in drying sessile drops leading to uneven film formation.³⁵ Film formation in inks with high solvent loading may be further disrupted by solvent-polymer interactions during drying which lead to diffusion of residual monomers or impurities and to surface roughness.¹¹⁶ Considerations must also be made of the choice of chemical as solvent, as volatile solvents can reduce ink working time and cause nozzle blockages, and flammable or harmful solvents pose a safety risk. Compatibility may be challenging as solvents must be compatible with not only the solute, but the printhead, fluid reservoir, and substrate materials; in fully inkjet-printed devices, it is necessary to use orthogonal solvents to deposit layers of the next material without distorting the previous material.²⁰⁸ Solvents, although removable, also affect the microstructure and the macroscopic properties of the cured material. For example, silicones that are crosslinked in the presence of solvent have reduced elastic moduli as locked chain entanglements are diluted,⁵⁷ which may or may not be desirable: greater chain mobility and higher CTE result in elastomers which are better able to absorb thermal stresses without cracking, but sensor readings may be more vulnerable to changes in expansion and discoloration.^{46,181,192} Polymers also swell when impregnated with a compatible solvent, which can be detrimental for device components; conversely, shrinkage may be seen upon solvent removal. This can complicate calibration of sensing materials and/or contaminate systems, necessitating either thermal-post treatment to fully remove solvent or sealing to isolate residual solvent.

Despite potential drawbacks, a strategy was required to lower viscosity to enable jetting. In terms of constituents that can be added to the commercial formulation, solvents do not alter the average crosslink chain length and are removable, which may be preferable to adding short chain vinyl-terminated PDMS or silicone oil, which would increase elastomer brittleness or lead to gradual leaching of oil from the matrix, respectively.⁵⁷ Increasing the amount of vinyl moieties in the elastomer would also promote the formation of Si-Pt and C-Pt clusters which are associated with greater discoloration.¹⁹² Therefore, inks were formulated with solvents, prioritising high polymer loading to reduce the negative impacts and improve printing efficiency.

Poor solvents will result in phase separation leading to inhomogeneous inks with inconsistent viscosity. For stable silicone inks, it is vital that silicones are soluble in or miscible with a chosen solvent. Solvent compatibility arises from the intermolecular bonding between the solute and the solvent, which may have contributions from a combination of dispersive forces, polarity and polarisability, and hydrogen bonding. There is an expansive range of parameters and models for polymer dissolution, e.g. steric factors and phase equilibria considerations; the relevant parameter(s), and appropriate solubility models, will depend on the dominant chemical properties and the conditions of interest. In broad terms, a good solvent is one in which the interactions between polymer segments and solvent molecules are energetically-favoured; in conformational models of polymer solvation, this leads the polymer chains to expand and uncoil in solution. In a poor solvent, polymer-polymer interactions are favoured, and polymer coils contract to decrease the polymer-solvent interface. A theta solvent is one in which neither interaction is preferred: at the theta point, polymer coils take the same conformation as the bulk polymer phase.²⁰⁷

A rule of thumb is “like dissolves like”²⁰⁷: silicones dissolve in non-polar and aprotic solvents. Silicones are soluble in a range of hydrocarbons, including aliphatic (n-alkanes), aromatic (xylene, toluene), and chlorinated (chloroform, perchloroethylene) molecules.^{17,53} They may also dissolve in hydrocarbons containing heteroatoms, such as 2°/3° amines (diisopropylamine, triethylamine), ethers (diethyl ether, tetrahydrofuran), and ketones (ethyl acetate, methyl ethyl ketone).^{17,53,209}

In PDMS-based devices and microfluidics research, solvent interactions with PDMS elastomers are of further interest for material compatibility issues. The use of orthogonal solvents or non-solvents during device manufacture can prevent distortion, swelling, and/or diffusion of materials from their desired placements, in addition to preventing

dissolution of impurities or oligomers from the PDMS elastomer and absorption of solutes into the PDMS elastomer.²⁰⁹ Crosslinked polymers do not dissolve, so solubility tests are unsuitable for assessing solvents, but they do expand when penetrated by solvent molecules; this swelling is an indication of solvent compatibility.

In binary, nonpolar systems, solubility can be related to swelling using the Hildebrand-Scatchard equation (Equation 10).²⁰⁹ The cohesive energy density c , often expressed as the Hildebrand solubility parameter δ , quantifies the intermolecular attraction per unit volume of material and is the principal energy barrier to mixing. For spontaneous mixing to be favourable, the change in free energy ΔG_m must be negative according to the Gibbs free energy equation, $\Delta G = \Delta H - T\Delta S$. As the enthalpy change of mixing ΔH_m is proportional to the difference in Hildebrand solubility parameters, swelling and solvation is maximal when the two constituents have the same Hildebrand values. A more complete thermodynamic model of solvent-polymer mixing is given by the Flory-Huggins equation, where the entropic factor in the free energy equation is included in the calculation; the solubility parameter used is the interaction parameter χ and is related to the Hildebrand parameter. The Flory-Huggins equation is used for polymer chains, while the Flory-Rehner equation considers elastomers by relating the molecular weight of crosslinks to swelling.²⁰⁷

Equation 10: The Hildebrand-Scatchard equation, where ΔH_m is the change of enthalpy upon mixing, V_m is the mixture volume, and δ and φ are the Hildebrand solubility parameters and volume fractions of the two constituents, respectively. The Hildebrand parameter relates to cohesive energy density c as $\delta = c^{1/2}$.

$$\Delta H_m = V_m(\delta_1 - \delta_2)^2 \varphi_1 \varphi_2$$

Whitesides *et al.* measured the swelling ratio by length and showed that PDMS swelling was predominantly determined by solvent compatibility, using the Hildebrand model where cohesive energy density relates to Hildebrand solubility parameters.²⁰⁹ Common organic solvents were ranked by swelling ratio by length S : chloroform (1.39) > ether (1.38) > tetrahydrofuran (1.38) > hexane (1.35) > toluene (1.31) > dichloromethane (1.22) > ethyl acetate (1.19).

Ziai *et al.* expanded on this,²¹⁰ utilising Hansen solubility parameters rather than Hildebrand: this uses the same model but subdivides solubility parameters into types of intermolecular interactions. R_a was used as a measure of overall similarity between polymer and solvent. Swelling ratios were calculated by weight (Q_w) and volume (Q_v); for common organic solvents ranked by swelling ratio Q_v , diethyl ether (3.3) > hexane (2.8) > tetrahydrofuran (2.4) > dichloromethane (2.3) > ethyl acetate (1.8) > toluene (1.7).

Swelling is not a direct measure of solvent compatibility; this metric does not take differences in solvent density and vapour pressure into account, which were observed to influence swelling.^{209,210} Nonetheless, swelling is a good indicator and a list of potential solvents for inks can be made based on this data.

Ideal parameters for potential solvents are given below in Table 9, grouped by desired features. The volatility of a solvent, i.e. its evaporation rate under ambient conditions, has an effect on print speed, film formation, ink working time, and nozzle failure. Inks with more volatile solvents have shorter drying times on the substrate which enables faster material deposition. However, higher volatility leads to greater Marangoni flow and coffee staining. It can also accelerate ink aging and changes in viscosity which cause deposition creep, nozzle blockages, and jetting failure.³⁵ Typical solvents for PDMS are volatile as they only have dispersive and dipole-dipole interactions, the weakest intermolecular forces; stable jetting performance is a priority and therefore compatible solvents with higher boiling point, lower vapour pressure, and higher vapour density were preferred.

Dipole moment and dielectric constant are selected as predictors of effective solvation; good compatibility is expected where solvent values match that of PDMS and the QD stabilising ligands. While the methyl groups of PDMS are hydrocarbons with weak, dispersive intermolecular forces, the Si-O bond of the siloxane backbone has 40% ionic character and a dipole moment of $\sim 0.6\text{-}0.9$ D.²¹¹ Silicones are amphiphilic polymers and the dipole moment of PDMS fluids is reported to scale with the number of repeat units according to $0.697 \mu n^{-0.5}$; the base polymer of SiliGlass (112.5 repeat units) is estimated to have a 7.4 D dipole moment.⁵³ Despite this, nonpolar solvents such as hexane are reported to be effective for silicones, and will be compatible with the alkyl-chain stabilising groups on the QDs; solvents with dipole moment equal to or lower than the Si-O bond dipole may be ideal. PDMS with a viscosity of 100 mPa s at 25 °C has a dielectric constant of 2.75,⁵³ and ideal solvents will have similar value.

In terms of rheology, the goal of the solvent is to bring the values for viscosity, surface tension and density closer to the ideal inkjet processing parameters, with viscosity as a priority. SiliGlass A and B are an order of magnitude more viscous than the jetting limit, so ideal solvents will have viscosity below the processing window (i.e. >2 mPa s). Viscosity will correlate with volatility as a function of the strength of intermolecular forces; as all solvents listed are inviscous, lower volatility was prioritised. The ideal values for surface tension are 28-33 mN m⁻¹ for the Dimatix,¹⁷⁵ whereas the surface tension of a 100 mPa s PDMS fluid is

lower, 20.9 mN m^{-1} at $25 \text{ }^\circ\text{C}$;⁵³ raising the surface tension with a solvent could improve jetting performance. Surface tension determines compatibility for contact with different substrates, e.g. wetting and spreading; increasing the surface energy may enable deposition of individually resolved droplets on a wider range of substrates than is possible for PDMS, which tends towards thin film formation. However, liquids that differ greatly in surface tension tend to not be miscible, so the surface tension of the solvent should not be too dissimilar to silicone. Lastly, the ideal density is $>1 \text{ g cm}^{-3}$,¹⁷⁶ while the mix density of SiliGlass is close at 0.97 g cm^{-3} ; solvents with higher density can make the ink more ideal.

Table 9: Ideal solvent parameters for ink formulation for reduced volatility, good compatibility with solutes, and inkjet processability.

Property	Parameter	Excellent	Good	Somewhat poor
Reduced volatility	<i>Boiling point</i> $^\circ\text{C}$	>200	100-200	<100
	<i>Vapour pressure</i> mmHg	<1	<100	>100
	<i>Vapour density</i> relative to air	>4.5	<4.5	<3.5
Material compatibility	<i>Dipole moment</i> D	<0.9	0.9-2.0	>2.0
	<i>Dielectric constant</i>	2.25-3.25	1.0-4.5	>4.5
Processability	<i>Viscosity</i> mPa s	>2.0	2.0-5.0	>5.0
	<i>Surface tension</i> mN m^{-1}	25-35	20-25	$<20, >35$
	<i>Density</i> g cm^{-1}	>1.0	0.8-1.0	<0.8

A list of suggested solvents for silicone and their properties is given below in Table 10. Solvents must not poison the platinum catalyst, so solvents containing amines or sulphides are excluded.¹⁷ While solvent MW can be an important factor in polymer dissolution, as large solvent molecules can lead to phase separation as described by the Flory-Huggins equation,²⁰⁷ this was not an issue in the case of SiliGlass as the polymer MW is low. Solvents must also be suitable for QD dispersions and have favourable interactions with QD stabilising ligands. Typical QD syntheses use coordinating ligands with hydrophobic tails in nonpolar solvents;¹¹³ the QDs purchased from Ocean Nanotech have similar composition, with octadecylamine ligands that have C18 alkyl chain tails that interface with the environment. Therefore, solvents that often feature in published QD syntheses are optimal.

Suitable solvents for PDMS are predominantly volatile, nonpolar solvents and, while high volatility does decrease the drying time of deposited material, it may lead to nozzle blockage in inkjet where solvent evaporation leaves material too viscous to jet.³⁵ Therefore, solvents with higher boiling points and lower vapour pressure were preferred; of the common organic solvents listed, toluene and octane have boiling points higher than water and relatively low vapour pressures. The less common solvents suggested are based on common organic solvents, with the goal of reducing their volatility while maintaining or enhancing their compatibility with PDMS: ethyl acetate is replaced with octyl acetate and diethyl ether is replaced with dibutyl ether, as longer hydrocarbon chains are expected to have more favourable interactions with the QD stabilising ligand. These solvents have higher boiling points and lower vapour pressures than the other, more common solvents listed. This is achieved at the cost of having relatively large dipoles and dielectric constants due to the polarity of the carbonyl bond, but good compatibility with silicones is expected despite this as their values are comparable to that of the chlorinated solvents.

Table 10: Suggested solvents for silicone inks for inkjet printing and their properties. Values are marked green (excellent), yellow (good), or orange (somewhat poor), in accordance with the ideal values stated above in Table 9.

Solvent	Boiling point ²¹² °C	Vapour pressure ²¹² mmHg	Vapour density relative to air	Dipole moment ²¹³ D	Dielectric constant ²¹³	Dynamic viscosity ²¹² mPa s	Surface tension ²¹³ mN m ⁻¹	Density ²¹²⁻²¹⁴ g cm ⁻³
Octyl acetate	211 °C ^{215,216}	0.4 (20 °C) ²¹⁵	5.9	1.78 ²¹⁷	4.13 (20 °C) ²¹⁸	1.85 (20 °C) ²¹⁷ ; 1.68 (25 °C) ²¹⁷	27.8 (20 °C) ²¹⁷ ; 27.3 (25 °C) ²¹⁷	0.867 (25 °C) ²¹⁶
Dibutyl ether	142 °C ^{213,219}	4.8 (20 °C) ²¹⁹	4.5	1.18	3.08 (20 °C) ^{213,214}	0.637 (25 °C) ²¹³	22.91 (20 °C); 22.45 (25 °C)	0.764- 0.769 (25 °C) ^{214,219}
Octane	126 °C ²¹³	10 (20 °C) ²¹⁴	3.9	0.00	1.948 (20 °C)	0.546 (20 °C) ^{213,214}	21.62-21.8 (20 °C) ^{213,214} ; 21.14 (25 °C)	0.703 (25 °C) ²¹⁴
Toluene	111 °C	22 (20 °C)	3.2	0.375; 0.31 (20 °C) ²¹²	2.38 (25 °C) ²¹²⁻²¹⁴	0.59 (20 °C); 0.553-0.56 (25 °C) ^{189,214}	28.52-28.6 (20 °C) ²¹²⁻²¹⁴ ; 27.9-27.93 (25 °C) ^{213,220}	0.862- 0.865 (25 °C)
Hexane	69 °C	124 (20 °C)	3.0	0.00; 0.08 (25 °C) ²¹²	1.89 (20 °C); 1.88 (25 °C) ^{212,214}	0.313 (20 °C) ^{212,213} ; 0.294 (25 °C) ²¹⁴	18.40 (20 °C); 17.89-17.95 (25 °C) ²¹²⁻²¹⁴	0.655 (25 °C) ^{212,214}
Chloroform	61 °C	158.4 (20 °C)	4.1	1.04; 1.15 (25 °C) ²¹²	4.81 (20 °C) ²¹² ; 4.807 (25 °C)	0.57 (20 °C); 0.54 (25 °C) ¹⁸⁹	27.16-27.32 (20 °C) ^{212,213} ; 26.67 (25 °C) ^{213,220}	1.480 (25 °C) ^{212,220}
Dichloro- methane	40 °C	350 (20 °C)	2.9	1.60; 1.14 (25 °C) ²¹²	9.14 (20 °C); 8.93 (25 °C) ²¹²⁻²¹⁴	0.44 (20 °C); 0.41 (25 °C) ¹⁸⁹	27.84-28.12 (20 °C) ²¹²⁻²¹⁴ ; 27.2 (25 °C)	1.317- 1.326 (25 °C)

Octyl acetate was selected as preferred solvent as it had the lowest volatility and has been used to formulate inks with silicones in literature.⁶⁰ It was miscible with the silicones and formed a stable ink; it is also very safe to work with and is categorised as harmless, a key advantage over the other solvent options. Dibutyl ether remains a viable alternative for low-volatility inks with faster drying in future work.

While octyl acetate was expected to work well for QD dispersion - as it contains a C8 alkyl chain that would interact favourably with the C18 alkyl chain of the QD stabilising ligands - it is a relatively polar solvent and was not seen to be used in literature, whereas others are well-documented. Therefore, a solvent that was more typical of QD colloidal dispersions was investigated as an alternative. Toluene was chosen as it is one of the least volatile of the common organic solvents and its polarity matches the QD stabilising ligand. However, octyl acetate is preferable to work with as toluene is volatile, flammable, and toxic.

Inks of different solvent loadings were then formulated using either octyl acetate or toluene. The rheological characterisation of these formulations is described below, identifying the solvent loadings for jettable inks and selecting ink compositions with polymer concentration as a priority.

4.2.2. Octyl acetate-based inks

Two-part inks were formulated from SiliGlass RTV using solvents as carrier vehicles to achieve the rheological properties required for inkjet printing (IJP). A 2-part ink strategy was selected over 1-part inks to extend the ink working life^{60,68} – as single inks crosslink and become unusable after 2-48 hours⁶¹⁻⁶⁴ – and to allow control over the molar ratio of silane to vinyl moieties to vary the mechanical properties.⁵⁷

For the Fujifilm Dimatix print cartridges, the ideal fluid properties are 10-12 mPa s viscosity,^{175,176} 28-33 mN m⁻¹ surface tension,¹⁷⁵ and >1 g cm⁻³ density.¹⁷⁶ As the viscosity of SiliGlass required a ten-fold reduction, viscosity measurements were carried out first to ascertain suitable solvent concentration to achieve values within the jettable range, before obtaining further parameters to calculate printability.

Viscosity

As the viscosity of undiluted SiliGlass exceeded the jettable limit, Ink A (crosslinker ink) and Ink B (catalyst ink) were prepared with varied polymer loadings to ascertain concentrations with suitable viscosity for jetting under ambient conditions. A solvent trap was used to prevent changes in viscosity arising from solvent evaporation; this enabled stable data acquisition but does not reflect inkjet conditions. Solvent evaporation during jetting or ink aging can occur and alter jettability, particularly if more volatile solvents and/or higher jetting temperatures are used.

The dynamic viscosities of different concentrations of silicone in octyl acetate are shown in Table 11. Inks with 30-50 wt% SiliGlass were found to be within the jettable range for inkjet printing at 25 °C⁵⁹: while the viscosities of the 40 wt% inks were within the ideal range for the Dimatix printer (10 - 12 mPa s),¹⁷⁵ the 50 wt% inks were selected as higher polymer concentration was prioritised. Higher polymer concentration does not necessarily lead to a significant reduction in layer drying time, as diffusion rates are observed to decrease as solvent concentration decreases,²²¹ but does lead to more efficient material deposition onto the printing substrate.

Table 11: Dynamic viscosity of 30, 40 and 50 wt% silicone in octyl acetate at 25 °C with a shear rate of 10 s⁻¹ and the percentage difference from the ideal range (as applicable).

Ink	Dynamic viscosity η , mPa s		
	30 wt% silicone	40 wt% silicone	50 wt% silicone
A	7.361 (-26.39%)	10.13 (ideal)	12.71 (+5.92%)
B	7.432 (-25.68%)	10.67 (ideal)	14.38 (+19.83%)

The temperature of the jetting nozzles was susceptible to its environment, as the printhead had an in-built heater but no cooling; 25 °C is close to the lower limit of maintainable printing temperature. Additionally, the Fujifilm Dimatix features platen heating, and there may be heat transfer from the platen to the nozzle plate during use. It had been determined by drop casting experiments that the addition of solvent slowed down the cure rate: at room temperature, 50 wt% inks took hours to cure, while at 60 °C, inks took 10 min to fully cure. As cure rate is diffusion-based²²² and the inkjet droplet volumes are much smaller (10 pL), which lead to an increased rate of solvent evaporation, 40 °C was selected to minimise thermal cycling on QDs and evaporation at the nozzle plate. Therefore, to confirm ink jettability in the case of 40 °C platen heating to accelerate curing, the viscosity was measured at 25, 30 and 35 °C to account for heat transfer.

A graph of dynamic viscosity versus temperature for 50 wt% silicone in octyl acetate is shown below in Figure 34. Viscosity decreased with increasing temperature to become closer to the ideal range; heat transfer from the platen to the nozzle plate would not be detrimental to printing outside of changes in evaporation rate. As a solvent trap was used during measurement, observation of printing is required to confirm that the jetting of the viscous inks is stable during inkjet. While octyl acetate was selected for its low volatility, and ambient jetting temperatures were chosen to reduce evaporation at the nozzles, the large surface-area-to-volume ratio of droplets produced during inkjet can accelerate evaporation; this would be most detrimental to jetting of the more concentrated inks, as the viscosity could exceed the jettable limit if significant evaporation occurred.

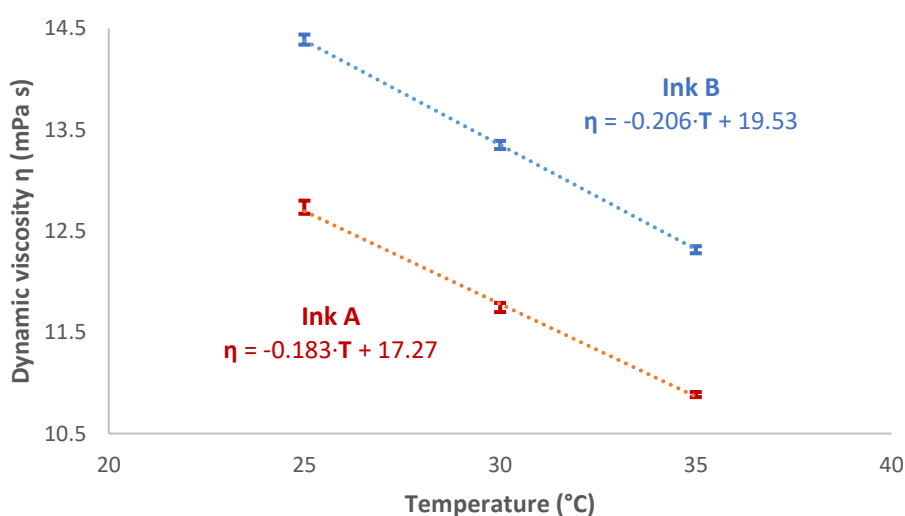


Figure 34: Dynamic viscosity of 50 wt% octyl acetate-based inks against temperature, showing Ink A in red and Ink B in blue. Bars display the range of values measured. Viscosity in mPa s (25 °C, 30 °C, 35 °C): (A) 12.71, 11.75, 10.88; (B) 14.38, 13.35, 12.32.

Density and Surface Tension

The densities of the 50 wt% octyl acetate inks were determined to be 0.92 g cm^{-3} for Ink A and 0.95 g cm^{-3} for Ink B, with $\pm 0.01 \text{ g cm}^{-3}$ equipment tolerance. These values are between density values for silicone (0.97 g cm^{-3})⁵³ and octyl acetate (0.867 g cm^{-3} at $25 \text{ }^\circ\text{C}$)²¹⁶. The silicone inks were effective at wetting surfaces inside the needle, which may have caused slight underestimation of density.

The surface tension was found by drop shape analysis (DSA) of pendant droplets, as shown in Figure 35. The inks showed wetting behaviour: solutions climbed the outside surface of the needle until the mass was sufficient for gravity to pull it into a droplet. In PDMS, the critical surface tension of wetting is higher than its liquid surface tension; this causes the aforementioned “creep”, where a silicone will migrate and spread over a film of itself.⁵¹

Values obtained for the surface tension were $23.94 (\pm 0.01) \text{ mN m}^{-1}$ for Ink A and $23.04 (\pm 0.04) \text{ mN m}^{-1}$ for Ink B with a 99.73% confidence interval (3x standard error). This is 14.50-17.71% lower than the ideal range given by the printhead manufacturer ($28 - 42 \text{ mN m}^{-1}$)^{175,176} but within the extended range for inkjet ($20\text{-}50 \text{ mN m}^{-1}$)³⁵.

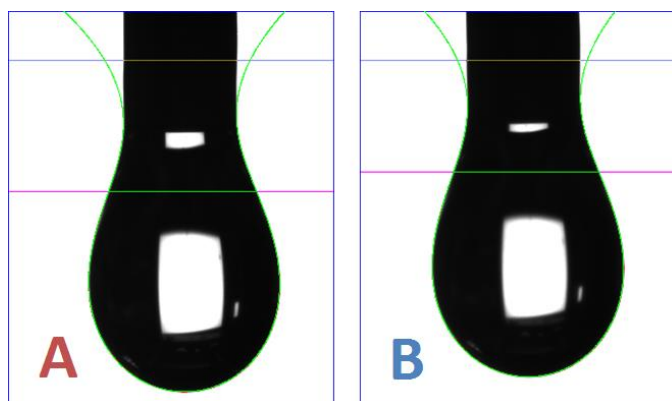


Figure 35: Representative images of pendant drop analysis of Ink A (left) and Ink B (right) for octyl acetate-based inks.

The low surface tension values are expected, as silicones are well-known to have low surface energy;¹⁷ PDMS surface tension increases with greater chain length and lower temperature, and is 20.9 mN m^{-1} for a 100 mPa s silicone at $25 \text{ }^\circ\text{C}$.⁵³ The values for the inks are higher, as the solvent has a higher surface tension than silicone: the surface tension of octyl acetate is 27.8 mN m^{-1} at $20 \text{ }^\circ\text{C}$ ²¹⁷ and 27.3 mN m^{-1} at $25 \text{ }^\circ\text{C}$ ²¹⁷. The shorter average chain length of SiliGlass A does not correlate with the lower surface tension of Ink A; this results from the substitution of methyl groups with more polar hydrogen atoms in the crosslinker, which leads to stronger intermolecular forces.⁵¹

Printability

The printability indicator Z - also known as the inverse Ohnesorge number - was used to identify the range of stable droplet formation, as defined in Equation 1.

$$Z = Oh^{-1} = \frac{\sqrt{\rho\sigma L}}{\mu} = \frac{Re}{\sqrt{We}}$$

Equation 1: Printability Indicator Z , where Oh , Re , and We are the Ohnesorge, Reynolds and Weber numbers, and ρ , η , σ , and L are density, dynamic viscosity, surface tension, and nozzle diameter respectively.

Rheological parameters for Ink A (crosslinker ink) and Ink B (catalyst ink) were used to predict printability as shown in Table 12. At 25 °C, Ink A and Ink B had viscosity values of 12.71 ± 0.01 mPa s and 14.38 ± 0.01 mPa s, respectively (99.73% confidence interval). Densities of 0.92 and 0.95 g cm⁻³ were obtained with 0.01 g cm⁻³ equipment tolerance, and surface tension values were 23.94 ± 0.01 mN m⁻¹ and 23.04 ± 0.04 mN m⁻¹ for Ink A and Ink B, respectively (99.73% confidence interval). Using Equation 1, the Z parameters for Ink A and Ink B - 1.71 and 1.51 respectively - are within range for stable droplet formation. As the viscosity was higher and the surface tension lower than ideal fluid properties for the Dimatix printer, a tendency to form long tails was expected in jetting. The similarity in printability parameter was advantageous for reactive inkjet of 2-part inks in that similar jetting behaviour and droplet mass are expected; if drop mass is identical or near identical, then calculation of and control over the mix ratio is simple and presents a facile strategy for varying the elastic modulus of the printed material.⁵⁷

Table 12: Printability of 50 wt% silicone in octyl acetate at 25 °C. Values of shear viscosity, density, surface tension, and the printability parameter Z are given for each ink.

	Viscosity η mPa s	Density ρ g cm ⁻³	Surface tension σ mN m ⁻¹	Diameter L μ m	Z
Part A 50 wt% octyl acetate	12.71 (± 0.01)	0.92 (± 0.01)	23.94 (± 0.01)	21.5	1.71
Part B 50 wt% octyl acetate	14.38 (± 0.01)	0.95 (± 0.01)	23.04 (± 0.04)	21.5	1.51

4.2.3. Toluene-based inks

As well as octyl acetate-based inks, inks were formulated using toluene solvent, which was selected as a common solvent choice for QD dispersion. The amount of solvent required for inks with printable viscosity was determined first, followed by other rheological measurements and calculation of printability.

Viscosity

The dynamic viscosities of different concentrations of inks at 25 °C are shown in Table 13, using a solvent trap as discussed above. Both 50 and 60 wt% SiliGlass inks were within the viscosity limits given by the Fujifilm Dimatix printer guidelines (2-30 mPa s)⁵⁹ and close to the ideal range of 10-12 mPa s^{175,176}: the 50 wt% inks were lower than ideal viscosity at 8.7-8.8 mPa s and the 60 wt% inks higher at 12.7 mPa s for Ink A (crosslinker) and 14.5 mPa s for Ink B (catalyst). Toluene-based inks were less viscous than octyl acetate-based analogues; viscosity of octyl acetate is three-fold that of toluene at 25 °C (1.68 mPa s²¹⁷ and 0.56 mPa s^{189,214}). Comparable viscosity values were obtained at 50 wt% SiliGlass using octyl acetate and 60 wt% SiliGlass using toluene.

Table 13: Dynamic viscosity of 50 and 60 wt% silicone in toluene at 25 °C with shear rate of 10 s⁻¹ and the percentage difference from the ideal range (as applicable).

Ink	Dynamic viscosity η , mPa s	
	50 wt% silicone	60 wt% silicone
A	8.676 (-13.24%)	12.72 (+6.00%)
B	8.789 (-12.11%)	14.53 (+21.08%)

Dynamic viscosity of inks as a function of temperature was obtained from 25-35 °C to account for potential heat transfer to the nozzle when 40 °C platen heating is used to accelerate cure rate; as a solvent trap was used during measurement, this data does not account for solvent evaporation. The graph for 60 wt% SiliGlass is shown below in Figure 36; the inks decreased in viscosity towards the ideal viscosity range, showing that higher nozzle temperature from heat transfer would not be innately detrimental for printing, although it may lead to nozzle blockages by increasing the evaporation rate of the solvent. In the graph for 50 wt% SiliGlass in Figure 37, viscosity deviated further from ideal values as the temperature increased, showing that heat transfer would be detrimental for printing if solvent evaporation does not counteract the predicted decrease in viscosity.

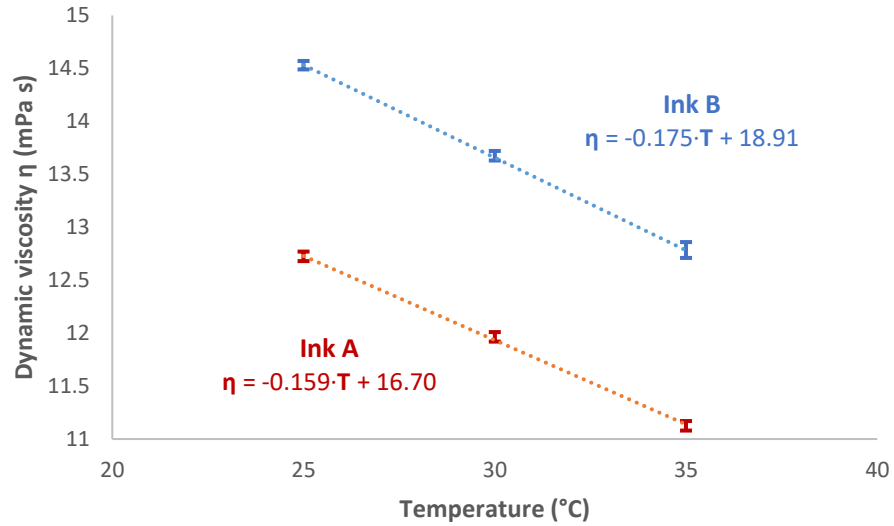


Figure 36: Dynamic viscosity of 60 wt% toluene-based inks against temperature, showing Ink A in red and Ink B in blue. Bars display the range of values measured. Viscosity in mPa s (25 °C, 30 °C, 35 °C): (A) 12.72, 11.95, 11.13; (B) 14.53, 13.66, 12.78.

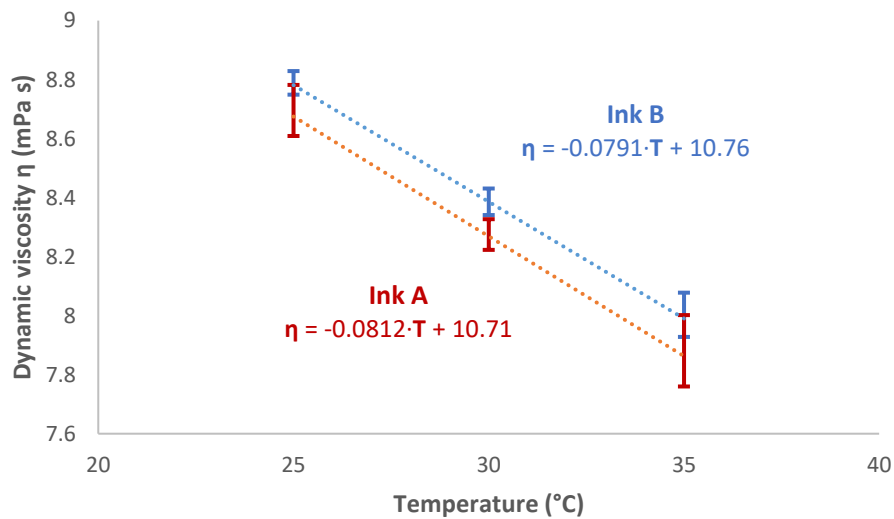


Figure 37: Dynamic viscosity of 50 wt% toluene-based inks against temperature, showing Ink A in red and Ink B in blue. Bars display the range of values measured. Viscosity in mPa s (25 °C, 30 °C, 35 °C): (A) 8.676, 8.265, 7.865; (B) 8.789, 8.371, 7.998.

While both 50 and 60 wt% SiliGlass lead to suitable viscosity for inkjet using toluene, the 60 wt% inks were prioritised as they had higher polymer loading and similar rheology to the 50 wt% octyl acetate inks. As a solvent trap was used during measurements, and toluene is more volatile than octyl acetate, the above inks may be susceptible to increases in viscosity and nozzle blockage from solvent evaporation at the nozzles; 50 wt% inks may be preferable if the 60 wt% inks display poor jetting performance during print trials, and therefore rheological characterisation and printability calculations were carried out for both concentrations of toluene-based inks.

Density and Surface Tension

The densities of the toluene-based inks were determined to be 0.92 g cm^{-3} for Ink A and 0.93 g cm^{-3} for Ink B at 60 wt% SiliGlass, and 0.95 g cm^{-3} for both inks at 50 wt% SiliGlass, with $\pm 0.01 \text{ g cm}^{-3}$ equipment tolerance. Ink density increased as solvent concentration increased even though the density of silicone exceeds that of toluene; as toluene-based inks displayed similar wetting behaviour to the octyl acetate-based inks discussed above, it may be that more residual material was unaccounted for when silicone concentration was higher, leading to greater underestimation of density. Between solvents, 50 wt% inks had the same density value for B (catalyst) but different densities for A (crosslinker), despite similar solvent densities (0.86 g cm^{-3} for toluene and 0.87 g cm^{-3} octyl acetate at $25 \text{ }^\circ\text{C}$);^{212-214,216} while this may be related to differences in solvent polarity and therefore their interactions with the crosslinker, this may just reflect the tolerance of the measurement.

Surface tension was determined using DSA, where toluene solutions displayed similar 'needle-climbing' behaviour to octyl acetate-based analogues. Surface tension values for all inks were lower than the ideal range given by the manufacturer ($28 - 42 \text{ mN m}^{-1}$)^{175,176} but within the extended range for inkjet printing ($20-50 \text{ mN m}^{-1}$)³⁵.

50 wt% toluene inks had surface tensions approximately $1-2 \text{ mN m}^{-1}$ higher than the analogous 50 wt% octyl acetate inks, despite similar surface tension values between the two solvents (27.9 mN m^{-1} for toluene^{213,220} versus 27.3 mN m^{-1} for octyl acetate²¹⁷).

Values obtained for surface tension were $22.41 (\pm 0.21) \text{ mN m}^{-1}$ for Ink A and $21.52 (\pm 0.04) \text{ mN m}^{-1}$ for Ink B at 60 wt% SiliGlass, and $24.32 (\pm 0.99) \text{ mN m}^{-1}$ for Ink A and $25.22 (\pm 0.17) \text{ mN m}^{-1}$ for Ink B at 50 wt% SiliGlass, with 99.73% confidence intervals. Surface tension of inks was seen to increase over time, moreso in inks with higher solvent concentration: over the course of measurement, surface tension values for Ink A increased, from $\sim 22.22 (\pm 0.25) \text{ mN m}^{-1}$ to $\sim 22.56 (\pm 0.12) \text{ mN m}^{-1}$ at 60 wt% SiliGlass, and from $\sim 23.33 (\pm 0.18) \text{ mN m}^{-1}$ to $\sim 25.31 (\pm 0.10) \text{ mN m}^{-1}$ at 50 wt% SiliGlass.

Increases in measured surface tension may arise from the evaporation of volatile solvents from the syringe, where drying rates are higher for higher solvent concentrations.²²¹ However, the surface tension of silicone (20.9 mN m^{-1})⁵³ is much lower than toluene, so evaporation would be expected to reduce the overall surface tension of the inks; as the calculation of surface tension used in DSA considered viscosity as a parameter, the lower values may instead reflect changes increased ink viscosity with evaporation. In addition, the

surface tension of Ink B was observed to be more stable as a function of time than for Ink A: the more polar silane moieties of the crosslinker have less favorable interactions with the aprotic toluene molecules than the methyl groups of PDMS do, which may lead to higher overall volatility in Ink A and account for these observations.

While surface tension was observed to vary over time in toluene-based inks, this was not observed in octyl acetate-based inks. This is likely indicative of the greater volatility of toluene and this suggests that changes in rheological properties will occur during printing, which may be detrimental for inkjet and lead to poor jetting performance and nozzle blockage. The surface tension of toluene inks had a smaller overall change at higher concentration, which may be due to diffusion rates decreasing as solvent concentration decreases,²²¹ which suggests that the jetting behaviour of the 60 wt% SiliGlass inks would be more stable over time despite their lower surface tensions.

Printability

The printability Z of toluene-based inks is calculated below in Table 14; 60 wt% SiliGlass inks (toluene) had similar rheological properties to Ink A and Ink B (50 wt%, octyl acetate).

At 25 °C, 60 wt% A and B in toluene had viscosity values of 12.72 ± 0.01 mPa s and 14.53 ± 0.01 mPa s, respectively (99.73% confidence). Densities of 0.92 and 0.93 g cm⁻³ were obtained and surface tension values were 22.41 ± 0.21 mN m⁻¹ and 21.52 ± 0.04 mN m⁻¹ for A and B respectively, lower than the 50 wt% octyl acetate inks. Using Equation 1, the Z parameters for 60 wt% A and B in toluene - 1.65 and 1.43 respectively - are within range for stable droplet formation. These Z parameters are very similar to 50 wt% silicone in octyl acetate inks and similar jetting behaviour is predicted.

At 25 °C, 50 wt% A and B in toluene had viscosity values of 8.676 ± 0.018 mPa s and 8.789 ± 0.008 mPa s, respectively. Ink density was found to be 0.95 g cm⁻³ and surface tension values were 24.32 ± 0.99 mN m⁻¹ and 25.22 ± 0.17 mN m⁻¹ for A and B respectively, higher than the 50 wt% octyl acetate inks. Using Equation 1, the Z parameters for 50 wt% A and B in toluene - 2.57 and 2.58 respectively - are within range for stable droplet formation. This suggests that the jetting performance of 50 wt% toluene-based inks could be superior to the octyl acetate-based analogues; however, the toluene-based inks were less stable due to solvent evaporation, which may lead to inconsistent jetting.

Table 14: Printability of 60 and 50 wt% silicone in toluene at 25 °C. Values of shear viscosity, density, surface tension, and the printability parameter Z are given for each ink.

	Viscosity η mPa s	Density ρ g cm ⁻³	Surface tension σ mN m ⁻¹	Diameter L μ m	Z
Part A 60 wt% in toluene	12.72 (± 0.01)	0.92 (± 0.01)	22.41 (± 0.21)	21.5	1.66
Part B 60 wt% in toluene	14.53 (± 0.01)	0.93 (± 0.01)	21.52 (± 0.04)	21.5	1.43
Part A 50 wt% in toluene	8.676 (± 0.018)	0.95 (± 0.01)	24.32 (± 0.99)	21.5	2.57
Part B 50 wt% in toluene	8.789 (± 0.008)	0.95 (± 0.01)	25.22 (± 0.17)	21.5	2.58

The 60 wt% SiliGlass inks were prioritised over the 50 wt% for the toluene-based inks, despite their lower surface tensions and Z parameters, as the properties were more stable over time than the inks with higher solvent content and the higher polymer concentration enabled faster polymer deposition.

4.2.4. Summary of SiliGlass inks

As the viscosity of pure SiliGlass parts exceeded the viscosity limits of the printer by an order of magnitude, two solvents were selected as carrier vehicles for their miscibility with PDMS, efficacy for dispersion of QDs, and parameters relating to inkjet printing: octyl acetate^{60,64} and toluene,⁶² both of which have been used for silicone IJP in literature. Octyl acetate was selected for low volatility to decrease the likelihood of nozzle blockages arising from solvent evaporation, while toluene was trialled because it is a common solvent for silicones and for QD dispersions, being better established in literature.

50 wt% octyl acetate-based inks were shown to be jettable with Z parameters of 1.71 and 1.51 for Ink A (crosslinker ink) and Ink B (catalyst ink) respectively, similar to analogous 25 wt% PDMS ink made from Sylgard 184 in work by Mikkonen *et al.*⁶⁴ As the viscosity was higher and the surface tension lower than ideal fluid properties for the Dimatix printer, a tendency to form long tails during droplet ejection was expected; if satellite droplets form, then the mix ratio may be non-homogenous in printed materials leading to inconsistent physical properties.

For toluene-based inks, 60 wt% SiliGlass inks had similar properties to the analogous 50 wt% octyl acetate inks and were expected to have comparable jetting behaviour. The Z parameters for 60 wt% A and B in toluene were 1.65 and 1.43 respectively, slightly lower than for the 50 wt% octyl acetate inks in line with the differences in surface tension.

50 wt% toluene inks had Z parameters of 2.57 and 2.58 for A and B, respectively. This suggests that the jetting performance of 50 wt% toluene-based inks could be superior to the octyl acetate-based analogues. However, measured surface tension was seen to increase over time in toluene-based inks; it is unclear whether this results from solvent evaporation, given the higher volatility of toluene, which could lead to inconsistent jetting. Therefore, inks which met Objective *O1* were prioritised by the stability of their rheology: 50 wt% octyl acetate inks were selected as the preferred formulation, and toluene inks could be used to enhance QD dispersion, with 60 wt% SiliGlass being the preferred loading and 50 wt% SiliGlass used if solvent evaporation at the nozzles were to impede printing.

The next subsection describes the jetting and printing of octyl acetate-based inks with 50 wt% silicone (henceforth referred to as Ink A and Ink B): despite higher viscosity and lower surface tension than the ideal for the Dimatix,^{175,176} jetting without satellite droplets was achieved and the ink formulation was demonstrated to print without nozzle blockage.

4.3. Printing of SiliGlass inks

In this section, the work to optimise and assess the jetting of 50 wt% octyl acetate-based inks – henceforth referred to as Ink A (crosslinker ink) and Ink B (catalyst ink) – is detailed for both the Fujifilm Dimatix printer (single printhead, Section 4.3.3) and the modified Suss Microtec PiXDRO LP50 printer (dual printhead, Section 4.3.4). This work meets objective O2 and includes:

- Substrate preparation for suitable ink contact angle
- Drop ejection and waveform optimisation from the Dimatix Model Fluid waveform
- Drop array analysis and determination of droplet mass
- Printing on single printhead printer using pinned grid strategy
- Waveform modification for compatibility with PiXDRO LP50
- Printing on dual printhead printer using line-by-line strategy.

4.3.1. Drop-on-drop inkjet process

As discussed earlier, inks formulated from 2-part RTV silicones may be 1-part or 2-part. 1-part inks have the advantage of simpler printing calibration and deposition, whereas printing of 2-part inks may require greater optimisation of deposition alignment, time-of-flight, and mix ratio of the two constituents to ensure that inks mix as intended to yield optimal mechanical properties. Nonetheless, 2-part inks were formulated for the sensing material for a number of reasons. 2-part inks have much longer working lives than 1-part inks,^{60,68} which crosslink and become unusable after 2-48 hours,⁶¹⁻⁶⁴ leading to greater material waste which is undesirable when using high-value quantum dots. Ink curing also renders print cartridges unusable unless a thorough cleaning cycle is implemented. In addition, a range of elastic moduli can be achieved with a single set of 2-part inks by varying the molar ratio;⁵⁷ this can enable functionally-graded materials and allow the mechanical properties of printed composite materials to be matched to specific sensing applications.

The inkjet process diagram used for the 2-part inks formulated from SiliGlass is shown below in Figure 38, whereby inks are deposited drop-on-drop (DoD) onto the substrate and cure *in situ*. The nozzle temperature was set as 30 °C and platen as 40 °C to accelerate cure. Inks were loaded into Dimatix cartridges made from liquid crystal polymer (LCP), as solvent incompatibility with polypropylene led to catalyst poisoning.¹⁷

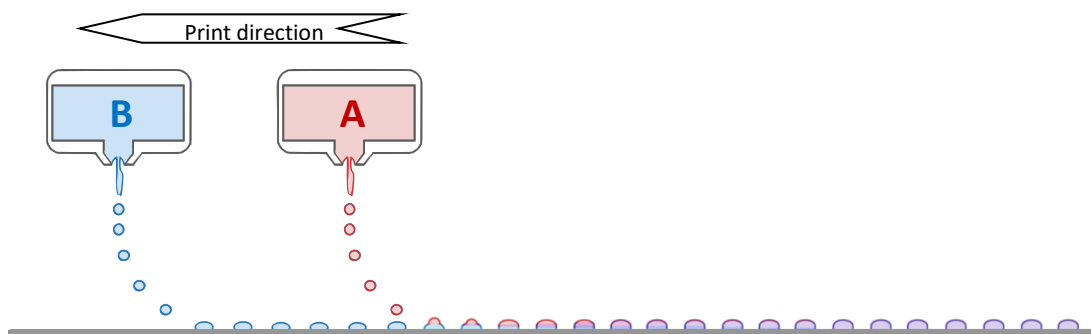


Figure 38: Drop-on-drop reactive inkjet scheme for addition cure silicone. Ink A (crosslinker) and Ink B (catalyst) are deposited drop-on-drop on the substrate and cure *in situ* via Pt-catalysed hydrosilylation. Here, Ink A is depicted as being deposited on Ink B using a dual printhead system; in practice, order of deposition was not seen to have a significant impact on printing.

Two printers were used, one with a single printhead (Fujifilm Dimatix) and one with dual printheads (PiXDRO LP50), the latter of which could deposit both inks near-simultaneously as shown in the scheme above. However, jetting could only be viewed when printing on the Dimatix printer; therefore, the Dimatix was used first to optimise and view jetting during waveform development.

4.3.2. Optimisation of jetting

Droplet ejection

Droplet ejection was investigated using the Fujifilm Dimatix printer (DMP-2830) so that droplet formation could be viewed by camera. A single pulse waveform was optimised from the Dimatix Model Fluid waveform, as described in Section 3.2.3.2. The initial waveform resulted in long tails which split into satellite droplets, but these satellites were eliminated in the final waveform (Waveform W_1 v1, Figure 138, Appendix), jetting at 32 V with shorter tails (<150 μm) that re-joined the primary drop as seen in Figure 39.

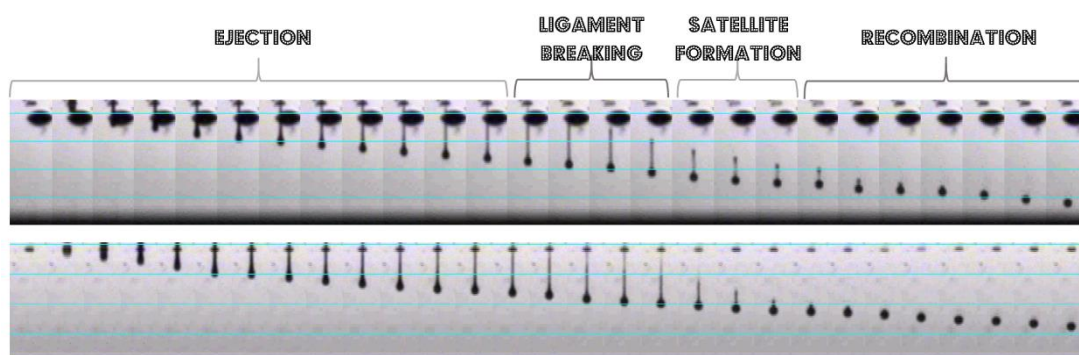


Figure 39: Droplet ejection of Ink A (top) and Ink B (bottom) at 32 V with waveform W_1 v1 using the Dimatix.

Minimal printhead maintenance was required in comparison to single-part RTV inks, as crosslinking did not occur at ambient temperature without catalysis. The Dimatix DMC-11610 print cartridges used in this thesis consist of a base and a nozzle plate cap, which act as both ink reservoir and printhead, respectively. The jettability of Ink A (crosslinker) and Ink B (catalyst) remained stable when stored at ambient temperatures and required no specialised storage conditions beyond those to prevent solvent evaporation, which would increase the viscosity. Although the manufacturer intended the print cartridge to be disposable, it was possible to use the cartridge reservoir indefinitely with no obvious detrimental impact on jetting performance, whereas single-part inks are reported to render cartridges unusable within days at most.^{61–64} While printability was not noted to degrade with ink aging over the course of weeks or even months – as long as vials and print cartridges were sealed and stored under ambient conditions out of direct sunlight to prevent solvent evaporation – further chemical changes in the inks may occur with aging. Commercial RTVs have recommended shelf lives of 6-18 months, depending on formulation; considerations for the shelf life of inks are discussed in Section 9.1.

The nozzle plate was also reusable, although its performance did degrade over time and occasional replacement was beneficial for jetting. Nozzles did not become permanently blocked after a period of disuse - as is the case for 1-part inks - and purge cycles were sufficient to clear out any ink that had undergone solvent evaporation. This ease of cleaning, despite the fact that the inks were more viscous than ideal, arises from the flexibility of the siloxane backbone, which confers lubricating properties.^{51,52} Nozzle blockage arising from solvent evaporation was not observed, indicating that the octyl acetate solvent was non-volatile under jetting conditions.³⁵ However, ink deposition creep on the nozzle plate arising from the low surface tension of silicones ($\sim 20.4 \text{ mN m}^{-1}$)⁵¹ was seen to alter or prevent drop ejection; the meniscus set point was raised to 4.0 to prevent excess ink flow from the nozzles.¹⁷⁶ Blotting was most effective strategy for in-print maintenance to absorb ink that had wet the nozzle plate due to low surface tension ($< 24 \text{ mN m}^{-1}$).

The low surface energy of the silicone inks also presented a challenge in obtaining a suitable substrate as inks tended to form thin films rather than discrete droplets. To assess suitable substrates for printing, sessile droplet analysis with 50 wt% octyl acetate inks was carried out as described in Section 3.2.2.3.

Sessile DSA

The tendency for a liquid to wet a surface is described by the spreading coefficient S (see Equation 11 below), which is the difference in energy between the dry surface and a wet surface, equivalent to the surface energy of the solid minus the surface energies of the liquid and solid-liquid interface.

$$S = [E_{substrate}]_{dry} - [E_{substrate}]_{wet} = \gamma_{solid} - (\gamma_{liquid} + \gamma_{solid-liquid})$$

Equation 11: The Young-Dupré equation, where S is the spreading coefficient, i.e. difference in energy between a wet and a dry surface, for a given system of solid and liquid with associated surface energies γ .

The system will default to the lowest energy configuration; if $S > 0$, then total wetting is observed. This is favoured for high energy substrates (large γ_{solid}) and low energy liquids (small γ_{liquid}). Silicones are known to have low surface energy ($\sim 20.4 \text{ mJ m}^{-2}$), which results in a strong tendency to form films.⁵¹ As controlled patterning requires a substrate upon which silicones form discrete droplets and do not spread into thin layers, comparably low energy substrates were needed for printing.

The surface tension was found to be $23.94 \pm 0.01 \text{ mN m}^{-1}$ and $23.04 \pm 0.04 \text{ mN m}^{-1}$ for Ink A and Ink B, respectively. Standard glass slides and slides coated in a thin layer of release agent both resulted in complete wetting when inks were dropcast; silicone inks spread into a thin layer and no contact angle could be detected by the software. This was as expected of glass, a high surface energy substrate (on the order of 70 mJ m^{-2}), while the release agent was designed for demoulding of silicone but was still insufficient to prevent wetting.

To produce a more strongly hydrophobic substrate, glass slides were silane-treated with PFOTS (Section 3.2.3.1). As polydimethylsiloxanes are able to orient their methyl groups due to the flexibility of the siloxane backbone, they are the polymer class with the lowest surface energy, with the important exception of fluoropolymers: the surface energy of carbon moieties decreases in the order $-\text{CH}_2- > -\text{CH}_3 > -\text{CF}_2- > -\text{CF}_3$ as the van der Waals interactions associated with them become weaker.^{51,223} PFOTS, a fluoroalkyl silane used in surface treatment,²²⁴ resulted in suitable contact angles: approximately 45° and 48° ($\pm 0.024^\circ$, 99.73% confidence) for Ink A and Ink B respectively, as shown in a representative image (Figure 40).

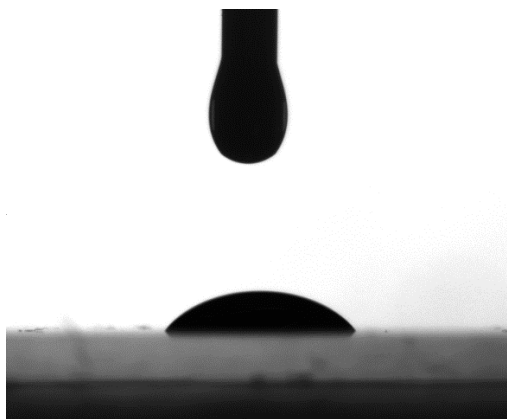


Figure 40: Ink B deposited onto a silane-treated glass slide, as viewed through the DSA100 camera.

A gradual decrease in contact angle was observed over a 5 min duration of measurement, likely corresponding to solvent evaporation: as the concentration of solvent in the ink decreases, the proportion of the constituent with lower surface energy (i.e. silicone) increases and the contact angle decreases. However, although higher SiliGlass concentration was expected to reduce contact angle, 60 wt% SiliGlass inks in octyl acetate were found to have contact angles of 55 ° on PFOTS-treated glass slides in work by Sturgess *et al.*,⁶⁰ larger contact angles than those obtained for 50 wt% inks here (Ink A 45 ° and Ink B 48 °). This may reflect differences between the treated surfaces as-prepared and after routine use: in this work, measurements have been taken with a slide that had been washed and reused to assess the working life of the substrate. Continuous reuse may gradually damage the silane monolayer, leading to deterioration of the substrate's hydrophobicity. This suggests a gradual decrease in the substrate's performance – larger contact angles are associated with higher resolution, although contact angles above 90° may be associated with bulging.¹⁷⁷ Nonetheless, this contact angle was sufficient and the ink formed stable droplets on the surface, indicating that the treated slides have suitable long-term performance.

In summary, glass slides treated with PFOTS were found to be a suitable printing substrate, leading to stable drops and contact angles of 45 ° and 48 ° for Ink A and Ink B. Droplet arrays were then deposited onto PFOTS-treated glass slides and analysed to determine droplet masses and diameters, as well as the mixing ratio of the two inks.

Droplet arrays

Droplet arrays of Ink A (crosslinker) and Ink B (catalyst) were deposited onto PFOTS-treated glass slides at a range of droplet spacings (Figure 41). Contact pinning on the substrate was observed to be insufficient to allow ink to coalesce into a continuous layer at any drop spacing. The coffee ring effect, where solutes are deposited at the edge of a sessile droplet as it dries due to Marangoni flow,³⁵ was not observed; it is known that reducing contact line pinning can eliminate coffee-staining.¹²⁹ 60 μm was the smallest spacing at which droplets did not merge and was used for drop sizing: both inks averaged approximately $890 \pm 25 \mu\text{m}^2$ SD (approx. 33.7 μm diameter) and had masses of 55 ± 1 mg per million drops, showing consistent jetting and similar behaviour to each other. Therefore, the two parts are expected to mix in the ratio the manufacturer intended, and mix ratio calculation is simple; this enables facile control over the molar ratio of silane to vinyl moieties, which could be used to tune the mechanical properties of the printed materials (e.g. the elastic modulus) towards the intended sensing application.⁵⁷

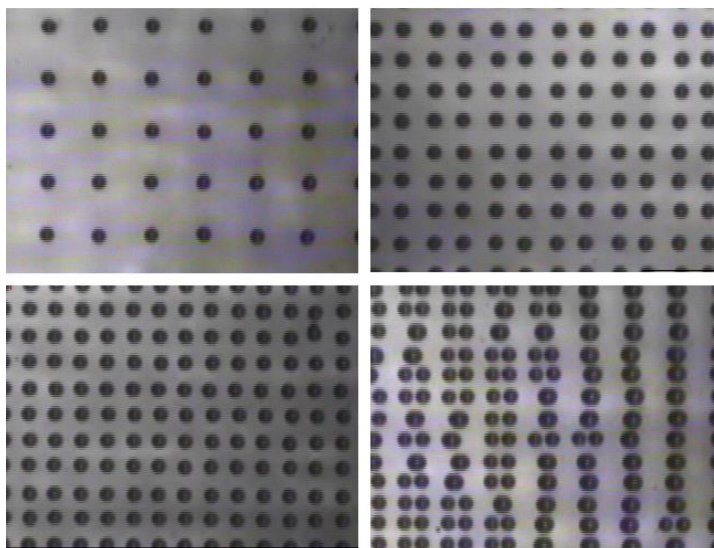


Figure 41: Droplet arrays of Ink A printed with 120, 70, 60 and 50 μm drop spacings, as viewed via fiducial camera. Droplets were ejected at 32 V with waveform W_1 v1 using the Dimatix. Representative of both inks.

At smaller drop spacings ($<60 \mu\text{m}$), continuous, flat layers of ink could not be deposited due to limited pinning to the substrate – the ink had more favourable interaction with itself than with the surface and did not adhere, as has been observed in literature.²²⁵ Instead, the ink coalesced into larger puddles, as seen below in Figure 42, although drop spacings around 30-40 μm did appear able to produce stable lines. Further layers led to increased coalescence, bulging, and curved profile.

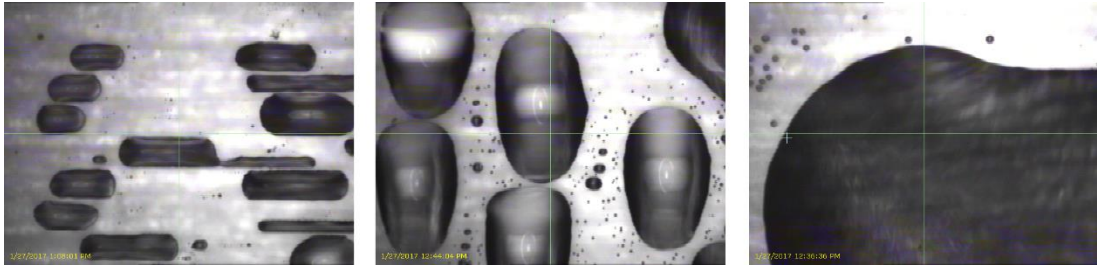


Figure 42: Images of one layer of deposited Ink A as viewed via the fiducial camera of the Dimatix printer. Droplet spacings decrease left-to-right: 30, 15, and 5 μm .

While it was not possible to obtain continuous films due to coalescence, the hemispherical dome shape of individual droplets may be beneficial: in LEDs, dome-shaped structures are used to reduce reflection arising from the mismatch in refractive index (RI) between the emitter and encapsulant, increasing the light extraction efficiency (LEE).^{186,187}

Overall, it was shown that it was possible to deposit dots or arrays of sensing material for the collection of point data. The spatial resolution of sensing would be on the order of 1000-2000 μm^2 (depending on the DoD diameter), orders of magnitude greater than current IJP thermal sensors which have maximum spatial resolutions on the order of tens of mm^2 (see Section 2.1.2). However, to achieve controlled, spatially-constant sensing material thickness (and therefore spatially-constant QD concentration) to enable planar sensing, further work was carried out to investigate the topology and geometries that could be produced in inkjet printing trials.

4.3.3. Single-headed reactive inkjet

Reactive inkjet was carried out using a drop-on-drop (DoD) method, depositing layers of Ink A (crosslinker) followed by layers of Ink B (catalyst). This is henceforth noted as $x\text{A}y\text{B}$, where x layers of Ink A are deposited, followed by x layers of Ink B DoD, followed by y layers of Ink A, followed by y layers of Ink B DoD, and so on. As previously stated, solvent was observed to slow the curing of SiliGlass and therefore $40\text{ }^{\circ}\text{C}$ platen heating was used to accelerate the crosslinking reaction and the solvent evaporation in deposited material.

Contact pinning had been observed to be insufficient to form continuous flat layers of inks, as discussed above; it was possible to deposit dots or assays with a potential spatial resolution of $1000\text{-}2000\text{ }\mu\text{m}^2$ (depending on the DoD diameter), which represents an improvement on existing IJP thermal sensors if it were to be demonstrated with the QD-silicone sensing material (see Section 2.1.2). Work was carried out to investigate the limitations of printing with this limited contact pinning and implications for sensing.

Print trials were carried out to investigate the effect of contact pinning on topography and geometry during reactive inkjet of squares with diameter $>1\text{ mm}$. At larger drop spacings ($\geq 60\text{ }\mu\text{m}$), the inks did not form a continuous shape, instead coalescing into disconnected shapes with rounded contact lines and dome-like topography (the inverse of coffee staining), as shown in Figure 43 (left). Printing with smaller drop spacing ($<60\text{ }\mu\text{m}$) did lead to a continuous shape, with dome-like topography and contact lines which deviated from the square pattern of deposition, showing bulging and curvature (Figure 43, right). While stable line formation was possible, deposition of continuous 2D shapes was limited.

As stated earlier, while domed topology is beneficial for light extraction efficiency in LEDs,^{186,187} this results in material thickness that varies spatially, which is not ideal for nanothermometry or planar imaging as emission intensity is concentration-dependent.¹

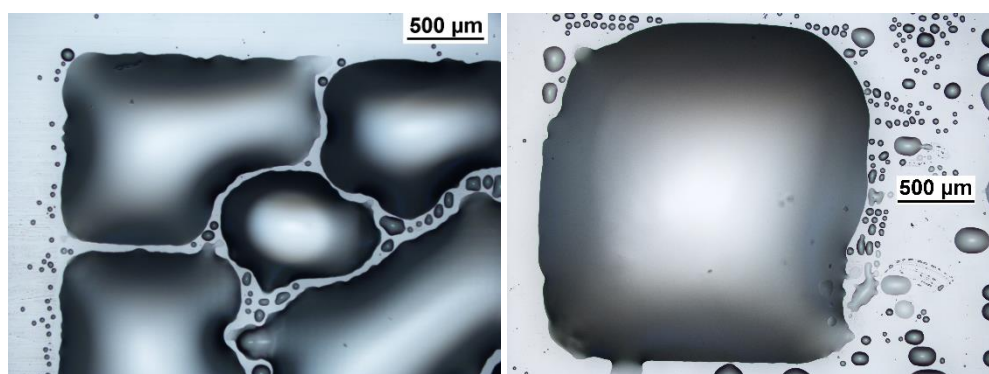


Figure 43: Micrographs of reactive inkjet-printed squares jetted at 32 V with waveform $W_1 v1$ using the Dimatix, demonstrating the effect of poor contact pinning. Left: A square printed at $60\text{ }\mu\text{m}$ spacing with 40A40B layers. Right: A $2\text{ }\mu\text{m}^2$ square printed at $30\text{ }\mu\text{m}$ spacing with 20A20B, showing bulging at edges and round profile.

Substrate microstructuring has been used to tailor contact angle and optimise contact pinning in the literature.^{60,226} Increased surface roughness is associated with higher hydrophilicity and contact pinning: this is known as the Wenzel effect.²²⁷ Therefore, a pinned grid was printed and cured before depositing subsequent layers. To reduce the time spent changing cartridges and recalibrating offset, the grid was printed at 60 μm spacing with 10 layers each of Ink A then Ink B (10A10B), as shown in the scheme in Figure 44. The pinned grid led to continuous films with flatter profile and less bulging than printing without a pinned grid (Figure 43, left), although edges were uneven and undulating where ink flowed to the pinned material; edges may be made more regular if the pinned material coalesces to smaller shapes in the grid, by increasing the droplet spacing or reducing the number of layers deposited. As shown in Figure 45, the surface texture of the printed material was bumpy, with some areas resembling a droplet array or the ‘moth-eye’ anti-reflective patterning used in LEDs,^{186,187} while smoother areas still showed peaks corresponding to the pinned grid. It was expected that the ink would flow to form a flat surface before curing; it appears that the subsequent ink deposited was insufficient to fully flow around and submerge anchor points. While it is beneficial to be able to control the surface roughness of silicone to control surface energy and adhesion in some applications – such as biological applications, where material could be printed with patterning to promote cell adhesion without the need for moulds – microscale surface roughness can reduce the transparency of an optical sensing material.

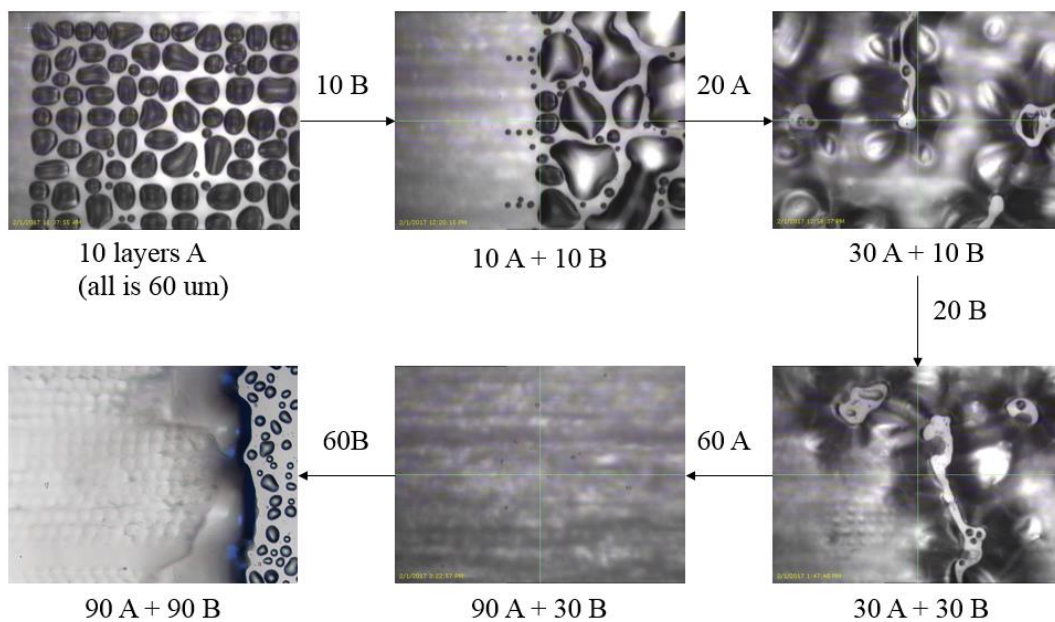


Figure 44: Stepwise printing of a 5 mm² square (consisting of layers 10A10B 20A20B 60A60B) at 32 V with waveform W₁ v1 and 60 μm drop spacing, as viewed in the fiducial camera of the Dimatix.

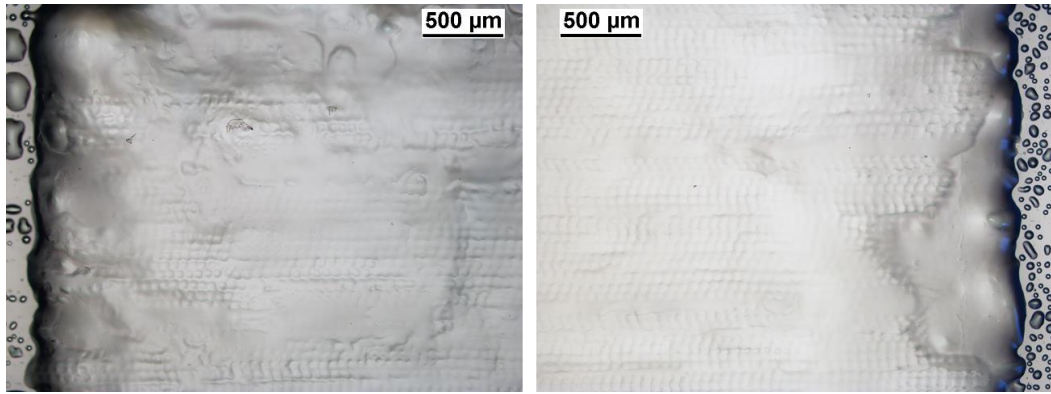


Figure 45: Micrograph of a 5 mm² square (consisting of layers 10A10B 20A20B 60A60B), printed at 32 V with waveform W₁ v1 and 60 μm drop spacing.

A test print was used to assess print quality with more complex, circular shapes, as shown in Figure 46. As cure rate is diffusion rate-limited,²²² sequential alternating layers of 1A1B were trialled to enhance mixing. While it was seen that it was possible to reproduce the geometric shape with >80 % coverage after alternating A and B at the outset, gradual deposition of subsequent material appeared to result in similar morphology to that of using an 10A10B grid: subsequent layers adhered to and increased the size of the anchor points.

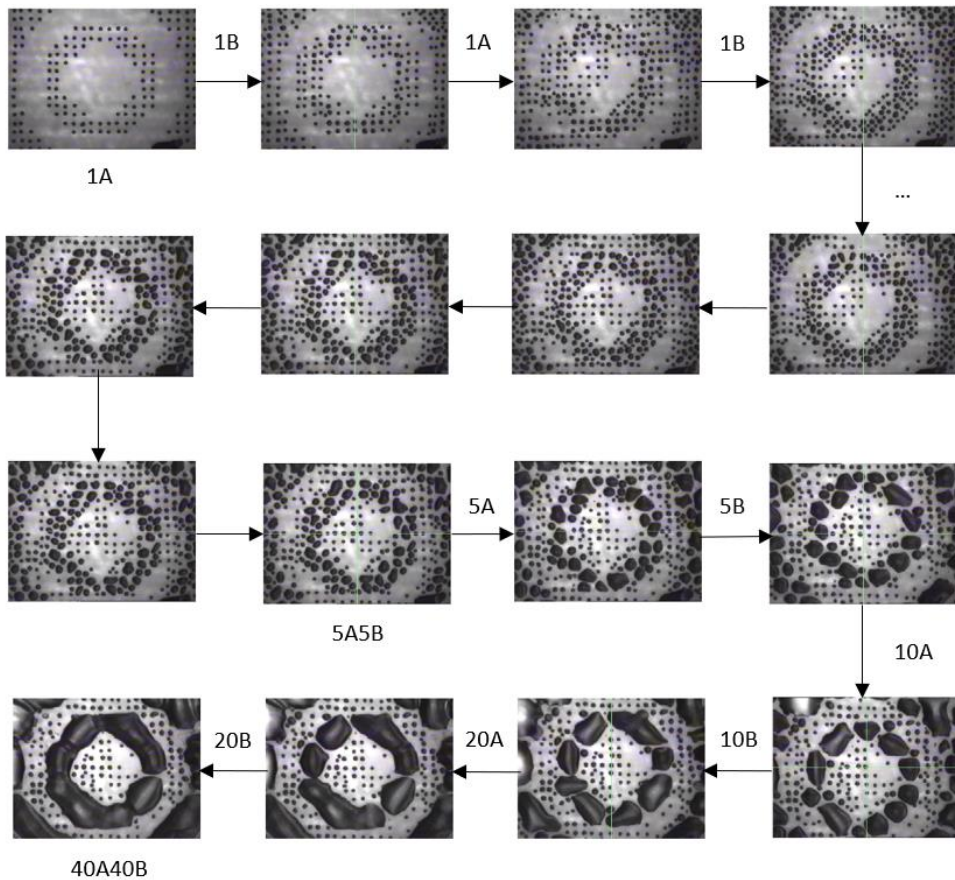


Figure 46: Stepwise printing of test pattern (with 1A1B grid) at 32 V with waveform W₁ v1 and 60 μm drop spacing, as viewed in the fiducial camera of the Dimatix. The print conformed to the pattern despite offsets.

The pinned grid caused rough surface texture, where the ink flowed around anchor points, as seen in Figure 47. While alternating arrays did not appear to have a detrimental impact on geometric accuracy as compared to a 10A10B grid, and can be used to enhance mixing, this suggests that such a strategy is associated with uneven surface texture. As subsequent material flows around the anchor points, the pinned grid can be used to control the morphology and topography of printed materials. While surface roughness in LEDs may be associated with higher REE, this is associated with submicron patterning;^{186,187} microscale surface roughness and microphases can lead to non-uniform scattering and RI, reducing transparency and generating optical aberrations, which would impede optical sensing. Flatter, more even surface textures can be achieved with smaller, sparser anchor points (1A1B grid with larger droplet spacings) and deposition of a greater volume of material at once after the grid cures (more layers of a single ink at a time or smaller droplet spacings) to allow ink to fill in the gaps around, rather than build upon, anchor points—albeit at the cost of reduced mixing of Ink A and Ink B.

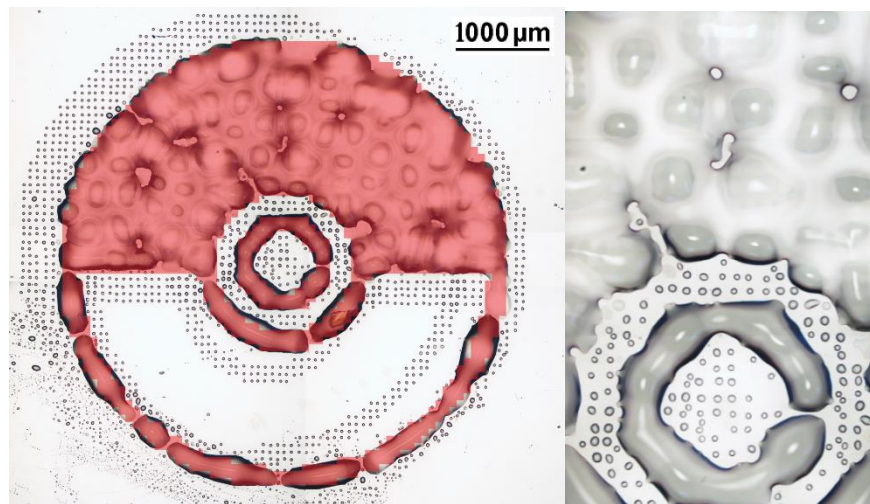


Figure 47: Left: Micrograph of test print with 5x objective, with print bitmap superimposed in red. Right: Closer view of surface texture, taken with 10x objective.

Overall, DoD reactive inkjet was demonstrated for the silicone inks, producing ordered arrays or continuous films with varied surface texture via a pinned grid microstructuring strategy. However, as the Dimatix printer had only one printhead, limited print strategies were possible and the printing process was inefficient as the ink cartridges had to be swapped regularly. Therefore, further print trials were carried out on a dual-headed assembly using line-by-line printing strategies.

4.3.4. Dual-headed reactive inkjet

Dual-headed reactive jetting was carried out on a PiXDRO LP50 that had been modified to be compatible with Dimatix cartridges (see Methodology, Section 3.2.3.3). This assembly allowed near-simultaneous jetting of Ink A (crosslinker) and Ink B (catalyst), which eliminated the need to swap cartridges. This also meant that it was not necessary to print entire layers of each ink at a time: it was possible to print Ink A and Ink B together in a line-by-line strategy,²²⁸ where drop-on-drop deposition was aligned by calibrating the printhead angle. Stable line formation^{229,230} was seen at drop spacings of 40-60 μm , eliminating the need for a pinned grid strategy. 'Reactive layers' are henceforth defined as 1AB, one layer of Ink B deposited DoD on one layer of Ink A.

Print strategy

Initial experiments utilising standard waveforms were carried out as an investigation of different print strategies and to assess need for complex line-by-line strategies. As the print assembly was limited to ≤ 30 V jetting voltage, waveform W₁ v1 could not be used.

The simplest line-by-line print strategy is unidirectional, meaning that Ink A and Ink B are deposited near-simultaneously in the y-direction on the downward pass of the printhead; lines are deposited from left-to-right by default at a defined spacing. A unidirectional, left-to-right line-by-line print strategy was used to print a continuous square, as shown in Figure 48, using 20 reactive layers at 60 μm spacing. Edge definition was improved as compared to pinned grid strategies in that greater linearity was observed, whereas deviations arose where material conformed to anchor points. The bottom and top edges appeared to have a slight waviness; this likely indicates gaps between lines, which would be resolved by a reduction in line spacing. Despite using non-optimised waveforms, the printed films were flatter and had more accurate geometric reproduction of edges than those obtained using a single printhead.

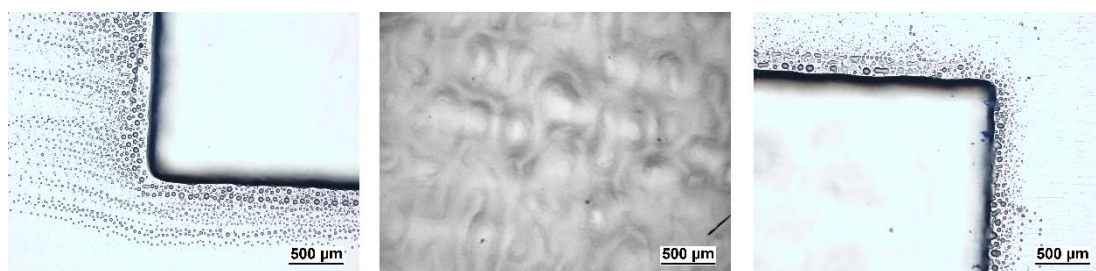


Figure 48: Micrographs of unidirectional line-by-line square, printed as 20AB with 60 μm spacing at 30 V with generic waveform using the PiXDRO. Contrast has been enhanced in the central micrograph.

While the film had much flatter surface texture than films produced with a pinned grid, microphases were observed which resembled gyroidal domains (Figure 48, centre; contrast has been enhanced). It appears that spinodal decomposition or polymerisation-induced phase separation occurs following ink deposition, leading to polymer-rich and solvent-rich domains.^{231,232} Solvents have been used to control polymer porosity arising from such mechanisms.²³³ As microscale variations in composition and refractive index can reduce the optical transparency²³⁴ and lead to inhomogenous material response during optical sensing, future studies to control phase formation are of interest to ensure that any domains present are nanoscale in size to prevent light scattering.

Further line-by-line print strategies are possible: bidirectional printing can be used to increase print speed, as inks are deposited on both the downward and upward passes of the printhead in the y-axis; this requires that the time-of-flight (ToF) of droplets is resolved for alignment. Printing strategies along the x-axis can be used to ensure flat films: as printing lines solely from left-to-right may lead to an excess of material on the left side of the print, alternating between left-to-right and right-to-left deposition can lead to films with more even material distribution. A stepped-line strategy may also be employed to print every other line, and fill in the other set of lines on the next pass along x. The above strategies may be combined in various ways to optimise print strategy.

A bidirectional stepped-line approach with alternating print direction was also run to investigate the effect of various strategies. Overall, this printed line-by-line with deposition on both the upward and downward y-axis pass; although the droplet time of flight had not been optimised for the silicone inks, the drops were aligned when tested with standard settings. Along the x-axis, material was deposited along every other line, left-to-right, and then the skipped lines were printed right-to-left. 30 reactive layers with 40 μm line spacing were printed using this approach; however, as seen in Figure 49 and Figure 50, the ink coalesced into separate round shapes, leading to the uneven texture associated with pinned grids. It is likely that the reaction rate of the silicone inks is incompatible with bidirectional printing under these conditions. As twice the amount of material is deposited in quick succession as compared to unidirectional printing, the ink from the downward pass may not have had time to cure and the additional ink led to line destabilisation. The material then cured to form a pinned grid around which subsequent ink flowed, filling the gaps but leading to bumpy surface texture and discontinuous edges.

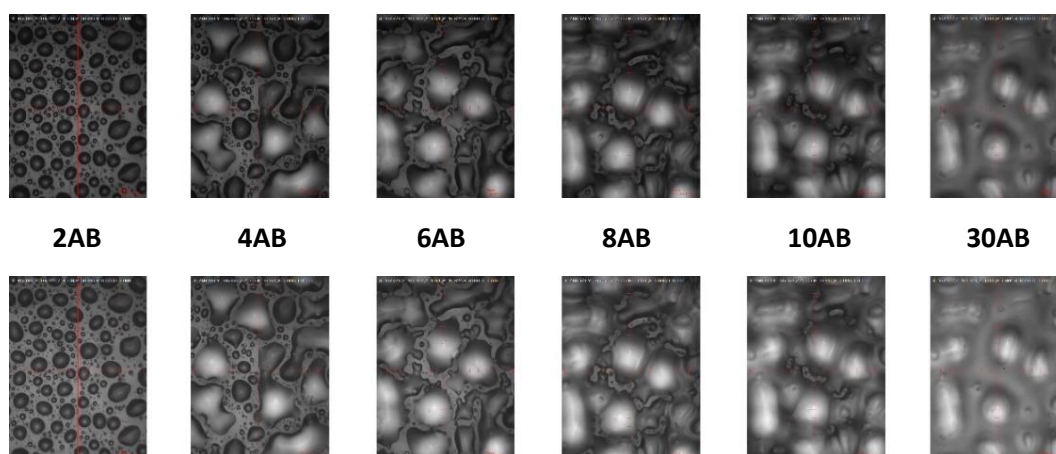


Figure 49: Consecutive runs of bidirectional stepped-line printing with alternating print direction, as viewed via fiducial camera. A 30AB square was printed with $40\ \mu\text{m}$ spacing at 30 V (generic waveform) using the PiXDRO. The bottom row consists of the same images where brightness and contrast have been digitally enhanced.

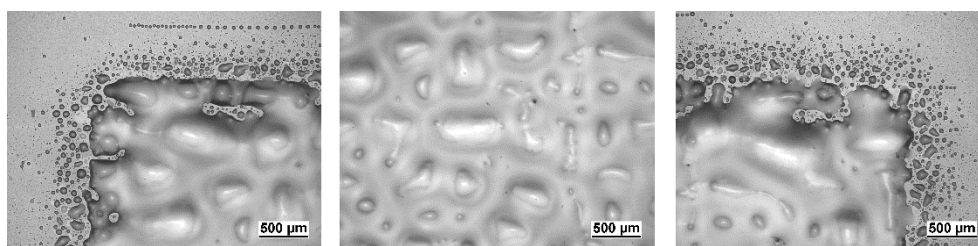


Figure 50: Micrographs of printed square using a bidirectional stepped-line strategy with alternating print direction. From left to right, images show the top-left corner, centre, and top-right corner of the 30AB square printed with $40\ \mu\text{m}$ spacing at 30 V with generic waveform using the PiXDRO.

The use of bidirectional printing to enhance the printing efficiency was not observed to be beneficial at the cure rate of the inks, as lines destabilised to form a pinned grid. While other complex line-by-line strategies could be used which would avoid this issue, the results of this trial suggest that the benefits of developing this print strategy may be limited at this stage of research: the excellent wettability of silicones ($\sim 20.4\ \text{mJ m}^{-2}$)⁵¹, the low ink viscosity ($>15\ \text{mPa s}$), and the curing time indicates that the material is expected to flow and become level. Therefore, as the simple line-by-line strategy was seen to be effective, further optimisation with complex line-by-line print strategies was not prioritised, although the effect of print strategy on QD distribution is of interest for further work.

Waveform optimisation

As the PiXDRO set-up was limited to jetting voltages ≤ 30 V, it was necessary to optimise the waveform for jetting at lower voltage (Waveform W_1 v2, see Figure 139, appendix). This was done on the Dimatix as droplet ejection could not be viewed on the modified PiXDRO.

Reducing the voltage to 28 V led to less consistent jetting than for the previous waveform at 32 V, observed as shaking in the strobe mode of the Drop Watcher. Droplet arrays were printed, imaged and sized: jetting at 28 V led to droplet masses of 49 ± 1 mg/million for both inks. Despite the smaller drop mass compared to W_1 v1 at 32 V, drops were much larger with an average size of $995 \pm 80 \mu\text{m}^2$ SD (Ink A, crosslinker) or $\pm 50 \mu\text{m}^2$ SD (Ink B, catalyst), corresponding to an average diameter of $35.6 \mu\text{m}$; this was larger than expected and indicated an issue with the substrate, which was discarded.

Drop ejection at 30 V (Figure 51) showed no satellites and tails re-joined the head, and the corresponding drop arrays in Figure 52 and Figure 53 were ordered and showed no satellites. Drop masses were 52 ± 1 mg/million for both inks and sessile drops were more uniform in size than was the case at 28 V: Ink A averaged $860 \pm 30 \mu\text{m}^2$ SD while Ink B averaged $840 \pm 32 \mu\text{m}^2$ SD (approx. $33.1 \mu\text{m}$ and $32.7 \mu\text{m}$ diameter, respectively).

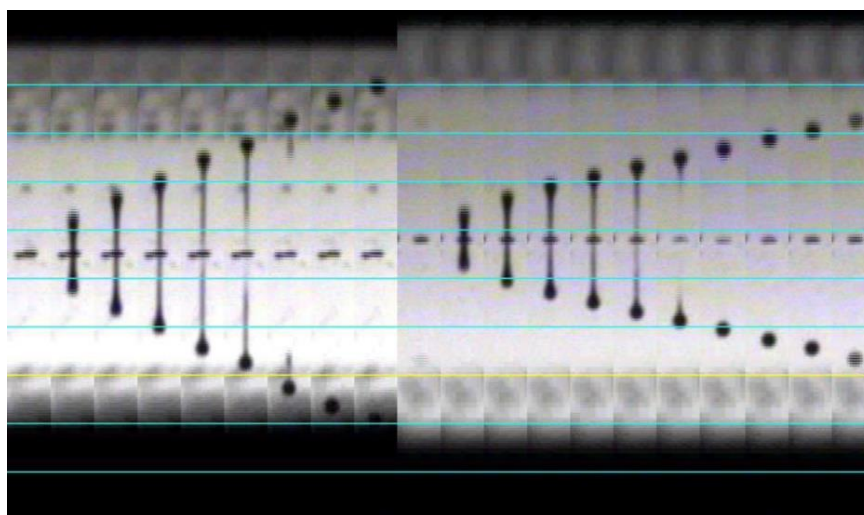


Figure 51: Droplet ejection of Ink A (left) and Ink B (right) at 30 V with waveform W_1 v2 using the Dimatix.

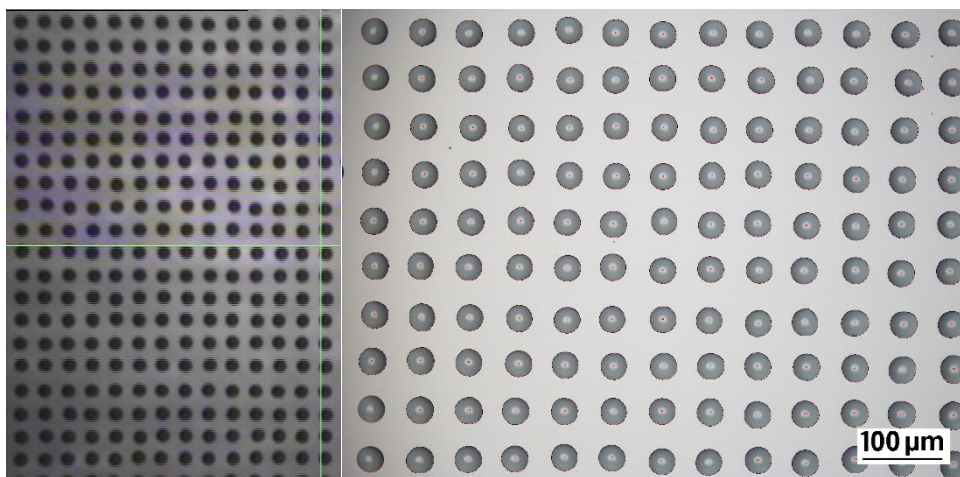


Figure 52: Droplet array of Ink A jetted at 30 V with waveform W_1 v2 using the Dimatix, as viewed via fiducial camera (left) and optical microscope (right). The droplets in the micrograph are circled and labelled for sizing.

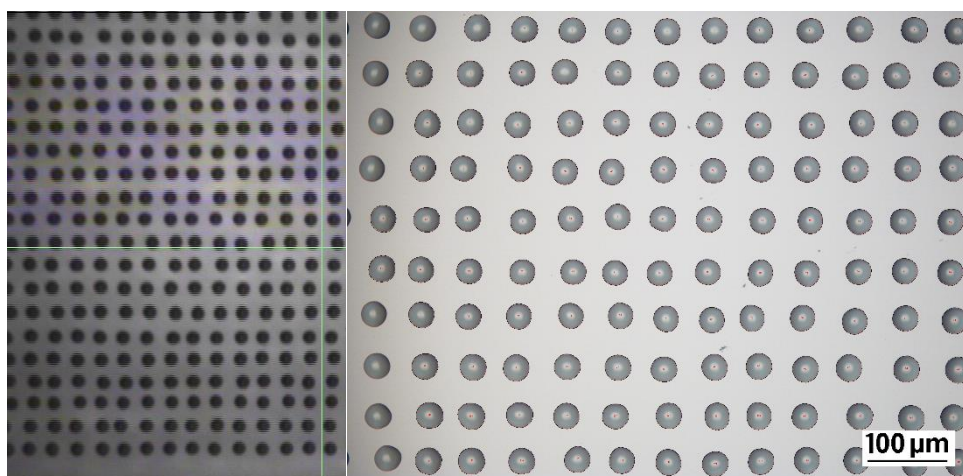


Figure 53: Droplet array of Ink B jetted at 30 V with waveform W_1 v2 using the Dimatix, as viewed via fiducial camera (left) and optical microscope (right). The droplets in the micrograph are circled and labelled for sizing.

Overall, jetting was optimised for a 30 V jetting voltage with an adjusted waveform W_1 v2. Reduced voltages yielded smaller droplets in both diameter and mass, as is typical:¹⁷⁶ average drop diameter decreased from 33.7 μm (W_1 v1 at 32 V) to around 32.9 μm (W_1 v2 at 30 V), with an anomalous value seen for W_1 v2 at 28 V (35.6 μm). Average drop mass decreased by 3 ng for each 2 V drop in jetting voltage (55, 52, and 49 ng for 32, 30, and 28 V). In all cases, both inks had identical drop mass, and so the 1:1 mixing ratio by weight of the SiliGlass formulation was expected to be conserved during drop-on-drop printing and calculations to modify the silane to vinyl ratio were expected to be simple.⁵⁷

Drop arrays were obtained using W_1 v2 at 30 V on the PiXDRO printer, as shown in Figure 54 and Figure 55, and subsequently imaged and analysed. Both Ink A (crosslinker) and Ink B (catalyst) showed the presence of infrequent secondary droplets when viewed via fiducial camera; these had merged into the primary droplets in the micrographs of Ink A. Sessile

droplets of Ink A averaged $1041 \pm 35 \mu\text{m}^2$ SD and Ink B $1015 \pm 25 \mu\text{m}^2$ SD, equivalent to average diameters of $36.4 \mu\text{m}$ and $35.9 \mu\text{m}$ respectively. To compare the area of all material deposited, the area of satellites was factored in and the average area of primary drops recalculated: Ink B averaged $1021 \mu\text{m}^2$ ($36.1 \mu\text{m}$ diameter).

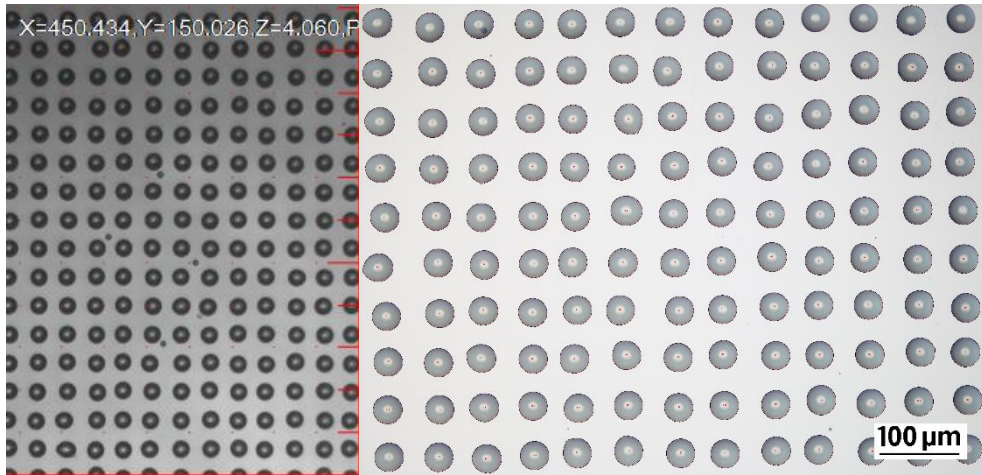


Figure 54: Droplet array of Ink A jetted at 30 V with waveform $W_1 v_2$ using the PiXDRO, as viewed via fiducial camera (left) and optical microscope (right). The droplets in the micrograph are circled and labelled for sizing.

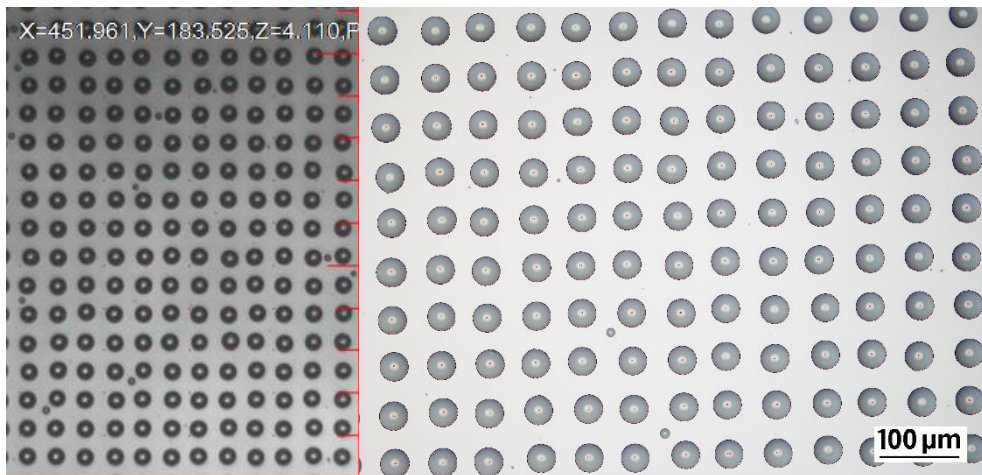


Figure 55: Droplet array of Ink B jetted at 30 V with waveform $W_1 v_2$ using the PiXDRO, as viewed via fiducial camera (left) and optical microscope (right). The droplets in the micrograph are circled and labelled for sizing.

The sessile drop sizes of the two inks were identical within standard deviation and the mixing ratio during printing is therefore expected to be close to 1, assuming that identical drop mass can be inferred from identical drop mass; however, this could not be confirmed as it was not possible to determine drop mass using the PiXDRO. The ink droplets were much larger than seen with printing using the Dimatix, and so potential print resolution was lower; the inability to set the meniscus point using the PiXDRO may have resulted in additional ink coating the nozzle plate, leading to a greater droplet mass. The jetting arrays obtained showed fewer satellite droplets than arrays deposited using a non-optimised PiXDRO waveform; further printing trials were then carried out with the $W_1 v_2$.

Complex test pattern

A complex test pattern was deposited by reactive inkjet using the PiXDRO dual-headed printer with the optimised waveform (W_1 v2 at 30 V): 30 reactive layers were printed using a simple line-by-line print strategy with 45 μm spacing, yielding patterned films as shown below in Figure 56 and Figure 57.

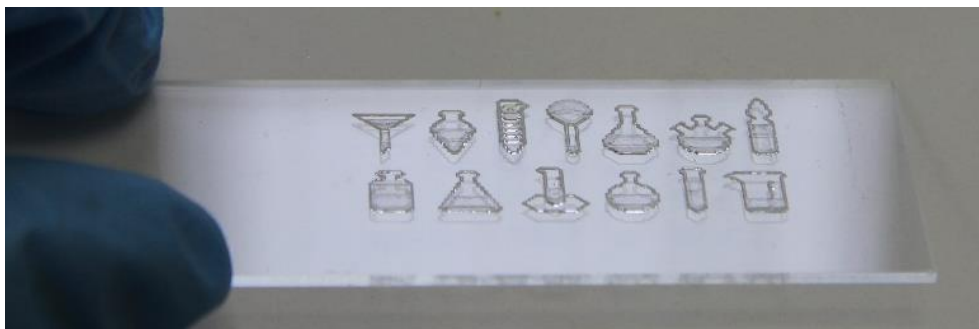


Figure 56: Photographs of a test print on a silanised glass slide. The pattern was printed unidirectionally and line-by-line as 30AB layers with 45 μm spacing at 30 V with waveform W_1 v2 using the PiXDRO.

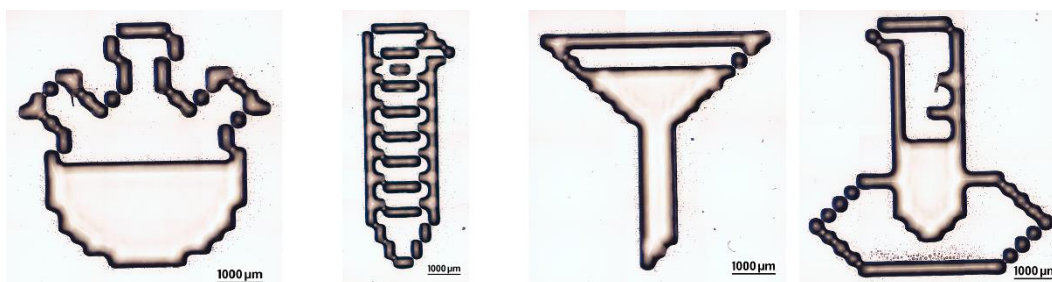


Figure 57: Stitched micrographs of representative elements of the 30AB pattern printed line-by-line with 45 μm spacing at 30 V with waveform W_1 v2 using the PiXDRO.

Convex edges were again observed, as in all printed SiliGlass samples, where inks receded from edges as driven by high initial contact angle ($\geq 45^\circ$) and limited contact pinning.⁶ The patterns printed with waveform W_1 v2 had improved edge definition compared to prints that had used the generic waveform: the top and bottom edges of prints at 60 μm spacing

had shown waviness when using the generic waveform (Figure 48), indicating that the line spacing was too large, whereas printed edges which showed greater linearity when using the optimised waveform $W_1 v_2$ (Figure 57); this indicates that the smaller spacing used ($45 \mu\text{m}$) was more ideal. Drop ejection appears to have been more repeatable using the optimised waveform compared to the generic waveform, as expected, with fewer satellites or 'spitting', although 'spitting' remains evident in places; the modified PiXDRO set-up means that only one nozzle may be used, which can lead to nozzle blockage and spray between cleaning cycles. While line formation was stable enough that the print pattern was reproduced, ink flow is observed in certain locations. Some pixels of the pattern merged together at the corners while others remained separate; this is likely to be deposition creep, which arises from the low surface energy of the inks ($<24 \text{ mN m}^{-1}$) and the weak contact pinning, as had been observed during rheological characterisation of the inks. This merging could be eliminated through the use of a stepped-line print strategy, as lines would have more time to cure before neighbouring lines were deposited.

Overall, print trials with the PiXDRO were able to yield flatter films with fewer optical aberrations than the Dimatix via a simple line-by-line print strategy, although convex edges and gyroidal microstructure were observed. QD-inks were then formulated so that print trials could be carried out with QD-silicone composites.

4.3.5. Summary of SiliGlass printing

Overall, reactive inkjet of addition cure silicones was carried out, fulfilling objective O2. IJP of 50 wt% octyl acetate-based inks with ambient nozzle temperature was carried out, inspired by the methodology in Sturgess *et al.*⁶⁰ Sessile DSA was carried out to characterise a suitably low-energy substrate for silicone printing; glass slides were coated with PFOTS to yield contact angles of 45 ° and 48 ° for Ink A (crosslinker) and Ink B (catalyst), respectively. It was not possible to deposit a uniform film as inks were poorly pinned to the surface, which necessitated specific print strategies.

Although alternative solvents were suggested (Section 4.2.1), they were not trialled as octyl acetate performed well: octyl acetate was not associated with nozzle blockages during printing, due to its low volatility, nor with a coffee ring effect, due to poor pinning and sufficient cure rate on the hydrophobic substrate,³⁵ meaning that a co-solvent was not required to suppress ring formation.^{81,82} However, octyl acetate did necessitate the use of LCP print cartridges due to incompatibility with polypropylene, which then poisoned the platinum catalyst;¹⁷ indeed, all solvents in Table 10 are incompatible with polypropylene.

The 2-part inks required no specialised storage conditions and nozzles did not become blocked, needing only a purge cycle to clear after a period of disuse, in agreement with Sturgess *et al.*⁶⁰ This is likely a result of the low surface energy of the inks (<24 mN m⁻¹, compared to the ideal 28-33 mN m⁻¹ for the Dimatix printer¹⁷⁵), for which the meniscus set point was set to the highest setting to prevent ink leakage from the nozzles and a blotting cleaning cycle was used to clear ink from the nozzle plate. In contrast, 1-part addition cure inks in literature have a worklife of ≤48 hours.⁶¹⁻⁶⁴ Waveform W₁ v1 was optimised from the Dimatix Model Fluid waveform, eliminating satellite droplets, which at 32 V yielded an average drop diameter of 33.7 μm and an average drop mass of 55 ng for both inks. Identical drop mass ensured that the intended 1:1 mixing ratio of SiliGlass was preserved.

Printing was demonstrated for the single-headed Dimatix printer using a pinned grid strategy, where substrate microstructuring was used to overcome issues with poor pinning^{226,227} - a 1A1B grid was deposited and cured to serve as anchor points for subsequent layers. Continuous patterns could be reproduced but the surface topography of prints was uneven where ink flowed around the anchor points of the pinned grid; Sturgess *et al.* reported that the grid remained visible in optical microscopy of thin films printed using a similar approach,⁶⁰ which could reduce the transparency of optical sensing materials.

Alterations were made to waveform W_1 v1 to enable reliable jetting at lower voltages for compatibility with the modified PiXDRO set-up. Waveform W_1 v2 at 30 V yielded an average drop diameter of approximately 33 μm and an average drop mass of 52 ng for both inks on the Dimatix, but an average diameter of approximately 36 μm on the PiXDRO; this is likely due to an inability to set the meniscus level when using the PiXDRO, leading to additional ink flow from nozzles and some satellite drops.

Printing was demonstrated on the dual-headed PiXDRO printer using a line-by-line strategy. As it was possible to form stable lines at 40-60 μm drop spacing, and Ink A and Ink B could be deposited DoD near-simultaneously, the lines could cure and retain their shape to enable printed patterns; this led to flatter film profile and straighter edges in prints, which could enable sensing material films with greater transparency.

While the centre of printed films was flatter, convex edges were observed where inks receded from edges, in line with earlier observations of observation creep; a margin should be left when taking concentration-dependent measurements of the sensing material, to ensure that the material thickness is consistent. The 'spitting' from nozzles may also be detrimental for printed device as this can contaminate other parts; however, as this was not observed when printing with the Dimatix printer, it is likely that this would be rectified in a dual-headed printer for which multi-nozzle jetting and meniscus control was possible. Lastly, while the line-by-line was advantageous in avoiding the need for microstructuring, the microphases observed in printed material similarly reduce the material homogeneity and transparency, which can reduce the accuracy and efficiency of optical sensing. The simple line-by-line printing strategy was an improvement over the pinned grid strategy, but it is of interest to investigate ways to control the microphase for future work.

Overall, it was demonstrated that dual-headed printing with line-by-line deposition was the best suited towards controlled deposition of QD-silicone temperature-sensing films. Printing was optimised for inks jetting at ambient nozzle temperature to reduce thermal cycling of nanoparticles in inks. These printing optimisation experiments led into formulation and printing of novel QD-silicone inks.

4.4. QD-ink formulation

This section reports the experiments carried out to formulate jettable composite inks (Objective O3). Quantum dots were loaded into Ink A; initial work with QD-Ink B found that curing was hindered when the catalyst and QDs were mixed. Work was carried out to find a suitable QD loading for satisfactory fluorescence, rheology, and dispersion stability.

In this section:

- The minimum loading for visible fluorescence and the detection limit for microscopy were determined
- The Einstein equation was used to predict the change in viscosity associated with particle loading, and therefore any changes in printability
- DLS was used to assess QD dispersion in octyl acetate as compared to hexane, a typical apolar solvent used in QD colloidal dispersions.

4.4.1. Minimum loading

To produce a material suitable for optical sensing, it was vital to determine whether a composite with suitable properties could be synthesised and to gain an understanding of the effect of the matrix on the fluorescence. The emission peak of the QDs as-received was listed as 630 nm with a full width at half maximum (FWHM) of 25 nm; the absorption and photoluminescence (PL) spectra given by the manufacturer are shown below in Figure 58.

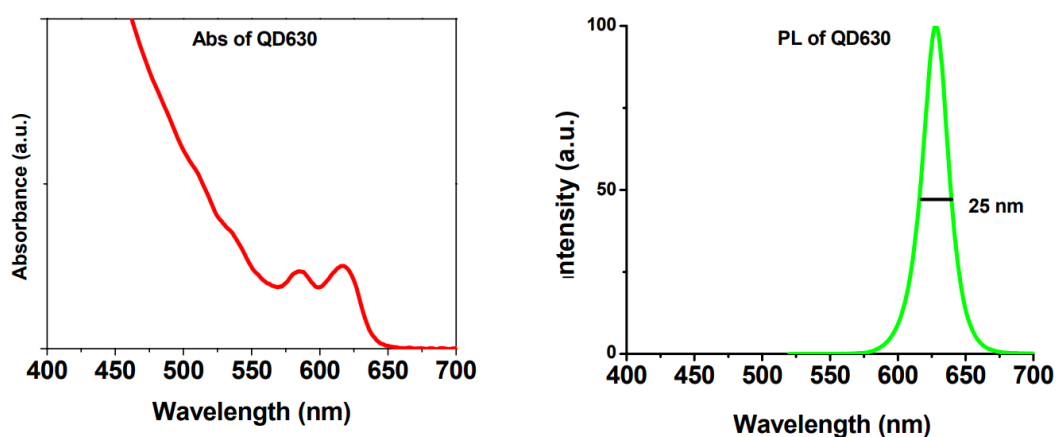


Figure 58: Absorbance (left) and photoluminescence (right) spectra of CdSe/ZnS quantum dots with 630 nm emission peak. Sourced from manufacturer Ocean Nanotech.²³⁵

In order to study the QD-silicone composite material and to assess the loading required for visible fluorescence, samples were prepared in vials by mixing 0.2 mL of Ink A of different QD loadings (QD-Ink A) with 0.2 mL of Ink B (see Section 3.2.4.1). Henceforth, addition cure

composites are listed with the weight percent of QDs in the QD-ink used to make them, which is equivalent to the weight percent of QDs to silicone matrix in the cured composites when disregarding residual solvent. Cure rate was retarded by higher QD loadings – samples made with 0.02 wt% QD-Ink A failed to cure at all, even at 70 °C – but all cured monoliths appeared transparent and fluorescence was visible and stable down to 0.0001 wt% QD-Ink A, albeit difficult to see with the naked eye, while 0.001 wt% QD-Ink A yielded composites with obvious fluorescence.

To determine the minimum QD loading that could be spectroscopically discriminated within the reactive inks, a detection limit experiment was carried out by preparing a series of QD-silicone composite inks across a range of QD concentrations (from 0.01-0.0001 wt% QD loading) (see Section 3.2.4.1). A well-plate was prepared PL point spectra were taken from the centre of each well to ascertain whether emission peaks could be detected. It was not possible to prepare cured samples in the well-plate due to solvent incompatibility with the polypropylene material which led to catalyst poisoning.

As shown in Figure 59, emission peaks were observed at 627.5, 627.2, and 626.9 nm for 0.01, 0.001, and 0.0001 wt% QD-Ink A respectively with FWHMs of approximately 21.5, 20.8, and 22.5 nm. No significant shift in the position or width of the emission peak ($\lambda_{\text{emission}} = 628 \text{ nm}$, FWHM = 22 nm) was observed with decreasing QD concentration, with intensity scaling in a near-linear fashion with QD concentration (within experimental error), to an apparent lower threshold of 0.0001 wt% below which QD emission could not be observed.

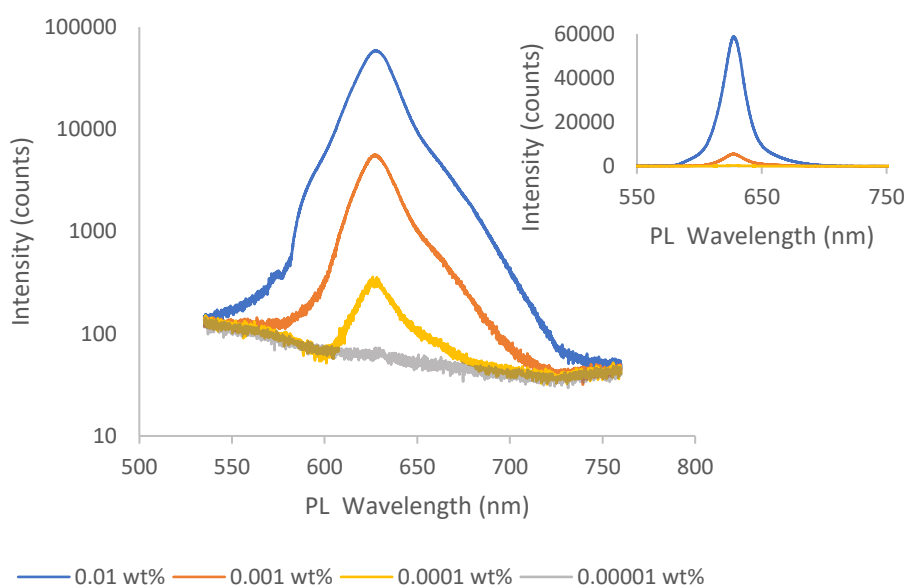


Figure 59: Detection limit experiment for serially-diluted quantum dots in addition cure silicone. Emission spectra with PL intensity on a logarithmic scale. Inset: Emission spectra with PL intensity on a linear scale.

The QD emission peak was blue-shifted from 630 nm to approximately 627 nm upon dispersion in the silicone ink as compared to the manufacturer's specifications. Both blue- and red-shift may be observed following immobilisation in a polymer matrix;¹⁵¹ the emission peak is sensitive to the QD surface environment and a shift is often seen upon solvent or ligand exchange.^{236,237}

While literature has reported that decreases in intensity increase at greater dilution, as labile stabilising ligands – particularly primary amines, which enhance PL in CdSe QDs^{236–238} – are also diluted and exchange with the solvent²³⁶, this was not observed. Blue-shift upon dilution is also observed in literature, attributed to decreased rates of Förster resonance energy transfer (FRET) and photon reabsorption as interparticle distances increase;^{239,240} blue-shift was minimal in this data, and may not be significant given experimental error.

As a trade-off was observed for QD loading between signal strength and polymer matrix curing in drop casting experiments, 0.005 wt% QD-Ink A was chosen as an initial target loading as it resulted in visible fluorescence and was not seen to significantly impede cure. Viscosity prediction was then carried out to assess whether the chosen loading would be detrimental to ink printability.

4.4.2. Viscosity prediction

Loading particles into inks may be associated with increased viscosity, which alters jettability, so it was important to determine whether the quantum dots in Ink A would be detrimental to printing at the chosen loading. While empirical measurement of QD-ink rheology was possible using the Kinexus rotational rheometer, the sample size required (~1-2 mL) made this option unattractive as the QDs were high-value components and toxic, the latter of which made it difficult to isolate and decontaminate the rheometer safely. Instead, the effect of quantum dots on viscosity was estimated using the Einstein equation (Equation 4, reproduced below), where μ_r is relative viscosity and ϕ is the volume fraction of hard sphere particles.

$$\mu_r = 1 + 2.5\phi$$

The Einstein equation is used for loadings under 1 vol%; the 0.005 wt% QD loading that had been selected based on detection limit experiments was within this limit. Henceforth, QD-Ink A refers to a loading of 0.005 wt% QDs in Ink A, and 0.005 wt% QD composite refers to composite synthesised with QD-Ink A.

QD properties are shown in Table 15, where mass is calculated using the density of wurtzite crystal structures. Using these values, the predicted relative viscosity for 0.005 wt% QDs in Ink A was found to be 1.00003, meaning that the addition of 0.005 wt% QDs would have no effect on printability.

Table 15: QD parameters, as determined from the manufacturer's specifications and crystallography data for wurtzite CdSe and ZnS.

<i>CdSe core diameter</i> nm	<i>ZnS shell thickness</i> nm	<i>Volume of a single QD</i> cm ³	<i>Estimated mass of a single QD</i> g
5.5	2	4.489 x 10 ⁻¹⁹	1.946 x 10 ⁻¹⁸

Stabilising ligands have not been considered here as it is difficult to ascertain surface coverage and therefore mass per quantum dot, and as the Einstein equation applies to hard sphere particles. This means that the mass of ligands is not accounted for, which gives an inflated volume of hard spheres. While a lower volume of hard spheres is implied by the Einstein equation to lead to a smaller change in viscosity and therefore be non-problematic for jetting of Ink A, it is also possible that this ligand sphere does make a significant contribution to viscosity which is not accounted for by this limited model.

Relative viscosity in the case of a much higher loading (0.5 wt%) has been calculated below in Table 16, to demonstrate that there is a wide error margin within which the jetting performance of inks is predicted to be unaffected. Given that even 0.5 wt% loading is predicted to increase viscosity by just 0.27% – which is insufficient to change the printability index – this margin is likely sufficient for any limitations of the model.

Table 16: Calculation of relative viscosity for 0.5 wt% QDs in 1 g of Ink A.

Mass of silicone solution in QD ink g	Density of silicone solution g cm ⁻³	Volume of silicone solution in QD ink cm ³	Volume percent of QDs in ink vol%	Relative viscosity μ_r
0.995	0.92 (± 0.01)	1.083	0.107	1.0027

Other researchers have utilised this equation for quantum dots in polymer: Elliot *et al.*¹⁸ applied the Einstein equation for inkjet of 0.5 wt% TOPO-capped CdSe quantum dots in photopolymer. The predicted viscosity increase was 0.23% and the experimental was lower than this at 0.15%. However, octadecylamine ligands have a longer chain length than TOPO ligands and may penetrate further into the surrounding medium. In one specific case in the literature, octadecylamine ligands on carbon nanotubes led to an intrinsic viscosity 40 times higher than any models investigated.²⁴¹ Regardless, even extreme examples are insufficient to change the printability index at the low loading of interest for 0.005 wt% QD-Ink A.

Overall, the quantum dots are predicted to have negligible effect on printability at this loading, even after considering extreme cases, and 0.005 wt% QD-Ink A was expected to have no issues with printability in terms of rheology. However, the tendency for aggregation needed to be assessed to ensure that nozzle blockage did not occur and to predict the size of aggregates in the sensing material, as aggregation is associated with scattering and red-shift.

4.4.3. Solvent assessment

It had been shown that 0.005 wt% QD-Ink A was expected to have suitable fluorescence and viscosity for sensing inks. However, initial jetting trials saw nozzle blockage arising from QDs settling out of the solution phase. Therefore, dynamic light scattering (DLS) was carried out to assess the suitability of the solvent.

Octyl acetate had been selected for its low vapour pressure and was therefore not expected to be susceptible to nozzle blockage. However, it was more polar than other typical solvents used in QD colloidal suspensions: toluene, for example, has a dipole moment of 0.375 D^{213} and a dielectric constant of $2.38 \epsilon_r$ (25 °C),^{212–214} although chloroform is an exception with a polarity of 1.04 D^{213} and dielectric constant $4.81 \epsilon_r$ (20 °C),²¹² values which are comparable to octyl acetate (1.84 D^{217} and $4.13 \epsilon_r$ (20 °C)²¹⁸). As it was thought that the solvent may have sub-optimal polarity which results in QD precipitation, DLS was chosen to compare octyl acetate to a typical ‘ideal’ solvent for quantum dots. DLS measures wet dispersions *in situ* and collects size data for agglomerates in solution, which allows for an understanding of the performance of the solvent.

A solvent was selected to represent a typical solvent for QD colloidal dispersions; while toluene was used in the alternate ink formulation, it is a strong scatterer and was not feasible for this study. Chloroform was considered but was observed to be a poorer solvent than octyl acetate for these QDs, as evidenced by the QDs settling out of solution over the course of a few days. Hexane was then selected as comparative solvent; as hexane is apolar, there was a contrast in polarity between the two solvents.

Data collection was complicated by the fact that the Malvern Zetasizer Nano-ZS uses a HeNe laser (633 nm) which is close to the QD emission peak (630 nm) – even with a small Stokes shift, the quantum dots may absorb the light and fluoresce strongly. QD fluorescence is a noted problem: an application note from Malvern describes a case-study where 655 nm emitting QDs could not be measured without a narrow band filter,²⁴² but it is not possible to filter out the laser without also excluding fluorescence at 630 nm.

Another potential factor in data collection is that, while DLS measurements require refractive indices (RI) of particles, the refractive indices of QDs are complex. However, measurements of small particles are less susceptible to refractive index values and intensity distribution is “always correct” as long as data quality is adequate, regardless of the refractive index.²⁴³ If fluorescence during DLS measurement was observed as noise in the baseline, the data may have been rendered unusable. Nonetheless, data from preliminary experiments passed the quality check of the software and appeared to be suitable for comparative studies.

Octyl acetate

A representative correlogram and size distribution obtained for 0.005 wt% QDs in octyl acetate are shown below in Figure 60. The correlogram showed a smooth sigmoidal curve which passed the software quality checks. The onset of decrease correlates to the intensity-weighted Z-average diameter, while the angle of this decrease correlates to the polydispersity index (see dotted line). The average value for the samples was 118.3 nm with a polydispersity index (PDI) of 0.137.

In the context of DLS, PDI values range from 0 to 1, where values less than 0.05 are considered highly monodisperse and values above 0.7 have a broader size distribution than is recommended for analysis using DLS.²⁴⁴ A PDI of 0.137 is low and indicates that the sample is moderately monodisperse, and the baseline was flat and showed no sedimentation or large aggregates. The graph of size distribution by intensity showed a single peak at approximately 138 nm with a standard deviation (SD) of around 56 nm.

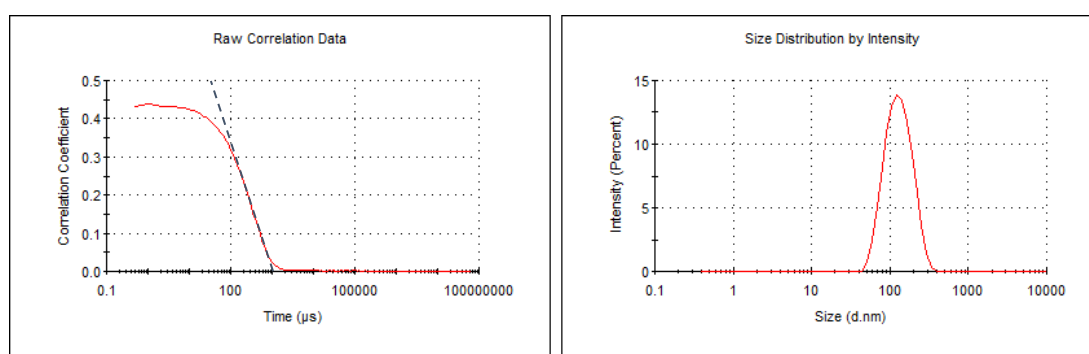


Figure 60: Representative measurement of 0.005 wt% QDs in octyl acetate at 20 °C. Left: Raw correlation data. Right: Size distribution by intensity.

Average diameters for 0.005 wt% QD solution in octyl acetate are summarised below in Table 17. The data showed clusters with a Z-average diameter of 118.3 nm, which corresponds to a cluster of 1931 QDs. This value is slightly smaller than the average diameter by intensity, which was 138.4 nm. In perfectly monodisperse samples, these values are equal; in practice, the cumulant is fit to the initial decay of the correlation function and has a small bias towards signal from smaller particles. Therefore, a smaller Z-average than peak average strongly implies the absence of large aggregates outside the measured size range, as supported by the flat baseline.

Only one peak was present in the size distribution by intensity, which is useful in identifying any aggregates as the signal strength is biased towards large particles,²⁴⁵ implying a lack of larger aggregates. Average diameter by volume has a smaller bias towards large particles but was very similar in value at 131.9 nm.²⁴⁵ The similarity between all values for average diameter confirmed the absence of smaller or larger species outside of the single peak seen in the size distribution, and that QDs exist in solution as clusters without single particles.

Table 17: Average diameters obtained from DLS of 0.005 wt% QDs in octyl acetate at 20 °C.

<i>Sample</i>	<i>Z-average diameter nm</i>	<i>PDI</i>	<i>Average diameter by intensity nm</i>	<i>SD nm</i>	<i>Average diameter by volume nm</i>
1	116.7	0.142	136.2	53.46	128.2
2	119.3	0.134	139.6	56.41	133.4
3	118.8	0.136	139.3	58.65	134.1
<i>Average</i>	<i>118.3</i>	<i>0.137</i>	<i>138.4</i>	<i>56.17</i>	<i>131.9</i>
<i>SD</i>	<i>1.380</i>		<i>1.882</i>		<i>3.223</i>

Hexane

A representative correlogram and size distribution obtained for 0.005 wt% QDs in hexane are shown below in Figure 61. The data quality appeared poorer than that of the octyl acetate solution: the correlogram showed discontinuities in the correlation curve, with greater fluctuations at smaller diameters. The data did pass quality checks, although the distribution was broader than for the octyl acetate solvent with a larger PDI (0.635). Values of PDI higher than 0.7 are considered to be polydisperse and unsuitable for DLS; this sample was within, but approached, this limit.²⁴⁴ The shallow decrease after the main decay is indicative of large particles, as seen in the graph of size distribution by intensity, but the baseline was flat and showed no sedimentation or large aggregates.

The graph of size distribution by intensity showed multiple peaks corresponding to approximate average diameters of 0.95, 41, and 1366 nm; the peak list is given below in Table 19. As the diameter of a single QD is 9.5 nm, the 0.95 nm peak is anomalous; this is typically a solvent or buffer peak and arises from additives.²⁴⁶ This is problematic as it was a strong peak, despite intensity favouring signal from larger particles. The larger diameter peaks were broad and overlapping, with standard deviations of around 30 and 1153 nm.

The discontinuities in the correlation curve were likely due to number fluctuations- DLS requires a consistent number of particles in the scattering volume for reliable results.²⁴⁷ Number fluctuations may arise from large particles, dust, or from low sample concentration and may be resolved by methods such as filtration, sonication, raising the sample concentration, centrifugation, and allowing time for large particles to sediment; however, a raised baseline was not observed, nor was noise reduction seen across consecutive runs.

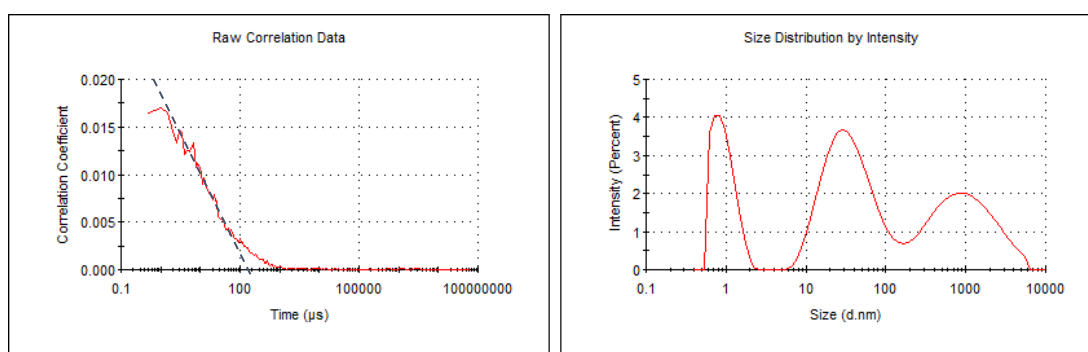


Figure 61: Representative measurement of 0.005 wt% QDs in hexane at 20 °C. Left: Raw correlation data. Right: Size distribution by intensity.

Average diameters obtained for 0.005 wt% QD solution in hexane are summarised below in Table 18. The data showed QD clusters with a Z-average diameter of 46.15 nm, which corresponds to a cluster of 115 QDs. This value was slightly larger than the average diameter by intensity of the central peak, as shown in the peak table below in Table 19, which was 40.53 nm. The overall average diameter based on the three intensity peaks is an order of magnitude larger at 432.6 nm, likely due to the bias towards larger particles with diameter by intensity.²⁴⁵

Table 18: Average diameters obtained from DLS of 0.005 wt% QDs in hexane at 20 °C.

<i>Sample</i>	<i>Z-average diameter nm</i>	<i>PDI</i>	<i>Average diameter by intensity nm</i>	<i>Average diameter by volume nm</i>
1	47.61	0.635	429.2	0.8037
2	48.52	0.650	402.9	0.7879
3	45.01	0.621	465.3	0.8147
<i>Average</i>	<i>46.15</i>	<i>0.635</i>	<i>432.5</i>	<i>0.8021</i>
<i>SD</i>	<i>1.330</i>	<i>0.0145</i>	<i>31.33</i>	<i>0.01347</i>

As stated previously, size by intensity has a strong bias towards larger particles which aids in identifying aggregates. When discounting the largest peak, the diameter is closer to the Z-average – albeit lower – at 25.93 nm. Size by volume has a lesser bias towards larger particles²⁴⁵ and the multiple peaks seen in the size distribution by intensity resolved into a single peak when distributed by volume, as shown in Table 18, corresponding to an average diameter of 0.8021 nm. However, the signal for <10 nm particles is anomalous as the diameter of a single QD is 9.5 nm; if this signal were excluded, a value close to or below the Z-average is expected.

Table 19: Peak list of size distribution by intensity for 0.005 wt% QDs in hexane at 20 °C.

<i>Peak</i>	<i>Sample</i>	<i>Average peak Int nm</i>	<i>Peak area int %</i>	<i>SD nm</i>
1	1	0.9605	22.6	0.3040
	2	0.9215	25.6	0.2663
	3	0.9787	28.3	0.3117
	<i>Average</i>	<i>0.9536</i>	<i>25.5</i>	<i>0.2940</i>
	<i>SD</i>	<i>0.02922</i>	<i>2.85</i>	
2	1	42.05	44.9	32.08
	2	33.30	39.3	23.76
	3	46.24	45.9	34.63
	<i>Average</i>	<i>40.53</i>	<i>43.4</i>	<i>30.16</i>
	<i>SD</i>	<i>6.603</i>	<i>3.56</i>	
3	1	1262	32.5	1111
	2	1110	35.1	1046
	3	1727	25.7	1301
	<i>Average</i>	<i>1366</i>	<i>31.1</i>	<i>1153</i>
	<i>SD</i>	<i>321.5</i>	<i>4.85</i>	

The data quality for QDs in hexane was questionable and the values obtained for diameter cannot be considered reliable. The issues with data collection are discussed below.

The correlogram of hexane showed number fluctuations, consistent with large particles or dilute samples.²⁴⁷ Samples were sonicated for 20 minutes prior to measurement and allowed 5-10 minutes to settle as required, which may still have been insufficient to prevent large aggregates or to allow potential contaminants such as dust time to settle. The presence of dust typically leads to weak peaks for large particles; this typically does not affect the Z-average diameter, and the back-scatter configuration that the Nano ZS uses further minimises the effect.²⁴⁷ While dust may be responsible for the micron-scale peak, this does not explain the erroneously small particle diameters seen.

A strong peak corresponding to an erroneously small particle diameter was seen, which is likely a solvent or buffer peak. In dilute samples, signal from additives may be seen and fluctuations in count rate add noise to the correlogram.²⁴⁶ It is possible that the QD ligands interfere during measurement, although it is unclear why number fluctuation was a significant problem for hexane but not octyl acetate. While it is possible that the hexane dispersion formed large aggregates rapidly, releasing ligands and lowering the concentration of free particles in comparison to the octyl acetate dispersion, large particles have a lower concentration limit for measurement as the intensity signal is much larger.

In summary, the data from the hexane is unreliable despite passing software quality checks. In contrast, the data quality of the octyl acetate-based dispersion was better and showed monodisperse particles with an average diameter of ~118 nm. The requirement for inkjet is that the largest particles must be no larger than 5% of the nozzle diameter,³⁴ which is 1.1 μm for the Dimatix print cartridge. Quantum dots in octyl acetate are within this limit, as long as adequate sonication is used to prevent QDs settling out of solution.

4.4.4. Summary of QD-inks

Reactive inks were formulated that cured to yield fluorescent bulk polymer nanocomposites, satisfying Objective O3. It was found that loadings as low as 0.0001 wt% QDs in Ink A yielded detectable fluorescence: the resulting fluorescence was visible to the naked eye for cured composites and detectable by microscopy of mixed inks. The QD emission peak was blue-shifted from 630 nm to approximately 627 nm upon dispersion in the silicone ink and ten-fold dilution was associated with lower intensity counts, resulting from fewer emitters, and to a lesser extent ligand depletion and decreased rates of photon reabsorption.^{236,239,240} The PL spectra were similar to the manufacturer's data: symmetrical peaks with narrow FWHMs (<25 nm). However, hindered curing was observed with increasing QD loading, as associated with platinum catalyst poisoning in literature.^{132,146,248}

0.005 wt% QD was chosen as a suitable ink formulation for signal strength and visibility under a UV lamp, for ease of monitoring and photography of printed composites. Henceforth, QD-Ink A refers to 0.005 wt% QD in Ink A.

The Einstein equation was used to estimate the change in viscosity associated with the selected QD loading for 0.005 wt% QD-Ink A and the predicted relative viscosity was 1.00003 μ_r . This calculation did not take stabilising ligands into account; however in work by Elliot *et al.*,¹⁸ the Einstein equation was found to overestimate the relative viscosity of 0.5 wt% TOPO-capped CdSe quantum dots in photopolymer. Higher intrinsic viscosity has been associated with octyldecylamine-capped carbon nanotubes,²⁴¹ but the quantum dots are predicted to have negligible effect on printability at this loading, even after considering extreme cases. 0.005 wt% QD-Ink A was not expected to present a rheological challenge.

DLS was carried out to assess the QD dispersion in the solvent as inks were observed to settle out of solution over time and block nozzles when jetted. Octyl acetate was compared to hexane, as an 'ideal' solvent for QD dispersion; however, the data quality for hexane was poor. Particles were monodisperse in octyl acetate with z-average diameter 118.3 nm and a polydispersity index (PDI) of 0.137; average diameters by intensity and volume were similar at 138.4 nm and 131.9 nm and no evidence of large aggregates was seen.

Octyl acetate was shown to be a suitable solvent, in which QDs form submicron clusters when adequate sonication is employed. This satisfies the requirement for inkjet: that the largest particles must be no larger than 5% of the nozzle diameter.³⁴ Adequate sonication must be used to prevent QDs settling out of solution; care needs to be taken that cartridges are loaded immediately before printing and that QDs do not settle during set-up.

Aggregation of QDs has implications for the performance of a sensing material: aggregation is associated with red-shift, leading to photon reabsorption and/or Förster resonance energy transfer (FRET) from smaller QDs to larger QDs.^{239,240} The rate of FRET increases with increasing particle size distribution and decreasing average inter-particle distance.²⁴⁹ Furthermore, adjacent QDs may also form larger particles via mechanisms such as thermal annealing,¹²² which may reduce the longterm stability of the sensing material.

In summary, reactive inks were formulated that cured to yield fluorescent bulk polymer nanocomposites, presenting the first QD-silicone composite inks and the synthesis of a new QD-silicone bulk composite (Objective O3). The inks were calculated to have suitable rheology for jetting and shown to have satisfactory fluorescence and QD dispersion. The next stage was to carry out printing trials to print fluorescent nanocomposites, as detailed in the next section.

4.5. Printing of QD-composites

This section describes the printing of fluorescent composites as well as the work carried out to enable this (Objective O4). In the previous section, jettable inks were formulated and it was noted that the presence of quantum dots slowed curing of the silicone matrix. This proved to be a challenge: jetting of QD-Ink A was then demonstrated during early print trials, but inks did not cure. Work was carried out to resolve issues with curing before printing.

In this section:

- Cure was characterised via drop casting experiments and FTIR and Raman spectroscopy
- Ink B was formulated with additional PtCl₂ catalyst to produce printable inks
- Printing was demonstrated using a single printhead printer, producing the first inkjet-printed QD-silicone composite.

4.5.1. Cure rate

It had been observed that higher quantum dot loading was associated with poorer curing in reactive inks (Section 4.4.1). During print trials following QD-Ink A formulation, it became evident that the reactive inks did not cure at 40 °C with 0.005 wt% QD-Ink A.

It was theorised that the QDs were poisoning the platinum catalyst and preventing addition curing; when inks were mixed without sufficient heating in vials, curing did not reach completion even if heating was applied later. Review of the literature found reports of platinum catalyst poisoning by labile amine ligands on the QD surface.^{132,146,248} It is probable that the octadecylamine ligands poison the platinum catalyst despite the low QD loading.

Drop casting

Work was carried out to assess whether print parameters or quantum dot loading could be changed to achieve suitable cure rates, or whether a change in formulation was necessary.

Drop casting experiments were carried out with varying QD loadings at 60 °C, as described in Chapter 3 (Section 3.2.5.1), mixing QD-loaded Ink A (crosslinker) with Ink B (catalyst). 60 °C was selected as the highest feasible substrate temperature as this is the maximum platen temperature of the Dimatix⁵⁹ - although alternate heating stages could be used - and

QD quenching is minimised. While core-shell CdSe-based QDs are known to have fully-reversible quenching up to 100 °C when immobilised in a polymer matrix, solution-phase QDs can lose capping ligands and are therefore vulnerable to irreversible generation of surface defects;¹⁶⁰ therefore, lower curing temperatures may be beneficial to help ensure that QDs are well-passivated and dispersed within the matrix to maximise their stability to thermal annealing.¹²² Ink A was prepared with 0.005 wt%, 0.001 wt%, or 0.0005 wt% QD loadings, which were selected to be within the detection limit (Figure 59).

The 0.005 wt% QD sample partially cured in 15 minutes: one section of the drop cured, while other areas remained uncured as the catalyst did not appear to have diffused. It took 40 minutes for all of the material to solidify. This observation was noted again in later drop casting experiments; tests were rerun when this occurred. It may be that samples with higher QD loading and lower catalyst concentration are more sensitive to the alignment of drop deposition, where catalyst complexes become poisoned during diffusion. The 0.001 wt% QD sample was almost fully cured in 15 minutes apart from a small patch in the centre of the droplet, and the 0.0005 wt% QD sample fully cured in 15 minutes. The fluorescence of all the samples was visible and stable throughout curing.

While it was clear that increasing the QD loading retarded the cure rate - or the overall cure quality or degree of conversion (DoC), as the cure time appeared to converge on 15 minutes - these cure times may not be indicative of cure times seen during inkjet. The cure rate is reliant on diffusion for the mixing of the two inks²²² and these simulated droplets have a volume of 20 µL, compared to the 50 nL that is expected during jetting. For these reasons, curing is expected to reach completion much faster during inkjet under the same conditions.

Ink A (crosslinker) and Ink B (catalyst) without QDs or additional catalyst were tested as a control and benchmark as they were known to cure at a rate suitable for printing. The control cured within 11 minutes; none of the QD-containing inks cured as quickly. It was evident that lower QD loading and higher substrate temperature alone were not sufficient to achieve the cure time of the unadulterated silicone inks. A change in formulation would be required to enable both reliable, controlled cure and strong emission signal.

Many strategies exist for controlling the QD surface environment – which are also beneficial for QD dispersion - such as ligand exchange, encapsulation, and alternate QD syntheses. These are discussed in Appendices - QD dispersion in polymer matrices, but often require time-consuming procedures. Increasing the amount of catalyst in the formulation was trialled as a simple, accessible route to QD-composite curing.

Increased catalytic loading is associated with longterm yellowing,^{181,192} even at low temperature (≤ 50 °C with 12 months accelerated aging),¹⁸¹ due to the formation of metallic nanoclusters during thermal aging or by photo-induced radical generation.⁴⁶ Discoloration reduces optical and UV transparency and accelerates further photodegradation, which is detrimental to optical sensing materials. Therefore, formulation should use the minimum amount of catalyst required for cure. The extent of yellowing is also affected by the molar ratio of silane to vinyl moieties and the chain mobility within the elastomer, which determine the type of metallic cluster and the rate of formation: while equimolar or excess silane is associated with Pt clusters and grey-brown discoloration, excess vinyl is observed to lead to Si-Pt and C-Pt clusters with darker brown discoloration.¹⁹² The high crosslink density and 1.68-fold molar excess of silane in SiliGlass may reduce discoloration; it may also be possible to lessen the impact of yellowing on sensing by using a SiliGlass sample without QDs to calibrate the QD-silicone composite. Further work could investigate the use of tetrakis (dimethylsiloxy) silane (TDS) crosslinking agent to minimise yellowing for a sensing range between 0-70 °C.¹⁸¹

PtCl₂ was selected as a simple and relatively cheap catalyst, suitable for a first trial to investigate the ideal amount of platinum to add, the achievable cure rate and degree of conversion, and the resultant material properties. Catalyst selection could be further optimised towards this application in future material development.

Minimum additional catalyst experiments were carried out using the drop-casting method above. Ink A contained 0.005 wt% QDs (hereafter referred to as 'QD-Ink A', as previously stated). Ink B was formulated with 0.005, 0.0025, 0.00125, and 0.00075 wt% loadings of PtCl₂ (hereafter called 'Pt-Ink B' and listed with the PtCl₂ wt%; an 'X wt% PtCl₂ composite' refers to the weight percent of PtCl₂ in the cured composite, assuming complete solvent evaporation such that it matches the loading of Pt-Ink B used to synthesise it, as has been described similarly for QD-Ink A). Controls were run with unadulterated Ink A and Ink B, and their toluene-based analogues (60 wt% SiliGlass in toluene).

Curing became slower and less repeatable as additional catalyst loading decreased. At higher PtCl₂ loadings, a decrease of 0.00125 wt% PtCl₂ was associated with 1 minute additional cure time: samples prepared from 0.005 wt% PtCl₂ Ink B cured within 4 minutes, 0.0025 wt% PtCl₂ within 6 minutes, and 0.00125 wt% PtCl₂ typically cured in 7 minutes. At lower loadings, curing was less consistent and frequently inhomogeneous, as described above; these were discounted and another slide prepared. 0.00075 wt% PtCl₂ cured within 9 minutes when it did cure homogeneously, and 0.0005 wt% PtCl₂ cured in 10.5 minutes on average, excluding an anomalous run which took 15 minutes.

All of the above inks prepared with additional catalyst met or exceeded the cure time of the control inks. However, cure behaviour was less reliable at lower concentrations of PtCl₂. In particular, samples prepared from 0.0005 wt% PtCl₂ Ink B had been seen to cure as slowly as samples prepared without added catalyst did and to frequently fail to cure uniformly; therefore, this catalyst loading was not used in further experiments.

Drop casting experiments were also carried out on control inks to compare octyl acetate-based inks to the toluene-based analogues (Section 4.2.3 above). The toluene analogues cured faster – within 7 minutes – which was expected due to toluene's higher volatility and the higher polymer loading of the inks (60 wt% SiliGlass). However, the toluene analogues had less reliable curing and frequently only one area of the drop cured. As stated above, this too is likely due to the diffusion rate-limited nature of curing:²²² inks solidified rapidly where the two inks had mixed, after which the catalyst was not able to diffuse to outer areas. This is less likely to be an issue during printing due to the numerous small drops involved. Overall, choice of solvent was shown to be a factor in cure rate.

Composites were produced in glass vials using different loadings of additional catalyst and compared. Samples appeared similar in transparency and colour, but upon excitation with UV light it became apparent that emission intensity differed. Increased platinum concentration was associated with reduced emission intensity, as shown below in Figure 62. Therefore, it was desirable to use the minimum amount of additional catalyst in order to control curing and preserve emission intensity.

Drop casting experiments assessed the suitability of different formulations based on cure rate quickly but with limited accuracy and in limited detail. Subsequently, spectroscopic methods were carried out to obtain quantitative data on conversion.

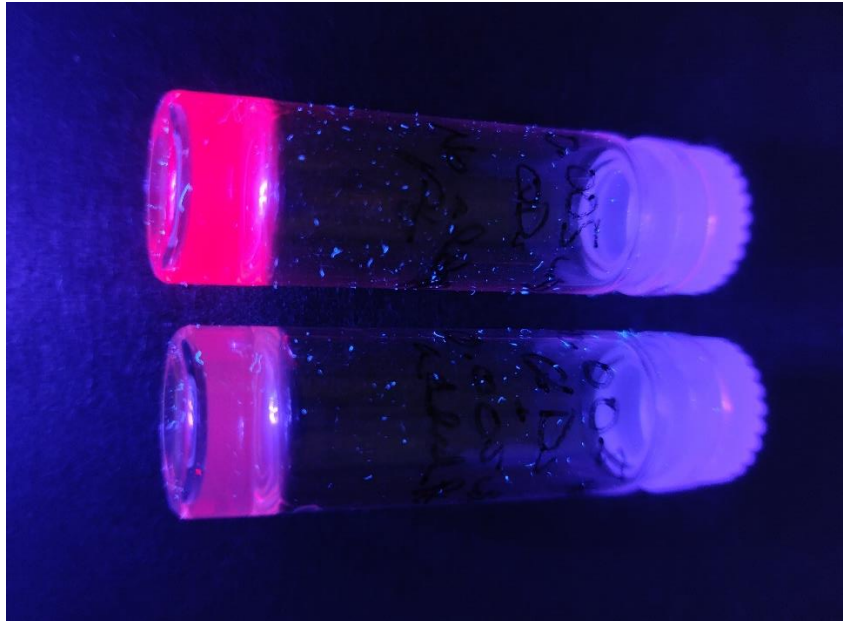


Figure 62: Photograph of 0.005 wt% QD composites excited by a UV lamp. The top sample has no additional platinum catalyst, whereas the bottom was synthesised with 0.005 wt% Pt-Ink B.

Spectroscopy

Spectroscopic methods were carried out using characteristic peaks of silicones.²⁰⁰ The peak of interest corresponds to the Si-H stretching mode around 2150 cm^{-1} , which is depleted as the silicone crosslinks via a Pt-catalysed reaction, and was monitored to assess extent of reaction. The carbonyl peak around 1740 cm^{-1} corresponds to the solvent (octyl acetate). FTIR data did not have a peak suitable for normalisation: the strong IR peak around 770 cm^{-1} present only in the silicones, assigned as a bending mode in the polymer backbone, was unideal as part of the changeable fingerprint region. For Raman spectroscopy, data was normalised to the Si-O-Si vibration at approximately 490 cm^{-1} .

Both data collected as a function of time and from fully cured samples were of interest to investigate cure rate and overall degree of conversion, respectively. In inkjet, the initial cure rate is important in ensuring that deposited layers will solidify quickly enough to hold their shape. Overall conversion determines the mechanical properties of the end product, as well as the amount of residual reactive groups which may undergo further reaction post-process.⁵⁷

Heat was required for composite curing; unfortunately, the equipment available was not capable of *in situ* heating. FTIR spectroscopy was employed for measurements as a function of time because the small sample volume, high sensitivity and ease of loading made sampling feasible. Raman spectroscopy was used to obtain degree of conversion as data could be normalised: characteristic modes of the silicone polymer were located in the so-called fingerprint region of the FTIR spectrum as discussed above, whereas this presents no issue in Raman spectroscopy.

A pilot study for time-dependant FTIR spectroscopy was carried out by mixing either control inks or QD-Ink A and Pt-Ink B (with varied PtCl_2 loadings) in pans at $60\text{ }^\circ\text{C}$ and sampling $1\text{ }\mu\text{L}$ at 3-minute intervals. While it was shown that FTIR spectroscopy is feasible for monitoring the Si-H stretching mode as a function of time in these samples, the data obtained during the pilot study proved difficult to normalise and could not be analysed. Experiments were time-consuming and, while FTIR spectroscopy could indeed be utilised in future works if data collection were further optimised to maximise the number of scans, this was not time-feasible in this project.

Raman spectroscopy was used to investigate degree of conversion (DoC) in fully-cured composite samples. Figure 63 shows the Raman spectrum of the cured inks as normalised to the Si-O-Si stretch around 490 cm^{-1} , and the inset shows the peak at centred at 2150 cm^{-1} corresponding to the Si-H stretching mode. The Si-H peak intensity decreased as reaction proceeded: the normalised intensity was 0.012, 0.0066, 0.0065, and 0.0091 for the control inks and 0.00125, 0.0025, and 0.005 wt% Pt-Ink B with QD-Ink A, respectively. The control inks had the most residual silane, approximately twice that of moderate PtCl_2 loadings (0.00125 or 0.0025 wt% PtCl_2).

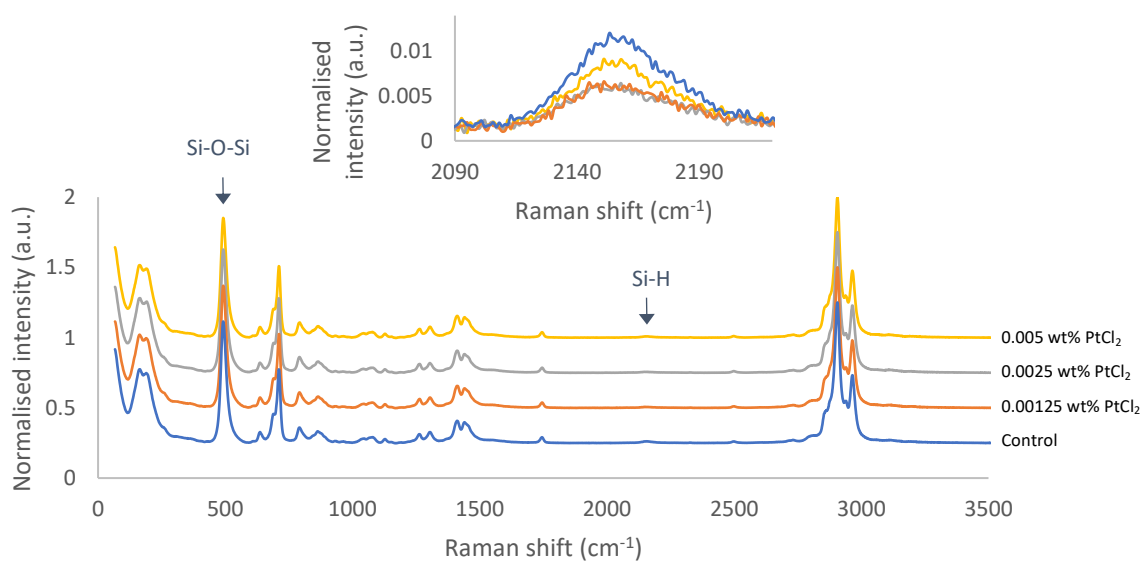


Figure 63: Mean Raman spectra of the cured inks ($N=10$); inset shows the Si-H stretching vibration centred at 2150 cm^{-1} . The blue line corresponds to the control sample, which does not contain QDs or PtCl_2 . Other samples contain QD-Ink A and Pt-Ink B: orange, grey, and yellow lines show data for 0.00125 wt%, 0.0025 wt%, and 0.005 wt% PtCl_2 . Spectra have been normalised to the intensity of the Si-O-Si mode at 490 cm^{-1} and offset on the y-axis for visual clarity.

Samples were prepared using an identical, short heat treatment (see Chapter 3, Section 3.2.5.1); 0.00075 and 0 wt% Pt-Ink B samples did not cure. Upon review, this method did not allow much heat conduction, and so the cure rate was too slow at lower catalyst loadings for samples to solidify before complete catalyst poisoning, under these conditions. Lower catalyst samples had otherwise been shown to be able to cure with sufficient heating, due to the faster reaction rate associated with increased thermal energy and increased rate of solvent evaporation.

The intensity ratio between the Si-H (2150 cm^{-1}) and Si-O-Si peaks (490 cm^{-1}) was used to calculate relative DoC, as shown below in Table 20. Values are relative to cured, undiluted SiliGlass A and B as a reference value, *i.e.* the expected silane depletion as formulated.

Table 20: Peak positions and intensities for Si-H and Si-O-Si modes obtained from cured samples.

<i>Sample</i>	<i>Si-H peak position</i> <i>cm⁻¹</i>	<i>Si-H peak intensity</i>	<i>Si-O-Si peak position</i> <i>cm⁻¹</i>	<i>Si-O-Si peak intensity</i>	<i>Intensity ratio</i>	<i>DoC %</i>
SiliGlass A + SiliGlass B Undiluted	2157.1 (±3.4 SD)	18904.6	491.9 (±0 SD)	643342.0	0.029 (±0.001 SD)	0 (ref)
Ink A + Ink B 50 wt% octyl acetate	2156.3 (±2.8 SD)	9185.1	491.9 (±0 SD)	503068.0	0.018 (±0.002 SD)	38
0.005 wt% QD-Ink A + 0.00125 wt% Pt-Ink B	2154.6 (±5.6 SD)	4815.0	492.2 (±0.7 SD)	520240.2	0.009 (±0.001 SD)	69
0.005 wt% QD-Ink A + 0.0025 wt% Pt-Ink B	2152.7 (±7.4 SD)	4638.3	492.1 (±0.5 SD)	531164.2	0.009 (±0.001 SD)	70
0.005 wt% QD-Ink A + 0.005 wt% Pt-Ink B	2154.5 (±4.9 SD)	7626.0	492.2 (±0.7 SD)	513275.6	0.015 (±0.001 SD)	49

The relative degree of conversion was 38, 69, 70, and 49 % for the control inks and for 0.00125, 0.0025, and 0.005 wt% Pt-Ink B mixed with QD-Ink A, respectively. Addition of solvent increased DoC relative to undiluted SiliGlass in all cases. This result was somewhat counter-intuitive to observations where solvent appeared to lengthen curing times; it is probable that the decrease in viscosity promotes mixing, which is beneficial to the overall conversion as the curing is diffusion rate-limited.²²²

QD-silicones had higher conversions than the control inks in all cases due to their higher catalyst loadings, despite the presence of quantum dots, in agreement with earlier drop casting experiments where it had been observed that these formulations cure faster than the control inks. Higher concentration of catalyst corresponds to a greater number of reaction centres, so that diffusion of species for crosslinking catalysis need to cover shorter distances on average. However, the DoC did not increase with increasing catalyst loading: DoC in the 0.005 wt% PtCl₂ sample was 20 % less than the value obtained for 0.00125 and

0.0025 wt% PtCl₂, corresponding to a 30% decrease in conversion. This inverse relationship implies that sufficiently high platinum concentration retarded conversion.

PL maps were obtained for the samples containing quantum dots, as shown below in Figure 64. PL intensity dropped with increasing platinum loading, as had previously been observed in samples prepared in glass vials (see Figure 62 above). At 626 nm emission, there were average intensity counts of 1650, 500, and 145 for composites made using 0.00125, 0.0025, and 0.005 wt% Pt-Ink B, respectively, which corresponds to a 70% decrease in emission intensity as PtCl₂ concentration doubles.

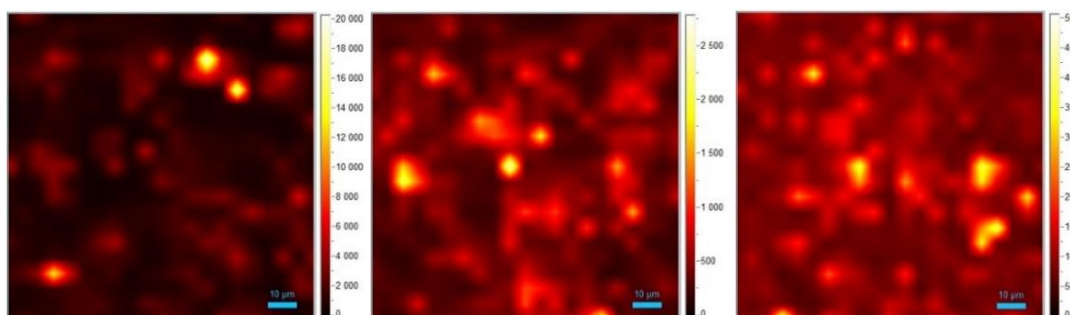


Figure 64: PL maps of 0.005 wt% QD-silicone composites synthesised with additional platinum catalyst in Ink B. From left to right: samples made using 0.00125, 0.0025, and 0.005 wt% Pt-Ink B. The intensity scale corresponds to the intensity of the emission maximum (in counts).

It is well-known that metal ions can impact the fluorescence of quantum dots; this behaviour has been exploited for optical sensing.²⁵⁰ There are four main interaction pathways that lead to quenching, all of which would also be associated with catalyst poisoning.

Firstly, metal chalcogenide QDs can undergo cation-exchange, generating surface defects.²⁵⁰ While ligand density has significant influence on these reactions, the ligands are not removed from the QD following metal displacement. Shifts are observed in absorption or PL wavelengths, due to the difference in bandgap of the substituted metal chalcogenide, along with peak broadening. The precise mechanism depends on composition; In CdTe QDs with Ag⁺ ions, silver has been observed to occupy surface vacancies and displace cadmium, which is driven by the higher solubility product value of Ag₂Te in aqueous media.²⁵¹ In contrast, for the case of CdSe QDs with Cu²⁺ ions, copper solely fills cadmium vacancies; the decrease in emission intensity plateaus as the QD surface becomes saturated.²⁵²

Secondly, metal ions may compete for ligands when they have higher affinity than the QD surface. This detaches the ligands from the QD surface, exposing surface traps.²⁵⁰ In the case of amine ligands on CdSe-based QDs, this also removes the PL enhancement from

primary amines.^{236–238} As ligand competition does not alter the chemical composition of the QD core, the PL and absorption wavelengths do not change, excepting any red-shift arising from the QD aggregation upon ligand removal. This is also known as metal-induced agglomeration.²⁵³

Thirdly, surface adsorbed metal can undergo reduction, particularly in the case of copper: Cu^{2+} is reduced by S^{2-} vacancies, which leads to quenching and a strong red-shift in emission wavelength.²⁵⁰ Lastly, metal ion attack on the core is impeded in QDs with a high surface density of ligands. Instead, metal ions can adsorb to the ligand shell by coordination or electrostatic forces, and quenching occurs where there is electron transfer from the QD conduction band to the metal ion.²⁵⁰ The Pearson theory of coordination can be used to predict interactions, *i.e.* soft acids like Pt^{2+} prefer to bind to nitrogen donor atoms and coordination is pH-dependent.

In practice, metal-induced quenching processes are complex and multiple pathways may be present; conclusions may not be drawn without further investigation. Platinum complexes are not likely to coordinate to the alkyl tails of the ligand shell, much preferring to complex with the amine head groups, so quenching via electron transfer is unlikely. As quenching was not seen to plateau, a cation-exchange mechanism where Pt^{2+} solely fills vacancies in the QD may be unlikely, although cation-exchange with displacement of cadmium and/or zinc may be feasible. X-ray Photoelectron Spectroscopy (XPS) of composites would determine whether such changes in QD elemental composition took place, and further PL spectroscopy of composites would identify emission peak shift and broadening that could elucidate the quenching mechanism.

However, as octadecylamine ligands on CdSe/ZnS QDs are known to be labile and amine groups are known to bind strongly to and poison platinum catalysts,^{132,146,248} ligand competition is likely the principal mechanism. Platinum has high affinity for nitrogen donor atoms and can complex with labile ligands and strip them from the QD surface, leading to aggregation. This also leaves the QD surface exposed and vulnerable to alternate quenching pathways. Reduced emission intensity would result from exposed surface defects, inter-particle reabsorption,^{239,240} and loss of the PL enhancement from the primary amine ligands.^{236–238} We propose that this metal-induced agglomeration leads to the decrease in conversion at higher catalyst loadings: as QDs aggregate, the stabilising ligands are lost from the joined QD surfaces. This results in more free ligands to poison catalysts, resulting in lower DoC. This would explain the time-dependent curing behaviour: increased

catalytic loading accelerates the initial cure rate, which is halted as ligands are rapidly liberated.

In summary, it was demonstrated using drop casting experiments that print parameters and lower QD loadings alone were not sufficient to enable printing, via comparison with control inks (Ink A and Ink B) as a benchmark. Instead, additional platinum catalyst was used to account for catalyst that was poisoned by ligands. More rapid crosslinking was observed with higher platinum loading; loadings as low as 0.00075 wt% Pt-Ink B were sufficient to produce 0.005 wt% QD composites with cure rate comparable to the benchmark. However, additional platinum catalyst was associated with lower QD emission intensity; this was corroborated by intensity mapping during microscopy, where a 70% decrease in emission intensity was observed as PtCl₂ concentration doubles.

Spectroscopic methods were used to investigate cure rate and degree of conversion by monitoring depletion of the Si-H mode at approximately 2150 cm⁻¹. FTIR spectroscopy was shown to be viable for measurements as a function of time, but challenges in normalisation of data meant that this was not time-feasible during this research project. Degree of conversion was obtained from Raman spectra, and addition of solvent led to higher conversion than seen in undiluted SiliGlass; the lower viscosity is thought to have aided mixing. Increased loadings of platinum catalyst resulted in higher conversion than for the control inks as the increased number of reaction centres had shorter distances to migrate on average. However, DoC was reduced at the highest catalyst loading, corresponding to a 30% decrease in conversion from moderate catalyst loadings. Metals are known to quench QD fluorescence through several pathways, including metal-induced agglomeration;^{250,253} the observed reductions in PL and DoC may be rationalised as higher concentrations of platinum inducing greater aggregation of QDs and thus greater liberation of surfactants.

Inks with optimised curing and fluorescence were obtained, showing that printing of fluorescent composites was possible. Print trials were subsequently carried out to demonstrate reactive inkjet of QD-silicone composites.

4.5.2. Single-headed reactive inkjet

Print trials of QD-silicone composites were conducted using a Fujifilm Dimatix printer (DMP-2830) and a pinned grid strategy as in Section 4.3.3 above, as the dual-headed set-up was not available. A platen temperature of 60 °C was used to maximise cure rate, which led to heat transfer to the nozzles. The nozzle temperature was then set to 35 °C, the lowest stable temperature; the inks remained jettable at this temperature, as expected from viscosity data (Figure 34).

Drop-on-drop printing of Part A (crosslinker ink) and Part B (catalyst ink) was carried out: QD-Ink A (0.005 wt%) was printed with either Ink B or Pt-Ink B (0.00125 wt% PtCl₂). Trials with Ink B were used to confirm whether additional catalyst, or a suitable alternate strategy, was necessary to enable curing of composites with controlled patterning and to compare printing performance.

The loading of Pt-Ink B was selected to maximise fluorescence without compromising curing: while 0.00075 wt% was the lowest loading that had led to the silicone matrix curing within a timeframe comparable to control inks during drop casting experiments, curing behaviour was less reliable and composites failed to cure when preparing samples for Raman spectroscopy with limited heating, and so 0.00125 wt% Pt-Ink B was used to print QD-silicone composites.

Test prints and 1A1B droplet arrays were deposited onto a treated glass slide, shown below in Figure 65; the test prints are described individually below.

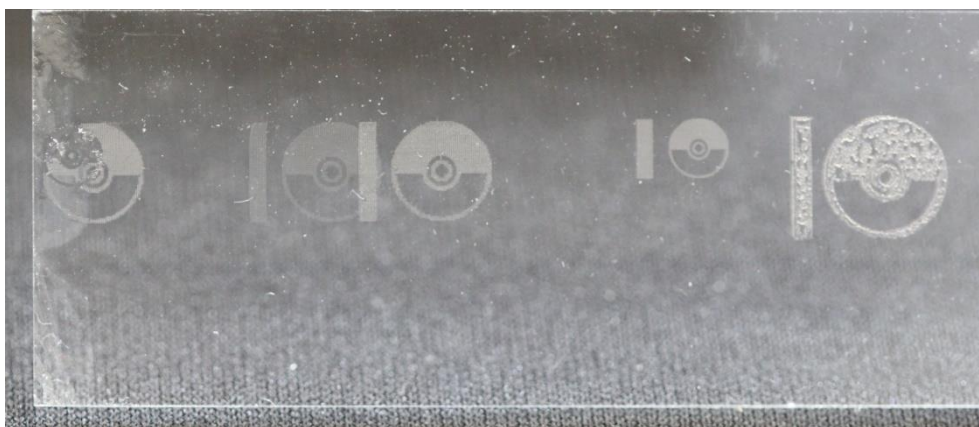


Figure 65: Photograph of glass slide of test prints of QD-silicone composites. Reactive inks were jetted at 30 V with waveform W₁ v2 using the Dimatix printer.

0 wt% Pt-Ink B

The test print with no added catalyst is shown below in Figure 66. The deposited layers were smaller than the pinned grid due to user error: the pattern size was automatically rescaled when drop spacing was decreased from 100 μm to 60 μm . The drop spacing was kept constant at 60 μm in subsequent print trials to minimise the need for realignment. Despite user error, the pattern appeared to have been reproduced, as seen below.

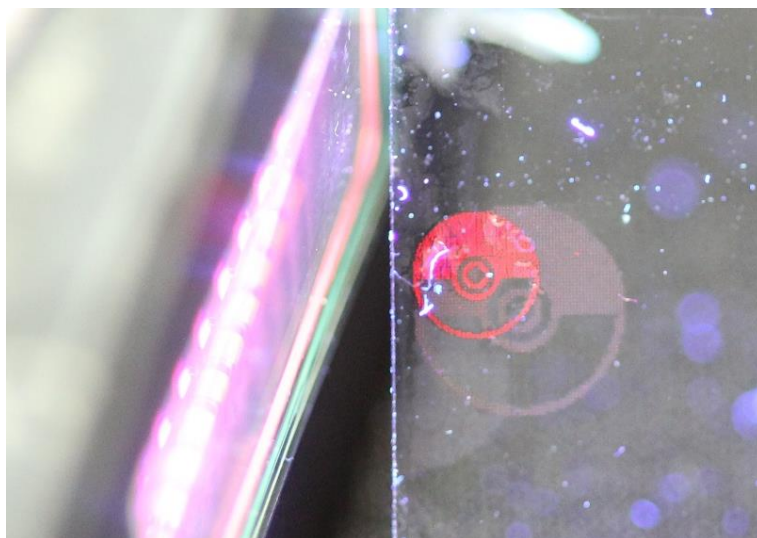


Figure 66: Photograph of the test print of 0.005 wt% QD-Ink A and 0 wt% Pt-Ink B, excited by a 395 nm UV lamp. Test pattern was printed with a 1A1B 2A2B grid at 100 μm spacing (6.5 mm diameter print pattern) and 10A10B layers at 60 μm spacing (4 mm diameter print pattern).

The micrograph in Figure 67 below shows that the inks did not cure fast enough to hold their shape, as the material was not pinned to the surface where it overlapped with the grid and the deposited pattern displays the same bulging seen in inks deposited without surface microstructuring (Figure 43). Upon further investigation, it was noted that the material had not solidified despite overnight substrate heating; therefore, increasing the delay between deposition of the grid and of subsequent layers was not a feasible solution.

It is unclear why the inks failed to cure, as they had been observed to cure at 60 $^{\circ}\text{C}$ in other experiments. It is possible that heat conduction from the platen to the glass slide was slow, despite having had time to heat during set-up. However, drop casting experiments already took thermal conduction into account: material was deposited onto glass slides at ambient temperature which were then placed onto the hotplate. It may be that the smaller drop volumes and greater extent of mixing - and therefore, shorter time frame to reach complete reaction and/or poisoning - made the composites more vulnerable to delays in warm up. Overall, this demonstrates that a strategy to enable curing is advantageous for controlled deposition and curing of composites.

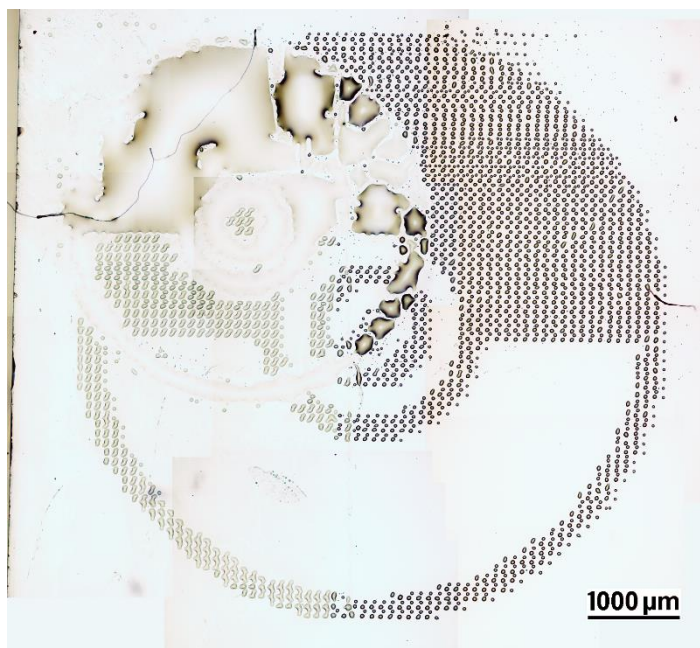


Figure 67: Composite micrograph of test print of 0.005 wt% QD-Ink A and 0 wt% Pt-Ink B, taken with 5x objective. Test pattern was printed with 1A1B 2A2B grid at 100 μm spacing (6.5 mm diameter print pattern) and 10A10B layers at 60 μm spacing (4 mm diameter print pattern).

0.00125 wt% Pt-Ink B

A photograph of a printed sample for the case of 0.00125 wt% PtCl₂ in Ink B is shown below in Figure 68; both grid and subsequent layers were deposited at 60 μm spacing to minimise realignment steps. The deposited material had visible fluorescence, though weaker than the print using 0 wt% Pt-Ink B, as increased platinum catalyst loading is associated with lower emission intensity. The material was solid and had cured; however, the surface texture was bumpy, as noted for printing with a pinned grid (see Section 4.3.3).

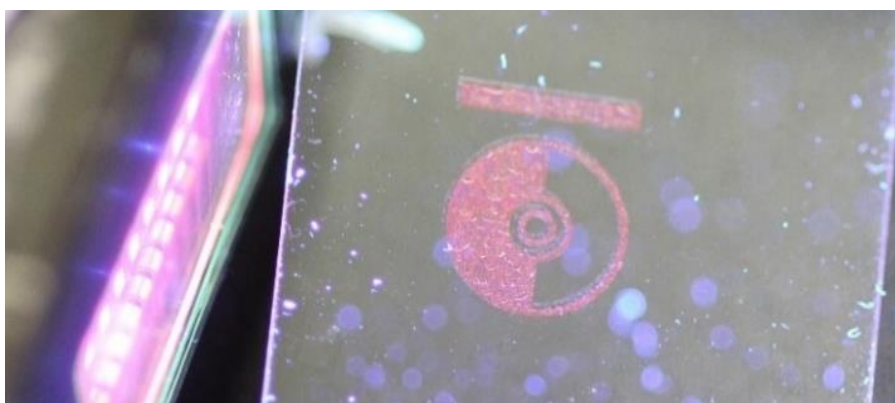


Figure 68: Photograph of the test print of 0.005 wt% QD-Ink A and 0.00125 wt% Pt-Ink B, excited by a 395 nm UV lamp. 1A1B 10A10B layers were deposited at 60 μm spacing (8 mm diameter print pattern).

The surface texture of the test print is shown in more detail in the micrograph in Figure 69. The deposited material was pinned to the grid: anchor points were visible at the edges and there was no bulging. However, the amount of ink deposited was insufficient to form a continuous film, as seen earlier in Figure 47. Convex edges were again observed, as in all printed SiliGlass samples, where inks receded from edges as driven by high initial contact angle ($\geq 45^\circ$) and limited contact pinning.⁶

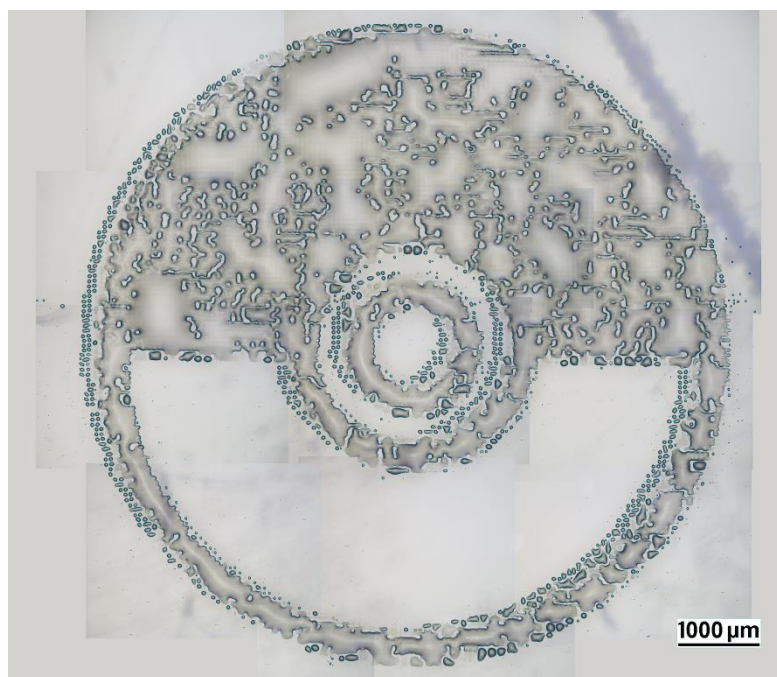


Figure 69: Composite micrograph of test print using 0.005 wt% QD-Ink A and 0.00125 wt% Pt-Ink B, taken with 5x objective. 1A1B 10A10B layers were deposited at 60 μm spacing (8 mm diameter print pattern).

Overall, the QD-silicone composite inks printed with similar behaviour to the SiliGlass inks and were demonstrated to be printable using a pinned grid strategy, although this method limits the transparency achievable. Printing with a single printhead is most suitable for deposition of sensing lines or arrays with $< 50 \mu\text{m}$ resolution.

Cluster imaging

Printed composites were imaged using confocal Laser Scanning Microscopy (cLSM), as seen below in Figure 70, to investigate the size and dispersion of QD clusters in the printed composites. No obvious differences in QD dispersion have been observed between the two samples with and without additional catalyst: both 0.005 wt% QD-composites, with or without added catalyst, typically had QD clusters with a mean Feret diameter of 2.3 μm with an approximate range of 1.5-6.1 μm. Catalyst was predicted to increase metal-induced aggregation,^{250,253} whereas failure to cure was expected to increase aggregation as QDs

were not immobilised in a solid matrix.¹²² Aggregation may have been limited by QD concentration and viscosity of the suspension media, leading to similar cluster distributions in both samples.

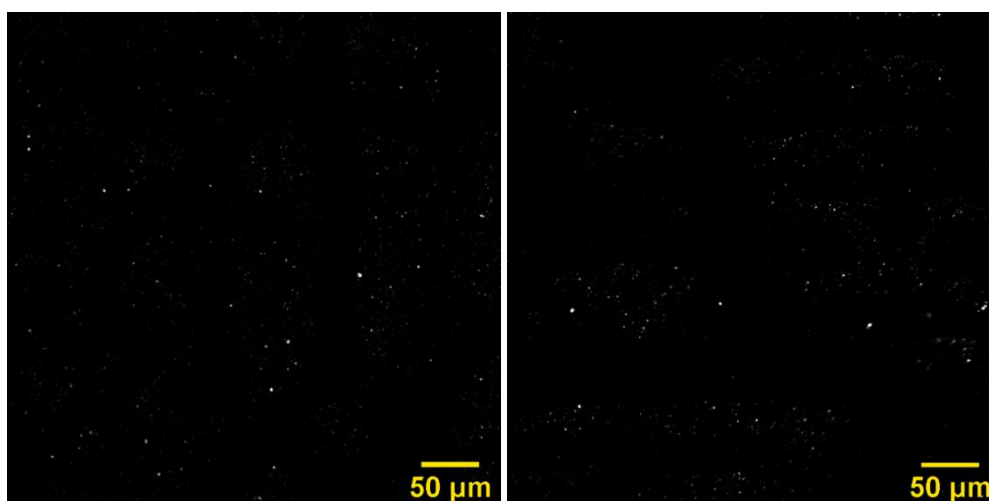


Figure 70: Greyscale micrographs of bulk composite of printed composites, imaged at 24 °C. Left: 0 wt% Pt-Ink B. Right: 0.00125 wt% Pt-Ink B.

Deposited grids were also analysed to assess potential use as sensing arrays. 1A1B grids with 100 μm spacing were deposited using 0 or 0.00125 wt% Pt-Ink B, as shown in Figure 71, left, without satellite droplets and with minimal nozzle spray. The average DoD area was $898.6 \pm 35.3 \mu\text{m}^2$ standard deviation (SD), corresponding to $33.82 \mu\text{m} \pm 0.66 \text{SD}$ diameter, and mean Feret diameter was $37.46 \mu\text{m} \pm 1.44$. The 1A1B 2A2B grid deposited without added PtCl₂ (Figure 71, right) was less ordered as material did not cure in 0 wt% Pt-Ink B print trials, so drop merging from dewetting was observed. Nozzle spitting and satellite droplets were also more noticeable and may accumulate with more layers.

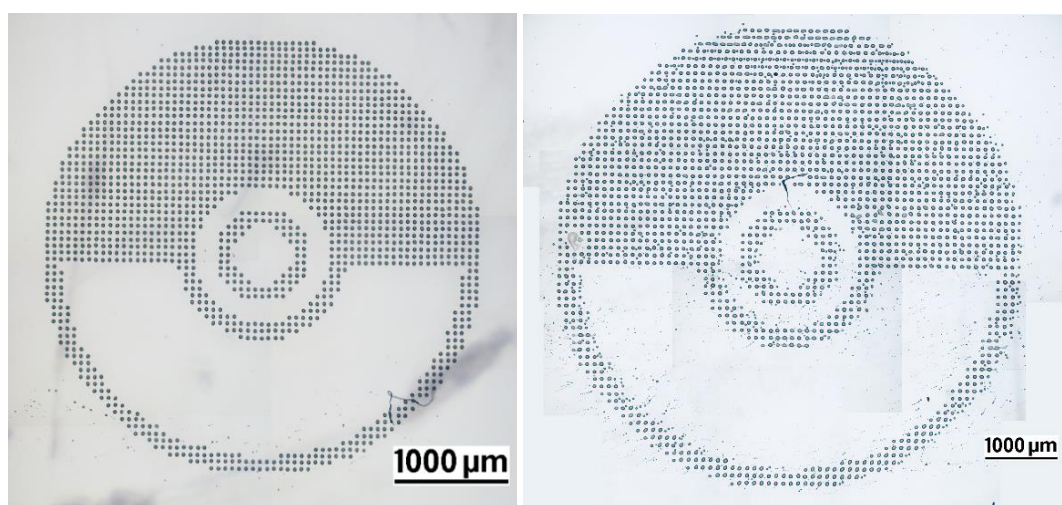


Figure 71: Composite micrographs of 1A1B grid deposited at 100 μm spacing, taken with 5x objective. Left: 1A1B grid using 0.005 wt% QD-Ink A and 0.00125 wt% Pt-Ink B, 4 mm diameter print pattern. Right: 1A1B 2A2B grid using 0.005 wt% QD-Ink A and 0 wt% Pt-Ink B, 6.5 mm diameter print pattern.

Arrays were imaged using fluorescence microscopy to investigate QD distribution in individual points for use as sensing points or arrays. Individual drops could not be discerned in the 1A1B arrays of either composite (Figure 71, left) as the lower number of emission centres resulted in lower emission intensity: the QDs formed irregular clusters and smaller clusters were difficult to differentiate from the background. However, individual drops could be seen in the 1A1B 2A2B array of 0 wt% PtCl₂ composite (Figure 71, right), as shown below in Figure 72. The dispersion of QDs bears superficial similarity to that seen in the 1A1B grids, but the increased number of layers resulted in a greater number of clusters, which made it possible to observe patterning *i.e.* individual drops in the grid. No obvious coffee staining was seen, as may be expected from the limited contact pinning: it appears that the ink was sufficiently viscous – and became more viscous as solvent evaporation proceeded due to high polymer loading – to oppose the generation of Marangoni flow.

The uniformity of individual drops was limited in terms of QD dispersion: the quantum dots were not evenly distributed and formed clusters of different sizes. The pattern of clusters deposited appears to be random: Elliot *et al.*¹⁸ observed similar random patterns when jetting CdSe QDs in VeroClear (an acrylate-based photopolymer) and such unclonable patterns have applications in anti-counterfeiting.^{18,254}

As a random distribution would regress towards the mean as more layers are deposited and lead to more equal intensity across the XY plane bulk measurements of printed composites may be suitable for sensing applications. For applications that require small volumes of material or nanothermometry, monitoring of specific clusters may be used to ensure that the number of emission centres is consistent between measurements. However, improving dispersion and reducing aggregation remains desirable to enable reliable sensing with minimal material, to reduce inter-particle re-absorption,^{239,240} and to improve thermal stability.¹²²

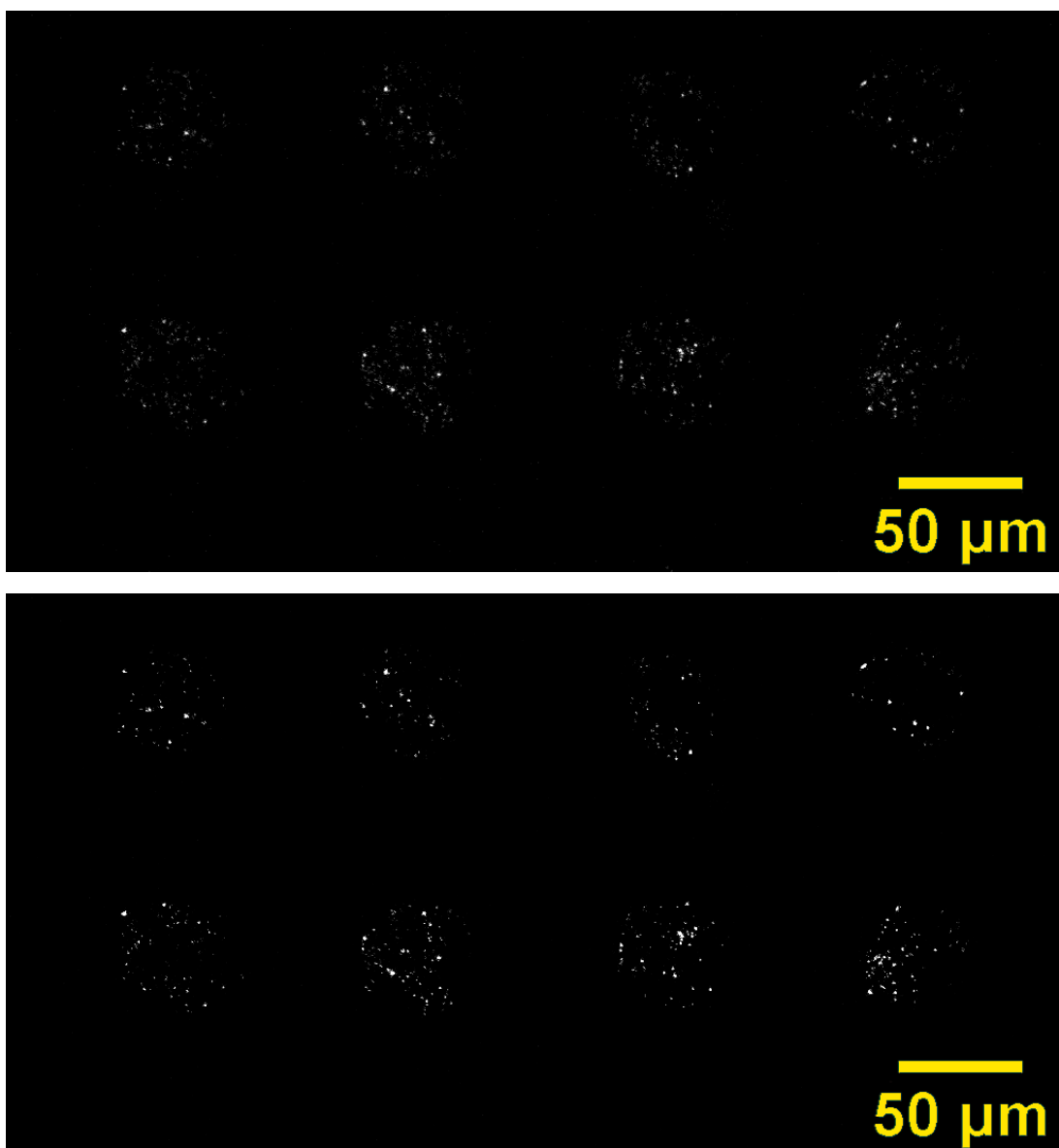


Figure 72: Greyscale fluorescence micrograph of 1A1B 2A2B grid (0.005 wt% QD-Ink A and 0 wt% Pt-Ink B) with 100 μm drop spacing, imaged at 24 $^{\circ}\text{C}$. Top: Raw data. Bottom: Contrast has been enhanced.

In summary, inkjet printing of QD-silicone nanocomposites was demonstrated for the first time. While only the composite with added catalyst cured, other experiments suggest that composites without added catalyst can cure at 60 $^{\circ}\text{C}$ substrate heating or higher. The composite without added catalyst had strong emission intensity despite low QD loading (0.005 wt%), while the composite with 0.00125 wt% PtCl_2 cured with ~ 37.5 μm DoD resolution and had weaker but visible emission. Fluorescence micrographs showed similar QD cluster distributions for both composites, and random patterning of individual points in arrays, which may find use in anti-counterfeiting applications.^{18,254} The next stage of research was to conduct temperature sensing experiments to assess the utility of printable formulations as temperature sensors.

4.5.3. Summary of QD-composite printing

Additional platinum catalyst was added to Ink B as curing in QD-composites was hindered: quantum dots retard cure rate in addition-cure silicones because the labile ligands poison the platinum catalyst.^{132,146,248} In drop casting experiments, loadings as low as 0.00075 wt% Pt-Ink B were sufficient to produce 0.005 wt% QD composites with cure rate comparable to the benchmark (Ink A and Ink B without any QDs or additional platinum catalyst). A trade-off between cure rate and QD emission intensity meant that lower catalytic loadings were preferred. A 70% decrease in emission intensity was seen as PtCl₂ concentration doubles. Degree of conversion was lower in the benchmark (Ink A mixed with Ink B) than in composites made by mixing QD-Ink A with Pt-Ink B containing PtCl₂ loadings of 0.00125 wt% and above. However, overall conversion decreased by 30% between moderate and high platinum concentration. Metal-induced aggregation is a plausible mechanism of fluorescence quenching in composites with high catalyst loading.^{250,253} Loss of QD stabilising ligands results in the loss of the PL enhancement by primary amines.^{236–238} This can also explain the decrease in conversion at high catalyst loading, assuming that metal-induced agglomeration can further lead to liberation of ligands from the joined QD surfaces, which accelerates catalyst poisoning.

Mixing was also observed to be an important factor in reaction, and a distinction was seen between rate of solidification and overall conversion. Inks took longer to solidify than undiluted SiliGlass; however, overall conversion was increased by the presence of solvent, as reduced viscosity enables more thorough mixing of catalyst and reagents, and therefore more complete reaction. Similarly, drop casting experiments with toluene-based inks - a more volatile solvent - showed faster initial cure rate as the polymer concentration was higher than in octyl acetate-based inks and the solvent evaporated more rapidly, but curing was nonhomogeneous. It appears that catalyst became immobilised at interfaces where material solidified and restricted diffusion to regions where inks had not mixed. While mixing is likely faster during inkjet than drop casting due to the difference in drop volume, it is noted that drop-on-drop mixing in reactive inkjet is solely diffusion-rate limited.²²²

Printing of QD composites was tested with and without added catalyst; a loading of 0.00125 wt% PtCl₂ was selected as the minimum loading for cure rate comparable to the SiliGlass inks as controls. Printed composites were imaged with confocal laser scanning microscopy: no differences were seen in QD cluster size and dispersion in composites of with catalyst loadings, and no coffee staining was observed in droplets of a printed grid.

The print trial with 0 wt% Pt-Ink B failed to cure, even though it was observed to cure at 60 °C in drop casting experiments. It is possible that heat transfer to the slide was delayed and that the smaller drop volume made the composites more vulnerable to delays in warm up. While higher substrate temperature may result in cured composites, the platen temperature was set to the maximum for the Fujifilm Dimatix.⁵⁹

The print trial with 0.00125 wt% Pt-Ink B did cure to produce the first inkjet-printed QD-silicone composite. While the layers deposited were insufficient to make a continuous film - leading to uneven surface texture - the print conformed to the pattern. While emission intensity was lower than in the composite with no added catalyst, fluorescence was visible. Line-by-line printing on a dual-headed printer without stepped-lines or interlayer delay could be carried out to produce films with controlled geometry and reduced optical aberrations, as was done for SiliGlass inks. Additionally, this composite required less heating than the one with no additional catalyst: Raman spectroscopy confirmed that 0.00125 wt% PtCl₂ composites cured well with limited heating, while inks without catalyst require immediate and consistent heating to prevent catalyst poisoning.

In summary, reactive composite inks were formulated with suitable curing for inkjet by addition of PtCl₂ catalyst to Ink B (Objective O4). Inkjet printing of QD-silicone nanocomposites was demonstrated for the first time with an intended application in thermal sensing. While composites did not cure without added catalyst, drop casting experiments suggest that they can be printed with 60 °C substrate heating or higher. Composites with 0.00125 wt% PtCl₂ had curing compatible with a range of print strategies and weaker but sufficient emission for optical sensing. Fluorescence micrographs show random patterning of QD clusters which means these inks may find use in anti-counterfeiting applications. The random distribution of clusters is expected to regress towards the mean as layers are deposited, so bulk printed material may be suitably distributed for sensing applications, while imaging of clusters could be carried out for temperature sensing with microscale resolution.

4.6. Summary of addition cure silicones

In this chapter, addition cure silicone reactive inks were formulated from a commercial 2-part RTV, PolyTek SiliGlass. Octyl acetate was selected as solvent due to its low volatility and non-toxicity and the printability of inks was confirmed from rheological measurement (Objective *O1*).

Reactive inkjet of 50 wt% silicone inks was demonstrated for single- and dual-headed printers without nozzle heating (Objective *O2*): Ink A (crosslinking ink) and Ink B (catalyst ink) were deposited drop-on-drop and a platen temperature of 40 °C was used to accelerate cure. Glass slides were treated to produce highly hydrophobic substrates but pinning to the treated substrate was poor, therefore thin films were produced using a pinned grid strategy or a line-by-line printing strategy to enable controlled patterning.

QD inks were formulated to optimise fluorescence, rheology, and dispersion (Objective *O3*). QDs were observed to retard curing of silicones: labile stabilising ligands poison the platinum catalyst. Additional catalyst was added to control curing and the effect on cure rate, conversion, and fluorescence were investigated for a range of PtCl₂ loadings.

Finally, reactive inkjet of QD-silicone composites was demonstrated for the first time using 0.005 wt% QD-Ink A and 0.00125 wt% Pt-Ink B with a platen temperature of 60 °C (Objective *O4*) to produce thin films in complex patterns with visible fluorescence. Composites without added catalyst are also thought to be printable at 60 °C - and have the benefit of much stronger emission intensity - but did not cure during the print trial.

Alternate schemes for reactive inkjet of QD-silicone composites were investigated next, by exploring another reaction mechanism: acrylate-based photopolymerisation. The experiments with UV cure silicone composites are described in Chapter 5 below.

The nanocomposites produced during this PhD are intended for use in optical sensing, so the final research stage was to assess the composites and to measure PL as a function of temperature. Temperature sensing experiments are carried out in Chapter 6.

Chapter 5. Results – UV cure silicones

In Chapter 4, reactive inkjet of addition cure QD-silicone composites was demonstrated. However, there were challenges associated with QD dispersion, cure rate, and platinum catalyst poisoning. UV cure formulations offer distinct advantages, including stable one-part inks, rapid curing, and solvent-free conditions. Furthermore, UV curable inks are compatible with a wide range of vat photopolymerisation-based AM processes.

In this chapter, UV cure silicone inks were formulated for inkjet using prepolymers with thiol-ene and/or (meth)acrylate moieties. Two popular photoinitiators were trialled and a range of novel QD-silicone composites were produced. A Fujifilm Dimatix DMP-2830 was used to print inks: deposited material was cured using an LED UV lamp under an inert nitrogen environment and drop spacing was optimised to achieve continuous films.

This chapter:

- Discusses the choice of reaction mechanisms and characterises prepolymers
- Explores two common photoinitiators: DMPA and TPO
- Characterises jettable ink formulations for a range of photoinitiator loadings
 - Viscosity
 - Density
 - Surface tension
 - Z number
- Details the synthesis and observations of fluorescent QD-silicone composites
 - Photoinitiator loading experiments
 - Effect of thiols on fluorescence
 - Loss of photoluminescence
- Describes the printing optimisation of silicone formulations
 - Assessment of cure in TPO-inks via differential scanning calorimetry (DSC)
 - Jetting observed and drop arrays analysed for two different waveforms
 - Assessment of printed patterns and print strategies on two substrates
 - Printing of UV cure silicone inks.

A range of novel QD composites were synthesised. However, QD fluorescence was unstable. Printing was demonstrated for silicone inks and shown to be feasible for composites. Further work to refine parameters and stabilise fluorescence would establish this as a viable route for functional siloxanes.

5.1. Prepolymer characterisation

This section provides the rationale for the selection of UV cure reaction mechanisms and reagents, discusses commercial photoinitiators, and describes the data collected to characterise prepolymers. In this section:

- ^1H Nuclear Magnetic Resonance (NMR) spectroscopy is used to determine molecular weight (MW) of the commercial silicone oligomer
- The rheological behaviour of the two acrylate-based prepolymers is examined to guide formulation for high-throughput screening (HTS).

5.1.1. Temperature sensor criteria

Addition cure silicones systems are used as LED encapsulants and were deemed to be attractive for optical sensing due to their lack of by-products and shrinkage, which may be associated with better transparency in comparison with other cross-linking mechanisms. However, the platinum catalyst is vulnerable to poisoning by a range of species and this presented a significant challenge during development of QD-silicone inks.

Photopolymerisable silicones are an attractive alternative as they can have faster, more robust cross-linking mechanisms, the photoinitiators required are cheaper than the platinum catalysts used in addition cure silicones, and efficient UV-LED lamps are used to accelerate cross-linking. This can enable UV curable silicone printing to be faster, more scalable, and cheaper. Increased reaction speed also makes contact pinning less of a problem as it halts droplet spreading on substrates and can improve resolution⁶⁵; this is advantageous for device manufacture, as the addition cure inks had required surface-treated substrates which used chemicals that could damage other components or materials. As UV curing requires an excitation source to initiate, single-part inks with longer working life than single-part addition cure inks are formulated, which simplifies the printing process and requires less calibration and less specialised printers than for two-part inks. UV curing materials are also more processable in terms of compatibility with additive manufacturing (AM) processes, which diversifies the potential deposition methods for development of complex printed devices to include vat photopolymerisation-based processes.

Criteria for the polymer matrix of a QD-based optical temperature-sensing material, as was summarised in Table 6, includes: thermal and photostability within the potential sensing range of 0-100 °C and the UV-LED excitation wavelengths 350-400 nm; >90% optical transparency ~350-750 nm and refractive index (RI) $\geq 1.4 n_D^{25}$; >30A Shore hardness; and

<1000 mPa s viscosity. These criteria (discussed in detail in Section 4.1.1) relate to material lifespan, sensing efficiency, prevention of material displacement, and inkjet processability, respectively. Both (meth)acrylates and silicones are utilised for LED encapsulation for their thermal stability, photostability, and transparency; therefore, both acrylate hydrocarbon and functionalised silicone precursors, and their copolymers, may lead to materials with suitable properties. Polymer encapsulants are compared in Section 2.1.2: while silicones and acrylates have similar transparency, acrylates are cheaper to produce than silicones and greater acrylate character in silicone-acrylate copolymers may increase the refractive index (RI values for n_D^{25} are ~ 1.4 for PDMS¹⁷ and ~ 1.5 for PMMA⁴⁸), leading to cheaper QD-polymer composites with higher light extraction efficiency (REE)^{186,187} and reduced scattering.¹⁸⁸ In turn, the siloxane chain offers higher thermal and chemical stability than (meth)acrylate polymers.⁴⁶ Both silicones and silicone-acrylate copolymers may be formulated with the properties desirable for optical temperature sensing applications.

While the addition cure inks produced elastomers which were softened by the presence of solvent, as this dilutes the locked chain entanglements,⁵⁷ a range of elastic moduli may be of use for thermal sensing. Elastomers with shorter crosslinks and higher crosslinking density are more rigid, which makes them less susceptible to changes in dimension but less able to absorb thermal stresses.^{57,181} Higher elastic moduli and greater chain mobility result in higher coefficients of thermal expansion (CTE), which can prevent crack formation as a result of thermal stress⁴⁶ and may enhance sensitivity,¹⁴ but thermal measurements may also be more vulnerable to changes in thermal expansion, solvent swelling, and mechanical changes arising from aging.^{46,57}

Addition cure inks had required dilution with a solvent to reduce the viscosity to meet inkjet requirements, as elastomers require long chain length precursors (<20 kg mol⁻¹ base polymers, corresponding to <270 repeat units)⁵⁷ and viscosity increases with chain length due to increasing entanglement.^{17,52} However, radical photopolymerisation is not limited by the initial chain length of precursors to the extent that addition cure crosslinking is, as it proceeds via a chain growth mechanism which can produce macromonomers. Therefore, polymers with a range of physical properties can be produced from a variety of low-viscosity monomers (<10 mPa s) so that inks with inkjet-compatible viscosity may be formulated for both rigid and flexible polymers without the need for a carrier vehicle.

Printing of solvent-free inks is less complex to optimise: solvents may be associated with slower curing, slower print rate due to less efficient deposition and interlayer drying times, a need for platen heating to accelerate evaporation, nozzle blockage due to evaporation, and Marangoni flow and other film defects arising from polymer-solvent interactions.^{35,116} Printed SiliGlass showed microphase formation (see Figure 48), possibly comprising polymer-rich and solvent-rich domains, which may reduce optical transparency;²³⁴ solvent-free inks prevent the formation of such solvent-associated microphases. Printing with solvents can also lead to material compatibility issues; orthogonal solvent strategies are required for printed components²⁰⁸ as solvents can distort deposited materials, swell polymers, and dissolve species.²⁰⁹ The SiliGlass addition cure inks required LCP print cartridges as the solvents were incompatible with the standard polypropylene-based cartridges, whereas acrylate monomers are compatible with polypropylene.²⁵⁵ The shelf life of a jetting ink may be limited by changes in viscosity: addition cure inks may increase in viscosity due to solvent evaporation, whereas the viscosity of solvent-free UV cure ink is expected to be stable in dark conditions, although reactive monomers may have their own shelf life limitations.²⁵⁵

Yellowing of polymers as a result of thermal and photo-aging is a key concern for LED encapsulants. PMMA is reported to have high photostability above 300 nm, although PMMA may be susceptible to oxidation even at <100 °C.^{46,255} Changes in optical properties appear to be limited within the intended maximum sensing range (30-100 °C), depending on the structure of the PMMA: Lu *et al.* reported that oxidation of PMMA was negligible after 3000 h at 85 °C and had little impact on the transmission spectra,²⁵⁶ while Estupiñán *et al.* reported a 1.01% decrease in transmission at 450 nm after 90 h at 72°C.²⁵⁷

While discoloration in addition cure silicones is associated with the formation of metallic nanoclusters, this is not the case for radical photopolymerisable silicones as they do not contain metal catalysts. Instead, radical-based UV curing mechanisms require photoinitiators (PI), and yellowing is linked to specific photoinitiator species and photo products. As discoloration degrades the optical performance of a sensing material, yellowing should be minimised by selecting photoinitiators with colourless by-products and using the minimal PI loading required for curing. As photoinitiators absorb at UV wavelengths, they also reduce the UV transmittance of QD-silicone composites and may reduce the efficiency of QD excitation, which may reduce the signal-to-noise ratio achievable at a given excitation source power. This concern is mitigated by the fact that the

CdSe/ZnS QDs used in this work have suitable absorption at all wavelengths ≤ 500 nm (see Figure 58), and so the excitation wavelength could be selected to avoid competition for photon absorption between QDs and PI during sensing and to minimise longterm polymer photoaging.

Overall, radical-based photopolymerisations are suitable for formulating solvent-free one-part inks with rapid crosslinking, which is greatly beneficial to inkjet printing calibration, throughput and resolution. This is advantageous for sensor production in a number of ways; firstly, material compatibility issues are lessened by solvent-free inks, which simplifies device production. UV cure inks are also less likely to require silanised substrates for controlled deposition, due to their fast reaction rate compared to hydrosilylation and as acrylate-functionalised oligomeric (co)monomers have higher surface energies than PDMS chains. Furthermore, free radical photopolymerisations are versatile due to a chain growth mechanism, which can allow for polymers and copolymers with a wide range of physical properties and microstructures from low viscosity precursors (<10 mPa s), which enables ink formulations towards materials with desirable optical and mechanical properties for specific sensing applications. Radical photopolymerisation is viable with a range of functionalised precursors including epoxide, vinyl, acrylate, and thiol groups; precursors and the rationale for their selection are discussed below.

5.1.2. Commercial reagents

Free-radical chain growth photopolymerisation is a versatile UV cure mechanism which can produce polymers with a wide range of properties, depending on the monomer(s), comonomer ratio(s), photoinitiator(s), additives, and reaction conditions. Monomers must contain suitable functional groups, which include epoxide, vinyl, acrylate, and thiol groups;⁵⁶ many short monomers and oligomers are suitable for synthesis of both rigid and flexible polymers as chain growth can produce macromonomers (macromers) during reaction.²⁵⁵ This enables the formulation of one-part, solvent-free jetting inks, which are deposited onto a substrate and cure rapidly at room temperature upon exposure to UV light, as shown below in Figure 73.

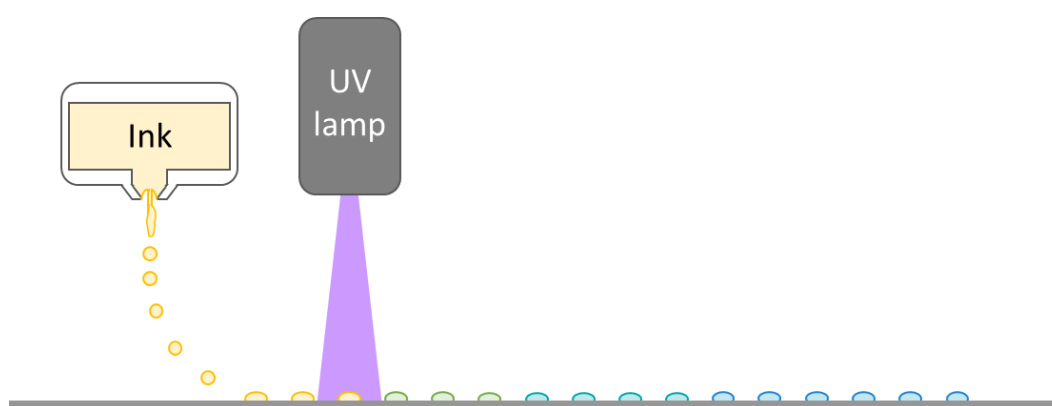


Figure 73: UV inkjet printing process diagram. Photopolymerisable ink is deposited onto the substrate and excited by a UV wavelength excitation source attached to the printhead assembly.

A vast number of potential monomers exist, in addition to further parameters that affect polymer curing, morphology, and macroscopic properties. Two inviscous monomers were selected for initial trials to enable polymers with varied properties in order to investigate their impact on QD-composite fluorescence. (Meth)acrylate-based free radical photopolymerisation was investigated as it is the most common mechanism for photopolymerisable silicones,⁵⁶ and has been used in the literature for both bulk QD-polymer composites^{160,258,259} and inkjet-printable QD-polymer composites.¹⁸ Rapid curing at ambient temperature is possible, which can enable higher inkjet print resolutions.⁵⁶ Acrylates, and PMMA in particular, are utilised for LED encapsulation and are suitable for optical sensing.⁴⁶

Various acrylate and methacrylate monomers may be used: the methyl group on the polymethacrylate backbone confers rigidity through steric factors, while polyacrylates are softer and more elastic due to higher chain mobility. Polymethylmethacrylate (PMMA) is used for LED encapsulation and has high UV transmittance and stability, but can discolour under high water absorption.⁴⁶ Acrylate-methacrylate copolymers have “outstanding”

photostability and are resistant to hydrolysis;²⁵⁵ acrylate comonomers can improve flexibility and impact strength as compared to pure polymethacrylates. In inkjet, acrylates are advantageous for faster reaction as they have less steric hindrance and less stable radicals (secondary) than for methacrylates (tertiary); this can result in gradient copolymers if reacted together. Bifunctional monomers can be used to crosslink polymers and improve UV and thermal stability,²⁵⁵ which is desirable for sensing materials.

Therefore, an acrylate and a methacrylate monomer, which were mono and bifunctional respectively, were chosen to enable one-part inks without carrier vehicles as shown below in Figure 74. α,ω -methylacryloxypropyl-terminated PDMS (abbr **AB116678**, 4-6 cP) was selected for printable viscosity (i.e. <40 mPa s viscosity³²) with methacrylate moieties to promote rigidity and crosslinking. An acrylate comonomer was selected to investigate faster reaction rate (which may be beneficial for inkjet) and to investigate copolymers with varying degrees of flexibility and its effect on thermal sensing.

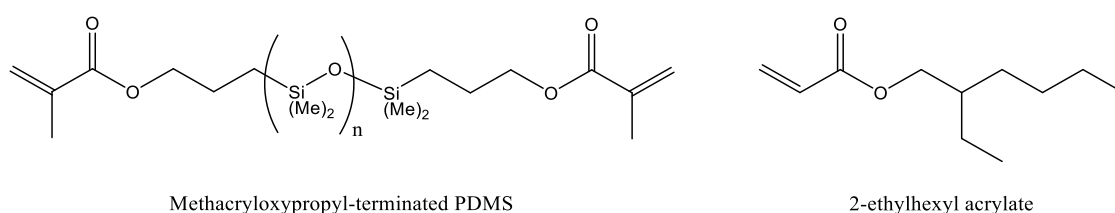


Figure 74: Precursors for UV-curable silicone and acrylate system.

Of the industrially-important acrylate monomers, 2-ethylhexyl acrylate (**2-EHA**) was selected for high refractive index ($1.4332 n_D^{25}$), hydrophobicity, and boiling point (217°C).²⁵⁵ Its hydrophobicity may promote compatibility with the silicone, and reduce water absorption and associated discoloration: acrylates with longer alkyl chains confer greater stability to hydrolysis.²⁵⁵ The high boiling point enables non-volatile jetting inks so that evaporation is not expected to occur and cause changes in formulation and printability.

The QDs purchased from Ocean NanoTech are capped with hydrocarbon chains. 2-EHA is a branched monomer with a C8 side chain, which may prevent exchange or reaction with QD ligands while promoting better interdigitation with stabilising ligands; this could improve QD dispersion and passivation, reducing scattering from aggregates and improving the thermal stability of QD-based sensing materials.^{122,239} However, branching reduces packing efficiency and may make polymers more susceptible to solvent swelling and increases porosity, which may lead to material incompatibilities during device fabrication and

operation, as well as reduce transparency in sensing materials. Variation of crosslinking density by polymerisation with the difunctional silicone could be used to reduce swelling.

Polymer precursors were characterised to inform formulation, as the manufacturer of AB116678 listed a viscosity range and did not provide data on molecular weight or polydispersity. Accurate rheological data was required for ink formulation and was collected using high throughput screening (HTS), while ^1H NMR spectroscopy was used to estimate number average molecular weight (M_n). The number of repeat units in a monomer chain has an effect on viscosity and the polymer properties: it determines the tendency for phase separation of prepolymers and the extent of silicone-like properties in the final material.²⁶⁰ As telechelic siloxane crosslinkers may react with acrylate monomers to form copolymers with a broad range of microstructures,²⁶¹ it was important to know chain length in order to interpret observations of copolymers and to inform sensor material development with regards to microphases which could reduce transparency.

Photoinitiators (PIs) are used to produce reactive free radicals to initiate polymerisation. The absorption spectrum of a PI determines the efficiency of radical generation with different excitation wavelengths and source powers as well as the quality of curing at different depths in the sample. Longer excitation wavelengths penetrate more deeply into a sample than shorter wavelengths: shortwave UV absorption (200-280 nm, UVC) is associated with preferential surface curing, longwave UV (340-400 nm, UVA-II) with preferential depth cure, and midrange UV (280-340 nm, UVB and UVA-I) with a combination. For inkjet-printable materials, ideal photoinitiators absorb longwave UV to match common excitation sources used in inkjet, provide some surface cure as inkjet deposits thin layers, and enable rapid photopolymerisation with minimal loadings, as high PI concentration can limit the mechanical properties of the material. For optical sensing materials, prevention of discoloration is a priority to ensure that QD emission is both accurately and consistently transmitted through the matrix across the sensing material lifetime; this can be achieved using low-yellowing PIs and/or minimal PI loadings.

Photoinitiators are divided into two main classes; Norrish Type I photoinitiators undergo homolytic cleavage to produce two radical fragments, which are incorporated into the end-product. In contrast, Norrish Type II photoinitiators must be paired with a hydrogen donor, typically a tertiary amine or amine synergist, which is incorporated into the end-product.²⁶² Commercial type I PIs include hydroxyacetophenones (HAPs), alkylaminoacetophenones

(AAAPs), dialkoxyacetophenones (DAAPs), and phosphine oxides (POs), which are described and contrasted below.²⁶²

HAPs are considered efficient PIs with strong shortwave UV absorption and weak midrange absorption. They are non-yellowing, as the alkyl radicals produce acetone and other colourless photoproducts. HAPs are used in coatings – including silicone-based coatings – due to effective surface cure from their absorption band at 230-270 nm, but also confer some depth cure from absorption ≤ 360 nm. However, much higher PI concentrations are needed for efficient surface curing in lower viscosity coatings, which limits their utility for inkjet.

AAAPs are much more reactive than HAPs, with rapid, versatile curing due to strong midrange UV absorption. Their high reactivity - among the highest of all commercial photopolymers²⁶² - means that they are employed in inkjet for their fast curing, although thick films tend to show yellowing. However, some AAAPs contain thiol moieties, which could quench QD fluorescence if used in QD-composite ink formulations.^{263,264}

DAAPs are another class of efficient PIs that can achieve rapid curing with strong shortwave UV absorption and fair midrange absorption. The most-successful example is Omnirad 651, which is considered a "good general-purpose photoinitiator"²⁶²; the main by-product is colourless methyl benzoate, though yellowing can occur via rearrangement of the benzyl radical. Omnirad 651 has reduced oxygen-sensitivity, as its short triplet lifetime leads to a narrow timeframe for oxygen to quench the excited state. Omnirad 651 is used in inks due to its broad absorption range, rapid crosslinking, surface cure, and high thermal stability.

Last of the commercial type 1, POs are a class of reactive PIs with strong longwave UV absorption leading to rapid and thorough depth cure. They are non-yellowing and residual PI photobleaches upon further exposure to UV or visible light, which aids transmission of light through the polymer. POs are therefore used to penetrate and cure thick films, composites, and pigmented formulations. However, the phosphinyl radical is very sensitive to oxygen and cannot be used to produce thin films in air. POs are also sensitive to nucleophilic attack and are incompatible with olamines.

Commercial type II photoinitiators include benzophenones (BPs), substituted benzophenones (sBPs), benzoylformate esters (BFs), and thioxanthenes (TXs).²⁶² BPs are cost-effective PIs, with strong shortwave absorption and some weak midrange absorption, that are used in varnishes and inks. They have high solubility and are used in relatively high

concentrations to give good surface cure in low viscosity coatings, similarly to HAPs. However, BPs suffer from long term yellowing. Substituted BPs are more reactive than BPs and have strong midrange UV absorption; in contrast to BPs, sBPs have limited solubility and may crystallise out of inks, which could cause nozzle blockages and inhomogeneity in printed samples. Substituted BPs which contain thiol moieties may quench QD fluorescence if used in an ink containing quantum dots.^{263,264}

BFs are unusual type II PIs: they do not require hydrogen donors, instead producing biradicals with low reactivity towards both acrylates and oxygen. Oligomeric radicals form which results in increased crosslink density and hardness, as well as minimal migration (i.e. photoinitiator does not leach out of the polymer). BFs are non-yellowing and are therefore used for transparent coatings.

Lastly, TXs are longwave UV absorbing PIs that are “used almost universally in ink formulations”²⁶² as they can sensitise certain type I PIs, leading to very fast cure rates. TXs yield excellent depth cure but are intrinsically yellow in colour and do not photobleach: POs are preferred for applications that require optical clarity. The thiol moiety in TXs may also result in PL quenching if interaction with the QD surface is significant.^{263,264}

The properties of different classes of commercial free radical photoinitiators are summarised below in Table 21. It is common to use blends of photoinitiators to optimise both surface and depth cure and to prevent oxygen inhibition of POs; POs are often combined with surface curing PIs in a 1:3 ratio for thick film curing.²⁶² For this study, two PIs were selected: one shortwave UV absorber and one longwave UV absorber, which could be combined in future work to optimise surface and depth cure.

Table 21: Performance of commercial classes of free radical photoinitiators.

Norrish Type I					
Class	Absorption bands <i>nm</i>	Surface cure	Depth cure	Yellowing	Shelf life
HAPs	230-270 Weak up to 360	Good	Fair	No	Good
AAAPs	280-350	Good	Good	Yes	Good
DAAPs	230-270 Weak up to 370	Good	Fair-Good	Yes	Excellent
POs	350-420	Poor	Excellent	No	Fair; avoid nucleophiles and light
Norrish Type II					
Class	Absorption <i>nm</i>	Surface cure	Depth cure	Yellowing	Shelf life
BPs	230-260 Weak around 330	Good	Fair	Yes	Good
sBPs	280-330	Good	Fair	Low	Good; poor solubility
BFs	230-260	Good	Poor	No	Good
TXs	350-410	Poor	Excellent	Yes - high	Fair; avoid light

The key considerations for photoinitiators in UV cure ink formulations are a) excitation wavelength and b) oxygen inhibition in air.²⁶⁵ As inkjet printers often use UV LEDs, which have monochromic emission at 365 or 395 nm, inks are prepared using one of the two classes which have strong absorption at these wavelengths (POs and TXs), and formulation strategies are used to enhance surface cure. Many inks utilise TXs (Omnirad DETX, ITX, and TX), either alone or combined with an AAAP or sBP co-initiator which is sensitised by TX to achieve accelerated surface cure (e.g. Omnirad 379 or Omnirad 4 PBZ, respectively). POs are used in pigmented inks (Omnirad 819 a.k.a. TPO, and TPO-L), though selection of a co-initiator which absorbs at 365 nm is difficult and various PIs are used (such as the AAAPs Omnirad 379 and 907).²⁶² HAPs are also suggested for use in inkjet (Omnirad 184 and 127, Esacure ONE, Esacure KIP 150 and 160), though these cannot be sensitised and are noted to require higher loadings in low viscosity fluids²⁶² including inks, which must have <40 mPa s viscosity to be inkjet-printable.³²

Suggested PI loadings are 5-10 wt% for inkjet²⁶⁵ to enable good surface cure in thin layers of deposited material: such high PI loadings are necessary to counteract oxygen inhibition and to achieve rapid curing when printing in air. However, higher PI loadings increase the extent of yellowing and are detrimental to mechanical properties: higher radical

concentration results in a larger number of shorter polymer chains with a wider MW distribution, in addition to a higher concentration of photo-products.²⁶² Printing under an inert atmosphere enables the use of lower PI loadings, which may be further lowered if reaction is accelerated using substrate heating.

In this thesis, two photoinitiators were selected for ink formulation trials: one associated with good depth cure and therefore strong absorption of typical UV-LED wavelengths, and one associated with good surface cure as the inkjet process deposits material in thin layers.

For depth cure, both POs and TXs have similar reactivity and absorption at the wavelengths of UV LED lamps and will both absorb light efficiently during the inkjet process. However, POs are preferred over TXs for optical sensing applications due to the strong yellowing of the latter class, in addition to potential issues with QD quenching by thiols. Omnirad 819, a.k.a. TPO, is attractive for optical sensing as it is photobleaching, which further allows UV-visible light to penetrate the polymer matrix, leading to high optical transparency and excellent depth cure and adhesion. However, TPO is oxygen-sensitive and may perform poorly in inkjet without a co-initiator or an inert atmosphere.

Omnirad 651, a.k.a. DMPA, is a DAAP-class PI and is the most widely-used PI for free radical crosslinking of PDMS.⁵⁶ It is considered a “general purpose” PI due to its broad, short-to-midrange UV absorption and will be able to confer some surface cure using a 365 nm UV LED. While some yellowing is possible, this is dependent on the by-products produced and can be mitigated by using low PI:acrylate ratios, particularly if using an inert atmosphere to enable lower loadings. The high thermal stability of DMPA is an ideal property for temperature sensing applications, as this prevents loss of transparency in the cured polymer from DMPA thermal decomposition products and may enhance ink shelf life.

As free radical acrylate photopolymerisation is limited by oxygen-inhibition, thiol monomers were also explored (see Section 5.3.2). Thiol-ene reactions are another photocuring mechanism compatible with solvent-free, ambient inkjet. Thiol-ene reactions have low oxygen-sensitivity and higher conversions than acrylate-based photopolymerisation, at the cost of shorter ink shelf-life.⁵⁶

Having selected ink constituents, it was necessary to characterise the prepolymers to gain a better understanding of the polymer system for the formulation stage, as described in the following section.

5.1.3. Spectroscopy

^1H NMR spectroscopy

^1H NMR was used to estimate number average molar mass (M_n) of the commercial oligomer, AB116678. The number of repeat units in a chain is related to viscosity, and to copolymer properties: it determines the tendency for phase separation of prepolymers and the extent to which the cured product will behave like a silicone.²⁶⁰ Telechelic siloxane crosslinkers may react with acrylate monomers to form copolymers with a broad range of microstructures;²⁶¹ M_n is important for understanding the formation of microstructures which could effect the optical behaviour of sensing materials.

The ^1H NMR spectrum of AB116678 is shown below in Figure 75; AB116678 is a methacryloxypropyl(MAP)-terminated PDMS, as shown in Figure 74 above. The methacrylate group generates two singlets (**a&a'**) centred at 5.8 parts per million (ppm) and a singlet around 2 ppm (**b**). The ^1H environments are distant to one another, so only very weak splitting is observed: **a&a'** are weakly split into quartets and **b** into a triplet. Each alkene group contains one hydrogen atom per peak, while the methyl group of each methacrylate moiety contains three hydrogen atoms. The propyl moieties have three distinct ^1H environments, each containing two hydrogen atoms: **c** is a triplet at 4.1 ppm; **d** is a double triplet at 1.7 ppm; and **e** is a multiplet around 5 ppm. The in-chain methyl groups (**f&g**) generate the multiplet at 0.1 ppm, which has six hydrogen atoms per silicon.

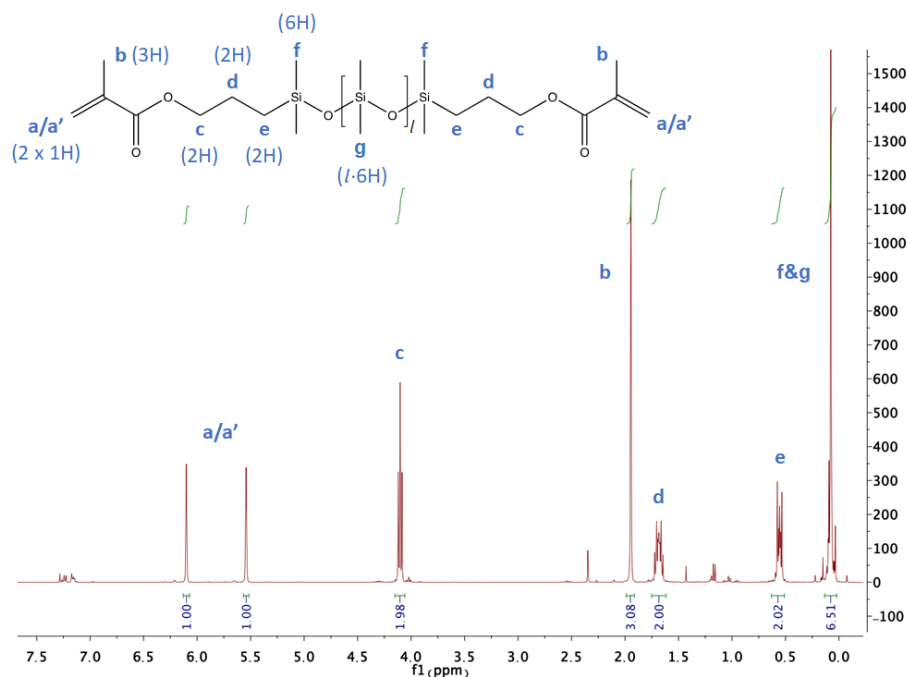


Figure 75: ^1H NMR spectrum of AB116678 with assigned peaks, corresponding to ^1H environments as labelled in inset siloxane.

The peaks observed in the ^1H NMR spectrum of AB116678 are listed below in Table 7 alongside typical ^1H NMR chemical shifts in siloxanes and hydrocarbons to summarise the assigned groups, observed and literature shift, and observed intensities.

Table 22: ^1H NMR correlation table for AB116678, relative to tetramethylsilane (SiMe_4 , TMS) with chloroform-D solvent (CDCl_3).

Group	Observed	Literature ^{17,266}	Intensity (AB116678)	
$\equiv\text{Si-CH}_3$	0.1	0	6.51	f,g
$\equiv\text{Si-CH}_2-$	0.5	0.5	2.02	e
$\equiv\text{C-CH}_2-\text{C}\equiv$	1.7	1.2-1.6	2.00	d
$=\text{C}=\text{C}-\text{C}-\text{H}$	2.0	1.6-2.2	3.08	b
$-\text{O}-\text{C}-\text{H}$	4.1	3.3-4.5	1.98	c
$=\text{C}=\text{CH}_2$	5.5, 6.1	4.5-6.5	1.00, 1.00	a,a'

Peak intensity ratios correspond to the number of hydrogen atoms and can therefore be used to estimate chain length according to Equation 6, where x and y are repeat unit (SiMe_2) and end group (MAP) moieties, a is peak area, n is the number of moieties in the average chain, and m is number of protons in group. The repeat moiety here is taken to be SiMe_2 rather than the repeat unit SiMe_2O , as the hydrogen atoms of the terminal SiMe_2 groups (**f**) do not resolve into a separate peak (from **g**) in the spectrum.

Equation 5: Calculation of number of repeat units n_x (i.e. degree of polymerisation) from ^1H NMR data, where x and y are the repeat unit and end group respectively, and a is area of peak, m is number of protons in the moiety, and n is number of moieties in the average polymer chain.¹⁹⁹

$$n_x = \frac{a_x \cdot m_y \cdot n_y}{a_y \cdot m_x}$$

From the spectrum of AB116678 above, the number of silicon atoms per bifunctional chain can be estimated based on the peak for one of the protons in the **a/a'** MAP group so that $n_{\text{SiMe}_2} = (6.51 \times 1 \times 2)/(1.00 \times 6) = 2.17$, or based on any of the other peaks associated with the MAP terminus (**b-e**). The number average molar mass M_n can then be calculated using Equation 7, which is the degree of polymerisation n multiplied by the molar mass of the repeat unit M_0 , plus the total molar mass of the end groups M_e .

Equation 6: Calculation of number average molar mass M_n , where n is the average number of repeat units, M_0 the molar mass of the repeat unit, and M_e the sum of molar masses of the end groups.¹⁹⁹

$$M_n = nM_0 + M_e$$

If the average chain contains 2.17 SiMe_2 moieties (average $l = 0.17$: $\text{M}^{\text{MAP}}\text{D}_{0.17}\text{M}^{\text{MAP}}$), then $M_n = (\text{SiMe}_2\text{O} \times 0.17) + \text{SiMe}_2\text{OMAP} + \text{SiMe}_2\text{MAP}$ and corresponds to $398.98 \text{ g mol}^{-1}$ for the bifunctional oligomer. This suggests that the typical oligomer contains two siloxane units,

although the dispersity is unknown as NMR spectroscopy is an averaging technique and can only be used to estimate the number average molecular weight M_n .¹⁹⁹

The molecular weights of the prepolymers are $398.98 \text{ g mol}^{-1}$ and $184.28 \text{ g mol}^{-1}$ for AB116678 and 2-EHA respectively and therefore phase separation of inks is unlikely: the 2-EHA may be considered a solvent and liquid-liquid phase separation is not expected from the Flory-Huggins equation.²⁰⁷ Polymers synthesised using AB116678 are not predicted to have PDMS-like surface energies as the silicone oligomer contains just two in-chain siloxane units on average and cannot orient these short segments to form a methyl surface in the manner that bulk PDMS would.⁵¹ The acrylate moieties are expected to lead to higher surface energies than PDMS due to hydrogen bonding and dipole-dipole interactions; the two monomers are expected to have favourable interactions with each other, while the alkyl branch on 2-EHA may interact favourably with QD stabilising ligands. While ink miscibility is predicted to be stable, a range of microstructures are possible in copolymers and microscale domains can increase scattering and reduce transparency.²³⁴ Experiments with the comonomer ratios and reaction conditions may be necessary to achieve microstructures desirable for optical sensing applications; chain transfer agents may be of interest in future studies.

As the rheological properties of an ink determines its printability,⁶ it was of interest to assess the precursors. The high throughput screening (HTS) method for rheological assessment of ink formulations required stable Newtonian fluids, as aspiration was used during measurement: ink constituents were identified and their intermolecular interactions and miscibility predicted, confirming that they were unlikely to undergo liquid-liquid phase separation.²⁰⁷ The precursors were mutually miscible, isotropic, and oligomeric or monomeric with $\leq 400 \text{ g mol}^{-1} M_n$, which precluded shear-dependant behaviour.^{17,178} Therefore, the precursors were compatible with the HTS method and rheological data was collected to inform ink formulation.

5.1.4. Rheology

Viscosity

Inkjet formulation has strict rheological requirements for printability; therefore, rheology of polymer precursors was assessed using a high-throughput screening (HTS) method developed by Zhou *et al.*,¹⁷⁸ as described in Section 3.2.2.4. The measured viscosities of the prepolymers are shown below in Table 23: for comparison, the manufacturer of AB116678 states that the viscosity is 4-6 mPa s and the density is 0.980 g cm⁻³, and literature values for 2-EHA at 20 °C are 1.7 mPa s viscosity and 0.887 g cm⁻³ density.²⁶⁷

Table 23: Viscosity of UV curing prepolymers at room temperature.

Chemical	Viscosity η mPa s			Mean mPa s	SD mPa s
AB116678	7.19	7.45	6.85	7.16	0.30
2-EHA	1.44	1.39	1.18	1.34	0.14

The average measured viscosity of AB116678 is 7.16 \pm 0.30 mPa s standard deviation (SD). This is higher than the viscosity range provided by the manufacturer, even when accounting for the accuracy reported by Zhou *et al.* (typically <10% difference in measurement between HTS and a conventional oscillatory rheometer¹⁷⁸). However, the manufacturer does not list the temperature associated with the viscosity value; if the value provided is viscosity at 25 °C, this accounts for the higher measured viscosity.

In contrast, the average measured viscosity of 2-EHA is 1.34 \pm 0.14 mPa s SD. This value is lower than the literature value of 1.7 mPa s. The HTS system typically underestimates viscosity, with percentage difference increasing as viscosity decreases: in the analytical model, different factors are dominant for low and high viscosity fluids.¹⁷⁸ Caution should be used in interpreting measured viscosity of low viscosity inks using the HTS.

The molecular weight of PDMS silicone fluids can be determined from their viscosity at room temperature (see Equation 8).¹⁷ However, ¹H NMR spectroscopy showed that there are very few repeating siloxane units in the AB116678 prepolymer, so the bulky terminating groups dominate intermolecular force contributions and the viscosity of AB116678 does not fit this model.

Surface tension

The surface tension values of AB116678 and 2-EHA were found to be $46.71 \pm 0.54 \text{ mN m}^{-1}$ and $43.57 \pm 0.42 \text{ mN m}^{-1}$ with 99.73% confidence intervals, respectively. Zhou *et al.*¹⁷⁸ reported that measured values for all test samples had <6% difference to conventional pendant DSA, and half of samples had <3% difference. Their paper reported a repeatability of $\pm 0.3\%$ deviation from the average; the deviation obtained here is higher at around 1%.

Contributions from the terminating groups dominate the rheological behaviour of AB116678. The acrylate moieties of both prepolymers give rise to stronger intermolecular forces than in bulk PDMS, originating from dipole-dipole interactions and hydrogen bonding, causing much higher surface tension values to be observed.

The printability is calculated from rheological parameters in Table 24 below according to the Printability Indicator Z , see Equation 1, where Z parameter values between 1 and 10 are printable. AB116678 has a Z parameter of 4.38, which is therefore inkjet compatible; its viscosity is lower than the ideal range (10-12 mPa s) and its surface tension higher than the ideal range ($28\text{-}42 \text{ mN m}^{-1}$),^{175,176} which can lead to the formation of satellite droplets. 2-EHA has an Z parameter of 21.5, which is therefore not compatible with inkjet; it has lower viscosity than the minimum limit (2 mPa s)⁵⁹ and is not printable without additives.

Table 24: Printability of UV curing prepolymers at room temperature. Values of shear viscosity, density, surface tension, and the printability parameter Z are given for each prepolymer.

Chemical	Viscosity η mPa s	Density ρ g cm ⁻³	Surface tension σ mN m ⁻¹	Diameter L μm	Z
AB116678	7.16 (± 0.30)	0.98	46.71 (± 0.54)	21.5	4.38
2-EHA	1.34 (± 0.14)	0.887 (lit) ²⁶⁷	43.57 (± 0.42)	21.5	21.5

5.1.5. Summary of UV cure reagents

Reagents were selected for formulations based on free radical photopolymerisation, using prepolymers with thiol-ene and/or (meth)acrylate moieties. Free radical photopolymerisation of acrylates is a common mechanism in UV inkjet, suitable for stable one-part inks with rapid curing at room temperature,⁵⁶ which can simplify calibration and increase throughput and resolution. For optical sensing materials, it was desirable as a route to materials with a range of macroscopic properties, with solvent-free inks which could prevent loss of transparency from microphases.²³⁴ While acrylate polymerisation is inhibited by oxygen and may require an inert printing environment, thiol-ene reactions are not, although thiols are well-known to quench QD fluorescence.^{263,264}

For optimal curing during inkjet printing with a longwave UV-LED source, two photoinitiators commonly used for silicone crosslinking⁵⁶ were selected for trials, for surface cure and depth cure properties respectively: DMPA and TPO. Acrylate-based prepolymers with jettable viscosity were selected so that copolymers with a range of macroscopic properties could be produced: a commercial methacryloxypropyl-terminated siloxane (AB116678), and 2-ethylhexyl acrylate (2-EHA). The siloxane was selected to produce more rigid polymers due to the steric hindrance of the methacrylate moiety and via crosslinking arising from bi-functionality. In contrast, 2-EHA was a mono-functional, branched monomer which could produce more flexible polymers, and was trialled to determine whether increased hydrocarbon content would improve dispersion of octadecylamine-capped QDs in the composite co-polymer. The molecular weight of the commercial silicone, AB116678, was determined to be $398.98 \text{ g mol}^{-1}$ using ^1H NMR spectroscopy, and monomers were predicted to form stable inks.

Rheological parameters of each prepolymer were obtained to assess needs for formulation. AB116678 was found to be jettable: viscosity was low ($7.16 \pm 0.30 \text{ mPa s}$) and surface tension high ($46.71 \pm 0.54 \text{ mN m}^{-1}$) as compared to the ideal values given by the printer manufacturer^{175,176}, corresponding to a printability parameter of 4.38. 2-EHA was much less viscous than AB116678 and was therefore found to not be jettable (Z parameter 21.5). There was a 21% difference between measured viscosity and the literature value of 2-EHA (1.7 mPa s)²⁶⁷; the HTS method appears to underestimate low viscosity fluids¹⁷⁸ and this was noted during subsequent formulation.

Overall, components for UV curable silicone inks were discussed and selected. The next section describes the screening of formulations of inks using the HTS method.

5.2. Ink formulation

As stated previously, the rheology of inks must meet requirements for stable drop formation to be printable via inkjet. A screening of prepolymers and photoinitiators was carried out to guide ink formulation (objective *O1*), as detailed below. In this section:

- Inks were prepared with varied photoinitiator loadings to assess their effect on rheology and to screen potential formulations
- Rheological parameters were obtained for inks (viscosity, density, surface tension)
- The *Z* parameter was calculated to confirm printability of inks.

Rheological measurements were carried out using high-throughput screening to identify suitable formulations as described in Methodology, Section 3.2.2.4. The surface tension and viscosity of potential formulations was calculated at room temperature using a HTS system as reported in Zhou *et al.*¹⁷⁸ The initial approach was to use an inert nitrogen atmosphere for printing to minimise yellowing and maximise mechanical properties, so low PI loadings were trialled (≤ 1 wt%); further work could be carried out with loadings between 3-10 wt% for air curing.²⁶⁵

Two prepolymers were investigated, as shown in Figure 74 above: methacryloxypropyl-terminated PDMS (abcr **AB116678**, 4-6 cP), and 2-ethylhexyl acrylate (**2-EHA**). Potential inks were formulated with 0.125-1.0 wt% of one of two photoinitiators: 2,2-dimethoxy-2-phenylacetophenone (**DMPA**), a.k.a. Omnirad 651 (see Section 5.3); and phenylbis(2,4,6-trimethylbenzoyl)-phosphine oxide (**TPO**), a.k.a. Omnirad 819 (Section 5.4). The HTS approach required formulations with Newtonian behaviour for accurate measurement, as fluids are subject to different shear rates during aspiration as part of the measurement process. The selected prepolymers were monomers or oligomers, mutually miscible, and isotropic, and therefore shear-dependant behaviour arising from polymer entanglement or flow-induced orientation does not occur with these prepolymers.^{17,178}

5.2.1. PDMS inks

Potential ink formulations were prepared and their rheological properties measured so that their printability could be calculated (see Equation 1) to confirm their compatibility with inkjet.⁶ PDMS-inks were formulated by adding one of two photoinitiators to AB116678 at different weight percent (wt%) loadings. Measurement of AB116678 using the HTS yielded a viscosity value of 7.16 ± 0.30 mPa s and a surface tension of 46.71 ± 0.54 mN m⁻¹; these values are compared to the measured properties of the inks below. Henceforth, X wt% DMPA-PDMS ink refers to AB116678 containing X wt% DMPA photoinitiator, and likewise for inks formulated with TPO photoinitiator.

DMPA-PDMS inks

The density of the inks was found to be 0.98 g cm⁻³ across the range of DMPA loadings, with 0.01 g cm⁻³ equipment tolerance, unchanged from that of AB116678. The viscosities of DMPA-PDMS with different PI loadings at room temperature are shown below in Table 25. Formulations at all PI loadings were within the viscosity limits given by the Fujifilm Dimatix printer guidelines (2-30 mPa s),⁵⁹ although lower than the ideal range of 10-12 mPa s.^{175,176}

Table 25: Viscosity of DMPA-PDMS inks at room temperature.

<i>PI loading</i> wt%	<i>Viscosity η</i> mPa s			<i>Mean</i> mPa s	<i>SD</i> mPa s
1	7.34	7.76	6.91	7.34	0.43
0.5	7.40	7.83	6.78	7.34	0.53
0.25	7.86	7.70	7.10	7.55	0.40
0.125	7.02	7.28	6.80	7.03	0.24

No obvious increase in viscosity was observed with increasing PI concentration, as plotted in the graph below (Figure 76). While the lowest loading (0.125 wt% DMPA) did have the lowest viscosity, this was lower than that measured for AB116678 (7.16 ± 0.3 mPa s SD) and the next lowest loading had the highest viscosity. The mean viscosity of all inks, 7.32 mPa s (26.8% lower than the ideal range) is within standard deviation of measured values. There is a slight increase in viscosity of 0.16 mPa s upon addition of DMPA to AB116678, but this would have negligible effect on printability and no clear trend is seen across this range of loadings.

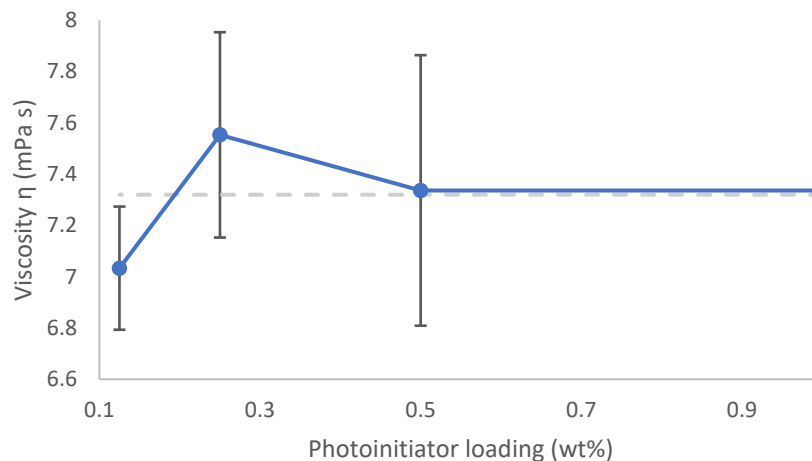


Figure 76: Viscosity of DMPA-PDMS inks as a function of DMPA loading. Error bars show standard deviation; the average viscosity is plotted as a grey dotted line (7.32 mPa s). Viscosity in mPa s (0.125, 0.25, 0.5, 1 wt% DMPA): 7.34, 7.34, 7.55, 7.03.

Surface tensions were obtained for inks, presented below in Table 26 with 99.73% confidence intervals. Surface tension values for all PI loadings were similar; more variance was seen in measurement than between average values for loadings. The average surface tension was 46.72 mN m^{-1} , unchanged from the value obtained for AB116678 ($46.71 \pm 0.54 \text{ mN m}^{-1}$, 99.73% confidence interval). This was 11.2% higher than the ideal range given by the manufacturer ($28 - 42 \text{ mN m}^{-1}$)^{175,176} but within the extended range typically recommended for inkjet ($20\text{-}50 \text{ mN m}^{-1}$)³⁵.

Printability indicators for each PI loading were calculated below in Table 26 according to the Printability Indicator, see Equation 1. The DMPA-PDMS inks have similar rheology and are therefore expected to have similar jetting behaviour. The average Z parameter was found to be 4.30 and therefore predicted to be jettable. As viscosity is slightly low and surface tension slightly high, a minor tendency to form satellite drops can be expected.

Table 26: Printability of DMPA-PDMS inks at room temperature. Values of shear viscosity, density, surface tension, and the printability parameter Z are given for each ink.

PI loading wt%	Viscosity η mPa s	Density ρ g cm ⁻³	Surface tension σ mN m ⁻¹	Diameter L μm	Z
1	7.34 (± 0.43)	0.98 (± 0.01)	46.82 (± 0.60)	21.5	4.28
0.5	7.34 (± 0.53)	0.98 (± 0.01)	46.78 (± 0.45)	21.5	4.28
0.25	7.55 (± 0.40)	0.98 (± 0.01)	46.51 (± 0.54)	21.5	4.15
0.125	7.03 (± 0.24)	0.98 (± 0.01)	46.77 (± 0.33)	21.5	4.47

TPO-PDMS inks

The density of the TPO-PDMS inks was found to be 0.98 g cm^{-3} ($\pm 0.01 \text{ g cm}^{-3}$ tolerance) across the range of PI loadings; neither photoinitiator had a significant effect on the density of AB116678 at these loadings. Viscosities of TPO-PDMS with different PI loadings at room temperature are shown below in Table 27 with standard deviation (SD). Viscosity was 2.73% higher than for DMPA-PDMS analogues on average, but values are still within viscosity limits at all PI loadings.

Table 27: Viscosity of TPO-PDMS inks at room temperature.

PI loading wt%	Viscosity η mPa s			Mean mPa s	SD mPa s
1	7.41	7.76	7.26	7.48	0.26
0.5	7.51	7.94	7.44	7.63	0.27
0.25	7.44	7.41	7.33	7.39	0.06
0.125	7.56	7.87	7.33	7.59	0.27

No obvious increase in viscosity was observed with increasing PI concentration of the TPO-PDMS inks, as plotted in the graph below (Figure 77). The mean viscosity was 7.52 mPa s, 24.8% lower than the ideal range.

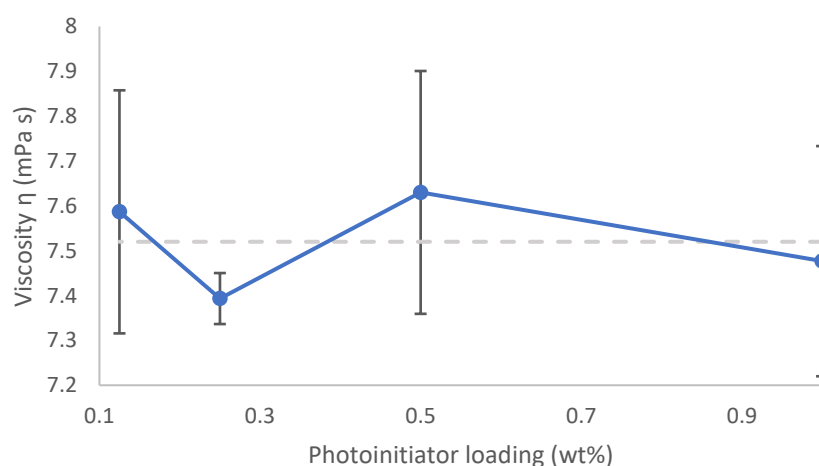


Figure 77: Viscosity of TPO-PDMS inks as a function of TPO loading. Error bars show standard deviation; the average viscosity is plotted as a grey dotted line (7.52 mPa s). Viscosity in mPa s (0.125, 0.25, 0.5, 1 wt% TPO): 7.48, 7.63, 7.39, 7.59.

Surface tension values are shown below in Table 28 with 99.73% confidence intervals. Surface tension was similar for all PI loadings with an average value of 46.71 mN m⁻¹, identical to DMPA-PDMS inks and AB116678; neither photoinitiator had a measurable effect on surface tension.

The Z parameter at each PI loading was calculated below in Table 28. TPO-PDMS inks have similar rheology across all PI loadings, and to DMPA-PDMS analogues and AB116678. Therefore, the printability was also similar, with the average Z parameter being 4.17.

Table 28: Printability of TPO-PDMS inks at room temperature. Values of shear viscosity, density, surface tension, and the printability parameter Z are given for each ink.

<i>PI loading</i> wt%	<i>Viscosity η</i> mPa s	<i>Density ρ</i> g cm ⁻³	<i>Surface tension σ</i> mN m ⁻¹	<i>Diameter L</i> μ m	<i>Z</i>
1	7.48 (\pm 0.26)	0.98 (\pm 0.01)	46.77 (\pm 0.27)	21.5	4.20
0.5	7.63 (\pm 0.27)	0.98 (\pm 0.01)	46.63 (\pm 0.57)	21.5	4.11
0.25	7.39 (\pm 0.06)	0.98 (\pm 0.01)	46.71 (\pm 0.27)	21.5	4.25
0.125	7.59 (\pm 0.27)	0.98 (\pm 0.01)	46.73 (\pm 0.54)	21.5	4.13

In summary, AB116678 formulations ('PDMS inks') containing different loadings of photoinitiator were all found to be jettable. Viscosity was not observed to increase with PI loading for either photoinitiator across the range of loadings tested. However, the presence of PI was associated with a small increase in average viscosity: a 2.23% increase in viscosity was seen upon addition of DMPA and a 5.03% increase upon addition of TPO. Neither photoinitiator at any loading was seen to have any effect on density nor surface tension as compared to AB116678. Formulations had average Z parameters of 4.30 (DMPA-PDMS) and 4.17 (TPO-PDMS), indicating that these are printable. Therefore, AB116678 inks have suitable rheology for inkjet at all PI loadings investigated - and viscosity is low enough that it is possible to use higher loadings - for both DMPA and TPO.

5.2.2. 2-EHA inks

2-EHA-inks were prepared for screening from a 1:1 ratio by weight of AB116678 and 2-EHA. While this is not necessarily the ideal ratio, it was selected as an upper limit in screening for rheology of formulations and further optimisation could be carried out in future studies. Henceforth, X wt% DMPA-2-EHA ink refers to a 50 wt% mixture of AB116678 in 2-EHA, to which X wt% DMPA photoinitiator is added. Analogous notation is used for inks formulated with TPO photoinitiator. During measurement of 2-EHA in Section 5.1.4, the HTS system was seen to underestimate viscosity. In interpreting the viscosity results below, it was important to consider that measured values are likely lower than the actual values, with greater percentage difference for lower viscosity fluids.

DMPA-2-EHA inks

The density of the inks was found to be 0.92 g cm^{-3} ($\pm 0.01 \text{ g cm}^{-3}$ tolerance) across the range of PI loadings, in between the densities of AB116678 (0.98 g cm^{-3}) and 2-EHA (0.887 g cm^{-3}). The room temperature viscosities of DMPA-2-EHA inks with different loadings are shown below in Table 29 with standard deviation (SD). Inks at all PI loadings were on the lower end of the viscosity limits given by the Fujifilm Dimatix printer guidelines (2-30 mPa s),⁵⁹ and much lower than the ideal range of 10-12 mPa s.^{175,176}

Table 29: Viscosity of DMPA-2-EHA inks at room temperature.

PI loading wt%	Viscosity η mPa s			Mean mPa s	SD mPa s
1	3.15	3.02	3.23	3.13	0.11
0.5	3.19	3.38	3.46	3.34	0.14
0.25	3.68	3.59	3.97	3.75	0.20
0.125	3.29	3.16	3.70	3.38	0.28

Viscosity as a function of PI loading is plotted below in Figure 78 and showed no obvious correlation. The average viscosity value across all loadings was 3.40 mPa s (66.0% lower than the ideal range), a 53.55% decrease from the DMPA-PDMS analogues. HTS may underestimate viscosity of inviscous fluids: assuming that fluids of similar viscosity have similar percentage differences to measurement by HTS, a 14.6% difference is expected,¹⁷⁸ which gives an estimate of 3.98 mPa s.

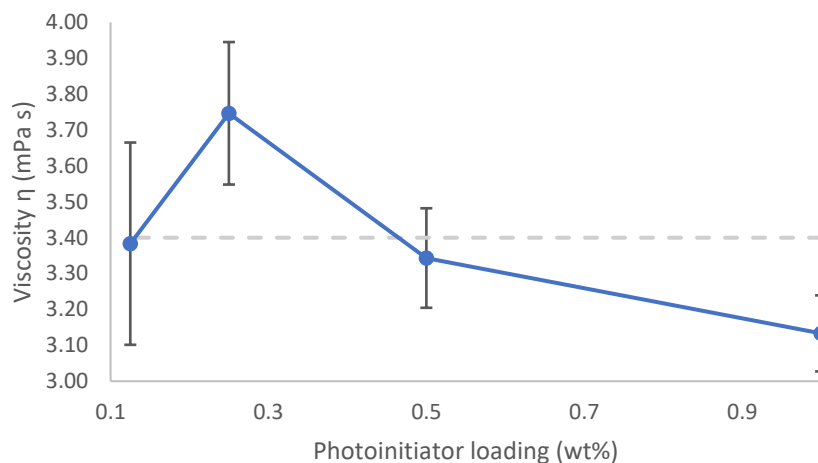


Figure 78: Viscosity of DMPA-2-EHA inks as a function of DMPA loading. Error bars show standard deviation; the average viscosity across all loadings is plotted as a grey dotted line (3.40 mPa s). Viscosity in mPa s (0.125, 0.25, 0.5, 1 wt% DMPA): 3.13, 3.34, 3.75, 3.38.

The surface tension values (shown in Table 30 with 99.73% confidence intervals) were similar for all PI loadings except for 0.5 wt%, which appeared to be anomalously low with greater deviation. The average surface tension was 44.20 mN m^{-1} , a 5.37% decrease from the DMPA-PDMS analogues, and an intermediate value between AB116678 (46.71 mN m^{-1}) and 2-EHA (43.57 mN m^{-1}).

Z parameters were calculated for inks at each PI loading in Table 30 below. The average Z parameter was 8.73, towards the upper limit for printability and indicating a strong tendency to form satellite droplets. If the actual viscosities are assumed to be higher than the measured values by a 14.6% difference, the average Z parameter becomes 7.46 which is more favourable.

Table 30: Printability of DMPA-2-EHA inks at room temperature. Values of shear viscosity, density, surface tension, and the printability parameter Z are given for each ink.

PI loading wt%	Viscosity η mPa s	Density ρ g cm ⁻³	Surface tension σ mN m ⁻¹	Diameter L μm	Z
1	3.13 (± 0.11)	0.92 (± 0.01)	44.66 (± 0.27)	21.5	9.50
0.5	3.34 (± 0.14)	0.92 (± 0.01)	43.06 (± 0.45)	21.5	8.74
0.25	3.75 (± 0.20)	0.92 (± 0.01)	44.63 (± 0.33)	21.5	7.92
0.125	3.38 (± 0.28)	0.92 (± 0.01)	44.46 (± 0.27)	21.5	8.77

TPO-2-EHA inks

The density of the TPO-2-EHA inks was also found to be 0.92 g cm^{-3} ($\pm 0.01 \text{ g cm}^{-3}$ tolerance) across the range of PI loadings, same as for the DMPA-2-EHA analogues; photoinitiators were not observed to have any effect on density at these loadings. The viscosities of TPO-2-EHA inks with different PI loadings at room temperature are shown below in Table 31. The average viscosity was 11.2% higher than for DMPA-2-EHA analogues but were still close to the lower limit for viscosity at all PI loadings.⁵⁹

Table 31: Viscosity of TPO-2-EHA inks at room temperature.

PI loading wt%	Viscosity η mPa s			Mean mPa s	SD mPa s
1	3.08	2.93	3.22	3.08	0.15
0.5	4.39	4.50	4.48	4.46	0.06
0.25	3.73	3.96	4.20	3.96	0.24
0.125	3.41	3.68	3.80	3.63	0.20

Viscosity as a function of PI loading is shown below in Figure 79. It is unclear whether PI loading correlates to viscosity: 0.5 wt% TPO has anomalously high viscosity and 1 wt% TPO anomalously low. The average measured viscosity value across all loadings was 3.78 mPa s (62.2% lower than the ideal range), approximately half that of the TPO-PDMS analogues. If assuming a 14.6% difference, the corrected value is estimated to be 4.42 mPa s.

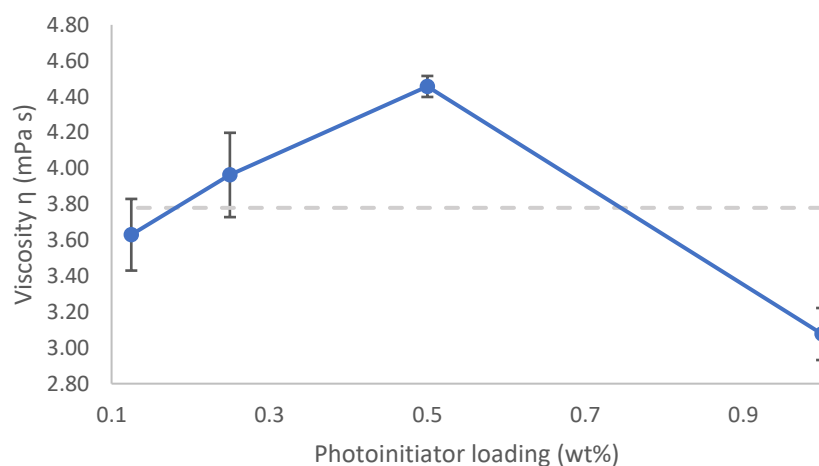


Figure 79: Viscosity of TPO-2-EHA inks as a function of TPO loading. Error bars show standard deviation; the average viscosity across all loadings is plotted as a grey dotted line (3.78 mPa s). Viscosity in mPa s (0.125, 0.25, 0.5, 1 wt% TPO): 3.08, 4.46, 3.96, 3.63.

Surface tension values at each loading are listed below in Table 32 with 99.73% confidence intervals. The average surface tension for all loadings is 43.92 mN m^{-1} , 0.63% lower than DMPA-2-EHA analogues and approximately 6% lower than TPO-PDMS analogues. The surface tensions of 0.5 and 1 wt% TPO were anomalously high and low respectively, as was observed for viscosity. As the average surface tension values for all other inks have had high repeatability with little variation, regardless of photoinitiator loading, this suggests that this may be a result of human error during sample preparation.

Printability indicators for each PI loading were calculated below in Table 32, with an average Z parameter of 7.93. If there is a difference between actual and measured viscosity of 14.6%, the average Z parameter becomes 6.77. There is a broad range of Oh^{-1} values due to the anomalous results for 0.5 and 1 wt% TPO: if the cause is assumed to be human error, then a Z parameter of 7.79 is obtained when calculated using average viscosity and surface tension values. This becomes 6.69 when assuming that measured viscosity is lower than actual viscosity.

Table 32: Printability of TPO-2-EHA inks at room temperature. Values of shear viscosity, density, surface tension, and the printability parameter Z are given for each ink.

<i>PI loading</i> wt%	<i>Viscosity η</i> mPa s	<i>Density ρ</i> g cm ⁻³	<i>Surface tension σ</i> mN m ⁻¹	<i>Diameter L</i> μm	<i>Z</i>
1	3.08 (± 0.15)	0.92 (± 0.01)	42.73 (± 0.33)	21.5	9.44
0.5	4.46 (± 0.06)	0.92 (± 0.01)	45.25 (± 0.45)	21.5	6.71
0.25	3.96 (± 0.24)	0.92 (± 0.01)	43.85 (± 0.42)	21.5	7.44
0.125	3.63 (± 0.20)	0.92 (± 0.01)	43.86 (± 0.27)	21.5	8.11

In summary, 2-EHA inks had viscosity values approximately half that of the corresponding PDMS inks, close to the lower limits given by the printhead manufacturer; while all inks were found to be jettable, they have correspondingly high Z parameters (8.73 and 7.93, for DMPA and TPO inks respectively) and are predicted to be vulnerable to satellite droplet formation. TPO inks were again observed to have slightly higher average viscosity than DMPA inks, although no clear correlation was seen between rheology and PI loading.

5.2.3. Summary of UV cure inks

Formulations were assessed using an HTS approach to determine printability and achieve objective *O1*. AB116678 and 50 wt% AB116678 in 2-EHA were formulated with DMPA or TPO with different photoinitiator loadings. Low loadings were tested to minimise yellowing in optical sensing materials as this could alter temperature readings.

Viscosity was not observed to increase with PI loading for any formulation across the range of loadings tested. However, the presence of PI was associated with a small increase in viscosity of PDMS inks: a 2.23% increase in viscosity was seen upon addition of DMPA (7.32 mPa s) and a 5.03% increase upon addition of TPO (7.52 mPa s). Similarly, TPO-2-EHA inks had higher average viscosity than DMPA-2-EHA inks (3.40 and 3.78 mPa s for DMPA-2-EHA and TPO-2-EHA inks respectively). The difference between viscosity of DMPA and TPO inks was 0.20 and 0.38 mPa s for PDMS and 2-EHA inks, respectively.

Neither density nor surface tension were observed to be affected by PI loading in any formulation tested. Surface tension was unchanged from that of AB116678 (46.71 mN m⁻¹) in all PDMS inks. However, there was a small difference in average surface tension between DMPA (44.20 mN m⁻¹) and TPO (43.92 mN m⁻¹) in 2-EHA inks.

PDMS inks had viscosities at the lower end of the ideal jetting range for the Dimatix, and surface tensions at the higher end of the ideal range.^{175,176} Average *Z* parameters were 4.30 (DMPA) and 4.17 (TPO), indicating that these are printable, and PDMS inks had suitable rheology for inkjet at low loadings of both DMPA and TPO.

2-EHA inks had lower viscosities than PDMS inks and slightly lower surface tensions; these were intermediate values between properties of AB116678 and 2-EHA. Average *Z* parameters were 8.73 (DMPA) and 7.93 (TPO), indicating that - while these are printable - the low viscosity of the 2-EHA inks makes them vulnerable to formation of satellite droplets. However, the HTS approach is noted to underestimate viscosity, particularly for low viscosity fluids. *Z* parameters using adjusted viscosity values (14.6% difference) are 7.46 (DMPA) and 6.77 (TPO).

Overall, objective *O1* was met, and all formulations tested were found to be jettable at room temperature; the next section covers the investigation of QD composite synthesis.

5.3. DMPA-containing composites

In this section, composites are synthesised using inks formulated with DMPA photoinitiator. This section describes:

- Inks formulated for acrylate-based free radical photopolymerisation with AB116678 and 2-EHA prepolymers
- Inks formulated for thiol-ene-based crosslinking with DODT and PETMP monomers
- Investigation into the effect of DMPA loading on photoluminescence.

2,2-Dimethoxy-2-phenylacetophenone (DMPA), or Omnirad 651, is the most commonly used photoinitiator for free-radical crosslinking of silicones.⁵⁶ It is a dialkoxyacetophenone-class PI which undergoes homolytic bond breaking to form a benzoyl radical and an acetal radical. DMPA is considered a “general purpose” PI due to its broad absorption and DMPA is able to absorb the 365 nm output of UV LEDs to give surface cure. DMPA has high thermal stability, which is ideal for optical temperature-sensing materials as decomposition products of residual photoinitiators could cause discoloration and affect measurement.

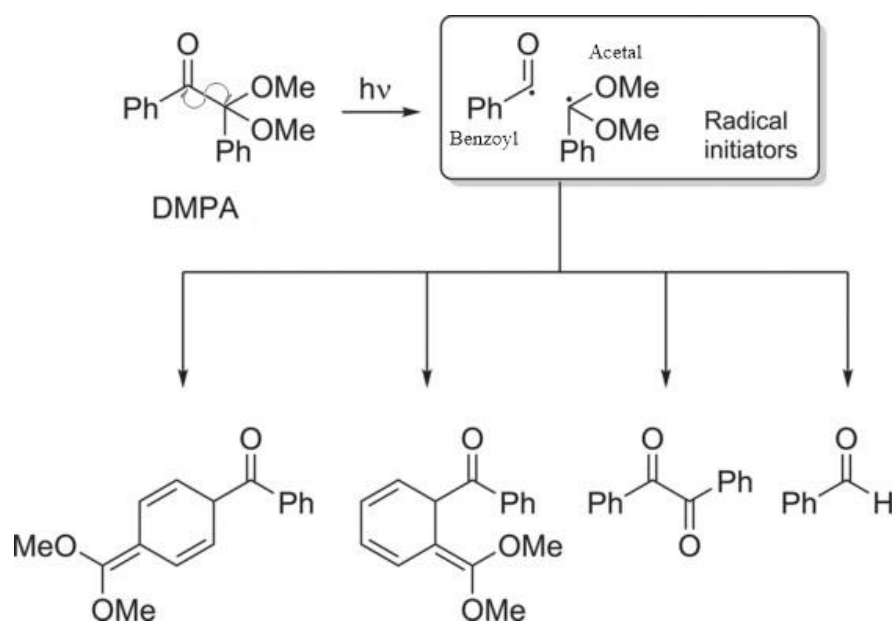


Figure 80: Photolysis of DMPA, showing the formation of benzoyl and acetal fragments (top right) and their recombination products below. Reproduced with permission from Wang *et al.*⁵⁶

The main disadvantage of DMPA is that there may be yellowing after curing, which is not desirable for a material intended for use in optical thermometry. Discoloration is due to radical recombination products, shown in Figure 80 above, which can be minimised by reducing the PI:acrylate ratio;⁵⁶ printing in an inert environment would facilitate lower PI loadings in ink. It may also be possible to account for yellowing when calibrating the material as a sensor by depositing a control sample which contains no QDs.

5.3.1. PDMS and 2-EHA inks

An initial test was carried out to confirm that QD composites could be produced (see Methodology, Section 3.2.5.2.). 0.5 wt% DMPA-PDMS was prepared, from which 0.25 wt% DMPA-2-EHA was also prepared. 10 μ L of quantum dot solution (0.005 wt% in octyl acetate) was added to each vial per 0.1 mL of prepolymer. The samples were deposited onto glass slides and cured under a 365 nm UV lamp; this was initially done in air to investigate oxygen-sensitivity.

The DMPA-PDMS ink cured but the QDs did not disperse well and there was no visible fluorescence. In the DMPA-2-EHA ink, the QDs appeared to disperse well and retained fluorescence, but the polymer did not cure. The PDMS ink contained more photoinitiator than the 2-EHA ink (0.5 wt% DMPA compared to 0.25 wt%); as photoinitiation is oxygen-sensitive, 0.25 wt% DMPA loading may be insufficient without de-gassing. It could also be that the greater free volume arising from the lower packing efficiency of 2-EHA ensured that oxygen was well-distributed through the sample and more thoroughly hindered curing. In terms of differences in QD dispersion, it appears that the hydrocarbon chain of the 2-EHA monomer may have led to a more favourable interaction overall with the octadecylamine ligands on the QDs, resulting in better dispersion. While the ligand shell of QDs in the 2-EHA composites may have been stabilised effectively and therefore better passivated,^{110,122} fluorescence in QD-PDMS may have been quenched by QD aggregation^{122,249} and poorly dispersed QDs are vulnerable to surface damage.

As discussed in Appendices, obtaining stable dispersions of QDs in polymers is challenging. Strong van der Waals attraction between QDs and large surface energy mis-match between silicones and CdSe/ZnS drives the formation of large QD agglomerates with interdigitisation of alkyl ligands to minimise contact with the matrix.^{122,268,269} QDs with grafted chains of similar composition to the host matrix can improve dispersion: morphology is dependent on multiple factors,²⁶⁹ of which grafting density and the ratio of grafted/matrix chain length are key parameters.¹²²

In this formulation, the octadecylamine ligands are dissimilar to AB116678 but have comparable composition to 2-EHA; the C18 tail is longer than the hydrocarbon chain in 2-EHA and octadecylamine contains no oxygen atoms. Better dispersion is expected in 2-EHA inks and therefore improved stability of the passivating ligand shell during photopolymerisation, which benefits sensing by improving QD photostability. However, the ligands are not bulky enough to fully screen core-core interactions, so aggregation is still expected and depletion flocculation may occur during photo-polymerisation.¹²²

Printing

A brief printing trial was carried out as described in Section 3.2.3.4. to confirm QD-ink jetting and to test the DMPA loading in an inert environment. 1 mL of 0.25 wt% DMPA-2-EHA ink was prepared and 10 μL of QD solution (0.005 wt% in octyl acetate) was added; one-tenth of the previous amount was used to conserve material. This was loaded into a Dimatix printer under a nitrogen atmosphere (1.1% O_2).

The ink was ejected using waveform W_2 (Figure 140, Appendices) to produce an ordered grid of droplets with approximately 35 μm diameter, as shown below in Figure 81, but the ink did not cure. The oxygen level may have been too high for the curing conditions of the printing process, or the DMPA loading may have been too low for curing even in an inert environment. It was also possible that octyl acetate solvent or QDs of the added solution interfered in radical crosslinking. While this confirmed that UV inks containing QDs can be jetted with controlled deposition, photoinitiator loading experiments were needed to determine the required concentration of DMPA and to explore factors affecting cure.

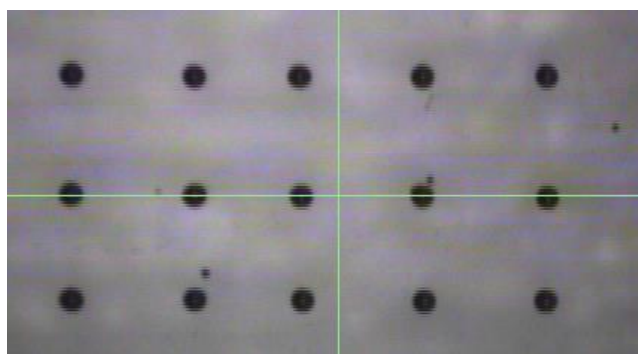


Figure 81: Drop array printed onto a silanised glass slide, viewed through the fiducial camera of a Dimatix printer. Droplet diameter is approximately 35 μm .

Photoinitiator loading

Photoinitiator loading experiments were carried out to ascertain ideal DMPA loadings to enable printing. Drop casting was carried out with 0.5, 1.25, and 2.5 wt% DMPA-2-EHA inks; loadings exceeded those tested in Section 5.2, to investigate accelerated cure rate and the effect of high radical concentration on PL. 10 μL of each ink was put on separate glass slides and cured in a glove box filled with nitrogen (0.5% O_2) and cured under a 365 nm UV lamp. All samples cured enough to solidify within 30 s: samples with more PI cured more rapidly.

It is well-known that higher photoinitiator loadings lead to faster curing. Reaction rate sharply increases as PI loading increases between 0 wt% to 3-4 wt% PI, after which it begins to level off, reaching a maximum at \sim 6-7 wt% PI.²⁶² Higher concentrations of radicals are produced which means that more reactions are initiated; high PI loadings are used to accelerate curing in air with oxygen-sensitive PIs, and IGM Resins recommends 5-10 wt% PI for inkjet.²⁶⁵ However, this approach limits the mechanical properties of the end-product: radicals initiate many chains, which leads to a large number of shorter polymer chains rather than long entangled chains. Excess PI leads to greater discoloration and may leach out of the matrix.²⁶² For material jetting AM, deposited material is required to cure rapidly enough to pin to the substrate and resist flow. Therefore, minimal PI loading is preferred to maximise mechanical properties and transparency and minimise discoloration and leaching in temperature sensing materials without sacrificing print quality.

Analogous QD composite inks were prepared by adding 10 μL of QD solution (0.005 wt% in octyl acetate) to 90 μL of each DMPA-2-EHA ink, and drop casting experiments were carried out as described above to produce QD-composites. As no discernible difference in cure rate was observed between samples with and without QDs, it appears that QDs did not significantly compete with PI for UV absorption. The fluorescence of each sample appeared to be stable and was similar regardless of photoinitiator concentration.

Overall, inks were observed to cure in inert conditions: 1.1% O_2 during the printing trial was sufficient to prevent cure at 0.25 wt% DMPA, while 0.5% O_2 allowed curing of solid polymer and composites at \geq 0.5 wt% DMPA. Faster curing was achieved by increasing PI loading; inks were expected to have reactivity compatible with the Dimatix printer, and the fluorescence of the QDs appeared to be unaffected by DMPA concentration. While it had been demonstrated that inks with low DMPA loading could cure under nitrogen, oxygen-sensitivity was shown to be a considerable challenge, and so initial tests were carried out with thiol monomers to investigate the thiol-ene crosslinking mechanism.

5.3.2. Thiol-ene inks

Thiol-ene reactions are another mechanism for UV-curable silicones and have been utilised for open-bench stereolithography (SLA) of silicones by Wallin *et al.*²⁷⁰ Thiol-ene inks offer some distinct advantages over acrylates: high conversions, low oxygen inhibition, and less shrinkage.⁵⁶ Acrylate thin films often have poor surface cure due to oxygen inhibition, which reduces transparency²⁷¹; thiol-ene inks may cure with lower PI loadings and/or without an inert atmosphere, leading to optical sensing materials with less discoloration and fewer optical aberrations. However, single-part inks have limited shelf life as thiol-ene reactions are thermally-activated and will occur over time. While thiols are well-known to quench CdSe/ZnS QDs,^{263,264} which would decrease or eradicate the signal for sensing, thiol-QD affinity has been used to improve QD dispersion in silicones.^{272–275} In thiol-acrylate systems, there is competition between two reactions: chain growth of the acrylate and step growth via thiol-ene mechanism. The molar ratio of thiol to ene is therefore important for determining microstructure and material properties.²⁷⁶

Two mercaptan monomers were obtained, shown below in Figure 82: pentaerythritol tetrakis(3-mercaptopropionate) (**PETMP**) and 2,2'-(ethylenedioxy)diethanethiol (also known as 3,6-dioxa-1,8-octanedithiol or **DODT**). PETMP was much more viscous and had 4 thiol moieties, which would lead to a higher crosslinking density and rigidity.

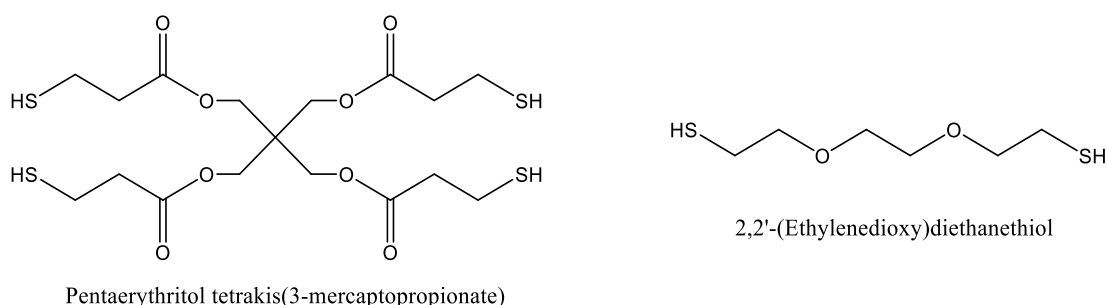


Figure 82: Mercaptan monomers PETMP (left) and DODT (right).

A preliminary test was done to determine whether it was feasible to use the thiol monomers, or whether they would quench the QD fluorescence. 0.2 ml of PDMS was mixed with 0.1 ml of DODT and 2 drops of the more viscous PETMP, and 2.5 wt% DMPA added. The sample was cured on a glass slide in an inert environment under a 365 nm UV lamp after the DMPA-2-EHA samples (see Section 5.3.1 and 3.2.5.2). Samples cured rapidly, with and without QDs, and the QD composite appeared transparent with visible fluorescence.

Compared to the DMPA-2-EHA composites, the cured polymer was harder, most likely due to higher crosslinking density from PETMP. The vials of DMPA-2-EHA and DMPA-PDMS-

DODT-PETMP prepolymers were examined under the UV lamp; the fluorescence of the PDMS-DODT-PETMP weaker, indicating quenching by QD ligand exchange.^{263,264} The PDMS-DODT-PETMP in the vial fully cured in seconds during examination. Overall, this preliminary investigation showed that there was potential to utilise thiol-ene reactions for QD-silicone composites.

5.3.3. Loss of photoluminescence

UV curing of QD-silicone composites with various monomers had seemed promising. However, all samples lost fluorescence once cured and were therefore unsuitable for sensing applications: the vials of uncured inks were put under the UV lamp to cure into monoliths with the intention of photographing them, but the red fluorescence disappeared in seconds. The droplets cured on glass slides were no more stable and appeared to have lost their fluorescence over the course of 48 hours. It was unclear what the quenching mechanism was and at which point(s) in the synthesis of the nanocomposites this occurred.

Inks with and without photoinitiator were prepared in vials to assess the effect of PI loading on photoluminescence, as detailed in Section 3.2.5.2. In brief, vials of DMPA-PDMS, DMPA-2-EHA, DMPA-DODT, and DMPA-PETMP inks were prepared with both 0 wt% and 2.5 wt% DMPA loadings. Additionally, a vial of 0.25 wt% DMPA-2-EHA was prepared to test low PI loading. 10 μ L of QD solution (0.005 wt% in octyl acetate) was added per 100 μ L sample and the vials were illuminated under a 365 nm UV lamp in a glove box (0.5% O₂).

Samples with DODT did not fluoresce, regardless of the presence or absence of photoinitiator. It is likely that ligand exchange occurred, and the quantum dots were quenched by the thiol group.^{263,264} DODT inks solidified via a thiol-ene mechanism and underwent a colour change to pale green. For the other ink formulations, all samples with photoinitiator initially showed bright fluorescence which faded to nothing as they cured under UV. The fluorescence of the 0.25 wt% DMPA-2-EHA sample did decrease more slowly but ceased in under a minute of irradiation.

Samples without photoinitiator did not lose fluorescence as quickly as the samples with photoinitiator did. A photograph of samples with 0 wt% DMPA taken after 48 hours is shown below in Figure 83. PDMS and 2-EHA ink samples retained their fluorescence under the UV lamp, but when monitored 24 hours later they appeared approximately half as bright, and within 48 hours there was no visible fluorescence. Only PETMP ink retained fluorescence; it solidified even without photoinitiator (most likely by thiol-ene reaction as DODT ink also solidified) and the intensity did not appear to decrease after 48 hours.

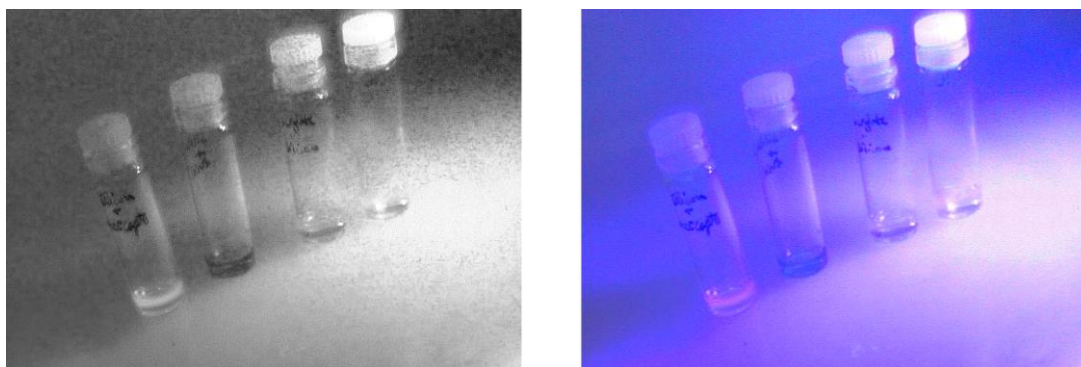


Figure 83: Photograph of vials of inks without DMPA, from left-to-right PETMP, DODT, 2-EHA, and PDMS inks. Right: Colour photograph of samples without photoinitiator after 48 hours, where only PETMP ink remains fluorescent. Left: Same image with the red channel isolated.

Overall, photoinitiator loading was demonstrated to lead to loss of PL, whether by a direct or indirect mechanism: all samples containing DMPA were rapidly quenched. Poor compatibility with the host matrix can lead to poor QD passivation and aggregation in QD-polymer composites, which severely reduces photostability.^{259,268,277,278} Phase separation and ligand detachment may be triggered by photopolymerisation.²⁷⁷⁻²⁷⁹ Furthermore, it is possible that radicals etched the exposed surface of the QDs in samples containing photoinitiator: photoinitiator concentration was and has been linked to QD quenching in QD-photopolymers,²⁸⁰ as particularly noted with nitroxyl radicals.²⁸¹

QD fluorescence was unstable in uncured inks: the amine ligand shell was insufficient to disperse the QDs long-term, resulting in aggregation and quenching.^{110,122,249} Loss of coordinated octadecylamine ligands in inks without photoinitiator likely led to gradual loss of fluorescence in PDMS and 2-EHA inks: a reduction in QY would be observed as ligands detach due to the PL enhancement associated with primary amines,²³⁶⁻²³⁸ while complete quenching would occur as surface defects are exposed and/or generated.¹¹⁰

The fluorescence of QDs was stabilised in thiol-containing composites without PI, as the polymer cured via the thiol-ene reaction to immobilise QDs and their ligand spheres; however, there was sufficient ligand exchange with DODT to fully quench PL.^{263,264} DODT is sufficiently small to migrate through polymer matrices,²⁶² and residual monomer could exchange with stabilising ligands before, during, or after photopolymerisation. A greater mass of DODT in ink was trialled than PETMP due to its lower viscosity. PETMP is a larger crosslinking agent with four reactive moieties: higher crosslinking density would lead to more rapid solidification and the molecule would quickly be immobilised in polymer chains, and the greater effective steric hindrance of PETMP impedes access to the QD surface.

5.3.4. Summary of DMPA photoinitiator

Overall, novel QD-photopolymers were produced (Objectives *O3-O4*) and jetting was demonstrated, but QD fluorescence was not found to be stable. QDs did not disperse well in DMPA-PDMS ink as it appears that the hydrocarbon chain of the 2-EHA monomer may have led to a more favourable interaction overall with the octadecylamine ligands on the QDs in DMPA-2-EHA inks. Observations of inks curing in air in Section 5.3.1 may be rationalised as the result of oxygen acting as a radical scavenger: loss of PL was observed in the 0.5 wt% DMPA-PDMS sample, which successfully cured, and PL was retained in the 0.25 wt% DMPA-2-EHA sample, which did not cure. QDs remained fluorescent where photopolymerisation was hindered, which prevented loss of passivating ligands arising from phase separation.^{259,277,278} Another contributing factor may be that lower PI loading led to a lower concentration of radical species that could damage QDs.

Jetting was demonstrated for 0.25 wt% DMPA-2-EHA ink under nitrogen to investigate drop ejection and oxygen-sensitivity. Ordered drop arrays were obtained with diameters on the order of 35 μm , partially fulfilling Objectives *O3-O4*, but ink did not cure. This indicated that the photoinitiator loading was too low for adequate cure rate under the UV conditions associated with printing, or that the 1.1% O_2 level was too high and led to significant oxygen inhibition – oxygen levels below 50 ppm are used industrially.⁵⁶ Subsequent photoinitiator loading experiments found that rapid photopolymerisation was achievable with 0.5% O_2 levels, with faster rates as PI loading increased. This is in agreement with common guidelines, which state that rapid acceleration is seen as loading increases between 0 wt% to 3-4 wt% and that a maximum cure rate is reached at 6-7 wt%.²⁶² It was predicted that printing is possible with loadings <3 wt% in nitrogen using the printer, despite relatively weak absorption of the 365 nm wavelength UV LED.

Thiol monomers were found to be promising additives during initial trials. Samples cured very rapidly, with or without QDs, and composites appeared to have good dispersion and transparency. The cured composite was noted to be harder than the equivalent DMPA-2-EHA composite due to higher crosslinking density from the multifunctional PETMP monomer. The fluorescence initially appeared to be stable and was visible, albeit slightly weaker than the DMPA-2-EHA analogue, likely resulting from a small amount of ligand exchange with DODT, leading to the QD quenching associated with thiols.^{263,264} Overall, thiol-ene reactions appeared to be a feasible route to fast cure times for QD-photopolymers.

However, loss of fluorescence was observed for all cured samples. Therefore, QD-inks were prepared with and without DMPA to assess the effect of photoinitiator on photostability. All samples containing DMPA were rapidly quenched, demonstrating that photopolymerisation and/or free radicals quench QD fluorescence in these formulations. Loss of QY with PI concentration dependency has been observed in literature.²⁸⁰ Poor compatibility with the host matrix is known to lead to QD aggregation and loss of passivation from stabilising ligands.^{259,268,277,278}

Fluid inks without photoinitiator lost fluorescence over a longer period of time; it is likely that the amine ligands gradually detach, leading to aggregation and quenching.^{110,122,249} As primary amines enhance PL of CdSe-based QDs, reduced coverage leads to an immediate, significant reduction in emission intensity.^{236–238} Inks which contained thiol monomers solidified via thiol-ene reaction. Emission of DODT ink was quenched by ligand exchange with thiols, whereas PETMP ink cured without significant ligand exchange and fluorescence remained stable. PETMP was shown to be a promising crosslinker for QD composites and can potentially improve cure rate and hardness without detrimental effect on PL; however, this formulation did not lead to stable fluorescence following photoinitiation with DMPA and is not suitable for UV curable fluorescent composites.

In summary, novel QD-composites were synthesised, and jetting was demonstrated; inks with suitable curing rates were investigated for acrylate and thiol-ene mechanisms. However, complete quenching of fluorescence occurred and therefore these materials are not suitable as temperature sensors. Concentration of DMPA photoinitiator was found to correlate with quenching. The cause may be two-fold: poor compatibility to the host matrix may lead to loss of passivating ligands; and free radicals may etch the QD surface.

It is not evident that DMPA is unsuitable for all formulations for QD-photopolymers; QDs could be stabilised or better dispersed through many methods, as discussed in Appendices. Nonetheless, the photobleaching properties of TPO were of interest, therefore experiments were carried out with this alternate photoinitiator to investigate whether photostability was improved.

5.4. TPO-containing composites

In this section, composites are synthesised using inks formulated with TPO photoinitiator.

This section describes:

- Inks formulated for acrylate-based free radical photopolymerisation with AB116678 and 2-EHA prepolymers
- Investigation into the effect of TPO loading on photoluminescence.

Bisacylphosphine oxide-based photoinitiators are used for depth cure in UV-curable silicones, of which Omnirad 819 – or phenylbis(2,4,6-trimethylbenzoyl)-phosphine oxide, TPO – is one of the most well-known. As discussed in Section 5.1.1, POs offer excellent depth cure and are photobleaching; this is ideal for optical sensing as it leads to materials with high optical transparency. As POs have high curing efficiencies in polymer composites and higher absorption in the near UV than the DAAP-based PIs,⁵⁶ this enables lower photoinitiator concentrations for inkjet printing under nitrogen than with DMPA.

However, POs are strongly oxygen-sensitive, and inkjet performance is poor without a co-initiator or inert environment. Co-initiators are recommended as the surface cure performance of TPO is limited. Additives to counter oxygen-sensitivity, such as thiolate oxygen scavengers and tertiary amines, should be used with caution as POs are susceptible to nucleophilic attack.²⁶²

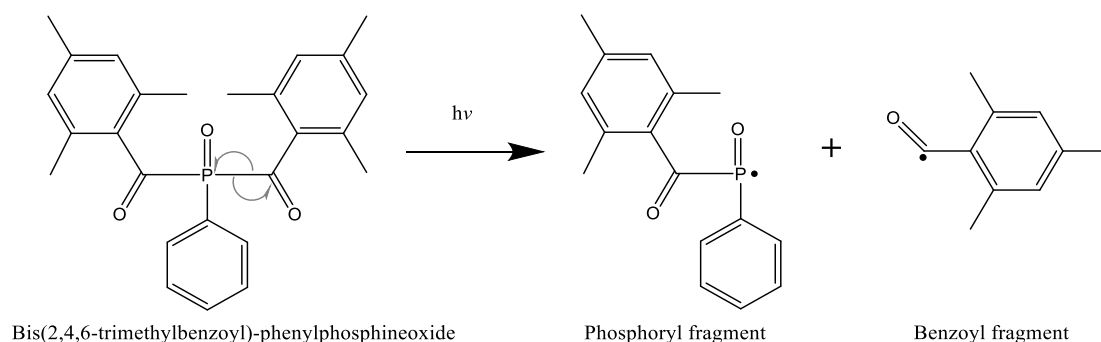


Figure 84: Photolysis of TPO.

Trials were carried out with TPO-2-EHA inks, where 'X wt% TPO-2-EHA ink' refers to a 50 wt% mixture of AB116678 in 2-EHA, to which X wt% TPO is added. The high absorption efficiency of TPO at 365 nm was beneficial for inkjet printing with UV LED excitation. It was also hoped that the bulkier radicals may be less able to reach the QD surface due to steric hindrance and therefore the PL of composites would be better preserved.

5.4.1. 2-EHA inks

1 wt% TPO-2-EHA ink was prepared for a preliminary experiment and 50 μl of QD solution (0.01 wt% in octyl acetate) was added to 0.2 ml ink. To assess the oxygen-sensitivity, these samples were cured in air rather than under nitrogen. A small volume was placed in a DSC pan and cured under a 365 nm UV lamp. The sample cured quickly with visible, stable fluorescence. A vial of sample also cured rapidly, but predominantly along the glass wall of the vial. As expected, significant oxygen sensitivity was observed; the sample in the DSC pan cured better as it had a smaller interface with air.

Fluorescence was stable enough to be photographed without any observed decrease in emission as seen in Figure 85. The DSC pan and a cured sample taken from the vial were stored for two weeks, after which fluorescence was mostly absent: some faint fluorescence was seen in the larger section of the sample extracted from the vial. It is possible that oxygen may protect the QD surface from photoinitiator by acting as a radical scavenger, but that the inhibited curing leads to poorer stability and eventual loss of passivation.

The photostability appeared to be greater than observed for DMPA inks, as fluorescence was not quenched under continuous illumination although it decreased during dark storage. However, it was difficult to compare results as a higher QD loading was used, and loss of fluorescence remained significant. As photoinitiator concentration has been associated with loss of QD fluorescence in QD-photopolymers,²⁸⁰ experiments were carried out to reduce photoinitiator loading and to investigate curing under inert conditions.

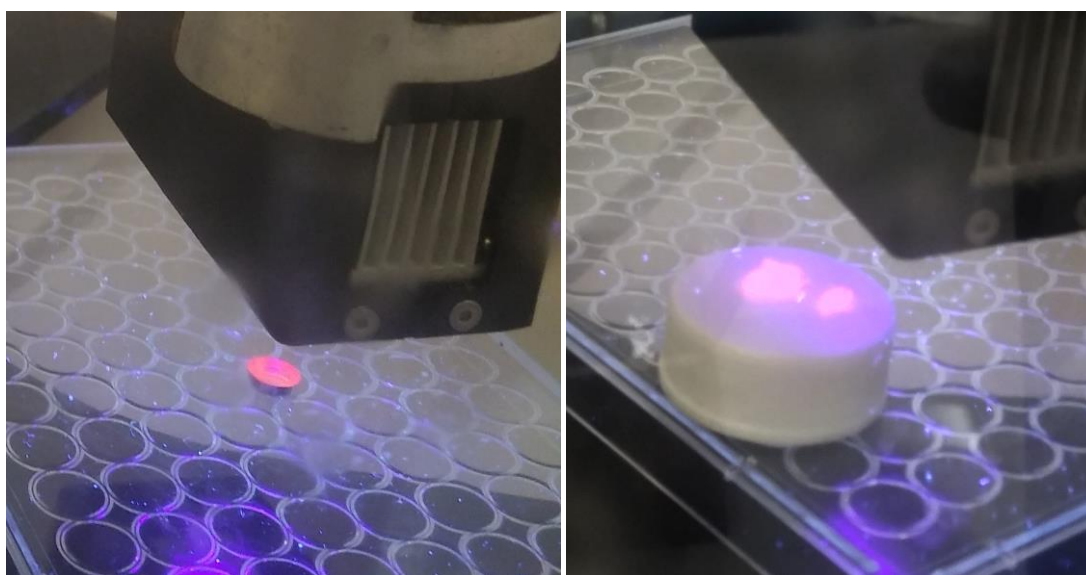


Figure 85: Samples prepared for initial feasibility tests with TPO, showing strong fluorescence after curing.

Photoinitiator loading

A preliminary experiment was run in order to assess the effect of concentration of photoinitiator and QDs on PL and cure rate. Vials were prepared with 0.2 mL each of 1 wt%, 0.1 wt%, or 0.01 wt% TPO-2-EHA. 25 or 50 μ L of quantum dot solution (0.01 wt% in octyl acetate) was added to each vial; the quantum dots appeared to be well-dispersed. These were then cured in the vials under a 365 nm lamp in a nitrogen atmosphere (0.5 wt% O₂) and their curing was visually monitored.

Samples with 0.01 wt% TPO required several minutes of exposure to cure, samples with 0.1 wt% TPO cured in approximately one minute and a half, and samples with 1 wt% TPO cured thoroughly in under thirty seconds. All samples retained fluorescence and appeared to be well-dispersed, presenting as transparent monoliths with no obvious sedimentation. No significant differences were seen in cure rates for samples with differing QD loadings, whereas cure retardation has been observed at higher QD loadings in literature.²⁸²

While a small initial decrease in fluorescence was observed after 24 hours, no sudden changes in emission intensity were observed over a 3-week monitoring period. There was no observable relationship between concentration of photoinitiator and fluorescence. The cause of the initial decrease in emission intensity is unclear but may relate to changes in the polymer after curing; acrylates are known to continue to react after initial irradiation, a process known as dark polymerisation, as macro-radicals propagate and terminate. Physical changes, such as diffusion of small molecules through the matrix and polymer relaxation, may have also taken place. Another possibility is that emission loss was halted by TPO photobleaching: emission decreased as radicals etched the QD surface, but upon exposure to UV the photoinitiator was bleached until no new radicals were produced.

While QD photostability was greater using this formulation than in DMPA analogues – whether as a result of choice of PI or increased QD loading – a short-term decrease in emission intensity was observed and long-term stability has not been confirmed.

5.4.2. Summary of TPO photoinitiator

Overall, novel QD-photopolymers were produced with visible emission using TPO photoinitiator. However, further work is needed to confirm long-term photostability of composites. Good dispersion and QD passivation is needed for photostability in QD-polymer composites.^{277,283,284} Poor compatibility between QD and polymer can lead to phase separation and depletion flocculation.²⁷⁷⁻²⁷⁹ Dispersion of QDs in polymers is complex and agglomeration occurs where interaction between particles is poorly shielded, leading to interdigitalisation of alkyl chain capping ligands instead of interaction with the host polymer.^{122,268,269} Furthermore, amine ligands are labile and temperature-dependant ligand detachment can occur,²⁷⁷⁻²⁷⁹ which is problematic as the crosslinking of acrylates is exothermic. This can cause stabilising ligands to be disrupted during photopolymerisation, leading to degradation of QD passivation and loss of QY from exposed surface defects.^{259,268,278} Poorly shielded quantum dot surfaces may be etched by radicals - as studied in the case of nitroxyl radicals²⁸¹ - and photoinitiator concentration has been associated with reduced QY.²⁸⁰ Additionally, oxygen may have been involved in photodegradation, despite the inert atmosphere, if adsorbed within the silicone ink. Photo-oxidation has even been reported in QDs with siloxane layers where oxygen was trapped.²⁶⁸ Conversely, other papers have observed photo-enhancement following UV curing and there are many different proposed mechanisms of enhancement.²⁶⁸ In summary, it seems clear that poor compatibility with the host matrix leads to aggregation, poor passivation, and quenching of QD fluorescence.

Overall, observed photostability was much greater for TPO-2-EHA composites than was seen for DMPA analogues; it is unclear whether this results from the photobleaching properties of TPO or whether it is merely the result of higher QD loading. TPO-based photopolymerisation may be attractive for QD-photopolymers, but long-term photostability was not confirmed – quantitative analysis is needed to elucidate the behaviour of polymer composites during curing.

In order to make effective use of research time, decisions were made to prioritise the research of addition cure inks as fewer issues with photostability were noted and an inert environment was not required. UV curable formulations remain of interest for future studies due to their fast curing and compatibility with a range of AM processes. Printing was then demonstrated for the UV inks, to demonstrate their viability for polymer printing and as proof-of-concept of inkjet for patterning of QD-photopolymers.

5.5. Printing of UV cure silicone inks

Although the fluorescence of QD composites had appeared unstable, it remained of interest to demonstrate printing of the UV curable inks. The polymers themselves have applications as printable materials and may further be used as matrices for other composite materials. Further work may elucidate the mechanism of QD quenching in the composites synthesised in Sections 5.3-5.4: if this issue were resolved then inkjet of these composites would enable printable materials for lighting and sensing. Work was carried out to demonstrate that the UV cure inks developed are inkjet-printable and to assess their performance.

In this section:

- Differential scanning calorimetry (DSC) was carried out on TPO-PDMS and TPO-2-EHA inks to investigate the effect of PI loading on cure rate and differences in curing behaviour between the two prepolymer formulations
- Jetting was investigated for PDMS and 2-EHA inks using two different waveforms and drop arrays were collected and analysed
- Reactive inkjet was demonstrated for 1 wt% TPO-PDMS ink and drop spacing optimised to produce continuous thin films.

Reactive inkjet of UV cure QD-silicone composites was not demonstrated due to the observed loss of photoluminescence. However, jetting of QD-loaded ink was demonstrated in Section 5.3.1, and work with curing QD composites with varied photoinitiator loading showed that QD ink would cure rapidly enough for the inkjet process. Therefore, printing of QD composites is feasible and would be of interest if issues with PL quenching were resolved.

5.5.1. Curing of silicone inks

Differential Scanning Calorimetry (DSC) was used to assess UV curing as function of the heat associated with reaction. A pilot study was carried out on 0.25, 0.5, and 1 wt% TPO-PDMS to match those tested during the rheological HTS (see Section 5.2). A 5-minute programme was run at 25 °C as described in Methodology Section 3.2.5.2. The UV lamp shutter was triggered to open for 10 s at 0.5 minutes and 3.5 minutes.

TPO-PDMS inks

DSC curves for TPO-PDMS inks are shown below in Figure 86. All samples hit a maximum approximately 30 seconds after the shutter was opened and a weak peak was seen when the shutter was opened again at 3.5 minutes, showing that few subsequent reactions occurred after resolution of the first peak. 1 and 0.5 wt% TPO-PDMS inks showed very similar curves, while the 0.25 wt% TPO-PDMS had a less steep onset and did not reach the same enthalpic maximum (6.32 W g^{-1} , lower than the 7.86 and 8.13 W g^{-1} seen for 1 and 0.5 wt% TPO samples respectively).

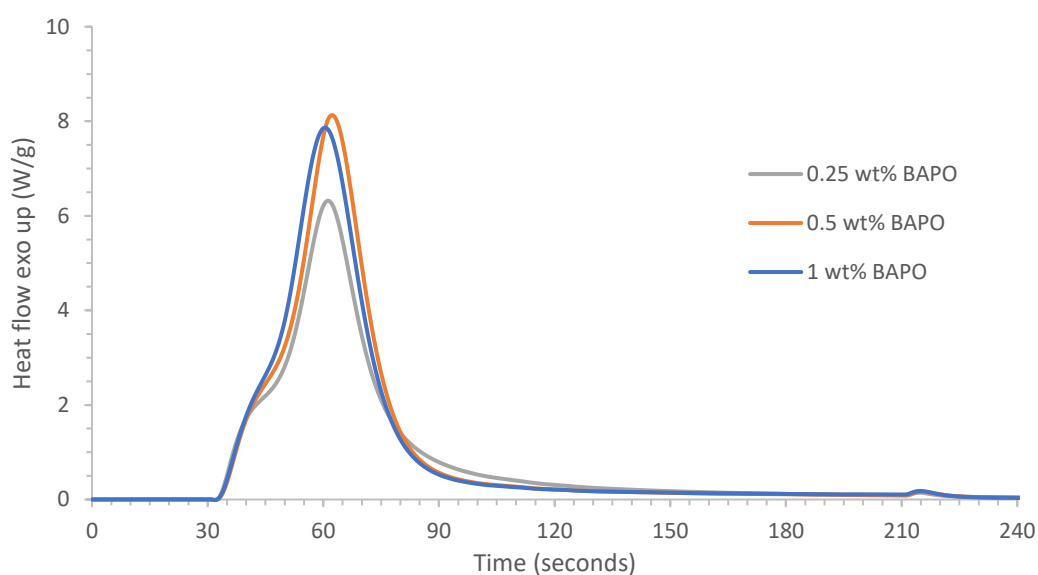


Figure 86: UV-DSC curves of 0.25, 0.5, and 1 wt% TPO-PDMS inks (grey, orange, and blue lines, respectively).

PDMS inks of different PI loading appeared to achieve similar degree of conversion following the first 10-second UV exposure as no significant curing was seen during the second UV exposure. However, higher TPO loading was associated with faster initial curing and return to the baseline after the first UV pulse. Lower PI loading resulted in fewer initiated chains, and therefore a longer propagation for reaction with free monomers and higher average chain length at termination.²⁶²

TPO-2-EHA inks

DSC curves for TPO-2-EHA inks are shown below in Figure 87. Onset of curing was less steep than in PDMS inks and there was a more pronounced curve between the shutter opening and closing at all PI loadings. While acrylate radicals have greater reactivity than methacrylate radicals,²⁵⁵ the rate of crosslinking may have been slowed by steric hindrance and entanglement of branched 2-EHA monomers. Exothermic peaks were approximately 45 seconds after shutter opening and delayed as PI loading decreased (45, 46, and 49 s for 1, 0.5, and 0.25 wt% TPO respectively); this was accompanied by peak broadening, indicating longer reaction times. Again, negligible heat flow was seen following the second shutter opening, which suggests that reaction completed following the first UV exposure.

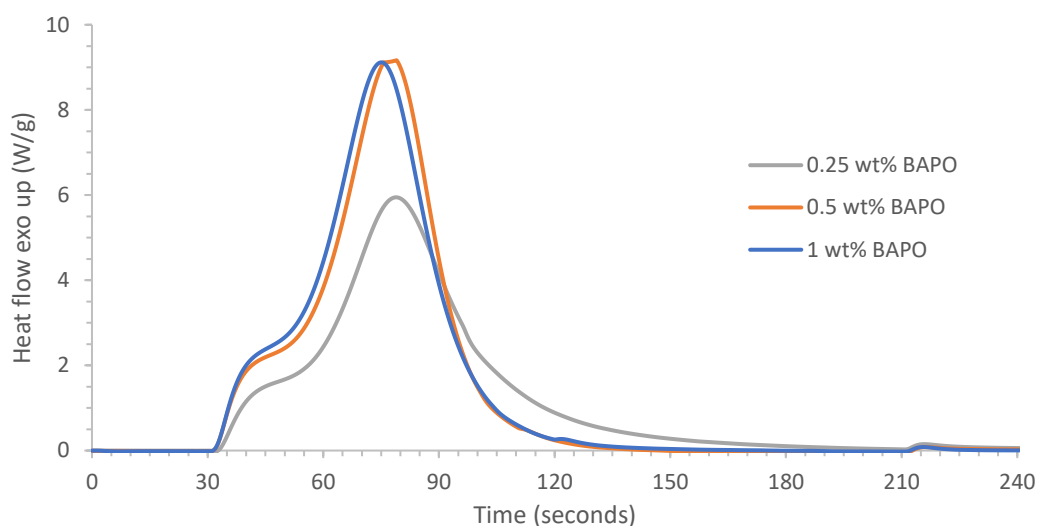


Figure 87: UV-DSC curves of 0.25, 0.5, and 1 wt% TPO-2-EHA inks (grey, orange, and blue lines, respectively).

The curves for 1 and 0.5 wt% TPO-2-EHA inks were again similar in appearance to each other, with 1 wt% having slightly faster reaction rate. 0.25 wt% had a broad peak and lower maximum heat flow (5.95 W g^{-1} compared to 9.12 W g^{-1} for 1 and 0.5 wt% TPO), indicating a much slower rate of reaction, and reaction continued for approximately 30 s longer.

In summary, all inks investigated reached their final conversion after the initial 10 second UV exposure and did not require further excitation. 1 and 0.5 wt% TPO inks behaved similarly to each other under nitrogen flow while 0.25 wt% TPO inks had slower onsets of curing and returned to the baseline more slowly. TPO-PDMS inks cured more rapidly than TPO-2-EHA inks, showing narrower exothermic peaks with earlier, steeper onset, and the difference in reaction rate was more pronounced in 0.25 wt% TPO inks. Print trials with 1 wt% TPO-PDMS inks were prioritised over other formulations for their faster reaction rate, as this could better preserve QD passivation and enhance print resolution.

5.5.2. Observation of jetting

Jetting was demonstrated for PDMS and 2-EHA inks using two different waveforms to show their viability for inkjet and observe drop formation. As it had been shown that the addition of photoinitiator did not have a detrimental effect on printability (see Section 5.2), inks were jetted without PI. Inkjet of UV cure silicones was carried out at room temperature on a Fujifilm Dimatix DMP-2831 with standard 10 pL cartridges. As the inks tested did not contain photoinitiator, a nitrogen atmosphere was not used during jetting optimisation.

PDMS and 2-EHA inks were jetted at 25 V with a single pulse waveform W_2 (Figure 140, appendix). Additionally, both were jetted at 20-22 V with the W_1 v2 waveform as used for addition cure inks (Chapter 4). Drop formation and ejection were observed and drop arrays were deposited onto silane-treated glass slides and analysed, as described in Section 3.2.3.

PDMS ink with waveform W_2 at 25 V

The rheology of AB116678 was assessed in Section 5.1.4 and found to be jettable with a Z parameter of 4.38. The Z parameters of PDMS inks calculated in Section 5.2.1 were lower at 4.30 and 4.17 for DMPA and TPO inks, respectively. These Z parameters correspond to printable inks; however, all fluids had slightly low viscosity and slightly high surface tension as compared to the ideal range suggested by the manufacturer,^{175,176} which indicates a tendency towards satellite drop formation.

Drop ejection of PDMS ink jetted at 25 V using waveform W_2 is shown below in Figure 88. Ink was seen to eject from nozzles with short tails ($\leq 100 \mu\text{m}$) which then re-joined the head; no satellite droplets were observed during jetting.

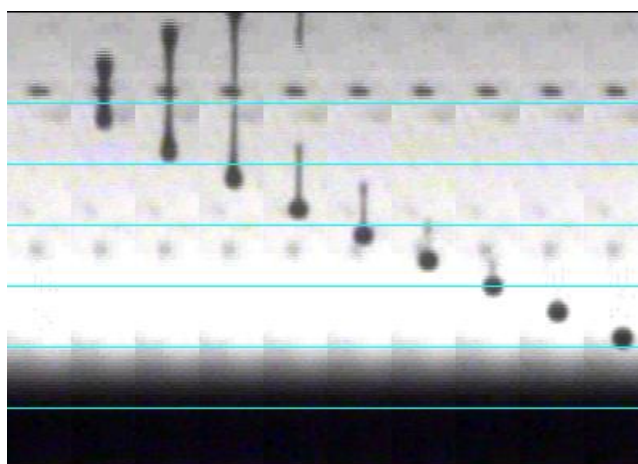


Figure 88: Droplet ejection of PDMS ink at 25 V with waveform W_2 using the Dimatix printer.

Droplet arrays at 60 and 100 μm spacing are shown below in Figure 89. Aside from the first row of the 60 μm -spaced array, inks were deposited into regular grids. Satellites and conjoined droplets were almost nonexistent at 60 μm spacing, despite the large drop diameter (approximately 40 μm).

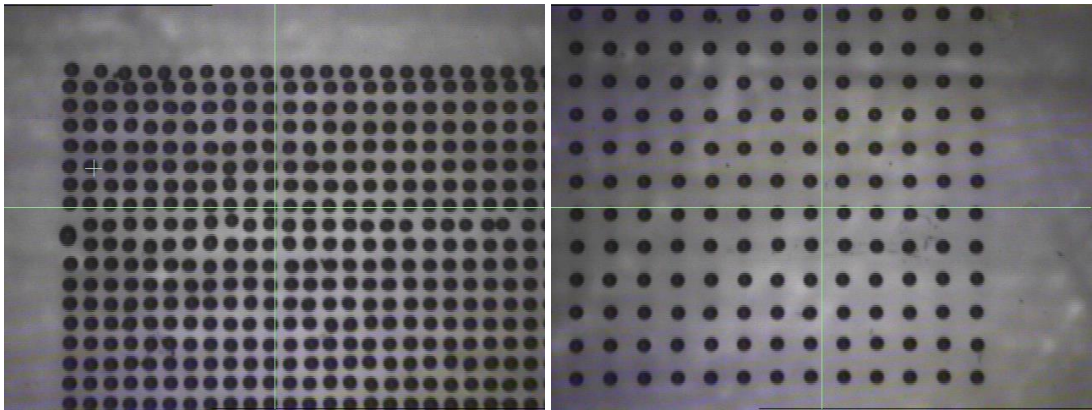


Figure 89: Droplet arrays of PDMS ink printed with 60 and 100 μm drop spacings, as viewed via fiducial camera. Droplets were ejected at 25 V with waveform W_2 using the Dimatix printer.

Sizing was carried out on micrographs, as shown in the example below (Figure 90). Sessile drops had an average area of $1397 \mu\text{m}^2 \pm 53.4 \mu\text{m}^2$ standard deviation (SD) with a 99.73% confidence interval of $7.4 \mu\text{m}^2$. This corresponds to an average diameter of $42.2 \mu\text{m} \pm 8.2 \mu\text{m}$ SD with a 99.73% confidence interval of 1.1 μm . Primary drops were uniform and circular; small droplets ($<20 \mu\text{m}^2$) were observed but did not cover a significant portion of the substrate.

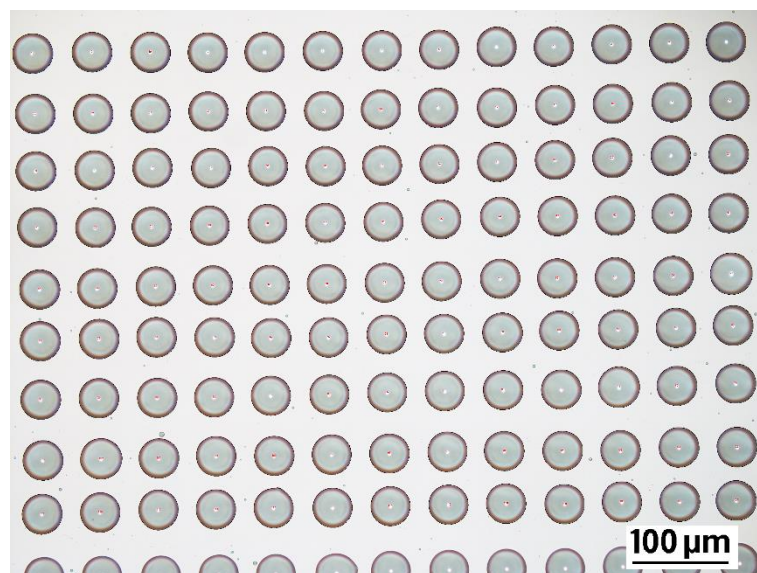


Figure 90: Droplet array of PDMS ink jetted at 25 V with waveform W_2 using the Dimatix, as viewed via optical microscopy. The droplets in the micrograph are circled and labelled for sizing.

PDMS ink with waveform W_1 v2 at 20 V

The droplet formation of PDMS inks jetted at 20 V using waveform W_1 v2 is shown below in Figure 91. Ink ejected from nozzles with short tails ($\leq 100 \mu\text{m}$) which then recombined with the head; satellite formation was not observed. Ink jetted from all nozzles, rarely failing when excess ink blocked a nozzle; trajectory was sometimes affected by this material.

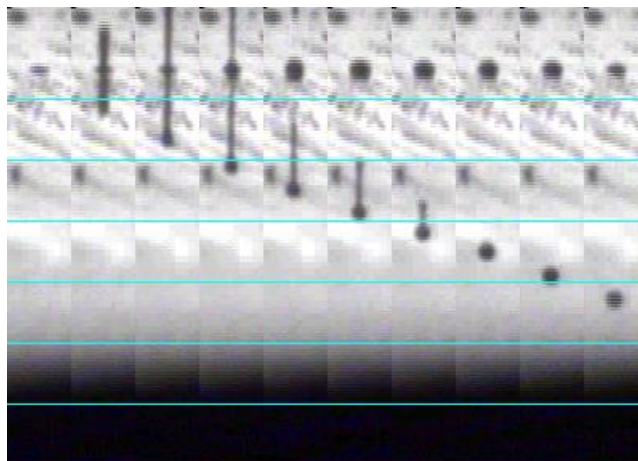


Figure 91: Droplet ejection of PDMS ink at 20 V with waveform W_1 v2 using the Dimatix printer.

Droplet arrays were collected at 60 and 100 μm , as shown in Figure 92. While it was possible to collect drop arrays, jetting was inconsistent at 60 μm spacing, particularly for the first eight rows of the array after which jetting stabilised. The deposited droplets do appear uniform despite this and there was no visual indication of nozzle blowouts. Droplets were much smaller than with the W_2 waveform, under 35 μm diameter; this reduced diameter was as expected as the jetting voltage was 5 V lower.¹⁷⁶ For this reason, merged droplets were not observed in grids at either spacing.

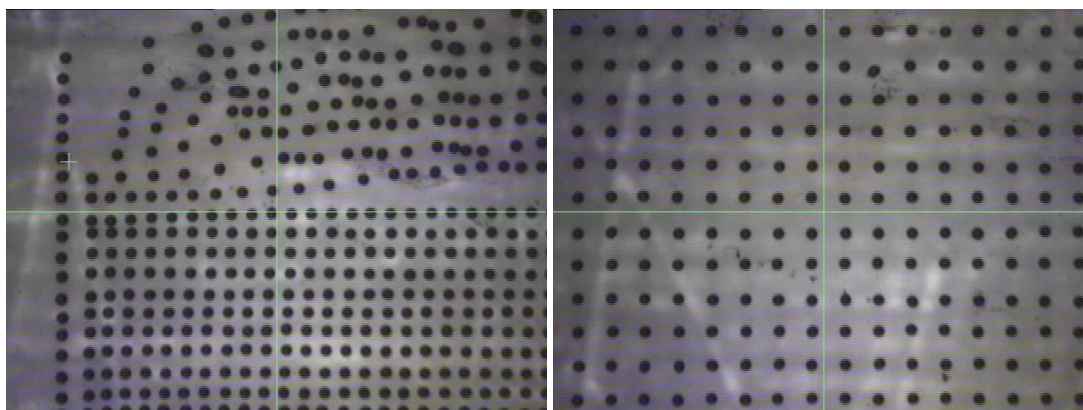


Figure 92: Droplet arrays of PDMS ink printed with 60 and 100 μm drop spacings, as viewed via fiducial camera. Droplets were ejected at 20 V with waveform W_1 v2 using the Dimatix printer.

Micrographs of arrays were sized as shown in Figure 93; drops had an average area of $847.5 \mu\text{m}^2 \pm 32.7 \mu\text{m}^2$ SD with a 99.73% confidence interval of $4.7 \mu\text{m}^2$. This corresponds to an average diameter of $32.9 \mu\text{m} \pm 6.5 \mu\text{m}$ SD with a 99.73% confidence interval of $0.9 \mu\text{m}$. The size and variance of drops were similar to that of the addition cure inks jetted using the same waveform at 30 V. However, some droplets appeared oblate and clusters of satellite droplets were observed. This may result from excess material at the nozzle plate, causing minor issues with nozzle spray and trajectory.

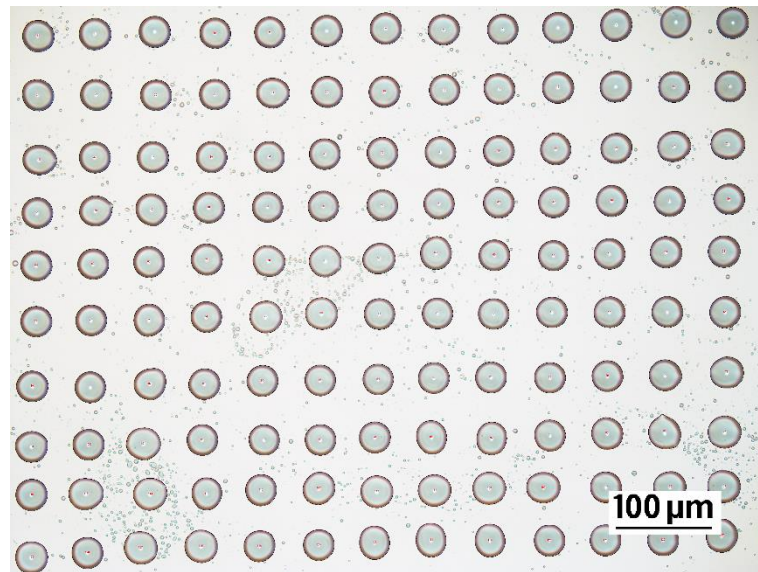


Figure 93: Droplet array of PDMS ink jetted at 20 V with waveform $W_1 v_2$ using the Dimatix, as viewed via optical microscopy. The droplets in the micrograph are circled and labelled for sizing.

PDMS ink with waveform $W_1 v2$ at 22 V

The $W_1 v2$ waveform was also tested at 22 V to see if nozzle spray was reduced at a higher jetting voltage. Drop ejection at 22 V is shown below in Figure 94: ink ejected from nozzles with short tails ($\leq 100 \mu\text{m}$) which then recombined with the head and satellite formation was not observed, although excess material at nozzles was observed.

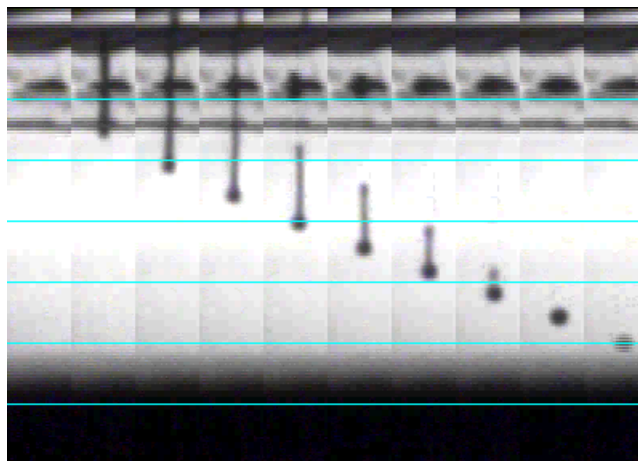


Figure 94: Droplet ejection of PDMS ink at 22 V with waveform $W_1 v2$ using the Dimatix printer.

A grid was deposited at $60 \mu\text{m}$ spacing as shown below in Figure 95. The array appears similar to that collected at 20 V, with some improvements: the jetting of the first several rows stabilised more quickly and produced droplets along straight lines. However, subsequent rows deposited the first several drops at an angle before jetting in straight lines. Some fine droplets were visible via fiducial camera, in addition to some larger satellite droplets which typically clustered together, suggesting these were transient occurrences. These issues may be possible to resolve by preventing excess material at nozzles via waveform optimisation.

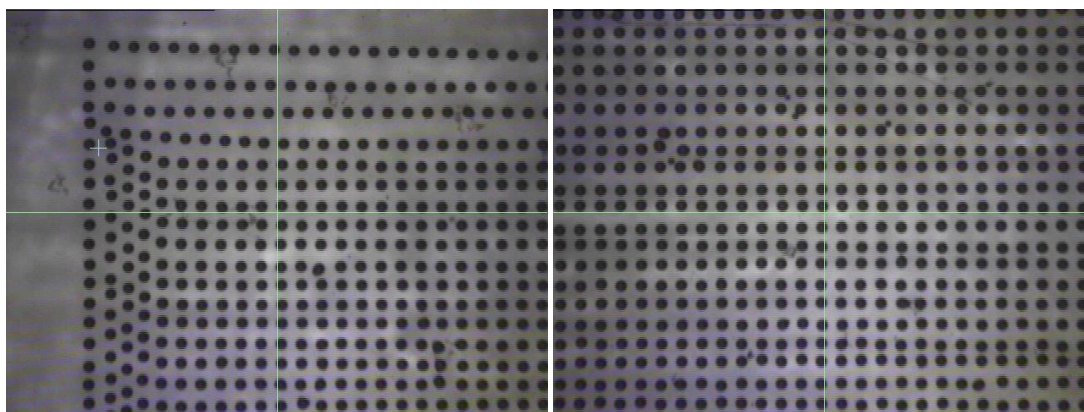


Figure 95: Droplet arrays of PDMS ink printed with $60 \mu\text{m}$ drop spacing, as viewed via fiducial camera. Droplets were ejected at 22 V with waveform $W_1 v2$ using the Dimatix printer.

Micrographs of drop arrays ejected at 22 V were obtained and sized (Figure 96). Sessile drops had an average area of $891.7 \mu\text{m}^2 \pm 26.9 \mu\text{m}^2$ SD with a 99.73% confidence interval of $3.6 \mu\text{m}^2$. This corresponds to an average diameter of $33.7 \mu\text{m} \pm 5.9 \mu\text{m}$ SD with a 99.73% confidence interval of $0.8 \mu\text{m}$. Droplets were larger than at 20 V, as expected,¹⁷⁶ but had lower variance. Increasing the jetting voltage was beneficial for drop uniformity: less nozzle spray was observed and droplets were less oblate and more uniformly circular.

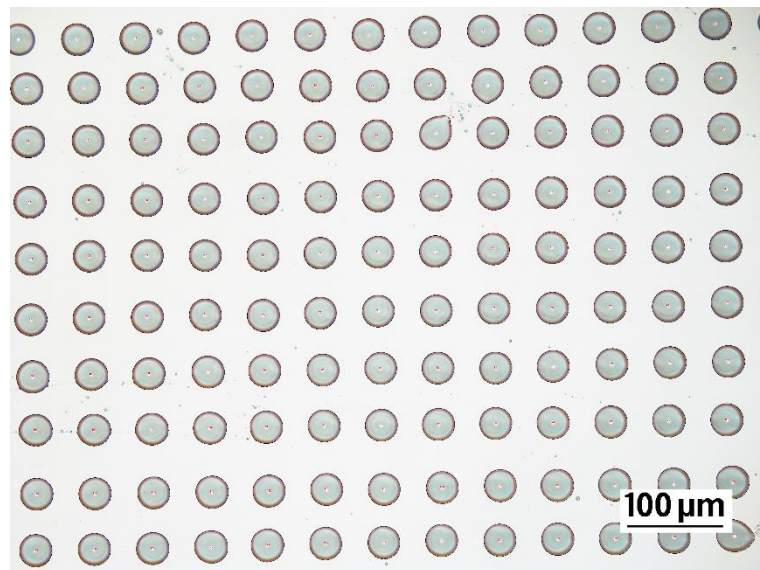


Figure 96: Droplet array of PDMS ink jetted at 22 V with waveform $W_1 v2$ using the Dimatix, as viewed via optical microscopy. The droplets in the micrograph are circled and labelled for sizing.

However, two drops were sometimes observed in drop arrays with repeatable patterning, as shown in Figure 97 below. As volume appeared consistent, the primary drop may have been split into two drops by the material at nozzles and by the relatively high surface tension of the ink. Adjustments to the waveform are needed to eliminate satellite drops and excess material at the nozzle, particularly refinement of the cancellation pulse.

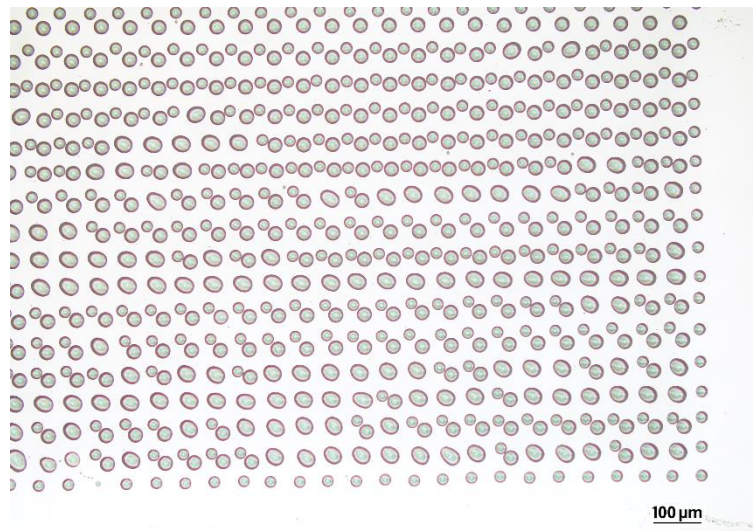


Figure 97: Droplet array of PDMS ink jetted at 22 V with waveform $W_1 v2$ using the Dimatix printer, as viewed via optical microscopy. Nozzles seem to deposit two smaller droplets, rather than one single drop, in a grid.

In summary, PDMS ink was jetted successfully with both waveforms, with little nozzle failure or satellite drops observed during ejection. Jetting at 25 V using waveform W_2 produced uniform drop arrays, but the drop diameter was large ($42.2 \pm 8.2 \mu\text{m}$), limiting printing resolution. Ejection at 20-22 V using waveform $W_1 v2$ showed inconsistent drop trajectory caused by the excess material observed at nozzles. While it was possible to obtain ordered arrays, the first rows of arrays at $60 \mu\text{m}$ were disordered though droplets were of uniform size. Furthermore, it was sometimes observed in drop arrays that the primary drop split into two; this deposition was repeatable and had similar volume to standard drops. In ordered regions, drops had excellent uniformity and much smaller diameter than W_2 ($33.7 \pm 5.9 \mu\text{m}$ at 22 V) - as expected given the reduced jetting voltage¹⁷⁶- showing a higher potential resolution.

Performance would benefit from further waveform optimisation to eliminate satellite droplets and prevent excess material at nozzles, which likely results from the relatively high surface tension of the ink compared to the ideal range for the Dimatix.^{175,176} The $W_1 v2$ waveform was designed for viscous, low surface energy inks (SiliGlass inks, $Z = 1.5-1.7$), rather than an inviscous, high surface energy ink such as this ($Z = \sim 4.3$). Issues with jetting can likely be resolved with alterations to the cancellation pulse of the waveform.

2-EHA ink with waveform W_2 at 25 V

2-EHA ink was jetted at 25 V using waveform W_2 and the drop formation is shown below in Figure 98. Drops were seen to eject from nozzles with short-to-medium tails (100-150 μm) which sometimes re-joined the head but often formed satellite droplets, as expected based on ink rheology. The viscosities obtained for 2-EHA inks (<4 mPa s) were close to the lower viscosity limit given by the printhead manufacturer (2 mPa s).⁵⁹ As a result, the inks had large Z parameters (8.73 and 7.93, for DMPA and TPO inks) and were predicted to be susceptible to satellite formation (see Section 5.2.2).

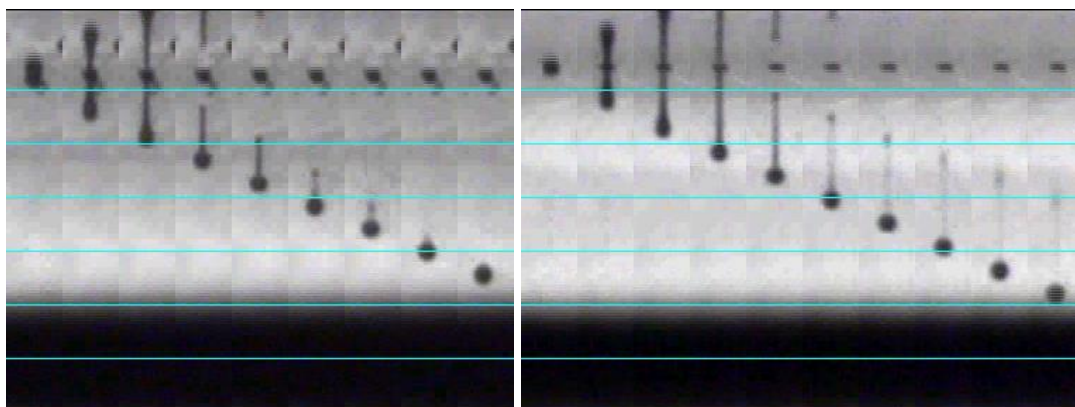


Figure 98: Droplet ejection of 2-EHA ink at 25 V with waveform W_2 using the Dimatix printer. Left shows jetting where the tail re-joins the head of the drop, while right shows formation of satellites.

Drop arrays were collected using a single nozzle at 60 and 100 μm spacings and are shown below in Figure 99. Drops appeared to be positioned well, forming regular arrays with no noticeable misalignments. Drops were large with diameters close to 40 μm , as observed with the PDMS ink, which resulted in some drops merging at 60 μm spacing. A high number of satellite droplets were present, as observed during droplet formation.

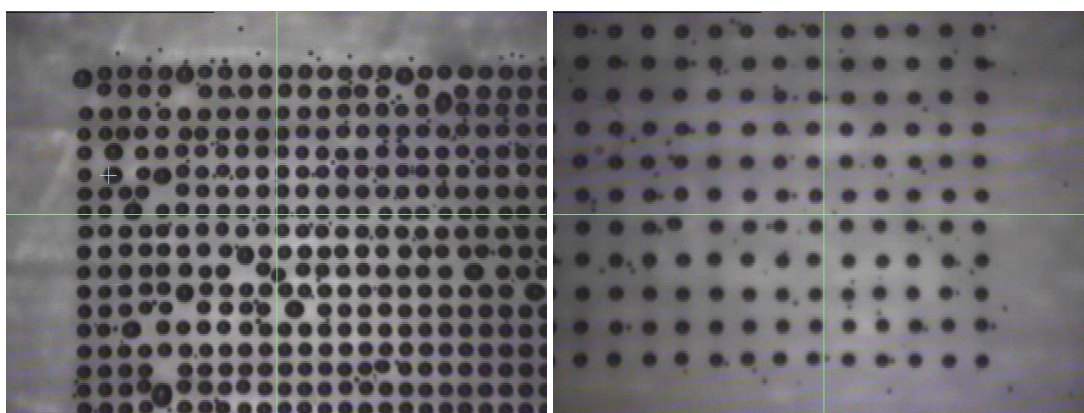


Figure 99: Droplet arrays of 2-EHA ink printed with 60 and 100 μm drop spacings, as viewed via fiducial camera. Droplets were ejected at 25 V with waveform W_2 using the Dimatix printer.

Droplet analysis was carried out on micrographs of the arrays, as shown in the representative micrograph below in Figure 100. Excluding conjoined drops and satellite droplets, drops had an average area of $1137 \mu\text{m}^2 \pm 47.0 \mu\text{m}^2$ SD with a 99.73% confidence interval of $6.6 \mu\text{m}^2$. This corresponds to an average diameter of $38.0 \mu\text{m} \pm 7.7 \mu\text{m}$ SD with a 99.73% confidence interval of $1.1 \mu\text{m}$. While primary droplets had repeatable size, the drop shape was not uniform: drop edges deviated from circularity where they merged with other drops, with satellite droplets, or with fine spray.

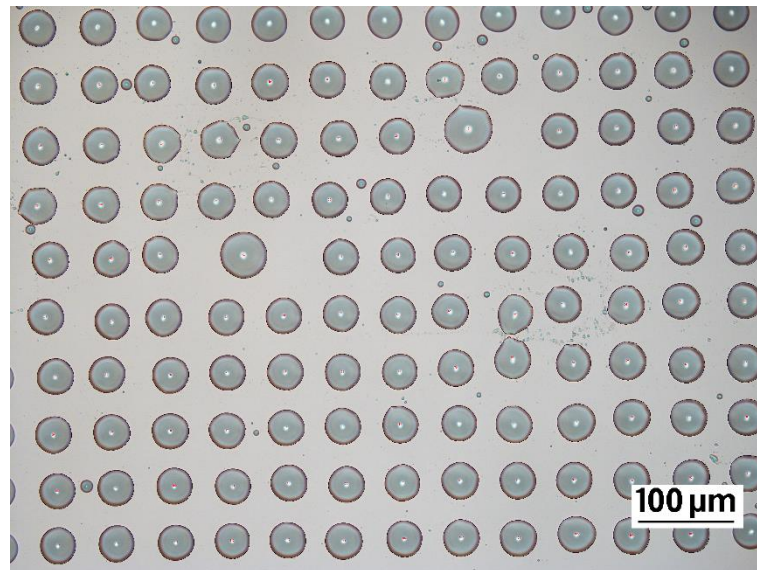


Figure 100: Droplet array of 2-EHA ink jetted at 25 V with waveform W_2 using the Dimatix, as viewed via optical microscopy. The droplets in the micrograph are circled and labelled for sizing.

Satellite droplets had a wide range of sizes: droplets varied from $<20 \mu\text{m}^2$ to $220 \mu\text{m}^2$ during sizing, with an average size of around $100 \mu\text{m}^2 \pm 60 \mu\text{m}^2$ SD. Size was varied by filament breakup during satellite formation. Conjoined drops were less numerous than satellites and had an average area of $1900 \mu\text{m}^2$, corresponding to a diameter of $49.2 \mu\text{m}$. These were much more uniform in size than the satellites as they were formed by the merging of two primary drops on the substrate. The average area was approximately $375 \mu\text{m}^2$ less than the sum of two separate drops; this is likely a result of poor substrate pinning, leading to receding contact with the surface.

In summary, 2-EHA inks did eject reliably at 25 V with waveform W_2 with no nozzle failures. Ink was deposited with controlled placement and drop diameter but had large drop diameter, which limited the potential print resolution, and satellite droplets were numerous. Further work to optimise a waveform and the voltage should produce a reliable ink with fewer satellites.

2-EHA ink with waveform $W_1 v2$ at 20-22 V

Droplet formation of 2-EHA ink jetted using waveform $W_1 v2$ was observed, as shown in Figure 101. At 20 V, drops ejected with short tails ($\leq 100 \mu\text{m}$) that re-joined the head, while tails were longer (approximately $150 \mu\text{m}$) at 22 V - as expected when increasing jetting voltage¹⁷⁶ - and frequently formed satellite droplets. Nozzle failure resulting from excess ink on the nozzle plate was observed.

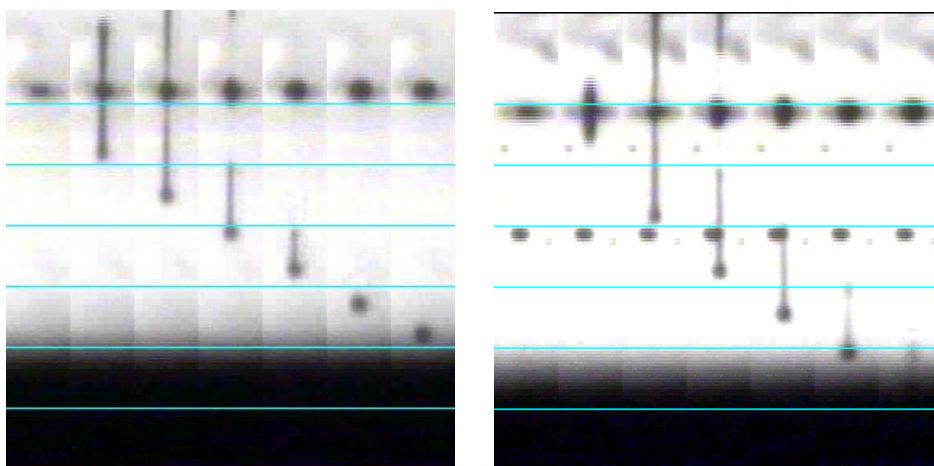


Figure 101: Droplet ejection of 2-EHA ink at 20 V (left) and 22 V (right) with waveform $W_1 v2$ using the Dimatix.

Overall, jetting of 2-EHA ink was achieved for both waveforms though satellite droplets were a considerable challenge, moreso than for PDMS ink. This is as expected based on the low viscosity ($<4 \text{ mPa s}$) and the high surface tension of the ink compared to ideal values for the Dimatix^{175,176}. Drop ejection at 25 V using waveform W_2 was reliable in that nozzles did not fail and drop trajectory was straight; drop tail length varied and satellite formation was observed. Drop arrays were aligned but conjoined drops and satellite droplets of varying sizes were seen. Drop diameter was repeatable and large ($38.0 \pm 7.7 \mu\text{m}$), limiting print resolution, while sessile drop shape deviated slightly due to satellites.

Jetting at 20-22 V using waveform $W_1 v2$ was successful, albeit with varied reliability: at 22 V nozzle failure was rare and drop trajectories were straight. Lowering the voltage to 20 V resulted in shorter tails but more frequent nozzle failure and issues with drop trajectory. Excess material was seen at nozzles, as observed with PDMS inks. While drop arrays were not obtained, the sessile drop diameter is expected to be smaller than that obtained using W_2 due to the lower jetting voltage.¹⁷⁶

In summary, both ink formulations were jettable using two different waveforms without further optimisation. The surface tensions of both inks were higher and viscosity lower than the ideal ranges for the Dimatix,^{175,176} leading to issues with satellite droplets as observed in drop arrays. PDMS ink had more minor issues with satellite droplets than 2-EHA inks, as predicted from their respective printability parameters.

Waveform W_2 showed stable jetting - leading to well-ordered drop arrays with minimal satellites - but drop diameters were large, limiting resolution. Waveform $W_1 v2$ had been optimised for the addition cure inks, which had lower surface energy than the UV cure formulations, which led to some excess material at nozzles. This resulted in more frequent nozzle misfire and issues with drop trajectory, leading to irregularities in arrays. However, drop diameter was small and well-controlled ($33.7 \pm 5.9 \mu\text{m}$ for PDMS ink at 22 V).

Therefore, PDMS ink was selected for print trials, as the viscosity was closer to ideal values and satellite droplets were less frequent. $W_1 v2$ was selected as higher resolution was achievable and only minor adjustments to the waveform are needed to eliminate satellite drops and excess material at the nozzle, particularly refinement of the cancellation pulse.

5.5.3. Reactive inkjet

Using the results from the previous sections, printing was demonstrated for 1 wt% TPO-PDMS at 22 V using waveform $W_1 v2$. During jetting of droplet arrays onto silane-treated substrates, the UV curable inks behaved similarly to the poorly pinned addition cure inks due to having higher surface energy than the silanised glass slide. Therefore, printing optimisation of the UV curable inks on the silanised substrates is predicted to be similar to that of addition cure inks: making use of pinned grid and line-by-line strategies. However, unlike the addition cure inks, it was possible to print onto slides coated with release agent as the UV curable inks did not fully wet the surface. As such, the formation of continuous films at different droplet spacings was tested on this substrate.

Single layers of ink were deposited at various drop spacings, as shown in Figure 102. Films became more continuous as spacing decreased: 30 μm spacing resulted in clusters of drops, indicating poor pinning, while 15 μm spacing yielded better coverage, but large gaps in the layer were apparent. 10 μm spacing resulted in a smoother monolayer to produce an almost fully continuous, flat film, and 5 μm spacing was too dense and led to bulging.

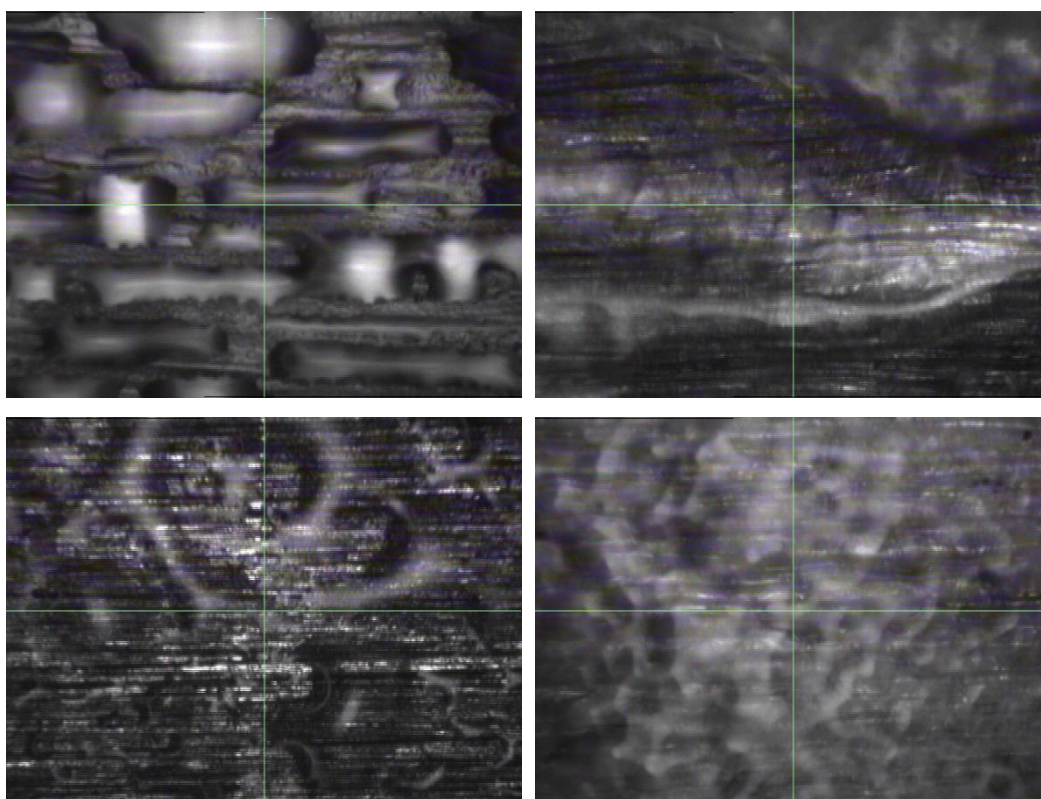


Figure 102: Single layers of 1 wt% TPO-PDMS ink deposited at drop spacings of 5, 10, 15, and 30 μm with waveform $W_1 v2$ at 22 V using the Dimatix, as viewed by fiducial camera. Larger-to-smaller drop spacing is shown, anti-clockwise from top-left.

The 1 wt% TPO-PDMS ink successfully cured on the release agent-coated substrate, as shown below in Figure 103. The surface textures of the monolayers with different drop spacings are apparent: the 30 μm spacing did not produce continuous films, 15-10 μm spacings resulted continuous films, and 5 μm spacing produced bulging at edges and a curved, wrinkled surface.

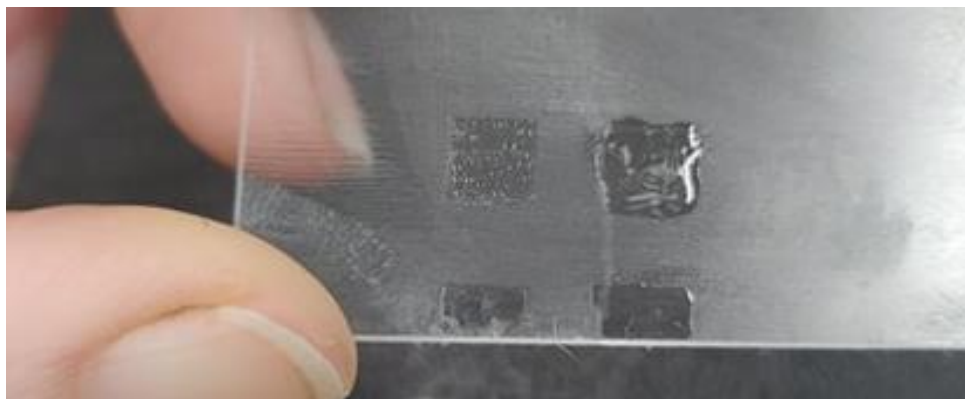


Figure 103: Photograph of monolayers printed onto a glass slide with release coating. 1 wt% TPO-PDMS ink was deposited at drop spacings of 5, 10, 15, and 30 μm . Larger-to-smaller drop spacing is shown, anti-clockwise from top-left.

Composite micrographs of the monolayer prints are shown below in Figure 104, where the monolayers at high and low drop spacing are compared. At 30 μm spacing, rectangular droplet clusters formed; stable line formation was seen as rows of ink. At 5 μm spacing, bulging was seen with visible wrinkles in the surface and trapped air bubbles.

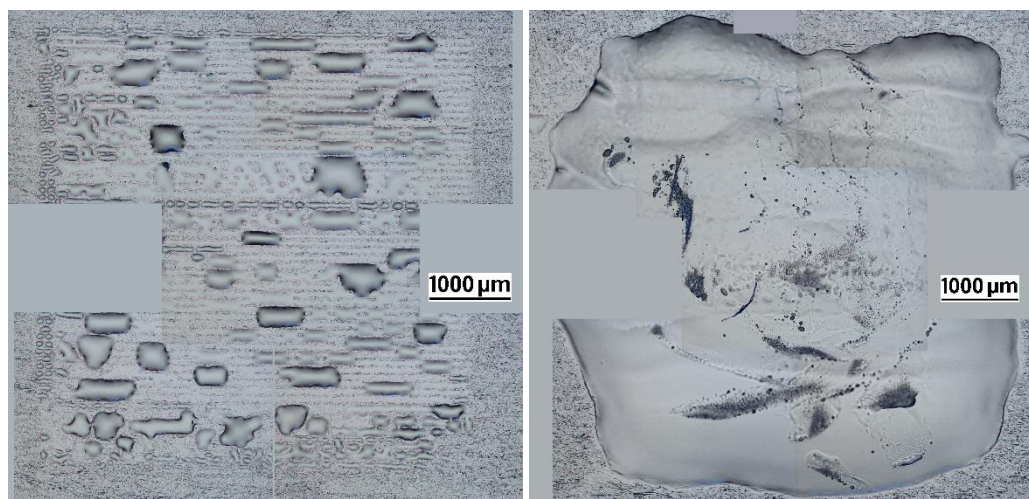


Figure 104: Composite micrographs of monolayers printed at unsuitable drop spacings. 1 wt% TPO-PDMS ink was deposited at drop spacings of 30 μm (left) and 5 μm (right) onto a glass slide with release coating.

Prints at intermediate drop spacings are shown below in Figure 105. The surface texture of both films appeared smooth and flat, although the texture of the print with 15 μm spacing resembled that of the release agent: it appears that there was not sufficient ink to fully

cover the release agent. Edges were reproduced in both films with some curvature and irregularity, resembling the undulation seen in prints using the pinned grid strategy (see Section 4.3.3). At 10 μm , the top-right corner was rounded, as seen in previous prints with poor pinning, while the top-left corner cured with straight edges at a right angle. These observations suggest that the release agent provided surface microstructuring and that deposition creep may have occurred as driven by surface tension ($\sim 47 \text{ mN m}^{-1}$). Profilometry would be of interest to assess whether whether ink receded at the edges.

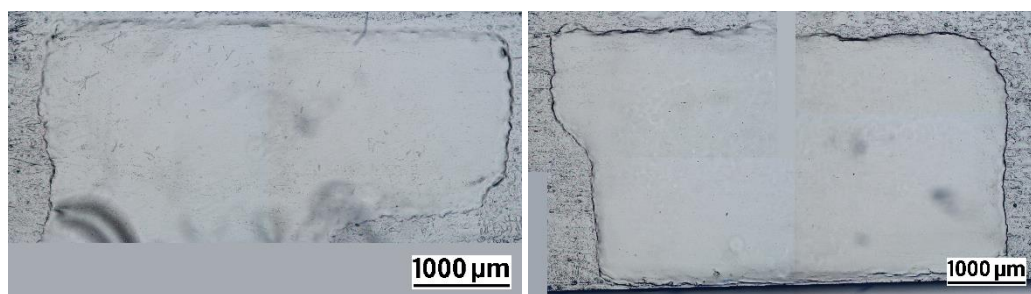


Figure 105: Composite micrographs of monolayers printed at intermediate drop spacings. 1 wt% TPO-PDMS ink was deposited at drop spacings of 15 μm (left) and 10 μm (right) onto a glass slide with release coating.

The texture of the release agent was visible through the films in the above micrographs, which reduces the transparency of the printed material and obscures observation of microstructure. Gyroidal microstructures with apparent polymer-rich and solvent-rich domains were observed in SiliGlass films printed line-by-line from inks with 50 wt% carrier vehicle loading. As the UV ink contained only PDMS precursor and TPO, the size and/or extent of polymerisation-induced phase separation (PIPS) may be small enough in scale that material transparency was not reduced by scattering,²³⁴ but a range of structures are possible which impact transmission and mechanical properties. Printing or spincoating onto untreated glass slides would be of interest in order to assess scattering and haze in the matrix. Additionally, acrylate thin films often have poor surface cure due to oxygen inhibition, reducing transparency and increasing surface roughness.²⁷¹

In summary, printing of a UV curable ink was demonstrated on slides coated in release agent, producing continuous monolayers at 10 μm spacing with smooth surface texture. The print quality was comparable to that of addition cure inks printed with a pinned grid strategy (Section 4.3.3) in terms of undulation at edges. The geometric control was poorer than seen for a line-by-line strategy (Section 4.3.4) as deposition creep and nozzle failures were evident; however, continuous thin films produced at 10 μm spacing appeared to have comparable flat surface texture.

5.5.4. Summary of UV inkjet printing

Overall, UV cure inks were shown to be jettable and printing was demonstrated for 0.1 wt% TPO-PDMS ink. TPO-inks were investigated using UV-DSC as TPO had more efficient absorption of the UV-LED wavelength and issues with quenching had been observed in composites containing DMPA. 1 and 0.5 wt% TPO inks had similar curing profiles while 0.25 wt% TPO inks cured more slowly. PDMS inks cured more rapidly than 2-EHA inks and had higher initial reaction rates and sharper exothermic peaks. 1 wt% TPO-PDMS ink reached a maximum 30 s after shutter opening and was identified as being the most suitable for inkjet under an inert atmosphere as it cured fastest.

Jetting was investigated for PDMS and 2-EHA inks without photoinitiator using two different waveforms. The surface tensions of both inks were high and viscosity low ($Z = \sim 4.3$ and $\sim 7.9-8.3$), leading to issues with satellite droplets as observed in drop arrays. Satellite formation was solely observed in jetting of 2-EHA ink, in both waveforms. The viscosity of the 2-EHA ink was low (< 4 mPa s, close to the 2 mPa s minimum for the Dimatix⁵⁹) and so satellites were a greater challenge than for PDMS ink.

Drop ejection using W_2 , a single pulse waveform (Figure 139, appendix), was observed to be stable: jetting nozzles and drop trajectory were reliable. However, the tail length was variable for the low-viscosity 2-EHA ink, and satellite droplet formation was frequently observed. Drop arrays were regular and well-ordered with excellent accuracy, but drop diameters were large, limiting resolution. $W_1 v_2$ was a dual pulse waveform (Figure 139, appendix) that was optimised for the addition cure inks ($Z = 1.5-1.7$). As the rheology was dissimilar to the UV curable inks, excess material at nozzles and satellite droplets were observed in all trials to varying extents. 2-EHA ink was associated with satellite droplets due to its low viscosity (< 4 mPa s, close to the 2 mPa s minimum for the Dimatix⁵⁹). Issues with drop trajectory were observed in PDMS ink arrays using $W_1 v_2$. However, where jetting was stable, drop diameter was uniform and small ($33.7 \pm 5.9 \mu\text{m}$ for PDMS ink at 22 V), suggesting that issues can be resolved with minor alterations to optimise the waveform.

Inkjet printing was demonstrated for 1 wt% TPO-PDMS ink using waveform $W_1 v_2$ at 22 V. While drop arrays were deposited onto silane-treated glass substrates, films would require strategies to overcome poor pinning. Instead, print trials were carried out on glass slides coated with release agent and inks produced monolayer films at $10 \mu\text{m}$ drop spacing. Overall, inkjet of a UV curable silicone was demonstrated (Objective O2) and smooth monolayer films were produced without the use of non-standard deposition strategies.

5.6. Summary of UV cure silicones

In this chapter, UV curable inks were formulated from methacrylate-terminated prepolymers to enable single-part, solvent-free inks for sensing materials: a commercial silicone (AB116678) and 2-EHA. Thiol monomers were selected to investigate thiol-ene reactions for reduced oxygen-sensitivity. Two photoinitiators were selected and the rheology of formulations were tested at a range of PI loadings to confirm printability (Objective O1). DMPA was chosen for its high thermal stability, good surface cure, and adequate absorption of 365 nm UV LED. TPO was selected for its low yellowing, photobleaching, excellent depth cure, and strong absorption at 365 nm.

A range of novel QD-photopolymer composites were produced, but oxygen-sensitivity and photostability were significant barriers to their use. Composites produced using DMPA photoinitiator were rapidly quenched once cured; precursors without PI did not quench under UV but QDs were not stable in the dispersion, with gradual loss of fluorescence over the course of 48 hours. Thiol monomers were found to be promising additives in the absence of PI: while DODT rapidly quenched QDs by ligand exchange, PETMP produced a cured composite with stable fluorescence. Composites produced using TPO were vulnerable to cure inhibition by oxygen; however, their fluorescence was more stable and - despite a decrease in emission intensity shortly after synthesis - was not quenched over an observation period of 3 weeks. Further work is required to ensure that the long-term photostability of composites is suitable for temperature sensing applications.

Jetting of PDMS and 2-EHA inks was observed with two different waveforms; 2-EHA inks were observed to have issues with satellite droplets due to their lower viscosity (<4 mPa s, close to the 2 mPa s minimum for the Dimatix⁵⁹). Printing of a UV curable reactive silicone was demonstrated using 1 wt% TPO-PDMS ink (Objective O2) and monolayer films were achieved at 10 μm spacing on a silicone release agent. Inkjet printing of QD-photopolymers was also shown to be viable, but issues with photostability require further investigation to produce materials for nanothermometry.

The next stage of research was to assess the structure and temperature sensing performance of QD-composites using spectroscopy and imaging. Well-plate reading was used for high throughput sensor material screening and comparison as bulk composites, and confocal laser scanning microscopy was used to image clusters within the silicone composites to characterise temperature-dependent fluorescence.

Chapter 6. Results – Temperature sensing

In Chapter 4 and Chapter 5, jettable reactive inks were formulated for inkjet processes to produce fluorescent QD-silicone composites. This chapter details the work carried out to monitor emission of composites as a function of temperature in fulfilment of Objective O5. The mechanism of temperature-dependent photoluminescence has been discussed, and the types of quantum dot-based temperature sensors reviewed, in Chapter 2, Section 2.3.4.

In this chapter, addition cure composite materials were characterised to assess their structure and fluorescence. High throughput measurements of emission intensity were taken using a fluorescence well-plate reader to compare all novel composites produced in this thesis (octyl acetate-based addition cure inks, toluene-based addition cure inks, and UV cure inks). Finally, imaging of QD clusters was carried out using confocal laser scanning microscopy (cLSM) to assess temperature-dependent fluorescence of addition cure composites in terms of emission intensity and wavelength.

This chapter:

- Characterises addition cure QD-silicone composites
 - Transmission electron microscopy (TEM) and electron-dispersive X-ray spectroscopy (EDS) to assess structure and composition
 - PL spectroscopy to observe changes in QD emission upon immobilisation
 - Confocal laser scanning microscopy (cLSM) for QD aggregate sizing and distribution
- Describes well-plate readings for high throughput investigation of emission intensity as a function of temperature, platinum catalyst loading, and/or photoinitiator loading
 - Octyl acetate ink-based QD-composites, both cured and uncured
 - Toluene ink-based QD-composites
 - UV cure QD-composites
- Demonstrates the use of cLSM to collect PL data from QD clusters in composites
 - Imaging of QD clusters and their dispersion
 - Measurement of reversible changes in intensity and peak shift (~30-50 °C)
 - Investigation of repeat thermal cycles (30-60 °C) and non-linear quenching (60-99 °C).

All QD-composites showed fluorescence with measurable temperature-dependence. Further optimisation of sample preparation would be beneficial to improve the degree of curing, distribution of clusters, and the uniformity of well-plate samples. Irreversible quenching was not observed in cLSM and samples appeared photostable, although changes in emission intensity between thermal cycles were noted. Further studies of thermal cycles of 25-99 °C or higher, collection of a wider range of PL parameters, and accelerated aging studies are needed to inform the use of the composites in sensing devices and applications.

6.1. Characterisation of QD addition cure silicone composite

As QD emission is highly sensitive to the surface environment, the structure and composition of QD-polymer composites is important for their fluorescence and long-term stability. Work was carried out to elucidate the properties of composites synthesised from octyl acetate-based addition cure inks and the implications for their performance as sensing materials.

In this section:

- Transmission electron microscopy (TEM) and electron dispersive spectroscopy (EDS) are used to investigate composite topography and elemental composition
- Photoluminescence (PL) spectroscopy is used to assess changes in emission after curing and possible causes
- Fluorescence microscopy (cLSM) is used to image micron-scale QD clusters for evaluation of distribution and size of aggregates.

As the UV cure composites had been observed to have issues with photostability in Chapter 5, only composites synthesised from octyl acetate-based addition cure inks were used in order to make effective use of research time. UV cure formulations remain of interest for further work but their optimisation is beyond the scope of this thesis.

6.1.1. TEM and EDS

Samples were prepared for TEM by cryosectioning, as described in Section 3.2.6.2. Samples were imaged in bright field mode for elemental contrast (Figure 106) and elements were identified by EDS (Figure 107).

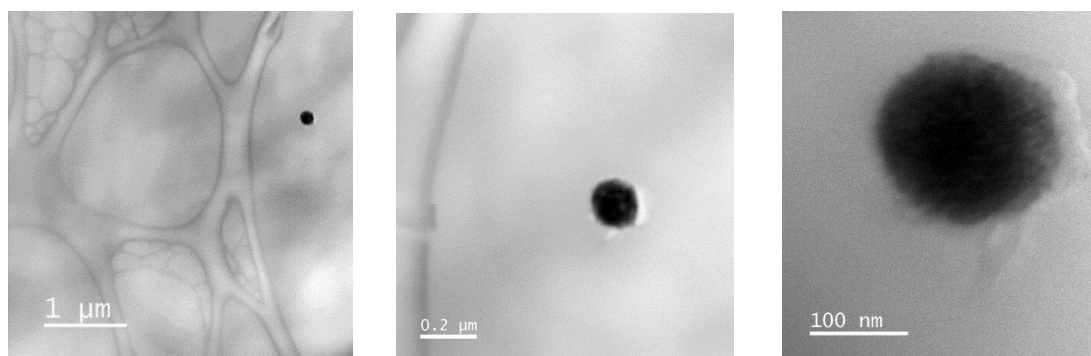


Figure 106: Transmission electron micrographs of sectioned 0.005 wt% QD silicone composite in bright field mode. These micrographs feature a single QD agglomeration, as identified by EDS in *Figure 107* below.

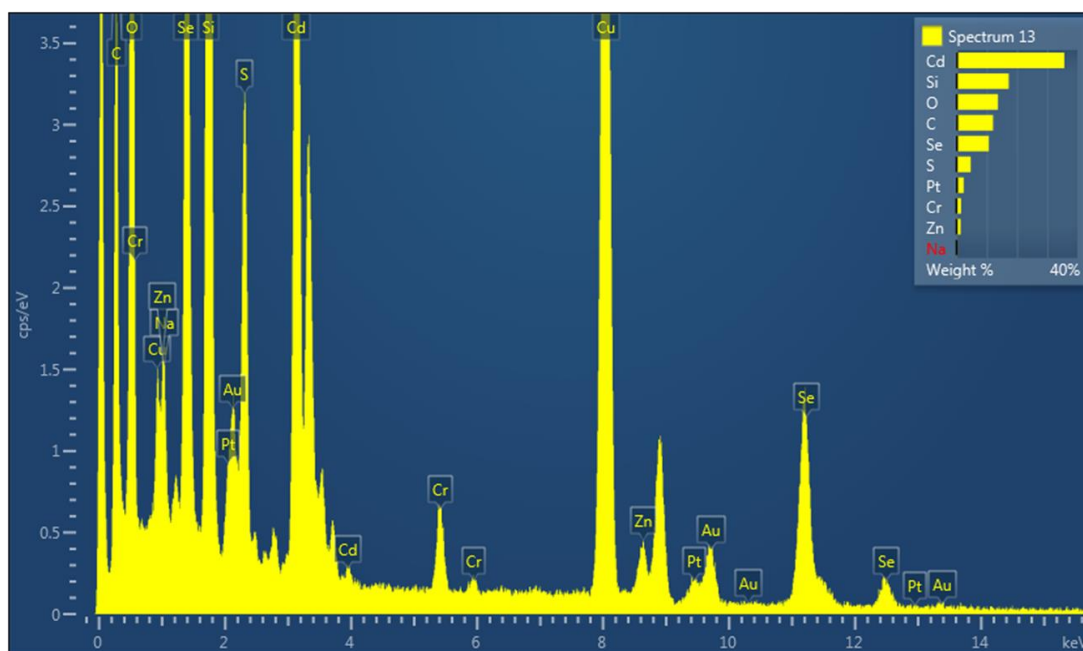


Figure 107: Electron-dispersive spectrogram of aggregate from 0.005 wt% QD-silicone sample, imaged in TEM.

In TEM, agglomerates of QDs of over 100 nm diameter were seen in the 0.005 wt% QD-silicone sample (Figure 106), similar to the 118.3 nm average diameter obtained from DLS of 0.005 wt% QDs in octyl acetate solution. EDS detected the presence of cadmium, selenium, zinc, and sulphur, confirming that the particle was indeed a cluster of quantum dots (Figure 107). An excess of cadmium was seen compared to selenium: different synthetic procedures and conjugating ligands can lead to surface enrichment to yield metal or chalcogenide rich QDs. Cd-rich surfaces are usually found to be brighter in SILAR studies and passivating amines bind to Cd sites and enhance PL.^{236,237,285,286} However, further measurements are needed to confirm an accurate Cd/Se ratio; comparison to the solid QD nanocrystals as supplied would also be of interest to determine whether changes in composition occur.²⁸⁶ Clusters were observed towards the bottom of the glass vial, indicating precipitation of quantum dots during curing: QDs tend towards settling into large aggregates in the silicone matrices.^{122,132}

TEM imaging appeared to show a microporous network structure, which may consist of an elastomeric siloxane network with solvent-rich domains. Gyroidal microphases were observed on a larger scale in optical micrographs of printed SiliGlass (see Figure 48, centre). It appears that phase separation occurs as the 50 wt% inks cure,^{231–233} leading to microdomains which may cause scattering and reduce the transparency of the sensing materials.²³⁴ Further work to control phase separation to enhance transmittance is of interest for future studies, as is the effect of solvent removal on QD-composite transparency, fluorescence, and photostability.

6.1.2. PL spectra

Confocal fluorescence microscopy was used to analyse PL of the addition cure composite. The emission spectrum of a 0.01 wt% QD-silicone composite (Figure 108 below) featuring a single peak at $\lambda_{\text{emission}} = 626 \text{ nm}$ (FWHM = 24 nm), was similar to manufacturer's data for the QDs supplied as powder ($\lambda_{\text{emission}} = 630 \text{ nm}$, FWHM = 25 nm - see Figure 58, Section 4.4.1). The position of the peak was subtly blue-shifted by the silicone matrix, consistent with a change in QD environment,^{151,236,237} but may also indicate some photo-oxidation in response to laser irradiation.^{236,287} While the peak width remained narrow, a small shoulder was seen around 655 nm post-cure, indicative of QD aggregation.^{122,239}

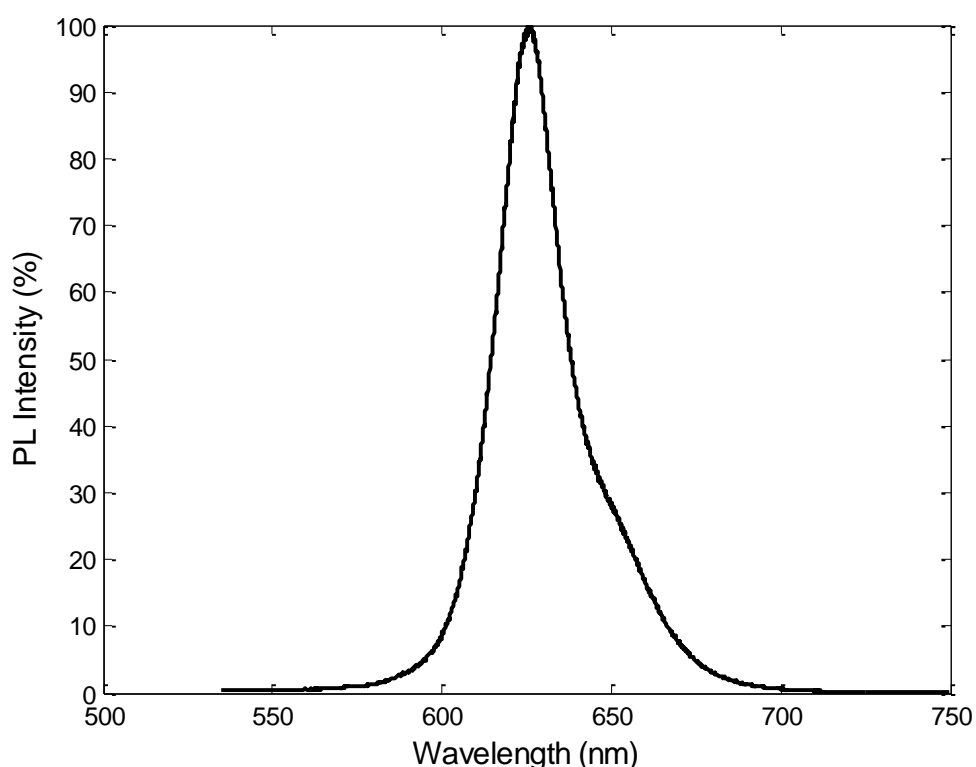


Figure 108: PL spectrum of 0.01 wt% QD-silicone composite ($\lambda_{\text{excitation}} = 532 \text{ nm}$).

Overall, the sample showed similar fluorescence to both the powder as supplied and the colloidal QD-ink samples in the detection limit experiments. Formation of agglomerates did not appear to be significantly detrimental to the photoluminescence of the bulk composite, other than the inherent self-quenching and reduced transparency that is associated with smaller inter-particle distances. However, aggregation is expected to reduce the thermal photostability due to thermal annealing processes.^{122,239}

6.1.3. Confocal LSM

The size and distribution of QD clusters throughout the matrix is an important factor in the performance of an optical temperature-sensing material: greater aggregation leads to weaker signal via self-quenching and Rayleigh scattering, and poorer thermal stability due to particle coarsening mechanisms.^{122,239} Confocal laser scanning microscopy (cLSM) was used to map large agglomerations throughout transparent polymer matrices, as seen in literature.^{18,131,132} Micrographs and z-stacks were obtained using a Zeiss LSM710, as described in Section 3.2.6.4. A micrograph of a bulk 0.005 wt% QD-silicone composite prepared from SiliGlass inks is shown below in Figure 109.

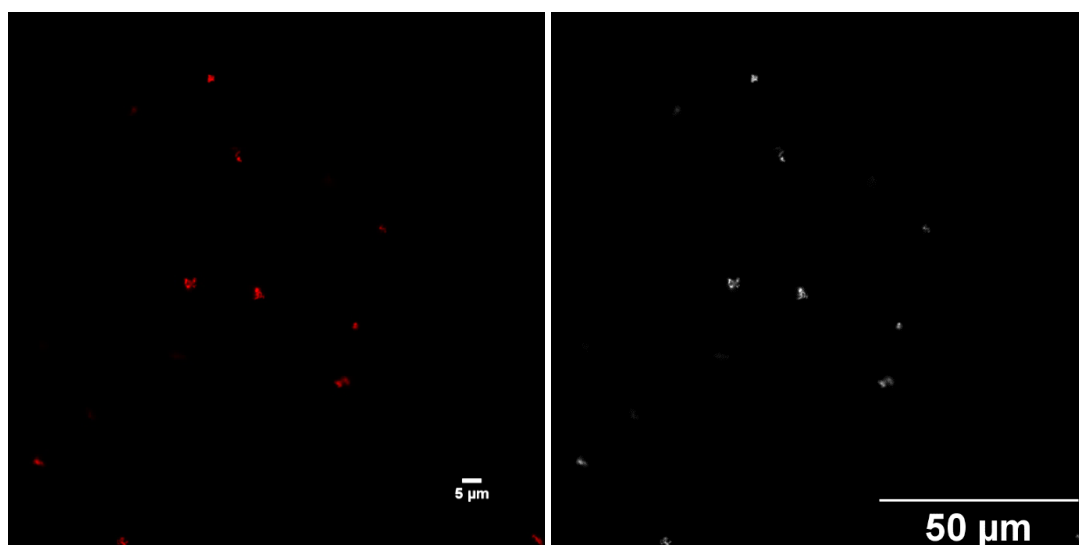


Figure 109: Representative fluorescent micrograph of QD aggregates in the silicone matrix of 0.005 wt% QD-silicone composite, in colour (left) and greyscale (right).

QDs were seen to aggregate in the silicone matrix to form micron-scale clusters, as expected based on the shoulder observed in the PL spectrum. Particle sizing was carried out on micrographs: mean Feret diameter was found to be approximately 1.8 μm with a range of 0.5-4.0 μm . The average cluster diameter was close to that of printed samples (2.3 μm , Section 4.5.2), both with and without added catalyst, suggesting that reaction volume did not have a significant impact on cluster sizes.

6.1.4. Summary of QD-SiliGlass analysis

0.01-0.005 wt% CdSe/ZnS QD-silicone composite was prepared from octyl acetate-based addition cure inks and analysed to better understand the behaviour of QDs in the matrix and their predicted impact on optical temperature sensing. TEM showed clusters on the order of 100 nm diameter while the optical microscopy showed larger micron-scale aggregates with a mean Feret diameter of 1.8 μm and a range of 0.5-4.0 μm . The aggregate

size and distribution seen in imaging is broadly in line with that seen in similar materials in literature: using TEM, Tao *et al.* reported well-dispersed QD-silicone composites with CdSe QD clusters on the order of 100 nm diameter in 0.2 wt% QD-silicone composites, and sub-micron sized CdSe agglomerates with 50 nm-sized clusters when precipitation rapidly occurs.¹²² Trung *et al.* observed 22 nm-sized CdSe/ZnS clusters in atomic force microscopy (AFM) and sub-micron to around 2 μm diameter agglomerates in cLSM in 0.1 wt% QD-silicone composite.¹³² Kim *et al.* reported much larger aggregates and clusters, which are likely due to the much higher loading (3 wt% QDs): large aggregates are seen with typically $\geq 10 \mu\text{m}$ diameter, in addition to some smaller clusters $\leq 5 \mu\text{m}$.¹³¹

The clusters observed in cLSM were slightly larger than expected for the low QD loading, given the sub-micron diameters that were observed by Trung *et al.* for a 0.1 wt% QD composite.¹³² Differences in sample preparation may explain this: Trung *et al.* prepared thin films by spin coating onto slides, whereas the sample preparation here was drop-casting. Additionally, a much higher curing temperature was used (150 °C) and the viscosity of the prepolymer mixture was much higher than that of the inkjet inks, leading to more rapid crosslinking and reduced QD mobility, which may have resulted in a shorter window for QD aggregation.

Despite the aggregation observed, the photoluminescence of the composite appeared largely unchanged from that of the manufacturer's specifications: a single narrow emission peak centred at 626 nm was seen in the PL spectra, with 24 nm FWHM and a small shoulder at around 655 nm, which suggests that some thermal annealing occurred during curing. The 4 nm blueshift observed upon immobilisation in the matrix may imply photo-etching occurred during measurement,^{236,287} however, peak shift often occurs following dispersion in different materials as the QD surface is sensitive to its environment.^{151,236,237}

The composite had measurable fluorescence that was temperature-dependent and therefore could be suitable for optical sensing applications. However, long term photostability needs to be established to ensure a good device lifetime. Additionally, sensor materials benefit from consistent spacing between quantum dots – this avoids self-quenching, reduces loss from Rayleigh scattering, and improves the stability of the material by preventing particle coarsening.^{122,239} Strategies for QD dispersion in polymer matrices are discussed in Appendices to inform future sensing material development.

6.2. Well-plate reading

A fluorescence plate reader was used to measure the emission intensity of bulk composite, as described in Section 3.2.6.3., to investigate intensity as a function of temperature and to compare the fluorescence of different formulations. This allowed high throughput (HTS) sensing material screening, although well-plate preparation was complicated by challenges in balancing sample uniformity with optimal curing conditions of different samples.

6.2.1. Octyl acetate-based addition cure composites

The temperature-dependent photoluminescence was investigated for a range of PtCl₂ loadings in 'X wt% PtCl₂ QD-composites', where X is the loading of PtCl₂ in Ink B (catalyst ink) and is mixed with 0.005 wt% QD Ink A (crosslinker ink). Measurement was carried out on both uncured and cured samples. The emission intensities of the uncured samples against temperature and Pt loading are shown in Figure 110 below.

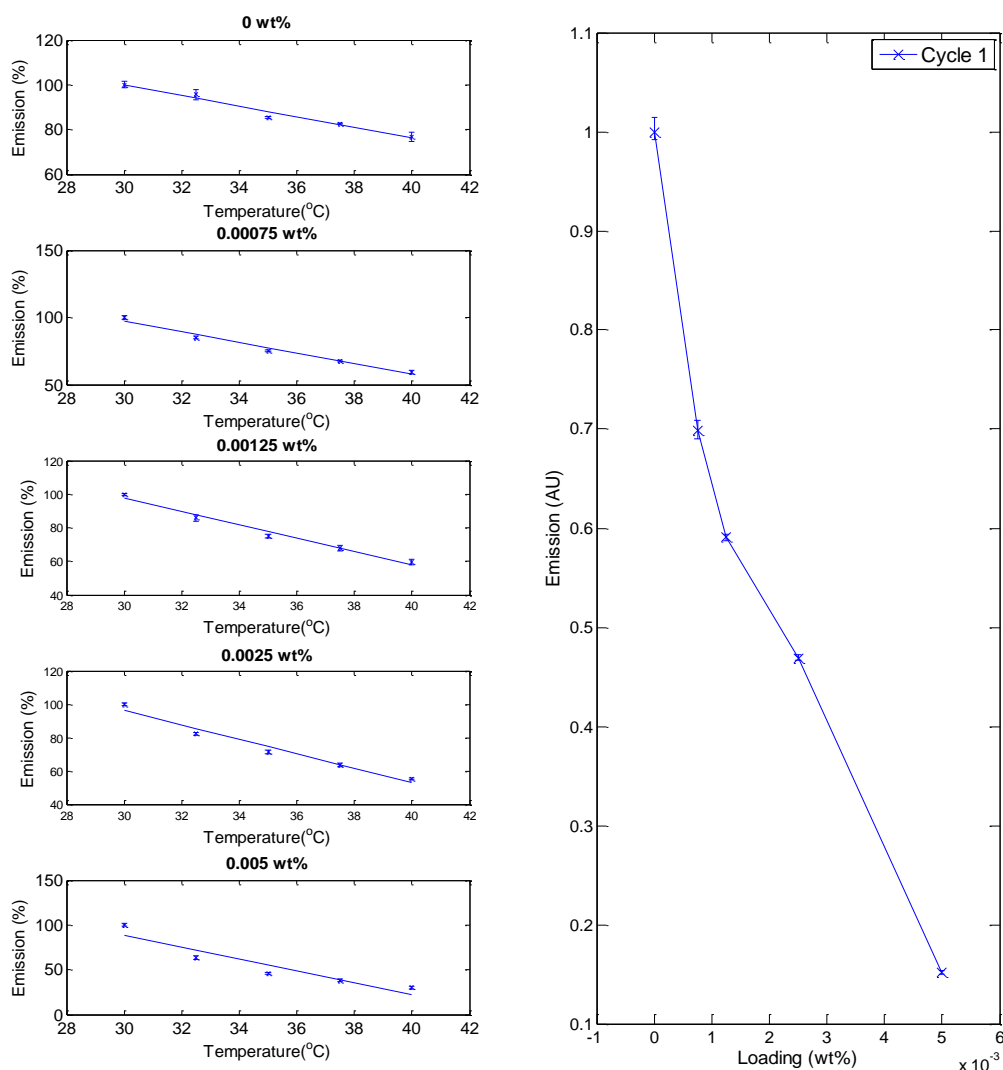


Figure 110: Emission of uncured QD-silicone composites. Bars display the range of values. Left: Emission as a function of temperature for each loading of additional catalyst. Right: Emission as a function of additional platinum catalyst at 30 °C.

Additional platinum catalyst was seen to decrease emission intensity from 1.0 to 0.15 arbitrary units (AU) for 0 and 0.005 wt% PtCl₂ respectively, in agreement with observations of bulk composites and PL maps, and is thought to result from Pt-mediated quenching. Samples with less additional platinum catalyst also retained a higher percentage of their intensity from 30 °C to 40 °C than those with greater loadings, which may reflect further Pt-mediated quenching or reduced transmission as a result of discoloration from the photo-induced formation of metallic clusters.^{181,192}

A linear decrease was seen from 30-40 °C in all uncured QD-silicone composites, i.e. mixtures of octyl acetate-based addition cure inks, as expected. QD emission intensity decreases with increasing temperature as a result of thermally-activated crossover.^{1,156} The change in intensity is linear and reversible in the ambient temperature range (approximately 5-60 °C), resulting in a constant thermal sensitivity desirable for sensing. Thermal sensitivity was collected from lines of best fit, as listed in Table 33. Percentage emission intensity thermal coefficients increased as PtCl₂ was added; however, this also correlated to lower overall emission intensities and the data for 0.005 wt% PtCl₂ appeared distinctly curved. Sensitivity as a function of intensity count decreased as signal strength was weakened by Pt-mediated quenching: 0.00075 wt% PtCl₂ had the highest sensitivity as a function of signal, followed by similar values for 0 and 0.00125 wt% PtCl₂. Therefore, PtCl₂ loadings below 0.0025 wt% were identified as more suitable to sensing as higher signal-to-noise ratios were expected.

Table 33: Percentage emission intensity thermal coefficients for temperature-dependent emission in uncured octyl acetate inks for each loading of additional platinum catalyst.

	<i>PtCl₂ loading in Ink B wt%</i>				
	0	0.00075	0.00125	0.0025	0.005
<i>Sensitivity</i> % °C ⁻¹	-2.3753	-3.9405	-3.9417	-4.3269	-6.6252

The emission intensities of the cured samples against temperature and Pt loading are shown in Figure 111 below. Emission intensity was reduced after curing: for 0 wt% PtCl₂, the intensity of cured samples was 26.7% that of the uncured.

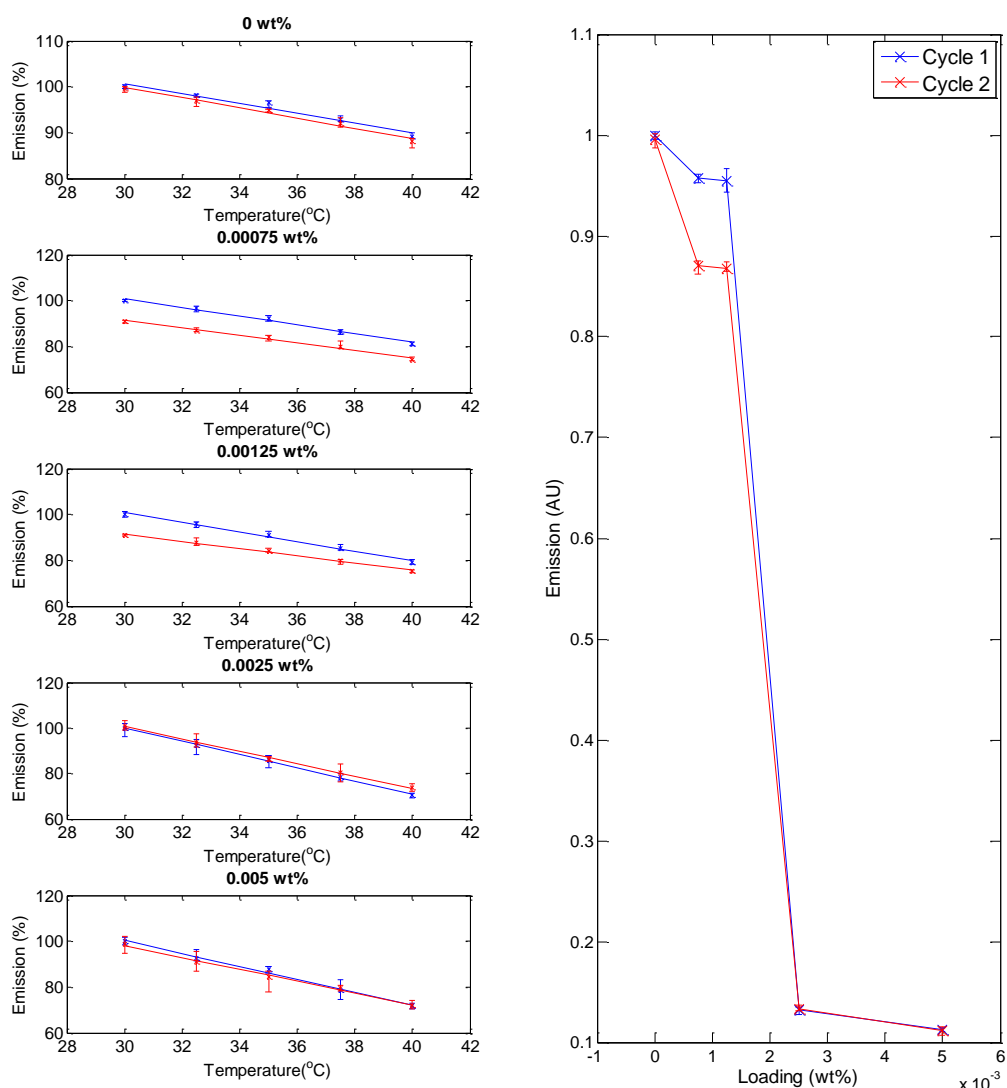


Figure 111: Emission of cured octyl acetate-ink QD-silicone composites. Bars display the range of values. Left: Emission as a function of temperature for each loading of additional catalyst. Right: Emission as a function of additional platinum catalyst at 30 °C.

Additional platinum catalyst was seen to decrease emission intensity - as in the case of uncured samples - from 1.0 to 0.11 AU for 0 and 0.005 wt% PtCl₂ respectively. However, there was a sharp drop in intensity between low PtCl₂ loadings (approximately 0.96 AU for 0.00075 and 0.00125 wt%) and high PtCl₂ loadings (approximately 0.12 AU for 0.0025 and 0.005 wt%). This is in contrast with the uncured samples, where emission intensity decreased at a relatively uniform rate with increasing catalyst concentration. This suggests a trade-off between Pt-induced quenching and the improved passivation arising from the

accelerated curing of the matrix. Therefore, it is recommended that loading does not exceed 0.00125 wt% Pt-Ink B as quenching becomes significant.

All samples showed linear decrease in emission intensity with increasing temperature for both thermal cycles. Sensitivities were typically half that of the uncured analogues; trendline gradients are listed in Table 34. Percentage emission intensity thermal coefficients increased with higher catalyst concentration and lower emission intensity, as platinum-induced quenching led to weaker signal strength. Sensitivity as a function of intensity count was highest for low PtCl₂ loadings (0.00075 and 0.00125 wt% PtCl₂) followed by the sample without added catalyst. The greater overall percentage decrease in emission between 30 to 40 °C in samples with higher catalyst loading could be interpreted as reduced photostability resulting from the platinum-induced quenching mechanism; this is supported by the change in thermal coefficients between thermal cycles. All samples with added catalyst showed decreased sensitivity on the subsequent thermal cycle, correlating with overall emission intensity; approximately 13.5 and 24.8% decreases were observed for 0.00075 and 0.00125 wt% PtCl₂, respectively. Therefore, although high loadings of catalyst led to higher apparent sensitivity, low loadings are recommended for higher signal-to-noise ratios and to minimise platinum-induced quenching.

Table 34: Percentage emission intensity thermal coefficients for temperature-dependent emission in cured octyl acetate ink QD-silicone composites for each loading of additional platinum catalyst.

	Cycle	<i>PtCl₂ loading in Ink B wt%</i>				
		0	0.00075	0.00125	0.0025	0.005
<i>Sensitivity</i> % °C ⁻¹	1	-1.0680	-1.9071	-2.0980	-2.9175	-2.8248
	2	-1.1349	-1.6473	-1.5755	-2.7395	-2.6175

Overall, emission intensity decreased with temperature in all samples and >90% PL was retained between thermal cycles of 30-40 °C. Sensitivity differed between cycles; decreases in sensitivity were associated with catalyst which may indicate reduced photostability. PtCl₂ loadings ≤0.00125 wt% appear most viable: while linear temperature-dependence was seen with higher catalyst loadings, samples yielded much weaker signals and had greater variance.

6.2.2. Toluene-based addition cure composites

The temperature-dependent photoluminescence of toluene-based addition cure analogues was investigated for a range of PtCl₂ loadings using analogous inks to prepare cured composites (see Methodology Section 3.2.6.1). Emission is plotted below in Figure 112 as a function of temperature (left) and PtCl₂ loading (right). For 0 wt% PtCl₂, toluene ink-based composites were approximately twice as bright as octyl acetate-based analogues (214.5% at 30 °C, cycle 1).

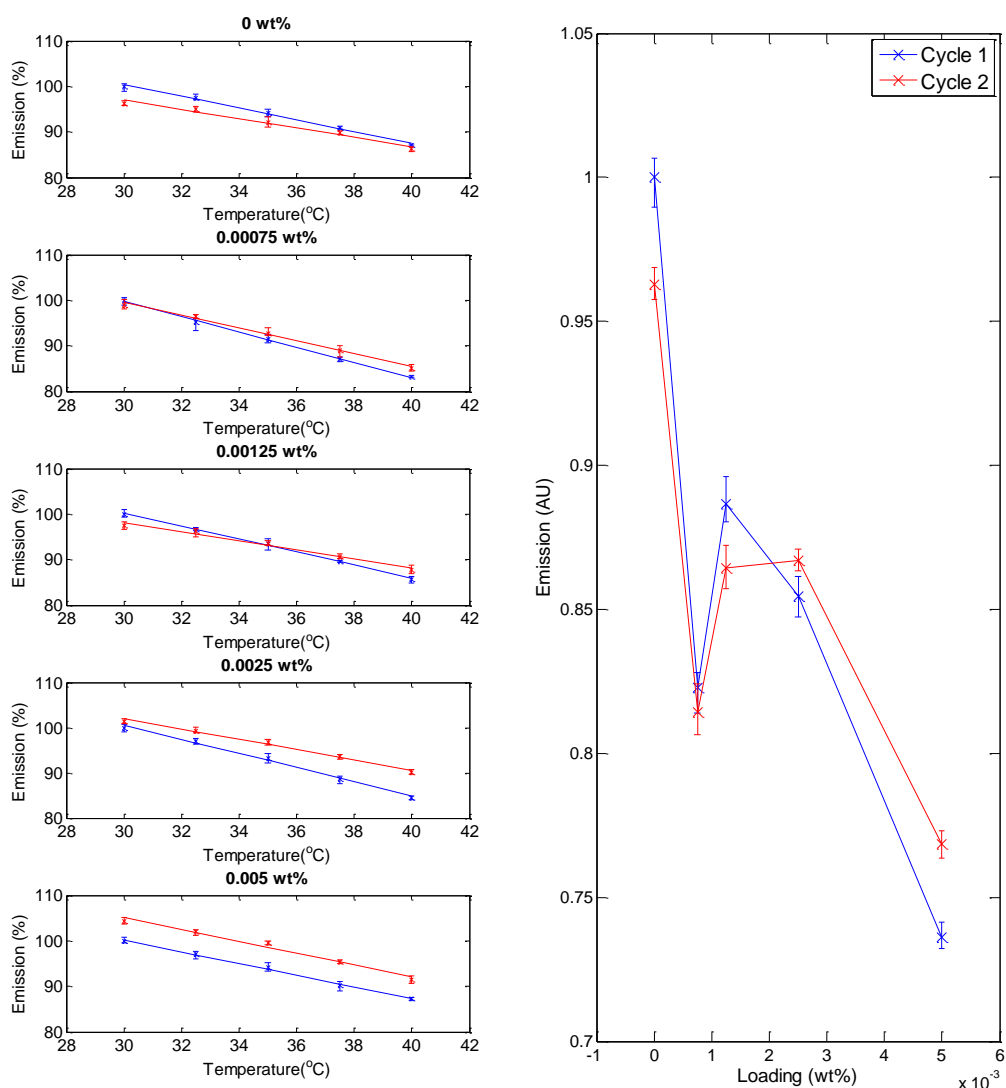


Figure 112: Emission of cured toluene ink QD-silicone composites. Bars display the range of values. Left: Emission as a function of temperature for each loading of additional catalyst. Right: Emission as a function of additional platinum catalyst at 30 °C.

Additional platinum catalyst was seen to decrease emission intensity - as in the case of octyl acetate-based samples - from 1.0 to 0.74 AU for 0 and 0.005 wt% PtCl₂ respectively. This is a much smaller decrease in emission intensity than was observed for octyl acetate-analogues; it is possible that differences in solvent properties limited the effectiveness of

Pt-mediated quenching, or that the more rapid reaction rate (as seen in Section 4.5.1) simply allowed less time for quenching mechanisms to occur. Emission intensity decreased with increasing PtCl₂ loading, with the exception of 0.00075 wt% PtCl₂ which was lower than expected. Smaller decreases in intensity were seen between intermediate PtCl₂ loadings than from 0 wt% (~0.15 AU higher than 0.00075-0.0025 wt%) or 0.005 wt% PtCl₂ (~0.11 AU lower than 0.00075-0.0025 wt%), in contrast to the octyl acetate analogues where a sharp drop in emission intensity was seen between low and high PtCl₂ loadings. The overall magnitude of intensity change between samples was smaller than seen for octyl acetate but the relative intensities changed between cycles; while toluene solvent may be advantageous in reducing Pt-mediated quenching, the samples showed less consistent thermal response and appear less suitable for sensing materials.

Percentage emission intensity thermal coefficients were collected from lines of best fit, as listed in Table 35. All samples showed linear decrease in emission intensity with increasing temperature for both thermal cycles, as expected of CdSe-based QDs immobilised in a polymer matrix.^{156,160,164} Percentage sensitivity and sensitivity as function of intensity count both appeared to be highest at intermediate Pt loadings (0.00075-0.0025 wt% PtCl₂) and all samples became less sensitive after a thermal cycle. In the second thermal cycle, emission intensities were >96% that of cycle 1 at 30 °C and >99% at 40 °C. Relative intensity between cycles increased with increasing Pt loading, with one exception: at 30 °C, 0.00075 wt% PtCl₂ had greater PL retention between cycles than 0.00125 wt% PtCl₂. Sensitivity trends in both cycles correlated with PL retention between cycles and the overall signal strength.

Table 35: Percentage emission intensity thermal coefficients for temperature-dependent emission in cured toluene ink QD-silicone composites for each loading of additional platinum catalyst.

	Cycle	<i>PtCl₂ loading in Ink B wt%</i>				
		0	0.00075	0.00125	0.0025	0.005
<i>Sensitivity</i> % °C ⁻¹	1	-1.2926	-1.6743	-1.4276	-1.5740	-1.2926
	2	-1.0555	-1.4244	-1.0163	-1.1126	-1.2397

Overall, while the emission intensity of the composites prepared from 60 wt% SiliGlass toluene-based inks was greater than that of the 50 wt% SiliGlass octyl acetate analogues, the relative intensities of different samples and their sensitivities were inconsistent, which was not ideal for sensing. The observed effect of Pt-mediated quenching is weak, whether due to faster reaction rates or different solvent properties between toluene and octyl acetate-based inks.

6.2.3. UV cure composites

The fluorescence of UV cure silicones was investigated in Chapter 5, where quenching of cured composites was observed; as a result, addition cure composites were prioritised. However, as UV cure formulations for QD-silicone composites remain of interest, wells were prepared as described in Section 3.2.6.1. UV inks were formulated with methacryloxy-terminated PDMS (AB116678), referred to as 'PDMS' in the context of UV inks, or 1:1 PDMS to 2-ethylhexyl acrylate by weight ('2-EHA' inks). Two different photoinitiators were investigated: DMPA and TPO. As high loadings of DMPA (but not TPO) were observed to lead to QD quenching (Section 5.3.3), wells were prepared with 0.1 or 0.001 wt% PI.

Emission intensity is shown for DMPA inks in Figure 113 below as a function of temperature and formulation (bottom). Intensity of 0.1 wt% DMPA-PDMS was similar to that of 0 wt% PtCl₂ octyl acetate ink-based composites (110.1% intensity at 30 °C, cycle 1).

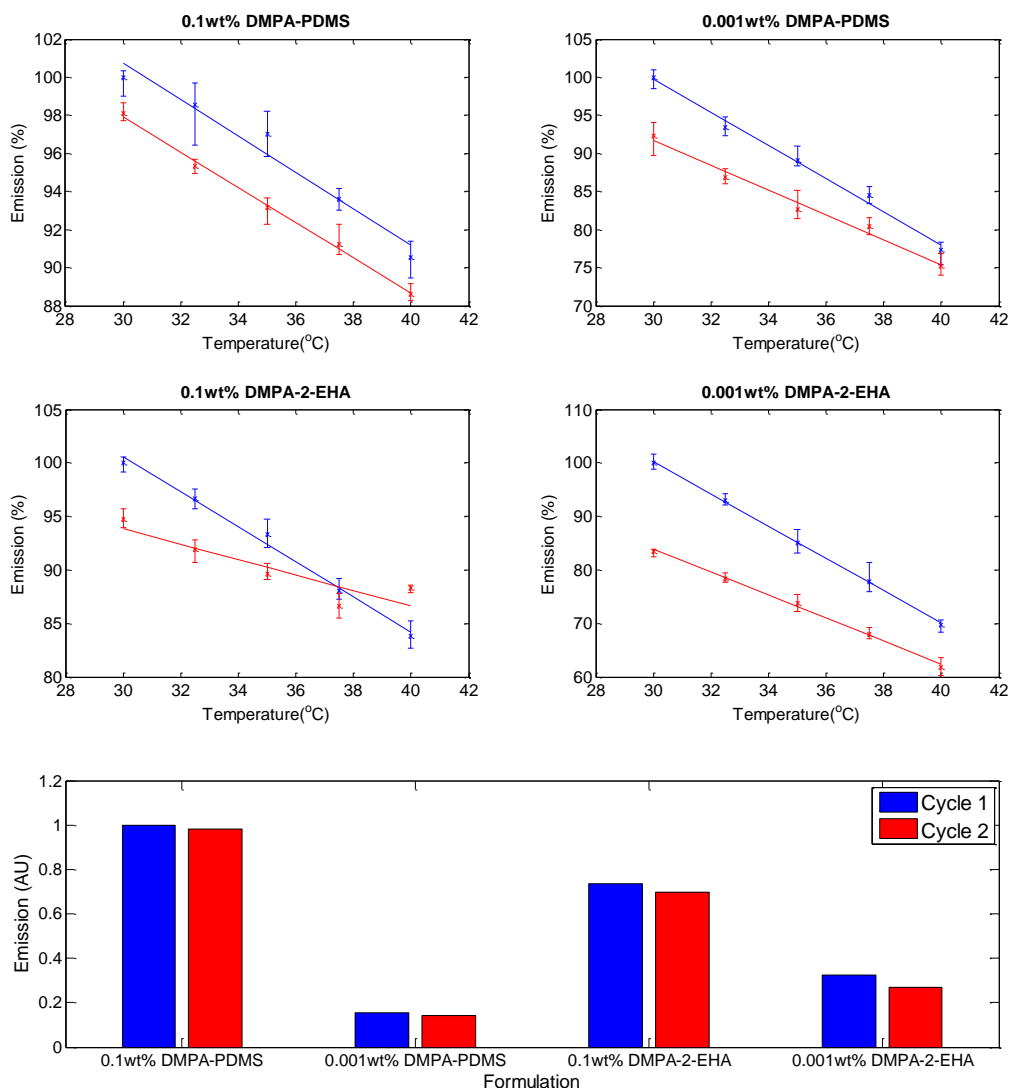


Figure 113: Emission of UV cured DMPA QD-silicone composites. Emission as a function of temperature for each formulation. Bars display the range of values. Bottom: Comparison of formulations at 30 °C.

All samples showed a decrease in emission intensity with increasing temperature in both thermal cycles, although 0.1 wt% DMPA-PDMS deviated from linearity in cycle 1 and 0.1 wt% DMPA-2-EHA in cycle 2. Percentage emission intensity thermal coefficients from trendlines are shown in Table 36; when plotted as a function of intensity count, samples with higher DMPA loadings typically had greater sensitivity, correlating with greater emission intensity. Lower loadings of DMPA were associated with lower emission intensity: it is likely that poor curing was achieved and that the QDs were less effectively immobilised, leading to loss of PL similar to that observed in uncured inks (Section 5.3.3). The 0.001 wt% DMPA inks had the lowest emission intensities, in line with earlier observations of QD photostability in uncured PDMS inks. However, 0.1 wt% DMPA-PDMS had the greatest emission intensities despite PDMS being less effective for QD dispersion; it may be that the increased free volume resulting from branched 2-EHA monomers led to more thorough oxygen dissolution which inhibited curing or entanglement which slowed curing, or that microphases formed which reduced the transparency of the cured polymer.

All composites became less sensitive to temperature after a thermal cycle of 30-40 °C and inks with lower DMPA loadings saw a greater loss in PL following a thermal cycle, which may indicate poorer curing and QD passivation. Of the 0.1 wt% DMPA samples, 2-EHA had the highest initial sensitivity but an anomalously low sensitivity in cycle 2 due to an increase in intensity at 40 °C in the second cycle. 0.1 wt% DMPA-PDMS had similar percentage intensity thermal coefficients in each cycle and the highest emission intensities overall, which suggests that this formulation was the most suitable for temperature sensing.

Table 36: Percentage emission intensity thermal coefficients for temperature-dependent emission in UV cured DMPA ink QD-silicone composites for each ink formulation.

	Cycle	<i>DMPA loading wt%</i>			
		DMPA-PDMS		DMPA-2-EHA	
		0.1	0.001	0.1	0.001
<i>Sensitivity</i>	1	-0.9553	-2.1703	-1.6408	-3.0225
<i>% °C⁻¹</i>	2	-0.9443	-1.7651	-0.7604	-2.5748

Emission intensity as a function of temperature and formulation is shown for TPO inks in Figure 114 below. The intensity of 0.001 wt% TPO-PDMS was greater than that of 0 wt% PtCl₂ octyl acetate ink-based composites (146.2% intensity at 30 °C, cycle 1) and of the DMPA analogues.

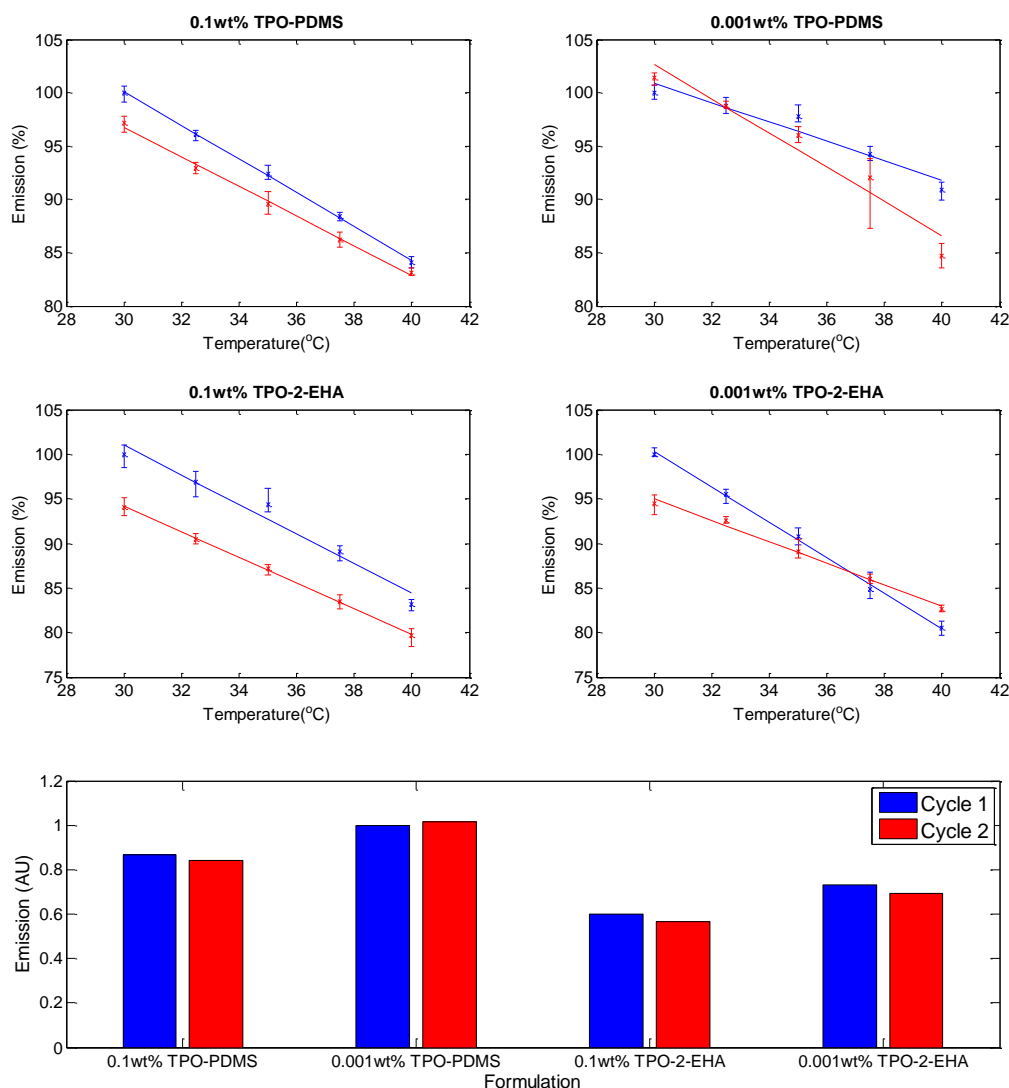


Figure 114: Emission of UV cured TPO QD-silicone composites. Emission as a function of temperature for each formulation. Bars display the range of values. Bottom: Comparison of formulations at 30 °C.

Unlike the DMPA inks, higher loadings of TPO were associated with lower intensities and sensitivities, even though TPO had not been observed to lead to greater quenching of emission (as DMPA had in Section 5.3.3). It is likely that this results from TPO's higher absorptivity of the UV-LED wavelength, which meant that curing occurred more effectively at low loadings of TPO than DMPA leading to a smaller difference in QD passivation between the two TPO loadings. Furthermore, differences in QD passivation may be less detrimental to fluorescence, due to the weaker quenching observed in the presence of TPO compared to DMPA. The comparatively small difference in intensity between the two PI loadings may result from competition for UV absorption between TPO and the QDs, weak TPO-mediated or polymerisation-induced quenching, or reduced transparency in cured materials, and further investigate is needed to determine the cause.

In both thermal cycles, all composites showed a decrease in emission intensity with increasing temperature, as expected of QDs. Sensitivities from lines of best fit are listed below in Table 37; when plotted as a function of intensity count, PDMS inks had consistently higher sensitivities than 2-EHA, correlating with greater emission intensity. Both PDMS inks had higher emission intensities than the 2-EHA inks, despite observations of poorer QD stability in PDMS precursor. As discussed above, the branching of the 2-EHA monomer may lead to difference in reaction rate that affect QD passivation in the cured polymer, or lead to the formation of microstructures that increase scattering and reduce transmittance.

All samples became less sensitive after a thermal cycle of 30-40 °C, with the exception of 0.001 wt% TPO-PDMS. Samples containing 0.1 wt% TPO had similar decreases in sensitivity to each other (PDMS and 2-EHA inks had sensitivities 90.6 and 91.8% that of the first cycle). While samples with 0.001 wt% TPO had greater emission intensities, they also had greater variance. 0.001 wt% TPO-PDMS deviated from linearity in both cycles and 0.1 wt% TPO-2-EHA in cycle 1; the data for cycle 2 of 0.001 wt% TPO-PDMS had very large error bars and appeared curved. 0.1 wt% TPO-PDMS and 0.1 wt% TPO-2-EHA showed the most consistent thermal responses and were therefore the most suitable for temperature sensing, although further optimisation is needed.

Table 37: Percentage emission intensity thermal coefficients for temperature-dependent emission in UV cured TPO ink QD-silicone composites for each ink formulation.

	Cycle	TPO loading wt%			
		TPO-PDMS		TPO-2-EHA	
		0.1	0.001	0.1	0.001
<i>Sensitivity</i> % °C ⁻¹	1	-1.5811	-0.9053	-1.6566	-1.9859
	2	-1.4320	-1.5829	-1.5209	-1.2792

Overall, emission intensity of the UV curable formulations was higher than that of the octyl acetate ink-based composites, but UV inks showed greater variance in temperature response. A more complete investigation is required to optimise photoinitiator loading and curing of UV cure samples to obtain consistent crosslinking density, emission, and photostability. 0.1 wt% DMPA-PDMS, 0.1 wt% TPO-PDMS, and 0.1 wt% TPO-2-EHA appeared to be the most promising UV formulations for temperature-sensing materials as they had comparatively strong emission, little loss in intensity between cycles, and more consistent thermal coefficients.

6.2.4. Summary of well-plate reading

Temperature-dependent photoluminescence was observed in all samples using well-plate reading to screen materials. Emission intensity varied between formulations: uncured octyl acetate inks had the highest emission intensity, followed by toluene ink-based composites, 0.001 wt% TPO-PDMS composite, 0.1 wt% DMPA-PDMS composite, and octyl acetate ink-based composites. The reasons for the observed differences are unclear but reaction rate appears to be a significant factor. Further optimisation of the heat program and UV curing program used in sample preparation would be ideal. Emission intensities were shown to decrease with temperature in all samples, the majority of which showed a linear relationship. Temperature sensitivity decreased between thermal cycles in the majority of samples; further experiments are needed to assess photostability.

For the addition cure composites, decreases in emission intensity for samples containing additional platinum catalyst agreed with prior observations of PL quenching in PL maps, composite monoliths, and printed materials (see Chapter 4); differences in sensitivity may indicate poorer photostability, likely arising from Pt-mediated quenching mechanisms. In octyl acetate-based inks, emission decreased evenly with increasing PtCl_2 loading in uncured inks while, in cured composites, 0-0.00125 wt% PtCl_2 had higher emission intensities than 0.0025-0.005 wt% PtCl_2 . In cured composites, PtCl_2 loadings ≤ 0.00125 wt% appeared most viable for sensing: higher Pt loadings led to much weaker signal and higher deviation. Observed Pt-mediated quenching was weaker in toluene-based inks, whether due to faster reaction rates or different solvent properties between toluene and octyl acetate-based inks. While toluene composites had stronger emission intensity at all PtCl_2 loadings, greater variances were seen between cycles: in particular, 0.005 wt% had almost unchanged sensitivity, but increased intensity, after a thermal cycle. 0.00075 wt% PtCl_2 had the most consistent behaviour between runs but more measurements are needed to ascertain reliable readings.

For the UV cured composites, emission intensity of TPO formulations was higher than all DMPA formulations. It is likely that this results from TPO's higher absorptivity of the UV-LED wavelength, which meant that curing occurred more effectively at low loadings of TPO than DMPA and that QDs were therefore better stabilised. Low loadings of DMPA were associated with lower emission intensity while the inverse is true of TPO: this was unexpected, as high loadings of DMPA were associated with PL quenching but this was not seen for TPO (Sections 5.3.3 and 5.4.1). PDMS inks typically had higher emission intensity than 2-EHA inks, which may correlate to their faster cure rate observed in DSC

(Section 5.5.1). Strong quenching of fluorescence was not observed during the course of measurement, despite having previously been observed in UV cure silicones. 0.1 wt% TPO-PDMS appeared to lead to the most reliable sensing and is also expected to be the most thoroughly cured UV-cure sample. Overall, the attempts to standardise the UV cure program for well-plate preparation likely led to the trends observed.

While well-plate readers were used as a tool for high throughput screening of temperature sensitive materials, well-plate preparation was challenging and further work to establish the optimal curing program for each formulation is advisable for more rigorous assessment of sensing behaviour and to prevent variations in heating, crosslinking, QD distribution, and residual solvent between samples. Material lifetime is another concern as repeatability was imperfect; photostability experiments and repeated measurements utilising more effective cooling between thermal cycles are needed to validate sensing performance. The utility of the HTS approach was demonstrated: multi-functional well-plate readers that are capable of high-resolution imaging, collection of detailed PL spectral data, and other common spectroscopic techniques present a powerful tool for material development of optical temperature-sensing composites.

6.3. Confocal microscopy

Confocal laser scanning microscopy (cLSM) was used to study the fluorescence of QD aggregates within silicone matrices as a function of temperature to assess the performance of printable sensing materials, as described in Section 3.2.6.4. Images were collected of composites cured from three addition cure ink formulations to assess their utility as printable temperature-sensing materials: 0.00125 wt% PtCl₂ octyl acetate-based inks, octyl acetate-based inks without added platinum, and toluene-based inks without added platinum.

In this section:

- Composites were imaged to compare dispersion and size of QD aggregates
- Lambda scans were collected to assess changes in emission intensity and wavelengths as a function of temperature, obtaining sensitivity values for the linear region (30-50 °C)
- Repeated thermal cycles of 25-60 °C were carried out to assess stability
- Non-linear PL quenching was investigated between 60-99 °C.

Current inkjet-printed temperature sensors are based on measurement of resistance across a circuit. However, there is a need for high-resolution and high-sensitivity temperature sensing in fields such as micro/nanoelectronics, integrated photonics, and biomedicine. Inkjet-printable QD-silicone composites for luminescence thermometry were developed to better meet these requirements and enable *in situ* sensing for a wider range of printed devices. Confocal microscopy was used to test and compare the performance of formulations via assessment of two different PL parameters.

QD nanothermometry may be conducted based on changes in photoluminescent (PL) intensity, band shape, spectral position, and lifetime,^{1,2} as described in Section 2.3.4. Intensity-based and spectral-based sensing were assessed using cLSM to compare the performance of materials prepared from inks to current inkjet printable temperature sensors and to QD-based temperature sensing in literature. The utility of different sensing parameters, need for normalisation and calibration, and hysteresis were also explored.

The emission intensity of QDs is well-known to show linear and reversible decrease as temperature increases in the ambient temperature range (approximately 5-60 °C), resulting in a constant thermal coefficient which is desirable for sensing^{1,2} and facile to compare to existing devices and materials. Intensity data was collected from lambda scans at different

temperatures, which resulted in collections of frames with varied emission wavelength. Frames were analysed and mean greyscale values obtained to assess emission intensity: greyscale values are from 0-65535, from black to white.

Calibration of emission intensity-based sensing is challenged by dependence on QD concentration.^{1,2} As the dispersion of QDs in the printable composites was random,¹⁸ images were taken of the same region of a sample using identical gain to ensure internal validity. To determine the extent to which apparent temperature coefficients varied with differences in image analysis, three image sectioning regimes were used: a 'strict' thresholding of clusters, with maximal background removal as would be used for particle sizing; a 'loose' thresholding of clusters, where dimmer clusters and some of the immediate vicinity around the brighter clusters were also selected; and full image analysis, where no background removal was performed. Data presented is collected using 'loose' thresholding unless stated otherwise.

In contrast, spectral-based measurements monitor emission peak shifts and are unaffected by concentration of emission centres. The mean emission wavelength λ_{mean} was estimated using Equation 5 below.

Equation 5: Estimated mean emission wavelength λ_{mean} , where λ is the midpoint emission wavelength of each frame and g_λ is the mean greyscale value.

$$\lambda_{mean} = \frac{\sum(\lambda \cdot g_\lambda)}{\sum g_\lambda}$$

6.3.1. Octyl acetate-based addition cure composite with 0.00125 wt% PtCl₂ In Chapter 4, additional platinum catalyst was used to compensate for catalyst poisoning by labile amine ligands on the QD surface. 0.00125 wt% PtCl₂ was used to enable sufficient curing without excessive loss of PL, successfully demonstrating printing.

The micrograph of the imaged section of the 0.00125 wt% PtCl₂ octyl acetate-based sample and corresponding spectral data for cycle 1 are shown below in Figure 115. The imaged clusters appeared dimmer and sparser than those in micrographs of the printed films (Figure 70) and clusters were larger than in printed films with 4.5 μm mean Feret diameter, 3.9 μm modal, and 1.5-7.5 μm range. This may result from reduced heating during curing (15 min compared to 24 hrs for printing) if slower curing allowed greater aggregation. Weaker emission intensity was seen relative to the composites without added catalyst, as expected: Pt-mediated quenching had been observed in PL mapping, well-plate studies, and in observations of printed samples. As expected of CdSe/ZnS QDs, emission peak intensity decreased as temperature increased and the peak broadened and redshifted; this was observed in microscopy as a decrease in image brightness at emission wavelengths below 627 nm relative to those above 627 nm. In the first thermal cycle, the emission intensity at 627 nm decreased by 10.5% and 29.0% from 30 °C to 45 and 60 °C, respectively.

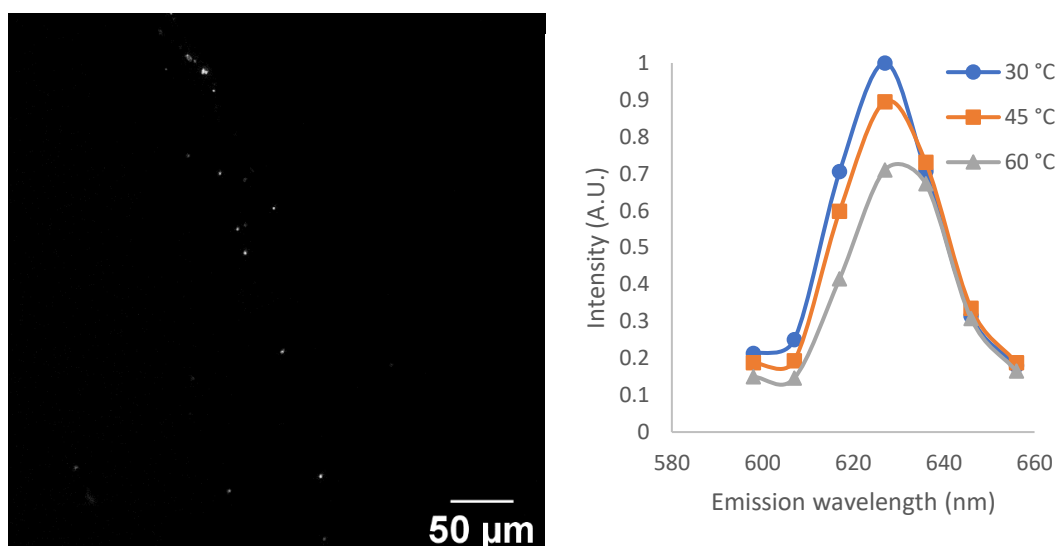


Figure 115: Left: Fluorescence micrograph of 0.00125 wt% PtCl₂ octyl acetate ink-based QD-silicone composite (cycle 1) at 27.5 °C ($\lambda_{\text{emission}} = 627$ nm). Right: Spectral profiles at 30, 45, and 60 °C.

Spectral data from the three thermal cycles are compared below in Figure 116 at 30, 45, and 60 °C. Emission intensity at 30 °C significantly decreased after a thermal cycle; differences in intensity between cycles were less significant at higher temperatures and intensities were very similar at 60 °C. At 30 °C, a relatively large decrease in emission intensity was observed between cycle 1 and 2 (approximately 10%), and a smaller loss

between cycle 2 and 3 (approximately 2%). Spectral profiles of different thermal cycles at 30 °C appear similar when intensities are normalised to the 627 nm emission; some changes are seen in the relative intensities of emission wavelengths. It appears that the samples had poor photostability, or that cooling was insufficient; however, inadequate cooling, particle coarsening, photo-oxidation, and/or yellowing were not likely to be primary mechanisms as mean emission wavelengths and spectral coefficients appeared stable between cycles (refer to Figure 118).

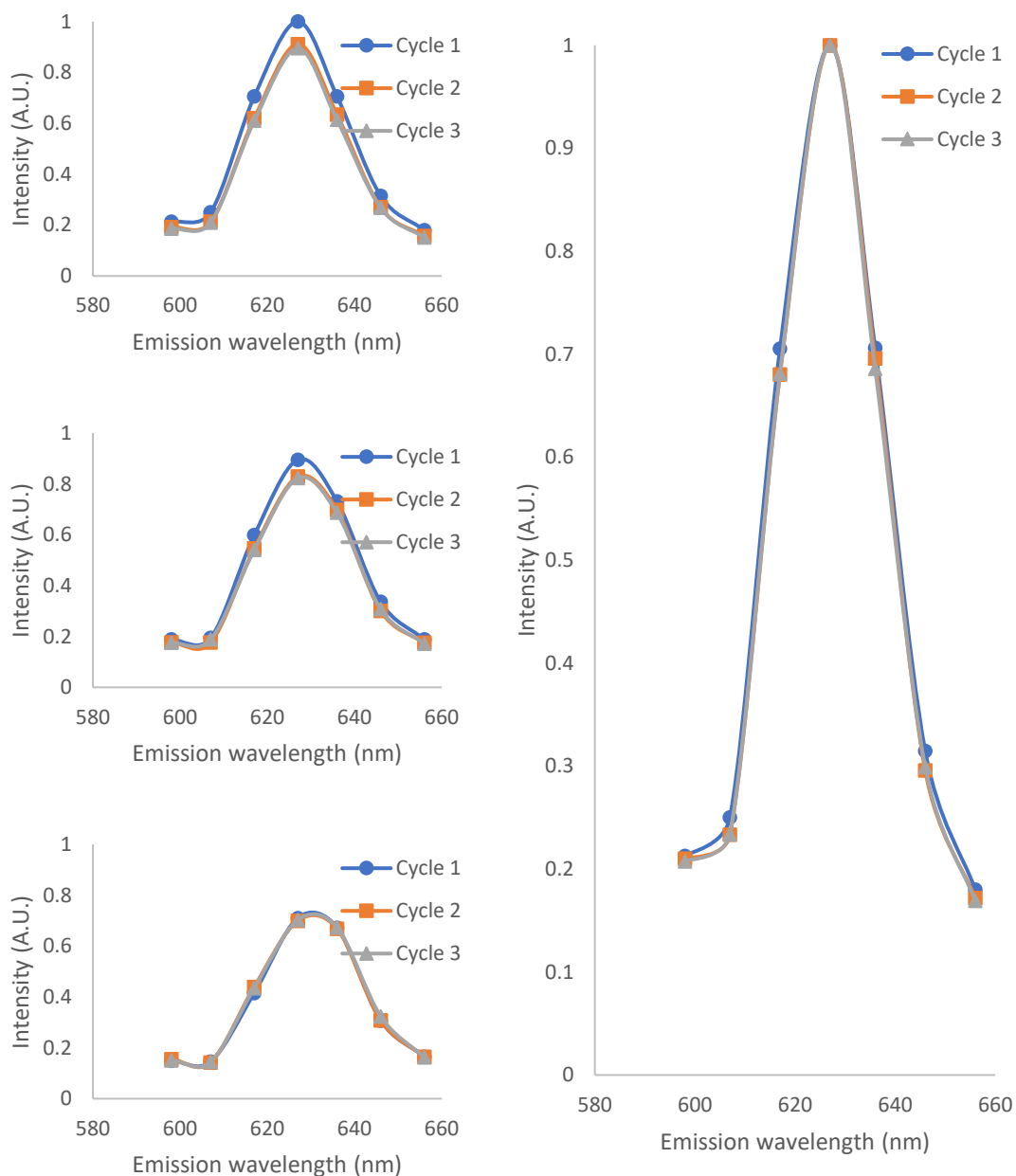


Figure 116: Left: Spectral profiles of subsequent thermal cycles at 30, 45, and 60 °C (top to bottom) of 0.00125 wt% PtCl₂ octyl acetate ink-based QD-silicone composite. Right: Normalised spectral profiles of subsequent thermal cycles at 30 °C.

Emission intensity of the 0.00125 wt% octyl acetate-based sample is plotted as a function of temperature in Figure 117 below, with representative graphs for cluster imaging and full image analysis. Emission intensity at wavelengths ≤ 627 nm decreased linearly between 30-50 °C, while emission intensity at wavelengths > 627 nm showed greater curvature: intensity initially increases as temperature increases and redshift occurs but begins to decrease at higher temperatures as thermal quenching increases.

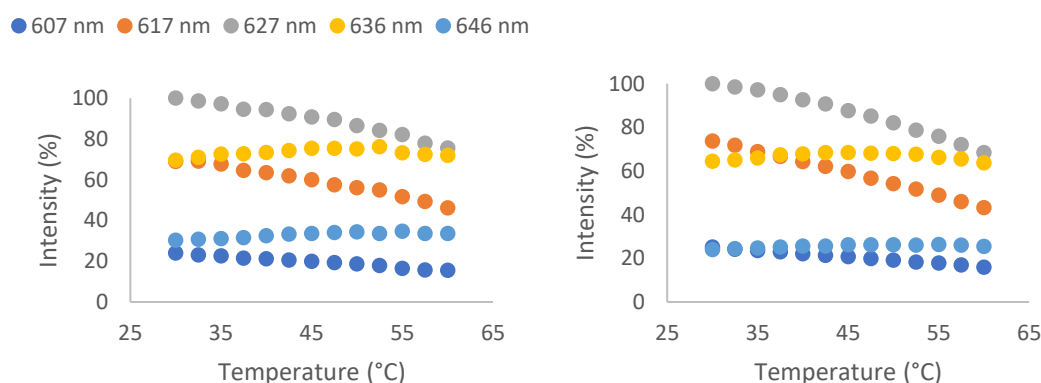


Figure 117: Representative graph of emission intensity as a function of temperature for the imaging of clusters (left) and the analysis of the full captured image (right) of 0.00125 wt% PtCl₂ octyl acetate ink-based QD-silicone composite at different emission wavelengths. Data shown is the average of the three thermal cycles.

Linear trendlines were applied to the data and the thermal coefficients of trendlines are listed in Table 38 below. As emission intensities > 627 nm showed greater curvature, the lines of best fit obtained for those emissions tended to have low R² values and their gradients are presented to give an indication of trend rather than expected sensing performance. Across the thermal cycles, thermal coefficients of emission intensity at all wavelengths tended to become more positive and R² values tended to increase, as emission intensities at 30 °C decreased, which implies thermal or photo-aging processes take place which quench QD fluorescence.

Table 38: Percentage emission intensity thermal coefficients (30-50 °C) at different wavelengths from images of 0.00125 wt% PtCl₂ octyl acetate ink-based QD-silicone composite using three image sectioning regimes.

Cycle 1 Emission nm	Strict threshold		Loose threshold		Full image	
	Sensitivity % °C ⁻¹	R ² value	Sensitivity % °C ⁻¹	R ² value	Sensitivity % °C ⁻¹	R ² value
607	-0.3610	0.9440	-0.3152	0.9563	-0.3334	0.9758
617	-0.7823	0.9690	-0.8369	0.9611	-1.1792	0.9979
627	-0.6258	0.9696	-0.6924	0.9842	-1.1560	0.9865
636	0.1383	0.8745	0.1333	0.6770	0.0034	0.0007
646	0.1119	0.8745	0.1375	0.6821	0.0395	0.3767

Cycle 2	Strict threshold		Loose threshold		Full image	
<i>Emission nm</i>	<i>Sensitivity % °C⁻¹</i>	<i>R² value</i>	<i>Sensitivity % °C⁻¹</i>	<i>R² value</i>	<i>Sensitivity % °C⁻¹</i>	<i>R² value</i>
607	-0.2800	0.9060	-0.2379	0.9502	-0.303	0.9718
617	-0.6379	0.9332	-0.6531	0.9636	-0.9185	0.9975
627	-0.6867	0.9189	-0.6737	0.9848	-0.8134	0.9805
636	0.2549	0.5705	0.2866	0.7708	0.2242	0.8202
646	0.2168	0.8306	0.1767	0.8659	0.1303	0.8659
Cycle 3	Strict threshold		Loose threshold		Full image	
<i>Emission nm</i>	<i>Sensitivity % °C⁻¹</i>	<i>R² value</i>	<i>Sensitivity % °C⁻¹</i>	<i>R² value</i>	<i>Sensitivity % °C⁻¹</i>	<i>R² value</i>
607	-0.2355	0.7652	-0.2219	0.8444	-0.2440	0.9594
617	-0.5890	0.9393	-0.6035	0.9575	-0.8214	0.9946
627	-0.5368	0.8940	-0.5495	0.9153	-0.7346	0.9747
636	0.3616	0.8530	0.4314	0.8830	0.3581	0.9131
646	0.3682	0.9331	0.3479	0.9643	0.1875	0.9610

Image processing had an effect on the observed thermal coefficients: while the value for average percentage intensity thermal coefficient at 627 nm was similar between strict and loose thresholding of clusters at -0.6164 and -0.6385 % °C⁻¹ respectively, a greater difference was seen when background removal was not performed. The full image led to lower signal-to-noise ratio, lower average greyscale values, and higher apparent percentage coefficients.

Sensitivities became more positive after a thermal cycle, except for strict thresholding at 627 nm emission where sensitivity increased from cycle 1 to 2. Sensitivities, and the magnitude of decrease after a cycle, correlated to average brightness of the image selection: across the three cycles, loose threshold and full image sectioning regimes were respectively 65.7% and 0.284% as bright on average as strict thresholding at 30 °C for 627 nm. Intensity of emission <627 nm decreased between cycles for all sectioning regimes while the opposite is true of emission >627 nm, implying thermal aging of QD-composites.

The average percentage intensity thermal coefficient obtained for the emission peak (approximately -0.6 % °C⁻¹ from 30-50 °C or -0.8 % °C⁻¹ from 30-60 °C for loose thresholding) is much higher than typical inkjet-printed sensors (0.1-0.3 % °C⁻¹)^{14,15} and is within range of those reported for intensity-based sensing using CdSe/ZnS core-shell QDs, as shown below in Table 39. However, intensity-based measurements are well-known to be dependent on concentration and laser power,¹ which makes both calibration and comparison between papers difficult. In this work, emission intensity-based measurements are complicated by the differences in patterning of the QD clusters throughout the matrix^{18,254} and the need to

set gain to minimise saturated pixels during image collection. In contrast, measurements based on spectral shift are independent of these factors and calibration is more facile. Therefore, the mean emission wavelength was estimated to assess redshift.

Table 39: Values reported for percentage intensity thermal coefficient for CdSe/ZnS quantum dots in literature. Papers where coefficients were not listed in text but could be obtained from the data presented are marked with an asterisk.

<i>Thermal coefficient</i> % °C ⁻¹	<i>Temperature range</i> °C	<i>QD emission wavelength</i> nm	<i>Dispersion medium</i>	<i>Author</i>
-0.3	24.4-43.6	655	PDMS polymer used to fix position of individual QDs	Li <i>et al.</i> ¹⁶⁸ *
-0.4 -0.7	20-70	655 620	Aqueous solution Unspecified polymer	Han <i>et al.</i> ¹⁶³ *
-0.7 -1.6	10-50	600 520	Unspecified, non-hydrolytic sol gel	Jorge <i>et al.</i> ¹⁵⁵
-1.0 -1.3	-23-42 (250-315 K) 5-40 (278-313 K)	600	PLMA polymer	Walker <i>et al.</i> ¹⁵⁶
-1.3	30-60	640	PS polymer	Liu <i>et al.</i> ¹⁶⁴

The emission peak λ_{max} was estimated using Equation 5 and plotted below in Figure 118. Average emission wavelength was seen to have a linear relationship with temperature using all three sectioning regimes, as is expected for CdSe/ZnS quantum dot fluorescence across a small, ambient temperature range.^{161,288} Values obtained using imaging of clusters were near-identical, while inclusion of the background (i.e. smaller signal-to-noise ratio) led to a decrease in estimated mean wavelength and a slight increase in the thermal coefficient of spectral shift.

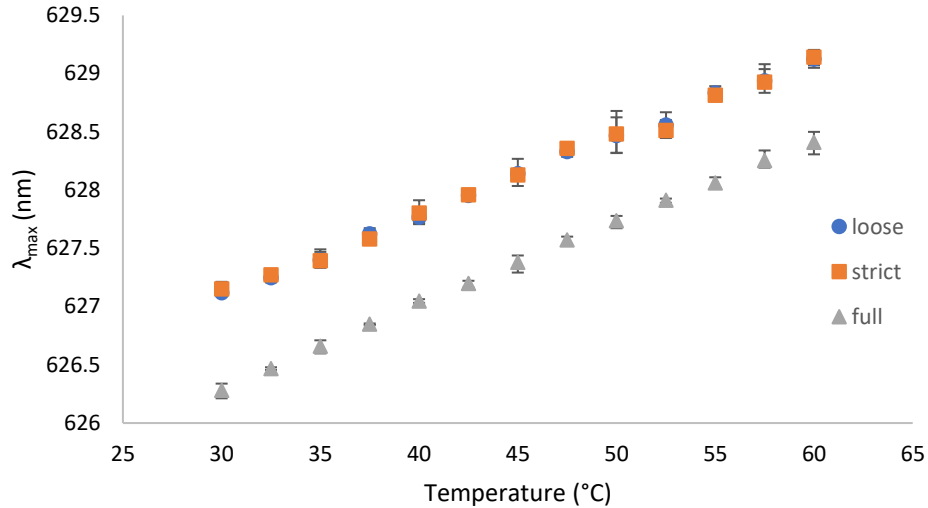


Figure 118: Estimated mean emission wavelength λ_{max} as a function of temperature for 0.00125 wt% PtCl₂ octyl acetate ink-based QD-silicone composite using three different image sectioning regimes. Data shown is the average of the three thermal cycles, with error bars denoting range.

Spectral shift thermal coefficients were obtained from lines of best fit and listed in Table 40 for different thresholding regimes. Between image sectioning regimes, apparent thermal coefficients increased as signal-to-noise ratio and average greyscale value decreased. The average spectral shift thermal coefficient for ‘loose’ thresholding was 0.0677 nm °C⁻¹, within the range of values reported for CdSe/ZnS QDs: 0.07-0.10 nm °C⁻¹.^{161,164,168,288} Values for mean emission wavelength at specific temperatures were similar between cycles and significant redshift was not observed, in contrast to changes in emission intensities. This may suggest that spectral-based sensing would remain reliable across thermal cycles at these temperatures, although further studies of thermal cycles with higher spectral resolution are needed to investigate thermal aging and to confirm repeatability. Changes in the QD ligand shell may rationalise the changes between cycles as a loss of labile species: amine ligands enhance PL of CdSe/ZnS QDs^{236–238} but are labile and temperature-dependant ligand detachment can occur,^{277–279} leading to a reduction in emission intensity. Solvent evaporation could also alter QD passivation within the matrix, though shrinkage would be expected but minimal thermal drift was observed.

Table 40: Spectral shift thermal coefficients (30-60 °C) from captured images of 0.00125 wt% PtCl₂ octyl acetate ink-based QD-silicone composite using three different image sectioning regimes.

Cycle	Strict		Loose		Full	
	Sensitivity nm °C ⁻¹	R ² value	Sensitivity nm °C ⁻¹	R ² value	Sensitivity nm °C ⁻¹	R ² value
1	0.0671	0.9838	0.0671	0.9914	0.0688	0.9954
2	0.0661	0.9836	0.0664	0.9914	0.0721	0.9953
3	0.0676	0.9773	0.0696	0.9897	0.0719	0.9967
Average	0.0669	0.9948	0.0677	0.9976	0.0709	0.9993

The non-linear intensity quenching region (approximately 50-99 °C) is shown below in Figure 119. Intensities followed curved profiles from approximately 50 °C onwards; an anomalous decrease in intensity was seen at 65-70 °C. Data overall showed greater fluctuation in intensity than seen in the 0 wt% octyl acetate ink-based composite (Section 6.3.2), likely due to comparatively poor dispersion of QD aggregates.

Above 70.0 °C, the emission intensity at 636 nm was greater than 627 nm and emission at all intensities decreased with increasing temperature. After heating to 99 °C, a 37.4% decrease in emission intensity at 627 nm was seen upon cooling to 60 °C, as compared to intensity at 60 °C before heating to elevated temperatures. This may indicate insufficient time was allowed for cooling; in temperature quenching studies of CdSe core-shell QD-polymer composites, intensity quenching was typically fully reversible up to 100 °C.¹⁶⁰ Repeated measurements are needed to assess non-linear quenching; fluorescence lifetime measurements would be of additional use in probing intrinsic quenching mechanisms.^{160,173}

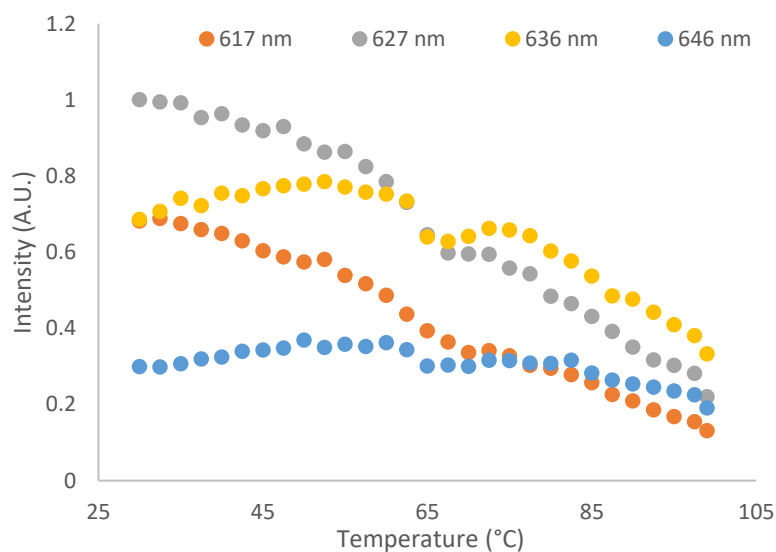


Figure 119: Left: Emission intensity of 0.00125 wt% PtCl₂ octyl acetate ink-based QD-silicone composite (cycle 3) as a function of temperature from 30-99 °C at different emission wavelengths. Data shown is for loose thresholding of clusters.

6.3.2. Octyl acetate-based addition cure composite without added catalyst
While catalyst poisoning was a significant barrier to printing addition cure QD-composites, octyl acetate-based addition cure QD-silicone composites were able to cure with sufficient heating. This formulation failed to cure during printing trials but samples for microscopy were produced with prolonged heating at 60 °C.

In this analysis, one thermal cycle of 25-60 °C was run on sample A and two cycles were run on sample B. Thermal cycles were taken from different regions of B; the gain was constant.

Sample A

The fluorescence micrograph of sample A of 0 wt% PtCl₂ octyl acetate-based composite and its corresponding spectral data are shown below in Figure 120. In comparison to the sample with added catalyst (Figure 115), a larger number of smaller and more evenly distributed clusters were seen with 2.6 μm mean Feret diameter, 1.9 μm modal, and 1.5-6.9 μm range. Fluorescence was brighter than that of the sample with 0.00125 wt% PtCl₂, as expected from previous observations of Pt-mediated quenching. Clusters also appeared brighter than in the samples from printing trials (Figure 70) due to better QD passivation as the inks did not cure during printing. The peak emission intensity decreased as temperature increased and appeared to redshift as the spectral profile broadened, as expected. Emission intensity at 627 nm decreased by 12.9% and 33.4% from 30 °C to 45 and 60 °C.

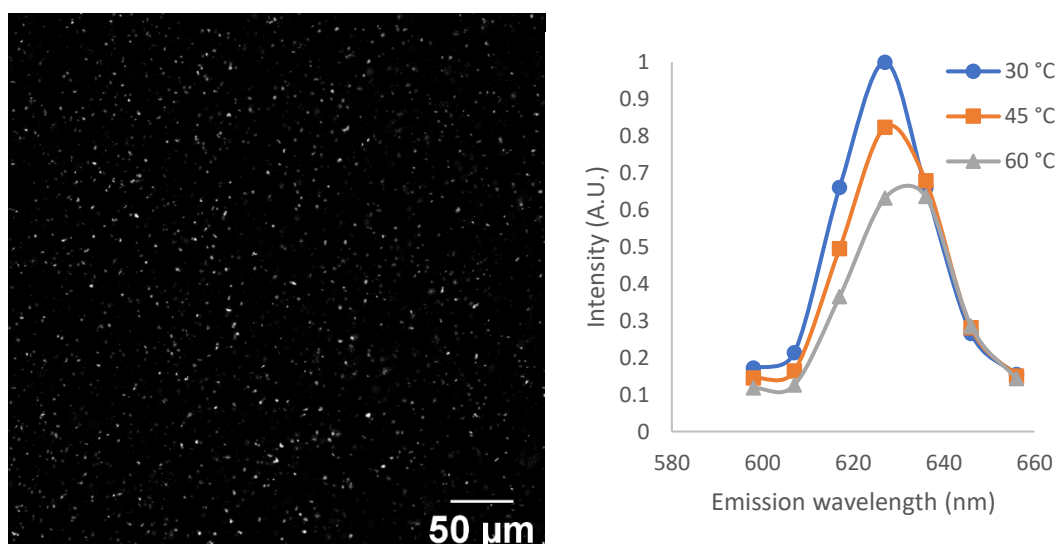


Figure 120: Left: Fluorescence micrograph of sample A of octyl acetate ink-based QD-silicone composite at 27.5 °C ($\lambda_{\text{emission}} = 627 \text{ nm}$). Right: Spectral profiles at 30, 45, and 60 °C.

Emission intensity as a function of temperature is shown below in Figure 121 with representative graphs for cluster imaging and full image analysis. Data was more linear in the full image analysis and R^2 values were larger; a sinusoidal pattern was seen in cluster imaging which may be a consequence of the image stabilisation process (for more details, see Section 3.2.6.4).

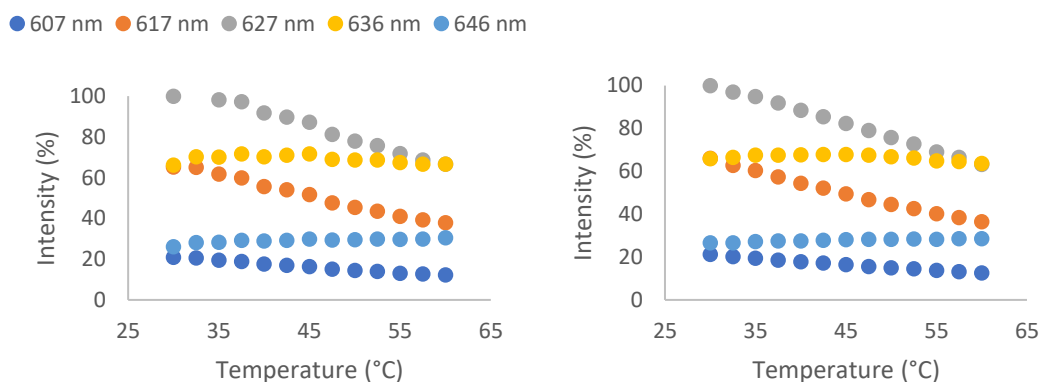


Figure 121: Emission intensity as a function of temperature for the imaging of clusters (left) and the analysis of the full image (right) of sample A of octyl acetate ink-based composite at different emission wavelengths.

Lines of best fit were applied to the data from 30-50 °C and the gradients of the trendlines are listed in Table 41 below. The percentage emission intensity thermal coefficient at 627 nm was -1.1779 , -1.2627 , and -1.2127 % °C⁻¹ for strict and loose thresholding of clusters and full image analysis, respectively, higher than observed in the sample with 0.00125 wt% PtCl₂, and more similar values were seen with different image sectioning regimes. Different image processing regimes had a smaller impact on the observed thermal coefficient than was seen for the sample with 0.00125 wt% PtCl₂, due to differences in QD cluster patterning: a greater proportion of visible QD clusters meant that a smaller proportion of background noise was present in the full image and that selection regimes were more similar in area and brightness.

Table 41: Percentage emission intensity thermal coefficients (30-50 °C) at different wavelengths from images of sample A of octyl acetate ink-based QD-silicone composite using three different image sectioning regimes.

Cycle 1	Strict threshold		Loose threshold		Full image	
	Sensitivity % °C ⁻¹	R ² value	Sensitivity % °C ⁻¹	R ² value	Sensitivity % °C ⁻¹	R ² value
607	-0.3409	0.9830	-0.3057	0.9908	-0.3122	0.9967
617	-1.0385	0.9745	-0.9938	0.9916	-1.0715	0.9984
627	-1.1779	0.9104	-1.2627	0.9816	-1.2127	0.9980
636	0.0631	0.0432	-0.0870	0.1961	0.0492	0.2542
646	0.1422	0.5785	0.0958	0.7106	0.0923	0.9500

The emission peak λ_{max} was estimated using Equation 5 and plotted below in Figure 122. All three sectioning regimes showed linear trends were close in both values for λ_{max} and the thermal coefficient; higher values were obtained when background removal was carried out, with little difference between loose and strict thresholding of clusters.

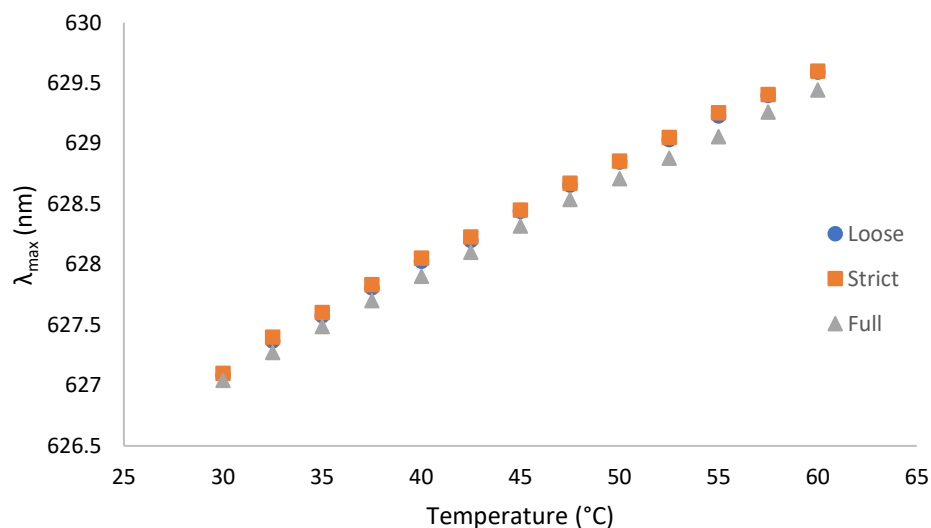


Figure 122: Estimated mean emission wavelength λ_{max} as a function of temperature for sample A of octyl acetate ink-based QD-silicone composite using three different image sectioning regimes.

Spectral shift thermal coefficients are listed in Table 42 for the different thresholding regimes. Similar values were obtained, suggesting that this sample was unsusceptible to variations in image analysis.

Table 42: Spectral shift thermal coefficients (30-60 °C) from images of sample A of octyl acetate ink-based QD-silicone composite using three different image sectioning regimes.

Cycle	Strict		Loose		Full	
	Sensitivity nm °C ⁻¹	R ² value	Sensitivity nm °C ⁻¹	R ² value	Sensitivity nm °C ⁻¹	R ² value
1	0.0821	0.9975	0.0826	0.9978	0.0795	0.9985

Sample B – Cycle 1

Two thermal cycles were carried out on sample B of 0 wt% PtCl₂ octyl acetate-based composite, but data was collected from different sections for each cycle to assess the effect of differences in QD patterning on measurement. The fluorescence micrograph of the imaged section of sample B for cycle 1 and its corresponding spectral data are shown below in Figure 123. The distribution and size of QD clusters appeared similar to sample A: mean Feret diameter was 2.6 μm, modal 1.9 μm, and ranged from 1.5-6.6 μm where 38.3% of clusters were <2 μm and 93.7% <4 μm.

The spectral profile showed intensity decrease, redshift, and broadening with increasing temperature, as is typical for QDs. The 627 nm emission intensity had lower overall change with temperature than was seen for sample A, which may reflect sample age (sample B was imaged 72 hours after sample A). Emission intensity at 627 nm decreased by 10.9% and 27.3% from 30 °C to 45 and 60 °C, respectively.

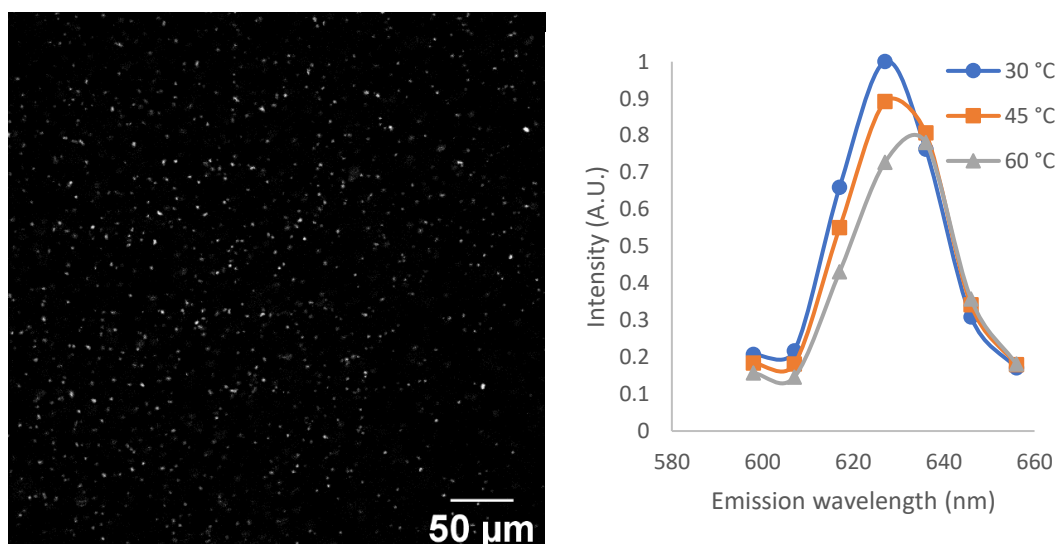


Figure 123: Left: Fluorescence micrograph of sample B of octyl acetate ink-based QD-silicone composite (cycle 1) at 27.5 °C ($\lambda_{\text{emission}} = 627$ nm). Right: Spectral profiles at 30, 45, and 60 °C.

Emission intensity as a function of temperature for cluster imaging and full image analysis is shown below in Figure 124 with representative graphs for cluster imaging and full image analysis.

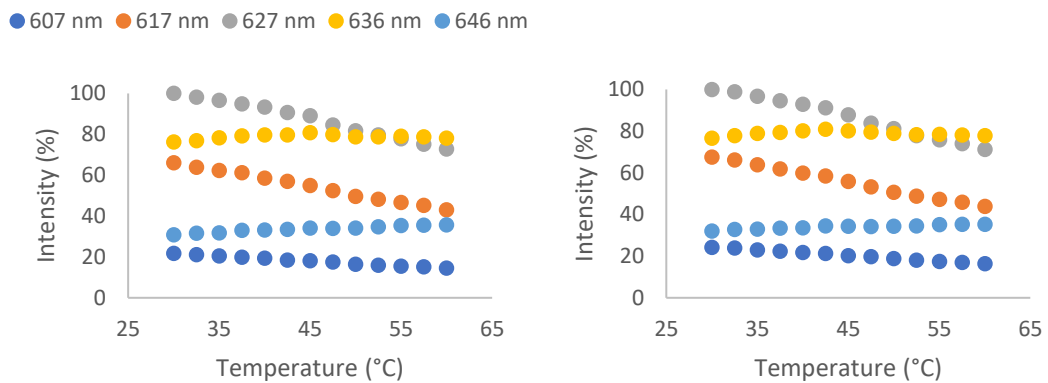


Figure 124: Emission intensity as a function of temperature for the imaging of clusters (left) and the analysis of the full captured image (right) of sample B of octyl acetate ink-based QD-silicone composite (cycle 1) at different emission wavelengths.

Lines of best fit were applied to the data from 30-50 °C and the percentage emission intensity thermal coefficients are listed in Table 43 below. The percentage emission intensity thermal coefficient at 627 nm was -0.8916, -0.9424, and -0.9419 % °C⁻¹ for strict and loose thresholding of clusters and full image analysis respectively, similar to but lower than values for sample A and correlating with the aforementioned smaller decrease in 627 nm emission intensity from 30-60 °C. This may indicate sample aging, although direct comparison is difficult due to the difference in gain used in data collection.

As in sample A, coefficients had similar values for different imaging approaches and loose thresholding of clusters had the highest sensitivity for 627 nm emission and the lowest for 607 nm. Sensitivity of regimes to different emission wavelengths correlated with their average brightness. At 30 °C for 627 nm emission, the average greyscale value for loose threshold and full image analysis was 55.6% and 3.37% that of strict threshold data respectively.

Table 43: Percentage emission intensity thermal coefficients (30-50 °C) at different wavelengths from sample B of octyl acetate ink-based QD-silicone composite (cycle 1) using three different image sectioning regimes.

Cycle 1 Emission nm	Strict threshold		Loose threshold		Full image	
	Sensitivity % °C ⁻¹	R ² value	Sensitivity % °C ⁻¹	R ² value	Sensitivity % °C ⁻¹	R ² value
607	-0.2615	0.9813	-0.2438	0.9955	-0.2687	0.9929
617	-0.8002	0.9860	-0.7802	0.9955	-0.8390	0.9933
627	-0.8916	0.9691	-0.9424	0.9895	-0.9419	0.9751
636	0.1002	0.3104	0.0459	0.1359	0.1185	0.4021
646	0.1628	0.8758	0.1556	0.9595	0.1163	0.8430

The emission peak λ_{max} was estimated using Equation 5 and plotted below in Figure 125. All three sectioning regimes showed linear trends and agreement with each other; full image analysis led to lower mean emission wavelengths and a smaller thermal coefficient than either of the cluster thresholds.

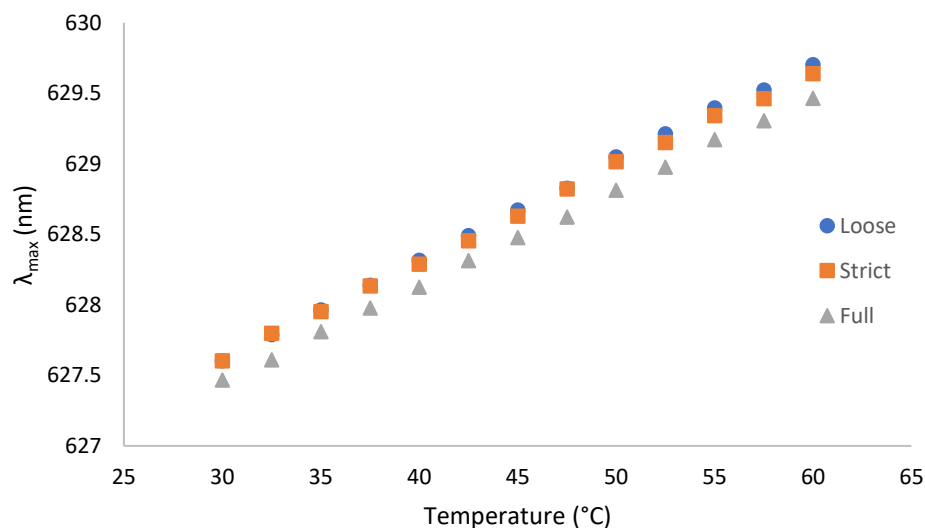


Figure 125: Estimated mean emission wavelength λ_{max} as a function of temperature for sample B of octyl acetate ink-based QD-silicone composite (cycle 1) using three different image sectioning regimes: strict and loose thresholding of clusters, and full image.

Spectral shift thermal coefficients are listed in Table 44 for the different thresholding regimes. All three image sectioning regimes had similar coefficients and R^2 values, suggesting insensitivity to image sectioning. Spectral shift thermal coefficient was lower than for sample A and values for λ_{max} higher, suggesting that sample aging associated with decreased intensity and redshift took place, such as particle coarsening or yellowing.

Table 44: Spectral shift thermal coefficients (30-60 °C) from images of sample B of octyl acetate ink-based QD-silicone composite (cycle 1) using three different image sectioning regimes.

Cycle	Strict		Loose		Full	
	Sensitivity nm °C ⁻¹	R ² value	Sensitivity nm °C ⁻¹	R ² value	Sensitivity nm °C ⁻¹	R ² value
1	0.0680	0.9993	0.0703	0.9995	0.0672	0.9995

Sample B – Cycle 2

A subsequent thermal cycle was run on the sample described above and a different region was imaged to assess the impact of variation in QD patterning. The fluorescence micrograph of the imaged section of sample B for cycle 2 and its corresponding spectral data are shown below in Figure 126. The distribution and size of QD clusters resembled other micrographs of this composite: mean Feret diameter was 2.8 μm , modal 2.4 μm , and ranged from 1.5-7.1 μm (21.0% of clusters were <2 μm diameter and 89.4% <4 μm).

The spectral profile showed intensity decrease, redshift, and broadening with increasing temperature. The emission intensity at 627 nm decreased by 9.1% and 19.3% from 30 °C to 45 and 60 °C, respectively. Average emission intensity at 30 °C was 2.4% lower than for cycle 1, similar to the difference between cycle 2 and 3 of the 0.00125 wt% PtCl₂ analogue.

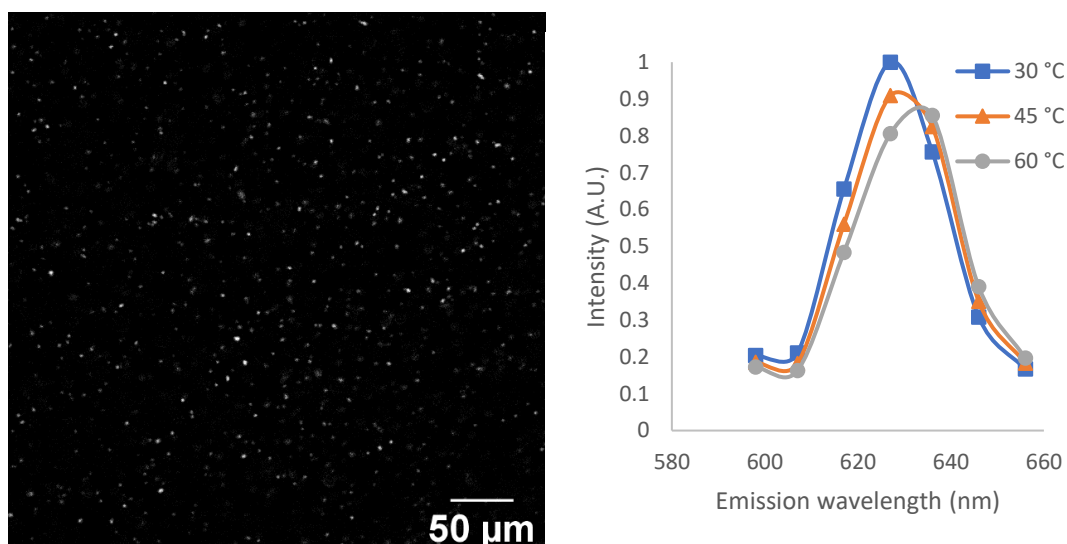


Figure 126: Left: Fluorescence micrograph of sample B of octyl acetate ink-based QD-silicone composite (cycle 2) at 27.5 °C ($\lambda_{\text{emission}} = 627 \text{ nm}$). Right: Spectral profiles at 30, 45, and 60 °C.

Emission intensity as a function of temperature is shown below in Figure 127 for cluster imaging and full image analysis.

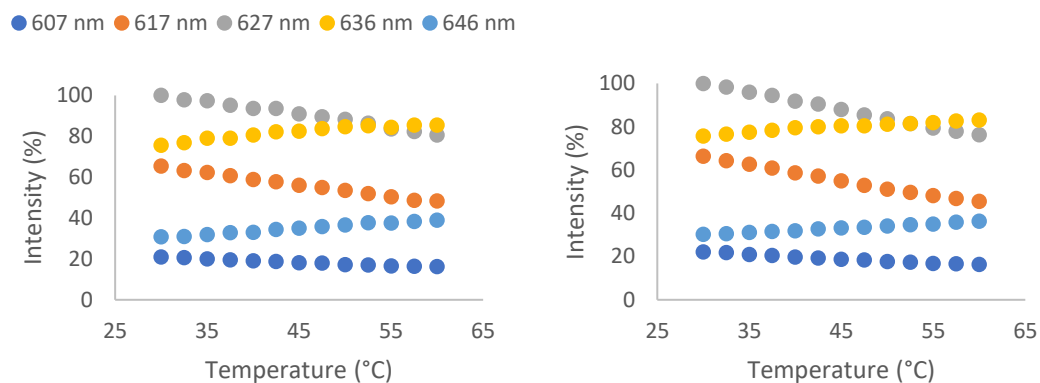


Figure 127: Emission intensity as a function of temperature for the imaging of clusters (left) and the analysis of the full captured image (right) of sample B of octyl acetate ink-based QD-silicone composite (cycle 2) at different emission wavelengths.

Lines of best fit were applied to the data from 30-50 °C and the gradients of the trendlines are summarised in Table 45 below; intensity appeared to vary linearly with temperature at all emission wavelengths. Signal-to-noise ratios of sectioning regimes, i.e. larger area and lower average greyscale value, correlated with higher sensitivities and R^2 values for emission at ≤ 627 nm, while the inverse was true of emission above 627 nm. At 30 °C for 627 nm emission, the average grey value for loose threshold and full image analysis was 54.01% and 2.96% that of strict threshold data respectively. Sensitivities and R^2 values for emission >627 nm increased after a thermal cycle: from 30-50 °C, emission at 636 nm increased by 3.3 and 12.0% and, at 646 nm, by 13.0 and 19.4% for cycles 1 and 2, respectively.

The temperature sensitivity at 627 nm was -0.5553 , -0.6381 , and -0.8272 % °C $^{-1}$ for strict and loose thresholding of clusters and full image analysis, respectively. All sensitivities were lower than Sample B cycle 1 in all image sectioning regimes, and image processing was observed to have a larger impact on observed coefficient.

Table 45: Percentage emission intensity thermal coefficients (30-50 °C) at different wavelengths in sample B of octyl acetate ink-based QD-silicone composite (cycle 2) using three different image sectioning regimes.

Cycle 2 Emission nm	Strict threshold		Loose threshold		Full image	
	Sensitivity % °C $^{-1}$	R^2 value	Sensitivity % °C $^{-1}$	R^2 value	Sensitivity % °C $^{-1}$	R^2 value
607	-0.1823	0.9712	-0.1657	0.9865	-0.2244	0.9920
617	-0.5782	0.9941	-0.5784	0.9966	-0.7606	0.9989
627	-0.5553	0.9765	-0.6381	0.9892	-0.8272	0.9973
636	0.4215	0.9729	0.3337	0.9249	0.2768	0.9538
646	0.3027	0.9854	0.2895	0.9880	0.2011	0.9905

The emission peak λ_{max} was estimated using Equation 5 and plotted below in Figure 128. All three sectioning regimes showed linear trends and similar values to each other.

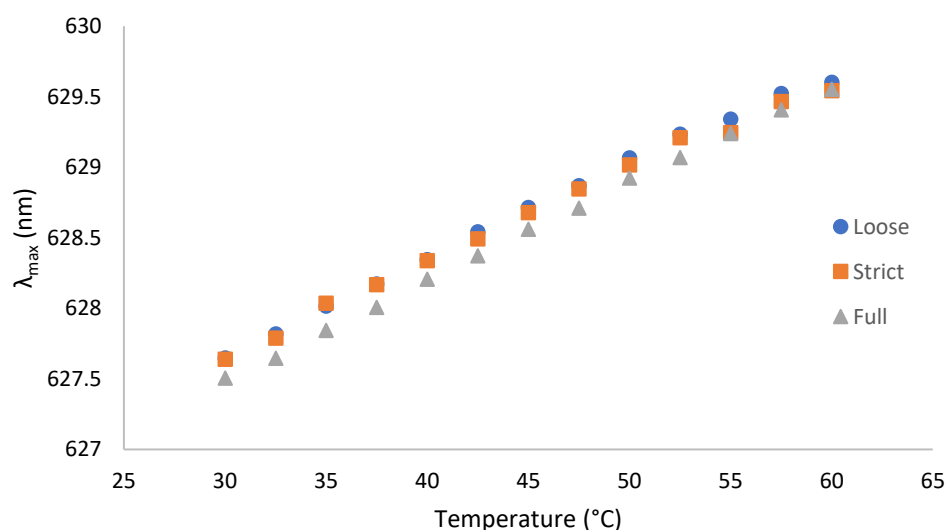


Figure 128: Estimated mean emission wavelength λ_{max} as a function of temperature for sample B of octyl acetate ink-based QD-silicone composite (cycle 2) using three different image sectioning regimes: strict and loose thresholding of clusters, and full image.

Spectral shift thermal coefficients are listed in Table 46 for the different thresholding regimes; values were similar between sectioning regimes, increasing as the selection size increased and the average grey value decreased in brightness. Values for mean emission wavelength and spectral coefficients were similar to those obtained for sample B cycle 1 and significant redshift was not observed, in contrast to changes in emission intensities. This implies that emission intensity measurement remained susceptible to variations in QD patterning, even when cluster distribution was greater than seen in the sample with added platinum catalyst. As expected, comparison of emission intensity between regions was difficult due to concentration-dependence; however, measured changes in peak shift may be consistent between regions of the same sample, although further testing is required to confirm this.

Table 46: Spectral shift thermal coefficients (30-60 °C) from images of sample B of octyl acetate ink-based QD-silicone composite (cycle 2) using three different image sectioning regimes.

Cycle	Strict		Loose		Full	
	Sensitivity nm °C ⁻¹	R ² value	Sensitivity nm °C ⁻¹	R ² value	Sensitivity nm °C ⁻¹	R ² value
2	0.0648	0.9951	0.0670	0.9969	0.0695	0.9993

The non-linear intensity quenching region (approximately 60-99 °C) is shown below in Figure 129. The emission intensity response was regular with no large anomalies and showed regular curves as emission decreased. Emission intensity at 636 nm overtook that of 627 nm between 55.0-57.5 °C and reached a maximum 65.0-67.5 °C.

After heating to 99 °C, a 22.2% decrease in emission intensity at 627 nm was seen upon cooling to 60 °C, as compared to intensity at 60 °C before heating to elevated temperatures. This may reflect poor photostability but it is also possible that insufficient cooling time was allowed; further work with better control over cooling would allow hysteresis loops to be collected and assessed.

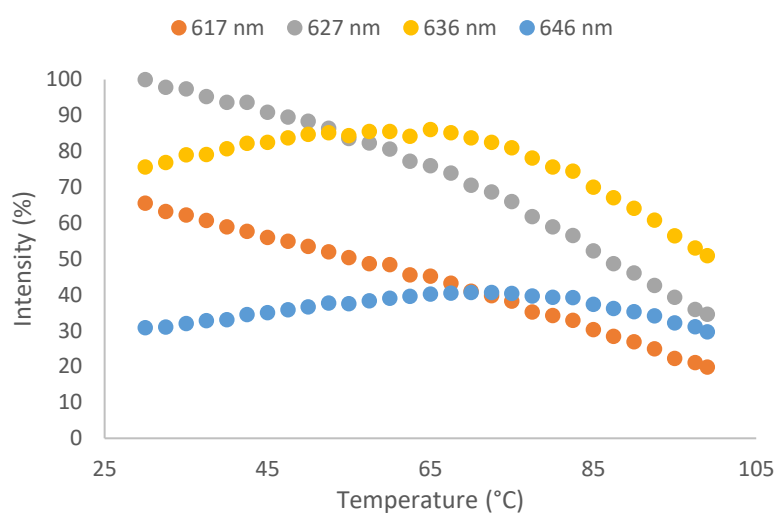


Figure 129: Left: Emission intensity of 0 wt% PtCl₂ octyl acetate ink-based composite (cycle 2) as a function of temperature from 30-99 °C at different emission wavelengths. Data shown is for loose thresholding of clusters.

6.3.3. Toluene-based addition cure composite without added catalyst

Lastly, toluene ink-based analogues were produced without additional platinum catalyst, as described in Section 3.2.6.1. One thermal cycle of 25-60 °C was run on sample A and two cycles were run on sample B.

Sample A

The fluorescence micrograph of sample A and its corresponding spectral data are shown below in Figure 130. Aggregates were brighter than those observed in octyl acetate-based composites, reflecting that toluene inks have faster reaction rate than the analogous octyl acetate inks: diameters were larger than in samples without added catalyst due to reduced heating (15 min vs 24 hr), and smaller than in samples with added catalyst and the same heat program. The mean Feret diameter was 3.0 μm , modal 2.4 μm , and the range 1.5-8.0 μm ; 15.0% of clusters had diameter <2 μm and 80.8% <4 μm . The emission intensity at 627 nm decreased by 11.9% and 26.6% from 30 °C to 45 and 60 °C, respectively.

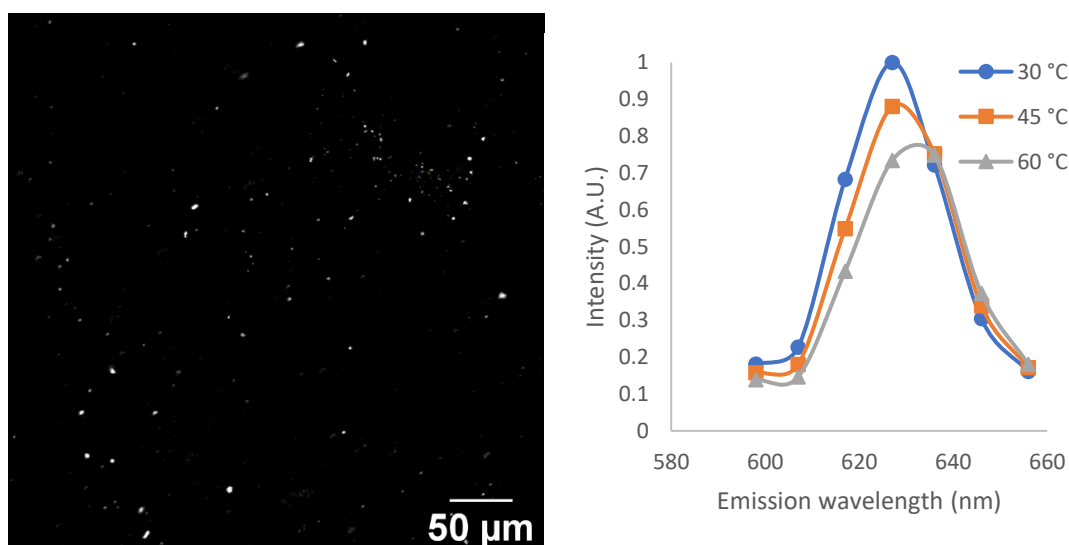


Figure 130: Left: Fluorescence micrograph of sample A of toluene ink-based QD-silicone composite at 27.5 °C ($\lambda_{\text{emission}} = 627 \text{ nm}$). Right: Spectral profiles at 30, 45, and 60 °C.

Emission intensity as a function of temperature is shown below in Figure 131 for cluster imaging and full image analysis. A reverse sigmoidal curve was seen in intensity data at all emission wavelengths, with an inflection point around 45 °C. This likely arose from the greater brightness of clusters compared to those in the octyl acetate samples, resulting in a greater number of saturated pixels; therefore, any decrease in emission intensity was masked until the pixels desaturated. This demonstrates the importance of optimising gain for intensity-based measurements.

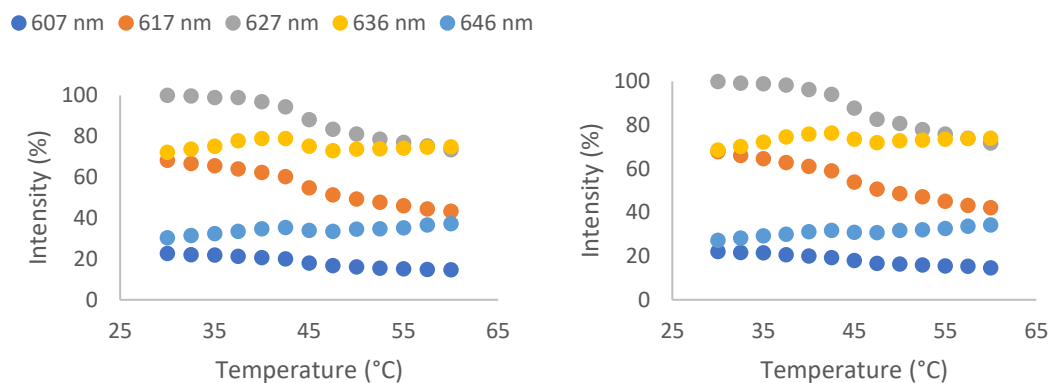


Figure 131: Emission intensity as a function of temperature for the imaging of clusters (left) and the analysis of the full image (right) of sample A of toluene ink-based QD-silicone composite at different emission wavelengths.

Lines of best fit were applied to the data from 30-50 °C and the gradients of the trendlines are summarised in Table 47 below. The most pronounced reverse sigmoidal curve was seen at 636 nm emission, leading to small R^2 values and gradients in trendlines.

The temperature sensitivity at 627 nm was -0.9076 , -1.0405 , and -1.0225 $\% \text{ } ^\circ\text{C}^{-1}$ for strict and loose thresholding of clusters and full image analysis, respectively. Loose thresholding had the greatest sensitivity for 627 nm emission and the highest R^2 values for emissions ≤ 627 nm: if saturated pixels are assumed to cause the reverse sigmoid, this observation may be rationalised as analysis of the greatest proportion of unsaturated, non-background pixels, leading to more linear profiles. Percentage sensitivity at 617 nm with full image analysis is greater than that using cluster thresholding; however, the average grey value of cluster data was much greater than that of the full image reflecting higher signal-to-noise. At 30 °C for 627 nm emission, the average grey value for loose threshold and full image analysis was 60.2% and 0.521% that of strict threshold.

Table 47: Percentage emission intensity thermal coefficients (30-50 °C) at different wavelengths from images of sample A of toluene ink-based QD-silicone composite using three different image sectioning regimes.

Cycle 1 Emission nm	Strict threshold		Loose threshold		Full image	
	Sensitivity $\% \text{ } ^\circ\text{C}^{-1}$	R^2 value	Sensitivity $\% \text{ } ^\circ\text{C}^{-1}$	R^2 value	Sensitivity $\% \text{ } ^\circ\text{C}^{-1}$	R^2 value
607	-0.3739	0.9392	-0.3104	0.9599	-0.3051	0.9552
617	-0.9607	0.9448	-0.9298	0.9753	-0.9878	0.9637
627	-0.9076	0.8734	-1.0405	0.9506	-1.0225	0.8749
636	-0.0044	0.0001	-0.0220	0.0099	0.1755	0.2233
646	0.1825	0.5560	0.1774	0.7912	0.2072	0.7805

The emission peak λ_{max} was estimated using Equation 5 and plotted below in Figure 132. All three sectioning regimes showed linear trends and had similar values to with each other. Background removal was associated with a small increase in values for λ_{max} .

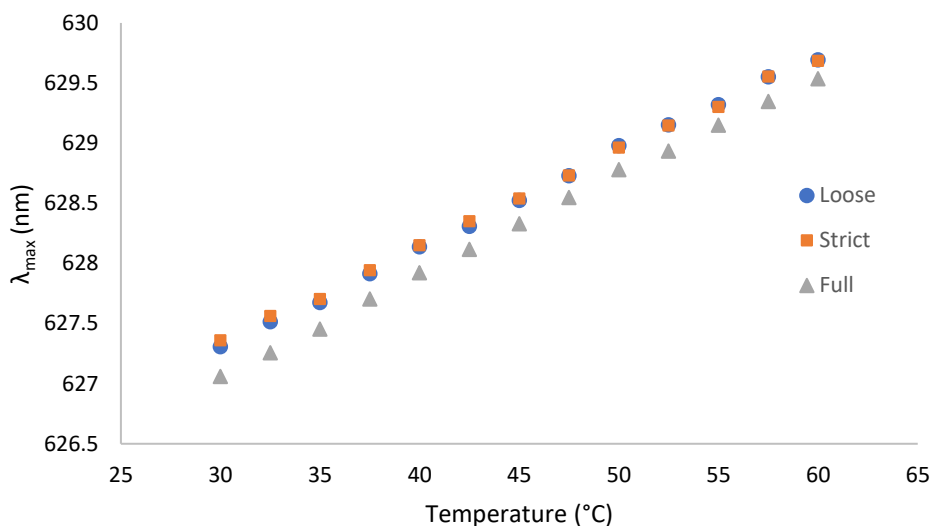


Figure 132: Estimated mean emission wavelength λ_{max} as a function of temperature for sample A of toluene ink-based composite using three different image sectioning regimes: strict and loose thresholding of clusters, and full image.

Spectral shift thermal coefficients are listed in Table 48 for different thresholding regimes and thermal cycles. Sensitivity varied with image sectioning regimes and increased as image selection size increased and average grey value decreased in brightness; background removal appeared to increase the impact of saturated pixels on apparent sensitivity due to a higher signal-to-noise ratio.

Table 48: Spectral shift thermal coefficients (30-60 °C) from images of sample A of toluene ink-based QD-silicone composite using three different image sectioning regimes.

Cycle	Strict		Loose		Full	
	Sensitivity nm °C ⁻¹	R ² value	Sensitivity nm °C ⁻¹	R ² value	Sensitivity nm °C ⁻¹	R ² value
1	0.0789	0.9991	0.0811	0.9990	0.0834	0.9992

Sample B

The fluorescence micrograph of sample B and its corresponding spectral data are shown below in Figure 133. QD clusters appeared similar in size and brightness to those in sample A, as expected. The mean Feret diameter was 3.4 μm and the modal was 2.4 μm ; values ranged from 1.5-10.0 μm , where 5.5% of clusters had diameters <2 μm and 75.9% <4 μm . The emission intensity at 627 nm decreased by 13.2% and 26.7% from 30 $^{\circ}\text{C}$ to 45 and 60 $^{\circ}\text{C}$, respectively, in cycle 1.

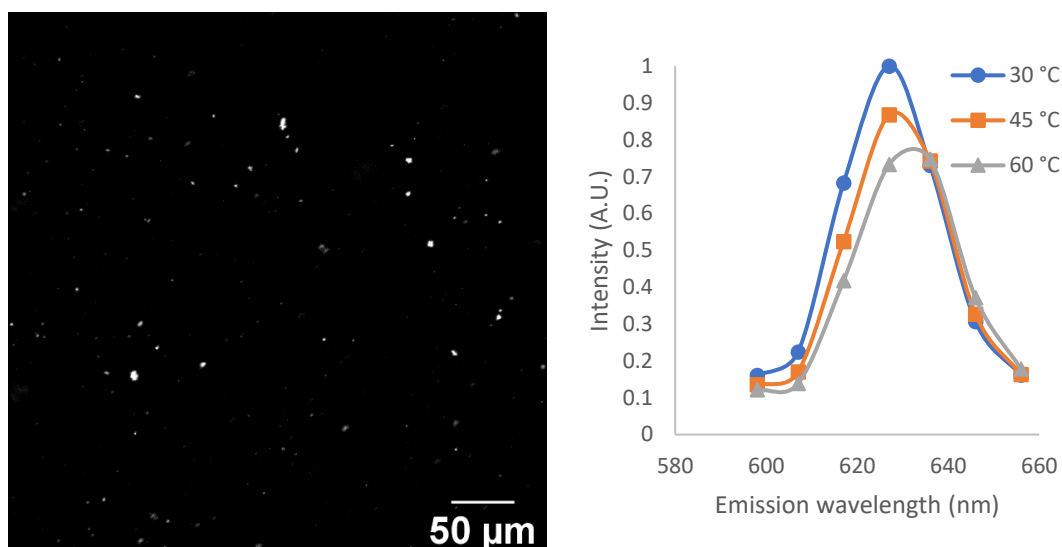


Figure 133: Left: Fluorescence micrograph of sample B of toluene ink-based QD-silicone composite (cycle 1) at 27.5 $^{\circ}\text{C}$ ($\lambda_{\text{emission}} = 627 \text{ nm}$). Right: Spectral profiles at 30, 45, and 60 $^{\circ}\text{C}$.

Spectral data of different thermal cycles are shown below in Figure 134 for 30, 45, and 60 $^{\circ}\text{C}$. Emission intensity at 30 $^{\circ}\text{C}$ decreased after a thermal cycle; differences in intensity between cycles became less significant as temperature increased and intensities were very similar at 60 $^{\circ}\text{C}$. At 30 $^{\circ}\text{C}$, a 5.5% decrease in emission intensity was observed between cycle 1 and 2. In contrast, the estimated mean wavelength appeared stable (Figure 136); changes in the QD ligand sphere may be associated with reduced emission intensity without significant immediate change in mean emission wavelength. If some labile amine ligands, which enhance PL in CdSe/ZnS QDs,²³⁶⁻²³⁸ were lost due to thermal ligand detachment,²⁷⁷⁻²⁷⁹ a reduction in emission intensity would be observed which may not be accompanied by immediate thermal annealing. Solvent evaporation could also alter the stability of QD surface states, though this would be associated with shrinkage of the polymer matrix but thermal drift was minimal during measurement.

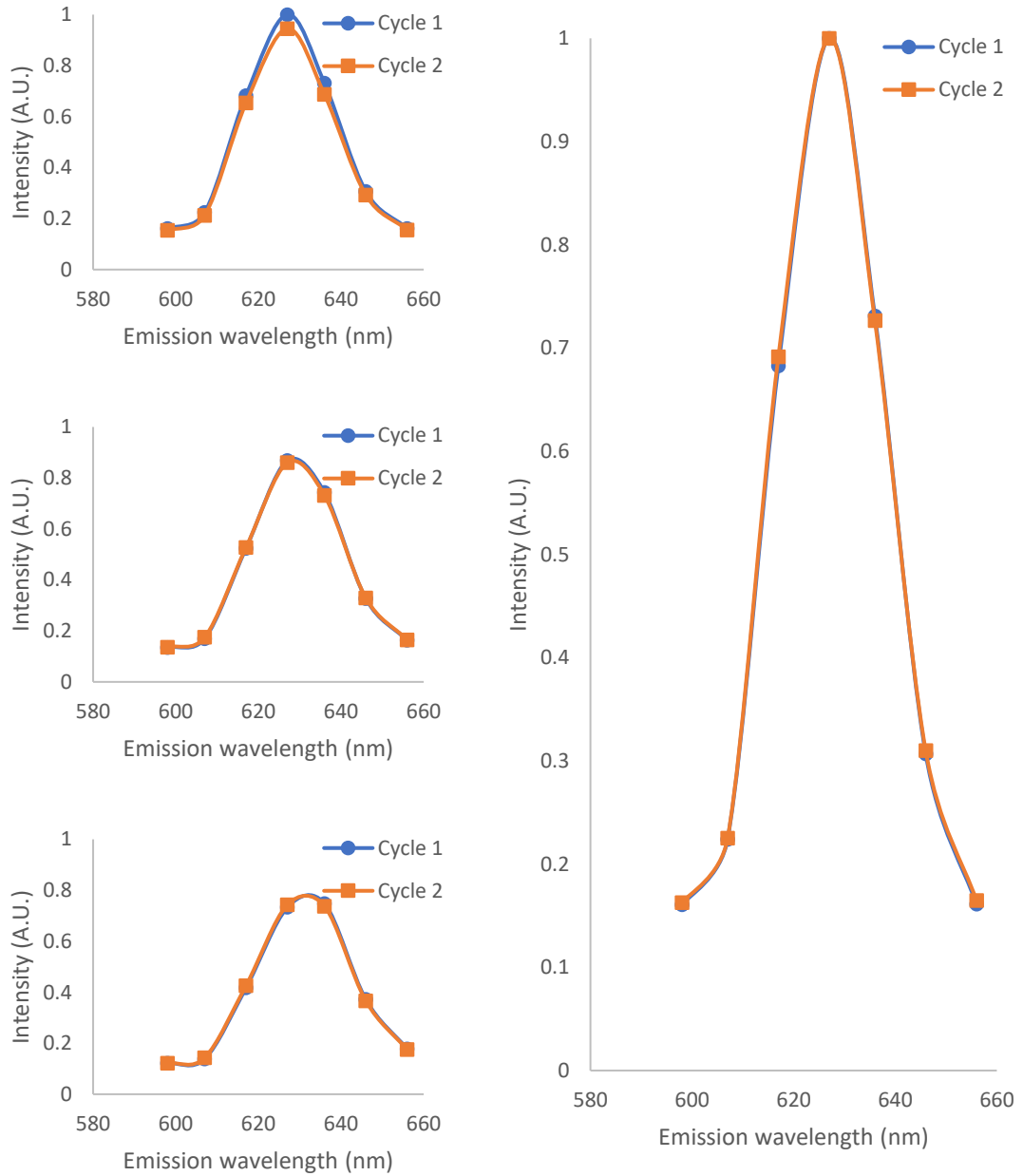


Figure 134: Left: Spectral profiles of subsequent thermal cycles at 30, 45, and 60 °C (top to bottom) of sample B of toluene ink QD-silicone composite. Right: Normalised spectral profiles of subsequent thermal cycles at 30 °C.

Emission intensity as a function of temperature is shown below in Figure 135 for cluster imaging and full image analysis. A similar reverse sigmoidal shape was observed, as was seen in sample A; the inflection point began earlier at 42.5 °C and appeared broader. This pattern was observed in both thermal cycles and did not become less pronounced following a cycle – the 5.5% decrease in emission intensity between cycles did not eliminate saturated pixels.

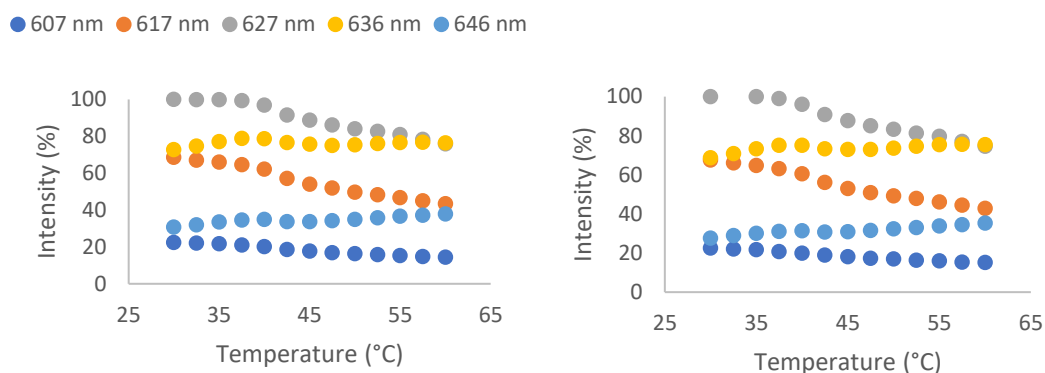


Figure 135: Representative graph of emission intensity as a function of temperature for the imaging of clusters (left) and the analysis of the full captured image (right) sample B of toluene ink-based QD-silicone composite at different emission wavelengths. Data shown is the average of the two thermal cycles.

Lines of best fit were applied to the data from 30-50 °C and the gradients of the trendlines are summarised in Table 49 below. Sensitivities became more positive after thermal cycles for all image sectioning regimes and wavelengths. Sensitivity correlated to average brightness of the image selection: across the two cycles, loose threshold and full image sectioning regimes were respectively 74.3% and 0.399% as bright as strict thresholding at 30 °C for 627 nm emission. The temperature sensitivity at 627 nm was -1.0026, -1.0124, and -1.1060 % °C⁻¹ in cycle 1 and -0.7818, -0.7859, and -0.8338 % °C⁻¹ in cycle 2, for strict and loose thresholding of clusters and full image analysis, respectively. Cycle 1 of samples A and B had more similar sensitivities than the two thermal cycles in sample B, which may reflect fewer saturated pixels with emission intensity decrease following a thermal cycle.

Table 49: Percentage emission intensity thermal coefficients (30-50 °C) at different wavelengths from images of sample B of toluene ink-based QD-silicone composite using three different image sectioning regimes.

Cycle 1	Strict threshold		Loose threshold		Full image	
	Sensitivity % °C ⁻¹	R ² value	Sensitivity % °C ⁻¹	R ² value	Sensitivity % °C ⁻¹	R ² value
607	-0.4010	0.9814	-0.3680	0.9832	-0.3243	0.9684
617	-1.1529	0.9804	-1.0865	0.9823	-1.0643	0.9848
627	-1.0026	0.9313	-1.0123	0.9364	-1.1060	0.9390
636	-0.1330	0.2554	-0.0418	0.0338	0.0760	0.1177
646	0.0795	0.2631	0.1080	0.4340	0.1464	0.6845
Cycle 2	Strict threshold		Loose threshold		Full image	
	Sensitivity % °C ⁻¹	R ² value	Sensitivity % °C ⁻¹	R ² value	Sensitivity % °C ⁻¹	R ² value
607	-0.3340	0.9303	-0.3045	0.9368	-0.2907	0.9699
617	-1.0013	0.9210	-0.9537	0.9295	-0.9285	0.9487
627	-0.7818	0.8130	-0.7859	0.8241	-0.8338	0.8628
636	0.0533	0.0174	0.1316	0.1200	0.2380	0.3817
646	0.1671	0.4695	0.1999	0.6155	0.2283	0.8055

The emission peak λ_{max} was estimated using Equation 5 and plotted below in Figure 136. All three sectioning regimes showed linear trends and had near-identical values λ_{max} ; data for loose thresholding is shown as representative.

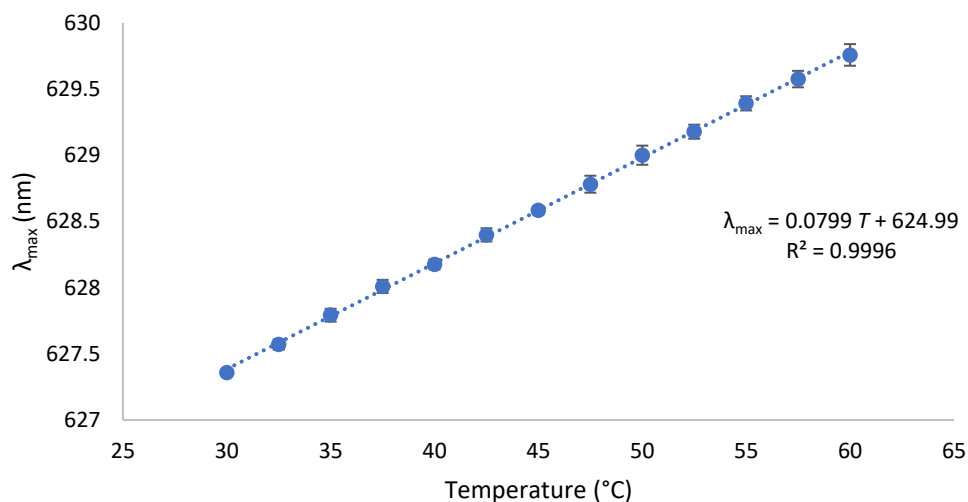


Figure 136: Estimated mean emission wavelength λ_{max} as a function of temperature for sample B of toluene ink-based QD-silicone composite using loose thresholding of clusters. Data shown is the average of the two thermal cycles, where error bars denote range of values.

Spectral shift thermal coefficients are listed in Table 50 for different thresholding regimes and thermal cycles. Values for mean emission wavelength and spectral coefficients were similar to data for sample A using background removal. Values between thermal cycles had close agreement, in contrast to changes in emission intensities, indicating that spectral-based temperature measurement may yield more consistent results than intensity-based.

Table 50: Spectral shift thermal coefficients (30-60 °C) from images of sample B of toluene ink-based QD-silicone composite using three different image sectioning regimes.

Cycle	Strict		Loose		Full	
	Sensitivity nm °C ⁻¹	R ² value	Sensitivity nm °C ⁻¹	R ² value	Sensitivity nm °C ⁻¹	R ² value
1	0.0798	0.9989	0.0813	0.9992	0.0792	0.999
2	0.0772	0.9991	0.0786	0.9996	0.0767	0.9991
Average	0.0785	0.9992	0.0799	0.9996	0.0779	0.9992

The non-linear intensity quenching region (approximately 60-99 °C) is shown below in Figure 137. During the first trial of measuring intensity as a function of temperature (left), data with significant waviness was obtained which otherwise followed the curves observed in other composites. This was caused by a sub-optimal heating program, which was subsequently not used in data collection of other composites: the sample was allowed to cool to 60 °C after certain temperatures were reached to monitor for irreversible

quenching, but it was evident that thermal conductivity led to undulating intensities under these trial conditions.

After cooling to room temperature, a subsequent cycle was run from 30-99 °C (right) to obtain more ordered data and had good agreement with the overall trends observed in the previous cycle. The anomalous 'dip' in intensity between 40 and 60 °C continued to be observed and was thought to be related to saturated pixels as discussed above. Emission intensity from 60-99 °C differed by less than 0.02 AU between the two runs for all emission wavelengths (where 1 AU is the 627 nm emission intensity at 60 °C in sample B cycle 2). This suggests that irreversible quenching is not observed for these composites at temperature below 99 °C, in agreement with research by Zhao *et al.*¹⁶⁰

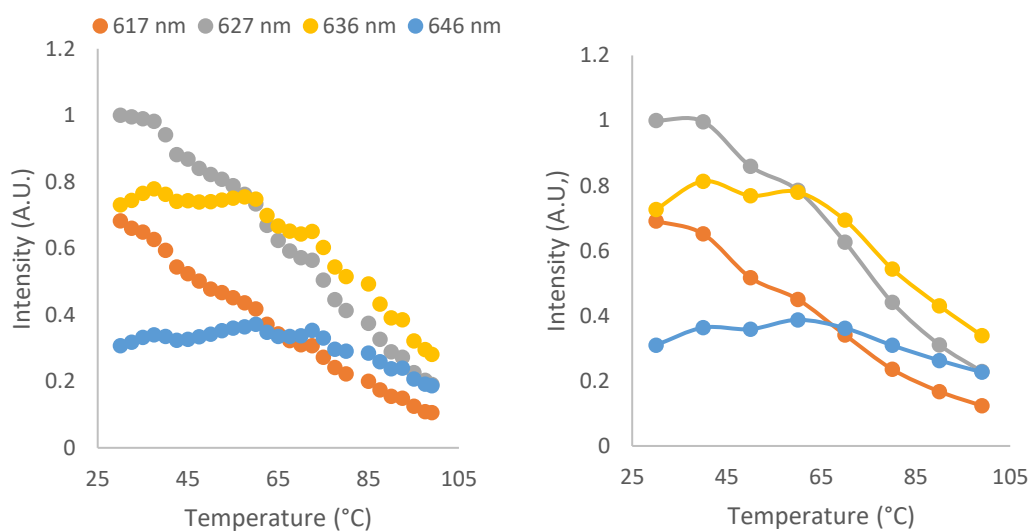


Figure 137: Left: Emission intensity of 0 wt% PtCl₂ toluene ink-based QD-silicone composite (sample B cycle 2) as a function of temperature from 30-99 °C at different emission wavelengths. Right: Emission intensity of sample B (cycle 3) as a function of temperature from 30-99 °C. Data shown is for loose thresholding of clusters.

6.3.4. Summary of microscopy-based sensing

Temperature sensing experiments were carried out on three different addition cure composites using confocal laser scanning microscopy. Lambda scans were collected and mean grey value obtained from frames to assess intensity and peak shift-based temperature sensing. Three different image sectioning regimes were trialled to determine the dependence of measured sensitivity on threshold levels. When average brightness of the full image was over 3% that of the strict threshold, similar percentage emission intensity thermal coefficients were obtained for all sectioning regimes.

In all samples, emission peak intensity at 627 nm decreased with increasing temperature and the peak appeared to broaden and redshift, as expected for QDs.^{1,160} Emission intensity for wavelengths below 627 nm fit linear trendlines between 30-50 °C while emission wavelengths above 627 nm showed greater curvature: intensity initially increased with temperature as redshift occurred but began to decrease at higher temperatures as thermal quenching increased.¹⁶⁰ The emission intensity at 627 nm decreased by 11-13% and 27-33% from 30 °C to 45 and 60 °C respectively in composites that had not undergone a thermal cycle. Emission intensity decreased between cycles for all sectioning regimes, with greatest decrease seen between values at 30 °C and little change seen between values at 60 °C, leading to smaller percentage intensity thermal coefficients in subsequent cycles. Given that mean emission wavelengths and spectral shift thermal coefficients were consistent between cycles, insufficient cooling and thermal annealing were unlikely to be the primary cause of the decreased intensity. Changes in the QD ligand shell may rationalise the changes between cycles: labile amine ligands enhance PL of CdSe/ZnS QDs²³⁶⁻²³⁸ but may thermally-detach,²⁷⁷⁻²⁷⁹ leading to a reduction in emission intensity. Solvent evaporation could also alter the stability of QD surface states, although shrinkage was not observed.

Pt-mediated quenching was observed to reduce the emission intensity of the 0.00125 wt% PtCl₂ octyl acetate ink-based composite relative to the other composites imaged and correlated with lower coefficients. Intensity coefficients at 627 nm emission were -0.69 to -0.54 % °C⁻¹ for cluster thresholds and -1.16 to -0.73 % °C⁻¹ for full image analysis, for cycle 1 and 3 respectively. Average spectral coefficients for the three thermal cycles were 0.0669, 0.0677, and 0.0709 nm °C⁻¹ for strict thresholding, loose thresholding, and full image analysis, respectively; mean emission wavelengths were stable across cycles and similar between imaging approaches despite the large proportion of background.

Micrographs of the octyl acetate ink-based composite without added catalyst showed more numerous, smaller clusters compared to the sample containing 0.00125 wt% PtCl₂,

resulting in a higher signal-to-noise ratio. In sample A, intensity coefficients were higher than observed for added catalyst at around $-1.2\% \text{ } ^\circ\text{C}^{-1}$, with greater similarity between different image sectioning regimes due to greater number and distribution of QD clusters. Spectral coefficients were also larger at 0.0821 , 0.0826 , and $0.0795 \text{ nm } ^\circ\text{C}^{-1}$ for strict thresholding, loose thresholding, and full image analysis, respectively. All coefficients were lower in sample B: -0.89 to $-0.56\% \text{ } ^\circ\text{C}^{-1}$ for strict cluster thresholds, -0.94 to $-0.64\% \text{ } ^\circ\text{C}^{-1}$ for loose cluster thresholds, and -0.94 to $-0.83\% \text{ } ^\circ\text{C}^{-1}$ for full image analysis, for cycle 1 and 2 respectively. Spectral coefficients for the two thermal cycles were similar, at 0.0680 , 0.0703 , and $0.0672 \text{ nm } ^\circ\text{C}^{-1}$ for strict thresholding, loose thresholding, and full image analysis respectively in cycle 1 and 0.0648 , 0.0670 , and $0.0695 \text{ nm } ^\circ\text{C}^{-1}$ in cycle 2. Cycle 1 and 2 were run on different regions of sample B to assess the effect of differences in cluster patterning on apparent sensitivity. Overall, intensity-based measurements were observed to vary, as expected based on its concentration-dependence, while spectral shift appeared consistent between regions of the same sample. Increase in mean emission wavelengths between sample A and B may indicate sample aging processes such as thermal annealing.

Lastly, toluene ink-based composites without added catalyst had brighter aggregates than octyl acetate ink-based composites, due to toluene inks having a faster reaction rate. Sigmoidal curves observed in graphs of intensity as a function of temperature were thought to correlate to saturated pixels and may lower apparent intensity-based sensitivity. In sample A, the intensity coefficient was around $-1.0\% \text{ } ^\circ\text{C}^{-1}$, and spectral coefficients were 0.0789 , 0.0811 , and $0.0834 \text{ nm } ^\circ\text{C}^{-1}$ for strict thresholding, loose thresholding, and full image analysis, respectively. In sample B, intensity coefficients were -1.00 to $-0.78\% \text{ } ^\circ\text{C}^{-1}$ for cluster thresholds and -1.11 to $-0.83\% \text{ } ^\circ\text{C}^{-1}$ for full image analysis, for cycle 1 and 2 respectively. Average spectral shift thermal coefficients for the two thermal cycles were 0.0785 , 0.0799 , and $0.0779 \text{ nm } ^\circ\text{C}^{-1}$ for strict thresholding, loose thresholding, and full image analysis, respectively.

Overall, all samples had larger thermal coefficients of measurement than typical inkjet-printed sensors ($0.1\text{-}0.3\% \text{ } ^\circ\text{C}^{-1}$)^{14,15} and values were within range of those reported for intensity and spectral-based sensing using CdSe/ZnS core-shell QDs. Spectral-based sensing yielded greater consistency between sample regions, imaging approaches, and thermal cycles.

6.4. Summary of temperature sensing materials

QD composites were characterised in terms of fluorescence and QD distribution through the silicone matrix, and optical temperature sensing experiments were carried out as measurements of bulk composite (well-plate reading) and micron-scale planar imaging (confocal fluorescence microscopy) to meet Objective O5.

QD clusters in addition cure composites were imaged and PL was largely unchanged from the manufacturer's specifications despite micron-scale aggregates: the emission peak was blue-shifted by 4 nm and a small shoulder was seen at approximately 655 nm. Intensity measurements were obtained using fluorescent plate readers and linear decrease in emission was observed with increasing temperature. The utility of the HTS approach was demonstrated: multi-functional well-plate readers that are capable of high-resolution imaging, collection of detailed PL spectral data, and other common spectroscopic techniques could present a powerful tool for material development of optical temperature-sensing composites and other advanced materials, particularly as combined with a pipetting liquid handling apparatus as a combinatorial approach to well-plate preparation of inkjet formulations.

Emission intensity at different wavelengths as a function of temperature was measured by using cLSM to obtain lambda scans to obtain thermal coefficients. Temperature was correlated to linear decrease in intensity and to spectral shift to higher emission wavelengths and sensitivities obtained from lines of best fit. All samples had larger thermal coefficients of measurement than than typical inkjet-printed sensors ($0.1-0.3\% \text{ } ^\circ\text{C}^{-1}$)^{14,15} and values were within range of those reported for intensity and spectral-based sensing using CdSe/ZnS core-shell QDs.

Overall, the fluorescence of inkjet-printable QD-silicone composites was shown to be suitable for temperature-sensing, using two different methods of data collection to fit a range of potential applications. More accurate sensitivities and data of the temperature-dependent fluorescence can be obtained by future research, but these initial measurements demonstrate the viability of inkjet for the deposition of composite sensing materials and as a potential route to advanced temperature-sensing products.

In the next chapter, the performance of the QD-composites is contextualised. Conclusions and suggestions for further work are then summarised in Chapter 8 and Chapter 9.

Chapter 7. Discussion

The aim of this thesis was to produce an inkjet-printable quantum dot-silicone composite that can be used for optical thermometry. Current inkjet-printed resistance-based thermal sensors have limited spatial resolution and do not achieve sub-degree thermal resolution in the physiological range, which is a barrier to their use in microdevices and in cell culture and biomedical applications. Novel inks for luminescence nanothermometry could better meet the requirements for integrated sensing in inkjet-printed micro-devices and other sensing applications. Inks were formulated for inkjet printing using either 2-part addition cure silicones or 1-part UV cure silicone in order to produce a quantum dot-silicone composite that can be used for optical thermometry. Quantum dots were selected as functional fillers for fluorescent composites due to their strong, narrow emission, complementary to the optical transparency and thermal stability of silicones. The QD-silicone composites were assessed using confocal laser scanning microscopy (cLSM) to confirm their suitability for optical thermometry. Addition of silicones and QD-silicone composites to the AM materials portfolio would expand the range of inkjet-printable devices.

The following sections discuss formulation and printing of addition cure inks, QD-silicone addition cure inks, and UV cure inks, followed by temperature sensing experiments. Lastly, suggested applications are described, and limitations of the materials are evaluated.

7.1. Formulation and printing of addition cure silicone inks

Addition cure silicones were identified as ideal for optical sensing due to their minimal shrinkage, use in commercial LED encapsulants, and suitable reactivity at ambient temperatures for inkjet printing. PolyTek SiliGlass, a commercial 2-part RTV silicone, was selected for its low viscosity (<1000 mPa s), optical transparency from 350-700 nm, and Shore A hardness (40A). These properties would enable formulation of inks with jettable viscosity even at high polymer loading (>25 wt%) and/or ambient temperature; allow efficient transmission of excitation and emission wavelengths; and limit displacement of sensing material during operation.

Characterisation data on SiliGlass provided by the manufacturer (Ocean NanoTech) and in literature was incomplete, therefore further characterisation was performed to fill in those gaps and inform material development. The α,ω -divinyl PDMS polymer in SiliGlass B was found to have an average of 112.5 repeat units using ^1H NMR spectroscopy, corresponding

to a molecular weight of 8528.28 g mol⁻¹. This chain length leads to a brittle 40A elastomer, which enables it to mimic glass shards.⁵⁷ Assuming that the base polymer is identical in both parts, a likely identity for the crosslinker in SiliGlass A is proposed to be PDMS-co-PMHS with an average MW of 2206.21 g mol⁻¹ and $f=7.6$. “The ratio of vinyl groups to silane groups in the NMR spectrum of SiliGlass A was 1 : 3.79, calculated to correspond to a 1.68-fold molar excess of silane when SiliGlass A and SiliGlass B are mixed in a 1:1 weight ratio. As shorter base polymers lead to reduced flexibility, higher crosslinking density, and higher elastic modulus (≥ 1 MPa) in the presence of excess silane,⁵⁷ SiliGlass is expected to have reduced solvent swelling and coefficient of thermal expansion. This may produce sensing materials with more consistent sensing performance across device lifetime as the overall magnitude of change in expansion associated with material aging is reduced.^{46,181} Furthermore, reduced chain mobility and excess silane can both hinder discoloration.^{181,192} The disadvantage of brittleness is greater vulnerability to crack formation, which may reduce sensor lifespan.⁴⁶ This may be of use to others in future ink formulation or guide others on achieving similar inks with silicone reagents. In particular, chain extenders or multifunctional silane crosslinkers could be used to increase polymer flexibility with low viscosity precursors.⁵⁷

As the viscosity of pure SiliGlass parts exceeded the viscosity limits of the printer by an order of magnitude, strategies for viscosity modification were required to meet the processing requirements. Solvents were selected as removable carrier vehicles which could be added to the commercial formulation without altering the average crosslink chain length or vinyl to silane ratio, thereby avoiding increased elastomer brittleness, leaching of silicone oils, and formation of Si-Pt and C-Pt clusters which are associated with greater discoloration^{57,192} Silicones that are crosslinked in the presence of solvent have reduced elastic moduli as locked chain entanglements are diluted,⁵⁷ which may improve the ability of the printed SiliGlass elastomer to absorb thermal stresses without cracking, but may make sensor readings more vulnerable to changes in expansion and discoloration.^{46,181,192}

Two solvents were selected as carrier vehicles for their miscibility with PDMS, efficacy for dispersion of QDs, and high boiling point and low vapour pressure to prevent nozzle blockages and to suppress the coffee ring effect.^{60,64,116,289} Both octyl acetate^{60,64} and toluene⁶² have been used for silicone IJP in literature: octyl acetate was selected for its low volatility to improve jetting performance, while toluene was trialled as it was better established in literature as a solvent for silicones and for QD dispersions. Nozzle blockage and coffee staining was not observed in print trials with octyl acetate, while

acetate solvents with greater volatility have yielded mixed results in literature: 25% PDMS in *n*-butyl acetate was inkjet printed by Peng *et al.*,⁶¹ while iso-butyl acetate inks were not suitable for jetting of Sylgard 184 in work by Mikkonen *et al.*⁶⁴ Toluene inks were formulated for comparative study of a typical nonpolar solvent for QD dispersions to ensure QD dispersion in composite inks. Toluene enabled higher polymer loadings for solutions of comparable viscosity to octyl acetate-inks (50 wt% octyl acetate inks had rheology comparable to 40 wt% toluene inks) and was associated with faster curing. Decreased initial concentration of precursors leads to slower initial reaction rate; therefore, higher initial concentration combined with greater volatility leads to faster overall curing.^{60–62} As printing with octyl acetate was satisfactory, printing of toluene-based inks was not demonstrated.

The rheology of silicone inks was characterised and the printability indicator *Z* calculated, as is standard practice in formulation for inkjet.⁶ A 2-part ink strategy was selected over 1-part inks to extend the ink working life^{60,68} – as single inks crosslink and become unusable after 2-48 hours^{61–64} – and to allow control over the molar ratio of silane to vinyl moieties to vary the mechanical properties.⁵⁷ Due to the low viscosity of SiliGlass compared to Sylgard 184 – a PDMS elastomer which is considered a benchmark for RTVs with viscosity <10 Pa s^{57,67} – it was possible to jet octyl acetate-based inks at 30 °C nozzle temperature with polymer loading twice that of analogous inks. Of the two 50 wt% SiliGlass inks, Ink A (crosslinker ink) had a *Z* value of 1.7 and Ink B (catalyst ink) had a *Z* value of 1.5. In contrast, Mikkonen *et al.* achieved comparable jetting (*Z* = 1.5) with 25 wt% Sylgard 184 at 30-35 °C nozzle temperature and a working life limited to 48 hours.⁶⁴ Elastic properties are more limited with less viscous precursors, as hard elastomers have network polymer chains >20 kg mol⁻¹ and soft elastomers >50 kg mol⁻¹, and viscosity increases with chain length.⁵⁷ However, high polymer loading is a priority in jetting inks for printing efficiency and film formation: dilution slows material deposition and necessitates interlayer drying times, while Marangoni flow and solvent-polymer interactions can lead to uneven material distribution, surface roughness, and/or microphase formation,^{35,116,231,232} which would reduce the homogeneity, accuracy, and efficiency of temperature sensing materials.

As two-part inks were used for drop-on-drop reactive inkjet, the working life of the inks was much greater rather than the 48 hours reported by Mikkonen *et al.*⁶⁴ Octyl acetate did necessitate the use of LCP print cartridges due to incompatibility with polypropylene which then poisoned the platinum catalyst;¹⁷ however, this limitation is true of all solvents currently used for silicone inkjet. Jetting was reliable with suitable cleaning cycle, and a

purge cycle with nozzle heating was sufficient to clear out residual material after a period of disuse, similar to that reported by Sturgess *et al.*⁶⁰ Silicone inks were observed to wet surfaces effectively, and to 'climb' the needle during pendant drop shape analysis due to deposition creep arising from low surface tension ($<24 \text{ mN m}^{-1}$); for this reason, it was necessary to set a meniscus set point during printing as excess silicone ink would wet the nozzle plate leading to misfire of jetting nozzles.

Controlled deposition was challenged by the tendency of inks to wet substrates due to the low surface energy of PDMS ($\sim 20.4 \text{ mJ m}^{-2}$)⁵¹. Inkjet was suitable for depositing thin films onto substrates, which are compatible with planar sensing applications; Peng *et al.* and McCoul *et al.* inkjet-printed PDMS layers as thin as $\sim 1.6\text{-}2.0 \mu\text{m}$.^{61,63} However, print resolutions finer than $150 \mu\text{m}$ have not been achieved in inkjet without optimised printing substrates due to silicone ink spreading,⁶¹⁻⁶³ which is unsuitable for deposition of material in controlled areas and preventing contamination in printed micro-devices where material deposition is not desired. Therefore, a substrate was selected to achieve sensing arrays and other sensing geometries. Effective substrates investigated for silicone inkjet include PTFE films, spin-coated PDMS on glass slides, and fluoroalkylsilane-treated glass slides.^{60,64} The highest contact angles in silicone inkjet so far are reported for PFOTS-treated glass slides, which produce fluoroalkyl surfaces; this was used to achieve contact angles of 45° and 48° for Ink A and Ink B, respectively, and enhance resolution. Inkjet printing of droplets was demonstrated with the highest resolution currently reported for silicone inkjet: $33.0\text{-}33.7 \mu\text{m}$ mean drop diameter and $52\text{-}55 \text{ ng}$ drop volumes were obtained using the Fujifilm Dimatix printer, and $\leq 35.7 \pm 1.4 \mu\text{m}$ mean drop-on-drop (DoD) diameter, while mean drop diameter was approximately $36 \mu\text{m}$ on the modified PiXDRO LP50 printer. Drop resolution was greater than that reported by Sturgess *et al.* for the same substrate, where 60 wt% SiliGlass inks in octyl acetate had contact angles of 55° at room temperature and a DoD diameter of $48 \pm 2 \mu\text{m}$.⁶⁰ As all the above values are reported for Dimatix cartridges with $21.5 \mu\text{m}$ nozzle diameter, resolution could be increased further using 1 pL Dimatix cartridges that have a smaller nozzle diameter of $9 \mu\text{m}$; waveform optimisation would be needed and ink viscosity may present a barrier to jetting through a smaller orifice.

However, large differences in surface energy between the ink and silanised substrate led to issues with poor contact pinning, which necessitated printing strategies. It was not possible to deposit a continuous film of ink due to poor pinning so the strategies developed for FRIJP by Sturgess *et al.* were replicated.⁶⁰ Substrate microstructuring was used to enable printing on the single printhead Dimatix printer: a pinned grid of PDMS was deposited and

cured to provide anchor points for ink. While this enabled controlled patterning, the grid pattern was visible in printed films: edges were wavy and surface texture was bumpy where ink flowed around anchor points. Therefore, while it was possible to produce sensing arrays with $\sim 36 \mu\text{m}$ resolution, surface microstructuring was not ideal for production of sensing films as optical aberrations were generated. The line-by-line strategy using the dual printhead PiXDRO LP50 printer had much improved edge definition, morphology, and printing efficiency. Simultaneous deposition of both inks reduced calibration steps and increased throughput. The edges of prints were less undulating as they were produced by stable line formation rather than by conforming to surface microstructures, but convex edges were observed in all printed SiliGlass samples, where inks receded from edges as driven by high initial contact angle ($\geq 45^\circ$) and limited contact pinning.⁶ Printed films deposited line-by-line appeared smoother with less visible texture as compared to those produced using pinned grids, and was suitable for production of lines, films, and complex planar sensing geometries with $< 50 \mu\text{m}$ resolution.

In sessile drops, solvent evaporation can generate Marangoni flow resulting in uneven deposition ('coffee staining') which is detrimental to the transparency of films and the homogeneity of sensing materials. No coffee ring formation was observed, in agreement with Sturgess *et al.*⁶⁰ This is likely due to three main factors: high polymer concentration (50 wt%), the low vapour pressure of octyl acetate (0.4 mmHg at 20°C)²¹⁵, and limited contact pinning.^{121,129} However, microscale gyroidal domains were observed in printed material and TEM of bulk composites, arising from spinodal decomposition or polymerisation-induced phase separation (PIPS).^{231,232} Microscale variations in composition and refractive index can increase scattering, reduce optical transmittance,²³⁴ and lead to inhomogeneous material response in optical sensing materials; further work to eliminate or reduce to size of solvent- and polymer-rich domains is of interest to enhance performance of luminescent thermal sensing materials.

Overall, printable addition cure inks were formulated (Objectives O1 and O2) with high polymer loading (50 wt%) and resolution ($< 50 \mu\text{m}$). 2-part inks were printed using drop-on-drop reactive inkjet: printers with single printheads were able to deposit sensing arrays with $36 \mu\text{m}$ DoD diameter, and line-by-line strategies with dual printheads were able to produce lines, films and complex geometries for sensing areas with greater transparency than achieved with surface microstructuring. The next stage was to demonstrate printing of QD-composites with temperature sensitive fluorescence.

7.2. Formulation and printing of addition cure QD-silicone composite inks

Work was carried out so that QD-inks, based on the SiliGlass inks, could be printed to produce QD-silicone composite temperature-sensing geometries. Photoluminescence (PL) as a function of QD loading was investigated and the detection limit determined in order to identify suitable QD loadings for optical sensing applications. QD emission peaks remained narrow but were subtly blueshifted upon dispersion in the silicone ink. Loadings as low as 0.0001 wt% QD-Ink A (crosslinker ink) could produce composites with detectable PL; each 10-fold dilution led to a linear decrease in intensity count and approximately -0.3 nm peak shift, arising from a combination of fewer fluorescent particles, QD ligand depletion, and decreased rates of photon reabsorption.^{236,239,240} As a trade-off was observed for QD loading between signal strength and polymer matrix curing in drop casting experiments, 0.005 wt% QD-Ink A was chosen as an initial target loading as it resulted in visible fluorescence and was not seen to prevent curing at 60 °C.

Addition of nanoparticles to ink may be associated with increased viscosity.³⁴ To ensure that Ink A would remain printable at the chosen loading, the Einstein equation was used to predict the effect of QDs on viscosity,^{18,34} and 0.005 wt% QD loading was calculated to have no impact on ink printability. Elliot *et al.* found that the Einstein equation overestimated relative viscosity for 0.5 wt% TOPO-capped CdSe QDs in VeroClear acrylic resin by comparing viscosity prediction with empirical measurements.¹⁸ However, octadecylamine ligands have a longer chain length than TOPO ligands and may penetrate further into the surrounding medium. In one report in the literature, a discrepancy was seen where octadecylamine ligands on carbon nanotubes led to an intrinsic viscosity 40 times higher than any models investigated.²⁴¹ Nonetheless, 0.005 wt% QD loading was calculated to be suitable for inkjet, even after accounting for this extreme case under the assumption that the ligands were inherently responsible for the discrepancy. An Einstein equation with an intrinsic viscosity of 200 corresponds to a 0.21% increase in viscosity in 0.005 wt% QD-Ink A, which is still insufficient to change the printability index Z .

Large QD aggregates in ink can block jetting nozzles and particle diameter should not exceed 5% of the nozzle diameter.³⁴ Stabilisation of QD dispersion by the ink solvent was therefore important for longterm jettability as strong van der Waals attraction between QDs and large surface energy mis-match between silicones and CdSe/ZnS drives the formation of large QD agglomerates.^{122,268,269} Dynamic light scattering (DLS) was used to assess *in situ* QD dispersion in the octyl acetate solvent by comparison with a typical solvent for colloidal hydrophobic QDs. The use of DLS to assess QD solutions is impeded by

complex QD refractive indices and fluorescence;²⁴² despite laser wavelength close to the QD emission, it was possible to conduct a comparative study of octyl acetate and hexane solvents with data quality deemed acceptable by the software user interface. Dispersions in octyl acetate yielded viable data which showed monodisperse 118-138 nm clusters with 0.137 PDI, in agreement with clusters observed in TEM of composites and within particle size limitations for inkjet. Hexane dispersions returned anomalous data: a strong peak corresponding to an erroneously small particle diameter was seen, which is likely a solvent or buffer peak,²⁴⁶ and the correlogram showed discontinuities in the correlation curve indicating number fluctuations,²⁴⁷ consistent with issues seen in samples too dilute for stable measurement via DLS. It is possible that differences in QD emission peak shift between the two solvents led to the differences in data quality.^{236,237} While the nominal 630 nm QD emission peak led to complications in data collection, so that octyl acetate could not be compared with the apolar solvent, DLS studies were demonstrated to be feasible to assess QD dispersion in solvents *in situ* which may be of use to future ink formulation, and octyl acetate solvent was shown to be suitable for QD dispersions compatible with inkjet.

Curing was the greatest challenge in reactive inkjet of QD-silicone composites, as QDs were observed to inhibit curing in addition cure silicones. It appeared that the labile amine ligands on the QD poisoned the platinum catalyst, as reported in various studies of QD-silicone composites.^{132,146,248,290} In dropcasting experiments, both reduced QD loading and heating to the maximum platen temperature of the printer (60 °C) were insufficient to enable composite cure times comparable to the SiliGlass control inks. Therefore, a change in formulation was required to accelerate cure. Increasing the amount of catalyst in the formulation was trialled as an accessible route to QD-composite curing, in contrast to time-consuming QD surface modifications which are associated with reduced fluorescence. As increased catalytic loading is associated with longterm yellowing^{181,192} even at low temperature (≤ 50 °C with 12 months accelerated aging)¹⁸¹ due to the formation of metallic nanoclusters during thermal or photo-aging,⁴⁶ the minimum platinum loading needed for curing was used in ink formulation for temperature sensing materials with improved transparency and photostability. The high crosslink density and 1.68-fold molar excess of silane in SiliGlass may also lessen the development of discoloration¹⁹²; in one study, was used to prevent yellowing below 80 °C, which could be suitable for a sensing range between 0-70 °C.¹⁸¹ A simple, inexpensive catalyst (PtCl₂) was selected for initial trials, but specialised catalysts which are known for non-yellowing properties or robustness are

preferable for future material development. ≥ 0.00075 wt% PtCl₂ in Ink B (catalyst ink) enabled curing of QD-composites with cure time comparable to or shorter than control inks without QDs in drop casting experiments; further characterisation was carried out to assess the effect of platinum on conversion and QD fluorescence.

Vibrational spectroscopy was used to assess curing of composites with added catalyst by monitoring modes associated with hydrosilylation.²⁰⁰ While FTIR spectroscopy can be used to assess cure in jetted silicones,⁶⁸ the solvent made data processing challenging as octyl acetate masked peaks in the PDMS spectrum that were suitable for normalisation. Raman spectroscopy was therefore used to enable normalisation using the Si-O-Si vibration at approximately 490 cm^{-1} ,^{60,64} an excitation wavelength of 785 nm was necessary to prevent QD fluorescence during data collection. Raman spectroscopy was used to compare the degree of conversion (DoC) of cured inks relative to undiluted SiliGlass by quantifying the unreacted silane moieties. Addition of solvent increased DoC relative to undiluted SiliGlass in all cases, despite being associated with longer cure time in dropcasting experiments. This was rationalised as the decrease in viscosity promoting mixing, which is beneficial to the overall conversion as the curing is diffusion rate-limited.²²² QD-silicones had higher conversions than the controls in all cases due to their higher catalyst loadings, despite the presence of quantum dots, in agreement with their shorter cure times. However, high platinum concentration was observed to retard conversion in QD-silicones and DoC decreased by 30% from ≤ 0.0025 wt% Pt-Ink to 0.005 wt% Pt-Ink B.

Addition of platinum catalyst was observed to reduce the emission intensity of QD-silicone composites in bulk samples and in PL maps obtained during Raman spectroscopy, where a 70% reduction in emission intensity was observed when PtCl₂ loading doubled. Similar observations of Pt-mediated quenching in QD-silicones are reported in literature.^{250,291} A metal-induced aggregation mechanism was proposed to explain reduced emission and lower overall conversion in cured composites with high catalyst loading; further characterisation is needed to confirm this. While PL reduction is a significant drawback to the use of higher catalytic loadings for fluorescent sensing materials, reduced QY is also common in surface modification strategies due to the removal of primary amine-associated PL enhancement^{236–238} and PL loss being associated with many QD modification steps. Such strategies do typically offer improved photostability, however, and are worth consideration in future formulations. 0.00125 wt% was selected as the loading in Ink B as the minimal loading showing reliable curing and high conversion at ambient temperatures, and for its temperature response in PL well-plate reading (discussed in Section 7.4).

Inkjet printing of a QD-composite was demonstrated for the first time and ordered arrays and patterned composites were jetted using a single printhead printer as described above for silicone inks. 60 °C substrate heating was used to accelerate curing *in situ* and printing using Ink B with and without 0.00125 wt% added PtCl₂ was compared. Ink without added catalyst had greater PL emission intensity but failed to cure, despite being observed to cure at 60 °C in drop casting experiments; it appears that curing was vulnerable to delays in heating and that printing without added catalyst is feasible with higher substrate heating than was possible using the Dimatix printer. In contrast, composites printed using 0.00125 wt% did cure with a 35.7 ± 1.4 μm mean drop-on-drop (DoD) Feret diameter, although Pt-mediated quenching was observed as expected. The printed QD-silicone composite had visible fluorescence at 0.005 wt% QD loading which was suitable for optical sensing and sensing arrays were demonstrated with resolution ~36 μm, which is among the highest reported for inkjet of QD-polymer composites thus far (approximately 30 μm and <50 μm from Bao *et al.*¹²⁹ and Hu *et al.*,¹²⁸ respectively). Print resolution is difficult to compare where papers list diameters for pixels which consist of many droplets to enhance repeatability despite size variation of individual droplets;^{124,125} resolutions of ≥100 μm are not infrequent in literature.^{18,126,127}

A 2-part ink strategy was used to obtain high polymer loading (50 wt%) using a single solvent as carrier vehicle: other solution phase QD-polymer inks typically contain ≤5 wt% polymer^{124–127} and do not exceed 16 wt% to the author's knowledge.¹²⁹ High polymer loading was a priority for bulk composite inks for printing efficiency and film formation, Marangoni flow and solvent-polymer interactions lead to inhomogeneity that hinders the accuracy and efficiency of temperature sensing materials.^{35,116,231,232} Conversely, visible fluorescence was achieved with low QD loading (0.005 wt% QDs in Ink A) to minimise catalyst poisoning and the size of aggregates in the composite. This would reduce scattering, photon reabsorption by neighbouring QDs, and thermal annealing. QD loading was low in comparison to other literature reports; while greater QD loadings were needed in order to achieve similar brightness in some cases,¹⁸ in the majority of papers QD loading was higher because composites were intended for lighting displays which require intense emission.^{124–127} QD loadings of up to 15 wt% in ink have been reported for inkjet of QD-polymers where a solvent was not employed.¹²⁸ The issue of platinum catalyst poisoning may be solvable using *in situ* or *ex situ* heating at ~120 °C as hydrosilylation can be thermally activated.¹⁷ While neither of the printers used in this research were capable of platen temperatures that high, the ink constituents are compatible with high temperatures

as the octyl acetate solvent is non-flammable, although thermal annealing of QDs may occur.

While octyl acetate colloidal dispersions were measured to have QD clusters <140 nm in size in DLS, high polymer loading appears to have resulted in greater QD aggregation in ink. Ink and composite morphology bore resemblance to the 0.5 wt% CdSe QD-acrylate photoresin developed by Elliot *et al.* for inkjet printing:¹⁸ ink sonication was required prior to printing to prevent QDs from settling and micron-scale aggregates were observed via fluorescence microscopy. Clusters observed in TEM were on the order of 100 nm diameter, in agreement with DLS measurements of QD solution, while micron-scale aggregates were viewed during optical microscopy: bulk composite had a mean Feret diameter of 1.8 μm and a range of 0.5-4.0 μm while printed materials, with or without added catalyst, had similar values with mean Feret diameter of 2.3 μm and a range of 1.5-6.1 μm . Clusters and aggregates were similar to those seen in literature of QD-silicone composites and reports of QD aggregate sizes appeared to have some correlation with QD loading. Trung *et al.* synthesised a 0.1 wt% CdSe/ZnS QD-silicone composite and characterised 22 nm diameter clusters using AFM and sub-micron to 2 μm diameter agglomerates using cLSM.¹³² Tao *et al.* reported QD clusters on the order of 100 nm diameter during TEM of well-dispersed 0.2 wt% CdSe QD-silicone composites, and sub-micron agglomerates with 50 nm-sized clusters with rapid precipitation.¹²² Kim *et al.* used a higher QD concentration (3 wt%) and described correspondingly larger aggregates: larger aggregates had $\geq 10 \mu\text{m}$ diameter, while smaller aggregates had diameters $\leq 5 \mu\text{m}$.¹³¹ The micron-scale aggregates observed during this thesis were similar in size to Trung *et al.* despite containing half the amount of QDs; Trung *et al.*'s use of spin-coating, high cure temperature, and viscous silicone precursors may account for this in terms of more rapid crosslinking and reduced QD motility. Maximum QD dispersion is optimal for sensing materials and aggregation was expected to impact sensing performance due to self-quenching, Rayleigh scattering, and thermal annealing.^{122,239} Aggregation of different addition cure formulations and their temperature sensing performance are discussed in Section 7.4, obtaining thermal coefficients of sensing inks that had been developed to be jettable and printable (Objectives O3 and O4).

7.3. Formulation and printing of UV cure silicone inks

UV curable silicone formulations presented another promising mechanism for the synthesis of QD-silicone composites for temperature sensing. Free radical photopolymerisations are suitable for formulating solvent-free one-part inks with rapid crosslinking, which is greatly beneficial to inkjet printing calibration, throughput and resolution.⁵⁶ This was advantageous for sensor production in a number of ways; firstly, material compatibility issues are lessened by solvent-free inks, which simplifies device production. Controlled deposition of UV cure inks can be achieved with a wider range of substrates due to their fast reaction rate compared to hydrosilylation and as acrylate-functionalised oligomeric (co)monomers have higher surface energies than PDMS chains. Furthermore, the chain growth mechanism of free radical photopolymerisations can produce polymers and copolymers with a wide range of physical properties from low viscosity precursors (<10 mPa s), which enables ink formulations towards materials with desirable optical and mechanical properties for specific sensing applications. Enhanced dispersion of QDs may also be achieved: Hu *et al.* 2020 achieved excellent QD dispersion in inkjet-printed QD colour conversion layers, despite using a 15 wt% QD loading in photopolymer without solvent as rapid photopolymerisation produced drops without coffee staining or QD aggregation.¹²⁸

Low viscosity precursors were chosen to enable inks without carrier vehicles: a commercial methacryloxypropyl-terminated PDMS (abcr AB116678, 4-6 mPa s) and 2-ethylhexyl acrylate (2-EHA, 1.7 mPa s²⁶⁷). The bifunctional methacrylate PDMS was chosen to promote rigidity and crosslinking. An acrylate comonomer was selected to investigate faster reaction rate (which may be beneficial for inkjet resolution⁵⁶ and QD dispersion¹²⁸) and to investigate copolymers with varying degrees of flexibility and the effect on thermal sensing. 2-EHA was selected for its branching alkyl chain to investigate the effect on QD dispersion and photostability, and as longer alkyl chains confer increased hydrolytic stability and therefore resistance to discoloration.²⁵⁵ Copolymers with varied flexibility were of interest for sensing to fit a range of applications, and to assess the effect of coefficient of thermal expansion (CTE) on sensing performance: high CTE can act to enhance the temperature sensitivity of thermal sensors¹⁴ and to prevent crack formation as a result of thermal stress, but leads to dimensional changes with temperature and solvent swelling, and may see greater changes in measured response over the sensing material lifespan.^{57,181}

During initial tests of QD-silicone composites carried out via dropcasting in air, 2-EHA comonomers were associated with greater oxygen inhibition and improved QD dispersion. Observations may be rationalised as the result of oxygen acting as a radical scavenger: loss

of PL was observed in the QD-PDMS polymer, which successfully cured, whereas PL was retained in the QD-PDMS-2-EHA copolymer, which did not cure, correlating with photoinitiator (PI) loading (0.5 wt% compared to 0.25 wt%, respectively). In QD-PDMS-2-EHA composites, 0.25 wt% PI loading was insufficient for curing even at 1.1% O₂, while curing was observed with 0.5 wt% PI at 0.5% O₂. This may indicate that 0.5 wt% was the minimum loading required for curing without thorough degassing, regardless of the presence of 2-EHA; however, the lower packing efficiency of 2-EHA would also be expected to lead to greater inhibition if oxygen were better-distributed through the greater free volume in the sample. QDs did not remain dispersed in QD-PDMS polymer that was dropcast in air and QDs appeared to separate from the polymer, leading to full quenching of PL. While QD dispersion was stable in the QD-PDMS-2-EHA sample, which may indicate more favourable interaction of the stearyl tail of the QD stabilising ligand with 2-EHA than with the PDMS,^{122,268,269} this may instead reflect differences in cure inhibition. QDs remained fluorescent where photopolymerisation was hindered, which prevented loss of passivating ligands arising from phase separation and heat from exothermic polymerisation.²⁷⁷⁻²⁷⁹ While poorer compatibility between QDs and the host polymer is known to lead to greater phase separation and/or depletion flocculation,²⁷⁷⁻²⁷⁹ it is not clear whether addition of 2-EHA comonomer, which was more similar in composition to the octadecylamine ligands, led to improved QD stabilisation. While 2-EHA appeared to prevent phase separation in dropcast samples, differences between cured composites with and without 2-EHA were observed in samples cured in vials were unclear, and aggregation was still expected as QD ligands were not bulky enough to fully screen core-core interactions.¹²²

In order to optimise curing of UV inks deposited by inkjet, photoinitiator blends are commonly employed to enable good surface and depth cure, and to mitigate oxygen inhibition of phosphine oxide-type photoinitiators.²⁶² Two photoinitiators were selected for testing: one midwave UV absorber 2,2-dimethoxy-2-phenylacetophenone (DMPA), and one longwave UV absorber phenylbis(2,4,6-trimethylbenzoyl)-phosphine oxide (TPO). PI loadings ≤1 wt% were used to minimise yellowing and leaching from photoproducts, and to maximise chain length in cured materials.²⁶² Ink rheology was rapidly characterised using the high-throughput screening (HTS) method developed by Zhou *et al.* 2019.¹⁷⁸ Inks were formulated solely with the PDMS precursor ('PDMS ink') or with a 1:1 mixture of PDMS and 2-EHA ('2-EHA ink') to establish the rheology of the minimum and maximum comonomer ratios for a range of copolymers. PDMS inks were found to have average *Z* numbers of 4.2-4.3, while 2-EHA inks had 7.9-8.7 as they had much lower viscosities which made them

vulnerable to formation of satellite droplets. However, the HTS approach is noted to underestimate viscosity of low viscosity fluids;¹⁷⁸ estimated Z parameters using adjusted viscosity values (14.6% difference) were 6.8-7.5.

2,2-Dimethoxy-2-phenylacetophenone (DMPA), a.k.a. Omnirad 651, is considered to be the most commonly used photoinitiator for free-radical crosslinking of silicones.⁵⁶ It is considered a general-purpose PI due to broad UV absorption, which confers both surface and depth cure, and its susceptibility to oxygen inhibition is limited by its short triplet lifetime.²⁶² DMPA was selected for printing of optical temperature sensors due to its capacity for absorption of wavelengths of typical UV LEDs used in printers and for its surface curing, as oxygen inhibition at the surface of acrylate thin films reduces transparency.²⁷¹ The high thermal stability of DMPA was also desirable to prevent discoloration from thermal decomposition products of residual photoinitiator. However, photo-products of DMPA may cause yellowing; to prevent this, PI loading was minimised.⁵⁶

Jetting of DMPA-2-EHA ink was demonstrated with 35 μm drop diameter on silanised glass slides, comparable to that seen for addition cure inks, but did not cure. Further experiments with PI loading were carried out to determine loadings compatible with inkjet printing and the necessary oxygen concentration. 1.1% O_2 during the printing trial was sufficient to prevent cure at 0.25 wt% DMPA, while 0.5% O_2 allowed complete solidification of polymer and composites in under 30 s at loadings ≥ 0.5 wt% DMPA. Faster curing was achieved by increasing PI loading, correlating to greater radical concentration leading to greater number of initiated chains²⁶²; no discernible difference in cure rate was observed between samples with and without QDs, and QDs did not affect cure rate via competition with PI for UV absorption.²⁸²

While it had been demonstrated that inks with low DMPA loading could cure under nitrogen, oxygen-sensitivity was shown to be a considerable challenge, and so initial tests were carried out with thiol monomers to investigate the thiol-ene crosslinking mechanism. Thiol-ene reactions have higher conversions, lower oxygen inhibition, and less shrinkage than acrylate chain growth photopolymerisation, although the working life of inks is limited as gradual reaction occurs at room temperature.⁵⁶ Oxygen inhibition of acrylate thin films leads to poor surface cure and reduced transparency²⁷¹, and the inkjet process facilitates oxygen inhibition as droplets have high surface area to volume ratio and therefore large interfaces with air. Thiol-ene inks may enable greater conversion than acrylates, or achieve comparable cure with lower PI loadings and/or at higher O_2 concentrations, potentially

leading to optical sensing materials with less discoloration and fewer optical aberrations. However, thiols are well-known to quench CdSe/ZnS QDs,^{263,264} and trials with monomers were needed to assess their suitability for inkjet printing of fluorescent composites for optical temperature sensing.

Two thiol monomers were trialled as additives, to compare their tendency towards QD quenching and to modify crosslinking density in copolymers: pentaerythritol tetrakis(3-mercaptopropionate) (PETMP) and 2,2'-(ethylenedioxy)diethanethiol (also known as 3,6-dioxa-1,8-octanedithiol or DODT), which contained four and two thiol moieties respectively. Thiol-ene inks underwent rapid crosslinking to form fluorescent composites, though quenching was observed and the extent of PL loss correlated with the concentration of thiol moieties; total quenching was observed for higher thiol loadings. Increasing crosslinking density and steric hindrance appeared to reduce QD quenching by reducing the ease of ligand exchange,^{263,264} where DODT was associated with greater quenching in the absence of PETMP. PETMP was a larger crosslinking agent with four reactive moieties: rapid solidification and higher crosslinking density would lead to more effective immobilisation of species within the polymer, and the greater steric hindrance of PETMP impedes access to the QD surface. In contrast, DODT is sufficiently small to migrate through polymer matrices,²⁶² and residual monomer could exchange with stabilising ligands before, during, or after photopolymerisation. While PETMP was identified as promising for rapid crosslinking of polymers with increased crosslinking density, direct comparison between the monomers is difficult as PETMP was more viscous and a lower mass was trialled in initial experiments. In future formulations, the thiol : ene ratio could be reduced to minimise QD ligand exchange, although this must be balanced with changes in properties that arise from competition between acrylate chain growth and thiol-ene step growth mechanisms. For optical temperature sensing inks, stoichiometry should be optimised for fluorescence signal strength and stability, oxygen inhibition, and mechanical and optical properties of the cured matrix.^{271,276}

Total quenching was associated with DMPA photoinitiator in all samples with more rapid quenching at higher PI loading, whether by a direct or indirect mechanism, which prevented their use for optical temperature sensing. Fluid inks without photoinitiator lost fluorescence over a longer period of time, indicating that the labile octadecylamine ligands were not able to stabilise QD dispersion in precursors^{110,122,249} and that quenching of composites was induced by photopolymerisation, DMPA photoproducts, or radicals. While QD quenching by photoinitiators has been reported in prior literature,²⁸⁰ discussion in the

context of QD-silicone composites is scarce as hydrosilylation is the reaction mechanism of choice for lighting applications (Section 2.3.3). The mechanism of quenching may be multifaceted: amine stabilising ligands can detach during exothermic photopolymerisation reactions, particularly with poor compatibility with the host matrix, which degrades the surface passivation.^{259,277,278} Furthermore, it is possible that radicals etched the exposed surface of the QDs in samples containing photoinitiator: photoinitiator concentration was and has been linked to QD quenching in QD-photopolymers,²⁸⁰ as particularly noted with nitroxyl radicals,²⁸¹ as has photo-oxidisation by oxygen adsorbed in silicones.²⁶⁸

Therefore, while printing silicones with DMPA concentration <3 wt% under a low oxygen environment was shown to be feasible, fluorescent composites suitable for temperature sensing were not obtained using DMPA. Photostable QD-silicone composites can be synthesised using DMPA photoinitiator if the QD surface is adequately protected, and several QD-silicone composites are described in literature, mainly for sol-gel silicone hybridisers. Kim *et al.* 2016 dispersed 0.5 wt% oleic acid-capped CdSe/ZnS QDs in an α,ω -diacrylate PDMS (Miramer M244) with 0.2 wt% Omnirad 651. The QD-silicone resin was subjected to nitrogen purging for several hours before curing to eliminate oxygen; quenching of QDs was not observed.¹³⁵ In later work, a QD-silicone hybridiser with high stability was produced using silica encapsulation. QD-resins were prepared by *in situ* sol-gel condensation with 5 wt% silane-treated QD-silica microspheres; these were then cured using 2 wt% DMPA with 365 nm excitation under argon, and post-cure thermal treatment was used to terminate radicals.²⁹² The same group proceeded to use mercapto-silane-capped QDs to enable photopatterning of QD-silicone hybridisers without oxygen inhibition. 10-20 wt% QD-silicone resins were prepared by *in situ* sol-gel condensation and were crosslinked after addition of 2 wt% DMPA and a pentaerythritol tetrakis(3-mercaptopbutylate) and excitation at 365 nm.^{273,274} Overall, these reports suggest that photo-oxidation is a likely cause of quenching: quenching was not observed where inert gas purging was used, and more thorough degassing may prevent loss of PL. However, prevention of ligand detachment – via silica encapsulation and/or binding QDs to the precursor – also appears to be effective, as thiol-ene photopolymerisation was successfully demonstrated without inert conditions or QD quenching. Discussion of quenching and the need for thorough degassing or a specific QD stabilisation strategy may advise future formulations for radical crosslinking of QD-silicone composites.

Phenylbis(2,4,6-trimethylbenzoyl)-phosphine oxide (TPO), a.k.a. Omnirad 819, is a reactive photoinitiator commonly used in silicones, which strongly absorbs longwave UV leading to

good compatibility with the UV LED wavelengths used in inkjet. TPO is attractive for optical sensing materials as it undergoes photobleaching, which would lead to high transparency in composites and may limit the radical concentration if the quenching mechanism in DMPA was related to radical etching of the QD surface. TPO has notable susceptibility to oxygen inhibition and is associated with depth cure, which made it unsuitable for curing thin films in air with suitable transparency for optical sensing.²⁷¹

Photoinitiator loading experiments in 0.5 wt% O₂ found that 2 mL samples of 2-EHA inks with 0.01 wt% TPO required several minutes of exposure to cure, samples with 0.1 wt% TPO cured in approximately one minute and a half, and samples with 1 wt% TPO cured thoroughly in under thirty seconds. No differences were observed in cure times for samples with differing QD loadings, in agreement with observations of the DMPA composites, despite observations of acrylate cure retardation by QDs in literature.²⁸² All samples retained fluorescence and there was no observable relationship between concentration of photoinitiator and fluorescence. While a small initial decrease in fluorescence was observed after 24 hours, no further changes in emission intensity were observed over a 3-week monitoring period. The cause of the initial decrease in emission intensity is unclear but may relate to changes in the polymer after curing; acrylates are known to continue to react after initial irradiation, a process known as dark polymerisation, as macro-radicals propagate and terminate. Physical changes, such as diffusion of small molecules through the matrix and polymer relaxation, may have also taken place. Another possibility is that emission loss was halted by TPO photobleaching or that TPO radicals scavenge oxygen which shields the QD surface from photooxidation.

Overall, novel QD-photopolymers were produced with visible emission using TPO photoinitiator and observed photostability was much greater for TPO-2-EHA composites than was seen for DMPA analogues. However, while TPO may be attractive for QD-photopolymers, long-term photostability was not confirmed and further work is needed to elucidate the quenching mechanism and the effect of thorough degassing. Therefore, jetting was demonstrated for UV cure silicones without QDs, Objective O2, as photostability had not been optimised, and TPO-inks were prioritised due to more efficient absorption of the UV-LED wavelength and as issues with quenching had been observed in composites containing DMPA. Curing of inks with varied TPO loading (0.25, 0.5, 1 wt%) was investigated using UV-DSC to compare cure behaviour, conversion, and cure rate. All inks investigated reached their final conversion after the initial 10 second UV exposure and did not require further excitation. 1 and 0.5 wt% TPO inks showed similar behaviour under

nitrogen flow while 0.25 wt% TPO inks had slower onsets of curing and broader exothermic peaks. TPO-PDMS inks cured more rapidly than TPO-2-EHA inks and the difference in reaction rate was more pronounced at 0.25 wt% TPO loading. Print trials with 1 wt% TPO-PDMS inks were prioritised over other formulations as it had the fastest reaction rate, which could better preserve QD passivation and enhance print resolution.

Jetting trials of PDMS and 2-EHA inks without photoinitiators were carried out, as inks had similar rheologies with and without photoinitiators. Neither density nor surface tension were observed to be affected by PI loading in any formulation tested. While viscosity was not observed to be correlated with PI loading across the range of loadings tested, the presence of PI was associated with a small increase in viscosity; between the PIs, TPO conferred higher viscosity than DMPA analogues, likely due to π -stacking between its aromatic rings. Average Z parameters for PDMS inks were 4.30 (DMPA) and 4.17 (TPO), which had viscosities at the lower end of the ideal jetting range for the Dimatix, and surface tensions at the higher end of the ideal range.^{175,176} A greater difference in average Z parameters for 2-EHA inks, 8.73 (DMPA) and 7.93 (TPO), was due to low initial viscosity. Inks were jetted onto silanised glass slides to produce drop arrays using two different waveforms, W_2 and $W_1 v_2$, which were single and dual pulse respectively. Satellite drops were observed for both PDMS and 2-EHA inks, due to their high surface tensions and low viscosities compared to the ideal ranges for the Dimatix;^{175,176} satellite formation was solely observed in jetting of 2-EHA ink and PDMS ink had more minor issues with satellite droplets than 2-EHA inks, as predicted from their respective printability parameters. PDMS inks had drop diameters of $42.2 \mu\text{m} \pm 8.2 \mu\text{m}$ using waveform W_2 at 25 V and $33.7 \pm 5.9 \mu\text{m}$ using waveform $W_1 v_2$ at 22 V. Waveform W_2 produced well-ordered drop arrays with minimal satellites, but drop diameters were larger, limiting resolution. Waveform $W_1 v_2$ had been optimised for the addition cure inks, which had lower surface energy than the UV cure formulations, which led to some excess material at nozzles that resulted in more frequent nozzle misfire and issues with drop trajectory. However, drop diameter was smaller and well-controlled ($33.7 \pm 5.9 \mu\text{m}$ for PDMS ink at 22 V). PDMS inks were selected for print trials, as the viscosity was closer to ideal values and satellite droplets were less frequent, and $W_1 v_2$ was selected as higher resolution was achievable and only minor adjustments to the waveform are needed to eliminate satellite drops and excess material at the nozzle, particularly refinement of the cancellation pulse.

During jetting of droplet arrays onto silane-treated substrates, the UV curable inks showed similar lack of pinning as addition cure inks due to having higher surface energy than the

silanised glass slide. Therefore, printing optimisation of the UV curable inks on the silanised substrates is predicted to be similar to that of addition cure inks: making use of pinned grid and line-by-line strategies. However, unlike the addition cure inks, it was possible to print onto slides coated with release agent as the UV curable inks did not fully wet the surface due to higher surface tension ($\sim 47 \text{ mN m}^{-1}$). Printing of cured silicones was demonstrated using 1 wt% TPO-PDMS with waveform $W_1 v_2$ at 22 V under an N_2 atmosphere, producing continuous monolayers at 10 μm spacing with smooth surface texture. The print quality was comparable to that of addition cure inks printed with a pinned grid strategy in terms of undulation at edges, which implied that the release agent provided surface microstructuring and that deposition creep may have occurred as driven by surface tension. The geometric control was poorer than seen for a line-by-line strategy as deposition creep and nozzle failures were evident; however, continuous thin films produced at 10 μm spacing appeared to have comparable flat surface texture, although the texture of the release agent was visible through the films, which reduced the transparency of the printed material and obscured observation of microstructure.

Overall, a range of UV curable QD-silicones were produced, and the first jettable UV cure silicone inks without carrier vehicles were developed (Objective O1). On PFOTS-treated glass slides, PDMS and 2-EHA inks were jetted with mean drop diameters of $\leq 35 \mu\text{m}$ and $\leq 42 \mu\text{m}$, depending on the waveform employed. Jetting of QD-DMPA-2-EHA composite ink was established with 35 μm drop diameters and DMPA loadings of $\geq 0.5 \text{ wt}\%$ were shown to enable curing suitable for inkjet printing under inert conditions. Reactive inkjet of a UV curable silicone was demonstrated using 1 wt% TPO-PDMS (Objective O2) and smooth monolayer films were produced without the use of non-standard deposition strategies. Jetting was demonstrated with the highest resolutions achieved for IJP of UV curable silicones; despite the fact that rapid photopolymerisation can minimise drop spreading,^{56,128} potential for high resolution, UV curable silicone drop diameters are limited to $>200 \mu\text{m}$ in inkjet literature.⁶³ Other UV silicone ink formulations in material jetting literature have aimed towards soft PDMS elastomers with high elongation,⁶⁷ resulting in ubiquitous use of carrier vehicles and greater drop spreading due to lower surface energy (close to that of bulk PDMS). While $<40 \mu\text{m}$ drop diameters were obtained using the PFOTS treated glass slides due to their low surface energy ($<20 \text{ mJ m}^{-2}$) which prevented droplet spreading, silanised substrates were not required as the inks had higher surface energy (44-47 mJ m^{-2}) than bulk PDMS. Demonstration of printing on a wider range of substrates could aid device design by assessing material compatibilities without intensive surface treatment.

7.4. Temperature sensing with QD-silicone composites

The temperature sensing performance of jettable QD-silicone composites was assessed using fluorescence spectroscopy, well-plate reading, and confocal laser scanning microscopy (cLSM), with emphasis on the octyl acetate-based addition inks which had been demonstrated for IJP of fluorescent QD-silicone composites. The PL spectra of a 0.01 wt% QD-silicone composite (octyl acetate-based inks, no added platinum catalyst) did not show significant degradation from the manufacturer's specifications (Ocean NanoTech, CdSe/ZnS QDs, $\lambda_{\text{max}} = 630 \text{ nm}$). The position of the emission peak as supplied in solid form was blue-shifted by 4 nm upon immobilisation in the silicone matrix, consistent with a change in QD environment.^{151,236,237} Greater dilution may also contribute to observed blueshift, from decreased photon reabsorption and from ligand detachment,²³⁶ as could photo-oxidation in response to laser irradiation.^{236,287} While peak width remained narrow, a small shoulder was seen around 655 nm post-cure, indicative of QD aggregation.^{122,239}

As the extent of QD aggregation in the matrix determines the transparency and stability of the composite, QD clusters were imaged via TEM and cLSM of the 0.005 wt% QD-silicone composite (octyl acetate ink-based, no added catalyst). TEM imaging appeared to show a microporous network structure associated with phase separation,^{231–233} which may consist of an elastomeric siloxane network with solvent-rich domains, and gyroidal microphases were observed on a larger scale in optical micrographs of printed SiliGlass. Microphases may cause scattering and reduce the transparency of the sensing materials.²³⁴ QD clusters of over 100 nm diameter were seen and confirmed by EDS, similar in size to the 118.3 nm average diameter obtained from DLS of 0.005 wt% QDs in octyl acetate solution. Micron-scale aggregates were viewed during cLSM optical microscopy, with a mean Feret diameter of 1.8 μm and a range of 0.5–4.0 μm . Similar values were obtained during cLSM of printed composites, both with and without added catalyst, which had mean Feret diameters of 2.3 μm with an approximate range of 1.5–6.1 μm . In samples prepared for temperature sensing measurements using cLSM, differences in cure may have led to differences in QD aggregate size and brightness. In samples with 0.00125 wt% PtCl₂, aggregates had 4.5 μm mean Feret diameter and were larger than in printed composite due to reduced duration of heating at 60 °C; it appeared that thermal acceleration of curing was less effective than that achieved during print trials, allowing further aggregation to occur. However, while a difference in cure accounts for the difference from the printed sample, mean Feret diameter was double that of the composite that had been printed without added catalyst and failed to cure. This may be indicative of a metal-induced agglomeration mechanism of

Pt-mediated quenching, or it could be a survivorship bias if smaller aggregates were unable to remain visible during imaging due to quenching. Aggregates in sensing samples prepared without added platinum were similar in size to the printed composite, with 2.6-2.8 μm mean Feret diameter. QD clusters appeared brighter than in the printed composite, which did not cure during print trials, and greater intensity may have resulted in a slight increase in measured size. Toluene ink-based samples without added catalyst had brighter aggregates than the octyl acetate ink-based samples, reflecting the faster cure time of toluene inks. Aggregates had a mean Feret diameter of 3.0-3.4 μm : compared to octyl acetate ink-based composites, diameters were larger than in samples without added catalyst due to reduced heating (15 min vs 24 hr), and smaller than in samples with added catalyst and the same heat program. Aggregation is detrimental to QD-based optical sensing materials as greater aggregation leads to weaker signal via self-quenching and Rayleigh scattering, and poorer thermal stability due to particle coarsening mechanisms.^{122,239} Larger aggregates were associated with shorter heating programs, octyl acetate (due to faster curing of toluene-based inks), and higher catalyst loading, despite faster curing, which may indicate metal-induced agglomeration. As the above factors also correlated with lower emission intensity, there may be selection bias if only larger clusters remained visible in dimmer samples.

Well-plate reading was used to compare the emission intensity of different QD-silicone formulations and to assess the repeatability of thermal response. QD emission intensity is well-known to decrease linearly with increasing temperature,^{1,2} which was observed in all samples and lines of best fit were applied to assess sensitivity. Emission intensity varied between formulations: toluene ink-based composites had the highest emission intensity, followed by 0.001 wt% TPO-PDMS, 0.1 wt% DMPA-PDMS, and octyl acetate ink-based composites. Toluene ink-based formulations had higher emission intensity than octyl-acetate based ones, in agreement with observations made during microscopy; this was thought to arise due to higher reaction rate, resulting in faster QD passivation. Sample age and/or polymerisation also appeared to factor in emission intensity, as uncured octyl acetate inks had higher emission intensity than all cured composites.

Pt-mediated quenching was observed in addition cure composites: in octyl acetate-based inks, emission decreased regularly for uncured inks while, in cured composites, 0-0.00125 wt% PtCl_2 resulted in a much higher intensity than 0.0025-0.005 wt% PtCl_2 . Therefore, octyl acetate ink-based composites with ≤ 0.00125 wt% PtCl_2 appeared most viable for sensing due to higher signal-to-noise. Pt-mediated quenching was less significant

in composites from toluene-based inks, although repeatability between thermal cycles was poorer. In UV cured composites, photoinitiator loading was 0.1 or 0.001 wt%, and composites containing TPO had greater emission intensity than those containing DMPA. This was likely due to its higher absorptivity of the UV-LED wavelength, leading to better curing and passivation. Lower loadings of DMPA were associated with lower emission intensity, despite previous observations of PL quenching, likely due to DMPA's weaker absorption of the UV-LED wavelength leading to poorer QD passivation. Higher loadings of TPO led to slightly reduced emission, possibly from competition for photon absorption. PDMS inks typically had higher emission intensity than 2-EHA inks despite being associated with poorer QD dispersion, which may correlate to faster cure rate (as seen in DSC). Full quenching of fluorescence was not observed during the course of measurement, despite being observed in all composites containing DMPA in prior work; however, data quality was relatively poor for DMPA formulations with large error bars, and composites with low PI loading were inconsistent between thermal cycles. Overall, 0.1 wt% TPO-PDMS was the most promising of the UV cure inks, but further work is required to assess and resolve issues with photostability in UV cure composites. Octyl acetate inks were selected with 0 wt% and 0.00125 wt% PtCl₂ loading for demonstration of reactive inkjet printing.

Composite samples were prepared using octyl acetate inks with 0 wt% and 0.00125 wt% PtCl₂ loading and toluene inks with 0 wt% PtCl₂ loading, and were imaged using cLSM to assess the temperature sensing performance of printable composite inks. Emission intensity at different wavelengths was collected as a function of temperature, obtaining lambda scans of addition cure composites. Linear decrease in emission intensity at 627 nm and redshift were observed in all samples, in agreement with the results of well-plate reading and with literature.^{1,160} Emission intensity at wavelengths below 627 nm fit linear trendlines between 30-50 °C while wavelengths above 627 nm showed greater curvature: intensity initially increased with temperature as redshift occurred but began to decrease at higher temperatures as thermal quenching increased.¹⁶⁰ Three different image sectioning regimes were trialed to determine the dependence of measured sensitivity on threshold levels. When average brightness of the full image was over 3% that of the strict threshold, similar percentage intensity thermal coefficients were obtained for all sectioning regimes. Emission intensity decreased between cycles for all sectioning regimes, with greatest decrease seen between values at 30 °C and little change seen between values at 60 °C, leading to smaller percentage intensity thermal coefficients in subsequent cycles. Given that mean emission wavelengths and spectral shift thermal coefficients were

consistent between cycles, insufficient cooling and thermal annealing were unlikely to be the primary cause of the decreased intensity. Changes in the QD ligand shell may rationalise the changes between cycles: labile amine ligands enhance PL of CdSe/ZnS QDs^{236–238} but may thermally-detach,^{277–279} leading to a reduction in emission intensity. Solvent evaporation could also alter the stability of QD surface states, although shrinkage of the polymer matrix was not observed during measurement.

Percentage intensity thermal coefficients at 627 nm emission (30-50 °C) were compared for the first thermal cycles of samples. In the printable formulation, the 0.00125 wt% octyl acetate ink-based composite, the percentage intensity thermal coefficient was approximately -0.7 % °C⁻¹ for cluster thresholds and -1.2 % °C⁻¹ for full image analysis. This was lower than the respective values obtained for the composite without added catalyst (-1.2 % °C⁻¹ for Sample A and -0.9 % °C⁻¹ Sample B) due to reduced emission intensity from Pt-mediated quenching. Toluene-based analogues without added catalyst had coefficients of -0.9 % °C⁻¹ for cluster thresholds and -1.0 % °C⁻¹ for full image analysis of Sample A and -1.0 and -1.1 % °C⁻¹ for Sample B. All samples had larger percentage thermal coefficients than typical inkjet-printed sensors (0.1-0.3 % °C⁻¹)^{14,15} and values were within range of those reported for intensity-based sensing using CdSe/ZnS core-shell QDs (see Table 39): Jorge *et al.* achieved sensitivities of -0.7 % °C⁻¹ to -1.6 % °C⁻¹ between 10-50 °C using CdSe/ZnS or CdTe/ZnS QDs,¹⁵⁵ and Liu *et al.* attained -1.3 % °C⁻¹ using CdSe/ZnS QDs between 30-60 °C.¹⁶⁴ However, emission intensity and thermal coefficients decreased between thermal cycles in all samples, so that the repeatability was not suitable for optical sensing materials. Apparent sensitivity also varied with differences in patterning of imaged QD clusters, as expected as intensity-based measurements are well-known to be concentration-dependent in literature.^{1,2}

Peak shift was estimated from histograms of emission wavelengths as spectral shift-based QD nanothermometry is not dependent on concentration or laser power, which was desirable for more consistent thermal response. Values for estimated mean emission wavelength and spectral coefficients showed lesser variance between samples and thermal cycles, and all coefficients obtained were within the range reported for CdSe/ZnS QD-based sensing: 0.07-0.10 nm °C⁻¹.^{161,164,168,288} The average spectral shift thermal coefficient across the three thermal cycles of the 0.00125 wt% octyl acetate ink-based composite was 0.07 nm °C⁻¹, the spectral coefficient of the octyl acetate ink-based composite varied from 0.08 nm °C⁻¹ for sample A and 0.07 nm °C⁻¹ for sample B, and the toluene ink-based composite had a coefficient of 0.08 nm °C⁻¹. No redshift was observed following a thermal

cycle, suggesting that significant particle coarsening or thermal annealing did not occur in the short term and that the observed redshift was reversible. Lower mean emission wavelengths were obtained where background removal was not performed and therefore lower signal-to-noise ratio was associated with a slight difference in thermal coefficient. In 0 wt% PtCl₂ octyl acetate-ink based composite, Cycle 1 and 2 were run on different regions of Sample B to assess the effect of differences in cluster patterning on apparent sensitivity. Overall, intensity-based measurements were observed to vary, as expected based on its concentration-dependence,^{1,2} while spectral shift appeared consistent between regions of the same sample. Increase in mean emission wavelengths between sample A and B may indicate sample aging processes such as thermal annealing. Different formulations had similar spectral thermal coefficients, suggesting that consistent temperature response can be obtained, but long term photostability measurements are required to assess the life span of composites for repeatable spectral-based temperature sensing at temperatures under 60 °C.

Overall, composites with temperature-responsive emission were demonstrated for inkjet for the first time. The first inkjet printable QD-silicone was demonstrated with $\leq 35.7 \pm 1.4 \mu\text{m}$ mean drop-on-drop (DoD) Feret diameter on a silanised glass substrate to print arrays and films using a pinned grid strategy. The printed formulation was shown to have temperature coefficients of -0.6 to $-0.7 \text{ \% } ^\circ\text{C}^{-1}$ and $0.07 \text{ nm } ^\circ\text{C}^{-1}$ for intensity- and spectral-based sensing in the physiological range, respectively. In all three jettable formulations for addition cure QD-silicone inks, the thermal coefficients were within the range of values reported for CdSe/ZnS QDs^{161,164,168,288} and higher than typical resistance-based inkjet-printed temperature sensors (0.1 - $0.3 \text{ \% } ^\circ\text{C}^{-1}$)^{14,15}. Jetting of UV curable silicones and QD-silicone composites with resolution $<40 \mu\text{m}$ was shown to be feasible, although photostability of composites impeded their use as sensing materials; TPO appeared to be a more promising photoinitiator and was not associated with PL quenching.

Inkjet printing of addition cure QD-silicone formulations was demonstrated to be capable of depositing sensing arrays with higher spatial and thermal resolution in the physiological range than any other inkjet-printable thermal sensor in literature, where sensing areas are on the order of tens of mm². While spectral-based sensing yielded repeatable measurements across thermal cycles, further work is needed to improve photostability, data collection, and to produce and test a demonstrative device.

Chapter 8. Conclusions

The aim of this thesis was to produce inkjet-printable quantum dot-silicone composites that can be used for optical thermometry to address needs for inkjet printable thermal sensors with high spatial and thermal resolution for integrated sensing in microdevices and biomedical applications. Inks for jettable silicone matrices were formulated using addition cure or ultraviolet (UV) cure mechanisms and reactive inkjet printing was demonstrated for a range of potential sensing geometries (Objectives O1 and O2). QD were then incorporated into the inks to produce the first inkjet printable quantum dot-silicone composite (Objectives O3 and O4). QD-silicone composites were characterised to assess their temperature sensing performance (Objective O5).

2-part addition cure inks were formulated from a commercial silicone: Ink A (crosslinker) and Ink B (catalyst). Drop-on-drop IJP was demonstrated with the smallest average drop diameters reported for silicone IJP to date (33-36 μm), which was achieved using PFOTS-treated glass slides. Contact pinning was limited so that surface microstructuring or line-by-line print strategies were required for controlled geometries: the former was most suitable for production of sensing arrays and the latter for thin films with maximum transparency. QD-inks were then formulated using detection limit experiments and the Einstein equation to guide QD loading for composites with visible fluorescence; 0.005 wt% QD loading in Ink A was selected as trade-off between signal strength and polymer matrix curing. Dynamic light scattering (DLS) was used to assess dispersion of colloidal QDs *in situ* with regards to particle size limitations for a set jetting nozzle diameter and for the extent of aggregation and scattering in the cured sensing material. Octyl acetate solvent yielded monomodal data with an average diameter of 118-138 nm, in agreement with clusters observed during transmission electron microscopy.

Curing was the greatest challenge in reactive inkjet of QD-silicone composites, as labile ligands on the QDs poisoned the platinum catalyst. PtCl_2 catalyst was added to enable curing and to explore the interactions between QDs and the catalyst. A low weight percent of a platinum catalyst (0.00125 wt% in Ink B, catalyst ink) was added to enable curing of printed composites with comparable cure rate to control inks without quantum dots. The minimum catalyst loading to enable curing was used to reduce Pt-mediated quenching^{250,291} and yellowing via formation of metallic clusters.^{181,192} A 70% decrease in emission intensity was observed as PtCl_2 loading in Ink B doubled, and high platinum concentration was observed to retard conversion in QD-silicones as DoC decreased by 30% from

≤ 0.0025 wt% Pt-Ink to 0.005 wt% Pt-Ink B. It was suggested that the QDs and catalyst competed for ligands, leading to metal-induced aggregation.

Printing of fluorescent QD-silicone composites was demonstrated with $\leq 35.7 \pm 1.4$ μm mean drop-on-drop (DoD) Feret diameter on a single printhead system to produce arrays or films using a pinned grid strategy. 0.005 wt% QD-Ink A and 0.00125 wt% PtCl_2 -Ink B were deposited to accurately reproduce a complex 2D shape. Inks with no PtCl_2 had stronger fluorescence but did not cure, despite the 60 °C platen temperature, showing greater vulnerability to delays or fluctuations in temperature. Both formulations were analysed for temperature sensing performance.

Novel ultraviolet (UV) curable silicone inks were formulated for inkjet to produce 1-part inks with rapid crosslinking. The printability of formulations was confirmed using a high-throughput screening method.¹⁷⁸ Two photoinitiators (PIs) were trialled: DMPA (2,2-dimethoxy-2-phenylacetophenone) and TPO (phenylbis(2,4,6-trimethylbenzoyl)-phosphine oxide). Jetting with 34 - 42 μm average drop diameter was achieved on silanised glass slides, while printing of films was demonstrated on glass slides coated in a release agent for 1 wt% TPO silicone inks, exceeding reported resolutions for UV cure silicones.⁶³ Continuous films with smooth surface finish were obtained at 10 μm droplet spacing. However, while it was shown that silicone-containing inks can be jetted and cure under nitrogen, DMPA was associated with rapid loss of fluorescence in QD-silicones. In contrast, quenching was not observed with TPO, a common photoinitiator in silicone AM. Detachment of passivating ligands followed by photo-oxidation was suggested as a possible mechanism of PI-associated QD quenching: TPO photobleaches to reduce radical concentration and TPO radicals are more susceptible to recombination with oxygen radicals than DMPA-derived radicals, which might result in better shielding of the QD surface.

The temperature sensing performance of novel QD-silicone composites was assessed, confirming the first inkjet printable optical sensing materials. Aggregation was investigated as it is well-known to lead to reduced transparency and thermal stability in QD-polymer composites, and was observed as a slight shoulder in the photoluminescence spectrum at around 655 nm post-cure, 100 nm diameter clusters in TEM, and micron-scale aggregates in optical microscopy. A high throughput method for emission intensity measurement was demonstrated using well-plate reading at 30 - 45 °C to compare formulations. Emission intensity decreased in the order of toluene ink-based, UV cure, and octyl acetate ink-based composites. Octyl acetate ink-based composites with ≤ 0.00125 wt% added catalyst

appeared most suitable in terms of signal strength and repeatability. Addition cure composites were imaged via confocal laser scanning microscopy as a function of temperature to assess for intensity and spectral shift based optical thermometry. Emission intensity was observed to decrease following a thermal cycle and to be sensitive to QD cluster patterning, which resulted in less repeatable thermal responses in sensing materials. Spectral shift was estimated from emission histograms and yielded more repeatable thermometry. Intensity decreased between thermal cycles of the same sample, although values at 60 °C were unchanged, while redshift of estimated mean emission wavelengths was not observed; this was theorised to relate to changes in the QD ligand shell, such as thermally-induced detachment of primary amine ligands.

Overall, composites with temperature-responsive emission were demonstrated for inkjet for the first time with greater spatial resolution than existing IJP thermal sensors. The first inkjet printable QD-silicone was demonstrated with $\leq 36 \mu\text{m}$ mean drop-on-drop (DoD) Feret diameter on a silanised glass substrate to print arrays and films using a pinned grid strategy. The printed formulation was shown to have temperature coefficients of -0.6 to $-0.7 \text{ \% } ^\circ\text{C}^{-1}$ and $0.07 \text{ nm } ^\circ\text{C}^{-1}$ for intensity- and spectral-based sensing in the physiological range, respectively. In all three jettable formulations for addition cure QD-silicone inks, the thermal coefficients were within the range of values reported for CdSe/ZnS QDs^{161,164,168,288} and higher than typical resistance-based inkjet-printed temperature sensors (0.1 - $0.3 \text{ \% } ^\circ\text{C}^{-1}$)^{14,15}. Further development of fluorescent sensing inks can better meet needs for non-invasive, *in situ* thermal sensing for accurate calibration and analysis during device operation, enabling economical production of devices with integrated sensing geometries that are challenging or impossible to achieve by conventional means.

Chapter 9. Further work

In this chapter, recommendations for further work are given to achieve formulations with improved curing, mechanical properties, and photostability). Commentary on further analysis and characterisation is presented with suggested techniques and workflows. Finally, potential applications of novel inkjet-printable silicone and QD-silicone composites are summarised.

9.1. Ink shelf life

Further work is needed to assess the shelf life of ink formulations as stored in vials and in loaded cartridges. Formulations may become non-homogeneous during storage, and agitation may be required to ensure that inks remain well-mixed for even, efficient curing. Solvent-based inks, i.e. the SiliGlass inks, are prone to changes in printability due to solvent evaporation leading to increased viscosity. Ink shelf life is also limited by the chemical stability of constituents, which can lead to changes in rheology, changes in curing, and/or changes in the properties of cured polymers.

The shelf life of addition cure silicone inks can be affected by fillers, moisture, and trace impurities; as reinforcing fillers such as fumed silica were not present in SiliGlass, phenomena such as crepe hardening (a reversible increase in viscosity during storage) are not expected in the inks.²⁹³ In Ink A (crosslinker ink), hydrolysis of the crosslinker with water may occur, and trace impurities that are acidic or basic can catalyse hydrolysis; crosslinks may form by condensation reactions between Si-OH and Si-H, altering the rheology of the inks, degree of vinyl conversion, and the physical properties of the cured polymer.^{17,181} In Ink B (catalyst ink), trace impurities, such as sulphur dioxide, can poison the platinum catalyst. The platinum catalyst itself can also degrade into clusters, particularly if exposed to sunlight, causing material discoloration and inhibiting cure.^{181,192}

UV cure formulations must be stored under dark conditions and may be limited by the stability of the photoinitiator and the monomers. Degradation of the photoinitiators can occur; when stored in the dark at >30 °C, typical commercial photoinitiators have a shelf life of 1-2 years, and similar stability in commercial photoresins. Aging of photopolymer resins may be associated with discoloration, reduced conversion and cure rate, and changes in photopolymer properties. Acrylate monomers are reactive and can spontaneously polymerise at temperatures <100 °C without photoinitiators, leading to

gellation;²⁹⁴ pure monomeric acrylates have a shelf life of a few weeks at 10 °C.²⁵⁵ Acrylate monomers are therefore supplied with a stabiliser and are stored <20 °C under air, and thoroughly de-gassed immediately before use.²⁵⁵ Residual ink inside a print cartridge reservoir may be difficult to fully de-gas if exposed to air, leading to cure inhibition in subsequent printing; if the cartridge reservoir is kept under nitrogen between uses to prevent dissolved oxygen, the stability of the acrylate is reduced and aging is accelerated. Experiments to find the acceptable cartridge reuse conditions and timeframes could minimise material waste while ensuring that rheology, curing, and material properties remain consistent for inkjet printing and optical sensing performance. The shelf life of one-part UV cure inks using thiol-ene mechanisms is limited as the reaction proceeds at room temperature even under dark conditions and is not oxygen-inhibited;⁵⁶ volatile thiols in general may be associated with changes in printability and changes in material properties due to changes in comonomer ratio.

The stability of QD dispersions is of concern for QD-silicone inks. Quantum dots may form larger aggregates and settle out of solution if inks are not sufficiently sonicated prior to use. Changes in the QD ligand shell, via ligand exchange, aggregation, or reaction of amine ligands with other species in the ink, will reduce the passivation of the QD surface and reduce the quantum yield. The fluorescence of QDs is sensitive to environmental factors, which can alter the emission intensity and wavelength- thiols quenching. Aggregation is associated with redshift due to photon reabsorption and/or Förster resonance energy transfer (FRET) from smaller QDs to larger QDs^{239,240,249} and accelerates thermal aging of QDs, which is associated with particle coarsening via mechanisms such as thermal annealing.¹²² Overall, aging of the QD-silicone ink will lead to changes in the fluorescence of the printed composites, and therefore changes in their uniformity and/or efficacy as sensing materials.

9.2. Material development

Future formulations could explore a wider range of solvents to enhance film formation and QD stability. While octyl acetate was shown to suppress coffee ring formation and had good biocompatibility, toluene was found to lead to faster crosslinking. Solvents or diluents with low oxygen solubility could be used in UV cure inks to potentially reduce oxygen inhibition. Two-solvent systems could also be trialled to aid mixing in drop-on-drop inkjet printing, where reaction rate is limited by diffusion.^{82,222}

TEM imaging appeared to show a microporous network structure, which may consist of an elastomeric siloxane network with solvent-rich domains, and gyroidal microphases were observed on a larger scale in optical micrographs of printed SiliGlass. It appears that phase separation occurs as the 50 wt% inks cure,^{231–233} leading to microdomains which may cause scattering and reduce the transparency of the sensing materials.²³⁴ Solvents have been used to control polymer porosity arising from such mechanisms.²³³ Microscale variations in composition and refractive index can reduce the optical transparency²³⁴ and lead to inhomogenous material response during optical sensing. Further work to control phase separation to enhance transmittance is of interest for future studies, as is the effect of solvent removal on QD-composite transparency, fluorescence, and photostability.

Minimal heating was used for inkjet printing to minimise thermal aging during curing. However, while inks were optimised for jetting and curing at ≤ 40 °C, the majority of QD-silicone composites in literature are LED films which are produced via thermal curing at over 100 °C and yield strong fluorescence. Future work could investigate thermal treatment as octyl acetate is non-flammable. Nozzle heating and higher substrate temperatures aids cure rate and crosslinking, while post-processing would help to eliminate residual solvent and radicals and ensure high conversion. Nozzle heating would also enable jetting of precursors with longer chain length, enabling greater elasticity.^{6,57}

Rapid crosslinking is important for shape retention, resolution, and throughput in printing. Selection and loading of curing agents could be further optimised to obtain ideal cure rate, crosslinking density, and optical properties. For addition cure inks, platinum catalysts could be selected to optimise optical transparency and selectivity (which minimises poisoning). For UV cure inks, a wider range of photoinitiators could be tested using high throughput methods; blends of photoinitiators are commonly used to enable good surface and depth cure, and these could be investigated similarly.²⁶² TPO photoinitiator, a.k.a. Omnirad 819, was found to strongly absorb the UV LED wavelength during inkjet and was not observed to

quench QDs: further investigation of TPO for inkjet printing of QD-silicone composites is recommended. In-depth studies of formulations with UV-DSC are recommended for optimal UV ink curing in future studies: degree of conversion (DoC) can be obtained by integrating the area under peaks and comparing this to literature values of reaction energies. The PI loading can be optimised for desired DoC and/or mechanical properties at a given temperature and lamp power, wavelength, and exposure time. An investigation of the impact of QD loading on would also be of interest for formulation of inks for QD-based sensing materials, as QDs have been noted to slow photopolymerisation in acrylates.²⁸²

Alternative UV cure mechanisms could eliminate the need for inert printing environments associated with acrylate-based photopolymerisation.⁵⁶ Thiol-ene reactions were only briefly investigated but are promising candidates for UV curable inks with reduced oxygen sensitivity. Despite demand for oxygen insensitive curing for AM, thiol-ene silicone inks are not known for conventional inkjet printing (IJP) but have been described for extrusion^{295,296} and vat photopolymerisation.^{270,297-300} Furthermore, the UV cure inks were limited to free radical photopolymerisation mechanisms; stereolithography of silicones in air via cationic photopolymerisation has been demonstrated using coumarin sensitisers³⁰¹ which may also be promising for future UV cure formulations. Mixed condensation/UV cure systems are increasingly used to enable fast shape retention (UV) with desired final mechanical properties (condensation).^{69,302-304} Orthogonal thiol-ene and condensation crosslinking was used to produce silicone double networks by vat photopolymerisation.³⁰⁰

The mechanical properties of the inkjet-printed silicones were limited as non-viscous precursors were required for inkjet compatibility.⁵⁷ Typical hard silicone elastomers require $\geq 20 \text{ kg mol}^{-1}$ precursors and soft elastomers $\geq 50 \text{ kg mol}^{-1}$ precursors.⁵⁷ However, longer chain length leads to higher viscosity, which is a challenge for ink formulation of soft elastomers and elastomers with greater elongation at break.^{6,17} Increased flexibility can be beneficial to sensing materials in that higher coefficients of thermal expansion (CTE) can prevent cracking due to thermal stress⁴⁶ and enhance the temperature sensitivity of thermal sensors.¹⁴ Nozzle heating,⁶⁰ silicone oil diluents,^{63,68} and solvents^{60-62,64} are commonly used to reduce viscosity and can be further explored. Low molecular weight, reactive precursors - rather than inert silicone oil - can also reduce overall viscosity,³⁰² though care must be taken to avoid phase separation. Furthermore, chain extenders can be used to obtain longer chain lengths *in situ* to enhance elasticity of printed polymers: Sirrine *et al.* achieved simultaneous chain extension and crosslinking of silicones for stereolithography.²⁹⁸ Heterobifunctional vinyl-hydride silicones leading to exceptional

elongation were described by Goff *et al.*³⁰⁵ and commercialised by Gelest. Gelest ExSil 50 has 500-700 mPa s viscosity – five times lower than Sylgard 184, which has been printed using inkjet^{61,62,64} – yet has 6000% elongation once cured, three times higher than the highest achieved in silicone AM.²⁹⁶ This has potential for inkjet formulations, although there are no reports of silicone AM with heterobifunctional precursors yet.

Silicone-acrylate copolymers were investigated, and 2-ethylhexyl acrylate appeared to aid QD dispersion in UV curable silicone inks. The printed silicone acrylate is expected to have considerable acrylate character, which may not significantly differentiate it from other existing acrylate inks. However, the extent to which silicone-like properties are present in printed co-polymers can be controlled by varying the chain length and ratios of precursors. This could be used to enable a range of inks for tunable physical properties; for example, greater oxygen-permeability for co-polymers with greater silicone character, for biological applications and/or exchange membranes. Crosslinking agents could similarly be used to vary crosslinking density.

The main challenge for future formulations is to improve QD dispersion and photostability, as well as reduce the platinum catalyst loading to minimise yellowing and quenching. The following methods prevent are likely to be of greatest use for silicone IJP. Tao *et al.* used bimodal silicone grafting to enhance polymer dispersion in silicone matrices, which prevented thermal annealing associated with QD aggregation.¹²² Silica encapsulation is a relatively well-established route to enhance photostability of QDs and compatibility with silicones. QD-silica microspheres can meet requirements for inkjet where particle diameter and suitable surface treatment are employed: hydrophilic silica is a reinforcing filler for silicones which leads to high viscosity even at low loadings.¹⁷ One particularly effective strategy is to use QDs with passivating ligands which have reactive functional groups that crosslink with the matrix, leading to good dispersion and stability of QDs anchored to the polymer.^{275,306,307} Kong *et al.* described a facile example by using oleic acid-capped QDs which reacted via hydrosilylation to produce addition cure silicone composites without the need for ligand exchange.¹³⁸ This is a simple, accessible route which is expected to transition easily to inkjet and is recommended for future formulation of QD-silicones with improved photostability.

9.3. Characterisation and applications

High throughput material development using well-plates was shown to have potential for screening of temperature sensing inks. Rapid screening of ink rheology for inkjet was carried out for UV curable formulations to assess jettability,¹⁷⁸ and well-plate reading was used to assess photoluminescence (PL) of composites for emission-based temperature sensing. Further work could make use of multi-model well plate readers which can image QD clusters in the polymer matrix, collect spectroscopic and other characterisation data, and carry out temperature sensing experiments with collection of PL spectra, in a single streamlined workflow.

Infrared and Raman spectroscopy were demonstrated to be feasible for cure investigation, but lack of *in situ* heating made time resolved measurements labour-intensive and a full study was not carried out for infrared spectroscopy with sampling intervals. This method was shown to be possible and could be carried out in future work. Additionally, oscillatory rheometry is suggested for *in situ* heating and time-resolved collection of mechanical data: this yields information on mechanical properties, shape retention, and curing, which is of great value for printing processes, but does require a much higher sample volume than infrared spectroscopy.

Platinum-mediated quenching of QDs was proposed but work to identify the mechanism was outside the scope of this thesis. Analytical techniques towards this could include X-ray photoelectron spectroscopy (XPS) or wavelength dispersive spectroscopy (WDS) of composites to determine whether changes in QD elemental composition took place. Further PL spectroscopy of composites could also identify emission peak shift and broadening that could elucidate the quenching mechanism. A wide range of techniques may be required to fully interrogate material behaviour.

Lastly, more thorough PL characterisation is required to confirm reliable performance of temperature sensing materials. Work to obtain quantum yields and to assess photostability of composites is required to assess changes in emission and emission efficiency over time. Repeated sensing experiments with thermal cycling are needed for calibration and to confirm that measurements are reliable, and more complete analysis of PL is beneficial to enable peak shift- and lifetime-based thermometry.^{1,2} Investigation of higher temperature ranges is of further interest to expand the sensing range, inspired by work by Zhao *et al.*,¹⁶⁰ as thermal quenching of QD-polymer composites is likely to be reversible <100 °C. This may enable a wider sensing range, or historical/exposure data where quenching is irreversible.

Production and testing of demonstrative devices are desirable to showcase the functional composite inks developed in this thesis to address the shortcomings of IJP resistance-based thermal sensors, which have limited spatial resolution and do not achieve the sub-degree thermal resolution in the physiological range required for use in microdevices and in cell culture and biomedical applications. Printable devices with embedded sensing is beneficial for microfluidics and labs-on-chips, as integrated sensors eliminate the need for manual sample collection, which is time-consuming, requires large working volumes, and can disturb the system.³ Choudhury *et al.* and Haro-González *et al.* have used QDs for *in situ* measurement of microchannels, but it has not yet been demonstrated via AM.^{172,173} Monaghan *et al.* reported the first AM lab-on-chip with embedded optical fibres for UV vis spectroscopy inside channels;³⁰⁸ inkjet printing of optical sensing composites and silicone waveguides can be used to enable printing of modular microfluidic devices with embedded sensors.³⁰⁹ These materials also have use as *in situ* temperature calibration in other sensing devices, for temperature monitoring in electronic devices, and as colour conversion layers for LEDs.¹⁰²

The materials may also have utility for applications unrelated to typical lighting devices. While the QD aggregation observed in the composites was not ideal for optical thermometry or lighting, QD-polymer composites have use in security inks as physically unclonable functions (PUFs).^{18,254} The formation of thin films on untreated glass substrates were facile due to the low surface energy of silicones ($\sim 20.4 \text{ mJ m}^{-2}$).⁵¹ This can enable gas exchange membranes³¹⁰ and planar sensing,^{164,165} materials with enhanced biocompatibility are of use for wearable sensors.³¹¹

Bibliography

- (1) Jaque, D.; Vetrone, F. Luminescence Nanothermometry. *Nanoscale* **2012**, *4* (15), 4301. <https://doi.org/10.1039/c2nr30764b>.
- (2) Dramićanin, M. D. Trends in Luminescence Thermometry. *J. Appl. Phys.* **2020**, *128* (4), 040902. <https://doi.org/10.1063/5.0014825>.
- (3) Madou, M. J. *Fundamentals of Microfabrication and Nanotechnology, Three-Volume Set*, 3rd ed.; CRC Press: Boca Raton, 2018. <https://doi.org/10.1201/9781315274164>.
- (4) Măriuța, D.; Colin, S.; Barrot-Lattes, C.; Le Calvé, S.; Korvink, J. G.; Baldas, L.; Brandner, J. J. Miniaturization of Fluorescence Sensing in Optofluidic Devices. *Microfluid. Nanofluidics* **2020**, *24* (9), 65. <https://doi.org/10.1007/s10404-020-02371-1>.
- (5) Moya, A.; Ortega-Ribera, M.; Guimerà, X.; Sowade, E.; Zea, M.; Illa, X.; Ramon, E.; Villa, R.; Gracia-Sancho, J.; Gabriel, G. Online Oxygen Monitoring Using Integrated Inkjet-Printed Sensors in a Liver-on-a-Chip System. *Lab Chip* **2018**, *18* (14), 2023–2035. <https://doi.org/10.1039/C8LC00456K>.
- (6) Derby, B. Inkjet Printing of Functional and Structural Materials: Fluid Property Requirements, Feature Stability, and Resolution. *Annu. Rev. Mater. Res.* **2010**, *40* (1), 395–414. <https://doi.org/10.1146/annurev-matsci-070909-104502>.
- (7) Gibson, I.; Rosen, D.; Stucker, B. *Additive Manufacturing Technologies*; Springer: New York, NY, 2015. <https://doi.org/10.1007/978-1-4939-2113-3>.
- (8) Nayak, L.; Mohanty, S.; Nayak, S. K.; Ramadoss, A. A Review on Inkjet Printing of Nanoparticle Inks for Flexible Electronics. *J. Mater. Chem. C* **2019**, *7* (29), 8771–8795. <https://doi.org/10.1039/C9TC01630A>.
- (9) Chung, S.; Cho, K.; Lee, T. Recent Progress in Inkjet-Printed Thin-Film Transistors. *Adv. Sci.* **2019**, *6* (6), 1801445. <https://doi.org/10.1002/advs.201801445>.
- (10) Hartwig, M.; Zichner, R.; Joseph, Y. Inkjet-Printed Wireless Chemiresistive Sensors—A Review. *Chemosensors* **2018**, *6* (4), 66. <https://doi.org/10.3390/chemosensors6040066>.

- (11) Waheed, S.; Cabot, J. M.; Macdonald, N. P.; Lewis, T.; Guijt, R. M.; Paull, B.; Breadmore, M. C. 3D Printed Microfluidic Devices: Enablers and Barriers. *Lab Chip* **2016**, *16* (11), 1993–2013. <https://doi.org/10.1039/C6LC00284F>.
- (12) Xu, Y.; Wu, X.; Guo, X.; Kong, B.; Zhang, M.; Qian, X.; Mi, S.; Sun, W. The Boom in 3D-Printed Sensor Technology. *Sensors* **2017**, *17* (5), 1166. <https://doi.org/10.3390/s17051166>.
- (13) Dankoco, M. D.; Tesfay, G. Y.; Benevent, E.; Bendahan, M. Temperature Sensor Realized by Inkjet Printing Process on Flexible Substrate. *Mater. Sci. Eng. B* **2016**, *205*, 1–5. <https://doi.org/10.1016/j.mseb.2015.11.003>.
- (14) Kuzubasoglu, B. A.; Bahadir, S. K. Flexible Temperature Sensors: A Review. *Sensors Actuators A Phys.* **2020**, *315*, 112282. <https://doi.org/10.1016/j.sna.2020.112282>.
- (15) Barmpakos, D.; Kaltsas, G. A Review on Humidity, Temperature and Strain Printed Sensors—Current Trends and Future Perspectives. *Sensors* **2021**, *21* (3), 739. <https://doi.org/10.3390/s21030739>.
- (16) Trudeau, C.; Beaupré, P.; Bolduc, M.; Cloutier, S. G. All Inkjet-Printed Perovskite-Based Bolometers. *npj Flex. Electron.* **2020**, *4* (1), 34. <https://doi.org/10.1038/s41528-020-00097-2>.
- (17) Moretto, H.-H.; Schulze, M.; Wagner, G. Silicones. In *Ullmann's Encyclopedia of Industrial Chemistry*; Wiley-VCH Verlag GmbH & Co. KGaA: Weinheim, Germany, 2000; pp 675–708. https://doi.org/10.1002/14356007.a24_057.
- (18) Elliott, A. M.; Ivanova, O. S.; Williams, C. B.; Campbell, T. A. Inkjet Printing of Quantum Dots in Photopolymer for Use in Additive Manufacturing of Nanocomposites. *Adv. Eng. Mater.* **2013**, *15* (10), 903–907. <https://doi.org/10.1002/adem.201300020>.
- (19) de Mello Donegá, C. Synthesis and Properties of Colloidal Heteronanocrystals. *Chem. Soc. Rev.* **2011**, *40* (3), 1512–1546. <https://doi.org/10.1039/C0CS00055H>.
- (20) Chern, M.; Kays, J. C.; Bhuckory, S.; Dennis, A. M. Sensing with Photoluminescent Semiconductor Quantum Dots. *Methods Appl. Fluoresc.* **2019**, *7* (1), 012005. <https://doi.org/10.1088/2050-6120/aaf6f8>.

- (21) Lee, J.; Sundar, V. C.; Heine, J. R.; Bawendi, M. G.; Jensen, K. F. Full Color Emission from II-VI Semiconductor Quantum Dot-Polymer Composites. *Adv. Mater.* **2000**, *12* (15), 1102–1105. [https://doi.org/10.1002/1521-4095\(200008\)12:15<1102::AID-ADMA1102>3.0.CO;2-J](https://doi.org/10.1002/1521-4095(200008)12:15<1102::AID-ADMA1102>3.0.CO;2-J).
- (22) Böberl, M.; Kovalenko, M. V.; Gamerith, S.; List, E. J. W.; Heiss, W. Inkjet-Printed Nanocrystal Photodetectors Operating up to 3 μm Wavelengths. *Adv. Mater.* **2007**, *19* (21), 3574–3578. <https://doi.org/10.1002/adma.200700111>.
- (23) Shi, L.; Kwon, O.; Miner, A. C.; Majumdar, A. Design and Batch Fabrication of Probes for Sub-100 Nm Scanning Thermal Microscopy. *J. Microelectromechanical Syst.* **2001**, *10* (3), 370–378. <https://doi.org/10.1109/84.946785>.
- (24) Nakabeppu, O.; Chandrachud, M.; Wu, Y.; Lai, J.; Majumdar, A. Scanning Thermal Imaging Microscopy Using Composite Cantilever Probes. *Appl. Phys. Lett.* **1995**, *66* (6), 694–696. <https://doi.org/10.1063/1.114102>.
- (25) Baffou, G.; Bon, P.; Savatier, J.; Polleux, J.; Zhu, M.; Merlin, M.; Rigneault, H.; Monneret, S. Thermal Imaging of Nanostructures by Quantitative Optical Phase Analysis. *ACS Nano* **2012**, *6* (3), 2452–2458. <https://doi.org/10.1021/nn2047586>.
- (26) Christofferson, J.; Shakouri, A. Thermoreflectance Based Thermal Microscope. *Rev. Sci. Instrum.* **2005**, *76* (2), 024903. <https://doi.org/10.1063/1.1850632>.
- (27) Sandell, S.; Chávez-Ángel, E.; El Sachat, A.; He, J.; Sotomayor Torres, C. M.; Maire, J. Thermoreflectance Techniques and Raman Thermometry for Thermal Property Characterization of Nanostructures. *J. Appl. Phys.* **2020**, *128* (13), 131101. <https://doi.org/10.1063/5.0020239>.
- (28) Bagnall, K. R.; Moore, E. A.; Badescu, S. C.; Zhang, L.; Wang, E. N. Simultaneous Measurement of Temperature, Stress, and Electric Field in GaN HEMTs with Micro-Raman Spectroscopy. *Rev. Sci. Instrum.* **2017**, *88* (11), 113111. <https://doi.org/10.1063/1.5010225>.
- (29) Kuball, M.; Hayes, J. M.; Uren, M. J.; Martin, I.; Birbeck, J. C. H.; Balmer, R. S.; Hughes, B. T. Measurement of Temperature in Active High-Power AlGaIn/GaN HFETs Using Raman Spectroscopy. *IEEE Electron Device Lett.* **2002**, *23* (1), 7–9. <https://doi.org/10.1109/55.974795>.

- (30) Bagnall, K. R.; Wang, E. N. Transient Thermal Dynamics of GaN HEMTs. In *2016 15th IEEE Intersociety Conference on Thermal and Thermomechanical Phenomena in Electronic Systems (ITherm)*; IEEE, 2016; pp 1551–1557.
<https://doi.org/10.1109/ITHERM.2016.7517733>.
- (31) ASTM International. *Standard Terminology for Additive Manufacturing Technologies – General Principles – Terminology*; 2015. <https://doi.org/10.1520/F2792-12A.2>.
- (32) Liravi, F.; Toyserkani, E. Additive Manufacturing of Silicone Structures: A Review and Prospective. *Addit. Manuf.* **2018**, *24*, 232–242.
<https://doi.org/10.1016/j.addma.2018.10.002>.
- (33) Guo, Y.; Patanwala, H. S.; Bognet, B.; Ma, A. W. K. Inkjet and Inkjet-Based 3D Printing: Connecting Fluid Properties and Printing Performance. *Rapid Prototyp. J.* **2017**, *23* (3), 562–576. <https://doi.org/10.1108/RPJ-05-2016-0076>.
- (34) Derby, B.; Reis, N. Inkjet Printing of Highly Loaded Particulate Suspensions. *MRS Bull.* **2003**, *28* (11), 815–818. <https://doi.org/10.1557/mrs2003.230>.
- (35) Hoath, S. D. *Fundamentals of Inkjet Printing: The Science of Inkjet and Droplets*; John Wiley & Sons, 2016. <https://doi.org/10.1002/9783527684724>.
- (36) Courbat, J.; Kim, Y. B.; Briand, D.; de Rooij, N. F. Inkjet Printing on Paper for the Realization of Humidity and Temperature Sensors. In *2011 16th International Solid-State Sensors, Actuators and Microsystems Conference*; IEEE, 2011; pp 1356–1359.
<https://doi.org/10.1109/TRANSDUCERS.2011.5969506>.
- (37) Mattana, G.; Kinkeldei, T.; Leuenberger, D.; Ataman, C.; Ruan, J. J.; Molina-Lopez, F.; Quintero, A. V.; Nisato, G.; Troster, G.; Briand, D.; et al. Woven Temperature and Humidity Sensors on Flexible Plastic Substrates for E-Textile Applications. *IEEE Sens. J.* **2013**, *13* (10), 3901–3909. <https://doi.org/10.1109/JSEN.2013.2257167>.
- (38) Ali, S.; Hassan, A.; Bae, J.; Lee, C. H.; Kim, J. All-Printed Differential Temperature Sensor for the Compensation of Bending Effects. *Langmuir* **2016**, *32* (44), 11432–11439. <https://doi.org/10.1021/acs.langmuir.6b02885>.
- (39) Lin, S.-C.; Liao, Y.-C. Integrated Humidity and Temperature Sensing Circuit Fabricated by Inkjet Printing Technology. In *2016 11th International Microsystems, Packaging, Assembly and Circuits Technology Conference (IMPACT)*; IEEE, 2016; pp 59–61. <https://doi.org/10.1109/IMPACT.2016.7800045>.

- (40) Vena, A.; Sydanheimo, L.; Ukkonen, L.; Tentzeris, M. M. A Fully Inkjet-Printed Chipless RFID Gas and Temperature Sensor on Paper. In *2014 IEEE RFID Technology and Applications Conference (RFID-TA)*; IEEE, 2014; pp 115–120.
<https://doi.org/10.1109/RFID-TA.2014.6934211>.
- (41) Bali, C.; Brandlmaier, A.; Ganster, A.; Raab, O.; Zapf, J.; Hübner, A. Fully Inkjet-Printed Flexible Temperature Sensors Based on Carbon and PEDOT:PSS1. *Mater. Today Proc.* **2016**, *3* (3), 739–745. <https://doi.org/10.1016/j.matpr.2016.02.005>.
- (42) Vuorinen, T.; Niittynen, J.; Kankkunen, T.; Kraft, T. M.; Mäntysalo, M. Inkjet-Printed Graphene/PEDOT:PSS Temperature Sensors on a Skin-Conformable Polyurethane Substrate. *Sci. Rep.* **2016**, *6* (1), 35289. <https://doi.org/10.1038/srep35289>.
- (43) Tao, X.; Jia, H.; He, Y.; Liao, S.; Wang, Y. Ultrafast Paper Thermometers Based on a Green Sensing Ink. *ACS Sensors* **2017**, *2* (3), 449–454.
<https://doi.org/10.1021/acssensors.7b00060>.
- (44) Wang, C.-T.; Huang, K.-Y.; Lin, D. T. W.; Liao, W.-C.; Lin, H.-W.; Hu, Y.-C. A Flexible Proximity Sensor Fully Fabricated by Inkjet Printing. *Sensors* **2010**, *10* (5), 5054–5062. <https://doi.org/10.3390/s100505054>.
- (45) Yang, S.; Kwak, S.-Y.; Jin, J.; Kim, J.-S.; Choi, Y.; Paik, K.-W.; Bae, B.-S. Thermally Resistant UV-Curable Epoxy–Siloxane Hybrid Materials for Light Emitting Diode (LED) Encapsulation. *J. Mater. Chem.* **2012**, *22* (18), 8874.
<https://doi.org/10.1039/c2jm16355a>.
- (46) Yazdan Mehr, M.; Bahrami, A.; van Driel, W. D.; Fan, X. J.; Davis, J. L.; Zhang, G. Q. Degradation of Optical Materials in Solid-State Lighting Systems. *Int. Mater. Rev.* **2020**, *65* (2), 102–128. <https://doi.org/10.1080/09506608.2019.1565716>.
- (47) Madkour, T. M. Polycarbonate. In *Polymer Data Handbook*; Mark, J. E., Ed.; Oxford University Press, 1999; pp 363–367.
- (48) Hsu, S. L. Poly(Methyl Methacrylate). In *Polymer Data Handbook*; Mark, J. E., Ed.; Oxford University Press, 1999; pp 655–657.
- (49) Su, W.-F.; Fu, Y.-C.; Pan, W.-P. Thermal Properties of High Refractive Index Epoxy Resin System. *Thermochim. Acta* **2002**, *392–393*, 385–389.
[https://doi.org/10.1016/S0040-6031\(02\)00124-7](https://doi.org/10.1016/S0040-6031(02)00124-7).

- (50) Johnston, I. D.; McCluskey, D. K.; Tan, C. K. L.; Tracey, M. C. Mechanical Characterization of Bulk Sylgard 184 for Microfluidics and Microengineering. *J. Micromechanics Microengineering* **2014**, *24* (3), 035017. <https://doi.org/10.1088/0960-1317/24/3/035017>.
- (51) Owen, M. J.; Dvornic, P. R. *Silicone Surface Science*; Owen, M. J., Dvornic, P. R., Eds.; Advances in Silicon Science; Springer: Dordrecht, Netherlands, 2012; Vol. 4. <https://doi.org/10.1007/978-94-007-3876-8>.
- (52) de Buyl, F. Silicone Sealants and Structural Adhesives. *Int. J. Adhes. Adhes.* **2001**, *21* (5), 411–422. [https://doi.org/10.1016/S0143-7496\(01\)00018-5](https://doi.org/10.1016/S0143-7496(01)00018-5).
- (53) Kuo, A. C. M. Poly (Dimethylsiloxane). In *Polymer Data Handbook*; Mark, J. E., Ed.; Oxford University Press, 1999; pp 411–435.
- (54) Falkiewicz-Dulik, M.; Janda, K.; Wypych, G. Silicones. In *Handbook of Material Biodegradation, Biodeterioration, and Biostabilization*; ChemTec Publishing, 2015; pp 346–347. <https://doi.org/10.1016/C2014-0-01354-8>.
- (55) Lorenz, G.; Kandelbauer, A. Silicones. In *Handbook of Thermoset Plastics*; Dodiuk, H., Goodman, S. H., Eds.; Elsevier, 2014; pp 555–575. <https://doi.org/10.1016/B978-1-4557-3107-7.00014-2>.
- (56) Wang, D.; Klein, J.; Mejía, E. Catalytic Systems for the Cross-Linking of Organosilicon Polymers. *Chem. - An Asian J.* **2017**, *12* (11), 1180–1197. <https://doi.org/10.1002/asia.201700304>.
- (57) Mazurek, P.; Vudayagiri, S.; Skov, A. L. How to Tailor Flexible Silicone Elastomers with Mechanical Integrity: A Tutorial Review. *Chem. Soc. Rev.* **2019**, *48* (6), 1448–1464. <https://doi.org/10.1039/C8CS00963E>.
- (58) Cramer, N. B.; Bowman, C. N. Kinetics of Thiol-Ene and Thiol-Acrylate Photopolymerizations with Real-Time Fourier Transform Infrared. *J. Polym. Sci. Part A Polym. Chem.* **2001**, *39* (19), 3311–3319. <https://doi.org/10.1002/pola.1314>.
- (59) Dimatix Materials Printer & Cartridge DMP-2800 Series Printer & DMC-11600 Series Cartridge FAQs. Fujifilm 2008.
- (60) Sturgess, C.; Tuck, C. J.; Ashcroft, I. A.; Wildman, R. D. 3D Reactive Inkjet Printing of Polydimethylsiloxane. *J. Mater. Chem. C* **2017**, *5* (37), 9733–9743. <https://doi.org/10.1039/C7TC02412F>.

- (61) Peng, Y.; Xiao, S.; Yang, J.; Lin, J.; Yuan, W.; Gu, W.; Wu, X.; Cui, Z. The Elastic Microstructures of Inkjet Printed Polydimethylsiloxane as the Patterned Dielectric Layer for Pressure Sensors. *Appl. Phys. Lett.* **2017**, *110* (26), 261904. <https://doi.org/10.1063/1.4990528>.
- (62) Mamidanna, A.; Lefky, C.; Hildreth, O. Drop-on-Demand Printed Microfluidics Device with Sensing Electrodes Using Silver and PDMS Reactive Inks. *Microfluid. Nanofluidics* **2017**, *21* (11), 172. <https://doi.org/10.1007/s10404-017-2010-8>.
- (63) McCoul, D.; Rosset, S.; Schlatter, S.; Shea, H. Inkjet 3D Printing of UV and Thermal Cure Silicone Elastomers for Dielectric Elastomer Actuators. *Smart Mater. Struct.* **2017**, *26* (12), 125022. <https://doi.org/10.1088/1361-665X/aa9695>.
- (64) Mikkonen, R.; Puistola, P.; Jönkkäri, I.; Mäntysalo, M. Inkjet Printable Polydimethylsiloxane for All-Inkjet-Printed Multilayered Soft Electrical Applications. *ACS Appl. Mater. Interfaces* **2020**, *12* (10), 11990–11997. <https://doi.org/10.1021/acsami.9b19632>.
- (65) Stieghorst, J.; Majaura, D.; Wevering, H.; Doll, T. Toward 3D Printing of Medical Implants: Reduced Lateral Droplet Spreading of Silicone Rubber under Intense IR Curing. *ACS Appl. Mater. Interfaces* **2016**, *8* (12), 8239–8246. <https://doi.org/10.1021/acsami.5b12728>.
- (66) Ligon, S. C.; Liska, R.; Stampfl, J.; Gurr, M.; Mülhaupt, R. Polymers for 3D Printing and Customized Additive Manufacturing. *Chem. Rev.* **2017**, *117* (15), 10212–10290. <https://doi.org/10.1021/acs.chemrev.7b00074>.
- (67) Herzberger, J.; Serrine, J. M.; Williams, C. B.; Long, T. E. Polymer Design for 3D Printing Elastomers: Recent Advances in Structure, Properties, and Printing. *Prog. Polym. Sci.* **2019**, *97*, 101144. <https://doi.org/10.1016/j.progpolymsci.2019.101144>.
- (68) Foerster, A.; Wildman, R.; Hague, R.; Tuck, C. Reactive Inkjet Printing Approach towards 3d Silicone Elastomeric Structures Fabrication. In *Proceedings of the 28th Annual International Solid Freeform Fabrication Symposium*; Austin, TX, 2017; pp 1795–1805.
- (69) Liravi, F.; Toyserkani, E. A Hybrid Additive Manufacturing Method for the Fabrication of Silicone Bio-Structures: 3D Printing Optimization and Surface Characterization. *Mater. Des.* **2018**, *138*, 46–61. <https://doi.org/10.1016/j.matdes.2017.10.051>.

- (70) Davoodi, E.; Fayazfar, H.; Liravi, F.; Jabari, E.; Toyserkani, E. Drop-on-Demand High-Speed 3D Printing of Flexible Milled Carbon Fiber/Silicone Composite Sensors for Wearable Biomonitoring Devices. *Addit. Manuf.* **2020**, *32*, 101016. <https://doi.org/10.1016/j.addma.2019.101016>.
- (71) Wilkinson, N. J.; Kay, R. W.; Harris, R. A. Electrohydrodynamic and Aerosol Jet Printing for the Copatterning of Polydimethylsiloxane and Graphene Platelet Inks. *Adv. Mater. Technol.* **2020**, *5* (6), 2000148. <https://doi.org/10.1002/admt.202000148>.
- (72) Weiss, F. M.; Töpfer, T.; Osmani, B.; Deyhle, H.; Kovacs, G.; Müller, B. Thin Film Formation and Morphology of Electrosprayed Polydimethylsiloxane. *Langmuir* **2016**, *32* (13), 3276–3283. <https://doi.org/10.1021/acs.langmuir.6b00476>.
- (73) Weiss, F. M.; Töpfer, T.; Osmani, B.; Peters, S.; Kovacs, G.; Müller, B. Electrospraying Nanometer-Thin Elastomer Films for Low-Voltage Dielectric Actuators. *Adv. Electron. Mater.* **2016**, *2* (5), 1500476. <https://doi.org/10.1002/aelm.201500476>.
- (74) Araromi, O. A.; Conn, A. T.; Ling, C. S.; Rossiter, J. M.; Vaidyanathan, R.; Burgess, S. C. Spray Deposited Multilayered Dielectric Elastomer Actuators. *Sensors Actuators A Phys.* **2011**, *167* (2), 459–467. <https://doi.org/10.1016/j.sna.2011.03.004>.
- (75) Reitelshöfer, S.; Landgraf, M.; Graf, D.; Bugert, L.; Franke, J. A New Production Process for Soft Actuators and Sensors Based on Dielectric Elastomers Intended for Safe Human Robot Interaction. In *2015 IEEE/SICE International Symposium on System Integration (SII)*; IEEE, 2015; pp 51–56. <https://doi.org/10.1109/SII.2015.7404953>.
- (76) Reitelshöfer, S.; Göttler, M.; Schmidt, P.; Treffer, P.; Landgraf, M.; Franke, J. Aerosol-Jet-Printing Silicone Layers and Electrodes for Stacked Dielectric Elastomer Actuators in One Processing Device. In *Proceedings Volume 9798, Electroactive Polymer Actuators and Devices (EAPAD)*; Bar-Cohen, Y., Vidal, F., Eds.; Las Vega, NV, 2016; p 97981Y. <https://doi.org/10.1117/12.2219226>.
- (77) Zhan, Z.; An, J.; Wei, Y.; Tran, V. T.; Du, H. Inkjet-Printed Optoelectronics. *Nanoscale* **2017**, *9* (3), 965–993. <https://doi.org/10.1039/C6NR08220C>.

- (78) Larmagnac, A.; Eggenberger, S.; Janossy, H.; Vörös, J. Stretchable Electronics Based on Ag-PDMS Composites. *Sci. Rep.* **2014**, *4*, 7254. <https://doi.org/10.1038/srep07254>.
- (79) Guo, S.-Z.; Qiu, K.; Meng, F.; Park, S. H.; McAlpine, M. C. 3D Printed Stretchable Tactile Sensors. *Adv. Mater.* **2017**, *29* (27), 1701218. <https://doi.org/10.1002/adma.201701218>.
- (80) Seerden, K. A. M.; Reis, N.; Evans, J. R. G.; Grant, P. S.; Halloran, J. W.; Derby, B. Ink-Jet Printing of Wax-Based Alumina Suspensions. *J. Am. Ceram. Soc.* **2001**, *84* (11), 2514–2520. <https://doi.org/10.1111/j.1151-2916.2001.tb01045.x>.
- (81) Tekin, E.; de Gans, B.-J.; Schubert, U. S. Ink-Jet Printing of Polymers - from Single Dots to Thin Film Libraries. *J. Mater. Chem.* **2004**, *14* (17), 2627. <https://doi.org/10.1039/b407478e>.
- (82) Hu, H.; Larson, R. G. Marangoni Effect Reverses Coffee-Ring Depositions. *J. Phys. Chem. B* **2006**, *110* (14), 7090–7094. <https://doi.org/10.1021/jp0609232>.
- (83) Park, J.; Moon, J. Control of Colloidal Particle Deposit Patterns within Picoliter Droplets Ejected by Ink-Jet Printing. *Langmuir* **2006**, *22* (8), 3506–3513. <https://doi.org/10.1021/la053450j>.
- (84) Oh, Y.; Kim, J.; Yoon, Y. J.; Kim, H.; Yoon, H. G.; Lee, S.-N.; Kim, J. Inkjet Printing of Al₂O₃ Dots, Lines, and Films: From Uniform Dots to Uniform Films. *Curr. Appl. Phys.* **2011**, *11* (3), S359–S363. <https://doi.org/10.1016/j.cap.2010.11.065>.
- (85) Paul, D. R.; Mark, J. E. Fillers for Polysiloxane (“Silicone”) Elastomers. *Prog. Polym. Sci.* **2010**, *35* (7), 893–901. <https://doi.org/10.1016/j.progpolymsci.2010.03.004>.
- (86) Attia, M. S.; Elsaadany, S. A.; Ahmed, K. A.; El-Molla, M. M.; Abdel-Mottaleb, M. S. A. Inkjet Printable Luminescent Eu³⁺-TiO₂ Doped in Sol Gel Matrix for Paper Tagging. *J. Fluoresc.* **2015**, *25* (1), 119–125. <https://doi.org/10.1007/s10895-014-1488-7>.
- (87) Pastoriza-Santos, I.; Pérez-Juste, J.; KICKELBICK, G.; Liz-Marzán, L. M. Optically Active Poly(Dimethylsiloxane) Elastomer Films Through Doping with Gold Nanoparticles. *J. Nanosci. Nanotechnol.* **2006**, *6* (2), 453–458. <https://doi.org/10.1166/jnn.2006.922>.

- (88) Shim, G. H.; Han, M. G.; Sharp-Norton, J. C.; Creager, S. E.; Foulger, S. H. Inkjet-Printed Electrochromic Devices Utilizing Polyaniline–Silica and Poly(3,4-Ethylenedioxythiophene)–Silica Colloidal Composite Particles. *J. Mater. Chem.* **2008**, *18* (5), 594. <https://doi.org/10.1039/b712766a>.
- (89) Lim, S.; Kang, B.; Kwak, D.; Lee, W. H.; Lim, J. A.; Cho, K. Inkjet-Printed Reduced Graphene Oxide/Poly(Vinyl Alcohol) Composite Electrodes for Flexible Transparent Organic Field-Effect Transistors. *J. Phys. Chem. C* **2012**, *116* (13), 7520–7525. <https://doi.org/10.1021/jp203441e>.
- (90) Kovalchuk, A.; Huang, K.; Xiang, C.; Martí, A. A.; Tour, J. M. Luminescent Polymer Composite Films Containing Coal-Derived Graphene Quantum Dots. *ACS Appl. Mater. Interfaces* **2015**, *7* (47), 26063–26068. <https://doi.org/10.1021/acsami.5b06057>.
- (91) Angelo, P. D.; Farnood, R. R. Deposition of PEDOT/SWCNT Composites by Inkjet Printing. *MRS Proc.* **2010**, *1260*, 1260-T07-02. <https://doi.org/10.1557/PROC-1260-T07-02>.
- (92) Porter, D. A.; Cohen, A. L.; Krueger, P. S.; Son, D. Y. Additive Manufacturing with Ultraviolet Curable Silicones Containing Carbon Black. *3D Print. Addit. Manuf.* **2018**, *5* (1), 73–86. <https://doi.org/10.1089/3dp.2017.0019>.
- (93) Porter, D. A.; Davis, N.; Krueger, P. S.; Cohen, A. L.; Son, D. Additive Manufacturing by Material Extrusion with Medical Grade Silicone Elastomers and IR Laser Curing. *Rapid Prototyp. J.* **2020**, *26* (1), 145–155. <https://doi.org/10.1108/RPJ-10-2018-0279>.
- (94) Tegtmeier, K.; Aliuos, P.; Stieghorst, J.; Schickedanz, M.; Golly, F.; Zernetsch, H.; Glasmacher, B.; Doll, T. Aligned Carbon Nanotube-Liquid Silicone Rubber Conductors and Electrode Surfaces for Stimulating Medical Implants. *Phys. status solidi* **2014**, *211* (6), 1439–1447. <https://doi.org/10.1002/pssa.201330405>.
- (95) Wei, H.; Li, K.; Liu, W. G.; Meng, H.; Zhang, P. X.; Yan, C. Y. 3D Printing of Free-Standing Stretchable Electrodes with Tunable Structure and Stretchability. *Adv. Eng. Mater.* **2017**, *19* (11), 1700341. <https://doi.org/10.1002/adem.201700341>.

- (96) Periard, D.; Malone, E.; Lipson, H. Printing Embedded Circuits. In *Proceedings of the 18th Annual International Solid Freeform Fabrication Symposium*; Austin, TX, 2007; pp 503–512.
- (97) Mannoor, M. S.; Jiang, Z.; James, T.; Kong, Y. L.; Malatesta, K. A.; Soboyejo, W. O.; Verma, N.; Gracias, D. H.; McAlpine, M. C. 3D Printed Bionic Ears. *Nano Lett.* **2013**, *13* (6), 2634–2639. <https://doi.org/10.1021/nl4007744>.
- (98) Sangermano, M.; Chiolerio, A.; Marti, G.; Martino, P. UV-Cured Acrylic Conductive Inks for Microelectronic Devices. *Macromol. Mater. Eng.* **2013**, *298* (6), 607–611. <https://doi.org/10.1002/mame.201200072>.
- (99) Ross, D.; Gaitan, M.; Locascio, L. E. Temperature Measurement in Microfluidic Systems Using a Temperature-Dependent Fluorescent Dye. *Anal. Chem.* **2001**, *73* (17), 4117–4123. <https://doi.org/10.1021/ac010370l>.
- (100) Samy, R.; Glawdel, T.; Ren, C. L. Method for Microfluidic Whole-Chip Temperature Measurement Using Thin-Film Poly(Dimethylsiloxane)/Rhodamine B. *Anal. Chem.* **2008**, *80* (2), 369–375. <https://doi.org/10.1021/ac071268c>.
- (101) Demchenko, A. P. Photobleaching of Organic Fluorophores: Quantitative Characterization, Mechanisms, Protection. *Methods Appl. Fluoresc.* **2020**, *8* (2), 022001. <https://doi.org/10.1088/2050-6120/ab7365>.
- (102) Moon, H.; Lee, C.; Lee, W.; Kim, J.; Chae, H. Stability of Quantum Dots, Quantum Dot Films, and Quantum Dot Light-Emitting Diodes for Display Applications. *Adv. Mater.* **2019**, *31* (34), 1804294. <https://doi.org/10.1002/adma.201804294>.
- (103) Hardin, J. O.; Ober, T. J.; Valentine, A. D.; Lewis, J. A. Microfluidic Printheads for Multimaterial 3D Printing of Viscoelastic Inks. *Adv. Mater.* **2015**, *27* (21), 3279–3284. <https://doi.org/10.1002/adma.201500222>.
- (104) Vetrone, F.; Naccache, R.; Zamarrón, A.; Juarranz de la Fuente, A.; Sanz-Rodríguez, F.; Martínez Maestro, L.; Martín Rodríguez, E.; Jaque, D.; García Solé, J.; Capobianco, J. A. Temperature Sensing Using Fluorescent Nanothermometers. *ACS Nano* **2010**, *4* (6), 3254–3258. <https://doi.org/10.1021/nn100244a>.

- (105) Brites, C. D. S.; Lima, P. P.; Silva, N. J. O.; Millán, A.; Amaral, V. S.; Palacio, F.; Carlos, L. D. A Luminescent Molecular Thermometer for Long-Term Absolute Temperature Measurements at the Nanoscale. *Adv. Mater.* **2010**, *22* (40), 4499–4504. <https://doi.org/10.1002/adma.201001780>.
- (106) Allison, S. W.; Gillies, G. T.; Rondinone, A. J.; Cates, M. R. Nanoscale Thermometry via the Fluorescence of YAG:Ce Phosphor Particles: Measurements from 7 to 77 C. *Nanotechnology* **2003**, *14* (8), 859–863. <https://doi.org/10.1088/0957-4484/14/8/304>.
- (107) Hlil, A. R.; Lima, B. C.; Thomas, J.; Boisvert, J.-S.; Iden, H.; Garcia-Puente, Y.; Maia, L. J. Q.; Ledemi, Y.; Messaddeq, Y.; Gomes, A. S. L.; et al. Rare Earth Doped PDMS Elastomeric Random Lasers. *Opt. Mater. (Amst)*. **2019**, *97*, 109387. <https://doi.org/10.1016/j.optmat.2019.109387>.
- (108) Hlil, A. R.; Thomas, J.; Garcia-Puente, Y.; Boisvert, J.-S.; Lima, B. C.; Rakotonandrasana, A.; Maia, L. J. Q.; Tehranchi, A.; Loranger, S.; Gomes, A. S. L.; et al. Structural and Optical Properties of Nd:YAB-Nanoparticle-Doped PDMS Elastomers for Random Lasers. *Sci. Rep.* **2021**, *11* (1), 16803. <https://doi.org/10.1038/s41598-021-95921-8>.
- (109) Kumi Barimah, E.; Rahayu, S.; Ziarko, M. W.; Bamiedakis, N.; White, I. H.; Penty, R. V.; Kale, G. M.; Jose, G. Erbium-Doped Nanoparticle–Polymer Composite Thin Films for Photonic Applications: Structural and Optical Properties. *ACS Omega* **2020**, *5* (16), 9224–9232. <https://doi.org/10.1021/acsomega.0c00040>.
- (110) Lim, S. J.; Ma, L.; Schleife, A.; Smith, A. M. Quantum Dot Surface Engineering: Toward Inert Fluorophores with Compact Size and Bright, Stable Emission. *Coord. Chem. Rev.* **2016**, *320–321*, 216–237. <https://doi.org/10.1016/j.ccr.2016.03.012>.
- (111) Srivastava, A. K.; Zhang, W.; Schneider, J.; Halpert, J. E.; Rogach, A. L. Luminescent Down-Conversion Semiconductor Quantum Dots and Aligned Quantum Rods for Liquid Crystal Displays. *Adv. Sci.* **2019**, *6* (22), 1901345. <https://doi.org/10.1002/advs.201901345>.
- (112) Reiss, P.; Protière, M.; Li, L. Core/Shell Semiconductor Nanocrystals. *Small* **2009**, *5* (2), 154–168. <https://doi.org/10.1002/smll.200800841>.

- (113) Bera, D.; Qian, L.; Tseng, T.; Holloway, P. H. Quantum Dots and Their Multimodal Applications: A Review. *Materials (Basel)*. **2010**, *3* (4), 2260–2345. <https://doi.org/10.3390/ma3042260>.
- (114) Litvin, A. P.; Martynenko, I. V.; Purcell-Milton, F.; Baranov, A. V.; Fedorov, A. V.; Gun'ko, Y. K. Colloidal Quantum Dots for Optoelectronics. *J. Mater. Chem. A* **2017**, *5* (26), 13252–13275. <https://doi.org/10.1039/C7TA02076G>.
- (115) Petryayeva, E.; Algar, W. R.; Medintz, I. L. Quantum Dots in Bioanalysis: A Review of Applications across Various Platforms for Fluorescence Spectroscopy and Imaging. *Appl. Spectrosc.* **2013**, *67* (3), 215–252. <https://doi.org/10.1366/12-06948>.
- (116) Haverinen, H. M.; Myllylä, R. A.; Jabbour, G. E. Inkjet Printing of Light Emitting Quantum Dots. *Appl. Phys. Lett.* **2009**, *94* (7), 073108. <https://doi.org/10.1063/1.3085771>.
- (117) Coe-Sullivan, S.; Steckel, J. S.; Woo, W.-K.; Bawendi, M. G.; Bulović, V. Large-Area Ordered Quantum-Dot Monolayers via Phase Separation During Spin-Casting. *Adv. Funct. Mater.* **2005**, *15* (7), 1117–1124. <https://doi.org/10.1002/adfm.200400468>.
- (118) Jiang, C.; Zhong, Z.; Liu, B.; He, Z.; Zou, J.; Wang, L.; Wang, J.; Peng, J.; Cao, Y. Coffee-Ring-Free Quantum Dot Thin Film Using Inkjet Printing from a Mixed-Solvent System on Modified ZnO Transport Layer for Light-Emitting Devices. *ACS Appl. Mater. Interfaces* **2016**, *8* (39), 26162–26168. <https://doi.org/10.1021/acsami.6b08679>.
- (119) Liu, Y.; Li, F.; Xu, Z.; Zheng, C.; Guo, T.; Xie, X.; Qian, L.; Fu, D.; Yan, X. Efficient All-Solution Processed Quantum Dot Light Emitting Diodes Based on Inkjet Printing Technique. *ACS Appl. Mater. Interfaces* **2017**, *9* (30), 25506–25512. <https://doi.org/10.1021/acsami.7b05381>.
- (120) Yang, P.; Zhang, L.; Kang, D. J.; Strahl, R.; Kraus, T. High-Resolution Inkjet Printing of Quantum Dot Light-Emitting Microdiode Arrays. *Adv. Opt. Mater.* **2020**, *8* (1), 1901429. <https://doi.org/10.1002/adom.201901429>.
- (121) Ho, S.-J.; Hsu, H.-C.; Yeh, C.-W.; Chen, H.-S. Inkjet-Printed Salt-Encapsulated Quantum Dot Film for UV-Based RGB Color-Converted Micro-Light Emitting Diode Displays. *ACS Appl. Mater. Interfaces* **2020**, *12* (29), 33346–33351. <https://doi.org/10.1021/acsami.0c05646>.

- (122) Tao, P.; Li, Y.; Siegel, R. W.; Schadler, L. S. Transparent Luminescent Silicone Nanocomposites Filled with Bimodal PDMS-Brush-Grafted CdSe Quantum Dots. *J. Mater. Chem. C* **2013**, *1* (1), 86–94. <https://doi.org/10.1039/C2TC00057A>.
- (123) Seo, Y.-S.; Justin Raj, C.; Kim, D.-J.; Chul Kim, B.; Yu, K.-H. Effect of CdSe/ZnS Quantum Dots Dispersion in Silicone Based Polymeric Fluids. *Mater. Lett.* **2014**, *130*, 43–47. <https://doi.org/10.1016/j.matlet.2014.05.011>.
- (124) Kim, J. Y.; Ingrosso, C.; Fakhfour, V.; Striccoli, M.; Agostiano, A.; Curri, M. L.; Brugger, J. Inkjet-Printed Multicolor Arrays of Highly Luminescent Nanocrystal-Based Nanocomposites. *Small* **2009**, *5* (9), 1051–1057. <https://doi.org/10.1002/smll.200801315>.
- (125) Schnee, V. P.; Bright, C. J.; Nallon, E. C.; Polcha, M. P. Contact Printing of a Quantum Dot and Polymer Cross-Reactive Array Sensor. *Sensors Actuators B Chem.* **2016**, *236*, 506–511. <https://doi.org/10.1016/j.snb.2016.06.036>.
- (126) Tekin, E.; Smith, P. J.; Hoepfner, S.; van den Berg, A. M. J.; Susa, A. S.; Rogach, A. L.; Feldmann, J.; Schubert, U. S. Inkjet Printing of Luminescent CdTe Nanocrystal-Polymer Composites. *Adv. Funct. Mater.* **2007**, *17* (1), 23–28. <https://doi.org/10.1002/adfm.200600587>.
- (127) Wood, V.; Panzer, M. J.; Chen, J.; Bradley, M. S.; Halpert, J. E.; Bawendi, M. G.; Bulović, V. Inkjet-Printed Quantum Dot-Polymer Composites for Full-Color AC-Driven Displays. *Adv. Mater.* **2009**, *21* (21), 2151–2155. <https://doi.org/10.1002/adma.200803256>.
- (128) Hu, Z.; Yin, Y.; Ali, M. U.; Peng, W.; Zhang, S.; Li, D.; Zou, T.; Li, Y.; Jiao, S.; Chen, S.; et al. Inkjet Printed Uniform Quantum Dots as Color Conversion Layers for Full-Color OLED Displays. *Nanoscale* **2020**, *12* (3), 2103–2110. <https://doi.org/10.1039/C9NR09086J>.
- (129) Bao, B.; Li, M.; Li, Y.; Jiang, J.; Gu, Z.; Zhang, X.; Jiang, L.; Song, Y. Patterning Fluorescent Quantum Dot Nanocomposites by Reactive Inkjet Printing. *Small* **2015**, *11* (14), 1649–1654. <https://doi.org/10.1002/smll.201403005>.

- (130) Yang, Y.; Shi, H.-Q.; Li, W.-N.; Xiao, H.-M.; Luo, Y.-S.; Fu, S.-Y.; Liu, T. Tunable Photo-Luminescent Properties of Novel Transparent CdSe-QD/Silicone Nanocomposites. *Compos. Sci. Technol.* **2011**, *71* (14), 1652–1658.
<https://doi.org/10.1016/j.compscitech.2011.07.015>.
- (131) Kim, T.; Yoon, C.; Song, Y.-G.; Kim, Y.-J.; Lee, K. Thermal Stabilities of Cadmium Selenide and Cadmium-Free Quantum Dots in Quantum Dot–Silicone Nanocomposites. *J. Lumin.* **2016**, *177*, 54–58.
<https://doi.org/10.1016/j.jlumin.2016.04.038>.
- (132) Trung, N. N.; Luu, Q.-P.; Son, B. T.; Sinh, L. H.; Bae, J.-Y. Preparation and Characterization of Silicone Resin Nanocomposite Containing CdSe/ZnS Quantum Dots. *Polym. Compos.* **2012**, *33* (10), 1785–1791. <https://doi.org/10.1002/pc.22320>.
- (133) Hirayama, R.; Naruse, M.; Nakayama, H.; Tate, N.; Shiraki, A.; Kakue, T.; Shimobaba, T.; Ohtsu, M.; Ito, T. Design, Implementation and Characterization of a Quantum-Dot-Based Volumetric Display. *Sci. Rep.* **2015**, *5*, 8472.
<https://doi.org/10.1038/srep08472>.
- (134) Xuan, T.-T.; Liu, J.-Q.; Xie, R.-J.; Li, H.-L.; Sun, Z. Microwave-Assisted Synthesis of CdS/ZnS:Cu Quantum Dots for White Light-Emitting Diodes with High Color Rendition. *Chem. Mater.* **2015**, *27* (4), 1187–1193.
<https://doi.org/10.1021/cm503770w>.
- (135) Kim, H. Y.; Yoon, D.-E.; Jang, J.; Lee, D.; Choi, G.-M.; Chang, J. H.; Lee, J. Y.; Lee, D. C.; Bae, B.-S. Quantum Dot/Siloxane Composite Film Exceptionally Stable against Oxidation under Heat and Moisture. *J. Am. Chem. Soc.* **2016**, *138* (50), 16478–16485. <https://doi.org/10.1021/jacs.6b10681>.
- (136) Li, J.-S.; Tang, Y.; Li, Z.-T.; Rao, L.-S.; Ding, X.-R.; Yu, B.-H. High Efficiency Solid–Liquid Hybrid-State Quantum Dot Light-Emitting Diodes. *Photonics Res.* **2018**, *6* (12), 1107.
<https://doi.org/10.1364/PRJ.6.001107>.
- (137) Chen, H.-S.; Hsu, C.-K.; Hong, H.-Y. InGaN-CdSe-ZnSe Quantum Dots White LEDs. *IEEE Photonics Technol. Lett.* **2006**, *18* (1), 193–195.
<https://doi.org/10.1109/LPT.2005.859540>.

- (138) Kong, L.; Zhang, L.; Meng, Z.; Xu, C.; Lin, N.; Liu, X.-Y. Ultrastable, Highly Luminescent Quantum Dot Composites Based on Advanced Surface Manipulation Strategy for Flexible Lighting-Emitting. *Nanotechnology* **2018**, *29* (31), 315203. <https://doi.org/10.1088/1361-6528/aac39c>.
- (139) Jang, E.; Jun, S.; Jang, H.; Lim, J.; Kim, B.; Kim, Y. White-Light-Emitting Diodes with Quantum Dot Color Converters for Display Backlights. *Adv. Mater.* **2010**, *22* (28), 3076–3080. <https://doi.org/10.1002/adma.201000525>.
- (140) Woo, J. Y.; Kim, K. N.; Jeong, S.; Han, C.-S. Thermal Behavior of a Quantum Dot Nanocomposite as a Color Converting Material and Its Application to White LED. *Nanotechnology* **2010**, *21* (49), 495704. <https://doi.org/10.1088/0957-4484/21/49/495704>.
- (141) Kim, K.; Woo, J. Y.; Jeong, S.; Han, C.-S. Photoenhancement of a Quantum Dot Nanocomposite via UV Annealing and Its Application to White LEDs. *Adv. Mater.* **2011**, *23* (7), 911–914. <https://doi.org/10.1002/adma.201002979>.
- (142) Lai, C.-F.; Tien, Y.-C.; Tong, H.-C.; Zhong, C.-Z.; Lee, Y.-C. High-Performance Quantum Dot Light-Emitting Diodes Using Chip-Scale Package Structures with High Reliability and Wide Color Gamut for Backlight Displays. *RSC Adv.* **2018**, *8* (63), 35966–35972. <https://doi.org/10.1039/C8RA07928E>.
- (143) Osman, H.; Li, W.; Zhang, X.; Chun, F.; Deng, W.; Moatasim, M.; Zheng, X.; Deng, W.; Zhang, H.; Yang, W. One-Step Hot Injection Synthesis of Gradient Alloy $\text{Cd}_x\text{Zn}_{1-x}\text{Se}_y\text{Se}_{1-y}$ Quantum Dots with Large-Span Self-Regulating Ability. *J. Lumin.* **2019**, *206*, 565–570. <https://doi.org/10.1016/j.jlumin.2018.10.089>.
- (144) Chen, Y.; Xing, W.; Liu, Y.; Zhang, X.; Xie, Y.; Shen, C.; Liu, J. G.; Geng, C.; Xu, S. Efficient and Stable CdSe/CdS/ZnS Quantum Rods-in-Matrix Assembly for White LED Application. *Nanomaterials* **2020**, *10* (2), 317. <https://doi.org/10.3390/nano10020317>.
- (145) Yang, Y.; Li, W.-N.; Luo, Y.-S.; Xiao, H.-M.; Fu, S.-Y.; Mai, Y.-W. Novel Ultraviolet-Opaque, Visible-Transparent and Light-Emitting ZnO-QD/Silicone Composites with Tunable Luminescence Colors. *Polymer (Guildf)*. **2010**, *51* (12), 2755–2762. <https://doi.org/10.1016/j.polymer.2010.03.056>.

- (146) Ziegler, J.; Xu, S.; Kucur, E.; Meister, F.; Batentschuk, M.; Gindele, F.; Nann, T. Silica-Coated InP/ZnS Nanocrystals as Converter Material in White LEDs. *Adv. Mater.* **2008**, *20* (21), 4068–4073. <https://doi.org/10.1002/adma.200800724>.
- (147) Kim, K.; Jeong, S.; Woo, J. Y.; Han, C.-S. Successive and Large-Scale Synthesis of InP/ZnS Quantum Dots in a Hybrid Reactor and Their Application to White LEDs. *Nanotechnology* **2012**, *23* (6), 065602. <https://doi.org/10.1088/0957-4484/23/6/065602>.
- (148) Park, J. P.; Kim, T. H.; Kim, S.-W. Highly Stable Cd Free Quantum Dot/Polymer Composites and Their WLED Application. *Dye. Pigment.* **2016**, *127*, 142–147. <https://doi.org/10.1016/j.dyepig.2015.12.029>.
- (149) Song, W.-S.; Yang, H. Fabrication of White Light-Emitting Diodes Based on Solvothermally Synthesized Copper Indium Sulfide Quantum Dots as Color Converters. *Appl. Phys. Lett.* **2012**, *100* (18), 183104. <https://doi.org/10.1063/1.4711019>.
- (150) Jang, E.-P.; Song, W.-S.; Lee, K.-H.; Yang, H. Preparation of a Photo-Degradation-Resistant Quantum Dot–Polymer Composite Plate for Use in the Fabrication of a High-Stability White-Light-Emitting Diode. *Nanotechnology* **2013**, *24* (4), 045607. <https://doi.org/10.1088/0957-4484/24/4/045607>.
- (151) Potyrailo, R. A.; Leach, A. M.; Surman, C. M. Multisize CdSe Nanocrystal/Polymer Nanocomposites for Selective Vapor Detection Identified from High-Throughput Screening Experimentation. *ACS Comb. Sci.* **2012**, *14* (3), 170–178. <https://doi.org/10.1021/co200112s>.
- (152) Zhao, Z.; Arrandale, M.; Vassiltsova, O. V.; Petrukhina, M. A.; Carpenter, M. A. Sensing Mechanism Investigation on Semiconductor Quantum Dot/Polymer Thin Film Based Hydrocarbon Sensor. *Sensors Actuators B Chem.* **2009**, *141* (1), 26–33. <https://doi.org/10.1016/j.snb.2009.06.036>.
- (153) Huang, Q.; Zeng, D.; Li, H.; Xie, C. Room Temperature Formaldehyde Sensors with Enhanced Performance, Fast Response and Recovery Based on Zinc Oxide Quantum Dots/Graphene Nanocomposites. *Nanoscale* **2012**, *4* (18), 5651. <https://doi.org/10.1039/c2nr31131c>.

- (154) Liu, H.; Li, M.; Voznyy, O.; Hu, L.; Fu, Q.; Zhou, D.; Xia, Z.; Sargent, E. H.; Tang, J. Physically Flexible, Rapid-Response Gas Sensor Based on Colloidal Quantum Dot Solids. *Adv. Mater.* **2014**, *26* (17), 2718–2724. <https://doi.org/10.1002/adma.201304366>.
- (155) Jorge, P. A. S.; Mayeh, M.; Benrashid, R.; Caldas, P.; Santos, J. L.; Farahi, F. Quantum Dots as Self-Referenced Optical Fibre Temperature Probes for Luminescent Chemical Sensors. *Meas. Sci. Technol.* **2006**, *17* (5), 1032–1038. <https://doi.org/10.1088/0957-0233/17/5/S16>.
- (156) Walker, G. W.; Sundar, V. C.; Rudzinski, C. M.; Wun, A. W.; Bawendi, M. G.; Nocera, D. G. Quantum-Dot Optical Temperature Probes. *Appl. Phys. Lett.* **2003**, *83* (17), 3555. <https://doi.org/10.1063/1.1620686>.
- (157) Vlaskin, V. A.; Janssen, N.; van Rijssel, J.; Beaulac, R.; Gamelin, D. R. Tunable Dual Emission in Doped Semiconductor Nanocrystals. *Nano Lett.* **2010**, *10* (9), 3670–3674. <https://doi.org/10.1021/nl102135k>.
- (158) Su, F. H.; Fang, Z. L.; Ma, B. S.; Ding, K.; Li, G. H.; Xu, S. J. Temperature and Pressure Behavior of the Emission Bands from Mn-, Cu-, and Eu-Doped ZnS Nanocrystals. *J. Appl. Phys.* **2004**, *95* (7), 3344. <https://doi.org/10.1063/1.1650894>.
- (159) Wang, C.; Wang, Q.; Zhou, Z.; Wu, W.; Chai, Z.; Gao, Y.; Kong, D. Temperature Dependence of Photoluminescence Properties in InP/ZnS Core-Shell Quantum Dots. *J. Lumin.* **2020**, *225*, 117354. <https://doi.org/10.1016/j.jlumin.2020.117354>.
- (160) Zhao, Y.; Riemersma, C.; Pietra, F.; Koole, R.; de Mello Donegá, C.; Meijerink, A. High-Temperature Luminescence Quenching of Colloidal Quantum Dots. *ACS Nano* **2012**, *6* (10), 9058–9067. <https://doi.org/10.1021/nn303217q>.
- (161) Valerini, D.; Cretí, A.; Lomascolo, M.; Manna, L.; Cingolani, R.; Anni, M. Temperature Dependence of the Photoluminescence Properties of Colloidal CdSe/ZnS Core/Shell Quantum Dots Embedded in a Polystyrene Matrix. *Phys. Rev. B* **2005**, *71* (23), 235409. <https://doi.org/10.1103/PhysRevB.71.235409>.
- (162) Munro, T.; Liu, L.; Glorieux, C.; Ban, H. CdSe/ZnS Quantum Dot Fluorescence Spectra Shape-Based Thermometry via Neural Network Reconstruction. *J. Appl. Phys.* **2016**, *119* (21), 214903. <https://doi.org/10.1063/1.4953223>.

- (163) Han, B.; Hanson, W. L.; Bensalah, K.; Tuncel, A.; Stern, J. M.; Cadeddu, J. A. Development of Quantum Dot-Mediated Fluorescence Thermometry for Thermal Therapies. *Ann. Biomed. Eng.* **2009**, *37* (6), 1230–1239. <https://doi.org/10.1007/s10439-009-9681-6>.
- (164) Liu, L.; Zhong, K.; Meng, L.; Van Hemelrijck, D.; Wang, L.; Glorieux, C. Temperature-Sensitive Photoluminescent CdSe-ZnS Polymer Composite Film for Lock-in Photothermal Characterization. *J. Appl. Phys.* **2016**, *119* (22), 224902. <https://doi.org/10.1063/1.4953591>.
- (165) Liu, W.; Zhang, Y.; Wu, H.; Feng, Y.; Zhang, T.; Gao, W.; Chu, H.; Yin, J.; Cui, T.; Wang, Y.; et al. Planar Temperature Sensing Using Heavy-Metal-Free Quantum Dots with Micrometer Resolution. *Nanotechnology* **2014**, *25* (28), 285501. <https://doi.org/10.1088/0957-4484/25/28/285501>.
- (166) Qiu, X.; Zhou, Q.; Zhu, X.; Wu, Z.; Feng, W.; Li, F. Ratiometric Upconversion Nanothermometry with Dual Emission at the Same Wavelength Decoded via a Time-Resolved Technique. *Nat. Commun.* **2020**, *11* (1), 4. <https://doi.org/10.1038/s41467-019-13796-w>.
- (167) Maestro, L. M.; Jacinto, C.; Silva, U. R.; Vetrone, F.; Capobianco, J. A.; Jaque, D.; Solé, J. G. CdTe Quantum Dots as Nanothermometers: Towards Highly Sensitive Thermal Imaging. *Small* **2011**, *7* (13), 1774–1778. <https://doi.org/10.1002/sml.201002377>.
- (168) Li, S.; Zhang, K.; Yang, J.-M.; Lin, L.; Yang, H. Single Quantum Dots as Local Temperature Markers. *Nano Lett.* **2007**, *7* (10), 3102–3105. <https://doi.org/10.1021/nl071606p>.
- (169) Gu, P.; Zhang, Y.; Feng, Y.; Zhang, T.; Chu, H.; Cui, T.; Wang, Y.; Zhao, J.; Yu, W. W. Real-Time and on-Chip Surface Temperature Sensing of GaN LED Chips Using PbSe Quantum Dots. *Nanoscale* **2013**, *5* (21), 10481. <https://doi.org/10.1039/c3nr02438e>.
- (170) Maestro, L. M.; Rodríguez, E. M.; Rodríguez, F. S.; la Cruz, M. C. I.; Juarranz, A.; Naccache, R.; Vetrone, F.; Jaque, D.; Capobianco, J. A.; Solé, J. G. CdSe Quantum Dots for Two-Photon Fluorescence Thermal Imaging. *Nano Lett.* **2010**, *10* (12), 5109–5115. <https://doi.org/10.1021/nl1036098>.

- (171) Maestro, L. M.; Zhang, Q.; Li, X.; Jaque, D.; Gu, M. Quantum-Dot Based Nanothermometry in Optical Plasmonic Recording Media. *Appl. Phys. Lett.* **2014**, *105* (18), 181110. <https://doi.org/10.1063/1.4901258>.
- (172) Choudhury, D.; Jaque, D.; Rodenas, A.; Ramsay, W. T.; Paterson, L.; Kar, A. K. Quantum Dot Enabled Thermal Imaging of Optofluidic Devices. *Lab Chip* **2012**, *12* (13), 2414. <https://doi.org/10.1039/c2lc40181a>.
- (173) Haro-González, P.; Martínez-Maestro, L.; Martín, I. R.; García-Solé, J.; Jaque, D. High-Sensitivity Fluorescence Lifetime Thermal Sensing Based on CdTe Quantum Dots. *Small* **2012**, *8* (17), 2652–2658. <https://doi.org/10.1002/sml.201102736>.
- (174) McLaurin, E. J.; Vlaskin, V. A.; Gamelin, D. R. Water-Soluble Dual-Emitting Nanocrystals for Ratiometric Optical Thermometry. *J. Am. Chem. Soc.* **2011**, *133* (38), 14978–14980. <https://doi.org/10.1021/ja206956t>.
- (175) Dimatix Materials Printer Jettable Fluid Formulation Guidelines. Fujifilm 2013.
- (176) Dimatix Materials Printer DMP-2800 Series User Manual. Fujifilm 2010.
- (177) Stringer, J.; Derby, B. Limits to Feature Size and Resolution in Ink Jet Printing. *J. Eur. Ceram. Soc.* **2009**, *29* (5), 913–918. <https://doi.org/10.1016/j.jeurceramsoc.2008.07.016>.
- (178) Zhou, Z.; Ruiz Cantu, L.; Chen, X.; Alexander, M. R.; Roberts, C. J.; Hague, R.; Tuck, C.; Irvine, D.; Wildman, R. High-Throughput Characterization of Fluid Properties to Predict Droplet Ejection for Three-Dimensional Inkjet Printing Formulations. *Addit. Manuf.* **2019**, *29*, 100792. <https://doi.org/10.1016/j.addma.2019.100792>.
- (179) Sturgess, C. Fully Reactive 3D Inkjet Printing of Polydimethylsiloxane and Polyurethane, Nottingham, 2018.
- (180) Rosato, D. V.; Rosato, D. V.; Rosato, M. V. Plastic Property. In *Plastic Product Material and Process Selection Handbook*; Elsevier, 2004; pp 40–129.
- (181) Brounstein, Z.; Zhao, J.; Geller, D.; Gupta, N.; Labouriau, A. Long-Term Thermal Aging of Modified Sylgard 184 Formulations. *Polymers (Basel)*. **2021**, *13* (18), 3125. <https://doi.org/10.3390/polym13183125>.

- (182) Ghosh, D.; Khastgir, D. Degradation and Stability of Polymeric High-Voltage Insulators and Prediction of Their Service Life through Environmental and Accelerated Aging Processes. *ACS Omega* **2018**, *3* (9), 11317–11330. <https://doi.org/10.1021/acsomega.8b01560>.
- (183) Winter, M. R.; Aeby, I.; Foresi, J. Performance and Reliability of Silicone Polymers in 1000X Concentration CPV Applications. *AIP Conf. Proc.* **2012**, *1477*, 285–288. <https://doi.org/10.1063/1.4753887>.
- (184) Zimmermann, C. G. On the Kinetics of Photodegradation in Transparent Silicones. *J. Appl. Phys.* **2008**, *103* (8), 083547. <https://doi.org/10.1063/1.2891243>.
- (185) Vaicekauskaite, J.; Mazurek, P.; Vudayagiri, S.; Skov, A. L. Mapping the Mechanical and Electrical Properties of Commercial Silicone Elastomer Formulations for Stretchable Transducers. *J. Mater. Chem. C* **2020**, *8* (4), 1273–1279. <https://doi.org/10.1039/C9TC05072H>.
- (186) Cho, H. K.; Jang, J.; Choi, J.-H.; Choi, J.; Kim, J.; Lee, J. S.; Lee, B.; Choe, Y. H.; Lee, K.-D.; Kim, S. H.; et al. Light Extraction Enhancement from Nano-Imprinted Photonic Crystal GaN-Based Blue Light-Emitting Diodes. *Opt. Express* **2006**, *14* (19), 8654. <https://doi.org/10.1364/OE.14.008654>.
- (187) David, A. Surface-Roughened Light-Emitting Diodes: An Accurate Model. *J. Disp. Technol.* **2013**, *9* (5), 301–316. <https://doi.org/10.1109/JDT.2013.2240373>.
- (188) Keaney, E.; Shearer, J.; Panwar, A.; Mead, J. Refractive Index Matching for High Light Transmission Composite Systems. *J. Compos. Mater.* **2018**, *52* (24), 3299–3307. <https://doi.org/10.1177/0021998318764787>.
- (189) *CRC Handbook of Chemistry and Physics*, 85th ed.; Lide, D., Ed.; CRC Press, 2004.
- (190) Liu, J.; Ueda, M. High Refractive Index Polymers: Fundamental Research and Practical Applications. *J. Mater. Chem.* **2009**, *19* (47), 8907. <https://doi.org/10.1039/b909690f>.
- (191) Gupta, N. S.; Lee, K.-S.; Labouriau, A. Tuning Thermal and Mechanical Properties of Polydimethylsiloxane with Carbon Fibers. *Polymers (Basel)*. **2021**, *13* (7), 1141. <https://doi.org/10.3390/polym13071141>.

- (192) Fischer, H. R.; Semprimoschnig, C.; Mooney, C.; Rohr, T.; van Eck, E. R. H.; Verkuijen, M. H. W. Degradation Mechanism of Silicone Glues under UV Irradiation and Options for Designing Materials with Increased Stability. *Polym. Degrad. Stab.* **2013**, *98* (3), 720–726. <https://doi.org/10.1016/j.polymdegradstab.2012.12.022>.
- (193) Kuo, A. C. M. Poly (Methylphenylsiloxane). In *Polymer Data Handbook*; Mark, J. E., Ed.; Oxford University Press, 1999; pp 664–671.
- (194) Meier, D. J. Poly (Diphenylsiloxane). In *Polymer Data Handbook*; Mark, J. E., Ed.; Oxford University Press, 1999; pp 450–451.
- (195) SYLGARD™ 184 Silicone Elastomer Kit Technical Data Sheet. Dow 2017.
- (196) PlatSil® 71-Series Silicone Rubbers Technical Bulletin. PolyTek 2016.
- (197) PlatSil® SILI GLASS Part A Safety Data Sheet. PolyTek 2012.
- (198) PlatSil® SILI GLASS Part B Safety Data Sheet. PolyTek 2012.
- (199) Izunobi, J. U.; Higginbotham, C. L. Polymer Molecular Weight Analysis by ¹H NMR Spectroscopy. *J. Chem. Educ.* **2011**, *88* (8), 1098–1104. <https://doi.org/10.1021/ed100461v>.
- (200) Cai, D.; Neyer, A.; Kuckuk, R.; Heise, H. M. Raman, Mid-Infrared, near-Infrared and Ultraviolet–Visible Spectroscopy of PDMS Silicone Rubber for Characterization of Polymer Optical Waveguide Materials. *J. Mol. Struct.* **2010**, *976* (1–3), 274–281. <https://doi.org/10.1016/j.molstruc.2010.03.054>.
- (201) Bistričić, L.; Borjanović, V.; Mikac, L.; Dananić, V. Vibrational Spectroscopic Study of Poly(Dimethylsiloxane)-ZnO Nanocomposites. *Vib. Spectrosc.* **2013**, *68*, 1–10. <https://doi.org/10.1016/j.vibspec.2013.05.005>.
- (202) Carteret, C.; Labrosse, A. Vibrational Properties of Polysiloxanes: From Dimer to Oligomers and Polymers. 1. Structural and Vibrational Properties of Hexamethyldisiloxane (CH₃)₃SiOSi(CH₃)₃. *J. Raman Spectrosc.* **2010**, *41* (9), 996–1004. <https://doi.org/10.1002/jrs.2537>.
- (203) Ma, T.; Yang, R.; Zheng, Z.; Song, Y. Rheology of Fumed Silica/Polydimethylsiloxane Suspensions. *J. Rheol. (N. Y. N. Y.)* **2017**, *61* (2), 205–215. <https://doi.org/10.1122/1.4973974>.

- (204) Zhang, G.-D.; Wu, J.-R.; Tang, L.-C.; Li, J.-Y.; Lai, G.-Q.; Zhong, M.-Q. Rheological Behaviors of Fumed Silica/Low Molecular Weight Hydroxyl Silicone Oil. *J. Appl. Polym. Sci.* **2014**, *131* (17), n/a-n/a. <https://doi.org/10.1002/app.40722>.
- (205) Understanding Yield Stress Measurements. Malvern 2015.
- (206) Ewoldt, R. H.; Johnston, M. T.; Caretta, L. M. Experimental Challenges of Shear Rheology: How to Avoid Bad Data. In *Complex Fluids in Biological Systems*; Spagnolie, S., Ed.; Springer: New York, NY, 2015; pp 207–241. https://doi.org/10.1007/978-1-4939-2065-5_6.
- (207) Sperling, L. H. *Introduction to Physical Polymer Science*, 4th ed.; Wiley, 2005. <https://doi.org/10.1002/0471757128>.
- (208) Kong, Y. L.; Tamargo, I. A.; Kim, H.; Johnson, B. N.; Gupta, M. K.; Koh, T.-W.; Chin, H.-A.; Steingart, D. A.; Rand, B. P.; McAlpine, M. C. 3D Printed Quantum Dot Light-Emitting Diodes. *Nano Lett.* **2014**, *14* (12), 7017–7023. <https://doi.org/10.1021/nl5033292>.
- (209) Lee, J. N.; Park, C.; Whitesides, G. M. Solvent Compatibility of Poly(Dimethylsiloxane)-Based Microfluidic Devices. *Anal. Chem.* **2003**, *75* (23), 6544–6554. <https://doi.org/10.1021/ac0346712>.
- (210) Rumens, C. V.; Ziai, M. A.; Belsey, K. E.; Batchelor, J. C.; Holder, S. J. Swelling of PDMS Networks in Solvent Vapours; Applications for Passive RFID Wireless Sensors. *J. Mater. Chem. C* **2015**, *3* (39), 10091–10098. <https://doi.org/10.1039/C5TC01927C>.
- (211) Diachun, N. A.; Marcus, A. H.; Hussey, D. M.; Fayer, M. D. Dynamics in Polydimethylsiloxane: The Effect of Solute Polarity. *J. Am. Chem. Soc.* **1994**, *116* (3), 1027–1032. <https://doi.org/10.1021/ja00082a025>.
- (212) Louisiana State University. Common solvent properties <https://macro.lsu.edu/HowTo/solvents.htm> (accessed Feb 12, 2017).
- (213) Dean, J.; Lange, N. *Lange's Handbook of Chemistry*, 15th ed.; Dean, J., Ed.; McGraw-Hill Education, 1999.
- (214) Elsevier. Basic Physical Properties of Common Solvents <https://app.knovel.com/hotlink/itble/rcid:kpKCTE000X/id:kt002VLY34/knovel-critical-tables/knovel-cri-basic-physical> (accessed Mar 30, 2018).

- (215) Safety Data Sheet AC310631000 Octyl Acetate. ThermoFisher Scientific 2018.
- (216) Safety Data Sheet O5500 Octyl Acetate. Sigma Aldrich 2019.
- (217) Mumford, S. A.; Phillips, J. W. C. 19. The Physical Properties of Some Aliphatic Compounds. *J. Chem. Soc.* **1950**, 75. <https://doi.org/10.1039/jr9500000075>.
- (218) Wohlfarth, C. Static Dielectric Constant of Octyl Acetate. In *Static Dielectric Constants of Pure Liquids and Binary Liquid Mixtures*; Springer: Berlin, Heidelberg, 2015; pp 197–197. https://doi.org/10.1007/978-3-662-48168-4_196.
- (219) Safety Data Sheet 802892 Dibutyl Ether. Merck Millipore 2018.
- (220) Yaws, C. *Thermophysical Properties of Chemicals and Hydrocarbons, Revised.*; William Andrew, 2008.
- (221) Siebel, D.; Scharfer, P.; Schabel, W. Determination of Concentration-Dependent Diffusion Coefficients in Polymer–Solvent Systems: Analysis of Concentration Profiles Measured by Raman Spectroscopy during Single Drying Experiments Excluding Boundary Conditions and Phase Equilibrium. *Macromolecules* **2015**, *48* (23), 8608–8614. <https://doi.org/10.1021/acs.macromol.5b02144>.
- (222) Castrejón-Pita, J. R.; Kubiak, K. J.; Castrejón-Pita, A. A.; Wilson, M. C. T.; Hutchings, I. M. Mixing and Internal Dynamics of Droplets Impacting and Coalescing on a Solid Surface. *Phys. Rev. E* **2013**, *88* (2), 023023. <https://doi.org/10.1103/PhysRevE.88.023023>.
- (223) Dalvi, V. H.; Rossky, P. J. Molecular Origins of Fluorocarbon Hydrophobicity. *Proc. Natl. Acad. Sci.* **2010**, *107* (31), 13603–13607. <https://doi.org/10.1073/pnas.0915169107>.
- (224) Pellerite, M. J.; Wood, E. J.; Jones, V. W. Dynamic Contact Angle Studies of Self-Assembled Thin Films from Fluorinated Alkyltrichlorosilanes 1. *J. Phys. Chem. B* **2002**, *106* (18), 4746–4754. <https://doi.org/10.1021/jp013820m>.
- (225) Wu, J.; Wang, R.; Yu, H.; Li, G.; Xu, K.; Tien, N. C.; Roberts, R. C.; Li, D. Inkjet-Printed Microelectrodes on PDMS as Biosensors for Functionalized Microfluidic Systems. *Lab Chip* **2015**, *15* (3), 690–695. <https://doi.org/10.1039/C4LC01121J>.

- (226) Vafaei, S.; Tuck, C.; Ashcroft, I.; Wildman, R. Surface Microstructuring to Modify Wettability for 3D Printing of Nano-Filled Inks. *Chem. Eng. Res. Des.* **2016**, *109*, 414–420. <https://doi.org/10.1016/j.cherd.2016.02.004>.
- (227) Quéré, D. Wetting and Roughness. *Annu. Rev. Mater. Res.* **2008**, *38* (1), 71–99. <https://doi.org/10.1146/annurev.matsci.38.060407.132434>.
- (228) Belgardt, C.; Sowade, E.; Blaudeck, T.; Baumgärtel, T.; Graaf, H.; von Borczyskowski, C.; Baumann, R. R. Inkjet Printing as a Tool for the Patterned Deposition of Octadecylsiloxane Monolayers on Silicon Oxide Surfaces. *Phys. Chem. Chem. Phys.* **2013**, *15* (20), 7494. <https://doi.org/10.1039/c3cp50331c>.
- (229) Stringer, J.; Derby, B. Formation and Stability of Lines Produced by Inkjet Printing. *Langmuir* **2010**, *26* (12), 10365–10372. <https://doi.org/10.1021/la101296e>.
- (230) Soltman, D.; Subramanian, V. Inkjet-Printed Line Morphologies and Temperature Control of the Coffee Ring Effect. *Langmuir* **2008**, *24* (5), 2224–2231. <https://doi.org/10.1021/la7026847>.
- (231) Wang, F.; Altschuh, P.; Ratke, L.; Zhang, H.; Selzer, M.; Nestler, B. Progress Report on Phase Separation in Polymer Solutions. *Adv. Mater.* **2019**, *31* (26), 1806733. <https://doi.org/10.1002/adma.201806733>.
- (232) Liu, Y. Polymerization-Induced Phase Separation and Resulting Thermomechanical Properties of Thermosetting/Reactive Nonlinear Polymer Blends: A Review. *J. Appl. Polym. Sci.* **2013**, *127* (5), 3279–3292. <https://doi.org/10.1002/app.38721>.
- (233) Schulze, M. W.; Hillmyer, M. A. Tuning Mesoporosity in Cross-Linked Nanostructured Thermosets via Polymerization-Induced Microphase Separation. *Macromolecules* **2017**, *50* (3), 997–1007. <https://doi.org/10.1021/acs.macromol.6b02570>.
- (234) Seo, M.; Hillmyer, M. A. Reticulated Nanoporous Polymers by Controlled Polymerization-Induced Microphase Separation. *Science* **2012**, *336* (6087), 1422–1425. <https://doi.org/10.1126/science.1221383>.
- (235) SPECIFICATION SHEET - QSP 630. Ocean Nanotech LLC 2016.
- (236) Krause, M. M.; Kambhampati, P. Linking Surface Chemistry to Optical Properties of Semiconductor Nanocrystals. *Phys. Chem. Chem. Phys.* **2015**, *17* (29), 18882–18894. <https://doi.org/10.1039/C5CP02173A>.

- (237) Hines, D. A.; Kamat, P. V. Recent Advances in Quantum Dot Surface Chemistry. *ACS Appl. Mater. Interfaces* **2014**, *6* (5), 3041–3057.
<https://doi.org/10.1021/am405196u>.
- (238) Morgan, D. P.; Kelley, D. F. Mechanism of Hole Trap Passivation in CdSe Quantum Dots by Alkylamines. *J. Phys. Chem. C* **2018**, *122* (44), 25661–25667.
<https://doi.org/10.1021/acs.jpcc.8b08798>.
- (239) Lunz, M.; Bradley, A. L.; Chen, W.-Y.; Gerard, V. A.; Byrne, S. J.; Gun'ko, Y. K.; Lesnyak, V.; Gaponik, N. Influence of Quantum Dot Concentration on Förster Resonant Energy Transfer in Monodispersed Nanocrystal Quantum Dot Monolayers. *Phys. Rev. B* **2010**, *81* (20), 205316. <https://doi.org/10.1103/PhysRevB.81.205316>.
- (240) Rinehart, B. S.; Cao, C. G. L. Concentration and Size Dependence of Peak Wavelength Shift on Quantum Dots in Colloidal Suspension. *Opt. Eng.* **2016**, *55* (8), 087106.
<https://doi.org/10.1117/1.OE.55.8.087106>.
- (241) Donovan, K. J.; Scott, K. Anomalous Intrinsic Viscosity of Octadecylamine-Functionalised Carbon Nanotubes in Suspension. *J. Chem. Phys.* **2013**, *138* (24), 244902. <https://doi.org/10.1063/1.4811279>.
- (242) Measuring Quantum Dots Using the Zetasizer Nano. Malvern 2017.
- (243) Malvern. Refractive index values of nanoparticles - Required?
<http://www.materials-talks.com/blog/2014/08/05/faq-how-important-are-refractive-index-absorption-for-nanoparticles/> (accessed Sep 7, 2020).
- (244) Dynamic Light Scattering - Common Terms Defined. Malvern 2020.
- (245) Intensity Volume Number - Which Size Is Correct? Malvern 2020.
- (246) Malvern. Solvent Peak - How to get rid of the buffer/salt/additive DLS contribution
<http://www.materials-talks.com/blog/2016/06/15/solvent-peaks-how-to-get-rid-of-the-buffersaltadditive-dls-contribution/> (accessed Sep 7, 2020).
- (247) Application Of Dynamic Light Scattering (DLS) to Protein Therapeutic Formulations: Principles, Measurements and Analysis - 4. FAQs. Malvern 2020.
- (248) Weaver, J.; Zakeri, R.; Aouadi, S.; Kohli, P. Synthesis and Characterization of Quantum Dot–Polymer Composites. *J. Mater. Chem.* **2009**, *19* (20), 3198.
<https://doi.org/10.1039/b820204d>.

- (249) Chou, K.; Dennis, A. Förster Resonance Energy Transfer between Quantum Dot Donors and Quantum Dot Acceptors. *Sensors* **2015**, *15* (6), 13288–13325. <https://doi.org/10.3390/s150613288>.
- (250) Wu, P.; Zhao, T.; Wang, S.; Hou, X. Semiconductor Quantum Dots-Based Metal Ion Probes. *Nanoscale* **2014**, *6* (1), 43–64. <https://doi.org/10.1039/C3NR04628A>.
- (251) Tang, Z.; Podsiadlo, P.; Shim, B. S.; Lee, J.; Kotov, N. A. The Effect of Stabilizer Density on Transformation of CdTe Nanoparticles Induced by Ag Cations. *Adv. Funct. Mater.* **2008**, *18* (23), 3801–3808. <https://doi.org/10.1002/adfm.200800691>.
- (252) Chan, Y.-H.; Chen, J.; Liu, Q.; Wark, S. E.; Son, D. H.; Batteas, J. D. Ultrasensitive Copper(II) Detection Using Plasmon-Enhanced and Photo-Brightened Luminescence of CdSe Quantum Dots. *Anal. Chem.* **2010**, *82* (9), 3671–3678. <https://doi.org/10.1021/ac902985p>.
- (253) Ke, J.; Li, X.; Zhao, Q.; Hou, Y.; Chen, J. Ultrasensitive Quantum Dot Fluorescence Quenching Assay for Selective Detection of Mercury Ions in Drinking Water. *Sci. Rep.* **2015**, *4* (1), 5624. <https://doi.org/10.1038/srep05624>.
- (254) Liu, Y.; Han, F.; Li, F.; Zhao, Y.; Chen, M.; Xu, Z.; Zheng, X.; Hu, H.; Yao, J.; Guo, T.; et al. Inkjet-Printed Unclonable Quantum Dot Fluorescent Anti-Counterfeiting Labels with Artificial Intelligence Authentication. *Nat. Commun.* **2019**, *10* (1), 2409. <https://doi.org/10.1038/s41467-019-10406-7>.
- (255) Penzel, E.; Ballard, N.; Asua, J. M. Polyacrylates. In *Ullmann's Encyclopedia of Industrial Chemistry*; Wiley-VCH Verlag GmbH & Co. KGaA: Weinheim, Germany, 2018; pp 1–20. https://doi.org/10.1002/14356007.a21_157.pub2.
- (256) Lu, G.; Yazdan Mehr, M.; van Driel, W. D.; Fan, X.; Fan, J.; Jansen, K. M. B.; Zhang, G. Q. Color Shift Investigations for LED Secondary Optical Designs: Comparison between BPA-PC and PMMA. *Opt. Mater. (Amst)*. **2015**, *45*, 37–41. <https://doi.org/10.1016/j.optmat.2015.03.005>.
- (257) Estupiñán, E.; Wendling, P.; Kostrun, M.; Garner, R. Accelerated Optical Polymer Aging Studies for LED Luminaire Applications; Jiao, J., Ed.; 2013; p 883502. <https://doi.org/10.1117/12.2024044>.

- (258) Ma, Y.; Zhang, B.; Gu, M.; Huang, S.; Liu, X.; Liu, B.; Ni, C. Bulk Synthesis of Homogeneous and Transparent Bulk Core/Multishell Quantum Dots/PMMA Nanocomposites with Bright Luminescence. *J. Appl. Polym. Sci.* **2013**, *130* (3), 1548–1553. <https://doi.org/10.1002/app.39338>.
- (259) Wei, W.; Xu, H.; You, Q.; Cheng, Q.; Liu, C.; Zou, L.; Liu, X.; Liu, J.; Cao, Y.-C.; Zheng, G. Preparation of Quantum Dot Luminescent Materials through the Ink Approach. *Mater. Des.* **2016**, *91*, 165–170. <https://doi.org/10.1016/j.matdes.2015.11.077>.
- (260) Kimble, E.; Arkles, B.; Cameron, R. Symmetric Silicone Macromers. *Polym. Prepr.* **2009**, *50* (2), 859.
- (261) Mazurek, M.; Kinning, D. J.; Kinoshita, T. Novel Materials Based on Silicone-Acrylate Copolymer Networks. *J. Appl. Polym. Sci.* **2001**, *80* (2), 159–180. [https://doi.org/10.1002/1097-4628\(20010411\)80:2<159::AID-APP1084>3.0.CO;2-P](https://doi.org/10.1002/1097-4628(20010411)80:2<159::AID-APP1084>3.0.CO;2-P).
- (262) Green, W. A. *Industrial Photoinitiators: A Technical Guide*; CRC Press, 2010.
- (263) Breus, V. V.; Heyes, C. D.; Nienhaus, G. U. Quenching of CdSe–ZnS Core–Shell Quantum Dot Luminescence by Water-Soluble Thiolated Ligands. *J. Phys. Chem. C* **2007**, *111* (50), 18589–18594. <https://doi.org/10.1021/jp075848p>.
- (264) Pong, B.-K.; Trout, B. L.; Lee, J.-Y. Modified Ligand-Exchange for Efficient Solubilization of CdSe/ZnS Quantum Dots in Water: A Procedure Guided by Computational Studies. *Langmuir* **2008**, *24* (10), 5270–5276. <https://doi.org/10.1021/la703431j>.
- (265) Inkjet Product Guide v2.1. IGM Resins.
- (266) McMurry, J. Chemical Shifts in ¹H NMR Spectroscopy. In *Organic Chemistry International edition*; Cengage Learning, 2011; pp 474–475.
- (267) Technical Data Sheet 2-Ethylhexyl Acrylate. BASF 2003.
- (268) Park, J.-J.; Prabhakaran, P.; Jang, K. K.; Lee, Y.; Lee, J.; Lee, K.; Hur, J.; Kim, J.-M.; Cho, N.; Son, Y.; et al. Photopatternable Quantum Dots Forming Quasi-Ordered Arrays. *Nano Lett.* **2010**, *10* (7), 2310–2317. <https://doi.org/10.1021/nl101609s>.
- (269) Green, P. F. The Structure of Chain End-Grafted Nanoparticle/Homopolymer Nanocomposites. *Soft Matter* **2011**, *7* (18), 7914. <https://doi.org/10.1039/c1sm05076a>.

- (270) Wallin, T. J.; Pikul, J. H.; Bodkhe, S.; Peele, B. N.; Mac Murray, B. C.; Therriault, D.; McEnerney, B. W.; Dillon, R. P.; Giannelis, E. P.; Shepherd, R. F. Click Chemistry Stereolithography for Soft Robots That Self-Heal. *J. Mater. Chem. B* **2017**, *5* (31), 6249–6255. <https://doi.org/10.1039/C7TB01605K>.
- (271) O'Brien, A. K.; Cramer, N. B.; Bowman, C. N. Oxygen Inhibition in Thiol–Acrylate Photopolymerizations. *J. Polym. Sci. Part A Polym. Chem.* **2006**, *44* (6), 2007–2014. <https://doi.org/10.1002/pola.21304>.
- (272) Yoon, C.; Kim, T.; Shin, M.-H.; Song, Y.-G.; Shin, K.; Kim, Y.-J.; Lee, K. Highly Luminescent and Stable White Light-Emitting Diodes Created by Direct Incorporation of Cd-Free Quantum Dots in Silicone Resins Using the Thiol Group. *J. Mater. Chem. C* **2015**, *3* (26), 6908–6915. <https://doi.org/10.1039/C5TC00660K>.
- (273) Kim, Y. H.; Koh, S.; Lee, H.; Kang, S.-M.; Lee, D. C.; Bae, B.-S. Photo-Patternable Quantum Dots/Siloxane Composite with Long-Term Stability for Quantum Dot Color Filters. *ACS Appl. Mater. Interfaces* **2020**, *12* (3), 3961–3968. <https://doi.org/10.1021/acscami.9b19586>.
- (274) Kim, Y. H.; Lee, H.; Kang, S.-M.; Lee, Y.; Bae, B.-S. Long-Term Stable Microlens Array-Integrated Quantum Dot/Siloxane Film for Thin White Backlight Units. *ACS Appl. Nano Mater.* **2020**, *3* (10), 10261–10269. <https://doi.org/10.1021/acsanm.0c02195>.
- (275) Nam, E.; Lee, C.; Kim, S. J.; Chung, H. K.; Chae, H. Stability and Dispersion Improvement of Quantum-Dot Films by Hydrosilylation between Quantum-Dot Ligands and a Siloxane Matrix. *Opt. Express* **2019**, *27* (14), 20037. <https://doi.org/10.1364/OE.27.020037>.
- (276) Hoyle, C. E.; Lee, T. Y.; Roper, T. Thiol-Enes: Chemistry of the Past with Promise for the Future. *J. Polym. Sci. Part A Polym. Chem.* **2004**, *42* (21), 5301–5338. <https://doi.org/10.1002/pola.20366>.
- (277) Li, X.; Kundaliya, D.; Tan, Z. J.; Anc, M.; Fang, N. X. Projection Lithography Patterned High-Resolution Quantum Dots/Thiol-Ene Photo-Polymer Pixels for Color down Conversion. *Opt. Express* **2019**, *27* (21), 30864. <https://doi.org/10.1364/OE.27.030864>.

- (278) Han, T.; Yuan, Y.; Liang, X.; Zhang, Y.; Xiong, C.; Dong, L. Colloidal Stable Quantum Dots Modified by Dual Functional Group Polymers for Inkjet Printing. *J. Mater. Chem. C* **2017**, *5* (19), 4629–4635. <https://doi.org/10.1039/C7TC00452D>.
- (279) Chou, C.-C.; Wang, T.-L.; Chen, W.-J.; Yang, C.-H. Quantum Dot–Acrylic Acrylate Oligomer Hybrid Films for Stable White Light-Emitting Diodes. *ACS Omega* **2019**, *4* (2), 3234–3243. <https://doi.org/10.1021/acsomega.8b03241>.
- (280) Bomm, J.; Büchtemann, A.; Chatten, A. J.; Bose, R.; Farrell, D. J.; Chan, N. L. A.; Xiao, Y.; Slooff, L. H.; Meyer, T.; Meyer, A.; et al. Fabrication and Full Characterization of State-of-the-Art Quantum Dot Luminescent Solar Concentrators. *Sol. Energy Mater. Sol. Cells* **2011**, *95* (8), 2087–2094. <https://doi.org/10.1016/j.solmat.2011.02.027>.
- (281) Dutta, P.; Beaulac, R. Photoluminescence Quenching of Colloidal CdSe and CdTe Quantum Dots by Nitroxide Free Radicals. *Chem. Mater.* **2016**, *28* (4), 1076–1084. <https://doi.org/10.1021/acs.chemmater.5b04423>.
- (282) Barichard, A.; Galstian, T.; Israëli, Y. Physico-Chemical Role of CdSe/ZnS Quantum Dots in the Photo-Polymerization Process of Acrylate Composite Materials. *Phys. Chem. Chem. Phys.* **2012**, *14* (22), 8208. <https://doi.org/10.1039/c2cp40746a>.
- (283) Du, L.; Liu, Z.; Jiang, S. Inkjet-Printed CdTe Quantum Dots-Polyurethane Acrylate Thin Films. *J. Nanomater.* **2017**, *2017*, 1–5. <https://doi.org/10.1155/2017/7409154>.
- (284) Lee, S. Design Principle of Reactive Components for Dimethacrylate-Terminated Quantum Dots: Preserved Photoluminescent Quantum Yield, Excellent Pattern Uniformity, and Suppression of Aggregation in the Matrix. *Macromol. Chem. Phys.* **2020**, *221* (5), 1900488. <https://doi.org/10.1002/macp.201900488>.
- (285) Jasieniak, J.; Mulvaney, P. From Cd-Rich to Se-Rich – the Manipulation of CdSe Nanocrystal Surface Stoichiometry. *J. Am. Chem. Soc.* **2007**, *129* (10), 2841–2848. <https://doi.org/10.1021/ja066205a>.
- (286) Anderson, N. C.; Hendricks, M. P.; Choi, J. J.; Owen, J. S. Ligand Exchange and the Stoichiometry of Metal Chalcogenide Nanocrystals: Spectroscopic Observation of Facile Metal-Carboxylate Displacement and Binding. *J. Am. Chem. Soc.* **2013**, *135* (49), 18536–18548. <https://doi.org/10.1021/ja4086758>.

- (287) Lee, S. F.; Osborne, M. A. Brightening, Blinking, Bluing and Bleaching in the Life of a Quantum Dot: Friend or Foe? *ChemPhysChem* **2009**, *10* (13), 2174–2191. <https://doi.org/10.1002/cphc.200900200>.
- (288) Joshi, A.; Narsingi, K. Y.; Manasreh, M. O.; Davis, E. A.; Weaver, B. D. Temperature Dependence of the Band Gap of Colloidal CdSe/ZnS Core/Shell Nanocrystals Embedded into an Ultraviolet Curable Resin. *Appl. Phys. Lett.* **2006**, *89* (13), 131907. <https://doi.org/10.1063/1.2357856>.
- (289) Kim, H. Y.; Yoon, D.-E.; Jang, J.; Choi, G.-M.; Lee, D. C.; Bae, B.-S. Heat- and Water-Proof Quantum Dot/Siloxane Composite Film: Effect of Quantum Dot-Siloxane Linkage. *J. Soc. Inf. Disp.* **2017**, *25* (2), 108–116. <https://doi.org/10.1002/jsid.542>.
- (290) Chen, W.; Wang, K.; Hao, J.; Wu, D.; Qin, J.; Dong, D.; Deng, J.; Li, Y.; Chen, Y.; Cao, W. High Efficiency and Color Rendering Quantum Dots White Light Emitting Diodes Optimized by Luminescent Microspheres Incorporating. *Nanophotonics* **2016**, *5* (4), 565–572. <https://doi.org/10.1515/nanoph-2016-0037>.
- (291) Xie, Y.; Geng, C.; Liu, X.; Xu, S.; Xing, W.; Zhang, X.; Zhang, Z.-H.; Zhang, Y.; Bi, W. Synthesis of Highly Stable Quantum-Dot Silicone Nanocomposites via in Situ Zinc-Terminated Polysiloxane Passivation. *Nanoscale* **2017**, *9* (43), 16836–16842. <https://doi.org/10.1039/C7NR05370C>.
- (292) Kim, Y. H.; Lee, H.; Kang, S.-M.; Bae, B.-S. Two-Step-Enhanced Stability of Quantum Dots via Silica and Siloxane Encapsulation for the Long-Term Operation of Light-Emitting Diodes. *ACS Appl. Mater. Interfaces* **2019**, *11* (25), 22801–22808. <https://doi.org/10.1021/acsami.9b06987>.
- (293) Shen, L.; Wang, T.; Goyal, S.; Lee, T.-H.; Lin, F.-Y.; Torres, S.; Robison, T.; Cochran, E. W. Easy-Processable and Aging-Free All-Polymer Polysiloxane Composites. *ACS Appl. Polym. Mater.* **2020**, *2* (12), 5835–5844. <https://doi.org/10.1021/acsapm.0c01088>.
- (294) Srinivasan, S.; Lee, M. W.; Grady, M. C.; Soroush, M.; Rappe, A. M. Self-Initiation Mechanism in Spontaneous Thermal Polymerization of Ethyl and n-Butyl Acrylate: A Theoretical Study. *J. Phys. Chem. A* **2010**, *114* (30), 7975–7983. <https://doi.org/10.1021/jp102772v>.

- (295) Schaffner, M.; Faber, J. A.; Pianegonda, L.; Rühls, P. A.; Coulter, F.; Studart, A. R. 3D Printing of Robotic Soft Actuators with Programmable Bioinspired Architectures. *Nat. Commun.* **2018**, *9* (1), 878. <https://doi.org/10.1038/s41467-018-03216-w>.
- (296) Zheng, S.; Zlatin, M.; Selvaganapathy, P. R.; Brook, M. A. Multiple Modulus Silicone Elastomers Using 3D Extrusion Printing of Low Viscosity Inks. *Addit. Manuf.* **2018**, *24*, 86–92. <https://doi.org/10.1016/j.addma.2018.09.011>.
- (297) Xiang, H.; Wang, X.; Ou, Z.; Lin, G.; Yin, J.; Liu, Z.; Zhang, L.; Liu, X. UV-Curable, 3D Printable and Biocompatible Silicone Elastomers. *Prog. Org. Coatings* **2019**, *137*, 105372. <https://doi.org/10.1016/j.porgcoat.2019.105372>.
- (298) Sirrine, J. M.; Meenakshisundaram, V.; Moon, N. G.; Scott, P. J.; Mondschein, R. J.; Weiseman, T. F.; Williams, C. B.; Long, T. E. Functional Siloxanes with Photo-Activated, Simultaneous Chain Extension and Crosslinking for Lithography-Based 3D Printing. *Polymer (Guildf)*. **2018**, *152*, 25–34. <https://doi.org/10.1016/j.polymer.2018.02.056>.
- (299) Zhao, T.; Yu, R.; Li, S.; Li, X.; Zhang, Y.; Yang, X.; Zhao, X.; Wang, C.; Liu, Z.; Dou, R.; et al. Superstretchable and Processable Silicone Elastomers by Digital Light Processing 3D Printing. *ACS Appl. Mater. Interfaces* **2019**, *11* (15), 14391–14398. <https://doi.org/10.1021/acsami.9b03156>.
- (300) Wallin, T. J.; Simonsen, L.-E.; Pan, W.; Wang, K.; Giannelis, E.; Shepherd, R. F.; Mengüç, Y. 3D Printable Tough Silicone Double Networks. *Nat. Commun.* **2020**, *11* (1), 4000. <https://doi.org/10.1038/s41467-020-17816-y>.
- (301) Abdallah, M.; Hijazi, A.; Dumur, F.; Lalevée, J. Coumarins as Powerful Photosensitizers for the Cationic Polymerization of Epoxy-Silicones under Near-UV and Visible Light and Applications for 3D Printing Technology. *Molecules* **2020**, *25* (9), 2063. <https://doi.org/10.3390/molecules25092063>.
- (302) Robinson, S. S.; O'Brien, K. W.; Zhao, H.; Peele, B. N.; Larson, C. M.; Mac Murray, B. C.; Van Meerbeek, I. M.; Dunham, S. N.; Shepherd, R. F. Integrated Soft Sensors and Elastomeric Actuators for Tactile Machines with Kinesthetic Sense. *Extrem. Mech. Lett.* **2015**, *5*, 47–53. <https://doi.org/10.1016/j.eml.2015.09.005>.

- (303) O'Bryan, C. S.; Bhattacharjee, T.; Hart, S.; Kabb, C. P.; Schulze, K. D.; Chilakala, I.; Sumerlin, B. S.; Sawyer, W. G.; Angelini, T. E. Self-Assembled Micro-Organogels for 3D Printing Silicone Structures. *Sci. Adv.* **2017**, *3* (5), e1602800. <https://doi.org/10.1126/sciadv.1602800>.
- (304) Greenwood, T. E.; Hatch, S. E.; Colton, M. B.; Thomson, S. L. 3D Printing Low-Stiffness Silicone within a Curable Support Matrix. *Addit. Manuf.* **2021**, *37*, 101681. <https://doi.org/10.1016/j.addma.2020.101681>.
- (305) Goff, J.; Sulaiman, S.; Arkles, B.; Lewicki, J. P. Soft Materials with Recoverable Shape Factors from Extreme Distortion States. *Adv. Mater.* **2016**, *28* (12), 2393–2398. <https://doi.org/10.1002/adma.201503320>.
- (306) Yoon, C.; Yang, K. P.; Kim, J.; Shin, K.; Lee, K. Fabrication of Highly Transparent and Luminescent Quantum Dot/Polymer Nanocomposite for Light Emitting Diode Using Amphiphilic Polymer-Modified Quantum Dots. *Chem. Eng. J.* **2020**, *382*, 122792. <https://doi.org/10.1016/j.cej.2019.122792>.
- (307) Wang, Y.; Yin, Z.; Xie, Z.; Zhao, X.; Zhou, C.; Zhou, S.; Chen, P. Polysiloxane Functionalized Carbon Dots and Their Cross-Linked Flexible Silicone Rubbers for Color Conversion and Encapsulation of White LEDs. *ACS Appl. Mater. Interfaces* **2016**, *8* (15), 9961–9968. <https://doi.org/10.1021/acsami.6b01511>.
- (308) Monaghan, T.; Harding, M. J.; Harris, R. A.; Friel, R. J.; Christie, S. D. R. Customisable 3D Printed Microfluidics for Integrated Analysis and Optimisation. *Lab Chip* **2016**, *16* (17), 3362–3373. <https://doi.org/10.1039/C6LC00562D>.
- (309) Lee, K. G.; Park, K. J.; Seok, S.; Shin, S.; Kim, D. H.; Park, J. Y.; Heo, Y. S.; Lee, S. J.; Lee, T. J. 3D Printed Modules for Integrated Microfluidic Devices. *RSC Adv.* **2014**, *4* (62), 32876. <https://doi.org/10.1039/C4RA05072J>.
- (310) Femmer, T.; Kuehne, A. J. C.; Wessling, M. Print Your Own Membrane: Direct Rapid Prototyping of Polydimethylsiloxane. *Lab Chip* **2014**, *14* (15), 2610. <https://doi.org/10.1039/c4lc00320a>.
- (311) Gao, M.; Li, L.; Song, Y. Inkjet Printing Wearable Electronic Devices. *J. Mater. Chem. C* **2017**, *5* (12), 2971–2993. <https://doi.org/10.1039/C7TC00038C>.

- (312) Durban, M. M.; Lenhardt, J. M.; Wu, A. S.; Small, W.; Bryson, T. M.; Perez-Perez, L.; Nguyen, D. T.; Gammon, S.; Smay, J. E.; Duoss, E. B.; et al. Custom 3D Printable Silicones with Tunable Stiffness. *Macromol. Rapid Commun.* **2018**, *39* (4), 1700563. <https://doi.org/10.1002/marc.201700563>.
- (313) Tumbleston, J. R.; Shirvanyants, D.; Ermoshkin, N.; Januszewicz, R.; Johnson, A. R.; Kelly, D.; Chen, K.; Pinschmidt, R.; Rolland, J. P.; Ermoshkin, A.; et al. Continuous Liquid Interface Production of 3D Objects. *Science* **2015**, *347* (6228), 1349–1352. <https://doi.org/10.1126/science.aaa2397>.
- (314) Calcagnile, P.; Cacciatore, G.; Demitri, C.; Montagna, F.; Esposito Corcione, C. A Feasibility Study of Processing Polydimethylsiloxane–Sodium Carboxymethylcellulose Composites by a Low-Cost Fused Deposition Modeling 3D Printer. *Materials (Basel)*. **2018**, *11* (9), 1578. <https://doi.org/10.3390/ma11091578>.
- (315) Udofia, E. N.; Zhou, W. Microextrusion Based 3D Printing – A Review. In *Proceedings of the 29th Annual International Solid Freeform Fabrication Symposium*; Austin, TX, 2018; pp 2033–2060.
- (316) Symes, M. D.; Kitson, P. J.; Yan, J.; Richmond, C. J.; Cooper, G. J. T.; Bowman, R. W.; Vilbrandt, T.; Cronin, L. Integrated 3D-Printed Reactionware for Chemical Synthesis and Analysis. *Nat. Chem.* **2012**, *4* (5), 349–354. <https://doi.org/10.1038/nchem.1313>.
- (317) Lipton, J. I.; Angle, S.; Lipson, H. 3D Printable Wax-Silicone Actuators. In *Proceedings of the 25th Annual International Solid Freeform Fabrication Symposium*; Austin, TX, 2014.
- (318) Johnson, B. N.; Lancaster, K. Z.; Zhen, G.; He, J.; Gupta, M. K.; Kong, Y. L.; Engel, E. A.; Krick, K. D.; Ju, A.; Meng, F.; et al. 3D Printed Anatomical Nerve Regeneration Pathways. *Adv. Funct. Mater.* **2015**, *25* (39), 6205–6217. <https://doi.org/10.1002/adfm.201501760>.
- (319) Jin, Y.; Plott, J.; Shih, A. J. Extrusion-Based Additive Manufacturing of the Moisture-Cured Silicone Elastomer. In *Proceedings of the 26th Annual International Solid Freeform Fabrication Symposium*; Austin, TX, 2015; pp 308–318.

- (320) Tian, K.; Bae, J.; Bakarich, S. E.; Yang, C.; Gately, R. D.; Spinks, G. M.; in het Panhuis, M.; Suo, Z.; Vlassak, J. J. 3D Printing of Transparent and Conductive Heterogeneous Hydrogel-Elastomer Systems. *Adv. Mater.* **2017**, *29* (10), 1604827. <https://doi.org/10.1002/adma.201604827>.
- (321) Holländer, J.; Hakala, R.; Suominen, J.; Moritz, N.; Yliruusi, J.; Sandler, N. 3D Printed UV Light Cured Polydimethylsiloxane Devices for Drug Delivery. *Int. J. Pharm.* **2018**, *544* (2), 433–442. <https://doi.org/10.1016/j.ijpharm.2017.11.016>.
- (322) Muth, J. T.; Vogt, D. M.; Truby, R. L.; Mengüç, Y.; Kolesky, D. B.; Wood, R. J.; Lewis, J. A. Embedded 3D Printing of Strain Sensors within Highly Stretchable Elastomers. *Adv. Mater.* **2014**, *26* (36), 6307–6312. <https://doi.org/10.1002/adma.201400334>.
- (323) Truby, R. L.; Wehner, M.; Grosskopf, A. K.; Vogt, D. M.; Uzel, S. G. M.; Wood, R. J.; Lewis, J. A. Soft Somatosensitive Actuators via Embedded 3D Printing. *Adv. Mater.* **2018**, *30* (15), 1706383. <https://doi.org/10.1002/adma.201706383>.
- (324) Jindal, S. K.; Sherriff, M.; Waters, M. G.; Smay, J. E.; Coward, T. J. Development of a 3D Printable Maxillofacial Silicone: Part II. Optimization of Moderator and Thixotropic Agent. *J. Prosthet. Dent.* **2018**, *119* (2), 299–304. <https://doi.org/10.1016/j.prosdent.2017.04.028>.
- (325) Walker, S.; Daalkhajav, U.; Thrush, D.; Branyan, C.; Yirmibesoglu, O. D.; Olson, G.; Menguc, Y. Zero-Support 3D Printing of Thermoset Silicone Via Simultaneous Control of Both Reaction Kinetics and Transient Rheology. *3D Print. Addit. Manuf.* **2019**, *6* (3), 139–147. <https://doi.org/10.1089/3dp.2018.0117>.
- (326) Zhou, L.; Gao, Q.; Fu, J.; Chen, Q.; Zhu, J.; Sun, Y.; He, Y. Multimaterial 3D Printing of Highly Stretchable Silicone Elastomers. *ACS Appl. Mater. Interfaces* **2019**, *11* (26), 23573–23583. <https://doi.org/10.1021/acsami.9b04873>.
- (327) Behrens, A.; Stieghorst, J.; Doll, T.; Froriep, U. P. Laser-Facilitated Additive Manufacturing Enables Fabrication of Biocompatible Neural Devices. *Sensors* **2020**, *20* (22), 6614. <https://doi.org/10.3390/s20226614>.
- (328) Courtial, E.-J.; Perrinet, C.; Colly, A.; Mariot, D.; Frances, J.-M.; Fulchiron, R.; Marquette, C. Silicone Rheological Behavior Modification for 3D Printing: Evaluation of Yield Stress Impact on Printed Object Properties. *Addit. Manuf.* **2019**, *28*, 50–57. <https://doi.org/10.1016/j.addma.2019.04.006>.

- (329) Duoss, E. B.; Weisgraber, T. H.; Hearon, K.; Zhu, C.; Small, W.; Metz, T. R.; Vericella, J. J.; Barth, H. D.; Kuntz, J. D.; Maxwell, R. S.; et al. Three-Dimensional Printing of Elastomeric, Cellular Architectures with Negative Stiffness. *Adv. Funct. Mater.* **2014**, *24* (31), 4905–4913. <https://doi.org/10.1002/adfm.201400451>.
- (330) Ozbolat, V.; Dey, M.; Ayan, B.; Povilianskas, A.; Demirel, M. C.; Ozbolat, I. T. 3D Printing of PDMS Improves Its Mechanical and Cell Adhesion Properties. *ACS Biomater. Sci. Eng.* **2018**, *4* (2), 682–693. <https://doi.org/10.1021/acsbmaterials.7b00646>.
- (331) Roh, S.; Parekh, D. P.; Bharti, B.; Stoyanov, S. D.; Velev, O. D. 3D Printing by Multiphase Silicone/Water Capillary Inks. *Adv. Mater.* **2017**, *29* (30), 1701554. <https://doi.org/10.1002/adma.201701554>.
- (332) Zheng, R.; Chen, Y.; Chi, H.; Qiu, H.; Xue, H.; Bai, H. 3D Printing of a Polydimethylsiloxane/Polytetrafluoroethylene Composite Elastomer and Its Application in a Triboelectric Nanogenerator. *ACS Appl. Mater. Interfaces* **2020**, *12* (51), 57441–57449. <https://doi.org/10.1021/acsaami.0c18201>.
- (333) Bhattacharjee, T.; Zehnder, S. M.; Rowe, K. G.; Jain, S.; Nixon, R. M.; Sawyer, W. G.; Angelini, T. E. Writing in the Granular Gel Medium. *Sci. Adv.* **2015**, *1* (8), e1500655. <https://doi.org/10.1126/sciadv.1500655>.
- (334) Hinton, T. J.; Hudson, A.; Pusch, K.; Lee, A.; Feinberg, A. W. 3D Printing PDMS Elastomer in a Hydrophilic Support Bath via Freeform Reversible Embedding. *ACS Biomater. Sci. Eng.* **2016**, *2* (10), 1781–1786. <https://doi.org/10.1021/acsbmaterials.6b00170>.
- (335) Abdollahi, S.; Davis, A.; Miller, J. H.; Feinberg, A. W. Expert-Guided Optimization for 3D Printing of Soft and Liquid Materials. *PLoS One* **2018**, *13* (4), e0194890. <https://doi.org/10.1371/journal.pone.0194890>.
- (336) Menon, A.; Póczos, B.; Feinberg, A. W.; Washburn, N. R. Optimization of Silicone 3D Printing with Hierarchical Machine Learning. *3D Print. Addit. Manuf.* **2019**, *6* (4), 181–189. <https://doi.org/10.1089/3dp.2018.0088>.
- (337) Kolesky, D. B.; Truby, R. L.; Gladman, A. S.; Busbee, T. A.; Homan, K. A.; Lewis, J. A. 3D Bioprinting of Vascularized, Heterogeneous Cell-Laden Tissue Constructs. *Adv. Mater.* **2014**, *26* (19), 3124–3130. <https://doi.org/10.1002/adma.201305506>.

- (338) Lv, J.; Gong, Z.; He, Z.; Yang, J.; Chen, Y.; Tang, C.; Liu, Y.; Fan, M.; Lau, W.-M. 3D Printing of a Mechanically Durable Superhydrophobic Porous Membrane for Oil–Water Separation. *J. Mater. Chem. A* **2017**, *5* (24), 12435–12444. <https://doi.org/10.1039/C7TA02202F>.
- (339) Plott, J.; Shih, A. The Extrusion-Based Additive Manufacturing of Moisture-Cured Silicone Elastomer with Minimal Void for Pneumatic Actuators. *Addit. Manuf.* **2017**, *17*, 1–14. <https://doi.org/10.1016/j.addma.2017.06.009>.
- (340) Qiu, K.; Zhao, Z.; Haghighiastiani, G.; Guo, S.-Z.; He, M.; Su, R.; Zhu, Z.; Bhuiyan, D. B.; Murugan, P.; Meng, F.; et al. 3D Printed Organ Models with Physical Properties of Tissue and Integrated Sensors. *Adv. Mater. Technol.* **2018**, *3* (3), 1700235. <https://doi.org/10.1002/admt.201700235>.
- (341) Kim, Y.; Yuk, H.; Zhao, R.; Chester, S. A.; Zhao, X. Printing Ferromagnetic Domains for Untethered Fast-Transforming Soft Materials. *Nature* **2018**, *558* (7709), 274–279. <https://doi.org/10.1038/s41586-018-0185-0>.
- (342) Luis, E.; Pan, H. M.; Sing, S. L.; Bajpai, R.; Song, J.; Yeong, W. Y. 3D Direct Printing of Silicone Meniscus Implant Using a Novel Heat-Cured Extrusion-Based Printer. *Polymers (Basel)*. **2020**, *12* (5), 1031. <https://doi.org/10.3390/polym12051031>.
- (343) Thomas, T.; Rubfiaro, A. S.; Nautiyal, P.; Brooks, R.; Dickerson, D.; He, J.; Agarwal, A. Extrusion 3D Printing of Porous Silicone Architectures for Engineering Human Cardiomyocyte-Infused Patches Mimicking Adult Heart Stiffness. *ACS Appl. Bio Mater.* **2020**, *3* (9), 5865–5871. <https://doi.org/10.1021/acsabm.0c00572>.
- (344) Lu, D.-X.; Zhang, Y.-L.; Han, D.-D.; Wang, H.; Xia, H.; Chen, Q.-D.; Ding, H.; Sun, H.-B. Solvent-Tunable PDMS Microlens Fabricated by Femtosecond Laser Direct Writing. *J. Mater. Chem. C* **2015**, *3* (8), 1751–1756. <https://doi.org/10.1039/C4TC02737J>.
- (345) Bhattacharjee, N.; Parra-Cabrera, C.; Kim, Y. T.; Kuo, A. P.; Folch, A. Desktop-Stereolithography 3D-Printing of a Poly(Dimethylsiloxane)-Based Material with Sylgard-184 Properties. *Adv. Mater.* **2018**, *30* (22), 1800001. <https://doi.org/10.1002/adma.201800001>.
- (346) Kim, D. S.; Suriboot, J.; Grunlan, M. A.; Tai, B. L. Feasibility Study of Silicone Stereolithography with an Optically Created Dead Zone. *Addit. Manuf.* **2019**, *29*, 100793. <https://doi.org/10.1016/j.addma.2019.100793>.

- (347) Coenjarts, C. A.; Ober, C. K. Two-Photon Three-Dimensional Microfabrication of Poly(Dimethylsiloxane) Elastomers. *Chem. Mater.* **2004**, *16* (26), 5556–5558. <https://doi.org/10.1021/cm048717z>.
- (348) Hasegawa, T.; Oishi, K.; Maruo, S. Three-Dimensional Microstructuring of PDMS by Two-Photon Microstereolithography. In *2006 IEEE International Symposium on MicroNanoMechanical and Human Science*; IEEE, 2006; pp 1–4. <https://doi.org/10.1109/MHS.2006.320261>.
- (349) Rekštytė, S.; Malinauskas, M.; Juodkazis, S. Three-Dimensional Laser Micro-Sculpturing of Silicone: Towards Bio-Compatible Scaffolds. *Opt. Express* **2013**, *21* (14), 17028. <https://doi.org/10.1364/OE.21.017028>.
- (350) Kim, D. S.; Kao, Y.-T.; Tai, B. L. Hydrostatic 3D-Printing for Soft Material Structures Using Low One-Photon Polymerization. *Manuf. Lett.* **2016**, *10*, 6–9. <https://doi.org/10.1016/j.mfglet.2016.08.002>.
- (351) Obata, K.; Slobin, S.; Schonewille, A.; Hohnholz, A.; Unger, C.; Koch, J.; Suttmann, O.; Overmeyer, L. UV Laser Direct Writing of 2D/3D Structures Using Photo-Curable Polydimethylsiloxane (PDMS). *Appl. Phys. A* **2017**, *123* (7), 495. <https://doi.org/10.1007/s00339-017-1104-1>.
- (352) Thrasher, C. J.; Schwartz, J. J.; Boydston, A. J. Modular Elastomer Photoresins for Digital Light Processing Additive Manufacturing. *ACS Appl. Mater. Interfaces* **2017**, *9* (45), 39708–39716. <https://doi.org/10.1021/acsami.7b13909>.
- (353) In, E.; Walker, E.; Naguib, H. E. Novel Development of 3D Printable UV-Curable Silicone for Multimodal Imaging Phantom. *Bioprinting* **2017**, *7*, 19–26. <https://doi.org/10.1016/j.bprint.2017.05.003>.
- (354) Liravi, F.; Vlasea, M. Powder Bed Binder Jetting Additive Manufacturing of Silicone Structures. *Addit. Manuf.* **2018**, *21*, 112–124. <https://doi.org/10.1016/j.addma.2018.02.017>.
- (355) Sun, S.; Fei, G.; Wang, X.; Xie, M.; Guo, Q.; Fu, D.; Wang, Z.; Wang, H.; Luo, G.; Xia, H. Covalent Adaptable Networks of Polydimethylsiloxane Elastomer for Selective Laser Sintering 3D Printing. *Chem. Eng. J.* **2021**, *412*, 128675. <https://doi.org/10.1016/j.cej.2021.128675>.

- (356) Riahi, M.; Karimi, F.; Ghaffari, A. Fabrication of 3D Microfluidic Structure with Direct Selective Laser Baking of PDMS. *Rapid Prototyp. J.* **2019**, *25* (4), 775–780. <https://doi.org/10.1108/RPJ-01-2018-0021>.
- (357) Wang, M.; Zhang, M.; Qian, J.; Zhao, F.; Shen, L.; Scholes, G. D.; Winnik, M. A. Enhancing the Photoluminescence of Polymer-Stabilized CdSe/CdS/ZnS Core/Shell/Shell and CdSe/ZnS Core/Shell Quantum Dots in Water through a Chemical-Activation Approach. *Langmuir* **2009**, *25* (19), 11732–11740. <https://doi.org/10.1021/la900614e>.
- (358) Tomczak, N.; Jańczewski, D.; Han, M.; Vancso, G. J. Designer Polymer–Quantum Dot Architectures. *Prog. Polym. Sci.* **2009**, *34* (5), 393–430. <https://doi.org/10.1016/j.progpolymsci.2008.11.004>.
- (359) Gomes, R.; Hassinen, A.; Szczygiel, A.; Zhao, Q.; Vantomme, A.; Martins, J. C.; Hens, Z. Binding of Phosphonic Acids to CdSe Quantum Dots: A Solution NMR Study. *J. Phys. Chem. Lett.* **2011**, *2* (3), 145–152. <https://doi.org/10.1021/jz1016729>.
- (360) Knauf, R. R.; Lennox, J. C.; Dempsey, J. L. Quantifying Ligand Exchange Reactions at CdSe Nanocrystal Surfaces. *Chem. Mater.* **2016**, *28* (13), 4762–4770. <https://doi.org/10.1021/acs.chemmater.6b01827>.
- (361) Zeng, B.; Palui, G.; Zhang, C.; Zhan, N.; Wang, W.; Ji, X.; Chen, B.; Mattoussi, H. Characterization of the Ligand Capping of Hydrophobic CdSe–ZnS Quantum Dots Using NMR Spectroscopy. *Chem. Mater.* **2018**, *30* (1), 225–238. <https://doi.org/10.1021/acs.chemmater.7b04204>.
- (362) Park, S.-Y.; Kim, H.-S.; Yoo, J.; Kwon, S.; Shin, T. J.; Kim, K.; Jeong, S.; Seo, Y.-S. Long-Term Stability of CdSe/CdZnS Quantum Dot Encapsulated in a Multi-Lamellar Microcapsule. *Nanotechnology* **2015**, *26* (27), 275602. <https://doi.org/10.1088/0957-4484/26/27/275602>.
- (363) Yoo, H.; Jang, H. S.; Lee, K.; Woo, K. Quantum Dot-Layer-Encapsulated and Phenyl-Functionalized Silica Spheres for Highly Luminous, Colour Rendering, and Stable White Light-Emitting Diodes. *Nanoscale* **2015**, *7* (30), 12860–12867. <https://doi.org/10.1039/C5NR02991K>.

- (364) Adam, M.; Gaponik, N.; Eychmüller, A.; Erdem, T.; Soran-Erdem, Z.; Demir, H. V. Colloidal Nanocrystals Embedded in Macrocrystals: Methods and Applications. *J. Phys. Chem. Lett.* **2016**, *7* (20), 4117–4123. <https://doi.org/10.1021/acs.jpcllett.6b01699>.
- (365) Erdem, T.; Soran-Erdem, Z.; Sharma, V. K.; Kelestemur, Y.; Adam, M.; Gaponik, N.; Demir, H. V. Stable and Efficient Colour Enrichment Powders of Nonpolar Nanocrystals in LiCl. *Nanoscale* **2015**, *7* (42), 17611–17616. <https://doi.org/10.1039/C5NR02696B>.
- (366) Gill, R.; Zayats, M.; Willner, I. Semiconductor Quantum Dots for Bioanalysis. *Angew. Chemie Int. Ed.* **2008**, *47* (40), 7602–7625. <https://doi.org/10.1002/anie.200800169>.
- (367) Kwak, J.; Bae, W. K.; Zorn, M.; Woo, H.; Yoon, H.; Lim, J.; Kang, S. W.; Weber, S.; Butt, H.-J.; Zentel, R.; et al. Characterization of Quantum Dot/Conducting Polymer Hybrid Films and Their Application to Light-Emitting Diodes. *Adv. Mater.* **2009**, *21* (48), 5022–5026. <https://doi.org/10.1002/adma.200902072>.
- (368) Zorn, M.; Bae, W. K.; Kwak, J.; Lee, H.; Lee, C.; Zentel, R.; Char, K. Quantum Dot–Block Copolymer Hybrids with Improved Properties and Their Application to Quantum Dot Light-Emitting Devices. *ACS Nano* **2009**, *3* (5), 1063–1068. <https://doi.org/10.1021/nn800790s>.
- (369) Koole, R.; van Schooneveld, M. M.; Hilhorst, J.; de Mello Donegá, C.; 't Hart, D. C.; van Blaaderen, A.; Vanmaekelbergh, D.; Meijerink, A. On the Incorporation Mechanism of Hydrophobic Quantum Dots in Silica Spheres by a Reverse Microemulsion Method. *Chem. Mater.* **2008**, *20* (7), 2503–2512. <https://doi.org/10.1021/cm703348y>.
- (370) Jing, L.; Yang, C.; Qiao, R.; Niu, M.; Du, M.; Wang, D.; Gao, M. Highly Fluorescent CdTe@SiO₂ Particles Prepared via Reverse Microemulsion Method. *Chem. Mater.* **2010**, *22* (2), 420–427. <https://doi.org/10.1021/cm9029962>.
- (371) Yang, P.; Ando, M.; Murase, N. Highly Luminescent CdSe/Cd_xZn_{1-x}S Quantum Dots Coated with Thickness-Controlled SiO₂ Shell through Silanization. *Langmuir* **2011**, *27* (15), 9535–9540. <https://doi.org/10.1021/la201213c>.

- (372) Cho, M.; Lim, K.; Woo, K. Facile Synthesis and Optical Properties of Colloidal Silica Microspheres Encapsulating a Quantum Dot Layer. *Chem. Commun.* **2010**, *46* (30), 5584. <https://doi.org/10.1039/c0cc00621a>.
- (373) Chan, Y.; Zimmer, J. P.; Stroh, M.; Steckel, J. S.; Jain, R. K.; Bawendi, M. G. Incorporation of Luminescent Nanocrystals into Monodisperse Core-Shell Silica Microspheres. *Adv. Mater.* **2004**, *16* (23–24), 2092–2097. <https://doi.org/10.1002/adma.200400237>.
- (374) Xie, B.; Cheng, Y.; Hao, J.; Yu, X.; Shu, W.; Wang, K.; Luo, X. White Light-Emitting Diodes With Enhanced Efficiency and Thermal Stability Optimized by Quantum Dots-Silica Nanoparticles. *IEEE Trans. Electron Devices* **2018**, *65* (2), 605–609. <https://doi.org/10.1109/TED.2017.2785772>.
- (375) Kim, Y.-K.; Choi, K.-C.; Ahn, S.-H.; Cho, Y.-S. A Facile Synthesis of SiO₂-Based Nanocomposites Containing Multiple Quantum Dots at High Concentration for LED Applications. *RSC Adv.* **2012**, *2* (16), 6411. <https://doi.org/10.1039/c2ra20780j>.
- (376) Kim, Y.-K.; Choi, K.-C.; Baek, Y.-K.; Shin, P.-W. Enhanced Luminescence Stability of Quantum Dot-Based Inorganic Nanocomposite Particles for White-Light-Emitting Diodes. *Mater. Lett.* **2014**, *124*, 129–132. <https://doi.org/10.1016/j.matlet.2014.03.017>.
- (377) Li, J.; Tang, Y.; Li, Z.; Ding, X.; Yu, B.; Lin, L. Largely Enhancing Luminous Efficacy, Color-Conversion Efficiency, and Stability for Quantum-Dot White LEDs Using the Two-Dimensional Hexagonal Pore Structure of SBA-15 Mesoporous Particles. *ACS Appl. Mater. Interfaces* **2019**, *11* (20), 18808–18816. <https://doi.org/10.1021/acsami.8b22298>.
- (378) Xie, B.; Liu, H.; Hu, R.; Wang, C.; Hao, J.; Wang, K.; Luo, X. Targeting Cooling for Quantum Dots in White QDs-LEDs by Hexagonal Boron Nitride Platelets with Electrostatic Bonding. *Adv. Funct. Mater.* **2018**, *28* (30), 1801407. <https://doi.org/10.1002/adfm.201801407>.
- (379) Kim, J.-S.; Yang, S.; Bae, B.-S. Thermally Stable Transparent Sol–Gel Based Siloxane Hybrid Material with High Refractive Index for Light Emitting Diode (LED) Encapsulation. *Chem. Mater.* **2010**, *22* (11), 3549–3555. <https://doi.org/10.1021/cm100903b>.

- (380) Kim, J.-S.; Yang, S. C.; Kwak, S.-Y.; Choi, Y.; Paik, K.-W.; Bae, B.-S. High Performance Encapsulant for Light-Emitting Diodes (LEDs) by a Sol–Gel Derived Hydrogen Siloxane Hybrid. *J. Mater. Chem.* **2012**, *22* (16), 7954. <https://doi.org/10.1039/c2jm16907j>.
- (381) Bae, J.; Kim, Y.; Kim, H.-Y.; Lim, Y.; Bae, B.-S. Sol–Gel Synthesized Linear Oligosiloxane-Based Hybrid Material for a Thermally-Resistant Light Emitting Diode (LED) Encapsulant. *RSC Adv.* **2013**, *3* (23), 8871. <https://doi.org/10.1039/c3ra41478g>.
- (382) Jun, S.; Lee, J.; Jang, E. Highly Luminescent and Photostable Quantum Dot–Silica Monolith and Its Application to Light-Emitting Diodes. *ACS Nano* **2013**, *7* (2), 1472–1477. <https://doi.org/10.1021/nn3052428>.
- (383) Jang, J.; Yoon, D.-E.; Kang, S.-M.; Kim, Y. H.; Lee, I.; Lee, H.; Kim, Y. H.; Lee, D. C.; Bae, B.-S. Exceptionally Stable Quantum Dot/Siloxane Hybrid Encapsulation Material for White Light-Emitting Diodes with a Wide Color Gamut. *Nanoscale* **2019**, *11* (31), 14887–14895. <https://doi.org/10.1039/C9NR04517A>.
- (384) Boudine, B.; Sebais, M.; Halimi, O.; Mouras, R.; Boudrioua, A.; Bourson, P. Characterization of CdS Nanocrystals Embedded in KCl Single Crystal Matrix Grown by Czochralski Method. *Opt. Mater. (Amst)*. **2004**, *25* (4), 373–377. <https://doi.org/10.1016/j.optmat.2003.09.005>.
- (385) Soran-Erdem, Z.; Erdem, T.; Hernandez-Martinez, P. L.; Akgul, M. Z.; Gaponik, N.; Demir, H. V. Macrocrystals of Colloidal Quantum Dots in Anthracene: Exciton Transfer and Polarized Emission. *J. Phys. Chem. Lett.* **2015**, *6* (9), 1767–1772. <https://doi.org/10.1021/acs.jpcclett.5b00685>.
- (386) Otto, T.; Müller, M.; Mundra, P.; Lesnyak, V.; Demir, H. V.; Gaponik, N.; Eychmüller, A. Colloidal Nanocrystals Embedded in Macrocrystals: Robustness, Photostability, and Color Purity. *Nano Lett.* **2012**, *12* (10), 5348–5354. <https://doi.org/10.1021/nl3027444>.
- (387) Adam, M.; Erdem, T.; Stachowski, G. M.; Soran-Erdem, Z.; Lox, J. F. L.; Bauer, C.; Poppe, J.; Demir, H. V.; Gaponik, N.; Eychmüller, A. Implementation of High-Quality Warm-White Light-Emitting Diodes by a Model-Experimental Feedback Approach Using Quantum Dot–Salt Mixed Crystals. *ACS Appl. Mater. Interfaces* **2015**, *7* (41), 23364–23371. <https://doi.org/10.1021/acsami.5b08377>.

- (388) Adam, M.; Wang, Z.; Dubavik, A.; Stachowski, G. M.; Meerbach, C.; Soran-Erdem, Z.; Rengers, C.; Demir, H. V.; Gaponik, N.; Eychmüller, A. Liquid-Liquid Diffusion-Assisted Crystallization: A Fast and Versatile Approach Toward High Quality Mixed Quantum Dot-Salt Crystals. *Adv. Funct. Mater.* **2015**, *25* (18), 2638–2645. <https://doi.org/10.1002/adfm.201500552>.
- (389) Zhang, X.; Sun, Z.; Zhou, C.; Zhu, Z.; Guo, Z.; Shen, J.; Lin, Y.; Xiao, S.; Chen, L.; Zheng, X.; et al. Synthesis and Enhanced Photo/Thermal Stability of High-Luminescent Red-Emitting CdTe@CaCO₃ Composite for LED Applications. *Ceram. Int.* **2019**, *45* (5), 6484–6490. <https://doi.org/10.1016/j.ceramint.2018.12.137>.
- (390) Kalytchuk, S.; Adam, M.; Tomanec, O.; Zbořil, R.; Gaponik, N.; Rogach, A. L. Sodium Chloride Protected CdHgTe Quantum Dot Based Solid-State Near-Infrared Luminophore for Light-Emitting Devices and Luminescence Thermometry. *ACS Photonics* **2017**, *4* (6), 1459–1465. <https://doi.org/10.1021/acsp Photonics.7b00222>.

Appendices

Waveforms

W₁ v₁

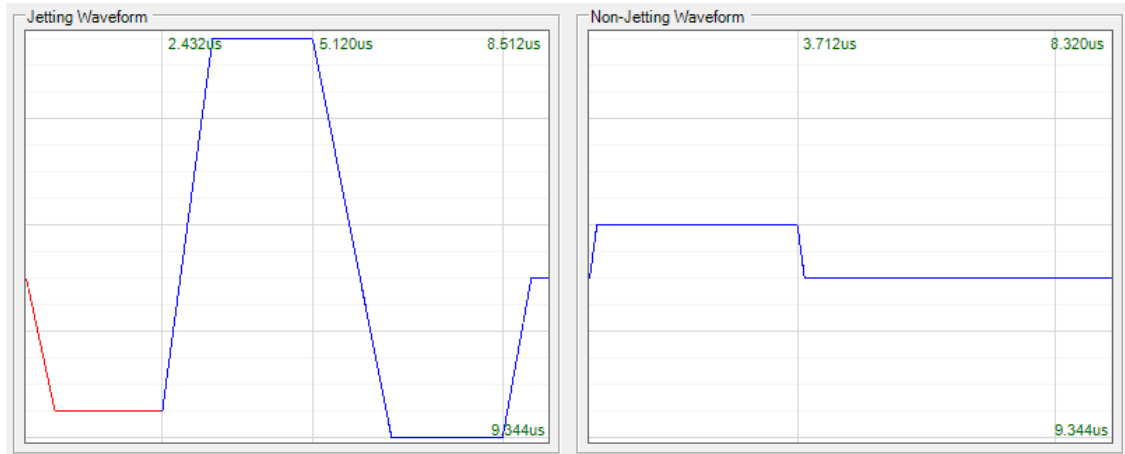


Figure 138: Single pulse waveform optimised for addition cure inks, jetting at 32 V. Referred to as W₁ v₁.

Segment	Length, μs	Slew rate	Pulse width, μs	Level, V%
Jetting 1: Fill	2.432	0.65	1.9	7
Jetting 2: Print	2.688	1	1.8	100
Jetting 3: Recovery	3.392	0.68	2.0	0
Jetting 4	0.832	0.8	0.35	40
Non-jetting	3.712	1	3.6	55

W₁ v₂

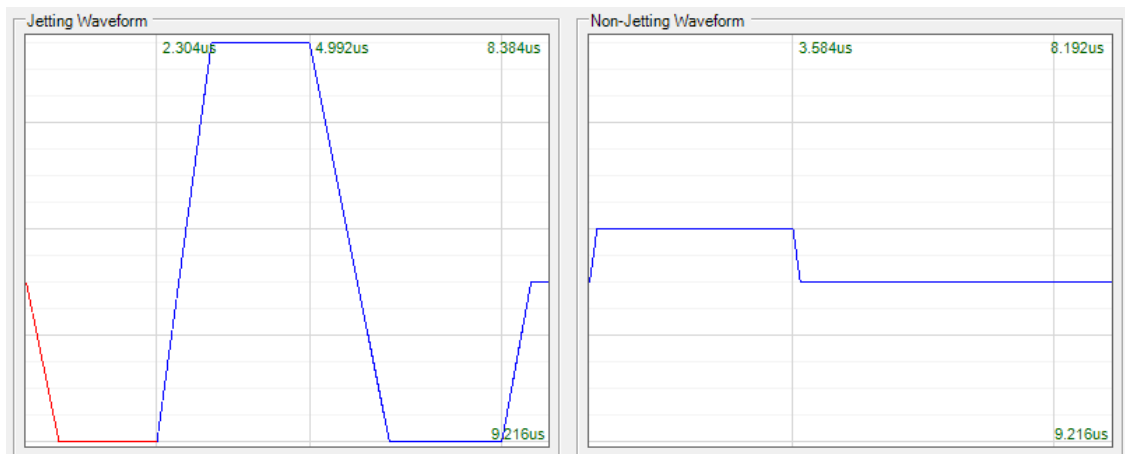


Figure 139: Single pulse waveform, optimised from previous in order to improve performance at lower jetting voltages. Referred to as W₁ v₂.

Segment	Length, μs	Slew rate	Pulse width, μs	Level, V%
Jetting 1: Fill	2.304	0.65	1.7	0
Jetting 2: Print	2.688	1	1.8	100
Jetting 3: Recovery	3.392	0.68	2.0	0
Jetting 4	0.832	0.8	0.35	40
Non-jetting	3.584	1	3.5	55

W₂

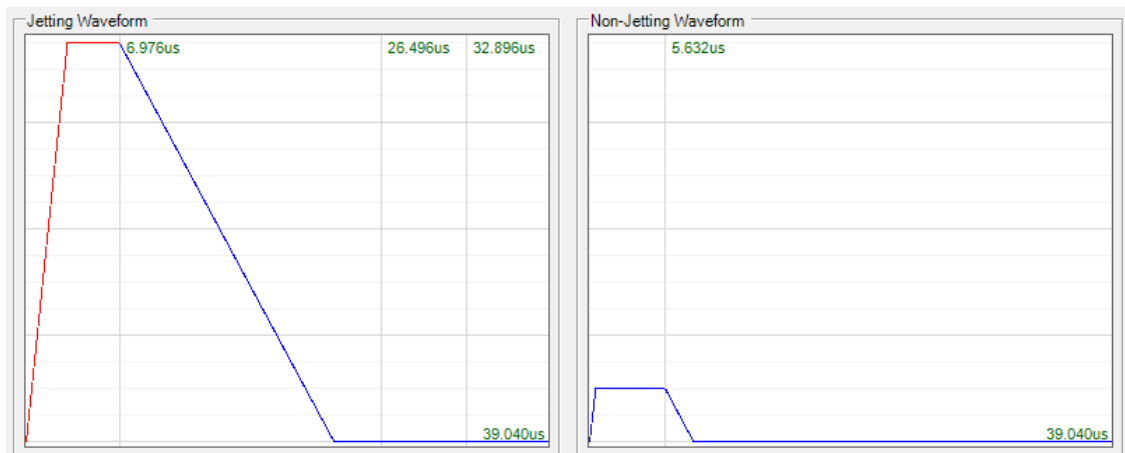


Figure 140: Single pulse waveform with forceful ink ejection; utilised here to demonstrate that UV cure inks can be jetted, but a waveform optimised from the Dimatix Model Fluid settings waveform is preferable. Referred to as W₂.

Segment	Length, μs	Slew rate	Pulse width, μs	Level, V%
Jetting 1: Print	6.976	0.31	4.0	100
Jetting 2: Recovery	32.064	0.06	16	0
Non-jetting	5.632	0.31	5.2	15

Waveform W₂ consists of a single pulse waveform for forceful ink ejection and long, slow recovery; a meniscus cancellation pulse is used to cut off tails during ink ejection. This waveform is not optimised towards efficient jetting of a specific ink but is compatible with a range of fluid properties and was used to demonstrate jetting of UV cure ink.

Silicones in alternate AM categories

Overview of AM

Additive manufacturing (AM) – also known as rapid prototyping (RP) and 3D printing (3DP) – selectively adds and fuses material to produce parts with controlled shapes, rather than selectively removing material or using moulds. Parts are created from CAD data which is sliced to give an STL file which instructs the printer; the three-dimensional shape is then built layer-by-layer. This enables geometric freedom, rapid customisation and small batch production, minimal assembly, low material waste, and multi-material printing: production of end-use parts is possible.⁷ However, within the AM materials portfolio, transparent and elastomeric materials such as silicone are limited; development of silicones compatible with AM processes would further enable production of functional end-use parts, particularly in microfluidic, soft robotic, or flexible electronic devices.

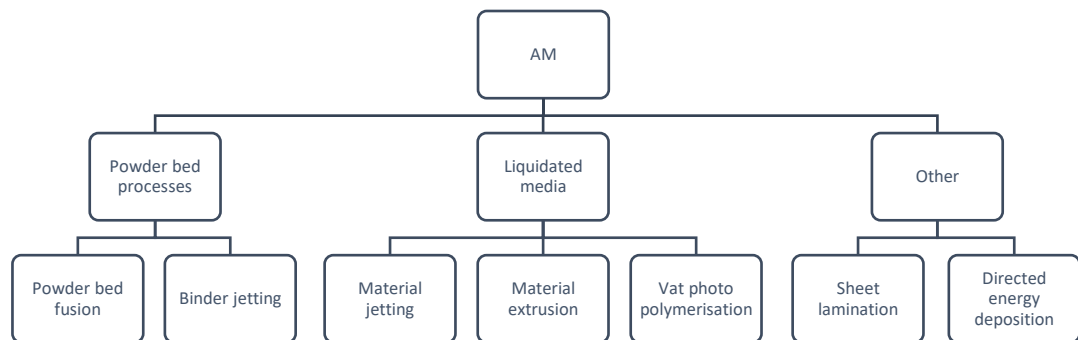


Figure 141: The seven AM process categories, as defined by the ASTM.

The American Society for Testing and Materials International (ASTM) defines seven categories of AM processes,³¹ as summarised above in Figure 141. In powder bed processes, a reservoir of powdered media is used as the printing feedstock and a new layer of powder is spread over the build platform for each sequential layer of the print file. The powder bed supports the structure of the part during printing. Some silicone powders are available from suppliers such as Shin-Etsu but have niche applications.

Powder bed fusion (PBF) processes use a high energy source - either a focused beam (electron or laser) or a thermal printhead - to selectively fuse powder particles together to form an object layer-by-layer (by melting or sintering). However, silicone elastomers are thermoset polymers and silicone fluids are amorphous, making PDMS fundamentally incompatible with PBF. Linear poly(methylphenylsiloxane) (PMPS) is semi-crystalline and is compatible in theory, although the low glass transition temperature is not ideal (approximately $-25\text{ }^{\circ}\text{C}$ and $35\text{ }^{\circ}\text{C}$ T_g and T_m respectively).¹⁹³ Crystallinity increases with increasing phenyl content: poly(diphenylsiloxane) (PDPS) is expected to have T_g $40\text{-}50\text{ }^{\circ}\text{C}$

and T_m 200-250 °C but it is not a commercial polymer.¹⁹⁴ While such materials could have use for applications requiring high radiation resistance, they do not have the elastomeric properties of PDMS, which is of most interest to the PBF materials portfolio.⁶⁶

Binder jetting combines material jetting and powder bed fusion: a liquid binder is selectively deposited by jetting onto the powder bed, which glues the powder together. This is a good route for multi-material printing but requires a significant amount of post-processing to remove excess powder, strengthen the part, and to improve surface finish. Green parts are typically weak and brittle due to low density, so thermal treatment is used to remove the binder and the part is then sintered or infiltrated with another material to improve mechanical properties. Production of composites by using reactive binders is also feasible.

For AM processes involving liquidated media, consideration must be given to the rheology and other physical properties of formulations. Silicones are thermoset polymers and are therefore not melt-processable, which can make formulation within viscosity limits challenging. Cured rubbers and resins have limited printability; while crosslinked silicones can be dissolved in some solvents, solutions have high viscosity and concentration is limited by low solubility. Therefore, crosslinking reactions are used, of which there are three main reactions that have been used in AM as they proceed under ambient conditions:

- Addition cure (hydrosilylation between α,ω -vinyl-PDMS and Si-H crosslinkers)
- Condensation cure (hydrolysis of α,ω -hydroxyl-PDM and organosilane crosslinkers)
- UV cure (predominantly free radical chain growth and thiol-ene reactions).

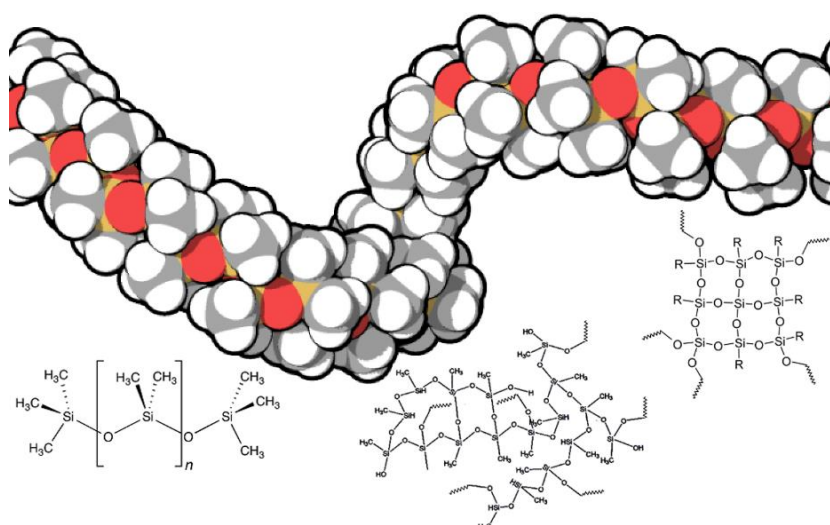


Figure 142: Top: A PDMS chain, created using MarvinSketch and Qutemol. Left to right: Representations of silicone fluids, elastomers, and resins.

Material jetting and extrusion both selectively deposit liquid material through a nozzle orifice which solidifies to produce a part layer-by-layer. In material jetting, ejected ink separates into droplets, whereas materials are deposited as a continuous filament in material extrusion. These processes typically offer less geometric freedom than powder bed fusion or vat photopolymerisation as overhangs are unsupported (excepting embedded processes); another support material can be deposited simultaneously and removed in post-processing to enable printing of overhanging geometries.

Vat photopolymerisation (VP) uses ultraviolet or visible light to selectively cure a vat of liquid photo-resin layer-by-layer. The vat material provides some support to parts, making VP somewhat analogous to PBF. This technique offers high resolution and good surface finish but requires expensive photopolymers and may require post-processing to remove structural supports and to fully cure parts. Photo-resins may yellow and are typically brittle.

These three categories have very different viscosity requirements for fluids. Extrusion-based processes have the widest range of viscosity, with a viscosity limit of ≤ 60 kPa s,³² but materials must be thixotropic in order to retain their shape once extruded; silicones with silica reinforcing fillers are ideal.^{295,312} Vat photopolymerisation requires viscosities of 300-5000 mPa s,³² while material jetting has the lowest viscosity limit at 10-100 mPa s and typically ≤ 40 mPa s for inkjet printing,³² compatible with low molecular weight silicone fluids,¹⁷ though piezoelectric/pneumatic valves are capable of jetting high viscosity inks (≤ 1 kPa s).³²

Commercial AM of silicones

There are a number of commercial systems that have demonstrated extrusion-based printing of silicones by various cure mechanisms. Companies including Momentive, Novagard, Wacker, Dow Corning, Bluestar Silicones, and Shin-Etsu produce commercial UV cure silicone formulations which may find application in AM technologies.³²

In 2000, EnvisionTEC developed the prototype BioPlotter extrusion printer: the first material printed was silicone. EnvisionTec currently offers a range of silicones for printing: for extrusion, Silicone TG is a medical-grade 1-part RTV (20A Shore hardness, 200-800 μm nozzle diameter, 6.5-40.5 mm s^{-1}) and UV Silicone 60A MG is a UV cure RTV (60A, 300-400 μm nozzle diameter, 5-20 mm s^{-1}). For vat photopolymerisation, they offer materials with 40-90A Shore hardness (E UA40, E-UA90) and validated 70A Shore hardness formulations E-5015 and E-3840 from LOCTITE 3D.

In 2011, Momentive partnered with Specialty Silicone Fabricators to develop an extrusion process with patented UV curing technology: a photo-sensitive platinum catalyst is activated by UV light and the silicone cures via hydrosilylation. This mechanism was not used for additive manufacturing, but is likely compatible with extrusion-based AM.

In 2013 and 2015, Hyrel demonstrated extrusion-based 3D printing of commercial silicones Sugru (a mouldable putty that sets into a silicone rubber) and an unspecified 1-part RTV silicone using their Emulsifiable Extruder (EMO-1). In 2019, printing of an unspecified 1-part RTV was demonstrated on the Hyrel Hydra 16A industrial extrusion printer; this features up to 5 printheads with programmable mixing ratios for 2- and 3-part formulations. Later printheads have photoinitiated crosslinking capabilities.

Similarly, Structur3d, a company developing Discov3ry extrusion printers, printed a commercial condensation cure RTV (DAP SiliconePlus) with resolution around 840 μm (nozzle diameter) in 2015-2016. Additionally, in 2019 Structur3d announced a desktop hybrid printer called Inj3ctor, combining extrusion and injection moulding. 2-part liquid rubbers are injected into 3D printed moulds with programmable mixing ratio and injection volumes, which presents an indirect route to silicone printing.

Due to the thermoset nature of silicones, there are three types of AM processes currently used in commercial AM specialised towards silicones: material extrusion, vat photopolymerisation, and material jetting.

Extrusion

stamos+braun Prothesenwerk (established 2013) was the first company to print high viscosity, heat cured, medical grade silicone rubbers. They produce high resolution, lifelike silicone prostheses; cushioning and internal structures are printed from addition or UV cure silicone by what appears to be an extrusion-based process. They hope to achieve full colour printing to better match skin tone.

A similar technology for the extrusion-based fabrication of silicone parts for medical applications, prosthetics, and high temperature applications is in development by Kühling&Kühling. Project Lapuna was showcased at FormNext 2017 and is currently

completing test and evaluation with industrial partners before launch of a printing service. Wax support material is used in a dual head system and an emphasis is put on hybrid manufacturing techniques and processing of soft elastomers (20-40 Shore A hardness).

In 2016, STERNE showcased SiO-Shaping 1601, a UV-cure extrusion process. Silicone filaments are deposited and crosslinked by photopolymerisation to give layer adhesion. The process is primarily intended for prototyping applications and has a 205 x 200 x 100 mm print volume and 100 μm resolution. Silicones were developed in collaboration with Momentive and have a hardness range of 30-60 Shore A. An antimicrobial silicone for medical prototyping was announced in 2019.

In 2019, German company RepRap launched the L320 silicone printer in collaboration with Dow Corning. It uses Liquid Additive Manufacturing (LAM), an extrusion process, where high viscosity liquid silicone rubber is thermally cured by a halogen lamp. The printer uses Dow Corning SILASTIC 3D 3335 2-part addition cure RTV, with 50A Shore hardness, 220-900 μm resolution, and 10-150 mm s^{-1} print rate.

San Draw, established 2014, produces full-colour silicone parts via a patented, extrusion-based technology called FAM: the acronym stands for either Fluid Additive Manufacturing or Full-colour, Adjustable-hardness, Multiple-materials. The company specialises in surgical simulation models and clinical training and provides a printing service. As of 2017, their FAM 3D printer offers layer thicknesses as low as 50 μm , multi-nozzle printheads with soluble support material, and a post-processing system for improved surface texture. In 2020, they released commercial printers, the San Draw S line, which offer 200-400 μm resolution printing of 1- and 2-part silicones.

Southern Methodist University has a patent pending for a similar full-colour extrusion printer (patent number US20180207863A1, submitted 2018). This method utilises thermal or UV curable silicones (including thiol-ene reagents) and is able to produce functionally-graded materials via a printhead containing a point-of-use, microfluidic mixing chamber.

PICSIMA by Fripp Design 2014 utilises a patented technique called Sub Surface Catalysation: catalyst is injected into a vat of unreacted 2-part RTV silicones via a syringe on an XY gantry. The company reported a range of Shore hardness down to 10A with 400 μm resolution. PICSIMA was notable for using commercial silicones rather than requiring in-house development of specialist materials to fit the printer; this allowed it to print facial prosthetics using materials already approved for medical use.

3Deus Dynamics, a spin-out company from Claude Bernard Lyon-1 University which launched in 2020, developed Dynamic Molding Technology for silicone printing. The printhead needle is immersed in a static powder bed and liquid silicone is injected into sugar or silica powder: the granular medium supports the printed part, analogous to other embedded-3D printing processes.

Vat photopolymerisation

Carbon3D produces M1 vat photopolymerisation printers (2015) which make use of a Continuous Liquid Interface Production (CLIP) process: an oxygen-permeable vat base is used to create a dead zone by inhibition of free radical photopolymerisation.³¹³ They offer a silicone-urethane resin Sil 30 with a Shore hardness of 35A.

SpectroPlast, a spin-off of ETH Zurich founded in 2018, is a 3D print service that manufactures silicone rubber parts via an undisclosed vat photopolymerisation process. They offer a range of silicones (TrueSil) with A20-A60 Shore hardness at 100 µm resolution.

Material jetting

In June 2015, Wacker announced the first commercial 3D printer for silicones and the first 3D-printable silicone elastomers. ACEO by Wacker uses material jetting valves with highly viscous, UV-curable silicones. They offer printable formulations with 400 µm resolution, 20-60A Shore hardness, and 200-800% elongation at break, as well as medical grade silicones. In 2018, ACEO printed conductive silicone composites and in 2019 they opened an Open Print Lab to interface with and offer training to customers. The ACEO Imagine Series K2 printer was announced in 2019 and is set to offer multi-material printing (four materials simultaneously) and novel automatic control technology (which measures silicone layers during printing and compares to the CAD file). In 2021, ACEO added a thermoset epoxy to its material portfolio which can be used to print composites with hard epoxy and soft silicone; this enables reinforcement of silicone parts.

Shortly after Wacker announced ACEO, in 2015 Keyence announced UV cure silicone inks for its AGILISTA 3200 inkjet printer: AR-G1L and AR-G1H are soft and hard silicone rubbers respectively, with 300 µm print resolution.

Summary

A range of commercial materials and processes for silicone exist, with typical resolutions of 200-400 μm (range 100-900 μm) and Shore hardness 20-60A (range 10-90A). Biomedical grade materials are available and enable prostheses and surgical models.

However, these processes have a limited range of materials: the vast majority of these use proprietary formulations. Current jetting and vat photopolymerisation processes require specialised UV cure silicones. All of the above processes use viscous materials, with the potential exceptions of PICSIMA and 3Deus Dynamics injection methods. Vat processes have limited multi-material capacity; jetting has great inherent capacity for multi-material and functionally-graded printing, and extrusion printers with multiple printheads and microfluidic mixers are becoming more common.

The capacity for advanced materials has not been fully explored. ACEO demonstrated jetting of a conductive silicone composite but reports of functional silicone printing materials are greatly limited as the focus so far has been on mechanical properties of elastomers. Expanding the material portfolio will further enable AM production of devices.

The following section describes silicone AM research. In academic literature, papers on direct AM of silicones begin around 2010. To date, the majority of research has been on dispersion-based material extrusion, followed by vat photopolymerisation-based processes; material jetting and powder bed fusion-based processes are also increasingly reported. Ligon *et al.* have written a review on all polymer AM processes,⁶⁶ while Liravi and Toyserkani³² and Herzberger *et al.*⁶⁷ have produced detailed reviews of silicone AM. An overview of the state-of-the-art is given below.

Material extrusion

Material extrusion of silicone is challenging due to its low elastic modulus and low surface energy, which lead to poor shape-retention. Fused filament fabrication (FFF) is not typically possible as silicones are thermoset, so there is only a single report of silicone FFF: printing of a thermoplastic containing >90% silicone was not successful.³¹⁴ In contrast, the other main material extrusion process - robocasting (RC) a.k.a. direct ink writing (DIW) - is the most common method of silicone 3DP. Research groups have successfully extruded silicones with commercial printers or with custom set-ups utilising pressurised dispensing systems; the latter is also known by the more descriptive acronym of pressure-assisted micro-syringe (PAM) printing within the field of pharmaceuticals. Such systems can handle a wide range of viscosities (up to 60 kPa s),³² which is advantageous as viscous prepolymers

better retain their shape and lead to better mechanical properties. Materials for RC/DIW require shear-thinning behaviour so that material behaves like a liquid in extrusion but has limited flow once deposited; fast reaction rates also aid 'solidification'. Extrusion-based silicone AM processes typically achieve 5-20 mm s⁻¹ print speeds with 200-400 μm XY resolution (dependent on nozzle diameter), with the notable exception of Udofia and Zhou who achieved XY resolutions of 10 μm (the highest to date).³¹⁵

In earlier papers, there is a roughly equal split between 1-part condensation cure RTVs^{96,97,302,316-319} and 2-part addition cure RTVs. Condensation cure has some significant disadvantages in comparison to addition cure in that reaction is slower, which does not aid shape-retention, and there is shrinkage from the release of by-products; however, commercial caulks which contain fillers are easy-to-use, low-cost, thixotropic silicones. Dow Corning SE 1700, a commercial addition cure silicone with the correct rheological properties for RC/DIW, has been widely investigated⁶⁷ and vinyl-terminated silicone formulations currently dominate literature. Photopolymerisable reactions have been increasingly utilised for rapid, controlled curing, using commercial UV-curable silicones,^{69,92,304,320,321} thiol-ene mechanisms,^{295,296} and mixed moisture/UV cure systems.^{69,302-304} 1-part extrusion mixtures are typically prepared, regardless of whether they are based on 1-part or 2-part RTVs, as printing a single material is simpler than the deposition of two reagents; however, this limits the working-life. Researchers have mitigated pot-life issues with the use of modifiers to slow reaction^{79,312,322,323} or by using a mixing printhead,^{103,296,324-327} the latter of which has the advantage of in process control over mix ratios of formulations which enables functionally-graded materials.

While high molecular weight PDMS fluids (where MW>M_c, 21000-33000 g mol⁻¹)⁵³ have intrinsic pseudoplastic behaviour due to chain entanglement,¹⁷ strategies for greater rheological control are used to improve resolution. Solvents, thinning agents,^{79,103,304,322,325} and thickening agents^{79,322,323} have been used to control rheology. A variety of polymeric additives and blends have been used to control rheology: Robinson *et al.* used a mixture of high and low MW silicones to achieve shear-thinning behaviour and rapid crosslinking.³⁰² Durban *et al.* tuned the stiffness of silicones by varying the proportion of pendant phenyl groups to control crystallinity and varying MW to control crosslinking density.³¹² Lipton *et al.* controlled rheology and other physical properties through the use of paraffin wax to

produce a thermo-actuator.³¹⁷ Courtial *et al.* used polyethylene glycol (PEG) additives to modify the rheology of printable silicones.³²⁸

Printable composites are also known, and a variety of fillers are used with silicones. Shear-thinning behaviour is frequently incorporated into silicones by adding fumed silica,^{295,312} a common reinforcing filler in silicones; silica NPs give Dow Corning SE 1700 properties ideal for RC/DIW, and work has been carried out by varying the silica loading using blends of commercial silicone formulations.^{103,312,329,330} Zheng *et al.* achieved the highest elongation to date (2000%) using thiol-ene precursors and 0-2 wt% silica.²⁹⁶ However, silica reduces the transparency of silicones, and leads to creep hardening if particles have not undergone hydrophobic surface-treatment.^{17,67} Roh *et al.* introduced a novel approach: using capillary forces to control rheology in water-based inks containing addition cure silicones and PDMS microbeads.³³¹ Zheng *et al.* presented poly(tetrafluoroethylene) (PTFE) micropowder as a novel thixotropic agent.³³² Carbon black (CB),^{92,93} carbon nanotubes (CNTs),^{94,95} and silver nanoparticles (NPs)^{79,96,97} are added for various specific applications. It is challenging to obtain good resolution without the addition of fillers that reduce transparency.

To address these challenges, novel processes which involve extrusion into a vat of material as support have been investigated by several groups. Embedded-3DP (e-3DP), in which material is extruded into an elastomeric reservoir, was used to print a conductive elastomer into a non-conductive elastomer reservoir; upon curing, a strain sensor with encapsulated wire tracks was produced.³²² Later, multi-material e-3DP was used to fabricate somatosensitive actuators.³²³ Extrusion into inert baths has also been investigated as a route to printed soft materials, a process called freeform reversible embedding (FRE).^{303,333,334} Bingham plastics or microgels act as support and are easily removed post-processing; the low stress requirement limits this to low viscosity silicones (3-4 Pa s) and lack of pressure may prevent adhesion in the XY direction.³² Abdollahi *et al.* and Menon *et al.* present parameter optimisation strategies to enable better printing of silicones via FRE.^{335,336}

Table 51: Direct additive manufacturing of bulk silicones and silicone composites via material extrusion in academic research.

<i>Paper</i>	<i>AM category</i>	<i>Application</i>	<i>Printer set-up</i>	<i>Silicone</i>	<i>Resolution</i>
Calcagnile <i>et al.</i> 2018 ³¹⁴	Material extrusion (fused filament fabrication, FFF)	Surgical models	TIPS 3DPRN LAB 3D printer, 400 μm tip Filament prepared by melt with twin-screw extruder (1750 μm filament diameter)	Wacker Geniomer 145 Thermoplastic (>90% siloxane) PDMS-only filaments or PDMS and 10 wt% Aqualon carboxymethylcellulose	Controlled printing was not achieved
Periard <i>et al.</i> 2007 ⁹⁶	Material extrusion (robocasting, RC, a.k.a. direct ink writing, DIW)	Embedded circuits	Fab@Home, 1270 μm diameter dispensing tip	Silicone Solutions 26F 1-part, AgNP-filled RTV; GE Silicone II 1-part RTV sealant; and 3M DP460NS 2-part epoxy	1.2mm X 0.8mm conductive ink
Symes <i>et al.</i> 2012 ³¹⁶	Material extrusion (RC/DIW)	Reaction vessels	Fab@Home, 838 μm diameter dispensing tip	Loctite 5366 1-part RTV	Unknown; 838 μm nozzle $\pm 5\%$ accuracy
Mannoor <i>et al.</i> 2013 ⁹⁷	Material extrusion (RC/DIW)	Bioprinting, auditory sensors	Fab@Home	Silicone Solutions 1-part AgNP-filled RTV; 3M 1-part RTV	Unknown
Kolesky <i>et al.</i> 2013 ³³⁷	Material extrusion (RC/DIW)	Bioprinting of vascular tissues	Nordson 800 Ultra dispenser, 200 μm tip diameter	Dow Corning SE 1700 2-part addition cure RTV Cured 1 hour, 80 $^{\circ}\text{C}$	Unknown; 200 μm nozzle diameter
Tegtmeier <i>et al.</i> 2014 ⁹⁴	Material extrusion (RC/DIW)	Conductive CNT-silicone electrode contacts for cochlear implants	Linear actuator controlled by electronic prototyping platform with nano-compounder (syringe, motor, helically ground wire) 610 μm nozzle	Dow Corning Sylgard 184 or Wacker RT 601 2-part addition cure RTVs, both with 7.5, 10, or 12.5% multi-walled CNTs (Baytubes C150P) Cured at 50 $^{\circ}\text{C}$ for 24 hr (Sylgard 184) or 70 $^{\circ}\text{C}$ for 20 min (RT601)	610 μm nozzle diameter Layer thickness 54 \pm 3.5 μm Flow rate 1.7-3.4 $\text{mm}^2 \text{min}^{-1}$

Duoss <i>et al.</i> 2014 ³²⁹	Material extrusion (RC/DIW)	Cellular architectures with negative stiffness	Nordson Ultimius IV 2800–30 dispenser, 610 μm diameter tip	Dow Corning SE 1700 2-part RTV (100-70%); Gelest DMS-V21 and HMS-082 as reagents without fumed silica Cured 1 hour, 150 °C	Features on par with nozzle diameter (610 μm); Unsupported features ≥ 2 cm
Lipton <i>et al.</i> 2014 ³¹⁷	Material extrusion (RC/DIW)	Wax-based soft actuators	Fab@Home, 18 gauge (838 μm) tips	Dow Corning 737 1-part RTV; Smooth-On Ecoflex 00-50 2-part addition cure RTV with paraffin wax	Unknown; 18 gauge tip (838 μm)
Hardin <i>et al.</i> 2015 ¹⁰³	Material extrusion (RC/DIW)	Multi-material microfluidic printhead	Custom multi-material printhead with microfluidic junction (nozzle diameter 400 μm)	Dow Corning SE 1700 2-part addition cure RTV; Anhydrous hexanes and silicone oil diluents; Smooth-On Red Silc Pig and CdSe/ZnS QDs for colour	≤ 420 μm ; seemingly on par with 400 μm diameter
Jin <i>et al.</i> 2015 ³¹⁹	Material extrusion (RC/DIW)	Process optimisation	Nordson Performus III dispenser, 410, 610, 840 and 1190 μm tips	Dow Corning 890-SL 1-part moisture cure RTV	Line width and height 840 μm , 25 mms^{-1} ; width 720 μm 30 mms^{-1}
Johnson <i>et al.</i> 2015 ³¹⁸	Material extrusion (RC/DIW)	Bioprinting	Fisner robotic dispenser, 108-210 μm tips	Loctite Superflex Clear 1-part RTV	Unknown; 27-32 gauge tips (108-210 μm)
Robinson <i>et al.</i> 2015 ³⁰²	Material extrusion (UV RC/DIW)	Elastic capacitive sensors	Custom dual-head printer, UV lamp Omnicure S1500, 330 and 250 μm tips	60 wt% Nuvasil Loctite 5039 1-part RTV, 40 wt% Wacker Semicosil 912 2-part addition cure RTV; Wacker Elastosil CAT UV	Unknown; 330 and 250 μm diameter tips
Tian <i>et al.</i> 2017 ³²⁰	Material extrusion (UV RC/DIW)	Stretchable electronic devices	KIMM SPS1000 Bioplotter with BlueWave 75 v2 UV lamp; 337 μm tip	Shin-Etsu KER-4690 2-part addition cure RTV 30 min UV cure (365 nm) and overnight bake (65 °C)	Unknown; sub millimeter

Lv <i>et al.</i> 2017 ³³⁸	Material extrusion (RC/DIW)	Superhydrophobic porous membrane	3-axis platform and Techcon TS500R screw-driven dispenser with 150 µm nozzles	Dow Corning Sylgard 184 3-butyn-1-ol (inhibitor) Thixotropic agent 0-20 wt% hydrophobic silica nanoparticles (20 nm) Post-cured at 120 °C for 1 h	800 µm typical layer height 370 µm pore RSM surface roughness 7-12 nm
Guo <i>et al.</i> 2017 ⁷⁹	Material extrusion (RC/DIW)	Stretchable tactile sensors	Aerotech AGS 1000 cartesian gantry and four dispensing apparatus (HP7x, Nordson) with 100 µm diameter nozzles	Smooth-On Dragon Skin 10 Slow (2-part addition cure RTV) with 0, 68, 75 and 80 wt% AgNPs. Rheology optimised using dichloromethane solvent and Thivex and Slo-Jo from Smooth-On	Unknown but ≤150 µm; 100 µm diameter nozzles
Roh <i>et al.</i> 2017 ³³¹	Material extrusion (RC/DIW)	Multiphase silicone/water capillary inks	Nordson Ultimius V dispenser with 22 gauge tips (413 µm diameter)	Dow Corning Sylgard 184 2-part addition cure RTV 10 µm PDMS microbeads, 2-30 vol% uncured PDMS, water Cured for 2 hours at 85 °C	Unknown. 10 µm CNC resolution; 413 µm nozzle diameter; cured filaments on the order of 300 µm
Wei <i>et al.</i> 2017 ⁹⁵	Material extrusion (RC/DIW)	Stretchable electrodes	Custom-built printer, 400 µm diameter nozzle	Dow Corning Sylgard 184 2-part addition cure RTV; Multi-walled carbon nanotubes (MWCNTs) Cured for 2 hours at 70 °C	400 µm nozzle diameter and resolution, 800 µm layer thickness
Plott <i>et al.</i> 2017 ³³⁹	Material extrusion (RC/DIW)	Print optimisation, pneumatic actuators	Modified commercial Lulzbot Taz 5 with Viscotec preflow eco-PEN 450 pump, 18-22 gauge tips	Dow Corning 737 1-part RTV	410 µm nozzle and 205 µm layer height, 489 µm spacing to fill voids

Durban <i>et al.</i> 2018 ³¹²	Material extrusion (RC/DIW)	3D printing formulations for tunable stiffness	Aerotech A3200 motion controller with Nordson Ultra 2800 dispenser and 250 µm nozzle diameter	Vinyl-terminated PDMS-co-PDPS; hexamethyldisilazane-treated (HMDZ) silica reinforcing filler; Karstedt catalyst; ETCH inhibitor Post cure 150 °C, 12-16 hr	Feature resolution 250 µm
Qiu <i>et al.</i> 2018 ³⁴⁰	Material extrusion (RC/DIW)	Prostate model with integrated sensors	Aerotech AGS 100 linear stage and two Nordson Ultimius V dispensers with 610 µm nozzle diameter, 500 µm layer height	Various ratios of Loctite SI 595 CL 1-part RTV with Trident LP20 silicone grease bulking agent, fumed silica (7 nm), and ICI Procyinyl Red GS colour. Two support ink formulae: unadulterated Loctite RTV, or 33 wt% Pluronic F127 in water as soluble support	Unknown; 610 µm nozzle diameter, 500 µm layer height 98% fidelity to STL file
Ozolat <i>et al.</i> 2018 ³³⁰	Material extrusion (RC/DIW)	Printability analysis; bioprinting	INKREDIBLE 3D bioprinter (Cellink), with 610, 510 and 410 µm deposition tips (Nordson).	Various mixing ratios of Dow Corning SE 1700 and Sylgard 184 2-part addition cure RTVs Cured at 80 °C	Line width <400 µm 78.45% fidelity to STL (±100µm) Mean deviation 189 µm
Liravi <i>et al.</i> 2018 ⁶⁹	Hybrid (material jetting and extrusion (RC/DIW))	Print optimisation	Three piezo-pneumatic jetting printheads (Pico Pulse, Nordson); two extrusion printheads (xQR41 MicroDot and Optimeter, Nordson); 365 nm UV lamp	Novagard RTV 800-400 with 3 wt% Omnirad 1173 photoinitiator Dual UV/moisture curing mechanism	320 µm line width 3 µm surface waviness Wq

Jindal <i>et al.</i> 2018 ³²⁴	Material extrusion (RC/DIW)	Maxillofacial prostheses	Custom, patented: XYZ gantry, two syringes and pumps, mixing chamber, 500 μm nozzle diameter	Base α,ω -vinyl PDMS: 70-80 wt% V46, 15-20 wt% V31, 5-10 wt% V21, Gelest; Pt catalyst (5 wt% in A); Crosslinker (Gelest HMS-301, 10 wt% in B); Inhibitors and thickeners; 20 wt% hydrophobic silica	Unknown; 500 μm nozzle diameter 10 mm s ⁻¹ print speed
Schaffner <i>et al.</i> 2018 ²⁹⁵	Material extrusion (RC/DIW)	Soft robotic actuators	regenHU 3D Discovery printer with 580 or 410 μm nozzle diameter	Smooth-On EcoFlex 00-30A and DragonSkin 30A; Dow Corning Sylgard 184; Gelest Q resin. Low MW thiol crosslinker, vinyl-terminated silicones, Omnirad 184, fumed silicas (H18 and V15, Wacker). 60 s UV cure under N ₂	Print resolution accuracy 300 μm Layer thickness is ~400 μm
Porter <i>et al.</i> 2018 ⁹²	Material extrusion (RC/DIW)	Carbon black to eliminate static between PDMS and nozzle	XY gantry, Z stage, linear step motors, hydraulic cylinder and pneumatic valve, Dymax Bluewave 200 UV light, 250 μm tip	Momentive Silopren UV 2030 or UV Electro 225-1, each with 0 or 0.15 wt% carbon black	Layer height 250 μm Extrudate width 500 μm
Kim <i>et al.</i> 2018 ³⁴¹	Material extrusion (RC/DIW)	Ferromagnetic, fast-transforming soft materials	Aerotech AGS1000 gantry, dispenser, magnetic field applied to nozzle, 50, 100, 200, 410 μm nozzle diameters	21.78 wt% Smooth-On Ecoflex 00-30B, 11.71 wt% Dow Corning SE 1700A, 1.17 wt% SE 1700B, 2.72 wt% fumed silica, and 62.62 wt% NdFeB. Support Wacker Elastosil CAT PT-F with fumed silica. Post-cured at 120 °C for 1 h	80-410 μm line width

Holländer <i>et al.</i> 2018 ³²¹	Material extrusion (RC/DIW)	Drug delivery devices	BioBots 1 desktop bioprinter, MTE UV303 365 nm light, 514 µm nozzle	Momentive Silopren 2030 UV LSR 0.0–1.5% prednisolone; up to 10% is possible with viscosity modifiers	Line width approximately 800-900 µm in finest grid 1 mm s ⁻¹
Udofia and Zhou 2018 ³¹⁵	Material extrusion (RC/DIW)	Microscale PDMS patterning	Custom: gantry, dispenser, 10 µm nozzle diameter	Dow Corning Sylgard 184 2-part addition cure RTV	10-15 µm line width 0.126 µm s ⁻¹
Zheng <i>et al.</i> 2018 ²⁹⁶	Material extrusion (RC/DIW)	Multiple modulus silicones from low viscosity precursors	Modified UNI-PRINT-3D printer, pump, custom multi-material printhead, 260-410 µm nozzles, Omnicure S1000 lamp, 150-350 µm layer spacing	Mercaptopropyl-PDMS and α, ω-vinyl PDMS (Gelest: SMS-142, SMS-022, DMS-V21, DMS-V31, DMS-V35), 0-2 wt% silica NPs (Aerosil) D ₅ silicone oil 10 mol% Omnirad TPO-L	≤70° overhang Shape holding within <2 s, full cure in <20 s Line width 300 µm, height 150-350 µm 12.7 µL s ⁻¹
Walker <i>et al.</i> 2019 ³²⁵	Material extrusion (RC/DIW)	Printability optimisation	Modified commercial Lulzbot Taz 6, custom mixing extruder with 335 µm tip diameter	87.3% Dragon Skin 10 Very Fast, 0.98% Thi-Vex, 9.8% Silicone Thinner, and 1.96% Silc-Pig dye (all Smooth-On)	335–500 µm
Zhou <i>et al.</i> 2019 ³²⁶	Material extrusion (RC/DIW)	Prosthetics, soft actuators, flexible electronics	EFL-BP6600 3D printer, digital pneumatic regulator, mixing printhead for 2-part silicones, 260, 330, and 410 µm nozzle	Commercial low viscosity 2-part addition cure RTV with typical 0, 4, and 8wt % hydrophobic silica NPs Post-cured at 80 °C, 30 min Various other formulations with commercial silicones	260 µm nozzle: 240 µm line width, 13 mm s ⁻¹ 410 µm nozzle: 360 µm line width, 22 mm s ⁻¹
Courtial <i>et al.</i> 2019 ³²⁸	Material extrusion (RC/DIW)	Rheological modifier for silicone 3DP	Tobeca COSMED 333 cartesian 3D printer with Nordson Ultimius V dispenser and 400 µm nozzles	Elkem Silbione LSR 4350 2-part addition cure RTV with polyethylene glycol Two-step thermal cure: ambient for 72 hr then 175 °C for 120 min	Unknown; 400 µm nozzle diameter, <5% XY deviation, <12% Z with 5° overhang

Porter <i>et al.</i> 2020 ⁹³	Material extrusion (RC/DIW)	IR laser curing for medical grade silicones	Miniature ram extruder (500 μm extrudate width), heated build platform, Innolume 1064 nm infrared laser with collimator and lens (1000 μm spot size)	NuSil MED4930 2-part addition RTV with 0.5 or 0.75 wt% NuSil MED1-4900-2 carbon black-based IR-absorbing dye	500 μm width extrudate, layer height 100, 175 or 250 μm ; raster spacing 262 or 562 μm . Tolerances of -2.9-3.1% in X (bulk -2.7%) and 0.98-1.4% in Y (bulk 0.55%)
Luis <i>et al.</i> 2020 ³⁴²	Material extrusion (RC/DIW)	Meniscus implants	Open-source CoreXY printer with syringe-extruder, 20-21 gauge tips (510-600 μm diameter), nozzle heating	Smooth-On EcoFlex 00-30 and 00-50 2-part addition cure RTV	Unknown; on the order of nozzle diameter $\leq 600 \mu\text{m}$ 1.2 mL min ⁻¹ 20 mm s ⁻¹
Thomas <i>et al.</i> 2020 ³⁴³	Material extrusion (RC/DIW)	Cardiac patches	Hyrel-System 30M with high torque printhead (VCD 400), 840 μm nozzle diameter	SILASEAL Professional Grade 100% RTV 1-part RTV Extraction with ethanol, plasma cleaned, silanised	350 μm layer thickness 100-200 μm pore size
Behrens <i>et al.</i> 2020 ³²⁷	Material extrusion (RC/DIW)	Biocompatible neural devices	Arduino-controlled XY gantry and step motor, platen heaters, Nordson Equalizer-2K dispensing system with static mixer, 250 μm nozzle diameter ULR-25 9.3 μm laser	Wacker Silpuran 2430 2-part addition cure RTV Post-cured 150 °C, 15 min Polyimide substrate	Min line width 447 \pm 10.7 μm Min line height 30.6 \pm 7.4 μm

Zheng <i>et al.</i> 2020 ³²²	Material extrusion (RC/DIW)	Triboelectric Nanogenerator	Syringe with compressed air, 260 and 610 μm nozzle diameters	Dow Corning Sylgard 527 2-part addition cure RTV 55 wt% PTFE micropowder Post-cure at 125 $^{\circ}\text{C}$, 75 min	270 μm XY 370 μm Z 36 μm surface waviness
Muth <i>et al.</i> 2014 ³²²	Material extrusion (embedded-3DP (e-3DP))	Strain sensors	Aerotech ABG 10000 gantry, extrusion under pressure through 410 μm nozzle (Nordson)	Smooth-On Ecoflex 00-30 2-part addition cure RTV Rheology optimised using Thivex, Slo-Jo and Thinner from Smooth-On	710 \pm 50 μm to 66 \pm 10 μm
Truby <i>et al.</i> 2018 ³²³	Material extrusion (e-3DP)	Soft somatosensitive actuators	Aerotech ABG 10000 gantry, Nordson 800 Ultra dispensing system	Smooth-On Ecoflex 00-30, Ecoflex 00-10, and SortaClear 40, all 2-part addition cure RTVs Rheology optimised using Thivex and Slo-Jo	Unknown
Bhattacharjee <i>et al.</i> 2015 ³³³	Material extrusion (Freeform Reversible Embedding (FRE))	3D printing of soft materials in granular gel media	Physik Instrumente stage and syringe pump with 50 μm silanised glass injection tips	Dow Corning Sylgard 184 2-part addition cure RTV with 0.1 w/v fluorescent polystyrene microspheres; Printed into Dow Corning 9041, 10 wt% in silicone oil	50 μm nozzle diameter
Hinton <i>et al.</i> 2016 ³³⁴	Material extrusion (FRE)	3D printing of PDMS in hydrophilic support bath	MakerBot Replicator with custom syringe pump extruder via 400 μm diameter stainless steel needle	Dow Corning Sylgard 184 2-part addition cure RTV Cured 2-8 hours, 65 $^{\circ}\text{C}$ Printed into Carbopol support bath, 0.7-1.2% w/v	140 μm \pm 10% XY 100 μm layer height 20 mm s^{-1}
O'Bryan <i>et al.</i> 2017 ³⁰³	Material extrusion (FRE)	3D printing of PDMS in self-assembled microgel support	Newport stage with Physik Instrumente syringe pump, glass needles (diameter 150-1000 μm)	Smooth-On Mold Max 10 2-part moisture cure RTV; Dow Corning Sylgard 184; Momentive UV Electro 225 Printed into self-assembled nonpolar microgels	450 μm ; 250 μm collapses upon support removal 30 μm for high viscosity inks 150 nm surface waviness

Abdollahi <i>et al.</i> 2018 ³³⁵	Material extrusion (FRE)	Expert-guided optimisation (EGO) of print parameters; printable pulse oximeters	MakerBot Replicator with custom syringe pump extruder with various diameter needles	Dow Corning Sylgard 184 2-part addition cure RTV Cured at 65 °C overnight Printed into Carbopol 940 support bath (0.2% w/v)	Average surface deviation $\pm 500 \mu\text{m}$
Menon <i>et al.</i> 2019 ³³⁶	Material extrusion (FRE)	Print optimisation using hierarchical machine learning	MakerBot Replicator with custom syringe pump extruder with various diameter needles	Dow Corning 3-4241 and Sylgard 567 2-part addition cure RTVs Printed into support bath, 1% w/v polymer (Carbopol 934, 940, 941, 974, 1342, ETD 2020 and Ultrez 10, and Pemulen 1621)	2.5 faster print speed with fidelity retained
Greenwood <i>et al.</i> 2021 ³⁰⁴	Material extrusion (FRE)	Vocal fold models	3-axis CNC mill with custom extruder, 260 μm diameter nozzles, 260 μm layer height	Momentive UV Electro 225-1 (15:1 base:catalyst ratio by weight) with Smooth-On thinner (1:3 UV-silicone:thinner ratio); Smooth-On Ecoflex 00-30; Dow Corning Sylgard 184. Extruded into a Smooth-On Thinner support matrix with 3 wt% fumed silica	250-1000 μm larger than specified in STL file

Vat photopolymerisation

It is challenging to obtain high resolution elastomers by vat photopolymerisation (VP): the typical materials are methacrylates, which meet the requirements for rapid gelation but produce hard polymers with high crosslinking density. However, vat photopolymerisation of silicones is challenged by low spatial resolution which arises from its long curing times and low surface energy. Additionally, dark-photopolymerisation is a particular issue in PDMS due to its low glass transition temperature.³¹⁰

Free radical chain growth polymerisation with vinyl and/or acrylate functionalised PDMS is the most commonly used mechanism. However, the high oxygen-permeability of silicones leads to cure inhibition of free radical photoinitiators. Thiol-ene reactions do not require inert atmospheres and are commonly utilised^{270,297-300} but have limited pot-life. Modifiers including sensitisers,^{270,300,310,344} UV blockers,³⁴⁵ and oxygen scavengers³⁴⁶ are used to control reaction rate and/or free radical concentration, although sensitisers sacrifice optical clarity. Combination moisture/UV formulations are also seen.³⁰⁰ Coenjarts *et al.* utilised an unusual method – one initiator photo-decomposed into an active platinum catalyst upon excitation, enabling UV-initiated hydrosilylation.³⁴⁷ Recently, Abdallah *et al.* have demonstrated the first 3D printing of silicones by cationic photopolymerisation: silicone epoxy was cured in air using various coumarins as sensitisers for the 405 nm laser diode.³⁰¹

Stereolithography (SLA) and digital light processing (DLP) are the most widely used VP processes in silicone AM, though top-down SLA printers are not seen in literature; this may be because bottom-up SLA printers are both cheaper than top-down and have less issues with oxygen inhibition as the build layer is not at the air-resin interface.⁶⁶ In literature of silicone AM, DLP is strongly favoured over SLA systems, likely due to their lower cost and the uniform exposure that projection-based systems offer: cure rate is height-dependant and planar objects (such as microfluidic or electronic devices) do not have longer printing times.⁶⁶ One challenge in bottom-up vat photopolymerisation is strong adhesion between the cured polymer and the vat base: silicones have low surface energies and are highly effective at wetting surfaces and therefore the vat base may require silane treatment to produce suitably non-stick interfaces. One strategy to tackle this is the creation of 'dead zones' – areas where photopolymerisation does not occur - at the interface by utilising oxygen inhibition of free radicals (CLIP process)³¹³ or establishing an optically-created dead zone.³⁴⁶

The low storage modulus of silicones may result in elastomers which are not robust enough to survive the printing process and support structures are often required.⁶⁷ Typical viscosity

limitations of vat photopolymerisation processes ($<5 \text{ Pa s}$)^{32,66} make higher storage moduli and other mechanical properties difficult to achieve in cured polymers: silicones with longer chain length lead to stronger, stretchable elastomers but have much higher viscosity.^{17,57} Serrine *et al.* used simultaneous chain extension to by-pass viscosity limits: shorter polymers react together to give a greater chain length in crosslinks.²⁹⁸ Wallin *et al.* recently presented an orthogonal crosslinking method, where thiol-ene and condensation reactions produced silicone double networks.³⁰⁰ Silica filler cannot typically be used to reinforce silicone elastomers as it reduces transparency and greatly increases viscosity,^{17,67} Zhao *et al.* used 0-20 wt% silica in thiol-ene silicone resin and achieved the highest elongation seen so far for VP-printed silicones (1400%), but this necessitated the use of a printer designed for ceramic slurries.²⁹⁹

Two photon polymerisation (2PP) has been explored for the production of microfluidics using vinyl-functionalised PDMS precursors which can react by hydrosilylation or free radical mechanisms; these silicones are biocompatible, unlike the acrylate-functionalised photopolymers typically used in 2PP.^{344,347-349} The utility of this process is limited by low throughput, though throughput is improving. Low one photon polymerisation (LOPP) has been demonstrated for hydrostatic 3D printing: this penetrates into the resin to cure at focused spots within vat reservoir, eliminating the need for a moveable build platform.^{346,350} While current resolution (500-2000 μm) and scan rate (1.2 mm min^{-1} , increased from 0.5 mm min^{-1} in first report) are poorer than other VP processes of silicone, this process confers some key advantages over SLA/DLP. The lack of build substrate and therefore flow in the vat eradicates issues associated with adhesion to the vat base and other forces. Both weaker and stronger elastomers are enabled as there are less forces to damage soft materials and the viscosity limit of the vat polymer is raised, as flow is not required to replace the previous layer. However, the cure time was long (over 100 s), although shape retention is aided by the higher resin viscosity limit, and the authors note that a stronger light source is needed. Silicone LOPP is a nascent technology but the advantages it offers are promising, if the process can be further optimised.

Table 52: Direct additive manufacturing of bulk silicones via vat photopolymerisation in academic research.

<i>Paper</i>	<i>AM category</i>	<i>Application</i>	<i>Printer set-up</i>	<i>Silicone</i>	<i>Resolution</i>
Coenjarts <i>et al.</i> 2004 ³⁴⁷	Vat photo polymerisation (2PP femtosecond direct laser writing (FsDLW))	Microfluidics	Olympus IX70 microscope, Ti:sapphire laser, motorised mirrors and stage	Dow Corning Sylgard 184 2-part addition cure RTV with 0.7 wt% Pt catalyst or 0.4 wt% radical photoinitiator	350 nm for Pt cure, 0.3-0.6 μm for radical $\sim 12 \mu\text{m}^3 \text{s}^{-1}$ throughput
Hasegawa <i>et al.</i> 2006 ³⁴⁸	Vat photo polymerisation (2PP FsDLW)	Microfluidics micro-rotors	CCD camera, Ti:sapphire laser, motorised mirrors and stage	Dow Corning Sylgard 184 2-part addition cure RTV 0.4 wt% radical photoinitiator	350 nm width, 750 nm depth, $\sim 12 \mu\text{m}^3 \text{s}^{-1}$ throughput
Rekštytė <i>et al.</i> 2013 ³⁴⁹	Vat photo polymerisation (2PP FsDLW)	Bio-compatible scaffolds	Pharos laser with galvanometric scanner and sample positioning system, or Ti:sapphire laser with galvano-mirror scanner and motors	Dow Corning Sylgard 184 2-part addition cure RTV 0-1 wt% various photoinitiators	Up to 5 μm with $720 \mu\text{m}^3 \text{s}^{-1}$ throughput
Lu <i>et al.</i> 2015 ³⁴⁴	Vat photo polymerisation (2PP FsDLW)	Microfluidics microlens	Piezo stage with galvano-mirror pair, Ti:sapphire laser	PDMS prepolymer with 0.1 wt% photosensitiser	Unknown; 200 nm focal diameter
Obata <i>et al.</i> 2017 ³⁵¹	Vat photo polymerisation (2PP DLW)	Direct laser writing of PDMS	Zouk Cobalt AB continuous laser (355 nm), galvano-mirror scanner, and linear piezo stage	Shin-Etsu KER-4690 2-part addition cure RTV Post-cured at 50 °C, 10 min Solvent extraction with tetrahydrofuran	18 μm line width 1 cm/s scan speed
Kim <i>et al.</i> 2016 ³⁵⁰	Vat photo polymerisation (LOPP hydrostatic 3DP)	Low 1PP (LOPP) for hydrostatic 3DP of silicone	UV lamp, optical lens array, 3-axis CNC stage (Moog Animatics)	Dow Corning non-commercial 2-part UV curable silicone Resin and photoinitiator	Estimated 500 μm voxel diameter, 0.5 mm min ⁻¹

Kim <i>et al.</i> 2019 ³⁴⁶	Vat photo polymerisation (LOPP hydrostatic 3DP)	Optical dead zones for reduced vat adhesion	375 and 385 nm LEDs, lens array, 3-axis CNC stage (Moog Animatics)	Synthesised α , ω -methacrylate PDMS Omnirad 1173 0.1 wt% <i>n</i> -vinyl pyrrolidone oxygen scavenger	Unknown. 1100 μm beam diameter >100 s to cure 1.2 mm min ⁻¹
Xiang <i>et al.</i> 2019 ²⁹⁷	Vat photo polymerisation (stereolithography (SLA))	3D printable biocompatible polymers	Formlabs Form 2 SLA printer; samples rinsed with ethanol and post-cured in an Intelli-Ray 400 UV Curing System 5min	Mercaptopropyl-functionalised PDMS with α , ω -vinyl PDMS, 4.4 and 46.5 kg mol ⁻¹ (1:1.25 ratio), thiol:ene ratio 1.5:1; 0.5 wt% Omnirad 819 photoinitiator	Unknown. Spot size 140 μm , layer thickness 50 μm
Abdallah <i>et al.</i> 2020 ³⁰¹	Vat photo polymerisation (SLA; initial DLW experiments)	Cationic polymerisation of silicone epoxies for 3DP	405 nm computer-controlled laser diode, spot size 50 μm	Elkem Silcolease UV POLY 200 silicone-epoxy 0.018-0.05% wt% coumarin sensitisers (commercial and synthesised) 0.36-1.0 wt% Lambson SpeedCure 939 initiator	50 μm XY, 1320 μm minimum print height reported <60 s cure
Femmer <i>et al.</i> 2014 ³¹⁰	Vat photo polymerisation (digital light processing (DLP))	Gas-liquid-contacting membrane with Schwartz-P geometry	Perfactory Mini Multi Lens, EnvisionTEC (440 nm lamp) 30 \times 30 μm pixel, 100 μm thick voxel	97.95 wt% (7-9 mol% methacryloxypropyl methylsiloxane)-PDMS copolymer with 2 wt% Omnirad TPO-L and 0.05 wt% Orasol Orange	150 μm lateral, 100 μm features 12 s cure
Wallin <i>et al.</i> 2017 ²⁷⁰	Vat photo polymerisation (DLP)	Soft robotics with self-healing elastomer	Autodesk Ember DLP printer (405 nm) 100 μm layer height	Mercaptopropyl-modified PDMS (2-6 wt% pendant thiol) with α , ω -divinyl PDMS, various MWs; 1 wt% Omnirad 819; Sudan I sensitiser	50 μm in plane, 175 μm Z axis

Thrasher <i>et al.</i> 2017 ³⁵²	Vat photo polymerisation (DLP)	Soft robotics, soft pneumatic gripper	SeeMeCNC Droplit DLP 3D Printer and an Acer X1161P projector 100 µm layer height	α, ω-propylacrylamide PDMS synthesised from Gelest DMS-A21 Two formulations: 95% PDMS, 5% toluene; 89% acrylate monomers, 9% PDMS, 2% cetrimonium bromide surfactant (2%). Both 0.25wt% Omnirad 819	Unknown; layer height 100 µm
In <i>et al.</i> 2017 ³⁵³	Vat photo polymerisation (DLP)	Medical phantoms	Characterised material but did not carry out print trials	Momentive UV Electro 225 and UV LSR catalyst with Smooth-On thinner (2:1 ratio); and Smooth-On hydrophilic silicone (10, 20 vol%) and deionised water (0-20 vol%)	Did not carry out print trials 20 s cure
Bhattacharjee <i>et al.</i> 2018 ³⁴⁵	Vat photo polymerisation (DLP)	Cytocompatible microfluidics	ILIOS HD kit printer with Wintech PRO4500 projector (385 nm), 52 µm pixel width, 50 µm layer height used	Commercially-available methacryloxypropyl-functionalised PDMS, different ratios of pendant to terminal groups; 0.6% Omnirad TPO-L; 0.3% UV blocker (isopropylthioxanthone, ITX); Overnight solvent extraction	250 µm lines (gaps below 200 µm are unresolved, but individual 50 µm pixels observed) Z resolution approximately 100-200 µm
Sirrine <i>et al.</i> 2018 ²⁹⁸	Vat photo polymerisation (DLP)	Simultaneous chain extension and crosslinking for SLA	Texas Instruments DLP 0.55 XGA DMD with BlueWave 75 UV spot curing lamp	α,ω-dithiol PDMS and α,ω-diacrylamide PDMS, various MWs 0.5 wt% Omnirad 819 with chloroform solvent	150 µm layer thickness

Zhao <i>et al.</i> 2019 ²⁹⁹	Vat photo polymerisation (DLP)	Stretchable electronics	Spaceworks DLP ceramic 3D printer (405 nm); 50 μm pixel DLP chip; layer thickness 100 μm	Branched mercaptan-PDMS (synthesised) with α,ω -divinyl PDMS (4.3 and 22 kg mol^{-1} , 0:1 or 3:1 ratios); 0-20 wt% reinforcing silica fillers (6-12 nm or 6-10 μm) 0.8-1.0 wt% Omnirad 1173 and/or 819	Unknown; layer height 100 μm , 50 μm pixel
Wallin <i>et al.</i> 2020 ³⁰⁰	Vat photo polymerisation (DLP)	Soft robotics, wearable electronics	Autodesk Ember DLP printer (405 nm) 50 μm pixel width	2-part moisture cure RTV (Reynold's Advanced Materials MM10T, MM14NV, MM29NV, or MM40) mixed with 61.7 wt% α, ω -vinyl PDMS (6000 kDa), 38.3 wt% mercaptopropyl-PDMS (SMS-042), both Gelest; Lambson Speedcure 2022 1 mL per 100 g thiol-ene resin Z resolution can be improved with Sudan I sensitiser	250 μm features 1000 μm gaps or holes

Other AM processes

Other AM processes are limited by the thermoset nature of silicones, which prevents melt-processing. Nonetheless, novel materials and reactivities have been used to enable different printing methods.

Powder bed processes have recently been demonstrated for silicones.^{354,355} In 2018, Liravi *et al.* published the first binder jetting of bulk silicones using a hybrid system. Silicone powder supplied by Shin-Etsu formed the powder bed which was fused by a two-binder process: a water-based binder was deposited via inkjet to form green parts; this was then infiltrated by a 2-part thermal cure silicone deposited by extrusion, and a thermal lamp was used for interlayer curing. Approximately 91.8% density was achieved following a thermal cure post-processing step.³⁵⁴

While PBF of conventional silicones is not possible due to their lack of melt point, Sun *et al.* 2021 presented an intriguing method for selective laser sintering of silicones using supramolecular chemistry. Aminopropyl-terminated PDMS formed covalent adaptable networks (CANs) with pyrazole urea bonds to linker molecules, enabling SLS printing and self-healing elastomers. Cryogenic freezing was used to produce powder on a kilogram scale and printing of an orthotic insole was demonstrated.³⁵⁵

Lastly, Riahi *et al.* introduced a process they called Selective Laser Baking in 2019. The process combines aspects of SLS and SLA: a CO₂ laser was used to selectively thermally-cure a vat of a commercial 2-part addition cure RTV. It is distinguished from SLA by the reaction mechanism: hydrosilylation rather than photopolymerisation.³⁵⁶

Table 53: Direct additive manufacturing of bulk silicones via powder bed processes and other AM techniques in academic research.

<i>Paper</i>	<i>AM category</i>	<i>Application</i>	<i>Printer set-up</i>	<i>Silicone</i>	<i>Resolution</i>
Livravi <i>et al.</i> 2018 ³⁵⁴	Hybrid (binder jetting and extrusion (RC/DIW))	First (and currently only) binder jet printed silicone	Custom system: 3 powder feed beds, roller recoater, thermal inkjet printhead, piezo inkjet printhead, pneumatic extrusion printhead (100 μm diameter, used for silicone binder), thermal curing lamp (100–120 $^{\circ}\text{C}$, 1 min)	Silicone powder bed Shin-Etsu KMP602 and KMP598 (average 30 μm , 13 μm); Water-based binder zb60, 3D Systems; Silicone binder Changzhou Juyou JY-9010 2-part thermal cure (100:1 A:B) modified silica and D4. Post-cured at 85 $^{\circ}\text{C}$: ~60% powder, ~ 30% silicone binder, and <10% air voids	1700 μm resolution with 100 μm layer thickness, 300 μm drop spacing, 1540 μm PDMS drop diameter 4 mm s^{-1} throughput 91.8% part density
Sun <i>et al.</i> 2021 ³⁵⁵	Powder bed fusion (Selective laser sintering (SLS))	First (and currently only) SLS-printed silicone, self-healing elastomers, orthopedics	Farsoon Tech HT251P SLS printer (55 W CO_2 -laser), 150 μm layer thickness, 80 μm scan spacing, 7.6 m s^{-1} scan speed	α , ω -aminopropyl PDMS (Gelest DMS-A15 and -21) was used to synthesise three covalent adaptable networks (CANs) with dynamic pyrazole urea bonds 1 kg powder prepared by cryogenic grinding 0.2-0.5 wt% silica NPs (10 nm) as flow agent	Powder diameter <177 μm (sieve mesh), average 92 μm diameter 7.6 m s^{-1} scan speed
Riahi <i>et al.</i> 2019 ³⁵⁶	Selective laser baking (μSLA but using CO_2 -laser for thermal curing of vat polymer)	Microfluidics	Custom: gantry, stepper motor, platform, 2D galvo-scanner, CO_2 laser	Dow Corning Sylgard 184 2-part addition cure RTV	260 μm XY, 200 μm Z

Summary of silicones in AM

Silicone AM has expanded greatly in recent years and there is a particular need for 3D-printable elastomers, which has driven demand for silicones. Most commercial and academic silicone printing utilises extrusion-based AM, due to its wide viscosity limits and simple compatibility with reinforcing fillers. To summarise extant processes:

Silicone extrusion solely uses robocasting/direct ink writing methods, where resolution is limited by nozzle diameter: this is typically 200-400 μm , though 10 μm has been achieved.³¹⁵ Print fidelity of extrusion-based AM is limited by rheology and cure rates of silicones, leading to slumping or wetting, but viscosity and cure rate modifiers alter crosslinking density which makes elastomers stiffer and less flexible. Embedded-3DP and FRE approaches use high viscosity support matrices to overcome this but are not well-established and the latter is limited to low viscosity materials.

VP-based AM has faster print rates than extrusion and the vat is inherently supportive; resolution is $<20\ \mu\text{m}$ for 2PP and typically 50-250 μm for SLA/DLP. Resin flow can damage soft elastomers and support structures are often needed for silicones. However, the lower viscosity limit prevents conventional formulations for strong elastomers. LOPP allows parts to be printed directly inside the vat and eliminates the need for a build platform but is a nascent process.

Material jetting processes vary: inkjet is particularly limited to low viscosities but is capable of high resolution ($<50\ \mu\text{m}$, dependent on nozzle diameter and substrate) at a reasonable throughput. Dual piezoelectric/pneumatic jetting valves have much higher viscosity limits than conventional inkjet printers and are suitable for jetting of high molecular weight silicones and silica fillers, better enabling elastomers with high mechanical strength. This has relatively low resolution (around 500 μm) but high print speed.

Academic research of silicone AM has focused on medical, microfluidic, soft robotic, and electronic applications. Multi-material AM is ideal to reduce the number of manufacturing and assembly steps for production of functional devices; vat photopolymerisation has limited capacity for multi-material printing, whereas material jetting is the most inherently suitable of the AM categories,⁷ although extrusion printers with microfluidic mixers and multiple printheads are becoming more common. Inkjet printing is increasingly used for inkjet-printed electronic devices and there is a demand for functional materials for jetting.^{8-10,77}

QD dispersion in polymer matrices

While QDs have excellent optical properties, their use in LEDs has been greatly limited by issues with aggregation and poor environmental stability in QD-polymer composites; a number of strategies have been employed to overcome these challenges.¹⁰²

It is inherently challenging to disperse CdSe/ZnS quantum dots in silicones: Strong van der Waals attraction between QDs and large surface energy mis-match between silicones and CdSe/ZnS drives the formation of large QD agglomerates to minimise contact with the matrix.¹²² Problems with curing are also noted for addition-cure silicones where labile capping ligands - particularly primary amines - poison the platinum catalyst.^{132,146,248} The high gas permeability of silicone is also problematic as QDs are poorly shielded from oxygen.⁵¹

While surface modification can address these challenges, dispersion and stabilisation is not as simple as selecting a strongly-attached, bulky ligand or overcoating a particle with another material: the surface chemistry of quantum dots has a large impact on their photo-electronic properties and careful consideration is needed to conserve fluorescence.^{110,236} As stated earlier, the optical properties of QDs arise from quantum confinement and can be described with the particle-in-a-box model. However, the surface forms a finite potential barrier which results in waveform leakage; therefore, the chemical environment of the surface must be given consideration in order to maximise quantum yield.^{110,236}

Photoluminescence (PL) occurs in QDs when electrons are excited from the valence band to the conductive band. These can electrostatically bond with the holes left in the valence band to form electron-hole pairs or excitons. Radiative recombination occurs when the electron relaxes back to the valence band and releases energy as a photon.¹¹⁰ Surface atoms differ from bulk as they are not surrounded and therefore have potential to form additional bonds. These so-called dangling bonds give rise to localised energy states which reduce the overlap between electrons and holes, decreasing the probability of exciton recombination. This effect is even stronger for surface defects, which are known as trap states, where carrier overlap is close to zero and relaxation proceeds via nonradiative pathways; defects can be generated via etching or photo-oxidation. For these reasons, surface passivation is vital to preserve photoluminescence.^{19,110,236}

Ligands on the quantum surface form a protective layer, typically consisting of the capping ligands used during synthesis to stop nanocrystal growth. Ligands passivate dangling bonds on the QD surface, eliminating trap states that can quench photoluminescence. They also act as the interface between quantum dots, which helps to stabilise them against thermal quenching and particle coarsening. These ligands are generally labile and their bonding to the surface is described using covalent bond notation (Figure 143).

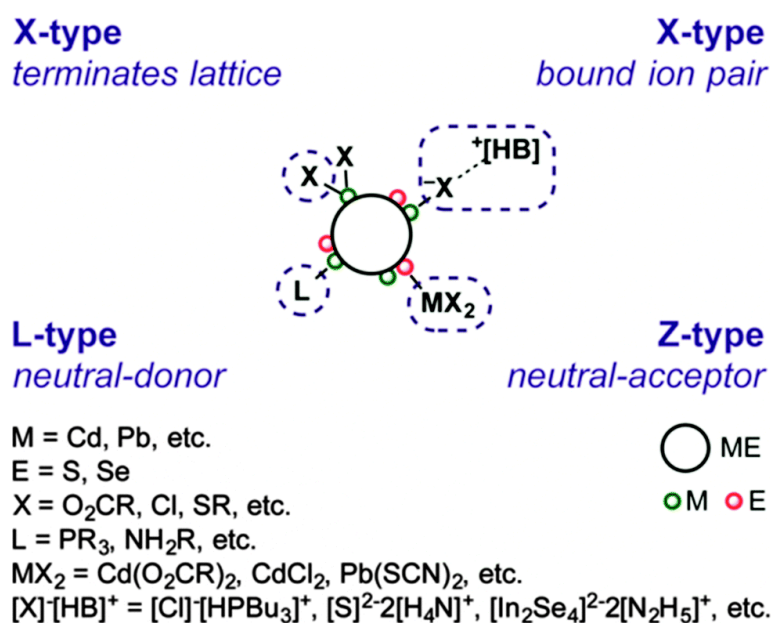


Figure 143: Classification of bonds at quantum dot surfaces using covalent bond notation. Reproduced with permission from Anderson *et al.* 2013.²⁸⁶ Copyright 2013 American Chemical Society.

CdSe/ZnS quantum dots are type I core shell QDs, meaning that the band gap of the shell is higher than the core so that charge carriers are confined to the core. The ZnS shell passivates dangling bonds and creates a potential energy well that reduces the effect of surface environment on emission, as shown below in Figure 144. Nonetheless, there is still some interaction with the surface and, although ZnS shells greatly reduce photo-oxidation,²⁸⁷ the shell distribution is highly anisotropic and does not uniformly shield the CdSe core.^{19,112} In CdSe core QDs, primary amines are well-known to enhance PL and thiols to quench it;²³⁷ this is also true of CdSe/ZnS QDs.^{263,264,357} It has been suggested that amines eliminate surface traps by raising their energy level, or that they create a higher energy barrier between core and surface. Thiols with redox energies higher than the QD valence band reduce quantum yield via ligand hole trapping.^{110,236}

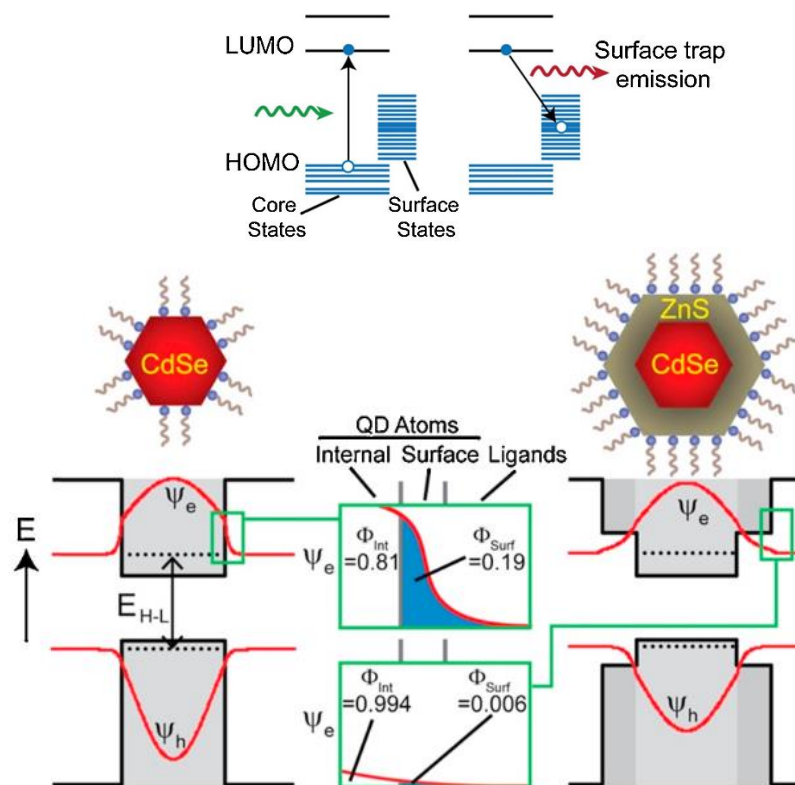


Figure 144: Top: Nonradiative relaxation of excitons as a result of surface trap states. Bottom: Confinement of excitons to the CdSe core by the potential well of the ZnS shell. Reproduced with permission from Lim *et al.*¹¹⁰

Surface states are also important in temperature-dependent emission, which is the most important material property for a temperature-sensing application. Different functional groups on ligands appear to change the energy barrier between core excitonic states and surface states, changing the thermodynamics of the exciton population and leading to temperature-dependant PL.²³⁶

Moon *et al.* 2020 review strategies for enhancing the photostability of QD-polymer composites for LEDs, dividing them into three main strategies: shell structure; ligand modification; and inorganic overcoating.¹⁰²

The most commonly approach for improving dispersion is ligand exchange. Ligands can be directly exchanged with monodentate, bidentate, and polydentate ligands according to the type of ligands involved (Figure 145). There are three main parameters for ligand exchange: ligand size, packing density on the surface, and binding affinity.¹¹⁰ Larger size ligands can more effectively shield the QD surface – and polymeric ligands are useful for increased stability or for incorporation into bulk polymer³⁵⁸ - but are more difficult to attach to the surface due to steric factors. Higher packing density on the surface means that more of the surface is shielded by the ligand; packing density may also affect the conformation of a ligand, particularly with regards to chain coiling. Finally, head groups with a stronger

affinity to the surface are less labile and are thus more effective in ligand exchange, not requiring an excess of reagent in order to drive exchange via mass action. Thiols and phosphonic acids are noted to bind strongly to CdSe QDs.^{359,360}

A. classes of ligand exchange reactions

X-type



L-type



Z-type



B. Z-type ligand displacement (L-promoted)



M = Cd, Pb, etc.
 E = S, Se
 X = O₂CR, Cl, SR, etc.
 L = PR₃, NH₂R, etc.



Figure 145: Classes of ligand exchange reactions at quantum dot surfaces. Reproduced with permission from Anderson *et al.* 2013.²⁸⁶ Copyright 2013 American Chemical Society.

A key disadvantage of ligand exchange is that it almost always lowers quantum yield due to damage to QD surfaces exposed during exchange. This is lessened where ligand reactivity makes it feasible to use mild conditions and there is a dense, compact coverage of new ligands on the surface; this ensures maximised protection of the surface with minimised environmental harshness. One example of such an optimised exchange is the room temperature exchange of TOPO for MPA ligands on CdSe/ZnS quantum dots described by Pong *et al.*,²⁶⁴ which utilises a strong base to activate the thiol ligand. Furthermore, it is well-known that primary amines enhance the photoluminescence of CdSe quantum dots, so replacing these with another head group with strong affinity to the ZnS surface (such as phosphonic acids)³⁶¹ will remove this benefit.

Alternate strategies may circumvent the issues associated with ligand exchange. For example, polymer encapsulation forms a polymeric shell around the original ligands so that the ligand shell is never disturbed and the surface is never exposed.³⁵⁸ Several papers describe QD surface coating with amphiphilic polymers— stability is driven by hydrophobic interactions so that no exchange is needed. The coating can then be further stabilised by crosslinking, as recently demonstrated for PDMS composites.³⁰⁶ However, silicones themselves are inherently amphiphilic, which may impede implementation.⁵¹ Microemulsion techniques may also be used.³⁶²

Another way to avoid the need for ligand exchange is to ensure that the QDs are synthesised with suitable ligands already attached from the outset. Capping ligands can be selected which lead to good dispersion in a polymer matrix,²⁹¹ but optimisation of synthetic conditions may be time-consuming, in addition to QD synthesis already being a specialised procedure.

Core-shell QDs have greater stability, but the maximum shell thickness (and therefore degree of protection) is limited by the lattice mismatch between materials. The use of multi-shell/gradient shell QDs to enable thick shells effectively passivates the QD surface, although capping ligands are still required to stabilise dispersions. Similarly, silica encapsulation overcoats particles with a silica shell, which eliminates labile ligands and prevents the platinum catalyst from being poisoned. This also improves the stability of the quantum dots. While this does reduce the quantum yield as the surface is exposed, the PL may increase overall due to the roughness of the silica shell.³⁶³ However, both strategies increase particle diameter and silica nanoparticles are associated with high viscosity in silicones,^{17,67} which may render this unsuitable for inkjet.

Quantum dots embedded in macrocrystals – particularly inorganic salt-encapsulation of water-soluble quantum dots – have also been used for LEDs.³⁶⁴ Ligand exchange is frequently required to achieve water soluble QDs or to generate charges on the surface, though oleic acid-capped QDs have been embedded into macrocrystals using nonpolar solvents.³⁶⁵ Dried crystals may be dispersed in polymer matrices; greater control over crystal size would be ideal to enable fine crystals for jetting inks.

Strategies for stabilisation and dispersion of quantum dots in polymer composites are discussed in greater detail below, specifically for silicone matrices.

Polymeric ligands

Polymeric ligands have been widely-used to synthesise bulk QD-polymer composites, with some inspiration taken from the principles of supramolecular chemistry. The many variations wide range of work has been carried out, as reviewed here,³⁵⁸ in both ligand exchange and in encapsulation of QDs driven by solvent interactions (mainly for biological applications where water solubility is a requirement). Some examples of the polymeric ligands used are shown below in Figure 146.

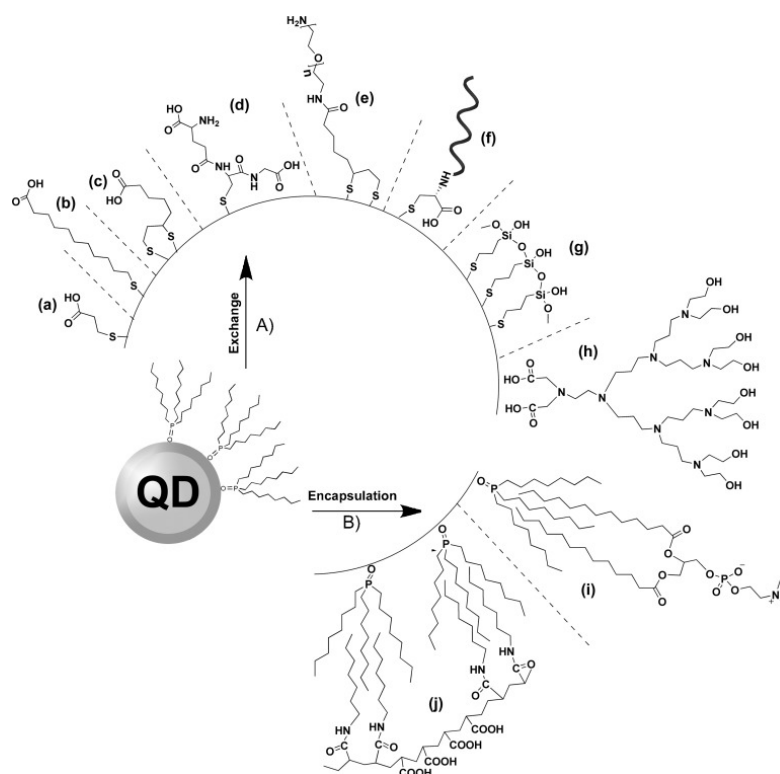


Figure 146: Dispersion strategies for QD-polymer composites utilising polymeric ligands. Reproduced with permission from Gill *et al.*³⁶⁶

One strategy to improve dispersion is to use bulkier ligands, where steric hindrance increases the distance between individual quantum dots and large ligands can interface with the polymer matrix. Quantum dots are commonly sold with long alkyl chain ligands, such as octadecylamine, a primary amine head group with a stearyl (C18) tail; longer chain lengths may improve the dispersion of QDs in silicone. Comb-shaped and dendritic polymers may also sterically protect the QD by effectively filling the coordination sphere.

Another important strategy is the use of multiple head groups, as bi- or polydentate ligands are more entropically stable, which drives ligand exchange. For an addition-cure silicone matrix, this reduces catalyst poisoning because these ligands are less labile. Dispersants based on long-chained succinic anhydrides are simple to prepare and may be effective.

Selection of head group requires consideration as relative energy levels can affect fluorescence. Primary amines enhance PL of CdSe/ZnS QDs and so replacement of them will remove this benefit.³⁵⁷ However, ligands with strong affinity are desirable to drive ligand exchange; thiol anchors have been used to strongly attach large polymeric ligands to a QD,^{367,368} although thiols are associated with PL quenching.^{263,264}

It is also possible to stabilise the ligand shells around QDs by spontaneously encapsulating them in an amphiphilic polymer, driven by differences in hydrophobicity; PL is preserved as the QD surface is not exposed. Seo *et al.* 2014 reported on stability of dodecyl amine-capped CdSe/ZnS QDs in various liquid silicones and silanes; they found that α,ω -hydride PDMS-co-PDPS silicone fluids led to good dispersion and stability of the passivating layer of ligands, forming a double layer.¹²³

Recently, Yoon *et al.* 2020 used CdSe@ZnS/ZnS and/or CdSe/CdZnS/ZnS QDs encapsulated in an amphiphilic polymer i.e. poly(styrene-co-maleic anhydride), which also functioned as a crosslinker, as shown below in Figure 147. Encapsulation enabled QDs to be dispersed without the need for ligand exchange and the associated reduction in QY. The matrix polymer cured via a ring-opening reaction between maleic anhydride groups of the encapsulating polymer and the amine groups of α,ω -diamine PDMS.³⁰⁶

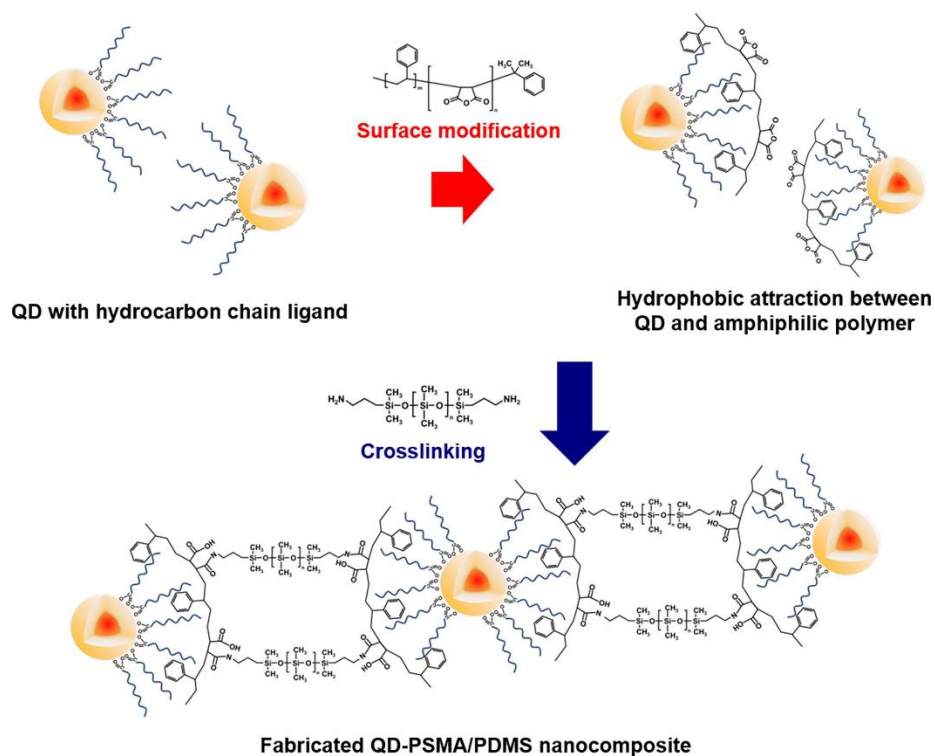


Figure 147: Reaction scheme for QD encapsulation in amphiphilic polymer followed by crosslinking between encapsulant and monomer to form QD-polymer composites. Reproduced with permission from Yoon *et al.*³⁰⁶

A similar encapsulation strategy was used by Park *et al.* 2015: octadecylamine-capped CdSe/CdZnS QDs were encapsulated in polyethylene wax to enable dispersion in Dow Corning OE6630 via a simple preparation step, reminiscent of Lipton *et al.*'s approach for silicone extrusion.³¹⁷ QD-loaded granules with multi-lamellar structure formed spontaneously in dilute solutions of polyethylene in wax, resulting in micron-scale capsules.³⁶² Photo-, thermal, and oxidative stability were improved, and FRET and thermal annealing were prevented as QDs were spaced apart at 12 nm distances.^{122,249} However, the micron-sized particles limit both transparency (as they led to scattering) and utility for inkjet (particle diameter should not exceed 5% that of the jetting nozzle).³⁴

QD ligands which are involved in crosslinking reactions show enhanced QD dispersion. In the aforementioned paper by Yoon *et al.* (Figure 147), the composite film was found to have high transparency and uniform QD distribution even at 30 wt% QD loading, where the encapsulating polymer was involved in crosslinking: the crosslinking was confirmed to be significant for dispersion, as QD-PSMA in Sylgard 184 showed aggregation even at 1 wt% QD loading.³⁰⁶ Wang *et al.* 2016 utilised PDMS-functionalised carbon QDs, where aminopropylmethylpolysiloxane ligands enabled self- or co-crosslinked QD-silicone composites, as shown below in Figure 148.³⁰⁷ Nam *et al.* 2019 used gradient alloy CdSe/ZnS QDs with vinyl-functional ligands which were involved in hydrosilylation curing. Oleic acid ligands were exchanged to 6-mercaptohexanol followed by reaction of the alcohol with allyl isocyanate to graft an allyl moiety via urethane linkage. Colour filters were prepared from mixing QDs, PMHS crosslinker (Gelest), tris(vinyl dimethylsiloxy)phenylsilane (TVDSP, Gelest), and Dow Corning Sylgard 184.²⁷⁵

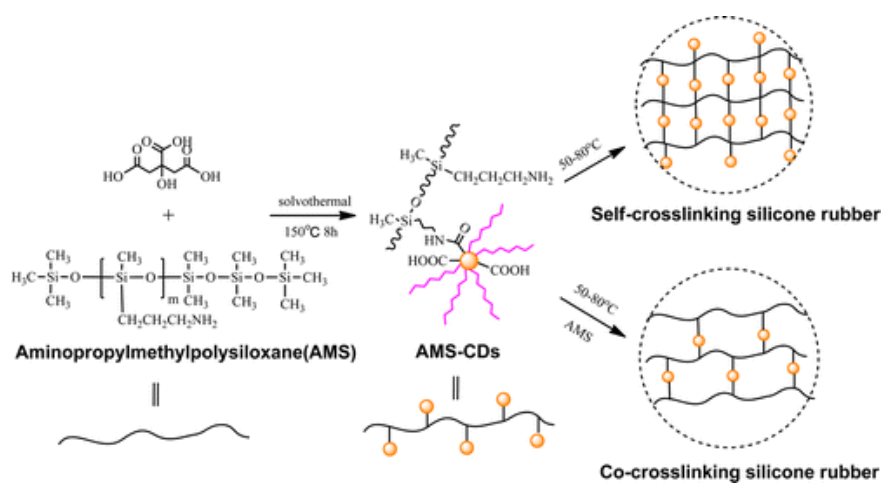


Figure 148: Reaction scheme for self- or co-crosslinking of QDs with reactive ligands to form silicone elastomers. Reproduced with permission from Wang *et al.*³⁰⁷ Copyright 2016 American Chemical Society.

Bimodal silicone grafting

There are two main limitations to the use of long alkyl hydrocarbons to disperse QDs in bulk PDMS: dispersion is best when QDs are grafted with polymers of similar composition to the host matrix. Siloxane chains are amphiphilic and have low surface energy compared to hydrocarbons⁵¹ and so, while silicones are excellent at wetting, maximum compatibility with the silicone matrix will occur with siloxane chain ligands. Dispersion morphology is dependent on nanoparticle composition, particle size and shape, grafting density, grafting chain length, host chain length, Flory–Huggins interaction parameter χ between the host and grafted chains, and film thickness.²⁶⁹ Therefore, grafted siloxane chains are more effective at aiding dispersion than typical hydrocarbon stabilising ligands.

The other issue is that, for polymer chains of uniform length, there is a trade-off between chain length and grafting density. Good dispersion is achieved when the entropic repulsion associated with the deformation of the grafted chains is greater than inter-particle enthalpic attraction between QDs. Grafting density and the ratio of grafted/matrix chain length are the two main parameters.¹²² For high molecular weight matrices, this leads to a narrow dispersion window where brushes are densely grafted enough to shield the QD surface but not so dense that they interact with each other, while having chain length comparable to the matrix. Bimodal grafting can help to fulfil these conflicting requirements: sparse longer siloxanes penetrate into the polymer matrix, while dense short siloxanes ensure good surface coverage and prevent longer ligands from coiling. A detailed summary of grafting regimes is given by Green (2011).²⁶⁹

This strategy has been very successful for dispersion of CdSe QDs in silicone matrices by Tao *et al.*¹²² Tao *et al.* used a platinum-catalysed, high molecular weight silicone, and functionalised siloxane ligands as shown in the reaction scheme in Figure 149. The exchange of hydrocarbons for siloxanes is driven by strong binding enthalpy of the phosphonic acid head groups to the CdSe surface, which displaces the weakly adsorbed carboxylic acids. This allows the reaction to proceed at a relatively low temperature of 75 °C and avoid particle coarsening. Phosphonic acids have stronger affinity than amines on CdSe/ZnS QD surfaces³⁶¹ in addition to CdSe surfaces.

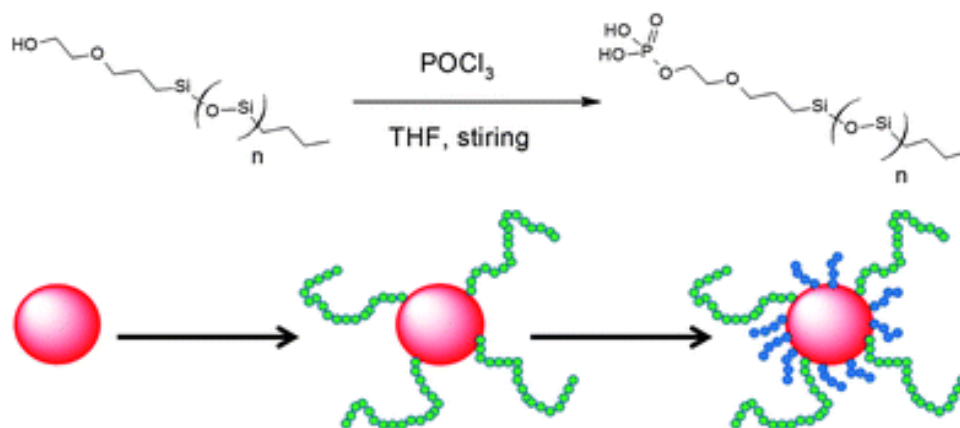


Figure 149: Reaction scheme for bimodal polymer grafting of CdSe QDs with phosphonic acid functionalised PDMS chains. Reproduced from Tao *et al.* 2013¹²² with permission from The Royal Society of Chemistry.

A highly-loaded QD-composite was obtained with homogeneous dispersion, high transparency, and unchanged PL peak, in a high molecular weight silicone. Even at 0.4 wt% QD, average QD separation is over 10 nm.^{122,249} Particles are not in proximity to fuse at this distance, enhancing the thermal stability of the composite: particle coarsening was prevented and so aging of the nanocomposite was slowed. However, the grafted QDs only had 50% residual quantum yield of the original colloidal suspension: thermal quenching occurred when bare surfaces were exposed during the 24-hour reflux at 75 °C. There are also synthetic disadvantages: preparation of the ligands requires the use of POCl₃, which is a considerable safety hazard.

In situ passivation

Capping ligands are typically the ligands present during QD synthesis; ensuring that ligands with desired properties are present during synthesis can by-pass the ligand exchange procedures that would otherwise be required to attach them, preserving PL. However, such synthetic procedures are challenging to design.

Xie *et al.* 2017²⁹¹ chose reagents to ensure that the quantum dots are synthesised with the desired ligands at the outset. The authors made use of zinc-terminated and primary amine-terminated PDMS ligands in the reaction mixture with the metal compounds during over-coating steps, as shown below in Figure 150. These quantum dots could then be dispersed in a commercial silicone resin as-synthesised, with good dispersion even at 4 wt% QD. The ligands shield the QDs from quenching by the platinum catalyst of addition cure silicones and result in high photo-stability and stability to oxygen and moisture – all desirable traits for temperature sensors. That said, quantum efficiency increased after thermal annealing so this would need to be considered for said sensor: 58% PL enhancement occurred upon heating, and 5 hours at 85 °C was required before the composite was photochemically stabilised. Investigation would be required to determine how emission varied with temperature following the thermal treatment.

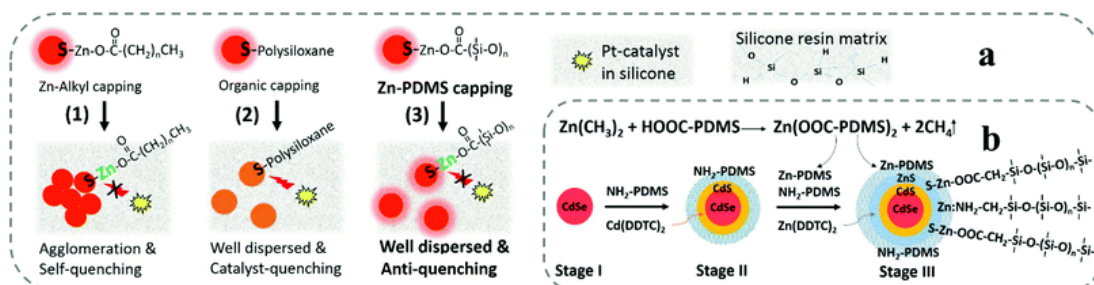


Figure 150: Synthesis of quantum dots with *in situ* PDMS capping ligands. Reproduced from Xie *et al.*²⁹¹ with permission from The Royal Society of Chemistry.

However, such quantum dots are not currently commercially available, which limits their ease of access and therefore their usage. The synthesis is intensive and has many safety concerns, as is typical of QD synthesis: a Schlenk line is needed to carry out inert synthesis, the cadmium precursor is profoundly toxic, and diethyl zinc is very strongly pyrophoric. Only specialist labs which are equipped for synthesis of heavy metal nanoparticles can carry out this procedure. It is also likely to be difficult to safely upscale production. Composites which make use of commercially available quantum dots are easier to study and to bring to market.

Silica encapsulation

Silica encapsulation of QDs has become a common method to improve QD stability and dispersion. There are two main synthetic routes: coating of silica on QDs^{369–371} and/or immobilisation of QDs in or on silica micro/nanospheres.^{372,373} A typical reaction scheme for silica sphere encapsulation of quantum dots is shown below in Figure 151. Layered particles abbreviate silica and QD, e.g. SQS refers to silica-immobilised QDs with a silica coating.

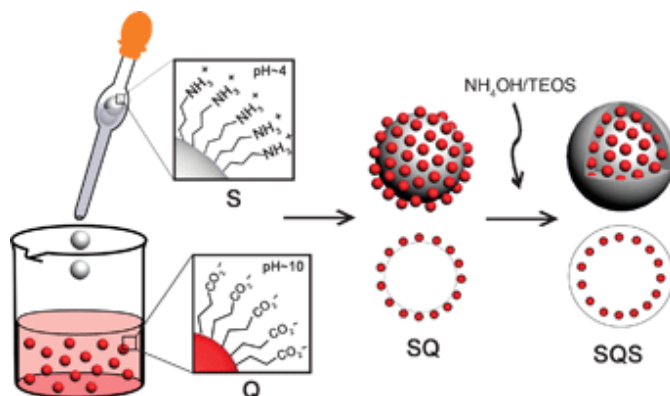


Figure 151: Schematic of silica sphere encapsulation of quantum dots, showing typical encapsulation and overcoating procedures. Reproduced from Cho *et al.*³⁷² with permission from The Royal Society of Chemistry.

Silica overcoating proceeds via two main synthetic strategies: the conventional Stöber method,^{372,373} as shown in Figure 151 above, and reverse microemulsion variants.^{369–371} The Stöber method is a sol-gel process which proceeds via hydrolysis and condensation of tetraethyl orthosilicate (TEOS) with ammonium catalyst in alcohol. QDs require ligand exchange to hydrophilic ligands, typically 3-mercaptopropionic acid (MPA), followed by silanisation to enable QDs to act as nucleation sites. Large PL losses are typically associated with the Stöber method, and silica is amorphous with relatively large and non-uniform particle diameters, containing multiple QDs. Reverse microemulsion methods use water-in-oil micelles for both hydrophobic and hydrophilic QDs: hydrolysis and condensation of the silica precursor occurs at the interface, which prevents damage to the QD surface, and no prior QD ligand exchange is required. Hydrophilic QDs occupy individual micelles due to electrostatic repulsion; for hydrophobic amine-capped QDs, QDs enter the aqueous micelle after ligands are replaced by hydrolysed TEOS. PL is better preserved via microemulsion routes and encapsulation of individual quantum dots is possible.

There are a number of advantages to these methods; the silica-encapsulated quantum dots are much safer to work with as the toxic species are contained. The silica spheres have greater compatibility with silicone matrices and do not have any labile ligands that could potentially poison the platinum catalyst of addition cure silicones. Lastly, QD-silica spheres show excellent thermal and chemical stability and, in some cases, enhanced PL intensity.³⁶³

Increasing the size of particles in this way is detrimental to dispersion: more mass means a stronger tendency for particles to settle. However, very small particles can be obtained using reverse microemulsion silica overcoating of individual QDs, with diameters as small as 10-30 nm.^{146,371} Additionally, reduction in PL is well-noted, particularly for ligand exchange to hydrophilic ligands and overcoating via the Stöber method. To tackle the former, Pong *et al.* describe an optimised, room temperature ligand exchange of TOPO-capped CdSe/ZnS quantum dots: a strong base is used to increase the activity of MPA, which results in better retention of PL due to less surface exposure and milder reaction conditions.²⁶⁴ A particular issue for silicones is that silica nanoparticles interact strongly with siloxane chains, leading to high viscosity even at low loadings. Strategic surface treatment of silica particles is required to enable loading of QD-silica in silicone inks.

There are a few reports of QS particles (silica-coated QDs) used for QD-silicone composites. Ziegler *et al.* 2008 encapsulated individual InP/ZnS QDs in silica using microemulsion (20 nm diameter QS) to prevent QD aggregation and platinum catalyst poisoning by labile QD ligands. Conversion layers for white LEDs were produced with QDs and phosphors using either Wacker Elastosil RT601 or Bayer Silicone IV S4312 and cured at 150 °C for 1 hr.¹⁴⁶ Similarly, Xie *et al.* 2018 used CdSe/ZnS QD silica nanoparticles (33 nm QS particles via microemulsion) with YAG:Ce phosphor in Dow Corning OE6550 for white LEDs.³⁷⁴

Kim *et al.* 2012 used an ultrasonic spray-drying technique to obtain 50 nm diameter, self-assembled mesospheres of CdSe/ZnS QDs from toluene solution. This was followed by Stöber method silica overcoating of QD assemblies to obtain highly loaded QS composites. Overcoating proceeded with time: the silica layer was 15 nm thick after 2 hours, but it was possible to obtain particles of several micrometer diameter. PL loss during overcoating was reduced via an initial silanisation strategy to obtain QD separation of 20 nm at lower QD loadings. A white LED was demonstrated by dispersion in an unspecified silicone encapsulant.³⁷⁵ In a later paper, Kim *et al.* 2014 used the same strategy but overcoating was carried out in the presence of triisopropyl borate. PL loss during overcoating was greatly reduced by borate, as the QD surface was passivated by a B₂O₃ and/or B(OH)₃ layer. Composite particles were <200 μm but irregularly-shaped. QD-borate-silica nanocomposites were dispersed in Dow Corning OE6636 with YAG:Ce phosphor to produce a white LED, with little decrease in emission after 672 hours of continuous operation.³⁷⁶

Kim *et al.* 2019 used silica encapsulation and a sol-gel hybridizer to maximise stability. Silica encapsulation was carried out via reverse microemulsion following room temperature

ligand exchange of oleic acid-capped CdSe/CdZnS QDs to 3-mercaptopropylmethyl dimethoxysilane (MPMDMS). QD-silica particles were treated with 3-methacryloxypropyl trimethoxysilane (MPTMS) to aid dispersion in sol-gel precursors and resin made by *in situ* condensation (see *Appendices: Sol-gel hybridizers*); dispersion of 5 wt% QD-silica resins was stable for ≥ 30 days.²⁹²

In work by Yoo *et al.* 2015,³⁶³ SQS particles were synthesised via a similar scheme to that shown in Figure 151. QDs were homogeneously distributed at 10 nm spacings on the surface of 50 nm silica spheres so that self-quenching was avoided. Photoluminescence intensities increased almost 4-fold to the original colloidal QDs: quantum yield decreased but light absorbance increased due to the rough silica surface. A white LED was demonstrated by encapsulating SQS in Dow Corning OE6630 with YAG:Ce phosphor; Yoo *et al.* used phenyl groups to enhance miscibility with the addition cure silicone resin, but the silica shell could be functionalised in other ways using sol-gel reactions with alternate silanes.

Encapsulation of QDs within mesopores, without the need for silica overcoating, is also known. Chen *et al.* 2016 encapsulated CdSe/ZnS QDs inside mesoporous silica microspheres using reversible swelling of silica in hexane solvent: quantum dots were trapped inside pores when drying silica shrank, fully isolating QDs and preventing platinum catalyst poisoning by labile ligands. A white LED was demonstrated with a conversion film of QD-silica microspheres and YAG:Ce phosphor in a Dow Corning OE6550 matrix.²⁹⁰

Li *et al.* 2019 also dispersed CdSe/ZnS QDs in mesoporous silica – specifically, SBA-15 silica particles, which have a 2D hexagonal pore structure. The QD-silica particle solution in chloroform was directly added to an unspecified Dow Corning silicone; solvent was evaporated and the mixture was cured at 150 °C for 1.5 hours to produce a conversion layer for a demonstrative white LED.³⁷⁷

Lastly, other inorganic QD encapsulants have been used in silicone composites. Xie *et al.* 2018 immobilised CdSe/ZnS QDs on boron nitride hexagonal platelets (hBN): the QD-hBN composite was dispersed in Dow Corning OE6550 with YAG:Ce phosphor for white LEDs.³⁷⁸ The hBN platelets act as conductivity filters for heat dissipation to prevent thermal QD quenching; this novel material may be unsuited to temperature sensing or may merely raise the temperature sensing range to temperatures at which this dissipation process is overwhelmed.

Sol-gel hybriders

Expanding on the sol-gel type reactions used to produce QD-silica particles, other researchers have developed silane sol-gel encapsulants. Sol-gel siloxane hybrid materials, also known as hybriders, are branched resins with polymerisable functional groups, which are prepared via silane-based sol-gel condensation reactions and can then further crosslink. They are of interest for their high refractive index and thermal stability.

Earlier research involved free radical curing of acrylate- or epoxy- silicones, which was associated with yellowing by thermal aging; to prevent this, Kim *et al.* 2010 proposed solely siloxane-based hybriders.³⁷⁹ They prepared a highly-branched, one-part phenyl-vinyl-oligosiloxane (PVO) resin from condensation of vinyltrimethoxysilane (VTMS) and diphenylsilanediol (DPSD) with a barium hydroxide basic catalyst. This was then crosslinked via hydrosilylation with a phenyltris(dimethylsiloxy)silane linker and a platinum catalyst. However, high shrinkage and by-products prevented *in situ* moulding using sol-gel precursors, while the hybridier had high viscosity: solvents were required for processability.

Subsequent work utilised two-part addition cure hybriders, analogous to 2-part RTVs: vinyl resins and hydride resins were created separately via sol-gel reactions (and by-products removed) and then mixed to crosslink via hydrosilylation.^{380,381} *In situ* hydrosilylation does not lead to shrinkage or by-products, and precursors were less viscous.

QD-siloxane films have been produced by incorporation of QDs with functionalised ligands into hybridier resins. However, while the two-step hybridier film preparation strategy does remove the problems of shrinkage and by-products from the final crosslinking, *in situ* sol-gel reactions to prepare resins in the presence of QDs are harmful to PL: alcohol by-products and the required acid or base catalysts can damage QDs, necessitating additional removal steps. Resin viscosity is also high, and reactive inks using precursors for *in situ* sol-gel condensation are precluded as described above. Nonetheless, these materials have promising thermal stability and refractive index, which is attractive for lighting and optical sensing; use of solvents and shorter sol-gel hybridier units may make this material class more compatible with conventional IJP, or higher viscosity jetting valves could be used.

Jun *et al.* 2013 produced QD-silica monoliths via *in situ* sol-gel condensation. 6-Mercaptohexanol-capped CdSe/CdS/ZnS QDs condensed with TEOS using a propylamine catalyst. Alternately, amine ligands can function as both as the initial QD ligand and catalyst, which preserves PL as ligand exchange is not needed; however, ligands with thiol groups served as effective anchors to the matrix and increased stability.³⁸² The silica matrix was limited in that its refractive index was lower than that of phenylsiloxane resins.

Yoon *et al.* 2015 prepared QD-PVO resin via barium hydroxide-catalysed sol-gel condensation in the presence of CIS/ZnS/ZnS QDs, with and without 3-(mercaptopropyl)trimethoxysilane: the mercaptosilane anchored the QDs to the resin via *in situ* ligand exchange and condensation reaction. Next, base resins were thermally cured with the hydride-resin crosslinker through hydrosilylation with a platinum catalyst (150 °C, 4 hr) to fabricate QD-containing phenylsiloxane hybrimer films for white LEDs.²⁷²

Jang *et al.* 2019 used 2-part addition cure hybrimer resins. QD-containing silicone hydride-resin was synthesised via *in situ* sol-gel condensation of a mixture of diethoxy-methylsilane (DEMS) and DPSD in the presence of 0.1 wt% oleic acid-capped CdSe/CdZnS QDs. PVO resin was prepared via sol-gel condensation of dimethoxy-vinylmethylsilane (MDVMS) and DPSD, then 0.2 wt% Karstedt's catalyst was added. The hybrimer resins were mixed to crosslink via hydrosilylation for 4 hours at 70 °C; the C=C bond of the QD ligand was involved in reaction and anchored QDs to the matrix.³⁸³

In addition to hydrosilylation mechanisms, photocurable hybrimer resins are also known. Kim *et al.* 2016 utilised free radical photopolymerisation reactions, shown in the reaction scheme in Figure 152 below. They encapsulated oleic acid-capped CdSe/ZnS QDs in resin via *in situ* sol-gel condensation with 3-methacryloxypropyltrimethoxysilane (MPTMS) and DPSD (barium hydroxide-catalysed), or in an acrylate-terminated PDMS (Miramer M244). QDs were spontaneously encapsulated due to hydrophobic interactions of ligands, initiating localised sol-gel reaction which was followed by sol-gel condensation of the rest of the resin. UV free radical reaction with 0.2 wt% Omnirad 651 was then used to crosslink carbon double bonds of the oleic acid ligand and the MPTS.¹³⁵

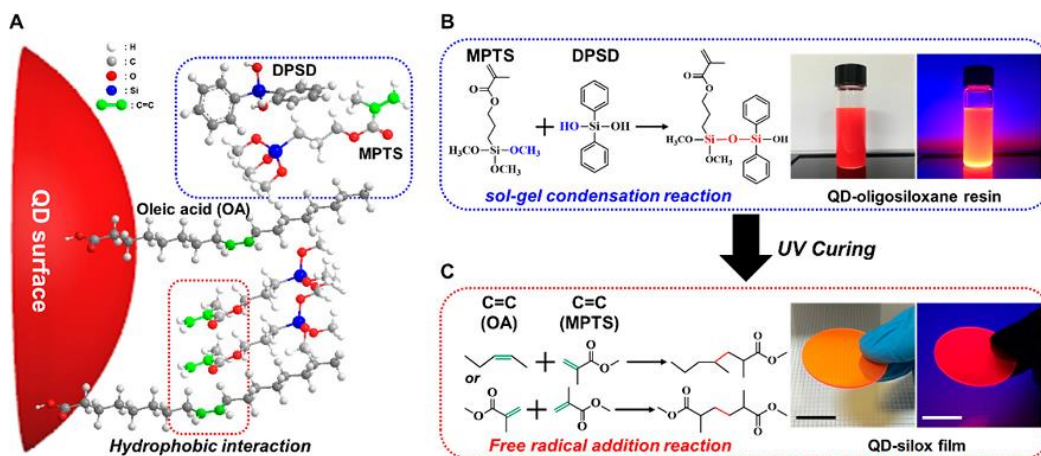


Figure 152: Reaction scheme for synthesis of QD-siloxane sol-gel resin (a and b), followed by free radical crosslinking to produce a cured QD-siloxane hybrimer (c). Reproduced with permission from Kim *et al.*¹³⁵ Copyright 2016 American Chemical Society.

Kim *et al.* 2019 used QD-silica NPs in a hybrimer to maximise stability to heat, moisture, and chemicals. 300 nm diameter QD-silica particles were prepared (see *Appendices: Silica encapsulation*) and 5 wt% QD-silica resins were synthesised by *in situ* sol-gel condensation of MPTMS, MPTMS-QD-silica, and DPSD. Resins were cured by free radical crosslinking of methacrylate groups with 2 wt% Omnirad 651, using 365 nm excitation under argon and post-cure thermal treatment (150 °C, 2 hours) to terminate radicals. QY was unchanged over the course of 30 days.²⁹²

Lastly, Kim *et al.* 2020 used oleic acid-capped CdSe/ZnS or CdSe/CdZnS QDs, with ligand exchange to mercapto-silane, to enable thiol-ene photopolymerisation for photo-patterning without oxygen inhibition. QD-siloxane resins were prepared with MPTMS and DPSD as previously described, and then 2 wt% Omnirad 651 photoinitiator and a pentaerythritol tetrakis(3-mercaptopbutylate) thiol monomer was added for thiol-ene crosslinking to demonstrate UV lithography (365 nm).^{273,274} While the authors suggest that this precursor could be used for inkjet and discuss drop casting morphology, there is no discussion of viscosity.

Macrocrystal embedding

Synthesis of quantum dots embedded in macrocrystals is another method of forming inorganic composite structures for QD stabilisation. Early work in salt-embedded QDs used the Czochralski method to impregnate molten KBr.³⁸⁴ Recent synthetic approaches are facile and proceed via salt precipitation; QD dispersions only need to be stable enough to avoid aggregation during incorporation. These crystals can then be ground down and dispersed into polymer to form composites where the inorganic crystal host imparts much greater oxygen-impermeability than that of the polymer matrix. Adam *et al.* 2016 published a review identifying three synthetic routes: direct incorporation by precipitation of QDs mixed with solutions of salts or organic molecules, either via slow solvent evaporation (days) or vacuum-assisted evaporation (minutes); and liquid-liquid-diffusion-assisted-crystallization (LLDC).³⁶⁴

The first method, slow solvent evaporation, is predominantly based on aqueous dispersions - which require QD ligand exchange to hydrophilic ligands - although ligand exchange-free embedding in chloroform has been demonstrated.³⁸⁵ Otto *et al.* 2012 embedded CdTe QDs in several inorganic salts (NaCl, KBr, or KCl) by gradual evaporation of saturated salt solutions at room temperature. However, only low loadings of QDs were embedded (<1 wt% QDs) as QDs had a strong tendency to aggregate.³⁸⁶ In a follow-up paper, Müller *et al.* 2014 repeated this method to investigate the effect of the salt host on QD PL. CdTe QDs with thiol-containing ligands (MPA or thioglycolic acid (TGA)) and CdSe/ZnS QDs with a gradient alloy shell (MPA or oleic acid ligands) were embedded into NaCl. PL enhancements of 1.1-3.0 times were observed for CdTe QDs, with 30-80% QY; the silicone matrix had negligible effect on PL. This is thought to arise from passivation or repair of surface defects, particularly as the enhancement was size dependent and not observed for CdSe/ZnS QDs, although enhancement was not dependent on ligand. Adam *et al.* 2015 achieved 3.4 times higher quantum dot loading by using borax as the host crystal for aqueous CdSe/ZnS QDs rather than sodium chloride. Solutions were precipitated for approximately one week at 30 °C; the solubilised borax is less ionic than sodium chloride and so QD aggregation was lesser.³⁸⁷ In all three papers, embedded crystals were ground into powder, dispersed into 2-part addition cure RTV (QSi218, ACC Silicones), and cured for 2 hours at 70 °C to make colour correction layers for white LEDs.

The second method, vacuum-assisted evaporation, is based on organic solvents; solvent removal under vacuum enables rapid production of crystals. In work by Erdem *et al.* 2015, oleic acid-capped gradient alloy CdSe/ZnS QDs were embedded into LiCl salt without ligand or solvent exchange. Saturated salt solution was added to QD solution, both in tetrahydrofuran, and dried in a vacuum desiccator. Powdered crystals were dispersed in epoxy to produce a white LED, which retained 95.5% of its emission intensity after 96 hours of operation. The authors noted that this strategy is also suitable for silicone matrices.³⁶⁵

The third method, LLDC, uses orthogonal solvents to induce crystallisation: an aqueous solution of QDs and salt is injected underneath an organic solvent layer leading to phase separation, and the organic solvent gradually diffuses into the water, lowering the solubility of the salt and triggering crystallisation. A seed-mediated strategy does not require QD ligand exchange: crystal seeding is carried out by adding salt-saturated organic solution to oil phase QDs. LLDC then proceeds with seeds in the organic phase and an aqueous salt solution. Adam *et al.* 2015 produced CdTe salts encapsulated in NaCl via both of the above LLDC routes using methanol and chloroform solvents. Crystals were dispersed in QSil218 2-part addition cure silicone to produce a white LED.³⁸⁸

More recently, Zhang *et al.* 2019 produced CdTe QDs embedded in calcium carbonate by an aqueous co-precipitation method. $\text{Ca}(\text{NO}_3)_2 \cdot 4\text{H}_2\text{O}$ was added to a solution containing QDs and Na_2CO_3 to produce embedded crystals in minutes. Crystals were rice-shaped with 1.5 μm average diameter and were dispersed in an unspecified silicone resin then cured for one hour at 150 °C to produce a layer for white LEDs.³⁸⁹

Salt-embedded QD-polymer composites have been investigated for use in temperature sensing. Kalytchuk *et al.* 2017 dispersed CdHgTe QDs embedded in NaCl in a PMMA matrix and investigated PL for spectral- and lifetime-based measurements. They achieved thermal sensitivities of up to 0.15 nm °C⁻¹ (0.02% °C⁻¹) and 0.09 ns °C⁻¹ (1.4% °C⁻¹) for peak shift and lifetime respectively.³⁹⁰ Similar work could be carried out on other polymers.

Inkjet is reported for *in situ* embedding of QDs in salts. Ho *et al.* 2020 produced aqueous gradient CdSe/ZnS QDs by ligand exchange to MPA to enable inks of 1-5 wt% QDs in aqueous NaCl solution. Embedding occurred spontaneously as droplets dried, and the high contact angle prevented contact pinning and led to high resolution: 20 μm diameter, cuboid 'pixels' were obtained.¹²¹ Macrocrystal embedding in the presence of reactive polymers is not established, and poisoning of platinum catalysts would be a concern for addition cure silicones. Therefore, *ex situ* methods are more accessible for silicone inks.

However, obtaining crystals of suitable fineness for inkjet is challenging, as particle diameter should not exceed 5% that of the jetting nozzle.³⁴ For 10 pL Dimatix print cartridges, which are commonly employed for ink research and development, this limits particle diameters to approximately 1.1 μm diameter: Zhang *et al.* approach this size, but the majority of papers report milling crystals before dispersing them in silicone resin. Further developments to gain control over crystal size are required.

Summary of dispersion strategies

The use of fluorescent QD-polymer composites is impeded by poor compatibility with polymer matrices, which can lead to aggregation and poor surface passivation, leading to materials with poor transparency, photostability, and emission intensity. Therefore, a wide range of strategies are used to enhance QD dispersion and stability. The surface state of quantum dots has a strong impact on fluorescence and selection of a strategy is complex.

Ligand exchange is the most common route to tune QD dispersion. Catalyst poisoning by labile ligands is a concern for QD-silicone composites which cure via hydrosilylation; multi-dentate or strongly bound ligands are used to reduce lability. Long, polymeric ligands are commonly used to increase interparticle distance and interaction with the polymer matrix, and QD with long hydrocarbon chains are available commercially. However, silicones have low surface energy and will interact more favourably with siloxane ligands. Additionally, there is a trade off between ligand chain length (and therefore inter-particle distancing via steric factors) and grafting density (and therefore surface passivation) – bimodal polymer grafting may be more effective. A critical weakness of ligand exchange is loss of PL as the QD surface is exposed in the process.

A variety of other strategies exist: QD encapsulation with an amphiphilic polymer can occur spontaneously without ligand exchange, driven by hydrophobic interactions. Functional QD ligands can be used to anchor QDs to prepolymers or react together to form polymeric films. QD syntheses can be carried out with suitable capping ligands *in situ*, so that no exchange steps are needed. QDs can be embedded in silica, table salt, and other inorganic materials to increase chemical and thermal stability of QDs and/or to improve dispersion in matrices.

However, QDs with these treatments are typically not well-established nor available commercially. Procedures are complex to design and optimise and additional steps are time-consuming to carry out and may require specialised equipment for steps. High viscosity, non-linear behaviour, and/or large particle sizes are concerns for their application to convention inkjet, although they may be compatible with high viscosity jetting.

Overall, these are exciting possibilities for design of future QD-polymer composites. Initial demonstration of jetting of commercial QDs in silicones for temperature sensing would provide proof of concept using more readily-available materials. Work could then be expanded at a later date to investigate jetting of QDs with various surface treatments to optimise the fluorescence of functional QD-silicones.